UNIVERSITY OF CALIFORNIA, SAN DIEGO

Spectral Binaries Hold the Key to the True Ultracool Binary Fraction

A dissertation submitted in partial satisfaction of the
requirements for the degree
Doctor of Philosophy

in

Physics

by

Daniella C. Bardalez Gagliuffi

Committee in charge:

Professor Adam J. Burgasser, Chair
Professor Daniel Arovas
Professor Quinn Konopacky
Doctor Alexei Kritsuk
Professor Mark Thiemens

2017

The dissertation of Daniella C. Bardalez Gagliuffi is approved, and it is acceptable in quality and form for publication on microfilm and electronically:

_____

_____

_____

_____

_____
Chair

University of California, San Diego

2017

DEDICATION

To my parents, who always showed me the value of education.

EPIGRAPH

Tan absurdo y fugaz es nuestro paso por el mundo,

que solo me deja tranquila saber que he sido auténtica,

que he logrado ser lo mas parecida a mi misma que he podido.

—Frida Kahlo

TABLE OF CONTENTS

LIST OF FIGURES

LIST OF TABLES

ACKNOWLEDGEMENTS

I must have been five, when one morning my dad was driving me to school. I asked him when would school end, expecting a time. He said I would first finish primary school, then secondary school, then I would go to university to earn my bachelor's degree, then I would specialize with a master's degree, and that I could even get a doctorate after that. Overwhelmed by the long laundry list of schooling I had to do, I cut my losses and tried to survive the school day until 3pm. Today, 25 years later, I graduate with a PhD and will voluntarily continue onto a postdoc, which I keep trying to convince my parents that is a job, not more school.

First and foremost, I want to thank my parents, Maritza Gagliuffi and Gonzalo Bardalez, for always encouraging me to do my best in everything I do, telling me there is nothing impossible and that I can achieve whatever I set my mind to. I love you so much and owe you everything. They really had no idea what I was getting into with the PhD (neither did I), but their unconditional love and blind certainty in my perseverance and abilities helped me stay afloat throughout the changing tides of grad school.

To my boyfriend, David Vidmar: you are my rock. Your support, patience and encouragement have kept me sane this last year, amongst job applications and thesis writing. Thank you for constantly telling me how proud I make you and for loving me and sticking around regardless of how irritable, difficult and stubborn I may have been. Thank you for always making me laugh. Thank you for discussing science with me and sharing your all-mighty coding knowledge. It will be your turn next year and I will be there for you.

I want to extend my deepest gratitude to my advisor, Prof. Adam Burgasser. I first met Adam when I was a bright-eyed and bushy-tailed freshman at MIT, while looking for a research project. In him, I found unwavering enthusiasm about science and more opportunities for growth as a scientist and as a person than I could say yes to. Thank

you, Adam, for introducing me to the astronomy profession, and for your mentorship and guidance these past 10 years. The skills I have learned through you will follow me throughout my career. Thank you for instilling in me the importance of outreach. Thank you for providing me with the opportunity to travel, it is definitely my favorite job perk. But most importantly, I want to thank you for believing in me, even when I did not believe in myself.

Thank you to my committee members: Prof. Adam Burgasser (again), Prof. Quinn Konopacky, Dr. Alexei Kritsuk, Prof. Dan Arovas and Prof. Mark Thiemens for taking the time to read the massive monster that is my thesis and providing thoughtful comments and questions to improve the draft.

A big thank you to Dr. Christopher Gelino, whose kind mentorship always provided me with the perfect balance between direction and freedom. I really enjoyed working with you while at Caltech, and later on while organizing the Cool Stars splinter session. Despite me being a student, you have always treated me like a colleague, and that has made me more confident in my knowledge and abilities.

Thank you to Prof. Adam Burgasser (again), Dr. Chris Gelino (again), Dr. Mark Marley and Prof. Stanimir Metchev, who wrote a million recommendation letters for me for postdoc applications. You must have written really nice things about me because I landed a sweet job. Thanks Mark for hosting me while at NASA Ames, it was a dream come true to work (even if only for a week) at a NASA facility. Thank you Stan for always having kind words about my work, and for willingly offering to write letters for me.

I am forever grateful to my PhD "exit buddy", the newly minted Dr. Sarah Logdson, who has been through the job application and thesis writing processes with me. We did it! Thank you for your kindness, empowering advice and constant support. Thank you for your pep talks at any time of the day. You are a smart and talented scientist, and I

admire your dedication.

To my dear friend, double-doctor Dr. Nazita Lajevardi, Esq., thank you for your continuous support. We have been through thick and thin together and you have been my partner in crime in so many situations. I am extremely impressed with all that you have accomplished in the time I have known you and incredibly lucky to call you my friend. I am indebted to my friend Dr. Olga Botvinnik, who taught me how to use python and pandas, and hosted office hours for me whenever I got stuck. If it hadn't been for you, this thesis would have taken twice as long. I admire your willingness to learn and teach and how you always strive for improvement. I am grateful to my friend Dianna Cowern, Miss Physics Girl, who still remembers me despite her celebrity status. You turned my life around when you came to San Diego and I have seen you grow and become an even more amazing version of you. I truly admire your perseverance and I am super proud of your accomplishments.

To my academic big sister, and soon-to-be coworker, Dr. Jackie Faherty: thank you for opening doors for me, everywhere you go. I am beyond excited to continue learning from you. Thank you to my officemates: Christian Aganze and Christopher Thiessen. For a while I was an only child in life and in research, but your company enriched my graduate school experience and knowledge. Thank you also for listening to my rants, whose frequency increased as deadlines approached.

To my astronomy graduate student cohort from universities all over the world plus/minus a couple of years: Miriam Aberasturi, Taisiya Kopytova, Elena Manjavacas, Will Best, Sarah Logdson (again), Emily Martin, Nathalie Skrzypek, Jonathan Gagné and many more. I am blessed to have found a large group of such intelligent, fun and kind people who also like brown dwarfs. I am lucky to call you colleagues and friends and I cannot wait to collaborate with you in the near future.

To the brown dwarf community as a whole: thank you for always encouraging

your students and advertising their work. I am lucky to be part of a supportive field. To my telescope operators at SpeX, Brian Cabreira, Dave Griep, Tony Matulonis, thank you for all your help. You guys made staying up all night and fighting sleep really fun, and I have learned a great deal from you. Special thanks to my LaTeX wizard Alex Kuczala, for your help and patience to make my thesis looks beautiful. I could thank a hundred more people who have had a strong impact on my PhD journey, but this thesis is already 400 pages long. I am truly humbled and grateful for the people in my life.

Chapter 3, in full, is a reprint of the material as it appears in the Astrophysical Journal 2014, Vol. 794, Num. 143. Bardalez Gagliuffi, Daniella; Burgasser, Adam; Gelino, Christopher; Looper, Dagny; Nicholls, Christine; Schmidt, Sarah; Cruz, Kelle; West, Andrew; Gizis, John; Metchev, Stanimir. The dissertation author was the primary investigator and author of this paper.

Chapter 4, in full, is a reprint of the material as it appears in the Astronomical Journal 2015, Vol. 150, Num. 163. Bardalez Gagliuffi, Daniella; Gelino, Christopher; Burgasser, Adam. The dissertation author was the primary investigator and author of this paper.

Chapter 5, in part, is currently being prepared for submission for publication of the material. Bardalez Gagliuffi, Daniella; Burgasser, Adam. The dissertation author was the primary investigator and author of this material.

Chapter 6, in part, is currently being prepared for submission for publication of the material. Bardalez Gagliuffi, Daniella; Burgasser, Adam. The dissertation author was the primary investigator and author of this material.

Chapter 7, in full, has been submitted for publication of the material as it may appear in The Astrophysical Journal Letters, 2017, Bardalez Gagliuffi, Daniella; Gagné, Jonathan; Faherty, Jacqueline; Burgasser, Adam. The dissertation author was the primary investigator and author of this paper.

VITA

2011	B. S. in Physics, Massachusetts Institute of Technology
2013	M. S. in Physics, University of California, San Diego
2017	Ph. D. in Physics, University of California, San Diego

PUBLICATIONS

J. Gagné, J. Faherty, A. Burgasser, É. Artigau, L. Albert, D. Lafreniére, R. Doyon, **D. Bardalez Gagliuffi**, *SIMP J013656.5+093347 is Likely a Deuterium Dwarf in the Carina-Near Moving Group*, submitted to ApJL.

D. Bardalez Gagliuffi, J. Gagné, J. Faherty, A. Burgasser, *A Spectral Binary with Possible AB Doradus Membership*, submitted to ApJL.

S. Fajardo-Acosta, D. Kirkpatrick, A. Schneider, M. Cushing, D. Stern, C. Gelino, **D. Bardalez-Gagliuffi**, K. Kellogg, E. Wright, *Discovery of a Possible Cool White Dwarf Companion from the AllWISE Motion Survey*, ApJ 832 62 (2016).

J. Robert, J. Gagné, E. Artigau, D. Lafrenière, D. Nadeau, R. Doyon, L. Malo, L. Albert, C. Simard, **D. Bardalez Gagliuffi**, A. Burgasser, *A Brown Dwarf Census from the SIMP Survey*, ApJ 830 144 (2016).

A. Burgasser, C. Blake, C. Gelino, J. Sahlmann, **D. Bardalez Gagliuffi**, *The Orbit of the L dwarf + T dwarf Spectral Binary SDSS J080531.84+481233.0*, ApJ 827 25 (2016).

M. Gillon, E. Jehin, S. Lederer, L. Delrez, J. de Wit, A. Burdanov, V. Van Grootel, A. Burgasser, A. Triaud, C. Opitom, B. O. Demory, D. Sahu, **D. Bardalez Gagliuffi**, P. Magain, D. Queloz, *Temperate Earth-sized planets transiting a nearby ultracool dwarf star*, Nature 533 7602 (2016).

A. Burgasser, C. Melis, J. Todd, C. Gelino, G. Hallinan, **D. Bardalez Gagliuffi**, *Radio Emission and Orbital Motion from the Close-encounter Star-Brown Dwarf Binary WISE J072003.20-084651.2*, AJ 150 180 (2015).

D. Bardalez Gagliuffi, A. Burgasser, C. Gelino, *High Resolution Imaging of Very Low Mass Spectral Binaries: Three Resolved Systems and Detection of Orbital Motion in an L/T Transition Binary*, AJ 150 163 (2015).

J. Sahlmann, A.J. Burgasser, E.L. Martín, P.F. Lazorenko, **D. Bardalez Gagliuffi**, M. Mayor, D. Ségransan, D. Queloz, S. Udry, *DE0823-49 is a juvenile binary brown dwarf at 20.7 pc*, A&A 579 61 (2015).

J. Faherty, K. Alatalo, L. Anderson, R. Assef, **D. Bardalez Gagliuffi**, M. Barry, D. Benford, M. Bilicki, B. Burningham, D. Christian, M. Cushing, P. Eisenhardt, M. Elvisx, S. Fajardo-Acosta, D. Finkbeiner, W. Fischer, W. Forrest, J. Fowler, J. Gardner, C. Gelino, V. Gorjian, C. Grillmair, M. Gromadzki, K. Hall, Z. Ivezi'c, N. Izumi, D. Kirkpatrick, A. Kovcs, D. Lang, D. Leisawitz, F. Liu, A. Mainzer, K. Malek, G. Marton, F. Masci, I. McLean, A. Meisner, R. Nikutta, D. Padgett, R. Patel, L. Rebull, J. Rich, F. Ringwald, M. Rose, A. Schneider, K. Stassun, D. Stern, C-W. Tsai, F. Wang, M. Weston, E Edward; J. Wu, J. Yang, *Results from the Wide-field Infrared Survey Explorer (WISE) Future Uses Session at the WISE at 5 Meeting*, arXiv:1505.01923.

A. Burgasser, M. Gillon, C. Melis, B. Bowler, E. Michelsen, **D. Bardalez Gagliuffi**, C. Gelino, E. Jehin, L. Delrez, J. Manfroid, C.H. Blake, *WISE J072003.20-084651.2: An Old and Active M9.5 + T5 Spectral Binary 6 pc from the Sun*, AJ 149 104 (2015).

D. Bardalez Gagliuffi, A. Burgasser, C. Gelino, D. Looper, C. Nicholls, S. Schmidt, K. Cruz, A. West, J. Gizis, S. Metchev, *SpeX Spectroscopy of Unresolved Very Low Mass Binaries. II. Identification of Fifteen Candidate Binaries with Late-M/Early-L and T Dwarf Components*, ApJ 794 143 (2014).

S. Schmidt, J. Prieto, K. Stanek, B. Shappee, N. Morrell, **D. Bardalez Gagliuffi**, C. Kochanek, J. Jencson, T. Holoien, U. Basu, J. Beacom, D. Szczygieł, G. Pojmanski, J. Brimacombe, M. Dubberley, M. Elphick, S. Foale, E. Hawkins, D. Mullins, W. Rosing, R. Ross, Z. Walker, *Characterizing a Dramatic $\Delta V\sim$-9 Flare on an Ultracool Dwarf Found by the ASAS-SN Survey*, ApJL 781 2 L24 (2014).

A. Burgasser, C. Luk, S. Dhital, **D. Bardalez Gagliuffi**, C. Nicholls, L. Prato, A. West, S. Lépine, *Discovery of a Very Low Mass Triple with Late-M and T Dwarfs Components: LP 704-48/SDSS J0006-0852AB*, ApJ 757 110 (2012).

A. Burgasser, **D. Bardalez Gagliuffi**, J. Gizis, *Hubble Space Telescope Imaging and Spectral Analysis of Brown Dwarf Binaries at the L Dwarf/T Dwarf Transition*, AJ 141 70 (2011).

D. Martinez-Delgado, R. Gabany, K. Crawford, S. Zibetti, S. Majewski, H. Rix, J. Fliri, J. Carballo-Bello, **D. Bardalez Gagliuffi**, J. Peñarrubia, T. Chonis, B. Madore, I. Trujillo, M. Schirmer, D. McDavid, *Stellar Tidal Streams in Spiral Galaxies of the Local Volume: A Pilot Survey with Modest Aperture Telescopes*, AJ 140 962 (2010).

ABSTRACT OF THE DISSERTATION

Spectral Binaries Hold the Key to the True Ultracool Binary Fraction

by

Daniella C. Bardalez Gagliuffi

Doctor of Philosophy in Physics

University of California, San Diego, 2017

Professor Adam J. Burgasser, Chair

Brown dwarfs bridge the gap between stars and giant planets. Lacking sufficient mass to sustain hydrogen fusion, these objects cool and dim as they age, evolving through a temperature-based sequence of spectral types M, L, T and Y. However, the essential mechanisms governing their formation are not well constrained. Binary statistics are a direct outcome of the formation process, and thus provide a means to test formation theories. Observational constraints on the brown dwarf binary fraction place it at $10-20\%$, dominated by imaging studies (85% of systems) with the most common separation at 4 AU. This coincides with the resolution limit of state-of-the-art imaging techniques, suggesting that the binary fraction is underestimated. I have developed a separation-

independent method to identify and characterize tightly-separated (< 5 AU) binary systems of brown dwarfs, so-called spectral binaries. To identify these systems I look for traces of methane, the hallmark of the cooler T dwarf class, in the spectra of late-M and early-L dwarfs. Imaging follow-up of 17 spectral binaries yielded 3 (18%) resolved systems, corroborating the observed binary fraction, but 5 (29%) known binaries were missed, reinforcing the hypothesis that the short-separation systems are undercounted. In order to find the true binary fraction of brown dwarfs, I compiled a volume-limited, unbiased, spectroscopic sample of M7-L5 dwarfs and searched for T dwarf companions. In the 25 pc volume, I found 4 candidates, three of which are already confirmed, leading to a spectral binary fraction of $0.95 \pm 0.50\%$, albeit for a specific combination of spectral types. To extract the true binary fraction and determine the biases of the spectral binary method, I have produced a binary population simulation based on different assumptions of the mass function, age distribution, evolutionary models and mass ratio distribution. The baseline model combination we chose is the Chabrier et al. (2005) IMF, a uniform age distribution, the Allen (2007) mass ratio distribution and the Baraffe et al. (2003) evolutionary models, which resemble observations most closely. Applying the correction fraction resulting from this method to the observed spectral binary fraction yields a true binary fraction of $31 \pm 17\%$, which is within 1σ of the binary fraction obtained from high resolution imaging studies, radial velocity and astrometric monitoring. This method can be extended to identify giant planet companions to young brown dwarfs.

Chapter 1

Introduction

1.1 Fantastic Brown Dwarfs and Where to Find Them

Brown dwarfs are "failed stars", substellar objects intermediate between stars and planets in terms of physical properties, with masses ranging between $13-80\ M_{\rm Jup}$ (Jupiter mass, $M_{\rm Jup} \sim 10^{-3} M_{\odot}$). They were theoretically proposed by Dr. Shiv Kumar in 1962, when he realized that there had to be a minimum mass for hydrogen burning, and that objects with masses below that limit would never reach thermodynamic equilibrium (Kumar 1962, 1963). Only after decades of observational searches and the improvement of near-infrared detector technology, were brown dwarfs incontrovertibly discovered (Nakajima et al. 1995; Rebolo et al. 1995).

As hybrids between stars and giant planets, brown dwarfs share physical properties and characteristics with both. Stars are thermodynamically stable spheres of plasma in which the force of gravity is balanced by the thermal pressure resulting from hydrogen fusion. They form by the gravitational collapse of a molecular cloud and its subsequent contraction, until their core reaches the temperatures and densities necessary for sustained nuclear fusion ($T_c \sim 3 \times 10^6$ K; Reid & Hawley 2005). When the fusion rate equals the

emitted flux, stars become self-luminous, enter the "main sequence" and remain stable for millions to trillions of years (depending on their mass) until they deplete their core hydrogen.

Young forming stars which fail to accrete enough mass to create or sustain the necessary conditions for core hydrogen fusion become brown dwarfs. Low-mass proto-stars collapse under their own gravity until electron degeneracy provides pressure support (Kumar 1963), reaching a radius similar to that of Jupiter. As a result, these objects never achieve thermal equilibrium, lacking a steady internal energy generation mechanism, and cool and dim over time. Their inability to sustain hydrogen fusion grants them special properties linking stars and giant planets.

Giant planets are theorized to form in disks around stars by either core accretion through the coagulation of dust grains and successive accretion of a gas envelope (Mizuno 1980; Pollack et al. 1996) or disk fragmentation into planet-sized clumps followed by the accretion of a gas-rich atmosphere (Lissauer 1993; Boss 1997). These formation pathways are fundamentally different from those of brown dwarfs and stars. While giant planets are less massive than brown dwarfs, their radii are similar and thus the former have lower surface gravity and atmospheric pressure. Brown dwarfs experience low surface gravity in the first couple hundred million years of their lives as they continue to contract after formation. Besides low surface gravity, giant planets and brown dwarfs overlap in temperatures, densities, and possibly masses.

Stars, brown dwarfs and planets, along with the gas and dust that forms them, are the main visible components of our galaxy. While stars have been observed with modern telescopes since the mid-1800s, observational searches for brown dwarfs only yielded irrefutable discoveries after the advent of infrared telescopes in the early 1980s. A few early candidates included: VB 8B (McCarthy et al. 1985), a companion to an M7

dwarf inferred by speckle imaging[1], and later disproved by infrared imaging (Skrutskie et al. 1987) and GD 165 B (Becklin & Zuckerman 1988; Kirkpatrick et al. 1999a), a companion to the white dwarf GD 165, which rests right on the hydrogen burning limit.

There is no doubt that 1995 was an exciting year for astronomy, when three brown dwarf discoveries were announced: PPl 15 (Basri et al. 1995) and Teide 1 (Rebolo et al. 1995, 1996), both objects in the Pleiades and at the hydrogen burning mass limit and Gl 229 B, the first incontrovertible brown dwarf showing signs of methane in its atmosphere, indicating a temperature around $T_{\rm eff} \sim 1000\,$K, firmly in the brown dwarf regime (Nakajima et al. 1995). The first exoplanet discovery, 51 Peg b (Mayor et al. 1995), was also announced that year.

Since then, almost 10,000 very low mass (VLM) stars and brown dwarfs[2,3] have been confirmed with large area surveys. The Sloan Digital Sky Survey (SDSS; York et al. 2000) in optical wavelengths ($0.38\,\mu$m$< \lambda < 0.75\,\mu$m) covered about half of the northern sky. The 2-Micron All Sky Survey (2MASS; Skrutskie et al. 2006), the DEep Near Infrared Survey of the Southern Sky (DENIS; Epchtein et al. 1997) and the United Kingdom Infrared Digital Sky Survey (UKIDSS; Lawrence et al. 2007) imaged the sky from the ground in near-infrared wavelengths ($0.75\,\mu$m$< \lambda < 2.50\,\mu$m). More recently, the space-based Wide-field Infrared Survey Explorer (WISE; Wright et al. 2010) surveyed the entire sky in mid-infrared wavelengths ($2.5\,\mu$m$< \lambda < 28\,\mu$m), furthering our understanding of the coldest brown dwarfs.

Presently, we know that brown dwarfs as a population span an ample range of properties: masses from $\sim 0.01 - 0.08\,M_\odot$, radii from $0.8 - 1.2\,R_{\rm Jup}$, luminosities from $10^{-2} - 10^{-7}\,L_\odot$, effective temperatures from $250 - 2700\,$K, and surface gravities from

[1] An imaging technique that consists on co-adding a large number of short exposures ($\lesssim 1$ s) to reduce the effect of atmospheric turbulence.

[2] Collectively referred to as ultracool dwarfs, $M_{UCD} \lesssim 0.1\,M_\odot$.

[3] A list of photometry, spectroscopy and astrometry of ultracool dwarfs can be found in the Dwarf Archives at http://spider.ipac.caltech.edu/staff/davy/ARCHIVE/index.shtml, at the List of All Ultracool Dwarfs at https://jgagneastro.wordpress.com/list-of-ultracool-dwarfs/ and on Best et al. (2017).

$3.0 \leq log\ g \leq 5.5$ cm s^{-2}. What we do not know are what the essential mechanisms for their formation and where the dividing line between brown dwarfs and planets lies (if there is such a division).

While the study of brown dwarfs is important in its own right, other subfields in astronomy have also realized their utility. Soon after their existence was theoretically proposed, brown dwarfs became prime candidates for baryonic dark matter (Daly & McLaughlin 1992). Extrapolating the initial mass function (IMF) distribution, which predicts the number of stars formed per unit mass (Salpeter 1955), below the hydrogen burning limit, implied that brown dwarfs should be more numerous than main sequence stars and thus could hide the "missing mass" from galaxy rotation curves. However, more recent observations find at least one brown dwarf for every six main sequence stars, thus disproving the dark matter candidacy of brown dwarfs (Kirkpatrick et al. 2011). Galaxy-wide studies of the interstellar medium (ISM) may also find brown dwarfs useful to probe the chemical composition and evolution of different regions of the galaxy, as these objects do not undergo significant fusion in their lives, preserving the composition of the ISM from where they formed mostly intact (Burgasser 2008). Additionally, brown dwarfs are excellent proxies for directly-imaged giant exoplanets (e.g. Faherty et al. 2013a; Burgasser 2009) since both kinds of objects have hydrogen-rich atmospheres with minimal stellar irradiation.

The question of brown dwarf formation is one that has interested me and countless other astronomers for a while. Several formation scenarios and simulations produce star and brown dwarf populations with slightly different statistical properties. These distributions are the blueprints against which observations are compared. In particular, the properties and configurations of low-mass binary systems hold a clue to the overarching formation problem, which is why observations must be well constrained. With this thesis

I hope to add my *granito de arena*[4] to the knowledge of brown dwarf binaries and their formation.

1.2 Physical Properties

1.2.1 The Hydrogen Burning Limit

At the low-mass end of the main sequence, the dividing line between a star and a brown dwarf is the hydrogen burning minimum mass (HBMM). Hydrogen fusion into helium provides the thermal pressure needed to balance the gravitational force, thus supporting the core from collapse. The net hydrogen fusion reaction is:

$$4\,{}^{1}_{1}\mathrm{H} \;\rightarrow\; {}^{4}_{2}He + 2\,{}^{0}_{1}e^{+} + 2\nu_e + 2\gamma \tag{1.1}$$

Known as the proton-proton or PP I chain, the net result of this reaction is the conversion of four hydrogen nuclei into one helium atom (Reid & Hawley 2005). For fusion to occur, interacting protons must overcome their Coulomb barriers to reach separations where the strong force dominates ($\sim 10^{-15}$ m; typical size of nuclei). The Coulomb barrier at nuclear scales is proportional to $V \sim \frac{Z_1 Z_2 e^2}{r} \approx Z_1 Z_2$ MeV. To overcome it, particles need at least that much energy, $kT = Z_1 Z_2$ MeV, implying temperatures exceeding $T \sim 10^{10}$ K, hotter than the center of the Sun, $T \sim 10^7$ K. However, thanks to the dual wave-particle nature of protons, there is a non-zero probability of tunneling through a potential barrier:

$$P(fusion) \propto \exp\left(-\frac{\pi Z_1 Z_2 e^2}{\varepsilon_0 h\nu}\right) \exp\left(-\frac{mv^2}{2kT}\right) \tag{1.2}$$

[4]Spanish expression meaning that if everyone adds their little bit, we can achieve something bigger.

where the first exponential encapsulates the probability of quantum tunneling, while the second one is the Maxwell-Boltzmann distribution which reflects the ideal gas nature of the protons. This convolved probability distribution is known as the Gamow peak.

Fusion rates throughout the star are regulated by a negative feedback mechanism colloquially known as the "stellar thermostat". As reaction rates increase, the energy generated will be trapped by opacity, thus heating up the core. The star expands to cool off and the density decreases, which lowers the reaction rates as well. In this way, stars can adjust their energy output to maintain hydrostatic equilibrium.

The lower mass of brown dwarfs renders them unable to heat up their cores to the point where nuclear reactions can be triggered or sustained (Kumar 1963; Hayashi & Nakano 1963), thus never achieving hydrostatic equilibrium. Instead, the compression of a colder electron gas leads to the onset of electron degeneracy pressure, since by the Pauli Exclusion Principle, no two electrons with the same spin can occupy the same quantum state. As greater fractions of a contracting protostar become electron degenerate, its potential energy is reabsorbed to tighten the packing of electrons rather than released as thermal energy, thus preventing its radius from contracting below R$\sim 0.1\,R_{\odot}$. As a consequence, the core temperature, T_c, reaches a maximum T_{max} about $10^7 - 10^8$ years after formation (see Figure 1.1). The ability of the contracting object to maintain T_c depends on the mass and nuclear reaction rate, leading to three possible scenarios (Reid & Hawley 2005):

1. The partially degenerate protostar is able to fuse hydrogen at a sufficient rate as to maintain $T_c \sim T_{max}$, and becomes a low-mass star that remains on the main sequence with constant luminosity and temperature ($M > 0.09\,M_{\odot}$).

2. T_c drops below T_{max} due to increasing degeneracy, yet hydrogen fusion is still thermodynamically favorable, resulting in a low-mass star that remains on the main sequence ($M \sim 0.08 - 0.085\,M_{\odot}$). At slightly lower masses, degeneracy in the

core limits the ability of this object to fuse hydrogen ($M \sim 0.075 M_{\odot}$).

3. T_c drops below critical temperatures preventing fusion from becoming a significant energy source (i.e. no hydrogen fusion, only deuterium) and the object becomes a fully degenerate brown dwarf ($M \sim 0.07 M_{\odot}$).

The original estimate of Kumar (1963) set the HBMM at $\sim 0.07 M_{\odot}$ at solar metallicity[5]. Metal-poor stars have lower opacities, hence higher luminosities and effective temperatures for a given mass. To achieve a higher luminosity, metal-poor objects require a higher core temperature, thus driving the HBMM to higher masses. HBMM ranges from $0.09 M_{\odot}$ at a metallicity of [Fe/H]$= -0.7$ in the disk of the galaxy, to $0.097 M_{\odot}$ at [Fe/H]$= -2.3$ in the halo (D'Antona & Mazzitelli 1996; Baraffe et al. 1997). On the other hand, metal-rich objects have larger opacities and optically thick atmospheres that block the energy release from the surface, thus enhancing central temperatures at a lower mass. All brown dwarfs down to $13 M_{\rm Jup}$ will fuse deuterium. However, the low cosmic abundance of deuterium ($D/H = (2.45 \pm 0.10) \times 10^{-5}$; Coc et al. 2015) and short period of fusion prevents the existence of a deuterium "main sequence" (Chabrier et al. 2007). Currently, the deuterium burning minimum mass (DBMM; Grossman & Graboske 1973) serves as the boundary between brown dwarfs and giant planets, yet this distinction is controversial because it lacks significance with respect to formation mechanisms and it is challenging to detect observationally.

Brown dwarfs with masses above $0.06 M_{\odot}$ can reach the critical temperatures to burn lithium. The detection of the Li I absorption line at 6708 Å in field ultracool dwarfs is a useful diagnostic test for substellarity (Rebolo et al. 1996). The only reasons for lithium to appear in the optical spectra of ultracool dwarfs are if the object is a very young, low-mass star and has not had time to burn its primordial lithium, or alternatively,

[5]Metallicity is defined as [Fe/H] $\equiv$ log_{10}[Fe/H]/[Fe/H]$_{\odot}$. The abundance of elements with atomic number $Z > 2$ in the universe is so small that in Astronomy we colloquially refer to these elements as "metals".

if the object is an old brown dwarf that still preserves its lithium. Brown dwarfs are fully convective, so if they are massive enough, it is only a matter of time for Li to be depleted.

1.2.2 Internal Structure

Hayashi & Nakano (1963) showed that pre-main sequence stars are fully convective, after their initial fast contraction and before they trigger hydrogen fusion and create a radiative layer, densely packed with matter and photons. Since brown dwarfs never reach the main sequence, their heat transfer occurs entirely through convection.

Ionized, partially metallic hydrogen and helium are the primary constituents of brown dwarfs due to their high core densities in the order of $10-1000\ g\ cm^{-3}$ (Burrows & Liebert 1993). Only during their initial contraction ($\leq 10^8$ years) are the internal densities low enough for brown dwarfs to be supported by ideal gas pressure (Burrows & Liebert 1993). As contraction continues, this assumption breaks down and a non-relativistic electron degenerate Fermi gas becomes a better description. The Pauli exclusion principle postulates that quantum states can only be occupied by one fermion; therefore only two electrons (accounting for spin up and spin down) can occupy the $p = 0$ momentum state. This means that all other electrons are forced to higher momentum states, such that even at $T = 0\,\mathrm{K}$, the pressure is non-zero.

The reduction in volume as brown dwarfs contract after the onset of degeneracy, pushes electrons into higher energy quantum states, increasing the overall pressure. Degeneracy pressure is independent of temperature, and only depends on the density of electrons. Therefore, it can maintain dense objects in equilibrium.

1.2.3 Evolutionary Trends

The fundamental parameters describing brown dwarf evolution are mass, radius, luminosity, temperature and surface gravity. The fact that brown dwarfs lack an internal energy generation mechanism implies that these objects continue contracting and therefore cool and dim with age. Observationally, this introduces a limitation in the characterization of brown dwarfs: given an observed luminosity (or luminosity proxies, i.e. spectral type, see Section 1.3.2), it is impossible to tell whether a brown dwarf is massive and old or low-mass and young. This is known as the mass-age-luminosity brown dwarf degeneracy.

The evolutionary models presented here were generated by Burrows et al. (1997b). Model versions from other authors (e.g. Baraffe et al. 1997; Saumon & Marley 2008) differ minimally in their treatment of opacities, molecular species, magnetic fields, and applicable mass ranges.

Figure 1.1 shows the evolution of the central temperature of ultracool dwarfs in the $0.3-211\,M_{\rm Jup}$ mass range (equivalent to $\sim 0.03-0.2\,M_{\odot}$). The blue lines correspond to stars, purple lines to brown dwarfs and red lines to planets. Objects with masses between $73-211\,M_{\rm Jup}$ experience a steady increase in temperature that ends in a stable core temperature for the rest of their lives. These objects are able to achieve hydrogen fusion and maintain steady nuclear reaction rates that counteract gravitational contraction. Objects between $13-73\,M_{\rm Jup}$ fuse deuterium, but never to the point where the energy generated can prevent further contraction, so they undergo a period of deuterium burning until ~ 300 Myr ($\sim 10^{8.5}$ years) when they deplete their deuterium, thus cooling off. The cores of planetary-mass objects below $\sim 5\,M_{\rm Jup}$ never reach minimum temperatures to begin any sort of fusion, so they roughly maintain their temperatures.

At the surface of these ultracool dwarfs, the survival of hydrogen or deuterium fusion affects their energy output. Figure 1.2 shows the luminosity evolution for the same

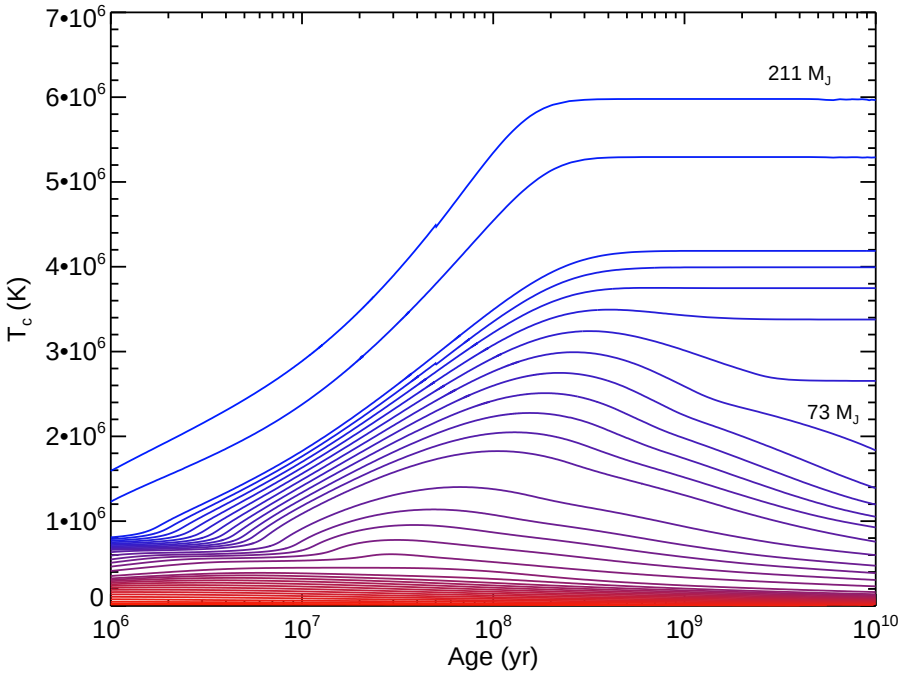

Figure 1.1 Evolution of central temperature for stellar and substellar objects with masses $211\,M_{\rm Jup}$ and below. Color-coding corresponds to Figure 1.4. the Burrows et al. (1997b) evolutionary models.

set of masses. At the beginning of the age axis, these objects have finished accreting material from their surroundings yet continue to contract. Objects with masses between $73-211\,M_{\rm Jup}$ start off losing energy but are able to stabilize their luminosities. These objects are massive enough to fuse hydrogen, and by the time they reach a billion years old, their nuclear reaction rates match their luminosity and thermal pressure is high enough to counteract their contraction, so they reach a stable radius and energy output. Between $73-13\,M_{\rm Jup}$, there are plateaux in luminosity until about 30 million years ($\sim 10^{7.5}$ years) that correspond to deuterium burning. Objects on the massive end of this range burn through their deuterium in a shorter period of time, suggesting that their reaction rates are higher. When the deuterium burning stops, luminosity decreases because the only energy generation mechanism is gone. From this point on, most of the energy released is left over from early gravitational contraction. Below $\sim 13\,M_{\rm Jup}$,

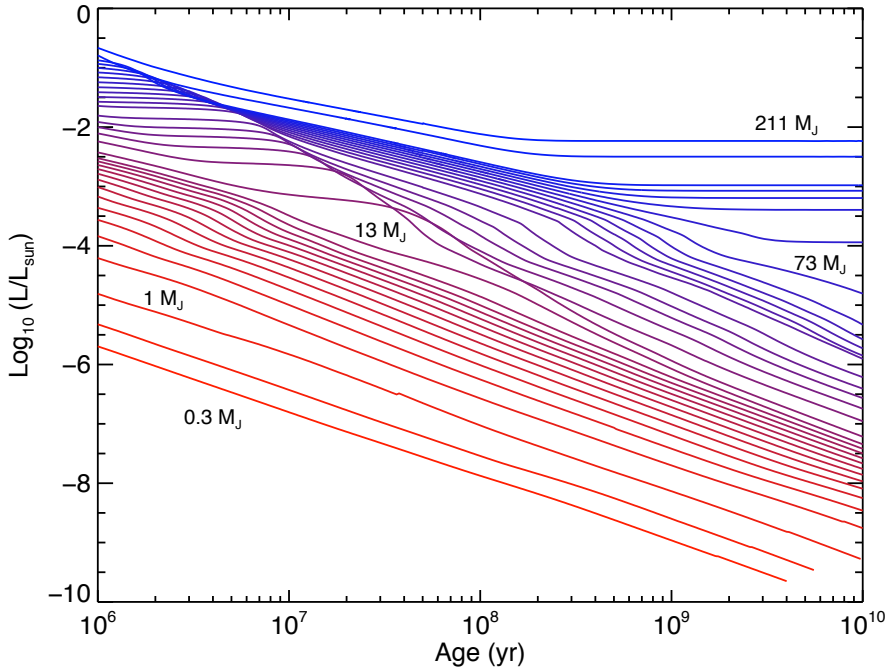

Figure 1.2 Luminosity in solar units as a function of age. Color-coding corresponds to Figure 1.4. At the higher mass end, low mass stars are able to stabilize their energy output by ~ 100 Myr, whereas objects with masses below $73\,M_{\rm Jup}$ never reach thermal equilibrium. Figure by Dr. Michael Cushing with the Burrows et al. (1997b) evolutionary models.

objects can deplete up to 50% of their primordial deuterium for a short period of time, until $\sim 10^7$ years old (Burrows et al. 1995). Objects less massive than $\sim 5\,M_{\rm Jup}$ do not fuse any elements in their cores, so their luminosity continuously falls as they get fainter with age.

The basic process underlying these evolutionary trends in temperatures and luminosity is the continued, yet slow, gravitational contraction of these objects. Figure 1.3 shows the evolution of radii as compared to effective temperatures and ages. Solid lines correspond to brown dwarfs (defined in this plot as objects with masses $13-80\,M_{\rm Jup}$, $0.08-0.015\,M_{\odot}$ in the figure), and dashed lines represent planetary-mass objects ($13\,M_{\rm Jup}$ and below). Isochrones are plotted in light gray. Faster contraction happens on brown dwarfs in the first ~ 100 Myr, while mostly maintaining their effective

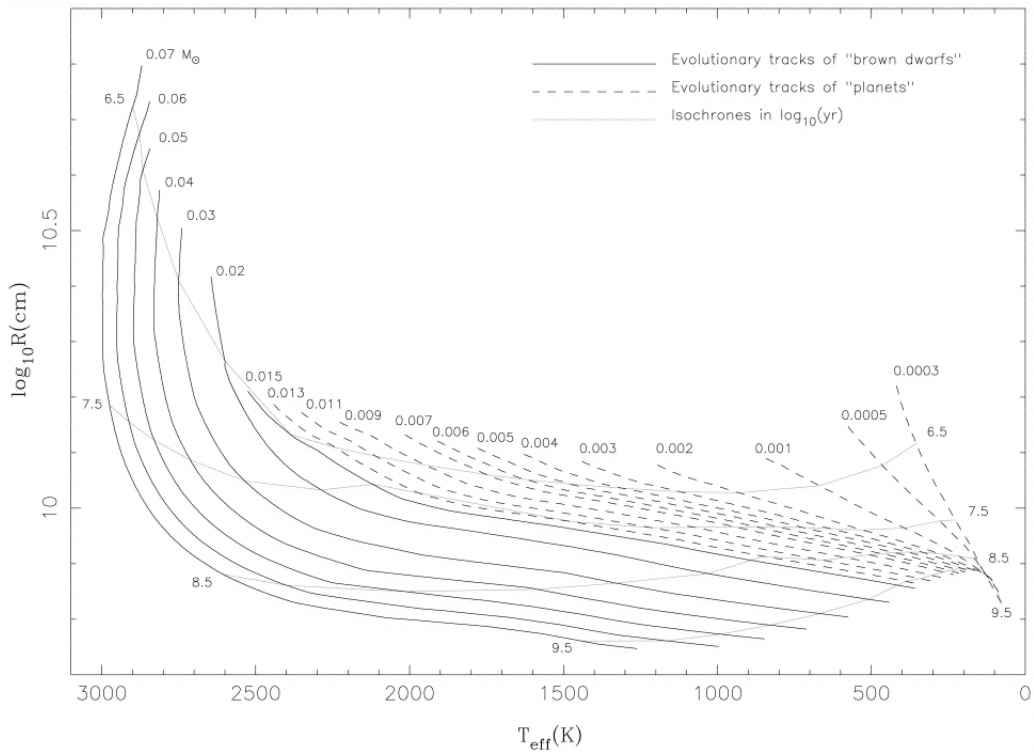

Figure 1.3 Evolution of radius compared to effective temperature and age. Solid lines correspond to brown dwarfs (defined in this plot as objects with masses $0.08-0.015\,M_{\odot}$), and dashed lines represent planetary-mass objects ($13\,M_{\rm Jup}$ and below). Isochrones are plotted in light gray. Figure from Burrows et al. (1997b).

temperature. Contraction slows down at later times at the onset of degeneracy reaching roughly the size of Jupiter (Burrows & Liebert 1993). Notice the scale on the radius y-axis only varies by one order of magnitude over the entire 10^6-10^9 year-long evolution of ultracool dwarfs. Planetary-mass objects do not experience fusion at any point in their lives and therefore contract slightly faster.

Effective temperature, radius and luminosity are related as $L \propto R^2T^4$. Following the same logic as for the previous two figures, on Figure 1.4, the blue lines for masses between $73-211\,M_{\rm Jup}$ correspond to stars which achieve a stable effective temperature. For objects between $13-73\,M_{\rm Jup}$, a small drop in temperature causes a large drop in luminosity, which happens at the end of the deuterium-burning phase between 10^7-

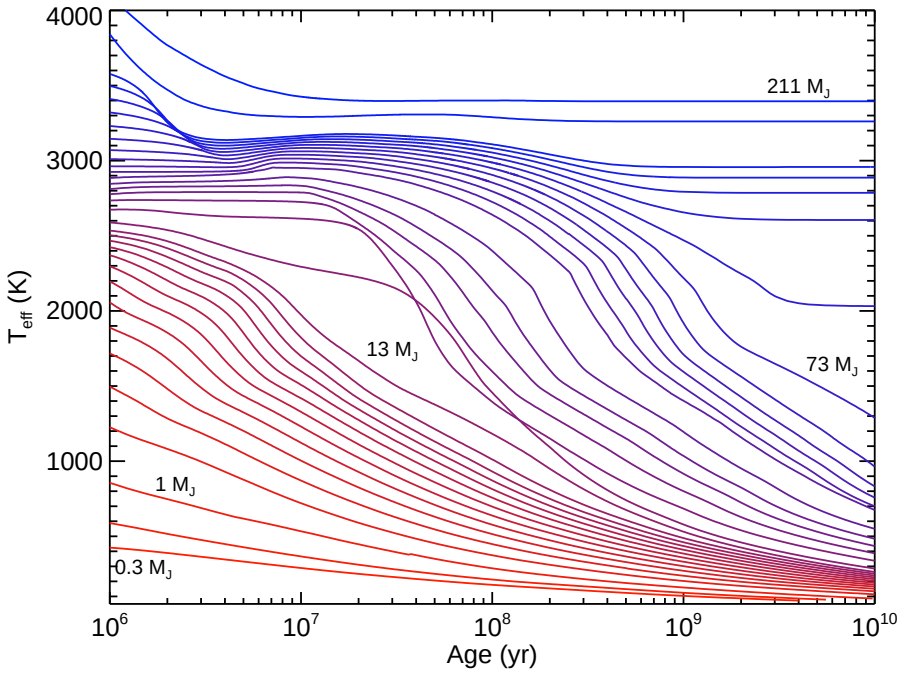

Figure 1.4 Cooling curves for stellar objects (blue), brown dwarfs (purple) and planets (red), as defined by mass and with the Burrows et al. (1997b) evolutionary models. Objects with masses down to $73\,M_{\rm Jup}$ are able to stabilize their temperatures and enter the main sequence. Figure by Dr. Michael Cushing.

10^9 years. The small kinks midway through the downward slopes, between effective temperatures of $1300-2500\,$K, correspond to the formation of silicate and iron grains in these atmospheres (Lunine et al. 1989). Section 1.3.1 explores this process in more detail. Objects with masses between $5-13\,M_{\rm Jup}$ cool off faster after $\sim 10\,$Myr where they stop fusing deuterium. Below $5\,M_{\rm Jup}$, planets which never fuse any elements cool off at a steady rate throughout their lives.

Surface gravity is $g \propto MR^{-2}$ or in terms of density, $g \propto \langle\rho\rangle R$. Figure 1.5 describes the change in surface gravity on a log scale with respect to effective temperature and age, following the color scheme of Figure 1.3. Overall, both planets and brown dwarfs contract and get denser over time, so their surface gravity always increases. Brown dwarfs start their lives with $log\ g \sim 3.5$, quickly increase their surface gravity during the

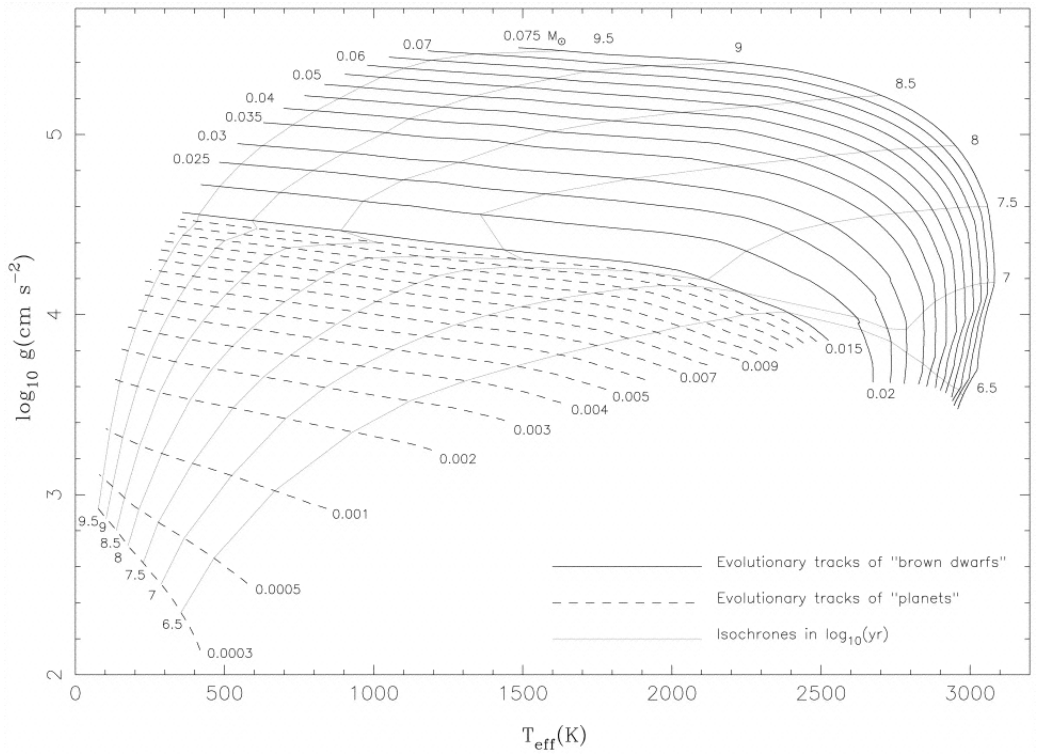

Figure 1.5 Evolution of surface gravity compared to effective temperature and age. Solid lines correspond to brown dwarfs (defined in this plot as objects with masses $0.08-0.015\,M_{\odot}$), and dashed lines represent planetary-mass objects ($13\,M_{\rm Jup}$ and below). Isochrones are plotted in light gray. Figure from Burrows et al. (1997b).

deuterium-burning phase until $\sim 10^{8.5}$ years for the more massive ones and after that, they continue contracting, increasing their density and as a consequence, their surface gravity. Planets contract over a longer period of time as their surface gravity increases slightly. During a short period in their youth, brown dwarfs have similar surface gravities as the more massive planets, making them analogs for parallel studies.

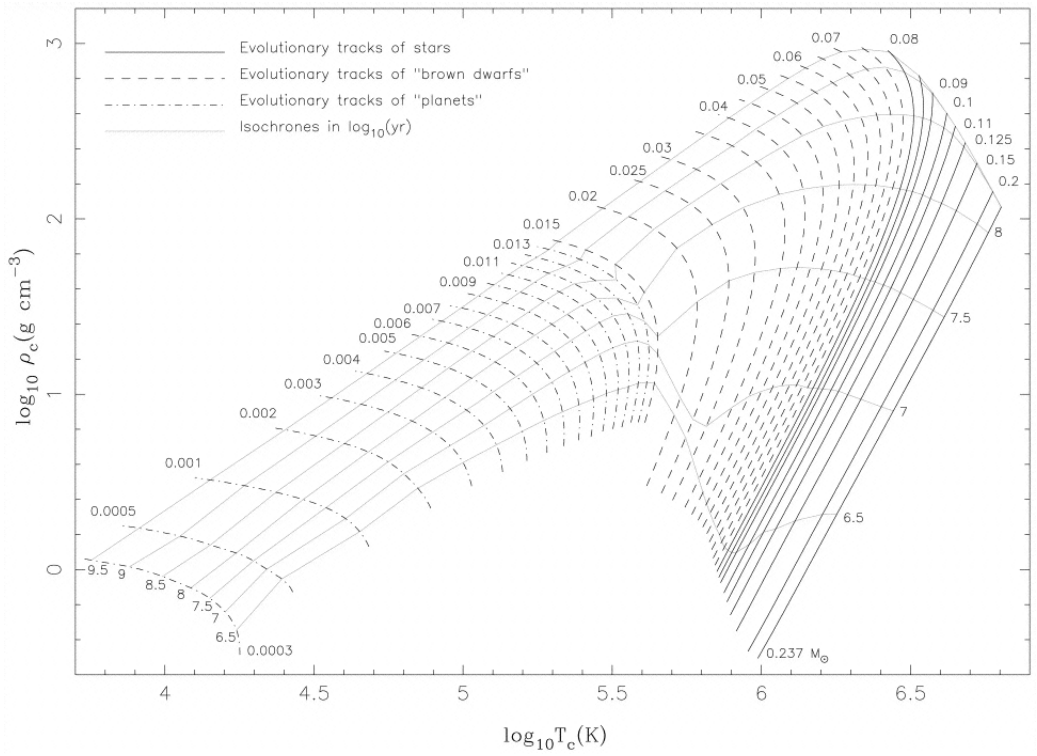

Figure 1.6 Evolution of central density compared to central temperature and age. Solid lines correspond to brown dwarfs (defined in this plot as objects with masses $0.08 - 0.015 M_{\odot}$), and dashed lines represent planetary-mass objects ($13 M_{\rm Jup}$ and below). Isochrones are plotted in light gray. Figure from Burrows et al. (1997b).

1.3 Atmospheres

1.3.1 Atmospheric Chemistry

As brown dwarfs cool over time, their atmospheres go through chemical transitions as gas and solid species achieve equilibrium at given temperatures and pressures. While Sun-like and more massive, hotter stars have completely ionized atmospheres closely approximating a black body energy distribution, cooler objects have important absorption contributions from neutral atoms and molecules that thrive in lower temperatures (Allard et al. 1997). Atmospheres cooler than $T_{\rm eff} \sim 5000$ K have an increasingly larger proportion of their hydrogen in the form of H_2. The high density of these atmo-

spheres raises the frequency of collisions between hydrogen molecules and other species, inducing dipole moments and producing collision-induced absorption (CIA; Linsky 1969). Below $\sim 4000\,\mathrm{K}$, most of the hydrogen is in molecular form and the rest is in metal hydrides like FeH, CaH and MgH. Oxygen is found primarily in VO, TiO, H_2O and CO and in a smaller proportion as OH (Fegley & Lodders 1996).

The temperatures and pressures in substellar atmospheres allow for the condensation of different species at different altitudes, as the species themselves find equilibrium between the condensate and gas phases. These cloud layers start becoming apparent in the spectra of late-M dwarfs. Molecular hydrogen and neutral helium can be found alongside H_2^-, H^- and He^- (Burrows & Liebert 1993). At colder temperatures ($T_{\mathrm{eff}} \lesssim 2800\,\mathrm{K}$) the gas phase is depleted of molecules by the condensation of O-rich compounds, e.g. TiO condenses into Perovskite, $CaTiO_3$.

The complete disappearance of TiO and VO from the spectral energy distributions (SED) of brown dwarfs at $T_{\mathrm{eff}} \sim 2000\,\mathrm{K}$, along with the emergence of metal hydrides like FeH, CaH, MgH and SiH, marks the onset of the L-type spectral type (Kirkpatrick et al. 1999b; Martin et al. 1997; Martín et al. 1998). This transition is caused by the condensation of refractory elements such as Al, Ca, Ti, Fe and V into dust grains at temperatures colder than $\sim 1800\,\mathrm{K}$, at the pressures of brown dwarf photospheres (1-10 bar), e.g. Al is integrated into corundum, Al_2O_3, Mg and Si into fosterite, Mg_2SiO_4, or enstatite, $MgSiO_3$, TiO into perovskit, $CaTiO_3$ and VO into VO_2, V_2O_3 and more complex vanadium oxides (Lodders 2002; Fegley & Lodders 1996; Tsuji et al. 1996b; Allard et al. 1997).

Below $T_{\mathrm{eff}} \sim 1300 - 1500\,\mathrm{K}$, carbon in the form of CO begins a transition to CH_4 (Fegley & Lodders 1996; Tsuji 1995; Allard & Hauschildt 1995). Methane bands around $7.8\,\mu$m (Saumon et al. 2003) appear in the mid-infrared spectra of L dwarfs as early as L5 Noll et al. 2000, and in the near-infrared spectra of late-L dwarfs, first

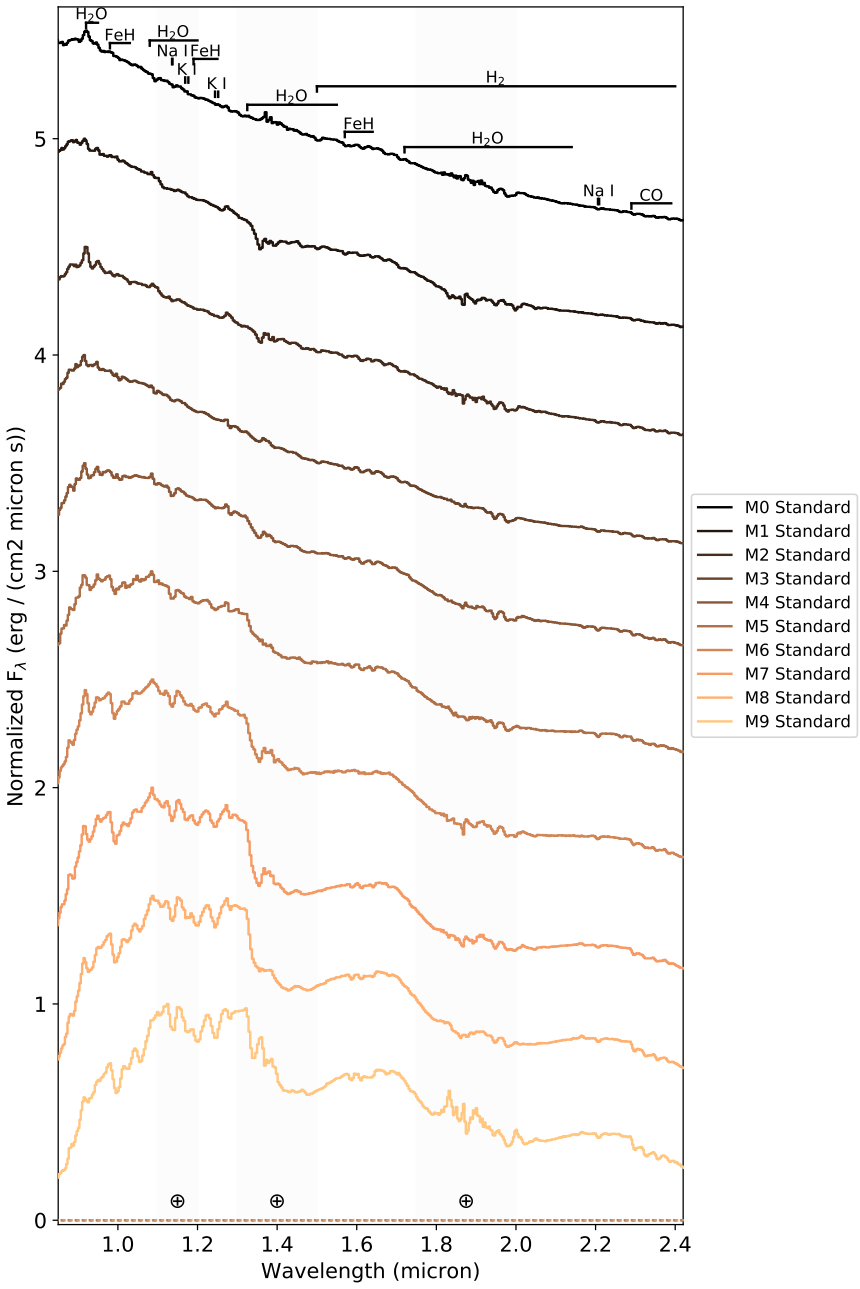

Figure 1.7 Spectral standards for M0−M9 dwarf subtypes.

at 2.2 μm, and then at 1.1 μm and 1.6 μm as the temperatures decrease (as early as L5 in mid-infrared bands; Noll et al. 2000). This defines a new spectral class: T dwarfs.

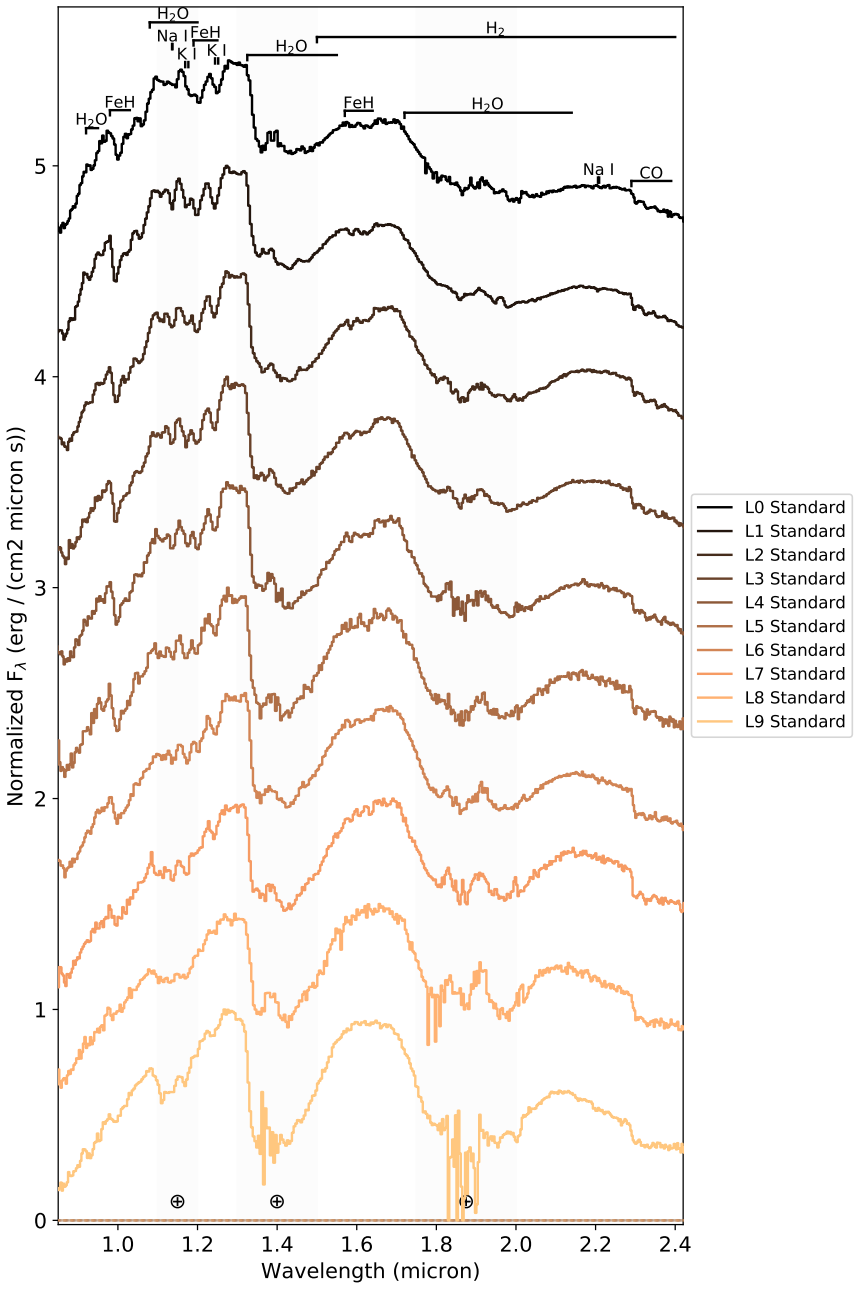

Figure 1.8 Spectral standards for L0−L9 dwarf subtypes.

The near infrared spectra of T dwarfs (600 K< $T_{\rm eff}$ <1400 K; Burgasser et al. 2002b) show deepening methane and water absorption lines and bands in the near-infrared, and

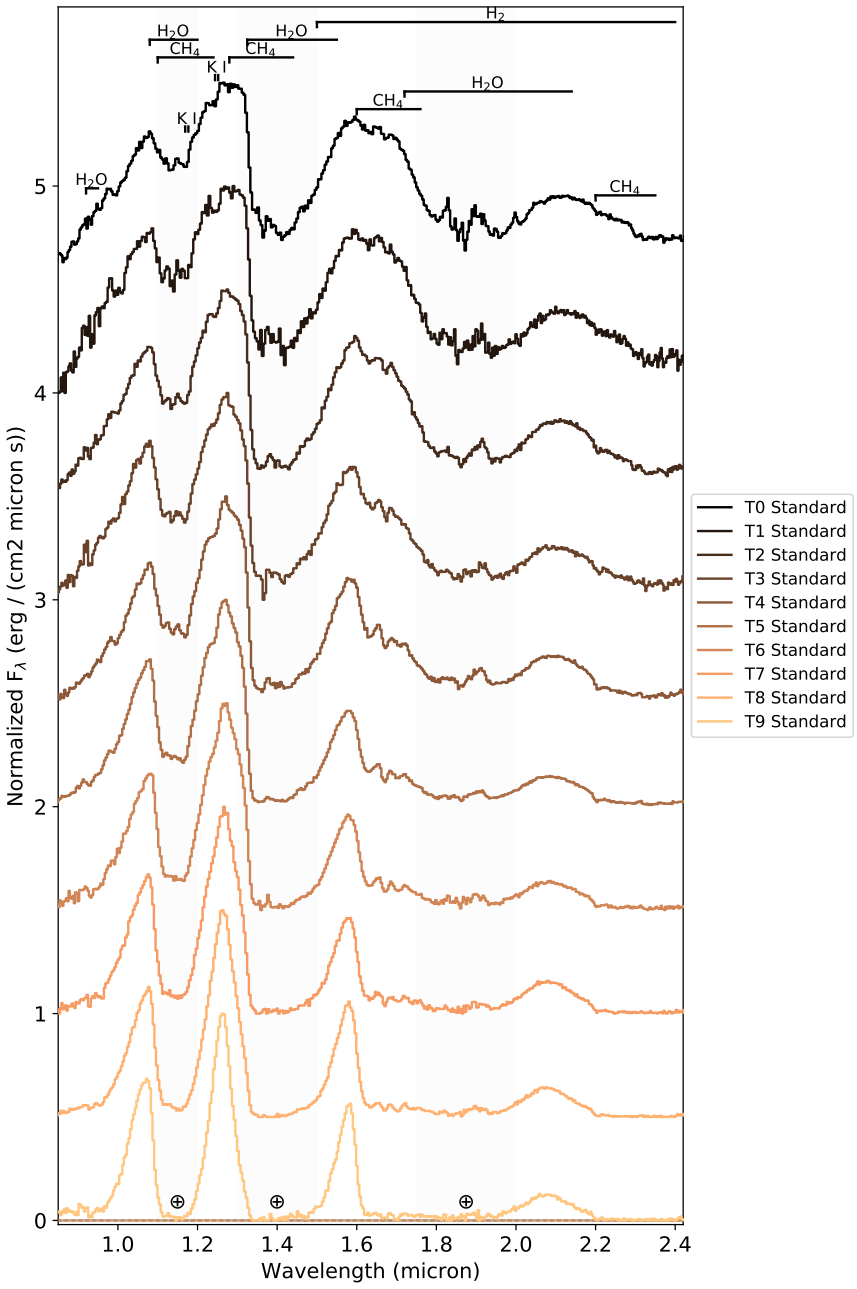

Figure 1.9 Spectral standards for T0−T9 dwarf subtypes.

decreasing dust (Tsuji et al. 1996a; Marley et al. 1996), indicating that dust sedimentation is part of the L to T dwarf transition.

At $T_{\rm eff} \sim 500$ K and below, Na and K reach their condensation temperatures and leave the gas phase as Na_2S and KCl, thus the Na I and K I lines become weaker in the red optical (Burgasser et al. 2003a; Leggett et al. 2003). The emergence of ammonia absorption in the near infrared at this temperature marks the beginning of the Y dwarf class. At $T_{\rm eff} \sim 350$ K and $T_{\rm eff} \sim 200$ K, respectively, water and ammonia are predicted to condense (Cushing et al. 2011). For Jovian-type effective temperatures ($\sim$125 K; Hanel et al. 1981), H_2O and NH_3 have completely condensed below the photosphere, and these bands disappear completely for $T_{\rm eff} < 150 - 80$ K (Guillot 1999).

The coldest brown dwarf currently known is WISE J085510.83−071442.5, a Y-dwarf with an effective temperature of $T_{\rm eff}$ $225 - 260$ K and a mass of $3 - 10$ $M_{\rm Jup}$ (Luhman 2014). Narrow-band, near-infrared imaging along with atmospheric models indicate the presence of water clouds in its atmosphere (Faherty et al. 2014). This object also holds the record for the closest brown dwarf to Earth at 2 pc.

1.3.2 Spectral Classification

1.3.2.1 M, L, T and Y classes

The spectral morphology of stellar and substellar objects can be ordered in a temperature sequence, thus defining the useful observational scale of *spectral types*. Stellar spectral types are labeled OBAFGKM for historical reasons[6], where O stars are the hottest (T$\gtrsim$30,000 K) and most massive (M$\gtrsim$15 $M_\odot$) and M stars are the coldest (T$\lesssim$3500 K) and least massive (M$\lesssim$0.5 $M_\odot$; Gray & Corbally (2009)). For context, our Sun is a G2-type star and has an effective temperature of $T_{\rm eff}$ $\sim$6000 K. As new discoveries reached colder temperatures, the brown dwarf spectral classes L, T and Y were added to the original stellar classes (Kirkpatrick et al. 1999b; Burgasser 2001;

[6]Women in astronomy worked with data taken from an extinct Peruvian telescope! Read more at: https://www.theatlantic.com/science/archive/2016/12/the-women-computers-who-measured-the-stars/509231/

Cushing et al. 2011). Both M and L spectral classes include stars and brown dwarfs. The T and Y spectral classes exclusively contain brown dwarfs and planetary-mass objects.

Since stars are capable of stabilizing their luminosity through hydrogen fusion, once they reach the main sequence, they adopt a relatively stable spectral type. On the other hand, brown dwarfs transition through spectral types as they cool down. For example, a 0.05 $M_{\odot}$ mass object at 10 Myr has a $T_{\rm eff} \sim 2800\,{\rm K}$ and is an M6. At 100 Myr, it will have cooled down to $T_{\rm eff} \sim 2500\,{\rm K}$ and is an M8.5. At 1 Gyr, its effective temperature is $T_{\rm eff} \sim 1500\,{\rm K}$ and is an L5.5. At 5 Gyr, its temperature has decreased to $T_{\rm eff} \sim 900\,{\rm K}$ and has a T6 classification. Finally at 10 Gyr, it will be as cold as $T_{\rm eff} \sim 800\,{\rm K}$ and have a T7.5 spectral type[7]. This is why independent measurements of age are crucial to determine brown dwarf masses.

Spectral classification is based on optical spectra for main sequence stars and M and L dwarfs. However, by Wien's law, $\lambda_{max} = (2.898 \times 10^{-3} m \cdot K)/T$, as stars get colder, their peak emission shifts to longer wavelengths. For detection and subsequent classification of the colder T and Y dwarfs, astronomers switched to near infrared spectra.

The spectral energy distribution of late-M dwarfs ($T_{\rm eff} \sim 3000 - 2400\,{\rm K}$; Gray & Corbally 2009) is dominated by VO and TiO absorption in the optical, and H_2O and CO in the near infrared (Chabrier & Baraffe 2000). The optical classification of M dwarf spectral subtypes uses indices that measure the strength of VO, TiO and CaH (Kirkpatrick et al. 1991; Gizis 1997; Lépine et al. 2003). Also present and strengthening as temperatures decline are metal hydride absorption bands from FeH, CrH, CaH and MgH.

Around $T_{\rm eff} \sim 2400\,{\rm K}$, while the CrH, FeH and water bands continue to strengthen in the optical, VO and TiO start to weaken, thus marking the transition to L-dwarfs ($1400\,{\rm K} < T_{\rm eff} < 2300\,{\rm K}$; Golimowski et al. 2004a). Figure 1.10 shows the contrast between the optical spectra of the M9 2MASSW J1239194+202952 with several TiO and

[7]Using Baraffe et al. (2003) models.

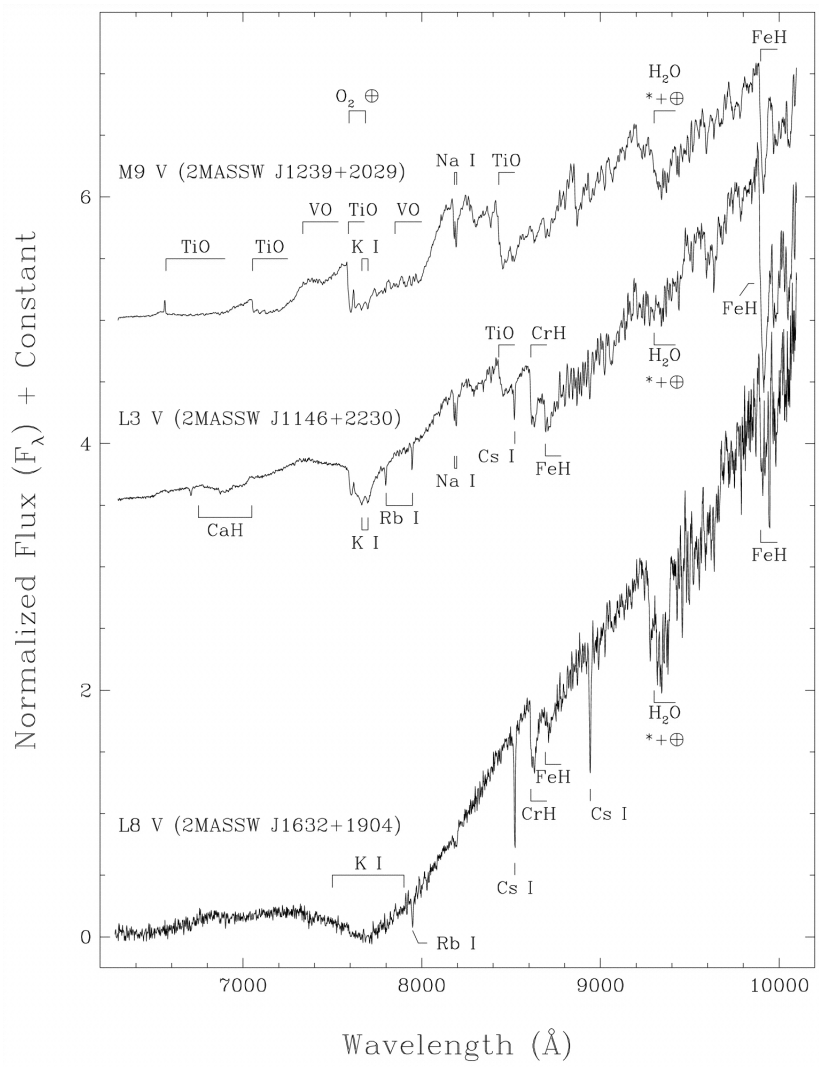

Figure 1.10 Optical spectra of selected M and L dwarfs indicating the molecular species absorbing at each spectral type. Figure from Kirkpatrick et al. (1999b).

VO bands, and the L3 2MASSW J1146344+223052 with much weaker TiO and no VO, while the CrH and FeH bands grow deeper up to the L8 2MASSW J1632291+190441 (Kirkpatrick et al. 1999b). Alkali lines from Na I, K I, Cs I, Rb I also become more prominent in the L class. In the near infrared, as brown dwarfs cool and transition from M to L-type, CO, CrH and FeH absorptions get stronger towards mid-L and get weaker at later types. In particular, FeH at 0.9896μm reappears strong in early-T dwarfs, becomes deepest around T5, and begin to decline towards the late-T, finally disappearing

at T8 (Burgasser et al. 2002b; Burgasser 2002).

In near-infrared wavelengths, CO absorption becomes prominent in L dwarfs until ∼T3 (Burgasser et al. 2002b; McLean et al. 2003). The T class is defined at the onset of methane absorption in the 1.6μm and 2.2μm regions. Methane appears in the mid-infrared at 3.3μm as early as L5 (Noll et al. 2000), and in the near infrared at 1.6μm and 2.2μm around L6.5−L8 (Nakajima et al. 2004; McLean et al. 2003). While the conversion of CO to CH_4 marks the beginning of the T-dwarf class, non-equilibrium mixing assures the presence of CO until T3 (see Section 1.3.3.1 for more on non-equilibrium chemistry).

Atomic doublets Na I (0.5890μm, 0.5896μm) and K I (0.7665μm, 0.7699μm) become stronger and pressure-broadened towards the end of the L sequence (Kirkpatrick et al. 1999b). The K I doublets in the near infrared (1.169μm, 1.177μm) become strongest at L3−L4 (McLean et al. 2003), weaken toward the late-L and peak again around T5−T6 in a way similar to FeH (Burgasser et al. 2002b).

The L to T dwarf transition is an area of active research. While L dwarfs show indications of clouds, these opacity sources do not exist in T dwarfs. The transition happens over narrow temperature ($\Delta T_{\rm eff} \simeq 200-400$ K) and luminosity ($\Delta\log_{10} \simeq 0.3$ dex; Golimowski et al. 2004a) ranges, thus implying a rapid atmospheric transformation. The most peculiar feature about this transition is the increase in surface brightness at 1μm, known as the "J-band bump" (e.g. Dahn et al. 2002; Tinney et al. 2003; Vrba et al. 2004). These characteristics have been observed in binary systems, thus excluding age, surface gravity and composition as culprits (Burgasser et al. 2006c). Hypotheses put forward to explain these effects include the fragmentation of the cloud layer, thus leaving a spotty atmosphere (Ackerman & Marley 2001; Burgasser et al. 2002a) or a global increase in sedimentation efficiency (Knapp et al. 2004).

Another hypothesis lets go of clouds altogether. Tremblin et al. (2016) pointed

out that the slow speed of CO to CH_4 and N_2 to NH_3 reactions in L and T dwarfs, respectively, generates a thermo-chemical instability akin to the fingering or chemical convective instability in oceans and the core/mantle boundary on Earth. The slowness of these reactions destabilizes the molecular weight gradient, which in turn generates local chemical convection that decreases the temperature gradient of the atmosphere. Taking into consideration this diminished temperature gradient and the quenching of CH_4 at the CO to CH_4 transition produces spectral models which reproduce the spectra of L dwarfs and self-luminous extrasolar giant planets. The instability would fade along the L/T transition, letting small scale turbulent dissipation warm up the deep layers of the atmosphere, increasing the temperature gradient. This process would explain the J-band brightening in early-T dwarfs as well as the resurgence of FeH in their near-infrared spectra. As of today, there is no smoking gun detection of clouds or fingering instabilities that would confirm either hypothesis.

Recently, the WISE mission has successfully discovered Y dwarfs, which mark the current limit of spectral classification (Cushing et al. 2011). At temperatures colder than $T_{\rm eff} \sim 500\,{\rm K}$ the major opacity sources are NH_3, CH_4 and H_2O, and the absorption is so strong that what is left of the continuum almost looks like an emission spectrum. About 20 Y dwarfs have been identified to date, with the coldest at $T_{\rm eff} \sim 250\,{\rm K}$ (WISE J085510.83-071442.5, and also the closest brown dwarf to the Sun at 2 pc; Luhman 2014).

1.3.2.2 Gravity effects

Since spectral lines and bands are prone to pressure broadening, surface gravity has a direct effect on spectral morphology. Young brown dwarfs ($\tau \leq 200\,{\rm Myr}$) have not finished contracting and therefore have low surface gravities compared to older brown dwarfs (Burrows et al. 2001; see Figure 1.11). This affects the atmospheric pressure,

reducing collision induced absorption (CIA) of H_2 and thus shaping the near infrared spectra between $1.4 - 1.8\mu$m (also known as the H-band) as a triangle (Allers & Liu 2013).

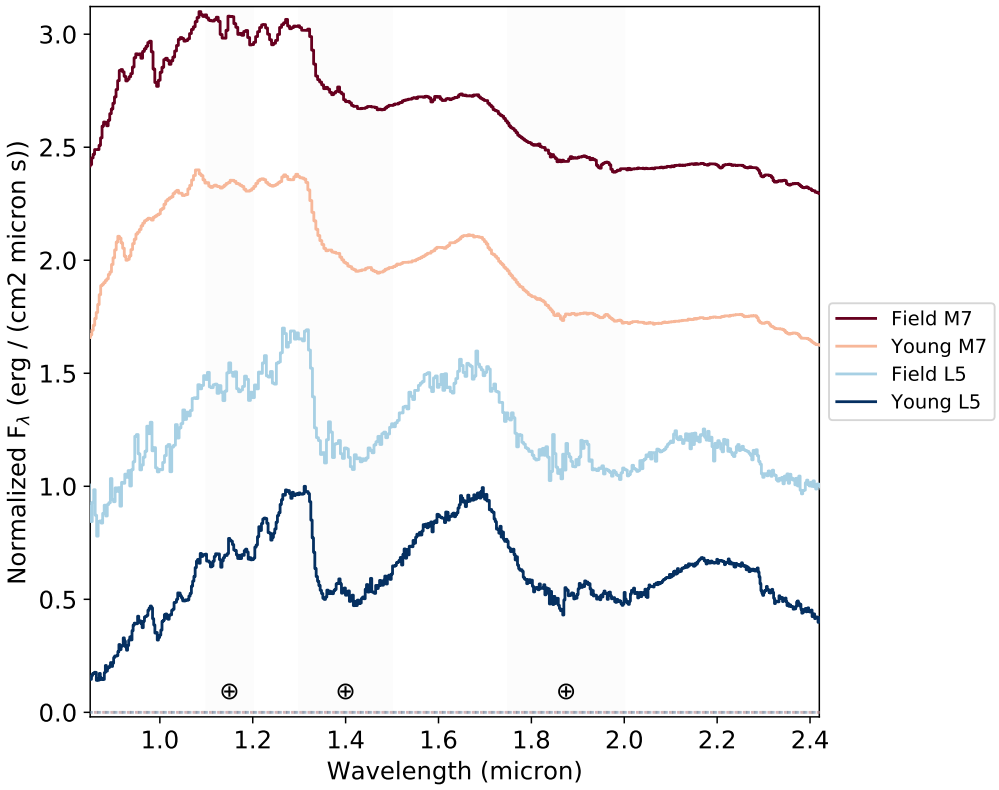

Figure 1.11 Comparison of field to young near-infrared spectra. The top two spectra show field and young M7 dwarfs, while the bottom two show field and young L5 spectra. In both young templates, the shape of the H band is triangular, denoting the lack of collision induced absorption of H_2.

Some features are more sensitive to gravity variations and therefore act as gravity indicators. FeH bands in the J-band, and K I, Na I, Rb I, and Cs I lines at optical and near-infrared wavelengths are weaker and narrower in young objects compared to equivalently-classified field ones (McGovern et al. 2004). Infrared absorption bands of

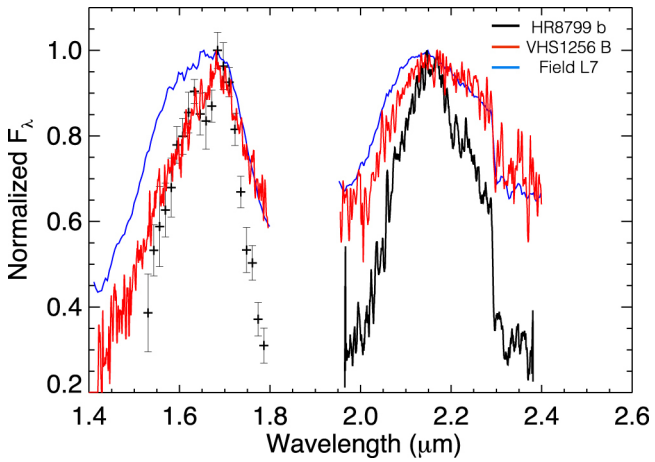

Figure 1.12 Comparison of near-infrared spectra from a field L7 (blue; Gagné et al. 2015c), VHS 1256 B (red), a young brown dwarf (Gauza et al. 2015), and HR8799 b (black), a giant planet spectrum (Barman et al. 2011; Oppenheimer et al. 2013). Figure from Faherty et al. (2016).

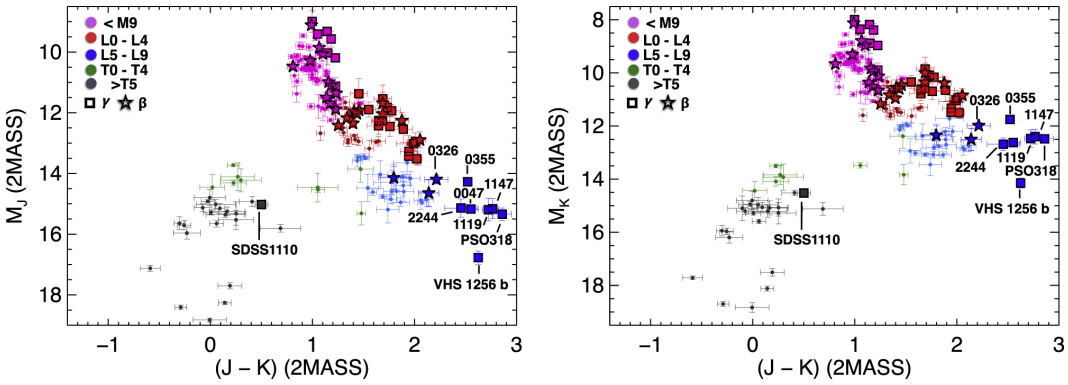

Figure 1.13 Color to absolute magnitude relations for 2MASS J and K_s filters showing field objects as solid dots, color-coded by their spectral subtype range, and young objects as stars and squares. Figure from Faherty et al. (2016).

TiO and VO, while weak in field dwarfs, are stronger in young objects (Allers & Liu 2013). These gravity indicators are important to identify and characterize the young brown dwarf population and the directly-imaged, giant exoplanets (Faherty et al. 2013a).

Recent population studies of young brown dwarfs as proxies to directly-imaged exoplanets (e.g. Faherty et al. 2016) show that low gravity objects are consistently brighter and redder in $J - K_s$ than field M and L dwarfs. Only four young T dwarfs have

been discovered to date: the T5.5 SDSS J111010.01+011613.1 (Gagné et al. 2015a), the T3.5 GU Psc b (Naud et al. 2014), 51 Eri b (Macintosh et al. 2015), and the T2.5 SIMP J013656.5+093347 (Gagné et al. 2017), and their brown dwarf or planetary status is debatable.

1.3.2.3 Metallicity effects

Most chemical elements up to iron ($Z = 56$) are made in the cores of main sequence stars through nuclear fusion (Burbidge et al. 1957). The interstellar medium (ISM) gets incrementally enriched with metals with supernova explosions and stellar winds from giant stars. New stars and brown dwarfs, which are born in this environment, share the composition of the natal ISM. The more metal-rich a star, the more generations of previous stars that have contributed to enriching the ISM environment. On the flip side, metal-poor stars are generally an older generation of stars which formed from a more pristine ISM, early in galactic history. Metal-poor ultracool dwarfs are called ultracool subdwarfs, and they have large velocities as the result of energy kicks from dynamical interactions throughout the galaxy (Burgasser et al. 2003c). The high velocities of these objects imply an older age than field dwarfs.

Since subdwarfs are metal-poor, most of their infrared opacity comes from collision-induced absorption of neutral hydrogen (Burgasser et al. 2003c). This leads to a much bluer near infrared spectra[8] than equivalently-classified normal field dwarfs. They are rare in the L and T classes, with only 36 L-type (Zhang et al. 2017) and 2 T subdwarfs (ULAS J131610.28+075553.0 from Burningham et al. 2014; and Wolf 1130C from Mace et al. 2013).

[8] "Blue" objects emit most of their flux in shorter, bluer wavelengths. Accordingly, "red" objects emit most of their flux in longer, redder wavelengths. A quantitative measure of color is the ratio of fluxes between two wavelengths or filters, $J - K_s$ being the most commonly used.

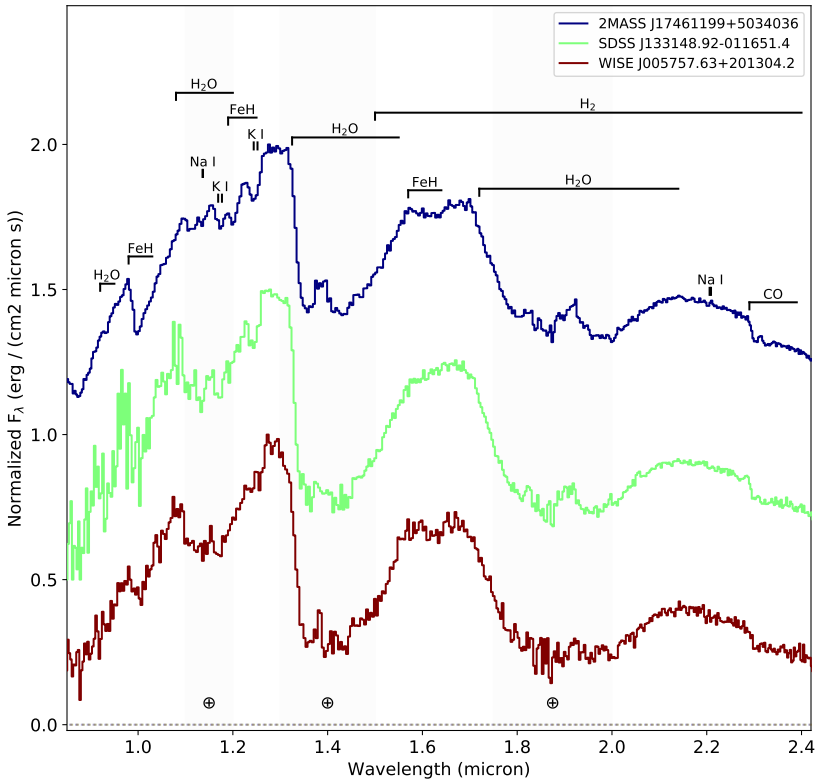

Figure 1.14 Example of a field L4 dwarf (top), an unusually blue L4 dwarf (middle), and an L4 subdwarf.

1.3.3 Atmospheric Dynamics

1.3.3.1 Non-equilibrium mixing

While the temperature and pressure profiles in brown dwarf atmospheres allow for local chemical equilibria, this static picture is incomplete, as it ignores dynamical mixing. Heat from the bottom of the atmosphere induces upward vertical transport of gases by turbulent diffusion (Griffith & Yelle 1999). As a consequence, the vertical distribution of certain gases will depend on the competition between the rate of transport and the rate of conversion to other species (Griffith & Yelle 1999). Non-equilibrium chemistry had been known to occur in solar system gas giants (e.g. Prinn & Barshay 1977; Fegley & Lodders

1994), and Fegley & Lodders (1996) suggested that it also happened in brown dwarfs.

Carbon and Nitrogen are integrated into different molecular compounds depending on the local atmospheric conditions. Their chemical balance is determined by the following equations:

$$CO + 2H_2 \longleftrightarrow CH_4 + H_2O \tag{1.3}$$

$$N_2 + 3H_2 \longleftrightarrow 2NH_3 \tag{1.4}$$

The triple covalent bonds coupling the CO and N_2 molecules have a higher binding energy than the CH_4 and NH_3 single bonds, so the rightward reactions tend to be slow. Rising hot gas, rich in CO and N_2 from the deep atmosphere maintains these species in the cooler upper layers and thus appear in non-equilibrium proportions (Saumon et al. 2006).

The conversion of the carbon reservoir from CO to CH_4 signals the transition from L to T dwarfs. By $T_{\rm eff} \sim 1000$ K, the conversion should be complete considering chemical equilibrium (Burrows & Sharp 1999), yet CO is observed as late as ∼T5 or $T_{\rm eff} \sim 700$ K over 1000 times as abundant as predicted by chemical equilibrium calculations (Noll et al. 1997; Oppenheimer et al. 1998). This CO excess indicates that non-equilibrium chemical processes are happening in substellar atmospheres.

1.3.3.2 Cloud formation

The range of effective temperatures encompassing L dwarfs ($T_{\rm eff} \sim 1400 - 2300$ K; Golimowski et al. 2004a) includes the condensation temperatures of many refractory species[9] found in late-M dwarfs (Lodders 2002). Those species will condense out of the gas phase onto dust grains, as early as in late-M dwarfs. Moreover, variance

[9]Opposite to volatile species, refractory species have high condensation temperatures.

among L dwarfs SEDs at infrared wavelengths shows that these grains are not mixed with the gas but rather assembled into cloud layers (Knapp et al. 2004).

It is possible that the disappearance and reappearance of FeH and K I on early-L and mid-T dwarfs, respectively, may be due to cloud formation above the photosphere, thus blocking the absorption of these compounds (Cushing et al. 2003). Clouds and their added opacity can affect the overall slope of near infrared spectra, in particular by blocking light in shorter wavelengths while letting through longer wavelengths, making spectra look "red". The subpopulation of unusually blue L dwarfs shows the opposite trend: enhanced flux in shorter wavelengths, along with stronger FeH, K I, and H_2O absorption (Cruz et al. 2003; Knapp et al. 2004; Chiu et al. 2006; Burgasser et al. 2008b). Kinematic studies of unusually blue L dwarfs have found that these objects have a higher dispersion of spatial velocities than average, which is consistent with older ages (e.g. Faherty et al. 2009; Schmidt et al. 2010) and high surface gravities.

1.4 Formation

1.4.1 Canonical Theory of Star Formation

Isolated low-mass star formation occurs by the collapse of unstable dense cloud cores within giant molecular clouds (GMCs) that have reached a density of the form $\rho(r) \propto r^{-2}$, characteristic of singular isothermal spheres (Shu et al. 1987). Giant molecular clouds (GMCs) are cold ($10-30\,\mathrm{K}$; Sargent & Welch 1993), vast ($5-200\,\mathrm{pc}$ in diameter; Murray 2011), massive ($10^5-10^6 M_\odot$; Williams et al. 2000), and sparse ($\langle n_{H_2}\rangle \sim 10^2\,\mathrm{cm}^{-3}$; Blitz 1993) interstellar clouds containing gas and dust irregularly arranged in large filaments, sheets, cores and clumps. The cold temperature of GMCs allows for the assembly of CO, CS and more complex molecules like HC_3N, CH_3OH, $HC_{11}N$, SO_2, while the most abundant species is H_2. Thermally-induced rotational and

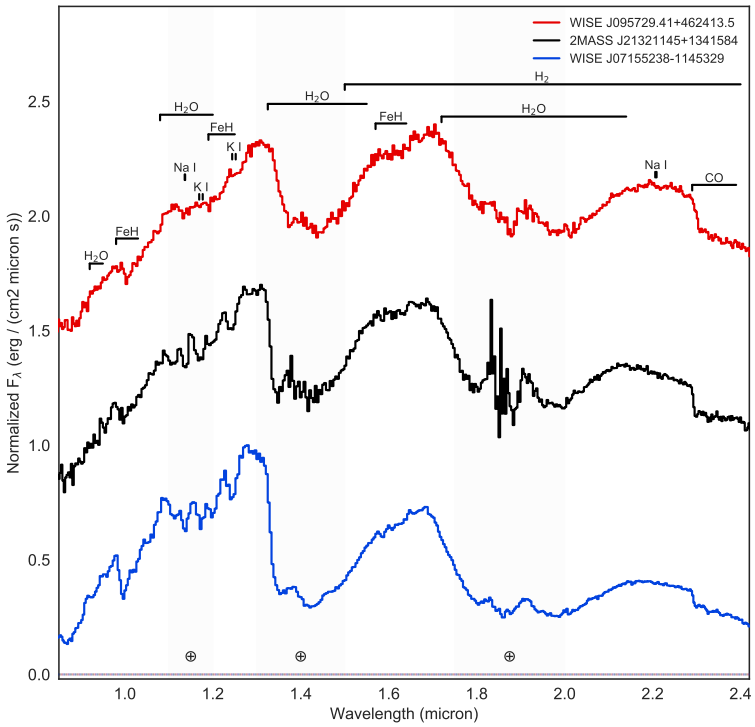

Figure 1.15 Examples of a red, average-color and blue L6 dwarf near-infrared spectra.

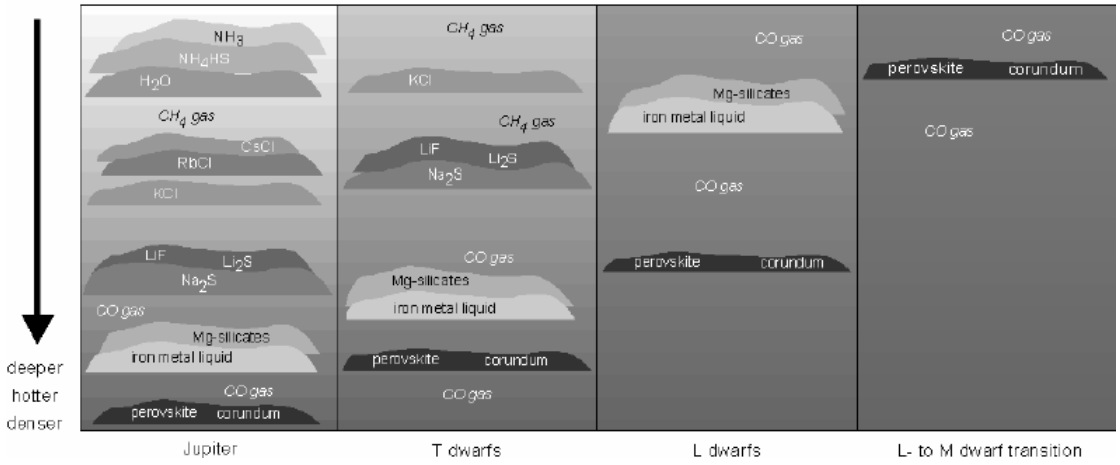

Figure 1.16 Illustration showing the different cloud layers and their vertical structure formed in M, L, T dwarfs and Jupiter. Figure from Lodders & Fegley (2006).

vibrational transitions in these molecules give rise to emission features at submillimeter wavelengths, where these clouds are seen (Sargent & Welch 1993). Turbulence, gas pressure and weak magnetic fields prevent these massive structures from collapsing under their own gravity. However, collapse can occur when a dense region exceeds its critical Jeans mass (see Section 1.4.2).

Clumps are $50-500\,M_{\odot}$ units, with similar velocities ($0.3-3\,\mathrm{km\,s^{-1}}$), extending $0.3-3$ pc with a mean number density of $10^3-10^4\,\mathrm{cm^{-3}}$ at a temperature of $10-20$ K. Cores are less massive ($0.5-5\,M_{\odot}$), smaller ($0.03-0.2$ pc), yet denser ($10^4-10^5\,\mathrm{cm^{-3}}$) units (see Bergin & Tafalla 2007).

When rapidly-rotating cores become unstable due to external large-scale gravitational perturbations (roughly after 10^6 years; Ward-Thompson 2002), they collapse into a central "Class 0" protostar or a multiple system to conserve angular momentum. Accretion rate is high at this stage ($\dot{M} \gtrsim 10^{-5}\,M_{\odot}\,\mathrm{yr^{-1}}$), only lasting for about 10^4 years. After half of the envelope mass has fallen in, accretion slows down to $\dot{M} \lesssim 10^{-6}\,M_{\odot}\,\mathrm{yr^{-1}}$, and the source is known as a Class I protostar (Lada & Wilking 1984), lasting for about 10^5 years until all the material is accreted, at which point it is referred to as a Class II protostar or classical T-Tauri star (Lada & Wilking 1984; Andre & Montmerle 1994). T-Tauri stars have massive circumstellar disks which could potentially form planets. After the inner part of the disk has dissipated, the source is known as a Class III or weak-line T-Tauri star and the phase of rapid contraction ends (Andre & Montmerle 1994). T-Tauri stars enter the main sequence by slowly contracting and losing luminosity but keeping roughly a constant surface temperature, until they develop a radiative zone or trigger nuclear fusion, formally entering the main sequence (Hansen et al. 2004).

From all available evidence (e.g. Luhman et al. 2007), brown dwarfs form in the same way as low-mass, hydrogen-burning stars: by gravitational instability on a dynamical timescale, typically in clusters, and with the same composition as the

interstellar medium from which they originate (Elmegreen 1999). A minimum mass is reached at very high densities where the core becomes adiabatic and opaque to its own radiation. This opacity limit is estimated to be between $0.003 - 0.007\,M_{\odot}$ (Boyd & Whitworth 2005).

1.4.2 The Challenges of Brown Dwarf Formation

The Jeans mass is a threshold mass above which the internal gas pressure is unable to balance the force of gravity in an isothermal sphere (Jeans 1902). For a virialized cloud, the magnitude of the potential energy is twice the kinetic energy, $U + 2K = 0$. From equipartition, assuming an ideal gas law, the kinetic energy of the cloud is $K = \frac{3}{2}NkT$, where $N = \frac{M}{m_H}$ is the number of particles in the cloud of total mass M and molecular mass m_H, k is the Boltzmann constant and T the average cloud temperature. The potential energy for a sphere of uniform density is $U = -\frac{3}{5}\frac{GM^2}{R}$. At virial equilibrium:

$$3NkT = \frac{3}{5}\frac{GM^2}{R} \tag{1.5}$$

Rearranging the terms and substituting a constant density, $\rho = \frac{3M}{4\pi R^3}$, we get a critical Jeans mass M_J, such that if exceeded, the cloud would collapse under its own gravity:

$$M_J = \left(\frac{5kT}{Gm_H}\right)^{3/2}\left(\frac{3}{4\pi\rho}\right)^{1/2} \tag{1.6}$$

The typical Jeans mass for a molecular cloud of $T = 10\,\mathrm{K}$ and $\rho = 100\,M_{\odot}\ \mathrm{pc}^{-3}$ is in the order of $\approx 1\,M_{\odot}$ (Larson 1985, 1999). This has been observationally supported by studies in ρ Ophiucus (Motte et al. 1998; Andre et al. 2000) and the Serpens cloud (Testi & Sargent 1998) which match the observed pre-stellar clump masses to the universal stellar IMF (Salpeter 1955).

From equation 1.6, we can see that mass is inversely proportional to the square root of the gas density, $M \propto \rho^{-1/2}$. This means that in order to collapse a smaller mass conducive to the formation of a low-mass star or brown dwarf, a gas clump needs to have a density higher than average, while halting the infalling mass onto a protostar in the subsequent stages of formation. This is the fundamental problem of brown dwarf formation.

1.4.3 Observations of Brown Dwarf Formation Outcomes

1.4.3.1 Initial Mass Function

The initial mass function (IMF) is an empirical distribution that describes the number of stars, dN, that form per mass bin, dM, in a given volume, and by extension, the redistribution of gas from a molecular cloud onto stars. The origin of the IMF is an active area of research. It is typically represented as a power law, a broken power law or a lognormal distribution. Salpeter (1955) provided the first measurement of the IMF from stars in the galactic disk following the relation:

$$dN \propto M^{-\alpha} dM, \quad \alpha = -2.35 \tag{1.7}$$

Salpeter's essential findings are that there are more low-mass stars than high-mass stars, that most of the mass lies in low-mass stars ($< 1 M_{\odot}$) and that most of the luminosity comes from high-mass stars. However, this shape of the IMF overestimated the number of low-mass stars, hinting there could be twice as many brown dwarfs as stars (Burgasser 2004).

Miller & Scalo (1979) introduced the IMF representation as a lognormal distribution. This shape can be understood by considering the star formation process as a complex transformation where the final stellar masses are determined by the product of

many independent variables, and by the central limit theorem, the distribution of $log(M)$ would converge onto a lognormal shape (Larson 1973; Zinnecker 1984). The newest formulation of the lognormal distribution is the one given by Chabrier (2005) for low masses:

$$dN = \frac{0.158}{M \ln 10} \exp\left[-\frac{\log(M)-\log(0.08)^2}{2\times 0.69^2}\right] dM, \quad \text{for } M < 1\,M_\odot \tag{1.8}$$

$$dN = M^{-\alpha} dM, \;\; \alpha = 2.3 \pm 0.3, \quad \text{for } M > 1\,M_\odot \tag{1.9}$$

Additionally, Kroupa (2001) introduced the broken power law to better model the low-mass end of the IMF:

$$dN \propto M^{-2.3} dM, \qquad M \geq 0.5\,M_\odot \tag{1.10}$$

$$dN \propto M^{-1.3} dM, \qquad 0.08 \leq M \leq 0.5\,M_\odot \tag{1.11}$$

$$dN \propto M^{-0.3} dM, \qquad M \leq 0.08\,M_\odot \tag{1.12}$$

Since brown dwarfs are affected by the mass-age-luminosity degeneracy, a well-calibrated IMF of field brown dwarfs is difficult to construct, especially for field objects. Constraints for α in the field include $\alpha \lesssim 0$ obtained through Monte Carlo simulations (Chabrier 2002), or $-1.5 \lesssim \alpha \lesssim 0$ via Bayesian inference (Allen et al. 2005). The IMF is continuous across the hydrogen-burning limit in star-forming clusters like σ Orionis ($\alpha = 0.8 \pm 0.4$; Béjar et al. 2001), α Persei ($\alpha = 0.59 \pm 0.05$; Barrado y Navascués et al. 2002), Taurus ($\alpha \sim 0.4$; Briceño et al. 2002; Luhman 2004a), IC348 ($\alpha \sim 0$; Luhman et al. 2003), and the Pleiades ($\alpha \sim 0.60 \pm 0.11$; Moraux et al. 2003). The ejection, turbulent and disk fragmentation scenarios reproduce the low-mass IMF observed in star-forming clusters and the field (Luhman 2005; Reid et al. 2002a).

1.4.3.2 Disks and Jets

The existence of disks around brown dwarfs is a strong indicator that they form as stars. Mid-infrared excess surveys have shown that $40-60\%$ of young brown dwarfs in $1-3$ Myr-old star-forming regions like IC 348, Chameleon I, ρ Ophiucus and Taurus have disks (Jayawardhana et al. 2003). The disk fraction of stellar sources, with masses in the $0.1\,M_{\odot} < M < 0.7\,M_{\odot}$ range, in IC 348 and Chameleon I is similar: $33 \pm 4\%$ and $45 \pm 7\%$, respectively (Apai et al. 2008). This parallel shows that there is material available for planet formation whether the central object is a star or a brown dwarf. Moreover, disks around stars have been studied for a range of stellar ages ($0.5-30$ Myr), yielding inner disk lifetimes of ~ 6 Myr (Hillenbrand et al. 1998; Haisch et al. 2001). While comprehensive studies of brown dwarf disks have been done in clusters younger than 2 Myr (e.g. IC 348 and Chameleon I; Jayawardhana et al. 2003), the existence of an actively accreting brown dwarf in the 10 Myr TW Hydrae young association (Mohanty et al. 2003), suggests that brown dwarf disk lifetimes could be comparable to those of stars, supporting similar formation pathways.

The typical mass for brown dwarf disks are $m_{disk} \sim 3 \times 10^{-5}\,M_{\odot}$ (Harvey et al. 2012), while the typical size is $20-40$ AU (Luhman et al. 2007), and up to $40-140$ AU in Taurus (Ricci et al. 2014). Accretion rates of brown dwarf disks range around $\dot{M} \sim 10^{-9.3} - 10^{-12}\ M_{\odot}\ \mathrm{yr}^{-1}$ (Riaz 2013), fairly smaller than those for solar-like classical T-Tauri stars, $\dot{M} \sim 5 \times 10^{-12}\ M_{\odot}\ \mathrm{yr}^{-1}$ (Gullbring et al. 1998). Brown dwarfs actively accreting material from their surrounding disks can produce large mass outflows collimated along their axis of rotation to regulate their angular momentum, in a similar way to those observed in stars. Recently, a proto-brown dwarf in the σ−Orionis cluster of only $36\,M_{\mathrm{Jup}}$ of total gas and dust mass, has been found to drive 0.26 pc jets (Riaz et al. 2017).

1.4.3.3 Multiplicity

The number of binary or higher order systems and their spatial configurations are a direct consequence of the formation mechanisms at play. In Section 2.4, we compare multiplicity observations with predictions from brown dwarf formation scenarios.

1.4.4 Formation theories and predictions

1.4.4.1 Turbulent Fragmentation

The theory of turbulent fragmentation adjudicates the formation of dense clumps and cores in molecular clouds to supersonic turbulence, whose kinetic energy is on the order of 100 times larger than the gas thermal energy for a scale of a few parsecs (Padoan et al. 2005). Gas compression by turbulence produces high density post-shock gas clumps with low Jeans masses. The role of gravity is limited to the collapse of the dense cores. In this model, turbulence can generate dense cores of any size, independent of the Jeans' mass. The ones whose mass exceeds their Jeans' mass will collapse under gravity into protostars, while the sparser ones will diffuse back into the turbulent flow (Padoan & Nordlund 2004).

This model reproduces the observed universal IMF. No predictions are presented regarding the formation of multiple systems. Bonnell et al. (2008) argue against this model based on their simulation which always produces brown dwarfs in stellar clusters, and are not scattered throughout the extent of the molecular cloud, in line with cores created by widespread turbulence. Turbulent fragmentation also predicts a ratio of brown dwarfs to stars sensitive and proportional to the Alfvénic Mach number (M_A), which is the ratio of the local flow velocity to the local Alfvén speed (the Alfvén speed is the speed of propagation of a plasma in the direction of the magnetic field lines; Whitworth et al. 2007). For a higher M_A, a higher proportion of brown dwarfs to stars is predicted.

While the Alfvénic Mach number seems to vary regionally within a molecular cloud, the observed ratio of brown dwarfs to stars appears to stay roughly constant over a range of star-forming environments (Luhman et al. 2007).

1.4.4.2 Disk Fragmentation

Stamatellos & Whitworth (2009a) envisioned a scenario where brown dwarfs form in the outskirts of prestellar disks, which are dense enough ($\rho \gtrsim 10^{-16}$ g cm^{-1}; Stamatellos & Whitworth 2010) to reach a low Jeans mass. The specific angular momentum of a rotating core is about three orders of magnitude larger than the angular momentum that can be contained in a star, thus the difference goes into forming a circumstellar disk. However, if the angular momentum is not efficiently dissipated, the disk can become unstable and fragment (Attwood et al. 2009). Fragmentation is viable if massive disks can overcome the stabilizing centrifugal and thermal support with their own gravity (Toomre 1964), and if they cool fast enough through radiation such that fragments continue to collapse (Gammie 2001; Rice et al. 2005).

The predicted IMF of this model agrees with observations of the Pleiades ($\alpha = 0.6 \pm 0.11$; Moraux et al. 2003) and σ-Orionis clusters ($\alpha = 0.6 \pm 0.1$; Lodieu et al. 2009). This formation scenario allows for brown dwarf disks of the order of a few Jupiter masses and few tens of AU to be retained within a larger prestellar disk.

The typical outcomes from this simulation are triple systems with a Sun-like star, a close low-mass star companion and a wide brown dwarf companion or a brown dwarf binary companion to the central Sun-like star. From the simulation of Stamatellos & Whitworth (2008) of a $0.5\,M_{\odot}$ star with a $0.07\,M_{\odot}$ disk of 40 AU evolving with smoothed particle hydrodynamics, 75% of the objects generated are brown dwarfs with masses between $20-30\,M_{\rm Jup}$ (including 4% planetary-mass brown dwarfs) and 25% are low-mass hydrogen-burning stars. Over 55% are ejected to the field. The resulting low-mass

binary fraction of 16% is similar to that measured in Taurus-Auriga ($\lesssim 20\%$; Kraus et al. 2006), Chameleon I ($11^{+9}_{-6}\%$; Ahmic et al. 2007), and the field (e.g. $15 \pm 5\%$; Gizis et al. 2003). Over half of the binaries produced (55%) have near-unity mass ratios, $q > 0.7$, in agreement with observations (e.g. Burgasser et al. 2007c).

1.4.4.3 Ejection of Pre-stellar Cores

Reipurth & Clarke (2001) proposed a scenario where a pre-stellar core collapses into an ensemble of protostellar embryos with a range of masses. As the embryos start growing by competitive accretion, the lowest mass objects are ejected out of the cluster by dynamical interactions, thus halting their accretion and preventing them from becoming hydrogen-burning stars. As Reipurth & Clarke (2001) point out in their original study, "With better luck, a brown dwarf would therefore have become a normal star."

The ejections occur in three steps: *interplay*, where the embryos follow chaotic motion; *close triple approach*, where three embryos come to proximity (~ 100 AU) of each other simultaneously in a small volume; and *ejection*, where one embryo is expelled from the group, exchanging energy and momentum with the other two. For ejection to be feasible, it either needs to occur on a shorter timescale than it takes for embryos to accrete gas up to the HBMM, or the embryos must accrete material unevenly. Ejections can lead both to isolated brown dwarfs, close brown dwarf binary systems ($20 - 30$ AU) if the lowest two members of the mini-cluster are ejected, or hierarchical triple systems if two low-mass embryos are ejected but remain bound to a more massive embryo.

While numerical simulations have reproduced this scenario (Bate et al. 2003; Goodwin et al. 2004), two problems remain. A primary prediction of this model is a population of brown dwarfs with a high velocity dispersion in the outskirts of open clusters and the vicinity of young protostars as a consequence of the ejection, yet such population has not been observed. However, the authors suggest this null result only

constrains the range of ejection velocities. Additionally, this scenario would truncate circumstellar disks around brown dwarfs and/or slow down accretion rates leading to lower far-IR excess emission, yet examples of brown dwarfs hosting disks are plentiful (e.g. Apai et al. 2008; Harvey et al. 2012).

The only way binary systems could form given this scenario would be by ejecting the two lowest-mass members of a mini-cluster, leading to an extremely low binary fraction estimated at $< 5\%$ (Bate et al. 2002a), which is much lower than observations ($\sim 10-20\%$; e.g. Close et al. 2003). The intrinsic difficulty to form binary systems in this scenario would explain the paucity of brown dwarf companions to main sequence stars at small separations, known as the "brown dwarf desert" (Marcy & Butler 2000). This model only allows for brown dwarf companions to higher mass stars at large separations (> 100 AU) if despite the ejection, the low-mass object remained gravitationally bound.

Some ejection theories (e.g. Reipurth & Clarke 2001; Boss 2001) predict a marked difference in the kinematic and spatial distribution of stars and brown dwarfs. As the brown dwarfs are ejected early from their originating cloud, their velocity dispersion should be higher than that of the hydrogen-burning stars that remain in the cluster and thus they should be more widely distributed in star-forming regions. Other ejection models (Bate et al. 2002b) where brown dwarfs form in similar ways as stars present the opposite prediction, that stars and brown dwarf populations should have the same spatial and velocity distributions.

Radial velocities from high resolution spectra of low-mass stars and brown dwarfs measured in the Chameleon I cloud ($\tau \sim 2$ Myr; $d = 160$ pc; Luhman 2007; Bayo et al. 2017) show no statistical difference between the velocity dispersions of brown dwarf and stellar populations ($v_{BD} = 0.9 \pm 0.3 \mathrm{km\,s^{-1}}$ versus $v_{stars} = 1.3 \pm 0.3 \mathrm{km\,s^{-1}}$; Joergens & Guenther 2001; Joergens 2006).

From the simulations of Kroupa & Bouvier (2003a), brown dwarfs and stars

share the same spatial distributions, while a small tail of high velocity brown dwarfs ($v > 1\mathrm{km\,s^{-1}}$) were more widely distributed than the stars. Additionally, a census of low-mass objects on the Taurus cluster ($\tau \sim 1\,\mathrm{Myr}$, $d \sim 140\,\mathrm{pc}$) by Luhman (2004a) shows no difference in their spatial distribution compared to earlier studies of stars in the same cluster (e.g. Briceño et al. 2002). These observations seems to disfavor the ejection scenario and support a common formation mechanism for stars and brown dwarfs (Luhman 2005).

1.4.4.4 Photoerosion of Pre-stellar Cores

This idea, originally put forward by Hester et al. (1996), and adapted to brown dwarfs by Whitworth & Zinnecker (2004), suggests that photoionizing radiation from newly-formed OB stars can halt the accretion of a forming pre-stellar core by removing material from its envelope while enhancing the density of its core with a compression wave driven by the ionization. This scenario gets around the requirement of a preexisting high density region in a molecular cloud, and laso halts the accretion of a core that otherwise would have birthed a stellar-mass object. Photoevaporation as a brown dwarf formation mechanism is robust, since it can operate in a range of initial conditions, yet inefficient, because it produces low-mass brown dwarfs from massive dense prestellar cores.

Evaporating gaseous globlues (EGGs) in the Eagle Nebula support the feasibility of this mechanism (Hester et al. 1996). Unassociated brown dwarfs found in the σ-Orionis cluster (Zapatero Osorio et al. 2000) in the vicinity of OB stars, also support formation by photoerosion. However, this scenario requires the presence of a source of ionizing radiation along with fine-tuning to blow away the outer layers of the core while keeping the center intact. It cannot explain the existence of brown dwarfs in lower-mass star-formation regions like Taurus (e.g. Luhman et al. 2017). It is unclear how binary

systems would form given this scenario.

1.4.5 Comparison to Brown Dwarf Formation Simulations

Large-scale hydrodynamical brown dwarf and star formation simulations including gravity, hydrodynamics, magnetic fields, radiative transfer, and chemistry, observe all of the scenarios discussed above. Early simulations (e.g. Bate 2009) assuming a barotropic equation of state, magnetohydrodynamics, and a power law shape for the turbulence spectrum, reproduced the correlation between primary mass and multiplicity, between the median separation of binary systems and primary mass, and the mass ratio distribution of VLM primaries peaking at near-equal masses. The results are indistinguishable between two exponents for the turbulence power law ($Pk \propto k^{-4}$ and $Pk \propto k^{-6}$), supporting the invariance in the properties of stars and brown dwarfs across different regions. However, this simulation overpredicts the number of brown dwarfs to stars by a factor of ~ 4 as compared to observations, which indicate that stars are $5-8$ times as abundant as brown dwarfs (Luhman et al. 2007). The overestimation was corrected with the introduction of radiative feedback (Bate 2012) in a later version of the simulation.

The brown dwarfs resulting from these simulations do not become stars because their accretion is halted by their ejection from unstable multiple systems. Disk fragmentation provides a more direct way to form brown dwarfs since they are born in a dense environment and can be easily ejected by dynamical interactions with other objects in the disk. Conversely, in a turbulent fragmentation scenario, brown dwarfs are form in isolation, thus can accrete more material until they get ejected, typically surpassing the HBMM (Whitworth et al. 2007).

On the other hand, simulations by Bate et al. (2003) and newer versions by Bate (2012) produce some brown dwarf disks truncated by tidal interactions between neighboring sources. 50% of disks have a truncation radius > 10 AU while 20% have a truncation

radius of > 20 AU. Therefore, most disks would need not be truncated to reproduce observations, disfavoring the ejection scenario (Luhman et al. 2007).

A problem with simulations in general is the difficulty to generate brown dwarf binary systems, with the typical binary fraction around 5% for systems closer than 20 AU, while observations report fractions of $10-20\%$ and a peak in the separation distribution at 4 AU (See Section 2.3.1). This shortcoming could be the result of computational limitations, as these simulations cannot resolve separations closer than 10 AU (Luhman et al. 2007).

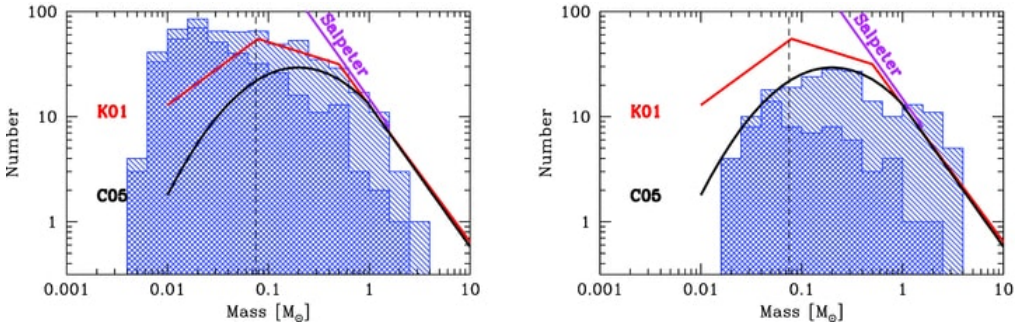

Figure 1.17 Initial mass function histograms from the simulations of Bate 2012 (left), which overpredicts the number of brown dwarfs due to the lack of radiative feedback on the simulations and Bate 2009 (right), that corrects for this effect. The double hatched areas represent objects that have stopped accreting, while the single hatched ones include objects still in the process of accretion, which could become low-mass stars rather than brown dwarfs. Overplotted are the IMF calculations from Salpeter (1955) (purple), Kroupa (2001) (red) and Chabrier (2005) (black). Figure from Bate (2012).

In summary, all of these formation scenarios could happen in nature and their prevalence possibly depends on the environment, which is why both the frequency and configuration of binary systems are valuable pieces of information to understand the conditions necessary for specific mechanisms of brown dwarf formation.

Chapter 2

Multiplicity

2.1 It takes two to tango

A natural consequence of the star formation process is the emergence of gravitationally bound systems of 2 or more objects. Binary systems are coeval and cospatial laboratories with a common chemical composition, crucial for the study of brown dwarf formation and evolution given their progressive cooling and dimming with age (see Section 1.2.3). In fact, prototypes for L, T and Y spectral types were all found as companions to more massive objects. In this thesis, we will refer to ultracool binaries as systems of two ultracool dwarfs, where the primary component has a mass of $M_{primary} \lesssim 0.1\,M_{\odot}$ at most, and the secondary component has a smaller mass than the primary. Additionally, ultracool dwarfs can be found as companions to hydrogen-burning, main sequence stars, and we will refer to the low-mass component as a companion.

Measuring the orbits of binary systems is one of the few ways to obtain direct measurements of masses[1]. Measured binary masses are used to calibrate evolutionary models and constrain empirical spectral type to absolute magnitude relations. The

[1]However, through microlensing, a single event can provide mass measurements.

characterization of single brown dwarfs relies entirely on these relations due to their mass-age-luminosity degeneracy, hence the prime importance to properly constrain them, especially since they are typically contaminated by unresolved binaries.

Additionally, binary systems are fossils of the formation process. Their population statistics, like the binary fraction, separation, eccentricity and mass ratio distributions, are the yardsticks by which we compare the results from formation simulations. To date, about ~ 150 low-mass binary systems[2] are known, accounting for about $10-20\%$ of the observed samples (e.g. Bouy et al. 2003; Burgasser et al. 2003b). Most systems have equal-mass components, and on average are separated by $4-7$ AU (Close et al. 2003; Burgasser et al. 2007c). However, it is possible that the observed brown dwarf binary sample is incomplete given the preference for equal-brightness systems by current detection methods. In this chapter, I review binary detection techniques and the statistical properties of the ultracool binary population, and presetnt a new technique to uncover binary systems of unequal brightness over a broad range of separations.

2.2 Detection techniques

2.2.1 Imaging

By far the most prolific method to detect binary systems is through direct imaging with over 80% of low-mass discoveries (Burgasser et al. 2007c; Bardalez Gagliuffi et al. 2015). In general, imaging is most sensitive to equal brightness or equal mass binaries, while faint companions to bright sources are difficult to detect.

The angular separation of a binary system determines its detectability by imaging. High resolution imaging is needed to resolve the typical close separations of most ultracool binaries. The resolution of a telescope depends on size of its aperture, as more

[2]Primary mass $M \lesssim 0.1 M_{\odot}$.

photons will be received in a larger collecting area. The practical limit to image quality is the seeing, which is a measure of the full width at half maximum of the point spread function (PSF) of a point source, denoting the intensity of local atmospheric turbulence. To minimize the effects of turbulence, adaptive optics (AO) systems have tip/tilt movable and deformable mirrors designed to counteract the distortion of incoming wavefronts. The movable mirror controls the first order corrections to atmospheric turbulence (tip/tilt, meaning corrections in the position of the science target), using a natural guide star (NGS) if a bright star is close to the science target. Alternatively, a laser guide star (LGS) can be generated by pointing a laser from the telescope to a sodium layer in the Earth's mesosphere at 90 ± 10 km of altitude, producing radiation from spontaneous emission which comes back to the telescope on the same beam (Foy & Labeyrie 1985). An example of a high resolution image taken with LGS-AO is shown in Figure 2.1. The other way to avoid turbulence effects is to use space-based telescopes.

High resolution imaging surveys to find companions to brown dwarfs have been pursued in young clusters (e.g. Neuhäuser et al. 2002; Kouwenhoven et al. 2005; Ahmic et al. 2007) and in the field (e.g. Reid et al. 2001b, 2002b; Burgasser et al. 2003b; Gizis et al. 2003), providing a glimpse into the relative brightnesses, separation distribution and binary fraction of low mass stars and brown dwarfs. Most field surveys have been magnitude-limited (e.g. Close et al. 2003; Gizis et al. 2003).

For widely-separated binaries (greater than a few arcseconds), the confirmation of common proper motion serves as the binary identification. Large area imaging surveys (e.g. SDSS, 2MASS, WISE) and follow up imaging provide multiple epochs of sky position, from which proper motion can be calculated. For two sources at the same distance and with the same velocities, the probability that they are not gravitationally bound is negligible. Figure 2.2 shows an example of the common proper motion of the wide triple system composed by the M9 LP 704−48 and the tight binary SDSS J0006−0852AB,

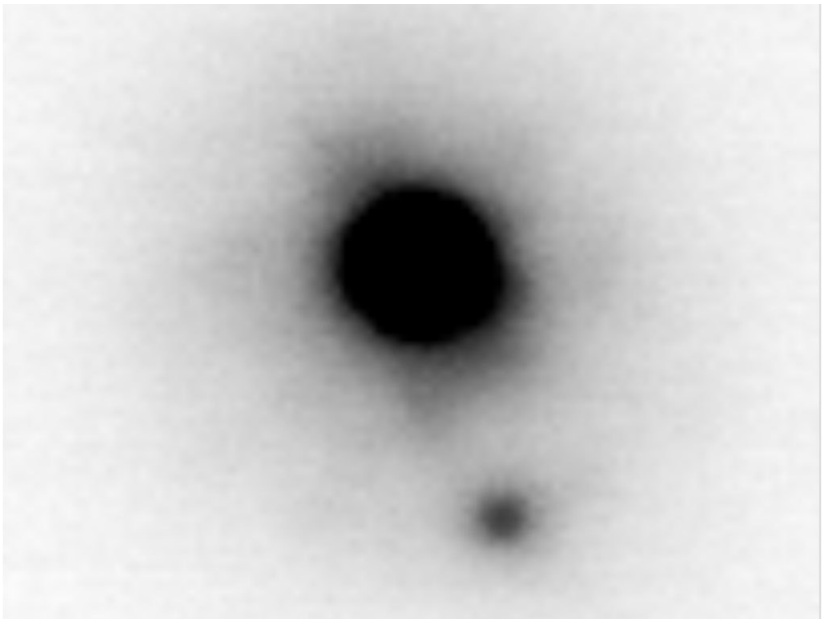

Figure 2.1 *J*-band high resolution image of 2MASS 1341−3052 obtained with Keck/NIRC2 using laser guide star adaptive optics (LGS-AO) by Dr. Adam Burgasser (priv. comm.). Its components are separated by 307 ± 15 mas or 8 AU, and their magnitude difference in *J* is 2.68±0.08 mag.

composed of M8.5 and T5 dwarfs, separated by 820 ± 120 AU (Burgasser et al. 2012). In addition to common proper motion, change in position angle can be detected from multi-epoch imaging, resulting in orbit characterization. Only ~ 20 ultracool dwarf binaries have fully characterized orbits (e.g. Dupuy & Liu 2011; Burgasser et al. 2016).

2.2.2 Radial Velocity Variability

The spectra of stars orbiting their common center of mass shifts towards shorter or longer wavelengths as the Doppler effect changes their radial velocity (RV) by approaching or moving away from the observer. Since this interaction is mediated by gravity, the shift will be more pronounced for small separations and larger component masses, as long as the orientation of the orbit is away from face-on. The main observable is the RV

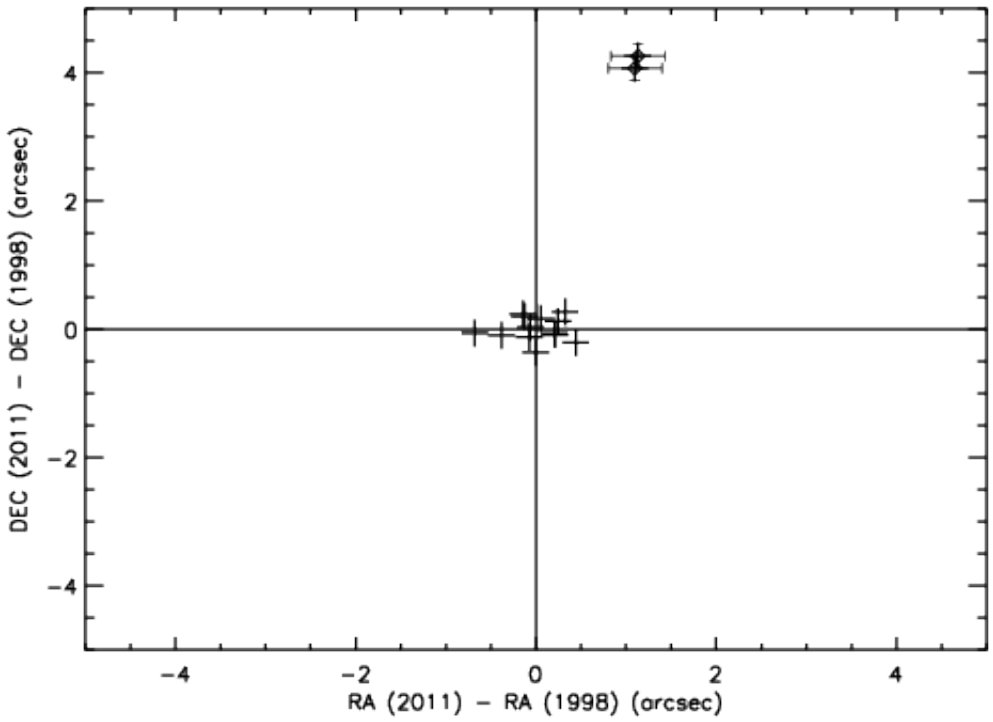

Figure 2.2 Common proper motion of M9 LP 704−48 (top) and the tight binary SDSS J0006−0852AB (top), composed of M8.5 and T5 dwarfs. Figure from Burgasser et al. (2012).

semi amplitude,

$$K_* = \sqrt{\frac{G}{1-e^2}}\, m_2 \sin i\, (m_1+m_2)^{-1/2} a^{-1/2} \tag{2.1}$$

where G is the gravitational constant, e is the orbit eccentricity, i is the orbit inclination, m_1 and m_2 are the component masses and a is the orbit semi-major axis (Lovis & Fischer 2010). For an average equal mass binary of 50 $M_{\rm Jup}$ components, separated by 1 AU, with close to circular eccentricity at $e = 0.3$ at a given inclination of $i = 45°$, we would find an RV semi-amplitude of 3.5 km s^{-1} , which can be easily detected with high resolution ($\Delta\lambda/\lambda$) spectroscopy. In addition to the five unknowns in the equation (m_1, m_2, e, i, a), we also need to know the epoch of observations, t, and the true anomaly, f, which is the angle between periastron (closest approach) and the position on the orbit from the

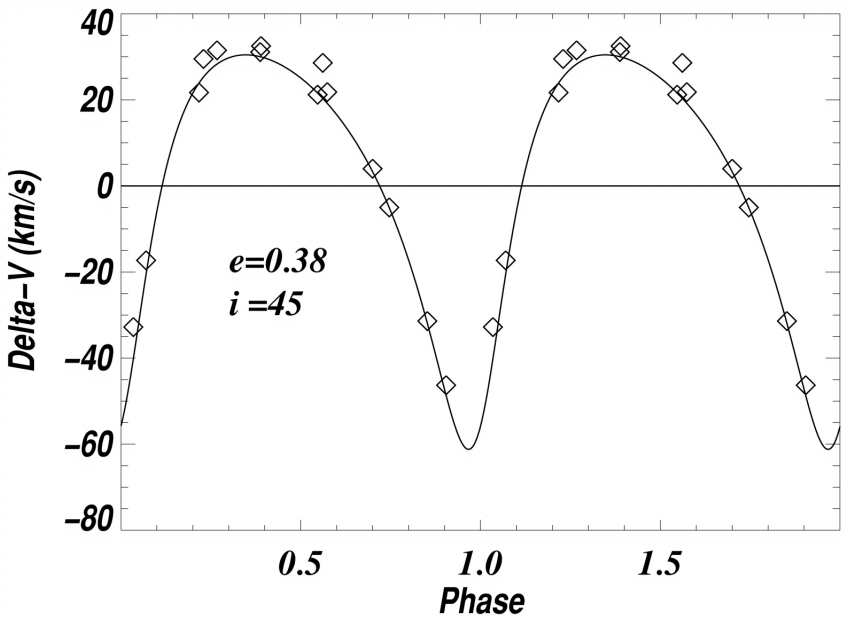

Figure 2.3 Solution to the orbit of PPl 15. Figure from Basri & Martín (1999).

center of mass frame. These seven parameters are needed to completely solve the orbit, otherwise masses are only expressed as a lower limit, function of sin *i*.

The first Pleiades brown dwarf identified by the presence of lithium in its optical spectrum, PPl 15 (Basri et al. 1995), was later established as the first brown dwarf spectroscopic binary (Basri & Martín 1999). Since then, high resolution spectroscopic surveys of ultracool dwarfs have uncovered about a dozen RV variables (e.g. Neuhäuser et al. 2000; Reid et al. 2002b; Guenther & Wuchterl 2003; Joergens et al. 2012; Zucker & Mazeh 2000). Sample sizes for high resolution spectroscopy tend to be small (e.g. 11 brown dwarfs in Chameleon; Joergens 2008) because of the high cost of telescope resources on repeated epochs, with the exception of the survey by Maxted et al. (2008) which obtained spectra of 218 ultracool dwarfs in σ-Orionis and λ-Orionis to find 11 binaries in the sample.

2.2.3 Astrometric Monitoring

Astrometry is the measurement of the coordinates and motions of stars over time. These motions include parallax, the apparent displacement of a source caused by Earth's orbit around the Sun; and proper motion, the apparent angular motion of a source with respect to background stars. A third motion occurs for binary systems as they orbit their center of mass, hence their components show periodic changes in coordinates. For binary systems with faint secondaries, where only the primary is discernible in images, wide-field imaging can detect motion of the center-of-light of the system over time.

This method is particularly suited for systems with low mass ratios and angular separations intermediate between those achievable by imaging and RV. This technique requires very high precision astrometry better than 1 mas and closer to $50-100$ microarcseconds for detecting planetary-mass companions to ultracool dwarfs (Lazorenko et al. 2009). The advanced technical requirements to execute this method result in small samples, the largest one targeting 20 low-mass dwarfs and finding one binary system (Sahlmann et al. 2014). Occasionally, systems are discovered through this technique in parallax surveys (e.g. SDSS J080531.84+481233.0; Dupuy & Liu 2012).

2.2.4 Microlensing

According to general relativity, mass curves spacetime. Light from a faraway source follows a straight path towards the observer, and will bend around a massive object following the curved spacetime (Einstein 1936). Microlensing events occur as the lens moves across the line of sight between the observer and the source.

The main observable of a microlensing event is the amplification of the brightness of the source over time, reaching a maximum at the closest angular approach between the lens and the source (Gould 2000). When the lens and source are perfectly aligned with

the observer, the light from the source is homogeneously magnified in an Einstein ring on the plane of the lens, whose radius is known as the Einstein radius. When the lens is a binary system, the light curve can show two peaks for each line-of-sight alignment with the source. Figure 2.4 shows an example of a microlensing event leading to the discovery of a brown dwarf binary.

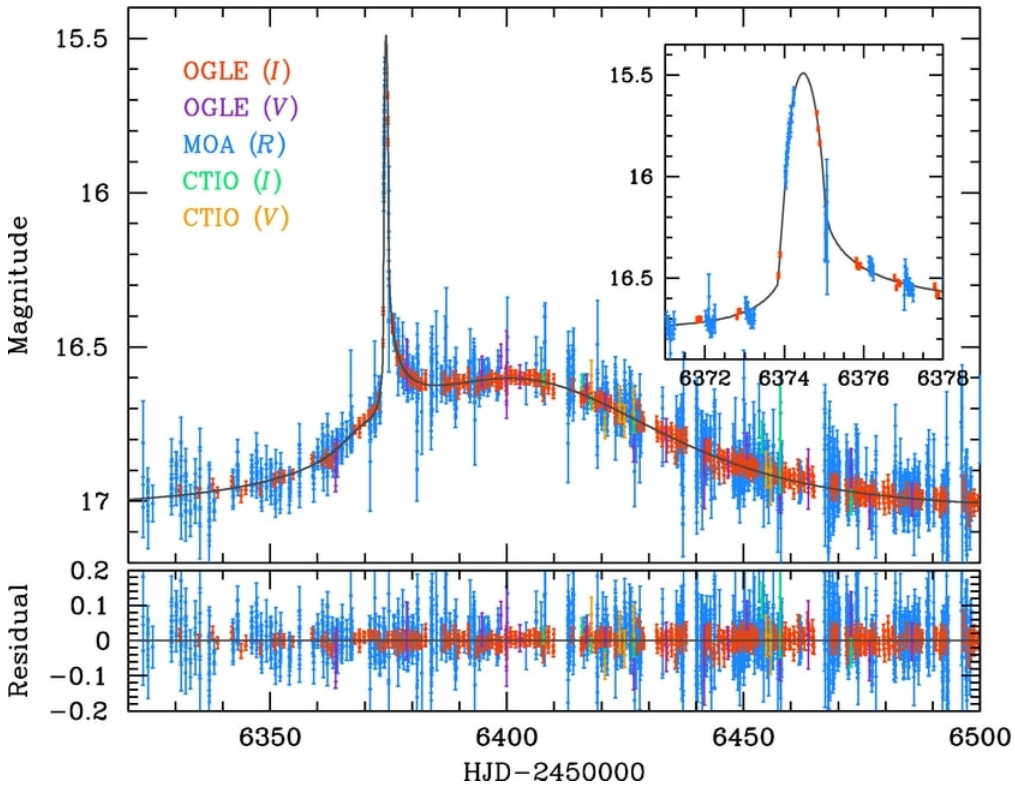

Figure 2.4 Light curve of the OGLE-2013-BLG-0102 microlensing event, with magnitude on the y-axis and heliocentric Julian date on the x-axis. The lens is a binary with a mass ratio of $q = 0.13$, with individual masses $M_1 = 0.096 \pm 0.013 M_\odot$ and $M_2 = 0.012 \pm 0.002 M_\odot$, right at the hydrogen and deuterium burning limits, respectively. The sharp peak corresponds to the lower-mass component passing in front of the source star. The lens is located at a distance of $d = 3.04 \pm 0.31$ kpc with a projected separation between components of 0.80 ± 0.08 AU. Figure from Jung et al. (2015).

Microlensing surveys usually point to dense stellar fields, such as the bulge of the galaxy, for the highest probability of events, as angular alignments need to be smaller than 1 *mas* on the plane of the sky for planetary-mass detections (Gaudi 2012). Microlensing

events are rare and only a handful of binary brown dwarfs have been discovered in this way (Bennett et al. 2008; Hwang et al. 2010; Choi et al. 2013).

2.2.5 Overluminosity in Color Magnitude Diagrams

Unresolved binary systems of near-equal brightness are outliers in absolute magnitude diagrams for a given spectral type or color. Single sources with measured parallaxes trace curves in spectral type- or color-absolute magnitude space (e.g. Looper et al. 2008a; Dupuy & Liu 2012; Faherty et al. 2016). Outliers to these empirical relations are too bright for a given spectral type or color, and could be unresolved binaries (e.g. 2MASS J11061197+2754225; Manjavacas et al. 2013). However, the outliers could be due to other factors such as unusually blue or red colors.

2.3 Statistical Properties of Multiple Systems

2.3.1 Binary fraction

The binary fraction is the number of binary systems as a fraction of the total number of systems, according to the following equation:

$$f_{bin} = \frac{B}{S+B} \tag{2.2}$$

where S and B are the number of single sources and binary systems, respectively (Reipurth & Zinnecker 1993).

Roughly $10-20\%$ of brown dwarfs are found in binary systems, including the first brown dwarf identified in the Pleiades, PPl 15 (Basri et al. 1995; Basri & Martín 1999). The flux-limited AO survey of Close et al. (2003) found 9 binaries in a sample of 39 very low mass stars with spectral types between M8−L0.5, all with $q > 0.7$, leading

to a binary fraction of $12 \pm 4\%$ after completeness corrections. Gizis et al. (2003) found 13 binary systems of M+L components in a sample of ~ 100 Hubble Space Telescope (HST) images, yielding a binary fraction of $15 \pm 5\%$ in the $1.6 - 16$ AU range, after correcting for completeness. Bouy et al. (2003) revised this value with HST images from a larger sample of 134 sources with spectral types later than M7, 26 of which are located within 20 pc. These authors determine a binary fraction of 15% for the 20 pc volume. On the T dwarf regime, Burgasser et al. (2003b) found 2 binaries in a sample of 10 T dwarfs imaged with HST, yielding a bias-corrected binary fraction of $9^{+15}_{-4}\%$. The resolved binary fraction is presumably a lower limit because of undetected, unresolved, closely-separated systems (Maxted & Jeffries 2005).

RV surveys provide a different perspective than imaging since they are sensitive to shorter binary separations. Reid et al. (2002b) ran a high resolution spectroscopic survey of 39 M6.5−L0.5 dwarfs, and found 2 double-lined binaries. Joergens (2008) surveyed the Chameleon I star-forming region and identified 2 binaries in a sample of 11 for a binary fraction of $10^{+18}_{-8}\%$. This study is the first one to close the gap in probed separations (earlier RV work sensitive to < 0.6 AU and imaging surveys sensitive to $> 3 - 10$ AU), and further suggest that direct imaging is not missing a significant fraction of binaries since their derived binary fraction is similar to those at larger separation ranges. However, their small sample is insufficient for generalized conclusions.

Only one astrometric variability survey has been attempted with the aim of finding planets around low mass stars. Sahlmann et al. (2014) followed up 20 M8−L2 dwarfs for 4 years with ~ 0.1 *mas* astrometric precision and found that DENIS J063001.4−184014 was in fact a binary with L1.5 and L4-L5 components in a 3-year orbit. Conversely, the overluminosity survey of Pinfield et al. (2003) finds $\sim 50\%$ of unresolved substellar binaries in the Pleiades cluster ($\tau = 115$ Myr; Basri et al. 1996). At later ages, Chappelle et al. (2005) finds a substellar binary fraction of $\sim 30\%$ in the Praesepe cluster ($\tau \approx$

500 Myr; Hambly et al. 1995). In summary, each observing technique is sensitive to different ranges of the separation distribution and therefore yields different binary fractions.

At wide separations ($\gtrsim 100$ AU), brown dwarf companions to stars have a $45^{+15}_{-13}\%$ chance of being in a binary systems themselves, thus making up a hierarchical triple system (Burgasser et al. 2005). This binary fraction is significantly higher than that of field brown dwarf binaries. Additionally, only a handful of very low mass triple systems with total masses $M_{tot} \lesssim 0.3\,M_{\odot}$ are known (e.g. Seifahrt et al. 2008; Stumpf et al. 2008; Burgasser et al. 2012). Very low mass wide binary and triple systems challenge ejection formation theories that rely on dynamics to restrict the mass of a forming brown dwarf, as these configurations are held together by small binding energies and could be easily disrupted.

2.3.2 Separation Distribution and Binding Energy

The separation distribution of ultracool dwarf binary systems peaks at 4 AU (Close et al. 2003), significantly closer than for main sequence stars. This peak may reveal a preferred binary formation scale, while the separations themselves are determined by the range of possible binding energies between the components of a binary system.

Figure 2.5 shows the projected separation distribution for all binary systems with primary masses below $\sim 0.1\,M_{\odot}$ reported in the literature and color-coded by detection method. This histogram shows a broad peak between $4-7$ AU, and the prevalence of direct imaging as a binary detection technique. Monte Carlo simulations by Maxted & Jeffries (2005) from RV surveys correctly constrain the separation distribution of very low mass stars and brown dwarfs.

For imaging techniques, the observable is the angular separation of the systems. Figure 2.6 shows the angular separation distribution of 120 ultracool binary systems. It

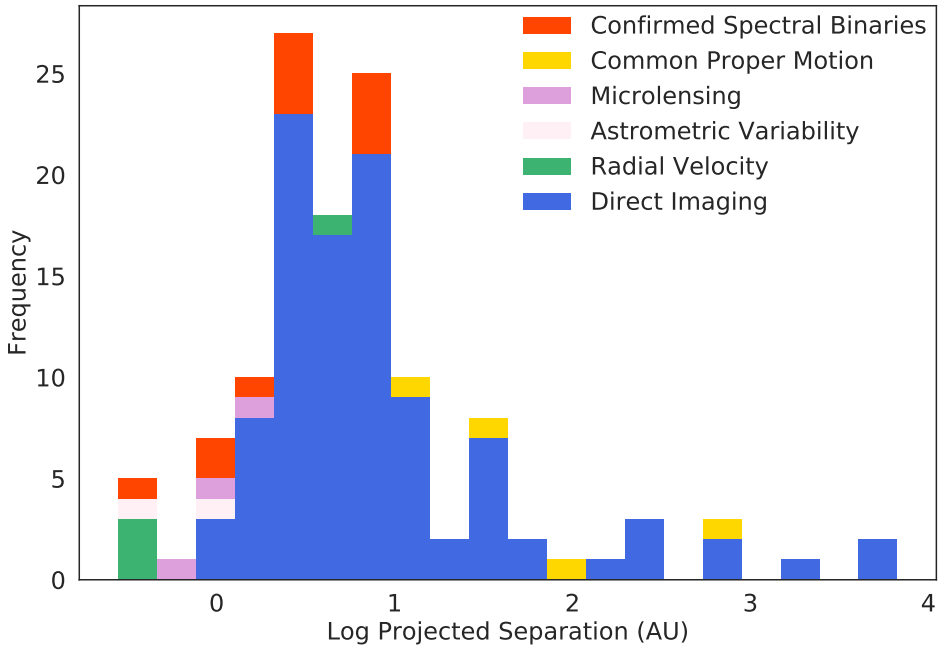

Figure 2.5 Projected separation distribution of ultracool binaries for which a separation has been measured (i.e. excludes RV variables lacking imaging follow-up).

is important to notice that there are no systems with angular separations smaller than $\sim 0\farcs05 - 0\farcs1$, and that angular separation is not a physical parameter, but it is dependent on the resolution of the telescope used. The lack of systems short-ward of $\sim 0\farcs05$ raises the question of completeness, and whether the true peak may lie at shorter separations than 4 AU. Radial velocity and astrometric monitoring are techniques more sensitive to small-separation systems, but their use requires a great deal of telescope resources.

Not only most ultracool binaries are separated by 4 AU, but there are extremely few examples separated by > 100 AU. The lack of observed wide ultracool binaries in both young clusters and field led Burgasser et al. (2003b) and Close et al. (2003) to suggest that wide binaries either do not form as such, or if they do, they get disrupted within 10 Myr, consistent with predictions from the ejection scenario. Through

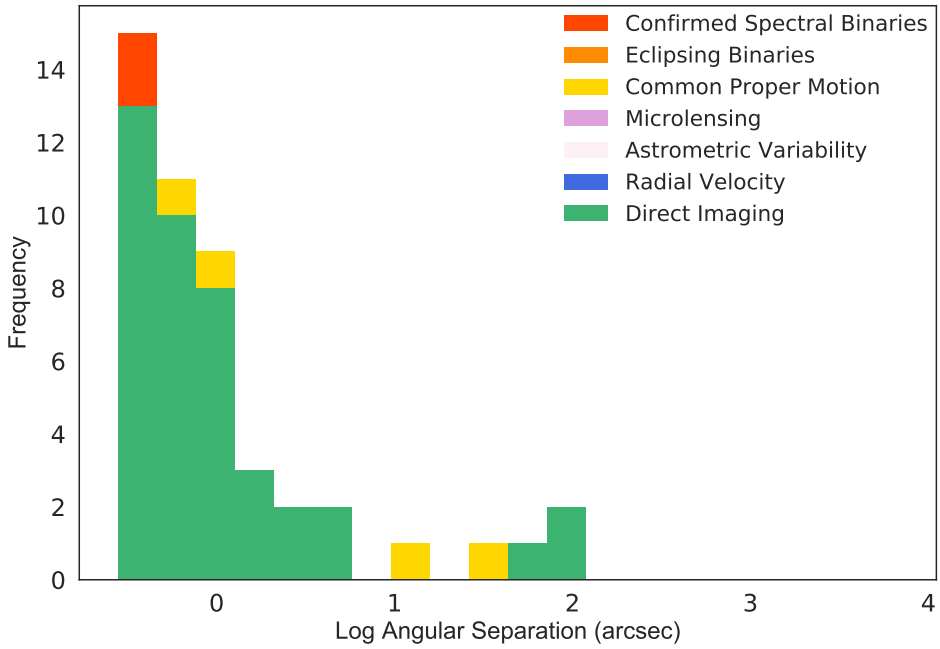

Figure 2.6 Angular separation distribution of ultracool binaries for which a separation has been measured (i.e. excludes RV variables lacking imaging follow-up).

ejection, wide ultracool binaries are very difficult to form, as they would likely get disrupted during ejection, and hardened once they are outside the gravitational field of the mini-cluster. However, the discovery by Luhman (2004b) of a low-mass binary in Chameleon (~ 2 Myr), separated by 240 AU counters the predictions of some ejection scenarios (Reipurth & Clarke 2001), but not others (Bate et al. 2003).

Close et al. (2003) found that the binding energy of VLM systems ($M_{tot} < 0.185\ M_{\odot}$) was 16 times larger than for main sequence binaries. Figure 2.7 shows the higher minimum in binding energy holding VLM binaries gravitationally bound, compared to more massive binaries. It is possible that these higher energies reflect the hardening of ejection processes.

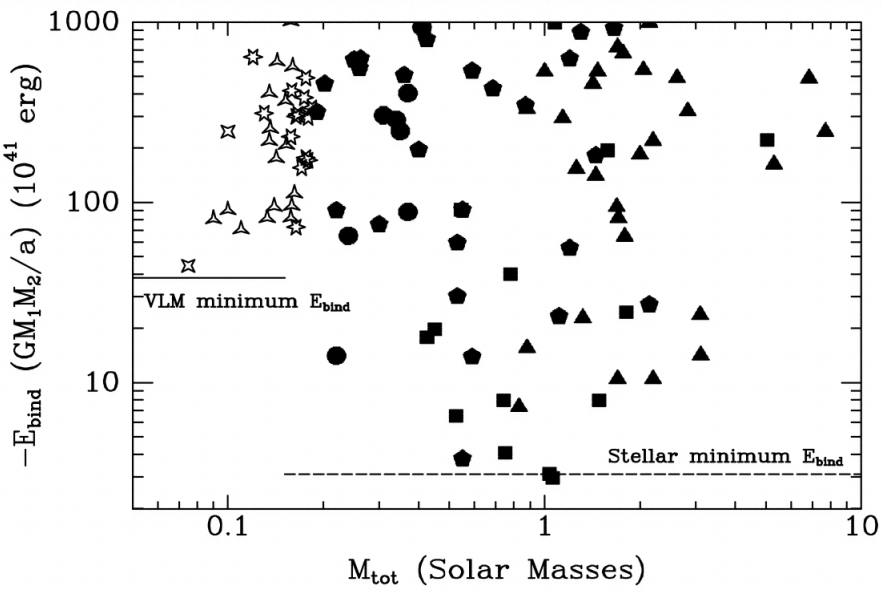

Figure 2.7 Binding energy as a function of total system mass for binary systems. 34 VLM binaries are plotted as open six-pointed stars for M dwarfs (Close et al. 2003), open triangles for L dwarfs (Koerner et al. 1999; Martin et al. 1999; Reid et al. 2001b; Bouy et al. 2003) and open four-pointed stars for T dwarfs (Burgasser et al. 2003b). Additionally, visual binaries in the M0-A0 range within 25 pc (Close et al. 1990) as shown as solid triangles. Low-mass binaries from the Hyades (Reid & Gizis 1997b) are drawn as solid circles, while low-mass field M-dwarfs (Reid & Gizis 1997a) are drawn as solid pentagons. Even the widest VLM binaries are ~ 16 times more strongly bound than main sequence binaries. Figure from Close et al. (2003).

2.3.3 Mass ratio distribution

Due to the mass-age-luminosity degeneracy, obtaining masses for brown dwarfs is a difficult task, so only a small fraction of brown dwarf binaries has measured masses (e.g. Konopacky et al. 2010; Dupuy & Liu 2017). For the rest of binaries, comparison to evolutionary models (e.g. Baraffe et al. 2003) and analytic relations (e.g. Burrows et al. 2001) are the only routes to a mass estimate. Most brown dwarf binaries have mass ratios close to unity, with $> 50\%$ of systems having a mass ratio $q > 0.9$ (Burgasser et al. 2007c).

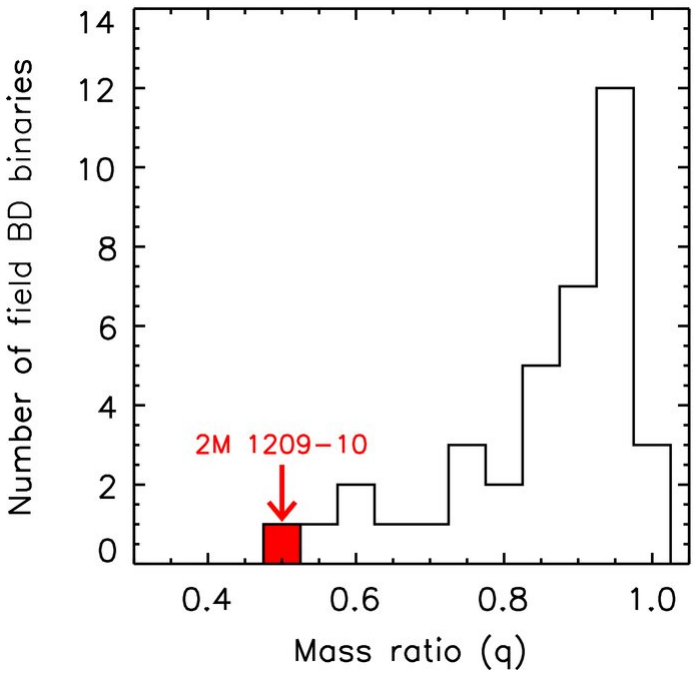

Figure 2.8 Mass ratio distribution of ultracool binaries. Figure from Liu et al. (2010).

A possible selection effect, also affecting the short end of the separation distribution, is the detectability of faint secondaries in low mass ratio systems through imaging or RV. On the other hand, wide-field surveys are more sensitive to equal brightness and equal mass systems. A few studies have tried to simulate the observed mass ratio distribution as a power law, q^{γ}. Allen (2007) found a power law index

2.3.4 Eccentricity distribution

The eccentricity of an orbit is a direct consequence of the dynamical history of a binary system. While separations, mass ratios and binary fractions can be studied with partial orbit information, the eccentricity distribution requires the full determination of the orbital parameters, which can only be done after repeated observations such that a relatively large fraction of the orbit is covered over time. These measurements are costly but extremely informative.

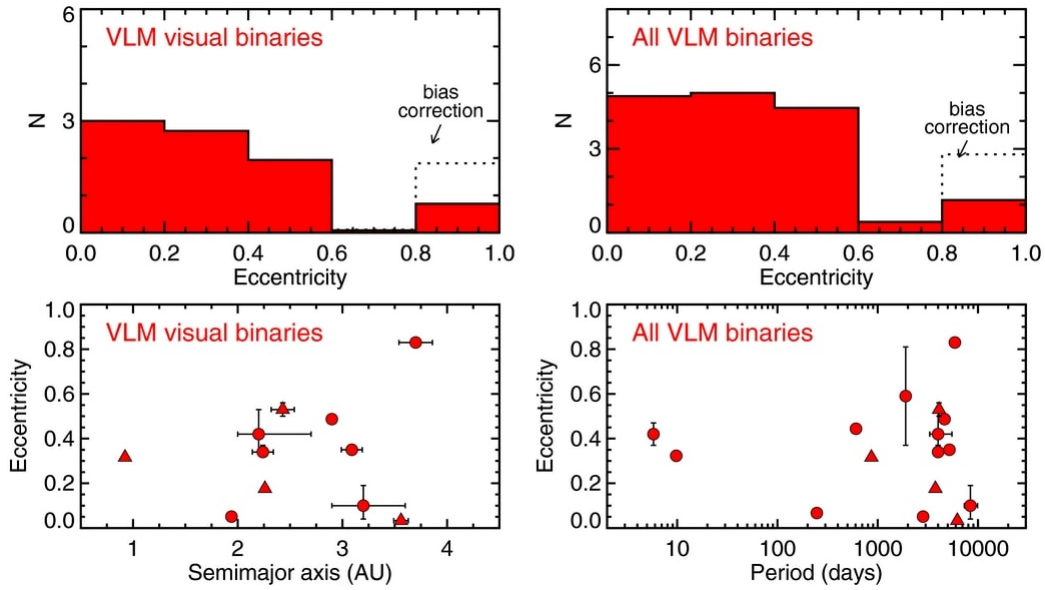

Figure 2.9 Eccentricity distribution of ultracool binaries. Figure from Dupuy & Liu (2011).

Dupuy & Liu (2011) combined eccentricities, semi-major axes and periods from 16 published very low mass binary orbits (Basri & Martín 1999; Stassun et al. 2006; Dahn et al. 2008; Seifahrt et al. 2008; Dupuy et al. 2009a; Blake et al. 2010; Dupuy et al. 2010; Dupuy 2010; Joergens et al. 2010; Konopacky et al. 2010) and performed a Monte Carlo simulation where they found that the eccentricity distribution covers the range $0.03 < e < 0.83$, and eccentricities below the mean and median of $e = 0.34$ are preferred, as seen in Figure 2.9.

This eccentricity distribution bears resemblance to that of Duquennoy & Mayor (1991) from a sample of solar-type binaries, thus suggesting similar formation mechanisms for stars and brown dwarfs. Nevertheless, Dupuy & Liu (2011) found no correlation between eccentricity and periods over 3 orders of magnitude (6 days$< P < 8 \times 10^3$ days) with a high confidence, which is opposite from observations of solar-type stars.

2.3.5 Binary Properties of Main Sequence Stars

The statistical properties of main sequence stars seem to follow a downward trend towards ultracool dwarfs according to primary masses. The binary fraction of O and B stars ($M \gtrsim 16\ M_\odot$) is close to $\sim 80\%$ (García & Mermilliod 2001), although sample sizes tend to be small since these stars are the most massive and short-lived. For A stars, the binary fraction is close to 50%, most binaries separated by 390 AU. Solar-type stars have a slightly lower binary fraction, $44 \pm 2\%$ with much smaller separations, peaking at 50 AU. The trend continues downward for M dwarfs whose binary fraction is $26 \pm 3\%$ at separations peaking at 16 AU. Finally, for VLM stars and brown dwarfs, the binary fraction is $\sim 10 - 20\%$ and the peak in the separation distribution is 4 AU (see Table 2.1). This downward trend with primary mass has served as evidence for a common formation mechanism between stars and brown dwarfs.

However, while the mass ratio distribution of main sequence binaries is uniform down to $q \sim 0.1$ for primary masses $M \gtrsim 0.3\ M_\odot$ (Reggiani & Meyer 2011), it is peaked towards equal masses for VLM stars and brown dwarfs (e.g. Bouy et al. 2003). Random pairing of binary components during formation as drawn from the IMF does not reproduce the observed mass ratio distribution of main sequence stars (Kouwenhoven et al. 2009; Reggiani & Meyer 2011).

Table 2.1 Binary Properties of Main Sequence Stars

Spectral Type	Mass Range ($M_\odot$)	Binary Fraction	Separation Peak (AU)	Reference
O	$\gtrsim 16$	82%, 100%	···	1, 2
B	$8-16$	74%	···	3
A	$1.5-5$	$\geq 50\%$	389	4, 5
FGK	$0.7-1.3$	$44\pm2\%$	50	6
M	$0.1-0.5$	$26\pm3\%$	16	7, 8, 9
VLM/BD	$0.01-0.1$	$22^{+6}_{-4}\%$	4	10, 11

References. — (1) García & Mermilliod (2001); (2) Mason et al. (1998a); (3) Verschueren et al. (1996); (4) De Rosa et al. (2012); (5) De Rosa et al. (2014); (6) Raghavan et al. (2010); (7) Bergfors et al. (2010); (8) Janson et al. (2012); (9) Delfosse et al. (2004); (10) Burgasser (2007a); (11) Thies & Kroupa (2007).

Note. — Table adapted from Duchêne et al. (2013) and Parker & Meyer (2014).

2.3.6 Multiplicity in Star-Forming Regions

Larson (1972) proposed the idea that all stars may be born in multiple systems and dynamical evolution reorganizes them into singles, binaries, triples and higher order systems. Observations of star-forming regions and young clusters seem to support this assertion at all masses (Reipurth et al. 2014). Pre-main sequence stars of A and B spectral types have binary fractions of $54\pm11\%$ (Baines et al. 2006). Kouwenhoven et al. (2007) compiled observations of pre-main sequence intermediate mass ($0.6-20M_\odot$) stars in the Upper Scorpius OB Association, yielding a binary fraction of $> 70\%$. Clearly the binary fraction of pre-main sequence stars is larger in star forming regions than in the field, supporting fragmentation theories and subsequent dynamical evolution.

For lower-mass stars, a high-resolution imaging survey directed by Kraus et al. (2011) in the Taurus-Auriga star-forming region, found a binary fraction of $\sim 60\%$ among $0.2-2.5\ M_\odot$ young stars, significantly higher than that found on the field. However, other star-forming regions like Chameleon I, Ophiucus and Upper Scorpius found lower binary fractions, in the order of $30\pm6\%$ (Lafrenière et al. 2008), $29\pm4\%$ (Ratzka et al. 2005) and $35\pm5\%$ (Kraus et al. 2008), respectively, suggesting that Taurus may be an outlier. However, these observations imply that star formation could occur differently

depending on the environment (Durisen & Sterzik 1994; Sterzik et al. 2003), and the evolution of multiple systems be affected by the stellar density in the cloud (Kroupa 1998; Kroupa & Bouvier 2003b). Dense star-forming regions like the Orion Nebula Cluster lack widely-separated young low-mass binary systems (Scally et al. 1999; Reipurth et al. 2007), whereas less dense ones like Taurus have a log-flat separation distribution in the $3-5000\,\mathrm{AU}$ range for $0.7-2.5\,M_{\odot}$ stars, meaning that there are more wide binaries composed of young stars than in the field (Kraus et al. 2011), again supporting the idea that dynamical interactions disrupt the lightly bound wide binaries during their evolution.

An earlier phase in the star formation process is the protobinary accretion, which will eventually determines the mass ratio. Young, intermediate mass binary systems in the Scorpius OB association show a preference for low mass ratio systems. For lower masses, the distribution increased towards unity mass ratios (Kraus et al. 2011; Kraus & Hillenbrand 2012), as seen in the field (e.g. Burgasser et al. 2007c).

2.4 Comparison to Formation Models

A crucial outcome of the star formation process is the assembly of objects into binary, triple, and higher order multiple systems. About $10-20\%$ of ultracool dwarfs are found in binary systems, down from $\sim 50\%$ for solar-type stars ($0.5-1.2\,M_{\odot}$; Raghavan et al. 2010; Duquennoy & Mayor 1991) and $26\pm3\%$ for M dwarfs ($0.1-0.5\,M_{\odot}$; Janson et al. 2012; Delfosse et al. 2004). Additionally, most ultracool binary systems have mass ratios close to unity (Burgasser et al. 2007c). However, the fraction of brown dwarf companions at small separations ($<5\,\mathrm{AU}$) to main sequence stars is minute (0.1% for primary masses $>0.5\,M_{\odot}$ within 3 AU; Marcy & Butler 2000), a shortage known as the "brown dwarf desert".

Ejection naturally explains the brown dwarf desert by the little chance that an

ejected low-mass object would remain gravitationally bound to one of the stars from the mini-cluster where it formed. Moreover, if the two lowest-mass objects are ejected, they can tighten into a closely-separated binary (Bate et al. 2002b). Disk fragmentation predicts a brown dwarf-brown dwarf binary fraction of 16% which is corroborated with observations. Turbulent fragmentation can produce wide binary systems (> 10 AU), but has difficulty forming close binaries, which could be a problem since most low-mass binaries are separated by ~ 4 AU (Close et al. 2003).

Radiation hydrodynamical simulations by Bate 2009, 2012 reproduce the binary fraction as a function of primary mass (Figure 2.10), except at low masses, where both simulations slightly underestimate the ultracool binary fraction: for the mass range $0.018 - 0.10 M_{\odot}$, Bate (2012) finds a binary fraction of 0.08 ± 0.05, twice as large as that one from Bate (2009).

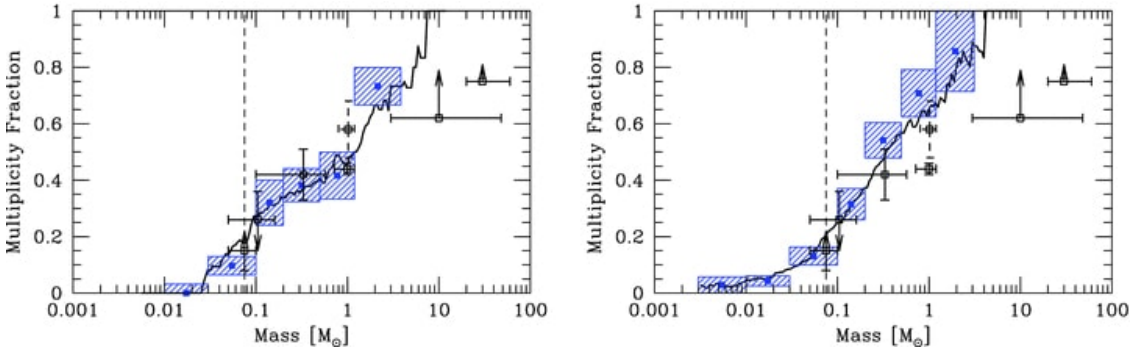

Figure 2.10 Multiplicity fraction as a function of primary mass for the hydrodynamical simulations of Bate (2012) (left) and Bate (2009) (right) compared against observations. The blue squares are the calculated multiplicity fractions from the simulations, and the solid lines are the continuous multiplicity fractions from a boxcar average. The black squares are the observed multiplicity fractions per mass bin from the surveys of Close et al. (2003), Basri & Reiners (2006), Fischer & Marcy (1992), Raghavan et al. (2010), Duquennoy & Mayor (1991), Preibisch et al. (1999), and Mason et al. (1998b) in order of ascending mass. The dashed line separates the stellar from substellar regime. Figure from Bate (2012).

2.5 Spectral Binary Technique

The peak in the projected separation distribution of ultracool binaries (see Figure 2.5) possibly points to a preferred formation scale. Measured at 4 AU, this peak coincides with the $0\farcs05 - 0\farcs1$ cutoff in the angular separation distribution (see Figure 2.6) at the typical distances achievable with ground-based AO[3]. Since most binaries have been identified as such by direct imaging, we need independent confirmation that the peak has a physical origin rather than the result of instrument detection limits. While radial velocity and astrometric variability are observational methods better suited to probe small binary separations (e.g. Joergens 2008; Sahlmann et al. 2014, see Section 2.2), both are resource-expensive as they require repeated measurements. An alternative method to identify and characterize unresolved binary systems is to search for spectral binaries: systems whose peculiar blended-light spectra shows features arising from both components. The highly structured spectra of low mass stars and brown dwarfs is filled with numerous absorption lines and bands that fully identify their spectral classes. When the secondary component is a T dwarf, its characteristic methane absorption bands superimposed on an otherwise typical late-M or L dwarf spectrum (acting as the primary component) generate a unique blended-light spectrum. The application of this method is independent of separation as long as both objects fit together in the spectrograph slit. Additionally, since this technique capitalizes on the identifying features of each component spectral type, it is best suited for unequal-mass binaries.

2.5.1 White dwarf/M dwarf spectral binaries

Prior to ultracool spectral binaries, this technique was applied to white dwarf/M dwarf pairs. This type of binary offers a unique look into stellar evolution. White dwarfs

[3]Limiting magnitudes are $K \sim 14$ for high resolution spectroscopy with Keck/NIRSPEC, corresponding to distances of 10 pc for the typical L5 dwarf ($M_K = 14$).

are the most common end stage for main sequence stars (Fontaine et al. 2001), and roughly half of the stars that become white dwarfs are found in binary systems (Fischer & Marcy 1992; Raghavan et al. 2010). Additionally, M dwarfs are the most plentiful stars in the galaxy (Bochanski et al. 2010). Over 2,000 white dwarf/M dwarf binaries have been reported in the literature (e.g Becklin & Zuckerman 1988; Heller et al. 2011).

White dwarfs and M dwarfs are very different objects. White dwarfs have $\sim 1.4\,M_{\odot}$ packed in a volume similar to that of Earth ($R_E \sim 0.01\,R_{\odot}$) at a temperature of $T_{eff} \sim 10,000$ K, while M dwarfs are low mass stars ($M \sim 0.1\,M_{\odot}$) with radii in the $0.08 - 0.6\,R_{\odot}$ range and effective temperatures $T_{\rm eff} \sim 3,000 - 4,000$ K (Reid & Hawley 2005). Their effective temperatures and pressures causes their luminosities to peak at different wavelengths and their spectral morphology to differ significantly, as seen in Figure 2.11.

2.5.2 Ultracool spectral binaries

Cruz et al. (2004) discovered a peculiar object while searching for late-M and L dwarfs in the solar neighborhood with 2MASS photometry. 2MASS J05185995−2828372 was selected for follow-up based on its red color, $J - K_s = 1.82$ mag. A near-infrared spectrum revealed an object with both L and T dwarf spectral features: carbon monoxide absorption at 2.3μm, consistent with an late-L dwarf; weak methane absorption at 2.2μm, typical of early-T dwarfs; strong methane and water absorption at $1.1 - 1.2\mu$m, and strong methane absorption at 1.6μm, characteristic of mid-T dwarfs. After exploring possible explanations due to youth, the L/T transition, and low metallicity, the authors conclude that the peculiarities are best reproduced by unresolved binarity. HST imaging later confirmed this binary as bona fide binary with L6 and T4 components separated by $0\farcs051 \pm 0\farcs012$ or 1.8 ± 0.5 AU (Burgasser et al. 2006c).

SDSS J080531.84+481233.0 was identified as a peculiar source from SDSS (Bur-

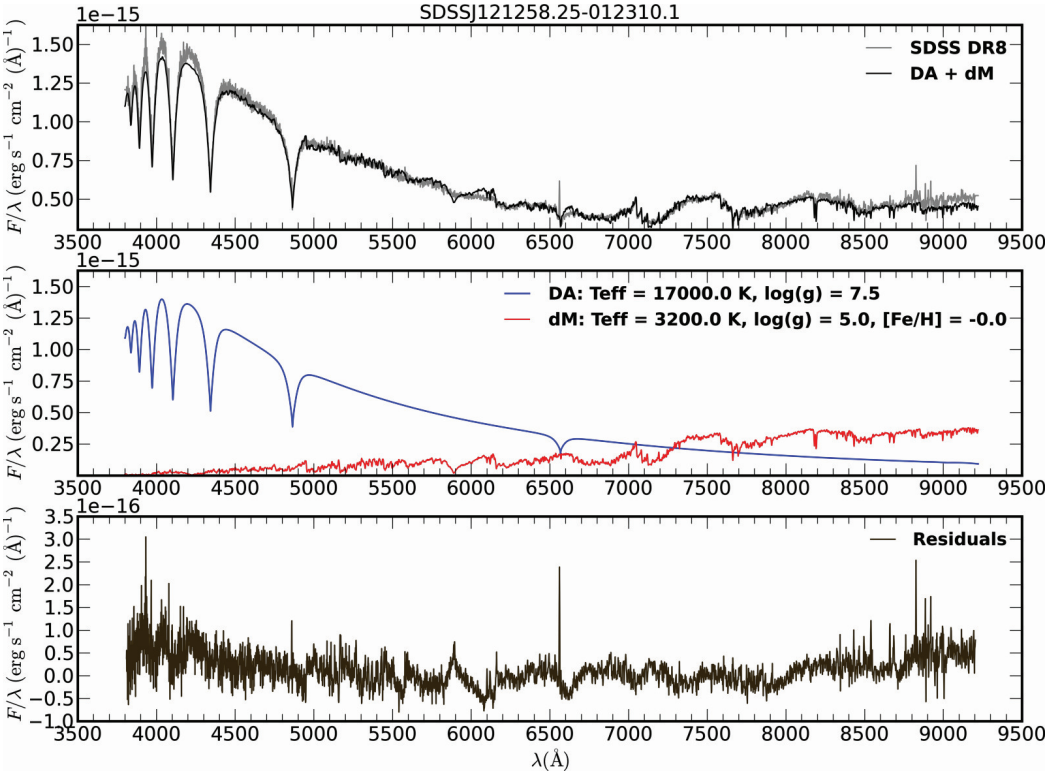

Figure 2.11 SDSS optical spectrum of a white dwarf/M dwarf spectral binary (top panel, black) compared to a binary model (top panel, gray). The template is generated by combining the two spectral models in the middle panel, one for the white dwarf and another for the M dwarf, correctly reproducing the observed spectrum. The negligible residuals are show in the bottom panel. Figure from Heller et al. (2011).

gasser 2007b) with highly discrepant optical and near infrared classifications: L4 (Hawley et al. 2002) and L9.5 $\pm$ 1.5 (Knapp et al. 2004; Chiu et al. 2006), respectively, and unusually blue colors for either classification ($J-K = 1.10 \pm 0.04$, compared to the average for L4, $\langle J-K \rangle = 1.52$, or L8-T0.5 dwarfs, $J-K = 1.58-1.74$; Vrba et al. 2004). The near infrared spectrum for this source shows strong FeH absorption at 0.99μm and deep Na I and K I absorption lines at $1.10-1.25\mu$m and no methane at 2.2μm, consistent with a mid-L classification, with simultaneous methane absorption at 1.6μm, characteristic of T dwarfs. Using near infrared spectra of 50 L and T dwarfs, the author generates over 1,000 binary templates to compare with the peculiar spectrum via a χ^2 minimization

routine, resulting in a L4.5 $\pm$ 0.7 and T5 $\pm$ 0.6 components. This source is both unusually blue and a binary system, as confirmed by astrometric monitoring and radial velocity variability (Dupuy & Liu 2012), with a 2-year orbital period (Burgasser et al. 2016).

A third serendipitous spectral binary was simultaneously found by Burgasser et al. (2008a) and Blake et al. (2008). 2MASS J03202839−0446358 also had discrepant optical and near infrared spectral types (M8: and L1, respectively). Low resolution, near infrared SpeX spectroscopy showed a subtle absorption feature at 1.6μm, resulting from overlapping FeH and CH_4 absorption from the M8.5 primary and T5 secondary, as suggested by binary template fitting Burgasser et al. (2008a). While LGS AO imaging was unable to resolve the faint secondary, Blake et al. (2008) reported this source as a single-lined spectroscopic binary from high resolution radial velocity measurements.

2.5.3 Systematic identification of L+T spectral binaries

Sparked by these examples, Burgasser et al. (2010a) devised a quantitative method to identify and characterize spectral binaries of L and T components from a sample of 189 near infrared SpeX[4] prism spectra of 178 sources. Their sample excludes sources from young clusters, subdwarfs and known binaries, except for six which they use as benchmarks. The SpeX spectra is classified with indices from Burgasser et al. (2006b) and the index/spectral type relations from Burgasser (2007a), while an additional spectral index is introduced to address the 1.6μm feature, summarized in Table 2.2. These eight spectral indices are compared against each other, leading to the identification of trends in six pairings where the known binaries clearly separated from the bulk, as shown in Figure 2.12. Candidate binaries were selected by satisfying two or more criteria. In order to characterize the binary candidates, their spectra was compared to single and binary

[4]SpeX is a near infrared spectrograph, which in low resolution ($\lambda/\Delta\lambda \approx 80-120$), prism mode covers wavelengths in the $0.9-2.5\mu$m range, and is mounted on the 3.0 m NASA Infrared Telescope Facility (IRTF; Rayner et al. 2003).

Table 2.2 Spectral Indices from Burgasser et al. (2010a)

Index	Numerator Range (μm)[a]	Denominator Range (μm)[a]	Feature	Reference
H_2O-J	$1.14-1.165$	$1.26-1.285$	$1.15\,\mu$m H_2O	1
CH_4-J	$1.315-1.34$	$1.26-1.285$	$1.32\,\mu$m CH_4	1
H_2O-H	$1.48-1.52$	$1.56-1.60$	$1.4\,\mu$m H_2O	1
CH_4-H	$1.635-1.675$	$1.56-1.60$	$1.65\,\mu$m CH_4	1
H_2O-K	$1.975-1.995$	$2.08-2.10$	$1.9\,\mu$m H_2O	1
CH_4-K	$2.215-2.255$	$2.08-2.12$	$2.2\,\mu$m CH_4	1
K/J	$2.060-2.10$	$1.25-1.29$	$J-K$ color	1
$H-$dip	$1.61-1.64$	$1.56-1.59+1.66-1.69$[b]	$1.65\,\mu$m CH_4[c]	2

References. — (1) Burgasser et al. (2006b); (2) Burgasser et al. (2010a).

[a]Wavelength range (in μm) over which flux density (f_λ) is integrated.

[b]Denominator is sum of these two wavelength ranges.

[c]Specifically, this index samples the sharp CH_4 feature present in the near-infrared spectra of the suspected L dwarf plus T dwarf binaries 2MASS J0805+4812 (Burgasser 2007b) and Kelu-1A (Stumpf et al. 2008).

templates from the SpeX sample by means of a χ^2 minimization routine, explained in detail in Chapter 3. This study identified 17 candidate binaries, 12 of which have been confirmed since then with high resolution imaging or RV variability.

The spectral binary candidacy of the T1.5 dwarf 2MASS J21392676+0220226 was ruled out by Radigan et al. (2012) in favor of photometric variability. Multi-epoch photometric monitoring of this source revealed a light curve with periodic variability ($P = 7.721 \pm 0.005$ hours) of an amplitude up to 26%, best reproduced by a patchy cloud layer or a continuous, thin cloud layer with cool clouds above it. The temperature differential between thin and thick patches is $175-425$ K. Photometric variability due to cloud patchiness is essentially the blend of two atmospheres so the spectrum effectively looks like that of a spectral binary. A systematic survey of photometric variability is needed to determine the frequency, prominence and weather of these sources.

The need for the spectral binary technique stems from the hypothesis that a large fraction of VLM binaries may be covert in closely-separated ($\rho \leq 2.6$ AU), unresolved systems, inaccessible by high resolution imaging (Maxted & Jeffries 2005). Simulations by Burgasser (2007a), assuming an exponential mass ratio distribution, predict a "binary

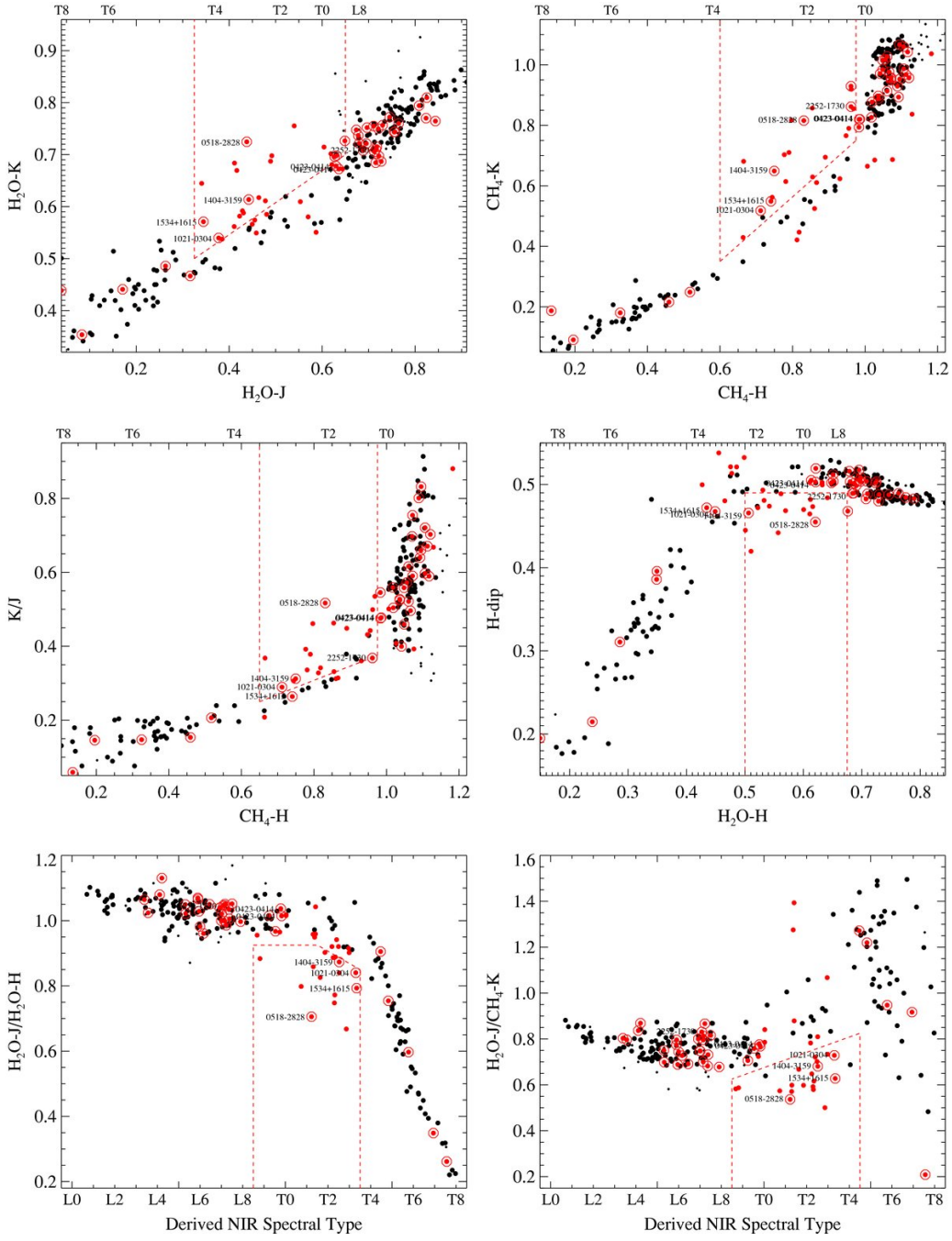

Figure 2.12 Spectral index selection criteria for L+T binary candidates. Sources from the spectral sample are shown as large black dots, known peculiar sources as small black dots, candidate binaries as red dots and confirmed binaries as encircled red dots. Regions of interest are demarcated with dashed red lines. Figure from Burgasser et al. (2010a).

excess" in the L/T transition (L7−T5), with a binary fraction as high as 40% compared to the underlying resolved binary fraction of 11^{+6}_{-3}%. This excess is possibly caused by the intrinsic flattening of the spectral type vs. absolute magnitude relation at the L/T transition, resulting in overluminous late-L+early-T binaries for their combined spectral type (typically an early-T classification).

2.5.4 Systematic identification of M+T spectral binaries

An extension to the Burgasser et al. (2010a) spectral binary technique was developed by Bardalez Gagliuffi et al. (2014) for binary systems composed of late-M/early-L plus T dwarfs. As aforementioned, M dwarfs are the most common stars in the galaxy (Bochanski et al. 2010), thus searching for faint companions to M dwarfs will result in a sizable sample. These objects are also brighter than L dwarfs, enabling a larger observable volume.

Binaries with M+T components are key probes of low-mass evolution, since the components straddle the hydrogen burning limit. Assuming coevality, masses above and below the hydrogen burning minimum mass are the only way to explain the large difference in spectral type, the M dwarf remaining stable for billions of years, while the secondary component has cooled down to T-type.

While the differences in morphology between late-M/early-L and T dwarf spectra are more pronounced than between late-L and T dwarfs, supposedly supporting an easier spectral binary identification, the larger flux difference in the former case makes the candidate selection more challenging as the T dwarf signatures subtly modify the spectrum of the primary. The most identifiable feature in the unresolved spectra of late-M plus T dwarfs is the superposition of FeH and CH_4 absorption features in the H-band, creating a "dip" at 1.62μm. The design of the M+T spectral binary technique is described in detail in the next chapter.

Chapter 3

SpeX Spectroscopy of Unresolved Very Low Mass Binaries

3.1 Introduction

Brown dwarfs are self-gravitating objects with physical and atmospheric properties intermediate between stars and planets. With masses below 0.075 $M_\odot$[1] (Kumar 1963; Hayashi & Nakano 1963), these objects cannot sustain hydrogen fusion, and hence cool and dim as they age, radiating primarily at infrared wavelengths. The evolution of their spectra spans the spectral classes M, L, T, and Y, with transitions demarcated by the appearance and disappearance of absorption lines and bands as molecules form and condense out of their atmospheres at different temperatures and pressures (Kirkpatrick 2005 and references therein).

Despite having a basic understanding of their evolution, brown dwarf formation remains an open question. Standard Jeans collapse of molecular clouds requires high densities so that gravity can overcome thermal pressure. Once the collapse has begun,

[1]Minimum mass for Hydrogen fusion may vary between 0.072-0.078 $M_\odot$ depending on age and metallicity. See Burrows et al. (1997b) for an extensive discussion of evolutionary models.

halting the accretion becomes problematic (Shu et al. 1987). Several mechanisms have been proposed to resolve this issue, including turbulent fragmentation of protostellar clouds (Padoan & Nordlund 2002), fragmentation of pre stellar disks (Stamatellos & Whitworth 2009b), ejection by dynamical interactions with other protostars (Reipurth & Clarke 2001), and photoerosion of prestellar cores (Whitworth & Zinnecker 2004). In principle, these formation mechanisms should leave traces on the statistical properties of brown dwarfs, including the occurrence of multiple systems and distributions of their separation, relative masses and eccentricity.

Observationally, it has been shown that multiplicity increases with primary mass, even at the lower mass end of the main sequence, with the G dwarf binary fraction being 57% higher than that for M dwarfs (Fischer & Marcy 1992; Delgado-Donate et al. 2004). Current estimates of the binary fraction of very low mass (VLM) late-M to T dwarfs (VLM $M_{total} < 0.1\ M_{\odot}$) are $20-25\%$, with a peak in separation at $\sim$ 4 AU and a mass ratio distribution peaking at nearly equal masses (Bouy et al. 2003; Close et al. 2003; Burgasser et al. 2006c; Allen 2007; Kraus & Hillenbrand 2012). However, these multiplicity statistics have been largely determined from resolved imaging programs, sampling separations greater than 3 AU. Burgasser et al. (2007c) pointed out that the current peak in the binary angular separation distribution is coincident with the resolution limit of HST and ground-based adaptive optics (AO) imaging, indicating that tight ($<$ 1AU) VLM binaries could be undercounted. Likewise, Pinfield et al. (2003) and Chappelle et al. (2005) report a higher unresolved binary fraction ($30-50\%$) based on overluminous binary candidates in color-magnitude plots. Conversely, spectroscopic radial velocity (RV) studies find binary fractions of 2.5% in systems separated by $<$ 1 AU (Blake et al. 2010) and $2-28\%$ up to 3 AU (Joergens 2008). For the 0-6 AU range, Basri & Reiners (2006) estimate a binary fraction of $26\% \pm 10\%$. However, the difficulty of obtaining high resolution spectra of faint VLM dwarfs results in small sample

size. Since total binary fractions for VLM stars and brown dwarfs could range between $2-50\%$, it is imperative to constrain this statistic to make conclusions about brown dwarf formation.

An alternative method for detecting tight unresolved binaries, developed by Burgasser (2007a), involves identifying blended light pairs, or spectral binaries. We will refer as *spectral* binaries to those objects whose combined-light spectrum shows distinct peculiarities that come from the highly structured spectra of single M, L and T dwarfs when blended together, as opposed to *spectroscopic* binaries which are binaries that show RV variations. The first brown dwarf spectral binary, 2MASS J05185995−2828372, was serendipitously identified by Cruz et al. (2004) based on its hybrid characteristics containing features of both L and T dwarfs. The superposition of L plus T dwarf spectra proved to be the simplest model of its peculiar spectrum and it was later resolved as a binary using the Hubble Space Telescope (Burgasser et al. 2006c). The unusually blue L dwarf SDSS J080531.84+481233.0 was next identified as a spectral binary with L4.5 and T5 components by Burgasser (2007b), based on a peculiar methane absorption band starting at 1.60 μm, and was later confirmed as an astrometric variable by Dupuy & Liu (2012). A third system, 2MASS J03202839−0446358, was concurrently identified as an unresolved M9+T5 spectral binary (Burgasser et al. 2008a) and a RV variable with an orbital period of eight months (Blake et al. 2008). These examples serve to illustrate how spectral binaries can encompass a broad range of system architectures. To date, 34 VLM spectral binaries and candidates have been reported (see Table 5.9), and ten have been confirmed by direct imaging, over luminosity, RV or astrometric variability (Burgasser et al. 2011a; Stumpf et al. 2011; Burgasser et al. 2012; Dupuy & Liu 2012; Faherty et al. 2012; Manjavacas et al. 2013; Gelino et al. in prep).

Table 3.1 Compilation of confirmed and candidate spectral binaries discovered to date

Name	Spectral Type				J mag	$J-K_s$	ΔJ	Separation[a] (AU)	Confirmation[b] method	Ref. SB; Conf.
	Optical	NIR	Primary	Secondary						
SDSS J000649.16−085246.3[c,d]	M9	···	M8.5±0.5	T5±1	14.14±0.04	1.01±0.05	3.15±0.31	0.29±0.01	RV	2; 2
ULAS J004757.41+154641.4	···	T2.0±2.0	L8.0	T7.0	17.83±0.05	1.41±0.07	···	< 65	···	22
2MASS J00521232+0012172	L5	···	L4	T3	16.36±0.11	0.90±0.19	···	<49	···	24
SDSS J011912.22+240331.6	···	T2	T0±0.7	T4±0.4	17.02±0.18	<-0.02	-0.42±0.19	<43	···	21
ULAS J020529.62+142114.0	···	T1.0±0.5	T1.0	T3.0	17.99±0.04	1.06±0.07	···	<71		22
2MASS J02060879+22355930	···	L5.5	L5.1±0.5	T3.2±2.3	16.56±0.11	1.39±0.17	1.61±0.89	···	···	26
2MASS J02361794+0048548	L6.5	···	L5.0±0.6	T1.9±1.1	16.10±0.08	1.43±0.12	1.05±0.48	<48	···	26
SDSS J024749.90−163112.6	···	T2.0±1.5	T0±0.2	T7±0.3	17.19±0.18	1.57±0.27	0.68±0.10	<36	···	21
2MASS J03202839−0446358[c,d]	M8:	L1	M8.5±0.3	T5±0.9	12.13±0.03	1.13±0.04	3.5±0.2	<0.58	RV	5; 1
SDSS J035104.37+481046.8	···	T1.0±1.5	L6.5±0.7	T5±0.7	16.47±0.13	1.47±0.18	0.31±0.31	<34	···	21
DENIS-P J04272708−1127143	···	dM7	M7.4±0.2	T5.1±1.5	13.74	0.99±0.14	4.13±0.62	···	···	26
2MASS J05185995−2828372[d]	···	···	L6	T4	15.98±0.10	1.82±0.12	0.13±0.19	1.80±0.50	DI	10; 7
2MASS J07354882+2720167	L1	···	L1	L4	16.94±0.13	1.28±0.21	···	<112	···	23
SDSS J080531.84+481233.0[c,d]	L4	L9.5	L4.5	T5	14.73±0.04	1.46±0.05	1.50±0.09	0.9−2.3	AV	6; 11
SDSS J090900.73+652527.2	···	T1.5	T1.5±0.5	T2.5±0.3	16.03±0.09	0.86±0.17	−0.12 ± 0.10	<29	···	21
SDSS J092615.38+584720.9	T4.5	···	T3	T6	16.77±0.14	< 1.57	0.4±0.2 [e]	2.6±0.5	DI	16; 7, 8
SDSS J093113.23+280227.1	L3	···	L1.4±0.1	T2.6±0.9	14.98±0.04	1.25±0.06	2.22±0.23	<37	···	26
2MASS J09490860−1545485	···	T2	T1±0.2	T2±0.2	16.15±0.12	0.92±0.20	−0.07±0.05	<25	···	21

Table 3.1 Continued

Name	Spectral Type				J mag	$J-K_s$	ΔJ	Separation[a] (AU)	Confirmation[b] method	Ref. SB; Conf.
	Optical	NIR	Primary	Secondary						
2MASS J10365305−3441380	L6	···	L5.2±0.4	T1.4±0.4	15.62±0.05	1.82±0.06	0.51±0.32	<30	···	26
SDSS J103931.35+325625.5	···	T1	L7±0.2	T4±0.2	16.41±0.15	1.25±0.22	0.26±0.09	<34	···	21
2MASS J10595138−2113082	L1	···	L0.6±0.4	T3.4±1.3	14.56±0.04	1.35±0.06	2.58±0.32	<52.5	···	26
2MASS J11061197+2754225[d]	···	T2.5	T0±0.2	T4.5±0.2	14.82±0.04	1.02±0.07	-0.37±0.06	<2.67	OL	4, 14; 15
SDSS J120747.17+024424.8	L8	T0	L6.5±0.7	T2.5±0.5	15.58±0.07	1.59±0.09	0.48±0.28	<17	···	21
2MASS J12144089+6316434	···	T3.5	T2	T6	16.59±0.12	0.71±0.26	···	<24	···	24
2MASS J13114227+3629235	L5pec	···	L4.8±0.6	T4.1±2.7	15.54±0.05	1.40±0.09	2.19±1.02	<27	···	27
2MASS J13153094−2649513[c,d]	L5	···	L3.5±2.5	T7±0.6	15.07±0.05	1.63±0.07	3.03±0.03	6.60±0.90	DI	3; 3
2MASS J13243559+6358284	···	T2:	L8±0.2	T3.5±0.2	15.60±0.07	1.54±0.09	−0.05±0.06	<23	···	21,2 4
2MASS J13411160−30525049	L3	···	L1.2±0.3	T6.3±1.0	14.61±0.03	1.53±0.04	3.28±0.53	<39	···	26
SDSS J141530.05+572428.7	···	T3±1	L8±0.5	T5±0.3	16.73±0.16	< 1.19	−0.13±0.20	<29	···	21
SDSS J142227.20+221557.5	L6.5	···	L4.2±0.6	T4.1±2.3	16.87±0.03	1.23±0.04	2.36±0.78	<43	···	26
2MASS J14232186+6154005	L4	···	L2	L5	16.63±0.15	1.35±0.2	···	···	···	23
SDSS J143553.25+112948.6	···	T2±1	L7.5±0.4	T6±0.3	17.14±0.23	< 0.23	0.41±0.12	<39	···	21
SDSS J143945.86+304220.6	···	T2.5	T1±0.2	T5±0.6	17.22±0.23	< 1.34	0.06±0.24	<45	···	21
2MASS J14532589+1420418	L1	···	L1.1±0.0	T6.0±1.1	15.07±0.04	1.18±0.05	3.27±0.46	<72	···	26
SDSS J151114.66+060742.9[†]	···	T0±2	L5.5±0.8	T5±0.4	16.02±0.08	1.47±0.13	0.54±0.32	<21	OL	4; 12
SDSS J151603.03+025928.9	···	T0:	L7.5±1.1	T2.5±2.2	17.23±0.20	1.80±0.27	0.30±0.65	<27	···	21, 24

Table 3.1 Continued

Name	Spectral Type				J mag	$J-K_s$	ΔJ	Separation[a] (AU)	Confirmation[b] method	Ref. SB; Conf.
	Optical	NIR	Primary	Secondary						
WISE J16235970−0508114	···	L1	L0.6±0.3	T6.0±0.8	14.94±0.04	1.39±0.06	3.39±0.40	···	···	26
2MASS J17072529−0138093	···	···	L0.7±0.5	T4.3±2.0	14.29±0.03	1.22±0.04	2.87±0.75	<31	···	26
2MASSI J17114573+2232044	L6.5	···	L1.5±0.6	T2.5±1.0	17.09±0.18	2.36±0.20	1.20±0.40	<35	···	21
2MASS J17310140+5310476	L6	···	L5	L8	16.37±0.11	1.52±0.18	···	<48	···	23,24
2MASS J17373467+5953434	L9	···	L5	T5	16.88±0.16	1.16±0.31	···	<50	···	23
2MASS J20261584−2943124	L1:	···	L0.1±0.5	T5.8±1.0	14.80±0.03	1.44±0.05	3.42±0.40	<9.00	DI	13
SDSS J205235.31−160929.8[d]	···	T1±1	L7.5±0.6	T2±0.2	16.33±0.12	1.21±0.19	0.04±0.18	3.20±0.50	DI	4; 17
2MASS J21265916+7617440	L7	T0	L7	T3.5	14.34±0.03	1.18±0.05	···	···	···	28
2MASS J21392676+0220226	···	T1.5	L8.5±0.7	T3.5±1.0	15.26±0.05	1.68±0.07	−0.14±0.21	<14	···	21
ULAS J222958.30+010217.2	···	T3.0±0.5	T1.0	T5.0	17.89±0.04	0.67±0.10	···	<62	···	22
ULAS J223348.82+002214.0	···	T0.0±0.5	L5.0	T4.0	18.07±0.05	1.43±0.07	···	<90	···	22
ULAS J235618.01+075420.4	···	T0.0±1.0	L7.0	T7.0	18.09±0.05	1.87±0.06	···	<58	···	22
ULAS J232315.39+071931.0	···	T2.0±0.5	T0.0	T2.0	17.30±0.02	1.01±0.04	···	<49	···	22
Kelu−1A	L3pec±1.5	L2.0±1.0	L0.5±0.5	T7.5±1	13.88±0.03	1.57±0.04	···	$6.4^{+2.4}_{-1.3}$	···	25

[a]Upper limits based on SDSS angular resolution (1″; York et al. 2000) and distance reported or estimated from absolute magnitudes (Looper et al. 2008a).

[b]RV = Radial Velocity, DI = Direct Imaging, AV = Astrometric Variability, OL = Overluminous.

[c]Used as M+T binary benchmark.

[d]Spectral binaries with confirmed separations. See figure 3.9.

[e]Estimated from F110W filter (Burgasser et al. 2006c).

References. — (1) Blake et al. (2008); (2) Burgasser et al. (2012); (3) Burgasser et al. (2011b); (4) Burgasser et al. (2010a); (5) Burgasser et al. (2008a); (6) Burgasser (2007b); (7) Burgasser et al. (2006c); (8) Carson et al. (2011); (9) Chiu et al. (2006); (10) Cruz et al. (2004); (11) Dupuy & Liu (2012); (12) Faherty et al. (2012); (13) Gelino & Burgasser (2010); (14) Looper et al. (2008a); (15) Manjavacas et al. (2013); (16) Metchev et al. (2008); (17) Stumpf et al. (2011);(21) Burgasser et al. (2010a); (22) Day-Jones et al. (2013); (23) Geißler et al. (2011); (24) Metchev et al. (2008); (25) Stumpf et al. (2008); (26) This paper; (27) Kirkpatrick et al. (2011); (28) Kirkpatrick et al. (2010).

Detecting binaries using the spectral binary method is particularly useful for multiplicity statistics, as the method is independent of separation within $0\farcs5$, which translates to $<$10-20 AU for field brown dwarfs at distances of 20-40 pc. The closest separation pairs can be followed-up to measure orbits and component masses, as well as infer ages by comparison to evolutionary models (Burgasser & Blake 2009). Systems with independent age constraints can also be used to test the evolutionary models directly (Dupuy et al. 2009b; Liu et al. 2010; Burgasser et al. 2011a). Finally, spectral binaries with late-M/early-L primaries and T dwarf secondaries can straddle the hydrogen burning limit, thus giving additional insight into brown dwarf evolution.

In this paper we adapt the technique of Burgasser et al. (2010a) to search for spectral binaries composed of late-M or early-L dwarf primaries with T dwarf secondaries. M dwarfs are the most common stars in the galaxy (Bochanski et al. 2010), and are the brightest VLM objects, enabling better statistics through larger magnitude-limited search volumes and sample sizes. M-dwarf spectra are also intrinsically distinct from T-dwarf spectra, but differ in brightness by several magnitudes, rendering peculiar features extremely subtle. In Section 3.2 we describe our spectral sample used to find spectral binaries, drawn from the SpeX Prism Libraries and new observations. In Section 3.3 we explain our two methods to identify spectral binary candidates: by visual examination (Section 3.3.1) and through spectral indices (Section 3.3.2). In Section 3.3.3, we perform single and binary template fitting to identify fourteen binary candidates. In Section 3.4, we describe the properties of the candidates. In Section 3.5.1 and Section 3.5.2, we discuss our major contaminant, blue L dwarfs, and show preliminary evidence that the separations of spectral binaries are tighter than the resolved population. Our results are summarized in Section 3.6.

3.2 SpeX Spectral Sample

The SpeX Prism Library is composed of low resolution ($\lambda/\Delta\lambda = 75-120$) spectra acquired with the SpeX $0.8-2.5$ μm spectrograph, mounted on the 3.0 m NASA Infrared Telescope Facility (IRTF), located in Mauna Kea, Hawaii (Rayner et al. 2003). All spectra were obtained using the prism-dispersed SpeX mode, which continuously samples wavelengths between $0.75-2.5$ μm at a dispersion of $20-30$ Å pixel^{-1}. The library includes close to 2,000 sources, both previously published data[2] and 530 new spectra acquired between November 2000 and December 2013 (Table 3.2). The new observations were obtained with the $0\farcs5$ or $0\farcs7$ slit, generally aligned with the parallactic angle. Total integration times ranged between 360 s and 1200 s, depending on source brightness and atmospheric conditions, and were obtained in an ABBA dither patter along the slit. Spectra of nearby A0 V stars were used to flux calibrate the raw spectra and correct for telluric absorption. Internal flat fields and argon arc lamps were observed with each flux standard for pixel response and wavelength calibration. All data were reduced with the SpeXtool package (Cushing et al. 2004; Vacca et al. 2003) using standard settings. A detailed description of our reduction procedures is given in Burgasser (2007b).

[2] e.g. Burgasser et al. (2010a); Chiu et al. (2006); Cruz et al. (2003).

Table 3.2 New SpeX Observations of M7−L6 Dwarfs

Source	Designation	Spectral Type			2MASS		Date	λ/Δλ	Ref[b]
		Opt	NIR	SpeX[a]	*J*	*J*-K_s			
2MASS J0000286−124515	J00002867−1245153	M8.5	···	M9.2	13.20	1.23	2013 Aug 14	120	44; 44
LEHPM 1−162	J00054768−2157176	M8.5	M8	M8.7	13.27	1.07	2006 Sep 03	120	32; 75
2MASSI J0006205−172051	J00062050−1720506	L2.5	···	L3.0	15.66	1.65	2008 Sep 08	120	25; 25
SDSS J000632.60+140606.4	J00063260+1406064	L1	···	L0.4	15.85	0.79	2009 Jun 30	120	48; 48
SDSS J000646.81+151225.8	J00064681+1512258	L4::	···	L4.3	16.22	1.41	2013 Sep 03	120	62; 62
2MASS J0007078−245804	J00070787−2458042	M7	···	M7.7	13.12	1.05	2013 Oct 23	120	44; 44
2MASS J00100009−2031122	J00100009−2031122	L0	···	M8.8:	14.13	1.25	2008 Jul 14	120	44; 44
2MASSI J0013578−223520	J00135779−2235200	L4	···	L5.7	15.78	1.74	2009 Nov 04	120	25; 25
2MASSW J0015447+351603	J00154476+3516026	L2	···	L1.0	13.88	1.61	2008 Sep 08	120	13; 13
SDSS J001608.44−004302.3	J00160843−00430209	···	L5.5	L4.3	16.33	1.78	2013 Sep 03	120	34; 34
SDSS J001637.62−103911.2	J00163762−1039112	L0	···	M8.9	15.46	0.92	2009 Nov 04	120	48; 48
SDSS J001911.65+003017.8	J00191165+0030176	L1	···	L0.4	14.92	1.35	2009 Nov 07	120	20; 20
DENIS−P J0020.9−4414	J00205982−4414340	M8V	···	M9.4	14.90	1.19	2007 Nov 10	120	6; 6
LEHPM 1−494B	J00210589−4244433	M9.5	···	L0.6:	13.52	1.22	2006 Aug 28	120	6; 15
SDSS J00220934−0110397	J00220934−0110397	L0	···	M8.9	15.82	1.12	2012 Sep 27	120	60; 60
BRI 0021−0214	J00242514−0158166	M9.5	···	L0.6	11.99	1.45	2007 Jul 04	120	80; 44
···	···	···	···	···	···	···	··· 2008 Jul 14	120	80; 44
LHS 1074	J00255117−0748069	sdM6	···	M7.9	14.68	0.81	2004 Sep 08	120	··· ; 39

Table 3.2 Continued

Source	Designation	Spectral Type			2MASS		Date	$\lambda/\Delta\lambda$	Ref[b]
		Opt	NIR	SpeX[a]	J	J-K_s			
LEHPM 1−606	J00271049−1813083	···	M8	M7.5	13.45	1.02	2006 Sep 03	120	32; 75
2MASSI J0028394+150141	J00283943+1501418	L4.5	L3	L6.1:	16.51	1.95	2009 Dec 07	120	13; 13, 34
2MASS J00285545−1927165	J00285545−1927165	L0:	···	L0.7	14.19	1.35	2009 Nov 04	120	49; 49
2MASSW J0030438+313932	J00304384+3139321	L2	···	L3.2	15.48	1.45	2008 Sep 08	120	11; 11
SIPS J0031−3840	J00311925−3840356	L2.5	L2	L1.2	14.10	1.18	2006 Aug 28	120	36; 59, 36
2MASS J00320509+0219017	J00320509+0219017	L1.5	M9	L0.4	14.32	1.52	2009 Jun 30	120	49; 49, 30
···	···	···	···	···	···	···	··· 2009 Nov 07	120	49; 49, 30
2MASSI J0032431−223727	J00324308−2237272	L1	···	M9.7:	15.39	1.43	2009 Dec 07	120	25; 25
EROS−MP J0032−4405	J00325584−4405058	L0γ	···	L0.5	14.78	1.51	2008 Sep 07	120	8; 56
2MASSI J0034568−070601	J00345684−0706013	L3	···	L4.3	15.53	1.59	2009 Nov 07	120	25; 25
SDSS J003843.99+134339.5	J00384397+13433950	L1	···	L0.6	15.91	1.15	2012 Sep 27	120	20; 20
SDSS J004154.54+134135.5	J00415453+1341351	L0	···	L0.6	14.45	1.22	2009 Jan 24	120	20; 20
···	···	···	···	···	···	···	··· 2009 Nov 08	120	20; 20
LHS 1135	J00433134+2054316	sdM6.5	···	M7.0	13.95	0.81	2004 Jul 24	120	··· ; 39
2MASSW J0045214+163445	J00452143+1634446	L2β	L3.5	L1.3::	13.06	1.69	2007 Sep 16	120	30; 56, 30
2MASS J00464841+0715177	J00464841+0715177	L0::	M9	M9.5:	13.89	1.34	2008 Jul 13	120	30; 49, 30
SIPS J0050−1538	J00502444−1538184	L1:	···	L0.5	13.78	1.13	2008 Sep 08	120	36; 44
SDSSp J005406.55−003101.8	J00540654−00310180	L1	···	L2.2	15.73	1.35	2012 Sep 25	120	19; 20

Table 3.2 Continued

Source	Designation	Spectral Type			2MASS		Date	λ/Δλ	Ref[b]
		Opt	NIR	SpeX[a]	J	J-K_s			
2MASS J00550460−3052000	J00550460−3052000	M8:	···	M7.2	13.03	1.12	2012 Dec 27	120	··· ; ···
LHS 1166	J00554418+2506235	sdM6.5	···	M7.2	14.26	0.69	2004 Sep 07	120	··· ; 39
SDSS J00570556−0846241	J00570556−0846241	L0	···	M9.3	15.70	1.34	2012 Sep 25	120	60; 60
2MASSW J0058425−065123	J00584253−0651239	L0	···	L0.0	14.31	1.41	2008 Jul 14	120	13; 13
LHS 132	J0102510−373743	M8	···	M8.1	11.13	1.06	2008 Sep 07	120	··· ; ···
SDSS J010311.51−004417.0	J01031151−0044170	M9.5	···	M8.5	14.29	1.12	2013 Oct 29	120	62; 62
2MASSI J0103320+193536	J01033203+1935361	L6	···	L5.4	16.29	2.14	2006 Sep 02	120	13; 13
2MASSI J0104075−005328	J01040750−0053283	L4.5	···	L5.8:	16.53	1.20	2009 Nov 07	120	29; 81
SDSS J010637.33+151855.0	J01063733+1518550	M8.5	M8 pec	M9.2	14.36	0.93	2013 Sep 03	120	62; 62, 66
SDSS J01071600−1517570	J01071600−1517570	M7	···	M7.2	13.34	1.06	2012 Dec 27	120	··· ; ···
SDSSp J010752.33+004156.1	J01075242+0041563	L8	L5.5	L6.6	15.82	2.12	2005 Oct 19	120	21; 20, 34
SDSS J01084048+1347392	J01084048+1347392	L0	···	M9.3	···	···	2012 Sep 27	120	60; 60
2MASS J01165457−1357342	J01165457−1357342	M9	···	M8.8	14.21	1.24	2009 Nov 08	120	49; 49
2MASS J01170586+1752568	J01170586+1752568	M9	M8	M8.6	14.14	1.20	2009 Nov 04	120	61; 61
SSSPM J0124−4240	J01235905−4240073	M8	L2.5	M8.4	13.15	1.12	2008 Sep 07	120	37; 49, 37
2MASSI J0125369−343505	J01253689−3435049	L2	···	L1.2	15.52	1.62	2008 Sep 07	120	25; 25
2MASS J01273917+2805536	J01273917+2805536	M8.5	···	M9.3	14.04	1.18	2013 Aug 14	120	··· ; ···
SDSS J012743.51+135420.9	J01274352+13542099	L5	L6±1	L5.5	16.83	1.40	2012 Sep 25	120	20; 20, 34

Table 3.2 Continued

Source	Designation	Spectral Type			2MASS		Date	$\lambda/\Delta\lambda$	Ref[b]
		Opt	NIR	SpeX[a]	J	J-K_s			
2MASSW J0129122+351758	J01291221+3517580	L4	···	L4.7	16.78	2.08	2009 Nov 07	120	11; 11
2MASS J01335299+0033017	J01335299+0033017	M9:	···	M9.1	15.84	1.21	2009 Jan 24	120	62; 62
NLTT 5282	J0134592−090442	esdM9.5?	···	M8.8	15.25	0.49	2008 Jul 14	120	··· ; ···
2MASSW J0135358+120522	J01353586+1205216	L1.5	···	L0.6	14.41	1.49	2009 Nov 04	120	13; 13
2MASSW J0141032+180450	J01410321+1804502	L1	L4.5	L0.8	13.88	1.38	2008 Sep 07	120	30; 44, 30
2MASS J01460119−4545263	J01460119−4545263	M9	···	M9.5	14.40	1.36	2008 Oct 12	120	49; 49
···	···	···	···	···	···	···	··· 2009 Dec 07	120	49; 49
2MASSW J0147334+345311	J01473344+3453112	L0.5	···	L1.0	14.95	1.37	2008 Sep 08	120	11; 11
2MASS J01490895+2956131	J01490895+2956131	M9.5	···	M9.7	13.45	1.47	2008 Sep 07	120	··· ; ···
SDSS J01535423+1404528	J01535423+1404528	L0	···	M9.0	15.21	1.25	2012 Sep 27	120	60; 60
LEHPM 2153	J02042212−3632308	M8:	···	M8.1	13.27	1.08	2013 Dec 05	120	49; 49
SDSS J020608.97+223559.2	J02060879+22355930	···	L5.5	L6.9:	16.56	1.39	2013 Dec 05	120	40; 40
DENIS J02065660−0735190	J02065660−0735190	M8.5	···	M8.5	14.34	1.35	2013 Aug 14	120	59; 59
SDSS J020735.60+135556.3	J02073556+13555639	L3	L3±1.5	L0.6	15.46	1.65	2012 Sep 27	120	20; 20, 34
2MASSW J0208549+250048	J02085498+25004880	L5	···	L5.9	16.21	1.80	2012 Sep 25	120	13; 13
2MASSI J0218291−313322	J02182913−3133230	L3	···	L3.8	14.73	1.57	2009 Nov 08	120	27; 27
2MASS J02192196+0506306	J02192196+0506306	L1:	L1	L3.0	14.97	1.49	2008 Sep 23	120	··· ; 55
SSSPM J0219−1939	J02192807−1938416	L1	L2.5	L0.6	14.11	1.20	2008 Sep 08	120	83; 37

Table 3.2 Continued

Source	Designation	Spectral Type			2MASS		Date	λ/Δλ	Ref[b]
		Opt	NIR	SpeX[a]	J	J-K_s			
2MASSI J0224367+253704	J02243669+25370419	L2	···	L2.3	16.58	1.89	2012 Sep 27	120	13; 13
2MASS J02284243+1639329	J02284243+16393299	L0:	···	M8.7	13.17	1.35	2012 Oct 27	120	49; 49
2MASS J02301551+2704061	J02301551+2704061	L0:	···	M9.4	14.29	1.31	2008 Sep 07	120	44; 44
DENIS J02304500−0953050	J02304500−0953050	L0	···	L0.9	14.68	1.69	2013 Aug 14	120	59; 59
SDSS J023547.56−084919.8	J02354755−08491980	L2	···	L2.0:	15.57	1.38	2012 Sep 27	120	20; 20
SDSSp J023617.93+004855.0	J02361793+00485479	L6	L6.5	L6.6:	16.10	1.43	2012 Sep 25	120	21; 20, 34
2MASSI J0239424−173547	J02394245−1735471	L0	···	M9.0	14.29	1.25	2009 Nov 08	120	27; 27
2MASSI J0241536−124106	J02415367−1241069	L2:	···	L1.9	15.61	1.67	2008 Sep 08	120	27; 27
2MASSW J0242435+160739	J02424354+16073920	L1.5	···	L1.7	15.78	1.43	2012 Oct 27	120	11; 11
SDSS J02511323+00473631	J02511323+00473631	M8	···	M8.2	13.77	1.09	2013 Sep 03	120	48; 48
2MASS J02522628+0056220	J02522628+0056220	M8	···	M8.3	13.13	1.16	2012 Dec 27	120	··· ; ···
SDSS J02540582−1934523	J02540582−1934523	M9	M9	M8.1	13.08	1.17	2009 Jan 25	120	49; 85
···	···	···	···	···	···	···	··· 2012 Dec 27	120	49; 85
2MASS J02594471+2254443	J02594471+2254443	M9	···	M9.5	14.11	1.25	2009 Dec 07	120	49; 49
2MASSI J0302012+135814	J03020121+13581419	L3	···	L2.7:	16.53	1.90	2005 Oct 19	120	13; 13
···	···	···	···	···	···	···	··· 2012 Sep 27	120	13; 13
LEHPM 1−3070	J03061185−3647417	M8	L0	M8.7	11.69	1.06	2006 Sep 03	120	32; 37
2MASSW J0306268+154514	J03062684+15451370	L6:	···	L6.0:	17.11	1.97	2012 Sep 25	120	13; 13

Table 3.2 Continued

Source	Designation	Spectral Type			2MASS		Date	$\lambda/\Delta\lambda$	Ref[b]
		Opt	NIR	SpeX[a]	J	J-K_s			
SDSS J03083243−08105138	J03083243−08105138	M8	···	M7.6	14.98	0.89	2013 Sep 03	120	48; 48
2MASSW J0309088−194938	J03090888−19493870	L4.5	···	L4.9	15.75	1.69	2012 Sep 25	120	13; 13
2MASS J03101401−2756452	J03101401−2756452	L5	···	L6.5	15.80	1.84	2009 Nov 08	120	44; 44
2MASS J03140344+1603056	J03140344+16030560	L0	···	M9.4	12.53	1.29	2012 Sep 25	120	49; 49
2MASSI J0316451−284852	J03164511−28485209	L0:	···	L1.0	14.57	1.46	2013 Dec 05	120	27; 27
2MASS J03201710−1026120	J03201710−1026120	M8	···	M7.6	13.87	1.15	2013 Aug 14	120	44; 44
2MASS J03250136+2253039	J03250136+22530390	L3	···	L3.3	15.43	1.65	2013 Sep 03	120	44; 44
2MASSW J0326137+295015	J03261367+2950152	L3.5	···	L4.6	15.48	1.65	2009 Dec 07	120	11; 11
2MASS J03264453+1919309	J03264453+1919309	M8.5	···	M8.6	13.12	···	2012 Sep 25	120	49; 49
SDSSp J032817.38+003257.2	J03281737+00325719	L3	···	L2.5:	15.99	1.83	2012 Sep 27	120	19; 20
LSPM J0330+3504B	J03301720+3505001	···	d/sdM7	M8.6	16.00	0.68	2005 Oct 17	120	··· ; 75
···	···	···	···	···	···	···	··· 2005 Dec 31	120	··· ; 75
SDSSp J033035.13−002534.5	J03303511−0025346	L4	···	L6.5	15.31	1.47	2009 Nov 04	120	12; 20
LEHPM 1−3365	J03303847−2348463	···	esdM7	M8.8	15.80	0.86	2004 Sep 09	120	32; 75
2MASS J03320043−2317496	J03320043−2317496	M8	···	M8.4	13.64	1.10	2013 Oct 29	120	49; 49
2MASS J03335134+0014068	J03335134+0014068	sdL	···	M7.6	16.43	−0.35	2013 Dec 05	120	62; 62
LEHPM 1−3396	J03340904−4953382	···	M8	M9.4	11.38	0.98	2004 Sep 06	120	32; 75
2MASS J03350236+2342407	J03350236+2342407	M8.5	···	M7.4	12.25	0.99	2013 Dec 05	120	14; 67

Table 3.2 Continued

Source	Designation	Spectral Type			2MASS		Date	$\lambda/\Delta\lambda$	Ref[b]
		Opt	NIR	SpeX[a]	J	J-K_s			
2MASS J03354535+0658058	J03354535+0658058	M8	···	M8.0	13.41	1.15	2012 Oct 27	120	49; 49
2MASSW J0337036−175807	J03370359−1758079	L4.5	···	L6.0:	15.62	2.04	2009 Nov 08	120	13; 13
2MASS J03395284+2457270	J03395284+2457270	M8	···	M7.7	12.84	1.10	2012 Dec 27	120	··· ; ···
SDSS J03440891+0111249	J03440891+0111249	L1	···	L2.9:	14.74	1.22	2012 Oct 27	120	60; 60
SDSS J03510002−00524587	J03510002−00524587	M8	···	M7.3	11.30	1.07	2012 Oct 27	120	48; 48
2MASS J03521086+0210479	J03521086+02104797	M9	L0±1	M8.6	13.08	1.12	2012 Oct 27	120	47; 49, 47
SDSS J035308.54+103056.0	J03530854+1030560	L1	···	L0.9	15.45	1.27	2013 Oct 29	120	60; 60
2MASS J03540135+2316330	J03540135+2316330	M8	···	M7.9	13.12	1.13	2012 Dec 27	120	··· ; ···
LEHPM 2−471	J03551067−1858173	···	M7	M7.6	13.81	0.93	2006 Sep 03	120	32; 75
2MASS J0355201+143929	J0355201+143929	M8	···	M8.8	13.81	1.11	2013 Oct 29	120	44; 44
2MASS J03552337+1133437	J03552337+1133437	L5γ	···	L4.8::	14.05	2.52	2009 Dec 07	120	49; 56
2MASSW J0355419+225702	J03554190+22570159	L3	···	L2.9:	16.11	1.83	2012 Sep 27	120	11; 11
DENIS−P J035729.6−441730	J03572695−4417305	L0β	···	L0.6:	14.37	1.46	2007 Sep 16	120	38; 56
2MASS J04012977−4050448	J04012977−40504488	L0:	···	L0.0	14.53	1.36	2012 Dec 27	120	49; 49
LSPM J0402+1730	J04024315+1730136	···	sdM7	M7.0	15.59	0.56	2005 Oct 17	120	··· ; 75
···	···	···	···	···	···	···	··· 2005 Dec 31	120	··· ; 75
2MASS J04070752+1546457	J04070752+1546457	L3.5	···	L3.9	15.48	1.92	2009 Dec 07	120	49; 49
2MASS J0407089−234829	J0407089−234829	M8:	···	M8.5	13.77	1.15	2013 Oct 29	120	44; 44

Table 3.2 Continued

Source	Designation	Spectral Type			2MASS		Date	$\lambda/\Delta\lambda$	Ref[b]
		Opt	NIR	SpeX[a]	J	J-K_s			
2MASS J04081032+0742494	J04081032+0742494	M8	···	M8.1	13.59	1.17	2013 Dec 05	120	49; 49
2MASSI J0408290−145033	J04082905−1450334	L2	L4.5	L1.3	14.22	1.40	2009 Nov 04	120	30; 27, 30
2MASSI J0409095+210439	J04090950+2104393	L3	···	L3.4	15.51	1.66	2009 Dec 07	120	13; 13
2MASS J0417474−212919	J0417474−212919	M8	···	M8.3	13.85	1.18	2013 Oct 29	120	44; 44
SDSS J04270723+0859027	J04270723+0859027	M8	···	M8.8	12.92	1.19	2012 Dec 27	120	··· ; ···
DENIS J0427270−112713	J04272708−1127143	M7	···	M7.9	13.74	1.07	2013 Dec 05	120	59; 59
2MASSI J0428510−225323	J04285095−22532270	L0.5	···	M9.9	13.51	1.39	2012 Sep 25	120	25; 25
LP 655−23B	J04305157−0849007	M8	···	M8.5	12.90	1.12	2013 Dec 05	120	28; 46
LP 775−31	J0435161−160657	···	M7	M8.0	10.41	1.05	2004 Sep 07	120	··· ; ···
2MASS J04362054−4218523	J04362054−42185236	L0:	···	L0.4	14.49	1.35	2012 Dec 27	120	49; 49
2MASSI J0443058−320209	J04430581−32020899	L5	···	L6.4:	15.27	1.40	2012 Sep 27	120	25; 25
SDSS J044337.61+000205.1	J04433761+0002051	M9	···	M9.0	12.51	1.29	2013 Dec 05	120	20; 44
2MASS 04441479+0543573	J04441479+0543573	M8	···	M7.9	13.67	1.15	2013 Dec 05	120	49; 49
2MASSI J0451009−340214	J04510092−34021500	L0.5	···	L0.6	13.54	1.25	2012 Sep 27	120	27; 27
2MASSI J0453264−175154	J04532647−1751543	L3:	···	L3.1	15.14	1.68	2009 Nov 04	120	27; 27
2MASS J05002100+0330501	J05002099+03305010	L4	···	L4.1	13.67	1.61	2012 Dec 27	120	49; 49
2MASSI J0502134+144236	J05021345+1442367	L0	···	M8.9	14.27	1.32	2013 Dec 05	120	60; 55
2MASS J05120636−2949540	J05120636−29495400	L4.5	···	L5.7::	15.46	2.18	2013 Oct 29	120	27; 52

Table 3.2 Continued

Source	Designation	Spectral Type			2MASS		Date	λ/Δλ	Ref[b]
		Opt	NIR	SpeX[a]	J	J-K_s			
2MASS J05170548−4154413	J05170548−4154413	M9	···	M8.8	13.46	1.19	2012 Dec 27	120	··· ; ···
LEHPM 2−183	J05173729−3348593	M8	M9	M9.4	12.00	1.17	2004 Sep 06	120	32; 27, 75
2MASS J05184616−2756457	J05184616−2756457	L0:	···	L1.0	15.26	1.65	2009 Jan 25	120	44; 44
2MASS J05264348−4455455	J05264348−4455455	M9.5	···	M9.8	14.08	1.38	2013 Dec 12	120	49; 49
2MASS J05301261+6253254	J05301261+6253254	L1	···	L1.1	14.05	1.34	2008 Jan 09	120	49; 49
2MASS J0534584−151143	J0534584−151143	M9	···	M8.9	13.15	1.15	2013 Oct 29	120	44; 44
SDSSp J053951.99−005902.0	J05395199−00590189	L5	L5	L5.0	14.03	1.51	2009 Jan 24	120	12; 12, 34
2MASS J05431887+6422528	J05431887+6422528	L1	···	L1.2	13.57	1.52	2008 Jan 09	120	49; 49
2MASS J05441150−2433010	J05441150−2433010	M8	···	M7.6	12.53	1.07	2012 Dec 27	120	··· ; ···
2MASS J06022216+6336391	J06022216+6336391	L1:	···	L1.5	14.27	1.58	2008 Jan 08	120	49; 49
LSR 0602+3910	J06023045+3910592	L1	···	L0.8	12.30	1.44	2009 Nov 04	120	88; 88
2MASS J06050190−2342260	J06050190−2342260	L0:	···	M9.8	14.51	1.37	2012 Dec 27	120	44; 44
2MASS J06050196−2342270	J06050190−2342260	L0:	···	L1.1:	14.51	1.37	2009 Jan 25	120	44; 44
2MASS J06085283−2753583	J06085283−2753583	M8.5 low g	L0 lg	M9.6	3.600	−8.78	2006 Sep 02	120	27; 59, 71
SIPS J0614−2019	J06141196−2019181	···	L4	L1.3	14.78	1.41	2006 Sep 01	120	··· ; 72
DENIS−P J0615493−010041	J06154934−01004158	L2±1	···	L1.0	13.75	1.21	2010 Jan 02	120	53; 53
···	···	···	···	···	···	···	··· 2012 Dec 27	120	53; 53
2MASS J06244595−4521548	J06244595−45215479	L5:	···	L5.1	14.48	1.88	2013 Oct 29	120	49; 49

Table 3.2 Continued

Source	Designation	Spectral Type			2MASS		Date	λ/Δλ	Ref[b]
		Opt	NIR	SpeX[a]	J	J-K_s			
SDSS J062621.22+002934.2	J06262121+00293410	L1	···	L0.3	15.93	1.07	2010 Jan 02	120	20; 20
2MASS J06411840−4322329	J06411839−43223290	L1.5	···	L2.4:	13.75	1.30	2012 Dec 27	120	49; 49
DENIS−P J0652197−253450	J06521977−25345058	L0	···	M9.2	12.76	1.24	2009 Jan 25	120	53; 53
···	···	···	···	···	···	···	··· 2009 Nov 04	120	53; 53
DENIS−P J0652197−253450	J06521977−2534505	L0	···	M9.2	12.76	1.24	2006 Sep 02	120	53; 53
LEHPM 2−461	J06591011−4747002	M6.5	M7	M7.4	13.64	0.92	2006 Dec 20	120	32; 87, 75
LEHPM 2−436	J07075333−4900574	M8.5	M8	M8.8	13.23	1.12	2006 Dec 20	120	32; 75
···	···	···	···	···	···	···	··· 2006 Dec 21	120	32; 37, 75
2MASSW J0708213+295035	J07082132+29503500	L5	···	L5.4:	16.72	1.95	2013 Dec 12	120	13; 13
DENIS−P J0716478−063037	J07164790−06303696	L1±1	···	L1.1	13.90	1.33	2010 Jan 02	120	53; 53
···	···	···	···	···	···	···	··· 2011 Apr 04	120	53; 53
2MASS J07200325−0846499	J07200325−0846499	M9:	···	M9.8	10.63	1.16	2013 Dec 05	120	70; 70
2MASS J07231462+5727081	J07231462+5727081	L1	···	L0.2	13.97	1.36	2008 Jan 08	120	49; 49
SDSS J07342570+30065792	J07342571+3006583	M8	···	M7.6	15.13	1.05	2009 Jan 25	120	48; 48
SDSS J07351959+4108503	J07351959+4108503	L0	···	M8.9	15.78	0.93	2010 Jan 26	120	60; 60
···	···	···	···	···	···	···	··· 2011 Mar 09	120	60; 60
2MASSW J0740096+321203	J07400965+32120320	L4.5	···	L4.0	16.19	1.97	2010 Jan 26	120	61; 61
···	···	···	···	···	···	···	··· 2012 Dec 27	120	13; 13

Table 3.2 Continued

Source	Designation	Spectral Type			2MASS		Date	$\lambda/\Delta\lambda$	Ref[b]
		Opt	NIR	SpeX[a]	J	J-K_s			
SDSS J074756.31+394732.9	J07475631+3947329	L0	···	M8.3	15.08	1.35	2008 Jan 11	120	20; 20
SDSS J074838.61+174332.9	J07483861+1743329	L7	···	L6.0	16.27	1.85	2013 Oct 29	120	54; 54
DENIS−P J0751164−253043	J07511645−2530432	L2.5	···	L1.1	13.16	1.17	2009 Nov 04	120	53; 53
2MASSI J0753321+291711	J07533216+29171190	L2	···	L2.0	15.52	1.67	2010 Jan 28	120	13; 13
···	···	···	···	···	···	···	··· 2011 Apr 03	120	13; 13
2MASS J07575274+0914103	J07575274+0914103	L4::	···	L3.7:	15.86	1.77	2013 Apr 26	120	54; 54
SDSS J080048.13+465825.5	J08004815+46582560	L2	···	L1.3	15.51	1.20	2011 Mar 09	75	20; 20
2MASS J08041429+0330474	J08041429+0330474	M8.5	···	M9.7	13.69	1.25	2013 Oct 29	120	49; 49
SDSS J080959.01+443422.2	J08095903+4434216	···	L6	L6.3:	16.44	2.02	2008 Jan 12	120	34; 40
DENIS−P J0812316−244442	J08123170−24444239	L2.5±1	···	L0.9	13.82	1.43	2010 Jan 03	120	53; 53
···	···	···	···	···	···	···	··· 2012 Dec 27	120	53; 53
SDSS J08175749+1824050	J08175749+1824050	L1	···	L2.0	15.09	1.27	2013 Apr 26	120	60; 60
SDSS J08181228+3310482	J08181228+3310482	L0	···	L1.3	15.99	0.93	2011 Apr 03	120	60; 60
SDSS J081946.02+165853.9	J08194602+1658539	M9	···	M8.6	13.79	1.17	2013 Dec 05	120	74; 74
DENIS J0823031−491201	J08230313−4912012	L1.5	L3	L2.7	13.55	1.48	2013 Nov 24	120	53; 53, 68
2MASS J08230838+6125208	J08230837+61252079	L2:	···	L2.5	14.82	1.62	2011 Apr 03	120	49; 49
SDSS J08264265+19392195	J08264262+1939224	L0	···	M9.2	14.78	1.20	2010 Jan 25	120	48; 48
2MASSW J0829066+145622	J08290664+1456225	L2	···	L1.0	14.75	1.58	2008 Jan 08	120	13; 13

Table 3.2 Continued

Source	Designation	Spectral Type			2MASS		Date	λ/Δλ	Ref[b]
		Opt	NIR	SpeX[a]	J	J-K_s			
GJ 1111	J08294949+2646348	M6.5	···	M7.2	8.230	0.97	2013 Dec 12	120	2; 58
2MASSW J0829570+265510	J08295706+26550990	L6.5	···	L6.4::	17.11	2.15	2013 Dec 12	120	13; 13
2MASS J08303256+0947150	J08303256+0947150	M8	···	M7.8	11.89	1.13	2012 Dec 27	120	··· ; ···
2MASS J08315564+1025466	J08315564+1025466	M9	···	M8.6	13.62	1.17	2009 Mar 21	120	··· ; 49
2MASSW J0832045−012835	J08320451−0128360	L1.5	···	L1.2	14.13	1.42	2008 Jan 10	120	13; 13
2MASS J08352366+1029318	J08352366+1029318	M7	···	M7.9	13.14	1.09	2013 Dec 05	120	49; 49
SDSS J08354533+2224308	J08354537+2224310	L0	···	M8.7	15.74	1.29	2010 Jan 25	120	60; 60
2MASS J08355829+0548308	J08355829+05483080	L3	···	L1.7	14.53	1.36	2010 Jan 24	120	49; 55
···	···	···	···	···	···	···	··· 2011 Apr 04	120	49; 55
SDSS J08362199+4949315	J08362199+4949315	L0	···	M9.3:	15.42	0.88	2011 Mar 09	120	60; 60
SDSS J08364634+0526426	J08364635+0526426	L0	···	M9.4	14.58	1.29	2008 Sep 23	120	60; 60
2MASS J08391608+1253543	J08391608+1253543	M9	···	M8.8	13.75	1.16	2013 Dec 12	120	74; 74
LHS 2034	J08402975+1824091	M6	···	M7.0	11.05	1.01	2013 Dec 12	120	1; 57
SDSS J08410685+6035063	J08410685+6035063	L4	···	L1.5	15.94	1.25	2011 Apr 03	120	60; 60
SDSS J08430794+3141292	J08430794+3141292	L3	···	L2.5	15.99	1.34	2011 Apr 03	120	60; 60
SDSS J08433328+1024435	J08433328+1024435	L1	···	L2.7:	14.87	1.20	2013 Dec 12	120	60; 60
SDSS J084403.46+043436.19	J08440346+04343619	M8	···	M8.7	13.46	1.05	2013 Dec 12	120	48; 48
SDSS J08475148+0138110	J08475148+0138110	L3	···	L3.2	16.23	1.82	2013 Dec 05	120	60; 60

Table 3.2 Continued

Source	Designation	Spectral Type			2MASS		Date	$\lambda/\Delta\lambda$	Ref[b]
		Opt	NIR	SpeX[a]	J	J-K_s			
2MASS J08490052+0220155	J08490052+0220155	M8	···	M7.3	12.93	1.03	2013 Dec 05	120	74; 74
2MASS J08533434−0329432	J08533434−0329432	M9e	···	M8.6	15.04	0.52	2009 Mar 21	120	··· ; ···
SDSS J08583697+2710508	J08583697+2710508	L0	···	L0.0	15.05	1.39	2011 Mar 09	120	60; 60
2MASSI J0859254−194926	J08592522−1949279	L6::	L8	L6.8	15.53	1.78	2008 Jan 12	120	27; 27, 69
2MASS J08593854+6341355	J08593854+6341355	L0	···	M8.6	13.70	1.31	2008 Jan 11	120	49; 49
2MASS J08594029+1145325	J08594029+1145325	M8	···	M8.4	12.74	1.25	2012 Dec 27	120	··· ; ···
LHS 2090	J09002359+2150054	M6.5	···	M7.3	9.440	1.00	2013 Dec 12	120	17; 58
SDSS J09002368+2539343	J09002368+2539343	L7	···	L6.7	16.43	1.77	2013 Dec 12	120	60; 60
SDSS J090206.90+003319.36	J09020690+00331936	M7	···	M7.3	12.11	0.95	2013 Dec 05	120	48; 48
SDSS J09094813+1940439	J09094813+1940439	L1	···	M9.9	14.73	1.29	2013 Apr 26	120	60; 60
DENIS−P J0909−0658	J09095749−0658186	L0	···	L0.2	13.89	1.35	2008 Jan 10	120	9; 52
2MASS J09161504+2139512	J09161504+2139512	M9	···	M9.8	13.22	1.15	2013 Dec 12	120	74; 74
2MASSW J0918382+213406	J09183814+21340580	L2.5	···	L2.7	15.66	1.76	2011 Apr 03	120	11; 11
SDSS J09230870+2340137	J09230870+2340137	L1	···	L2.3	13.85	1.04	2011 Mar 09	120	60; 60
2MASSW J0928397−160312	J09283972−1603128	L2	···	L1.7	15.32	1.71	2008 Jan 12	120	13; 13
SDSS J09311323+2802271	J09311323+2802271	L3	···	L2.5:	14.98	1.25	2011 Mar 09	120	60; 60
SDSS J093128.22+052821.93	J09312822+05282193	M7	···	M8.4	12.86	1.06	2013 Dec 05	120	48; 48
SDSS J09323747+6725145	J09323747+6725145	L0	···	M9.4	15.91	0.92	2011 Apr 03	120	60; 60

Table 3.2 Continued

Source	Designation	Spectral Type			2MASS		Date	$\lambda/\Delta\lambda$	Ref[b]
		Opt	NIR	SpeX[a]	J	J-K_s			
2MASS J09340617+0536234	J09340617+0536234	M8 pec	···	M7.5	15.57	0.81	2004 Mar 11	120	45; 45, 75
2MASS J09352803−2934596	J09352802−29345959	L0	···	L0.3	14.04	1.21	2012 Dec 27	120	49; 49
SDSS J09385888+0443439	J09385888+0443439	L0	···	M7.8	15.24	1.24	2013 Apr 26	120	60; 60
SDSS J09404788+2946530	J09404788+2946530	L1	···	L0.4	15.29	1.37	2013 Apr 26	120	60; 60
SDSS J09413492+1009421	J09413492+1009421	L0	···	M8.7	14.58	1.21	2013 Apr 26	120	60; 60
2MASSW J0944027+313132	J09440279+3131328	L2	···	L1.7	15.50	1.49	2008 Jan 09	120	13; 13
2MASS 09474477+0224327	J09474477+0224327	M8:	···	M8.2	13.17	1.09	2013 Dec 05	120	49; 49
LHS 2195	J09492223+0806450	M8.5	···	M8.5	12.31	1.10	2013 Dec 12	120	49; 49
2MASS J09524622+0620410	J09524622+0620410	M8	···	M7.3	12.45	0.99	2013 Dec 12	120	74; 74
2MASS J09532126−1014205	J09532126−1014205	L0	···	M9.4	13.47	1.33	2008 Jan 12	120	44; 44
2MASS J09532126−1014205	J09532126−10142056	L0	···	L0.0	13.47	1.33	2006 Dec 20	120	44; 44
NLTT 22851B	J09532455+0526583	M9.5	···	M9.8	15.67	1.28	2013 Dec 05	120	62; 62
SDSS J100319.17−010508.15	J10031917−01050815	M7	···	M8.0	12.33	1.09	2013 Dec 12	120	48; 48
G 196−3B	J10042066+5022596	L3β	···	L5.6::	14.83	2.05	2006 Dec 23	120	7; 56
LHS 5166B	J10043929−33351889	L4	···	L4.5:	14.48	1.56	2013 Apr 26	120	22; 22
LHS 2243	J10163470+2751497	M8 V	···	M7.4	11.99	1.03	2013 Dec 12	120	5; 5
2MASSI J1017075+130839	J10170754+1308398	L2:	L1	L1.1	14.10	1.39	2008 Jan 12	120	27; 27, 30
SDSS J10174251+4310579	J10174251+4310579	L1	···	L0.9	15.55	1.03	2011 Mar 09	120	60; 60

Table 3.2 Continued

Source	Designation	Spectral Type			2MASS		Date	$\lambda/\Delta\lambda$	Ref[b]
		Opt	NIR	SpeX[a]	J	J-K_s			
2MASSW J1018588−290953	J10185879−29095349	L1	···	L0.3	14.21	1.42	2012 Dec 27	120	22; 22
DENIS J1019245−270717	J10192447−2707171	L0.5	···	M9.1	13.53	1.06	2013 Dec 12	120	59; 59
2MASS 10213232−2044069	J10213232−2044069	M9	···	M8.5	13.19	1.13	2013 Dec 12	120	49; 49
2MASS J10220489+0200477	J10220489+0200477	L0	···	M9.0	14.10	1.20	2008 Jan 10	120	49; 49
2MASS J10224821+5825453	J10224821+5825453	L1β	···	L0.6	13.50	1.34	2008 Jan 11	120	49; 49
SDSS J102552.43+321234.0	J10255227+3212349	···	L7.5±2.5	L5.8:	15.91	0.84	2008 Jan 08	120	40; 40
2MASSI J1029216+162652	J10292165+1626526	L2.5	···	L2.8	14.29	1.67	2008 Jan 12	120	13; 13
SDSS J10330910+1216259	J10330910+1216259	L0	···	M8.9	15.07	1.12	2013 Apr 26	120	60; 60
SDSS J10340567+0350163	J10340567+0350163	L0	···	M8.7	14.70	1.07	2013 Apr 26	120	60; 60
2MASSW J1035245+250745	J10352455+2507450	L1	···	L1.1	14.76	1.47	2008 Jan 08	120	13; 13
DENIS J104617.0−421237	J10461703−4212372	···	M8	M8.2	14.29	1.01	2008 Jan 24	120	··· ; 84
LP 213−68	J10471381+4026493	M8	···	M8.2	12.44	1.18	2013 Dec 12	120	16; 16
DENIS−P J1047−1815	J10473108−18155739	L2.5	···	L0.3	14.20	1.31	2012 Dec 27	120	10; 10
SDSS J104922.45+012559.2	J10492244+01255930	L5	···	L3.5:	15.88	1.77	2011 Apr 04	120	54; 54
2MASS J10511900+5613086	J10511900+56130860	L2	···	L0.8	13.24	1.34	2012 May 30	75	49; 49
SDSS J10515124+13111633	J10515124+13111633	L0	···	M9.5:	14.83	1.20	2013 Apr 26	120	48; 48
SDSS J105547.29+080842.64	J10554729+08084264	M9	···	M8.5	12.55	1.18	2013 Dec 12	120	48; 48
2MASSI J1059513−211308	J10595138−21130819	L1	···	L2.8:	14.56	1.35	2012 Dec 27	120	27; 27

Table 3.2 Continued

Source	Designation	Spectral Type			2MASS		Date	$\lambda/\Delta\lambda$	Ref[b]
		Opt	NIR	SpeX[a]	J	J-K_s			
LHS 2351	J11061897+0428327	M7	···	M7.6	12.33	1.00	2013 Dec 12	120	4; 39
2MASS J11073750−2759385B	J11073750−2759385	···	M7	M7.0	···	···	2009 Dec 29	120	··· ; 84
Gliese 417BC	J11122567+35481310	L4.5	···	L4.8	14.58	1.86	2007 Mar 16	120	13; 13
LHS 2397a	J11214909−1313082	M8	···	M8.5	···	···	2011 Mar 09	120	··· ; ···
2MASSW J1122362−391605	J11223623−39160540	L3	···	L3.7::	15.71	1.83	2012 Dec 27	120	22; 22
SDSS J11264703+5816322	J11264703+5816322	L3	···	L1.3	15.84	1.30	2011 Apr 03	120	60; 60
LEHPM 2−333	J11414421−2232204	···	M8	M8.8	12.63	1.06	2006 Apr 09	120	32; 75
SDSS J11491231−0153006	J11491231−0153006	L1	···	M8.5	14.67	0.96	2011 Mar 09	120	60; 60
2MASS J11533966+5032092	J11533966+5032092	L1:	···	L0.3	14.19	1.34	2008 Jan 11	120	49; 49
GJ 3693	J11535267+0659561	M8	···	M7.0	11.26	0.99	2013 Dec 12	120	4; 63
2MASS J11544223−3400390	J11544223−3400390	L0	···	L0.5	14.20	1.34	2008 Jan 09	120	38; 52
2MASSW J1155395−372735	J11553951−37273499	L2	···	L2.3	12.81	1.35	2012 Dec 27	120	22; 22
LP 851−346	J11554286−2224586	M7.5	···	M7.7	10.93	1.05	2013 Dec 12	120	24; 24
DENIS−P J1157480−484442	J11574809−48444283	L0.5±1	···	M9.4	14.01	1.21	2008 Jan 24	120	53; 53
DENIS−P J1159+0057	J11593850+00572679	L0	···	L0.4	14.08	1.27	2013 Apr 25	120	10; 20
SDSS J11594072+5409386	J11594072+5409386	L2	···	L0.9	15.22	1.46	2013 Apr 24	120	60; 60
SDSSp J120358.19+001550.3	J12035811+00155000	L3	···	L5.0	14.01	1.53	2011 Apr 04	120	12; 12
2MASSI J1204303+321259	J12043036+32125950	L0	M9	M9.6	13.82	1.30	2013 Apr 24	120	27; 27, 30

Table 3.2 Continued

Source	Designation	Spectral Type			2MASS		Date	$\lambda/\Delta\lambda$	Ref[b]
		Opt	NIR	SpeX[a]	J	J-K_s			
SDSS J12061049+6242572	J12061049+6242572	L1	···	L2.1	15.65	1.70	2011 Mar 09	120	60; 60
DENIS J1206501−393725	J12065011−3937261	L2	···	L1.9	14.32	1.22	2007 Mar 17	120	59; 59
2MASS J12073804−3909050	J12073803−39090500	L2:	···	L0.9	14.69	1.44	2011 Mar 11	120	49; 49
2MASSI J1213033−043243	J12130335−04324369	L5	···	L4.2	14.68	1.67	2011 Apr 04	120	27; 27
BRI 1222−1222	J12245222−1238352	M9	···	M8.5	12.57	1.22	2006 Jun 01	120	89; ···
2MASS J12312141+4959234	J12312141+49592339	L2	···	L3.4	14.62	1.48	2013 Apr 24	120	44; 44
2MASS J12321827−0951502	J12321827−0951502	L0	···	M9.5	13.73	1.17	2008 Jan 14	120	49; 49
SDSS J12455566+4902109	J12455566+4902109	L1	···	M7.8:	15.95	0.75	2011 Mar 09	120	60; 60
2MASSW J1246467+402715	J12464677+40271500	L4	···	L4.0	15.09	1.81	2011 Apr 03	120	13; 13
SDSS J125128.43+624310.7	J12512843+6243107	L4	···	L4.2	15.49	1.13	2013 Apr 24	120	54; 54
2MASS J12565688+0146163	J12565688+0146163	L2:	···	L1.6	14.48	1.69	2009 Jun 30	120	49; 49
SDSSp J125737.26−011336.1	J12573726−0113360	L4	L5	L5.8	15.94	1.82	2009 Jun 30	120	21; 20, 34
2MASSW J1300425+191235	J13004255+1912354	L1	L3	L1.7	12.72	1.09	2006 Apr 10	120	14; 14, 50
2MASS J13015465−1510223	J13015464−15102229	L1	···	L0.5	14.54	1.44	2013 Apr 26	120	49; 49
GJ 499C	J13054106+2046394	L4:	···	L6.5	15.20	1.83	2009 Jun 30	120	27; 27
2MASS J13061727+3820296	J13061726+38202960	L0	···	L0.6	14.63	1.41	2011 Apr 03	120	49; 49
SDSS J131142.1+362923.9	J13114192+3629247	L6	L5 pec (blue)	L6.8	15.55	1.40	2012 Jul 09	120	54; 54, 66
2MASS J13120700+3937440	J13120700+3937440	L0:	···	M8.8	14.14	1.25	2012 May 30	75	··· ; ···

Table 3.2 Continued

Source	Designation	Spectral Type			2MASS		Date	$\lambda/\Delta\lambda$	Ref[b]
		Opt	NIR	SpeX[a]	J	J-K_s			
2MASSI J1315309−264951	J13153094−2649513	L5.5	···	L6.7	15.20	1.73	2009 Jun 30	120	79; 52
2MASS J13204427+0409045	J13204427+04090450	L3::	···	L2.5	15.25	1.63	2013 Apr 24	120	49; 49
DENIS−P J1323−1806	J13233597−18063790	L0	···	L0.0	14.90	1.24	2013 Apr 26	120	10; 10
2MASSW J1326201−272937	J13262009−2729370	L5	···	L6.6:	15.85	1.99	2009 Jun 30	120	22; 22
SDSS J13271521+0759375	J13271521+0759375	L1	···	L0.5	14.60	1.36	2013 Apr 25	120	60; 60
2MASSW J1328550+211449	J13285503+2114486	L5	···	L4.1	16.19	1.93	2009 Jun 30	120	11; 11
SDSS J133148.92−011651.4	J13314893−01165000	L6	L8±2.5	L6.1	15.46	1.39	2011 Mar 09	120	20; 20, 34
SDSS J13331279+1509566	J13331279+1509566	L0	···	M7.8	15.84	0.75	2011 Mar 11	120	60; 60
SDSS J13334536−0216002	J13334536−0216002	L3	···	L2.2	15.38	1.53	2013 Apr 25	120	60; 60
2MASS J13364062+3743230	J13364062+3743230	L1	···	L0.4	14.41	1.31	2013 Apr 26	120	44; 44
2MASS J13373116+4938367	J13373115+49383670	L0	···	M8.9	13.77	1.19	2012 May 30	75	44; 44
2MASSW J1338261+414034	J13382614+41403420	L2.5	···	L2.4	14.22	1.45	2012 May 30	75	13; 13
2MASS J13384944+0437315	J13384944+04373150	L1	···	L0.0	14.16	1.42	2012 May 30	75	49; 49
2MASS J13411160−3052505	J13411160−30525049	L2::	···	L2.7:	14.61	1.53	2012 Jul 09	120	49; 49
2MASSW J1343167+394508	J13431670+39450870	L5	···	L5.3::	16.16	2.01	2013 Apr 24	120	13; 13
SDSS J13571490−1438520	J13571490−1438520	M7	···	M8.5	12.85	1.11	2012 May 30	75	··· ; ···
2MASS J13595510−4034582	J13595510−40345819	L1	···	L3.1:	13.65	1.08	2013 Apr 25	120	49; 49
2MASS J14022235+0648479	J14022235+0648479	M9	···	M8.9	13.72	1.21	2010 Jul 07	120	··· ; ···

Table 3.2 Continued

Source	Designation	Spectral Type			2MASS		Date	λ/Δλ	Ref[b]
		Opt	NIR	SpeX[a]	J	J-K_s			
2MASS J14044495+4634297	J14044495+4634297	L0:	···	M9.7	14.34	1.28	2008 Jul 13	120	44; 44
SDSS J14060148+5249309	J14060148+5249309	L0	···	M9.8	15.56	1.00	2011 Mar 09	120	··· ; 60
2MASS J14090310−3357565	J14090310−3357565	L2	···	L1.3	14.25	1.38	2010 Jul 07	120	52; 52
2MASSW J1411175+393636	J14111735+3936363	L1.5	···	L1.5	14.64	1.40	2008 Jul 13	120	13; 13
2MASS J14122270+2354100	J14122270+2354100	M9	···	M7.8	13.73	1.08	2009 Jun 30	120	··· ; ···
2MASSW J1412244+163312	J14122449+1633115	L0.5	···	M9.9	13.89	1.37	2008 Jul 30	120	13; 13
SDSS J14205830+2131566	J14205830+2131566	L1	···	L0.0:	15.12	1.06	2011 Mar 11	120	60; 60
2MASSW 1421314+182740	J14213145+1827407	L0	···	M8.9	13.23	1.29	2008 Jul 30	120	14; 49
SDSS J142227.25+221557.1	J14222720+2215575	···	L6.5±2	L5.4:	17.06	1.42	2009 Jun 30	120	40; 40
SDSS J14225715+0827521	J14225715+0827521	L2	···	L2.1	15.10	1.45	2013 Apr 25	120	60; 60
2MASS J14232186+6154005	J14232186+6154005	···	L4	L4.5	16.60	1.32	2013 Apr 26	120	65; 65
GD 165B	J14243909+0917104	L4	L3±2	L4.4	15.69	1.52	2009 Jun 29	120	3; 11, 34
DENIS−P J142527.97−365023.4	J14252798−3650229	L3:	L5	L4.5::	13.75	1.94	2010 Jul 07	120	31; 49, 31
2MASS J14261286+3130394	J14261286+3130394	L4	···	L4.0::	16.62	1.90	2013 Apr 25	120	54; 54
2MASS J14283132+5923354	J14283132+59233546	L4	···	L4.4	14.78	1.52	2012 Jul 09	120	49; 49
LHS 2924	J14284313+3310368	M9 V	···	M9.1	11.99	1.25	2007 Jul 04	120	··· ; ···
2MASSI J1430435+291540	J14304358+2915405	L2	L0.5	L1.5	14.27	1.50	2008 Jul 13	120	30; 27, 30
SDSS J14324210+3451427	J14324210+3451427	L1	···	L1.2	15.75	0.98	2011 Apr 19	120	60; 60

Table 3.2 Continued

Source	Designation	Spectral Type			2MASS		Date	λ/Δλ	Ref[b]
		Opt	NIR	SpeX[a]	J	J-K_s			
SDSS J14380829+64083631	J14380829+64083631	L0	···	L0.2	12.98	1.33	2011 Mar 11	120	48; 48
SDSS J143832.63+572216.9	J14383259+5722168	L5	···	L4.6	15.96	1.59	2010 Jul 07	120	54; 54
2MASSW J1438549−130910	J14385498−13091029	L3:	···	L3.1	15.49	1.63	2012 Jul 09	120	13; 13
SDSS J143933.44+031759.2	J14393342+03175909	L1	···	L0.7	15.99	1.18	2011 Apr 19	120	20; 20
SDSS J14403025+12333391	J14403025+12333391	M9	···	M8.6	14.41	1.22	2013 Mar 27	75	48; 48
2MASSI J1441045+271932	J14410457+27193234	M7	···	M7.0	12.99	1.02	2013 Mar 27	75	44; 44
G 124−62BC	J14413716−09455900	L0.5	···	L0.4	14.02	1.36	2008 Jul 14	120	10; 13
···	···	···	···	···	···	···	··· 2011 Mar 09	120	10; 13
G 239−25 B	J14422175+6603198	···	L0±1	M8.1	11.51	1.18	2010 Jul 07	120	35; 78
SSSPM 1444−2019	J14442067−2019222	d/sdM9	d/sdM7	M9.0	12.55	0.61	2005 Mar 23	120	33; 45, 75
2MASS J14442946+0048530	J14442946+0048530	M9	···	M8.1	15.95	0.76	2009 Jun 30	120	··· ; ···
SDSSp J144600.60+002452.0	J14460060+00245190	L6	L5	L4.2	15.89	1.96	2011 Mar 11	120	21; 20, 34
2MASSW J1449378+235537	J14493784+2355378	L0	···	M9.5	15.82	1.51	2008 Jul 13	120	13; 13
2MASS J14520183+1114590	J14520183+1114590	L2	···	L2.9	15.52	1.18	2013 Apr 26	120	77; 62
SDSS J14525558+2723244	J14525558+2723244	L0	···	L0.2:	14.92	0.84	2011 Mar 09	120	60; 60
SDSS J14532589+1420418	J14532589+1420418	L1	···	L4.1:	15.07	1.18	2013 Apr 26	120	60; 60
LEHPM 2−50	J14560172−2747288	···	L1	M9.3	13.25	1.06	2006 Mar 12	120	32; 75
LHS 3003	J1456383−280947	M7	···	M7.7	9.970	1.04	2008 Jul 29	120	··· ; ···

Table 3.2 Continued

Source	Designation	Spectral Type			2MASS		Date	$\lambda/\Delta\lambda$	Ref[b]
		Opt	NIR	SpeX[a]	J	J-K_s			
LEHPM 2−498	J14565736−2631265	···	M8	M7.7	13.56	0.95	2006 Mar 12	120	32; 75
PSS 1458+2839	J1458245+283958	M8.5	···	M8.5	13.08	1.23	2008 Jul 13	120	··· ; ···
2MASS J15004572+4219448	J15004572+4219448	M9	···	M8.4	13.77	1.13	2012 May 30	75	··· ; ···
TVLM 513−46546	J1501081+225002	M8.5	···	M9.3	11.87	1.16	2008 Jul 30	120	··· ; ···
2MASS J15101685−024107	J15101685−024107	M9	···	M9.3	12.61	1.27	2009 Jun 29	120	··· ; ···
SDSS J15102955+36194699	J15102955+36194699	M9	···	M8.3	14.00	1.18	2013 Aug 14	120	48; 48
2MASS J15111091+4340363	J15111091+4340363	L5	···	L5.8	16.60	1.90	2013 Apr 25	120	54; 54
SDSS J15124067+3403501	J15124067+3403501	L3	···	L0.7	15.04	1.63	2013 Apr 25	120	60; 60
2MASS J15230657−2347526	J15230657−2347526	···	L2.5	L0.3	14.20	1.30	2008 Jul 29	120	47; 82
SDSS J153453.33+121949.2	J15345324+12194950	···	L4±1.5	L5.5	15.33	1.51	2012 Jul 09	120	40; 40
2MASS J15345700−1418480	J15345700−1418480	M7	···	M8.6	11.39	1.08	2012 May 30	75	··· ; ···
DENIS−P J153941.96−052042.4	J15394189−0520428	L4:	L2	L4.2	13.92	1.35	2008 Jul 14	120	31; 52, 31
LEHPM 2−287	J15453990−2255167	···	M8	M8.2	13.71	1.09	2006 Apr 09	120	32; 75
2MASS J15474719−2423493	J15474719−2423493	M9	···	M9.0	13.97	1.23	2008 Jul 29	120	49; 49
SDSS J154849.02+172235.4	J15484911+17223590	···	L5	L6.6	16.10	1.65	2013 Aug 14	120	40; 40
2MASS J15485834−1636018	J15485834−1636018	···	L2±1	M8.8	13.89	1.26	2010 Jul 07	120	47; 47
SDSS J15512086+4329303	J15512086+4329303	L3	···	L3.1	15.13	1.50	2011 Apr 19	120	60; 60
SDSS J15525232−0035019	J15525232−0035019	L0	···	M9.6:	15.99	0.98	2011 Apr 19	120	60; 60

Table 3.2 Continued

Source	Designation	Spectral Type			2MASS		Date	$\lambda/\Delta\lambda$	Ref[b]
		Opt	NIR	SpeX[a]	J	J-K_s			
2MASSW J1552591+294849	J15525906+2948485	L0β	L1	L0.5:	13.48	1.46	2008 Jul 30	120	30; 56, 30
2MASSW J1553214+210907	J15532142+2109071	L5.5	···	L6.6:	16.70	2.02	2009 Jun 29	120	11; 11
2MASSW J1555157−095605	J15551573−0956055	L1	···	L1.6	12.56	1.11	2008 Jul 14	120	22; 22
SDSS J15564435+1723089	J15564435+1723089	L0	···	L0.7	14.67	1.32	2013 Aug 14	120	60; 60
2MASS J15573270+1752380	J15573270+1752380	M7.5	···	M8.3	13.54	1.09	2013 Aug 14	120	44; 44
2MASSI J1600054+170832	J16000548+1708328	L1.5	···	L1.8	16.05	1.37	2008 Jul 12	120	13; 13
2MASS J16082460+195747	J16082460+195747	M9	···	M8.6	13.52	1.17	2009 Jun 29	120	··· ; ···
LSR 1610−0040	J16102900−0040530	sdL:	d/sdM6	M7.0:	12.91	0.89	2004 Mar 12	120	26; 26, 42
2MASS J16134550+1708270	J16134550+1708270	M9.5	···	M9.6	13.47	1.28	2009 Jun 29	120	··· ; ···
2MASSW J1615441+355900	J16154416+3559005	L3	···	L3.6	14.54	1.60	2009 Jun 30	120	13; 13
2MASS J16184503−1321297	J16184503−1321297	L0:	···	M9.3	14.25	1.33	2010 Jul 07	120	52; 52
SDSS J161928.31+005011.9	J16192830+0050118	L2	···	L1.3	14.39	1.20	2008 Jul 30	120	20; 20
LEHPM 2−1973	J16202207−2446025	···	M7	M7.0	14.32	0.94	2006 Apr 09	120	32; 75
GJ 618.1B	J16202614−0416315	L2.5	···	L2.4	15.28	1.69	2008 Jul 30	120	18; 18
2MASS J16203450−2430200	J16203456−2430205	M6.5	···	M9.4::	14.20	1.66	2008 Jul 29	120	··· ; ···
2MASS J16210822+2938480	J16210822+2938480	M9	···	M9.4	15.17	0.84	2009 Jun 30	120	··· ; ···
SDSS J16260303+2113130	J16260303+2113130	L3	···	L4.7:	15.48	1.56	2013 Apr 24	120	60; 60
2MASS J16301770−2120010	J16301770−2120010	···	M9:	M9.4	14.51	1.32	2008 Jul 29	120	77; ···

Table 3.2 Continued

Source	Designation	Spectral Type			2MASS		Date	$\lambda/\Delta\lambda$	Ref[b]
		Opt	NIR	SpeX[a]	J	J-K_s			
...	...	...	...	...	...	...	... 2008 Aug 28	120	77; ...
2MASS J16304139+0938446	J16304138+09384459	L0::	...	L0.4:	14.87	1.57	2011 Apr 19	120	49; 49
SDSS J16311227+32271141	J16311227+32271141	M7	...	M8.2	13.15	0.91	2013 Apr 26	120	48; 48
SDSS J163256.1+350507.3	J1632561+3505073	L1	...	L0.7	14.65	1.35	2012 Jul 09	120	74; 74
SDSS J16351918+42230531	J16351918+42230531	M8	...	M8.6	12.88	1.09	2013 Apr 26	120	48; 48
SDSSp J163600.79−003452.6	J16360078−0034525	L0	...	M9.0	14.59	1.18	2008 Jul 30	120	12; 12
2MASS J16452207+3004071	J16452207+3004071	L3	...	L2.3	15.19	1.60	2008 Jul 13	120	44; 44
2MASS J16452207+3004071	J16452207+30040718	L3	...	L3.0	15.19	1.60	2012 Jul 09	120	44; 44
2MASS J16490419+0444571	J16490419+0444571	M8	...	M8.1	12.96	1.08	2013 Aug 14	120	49; 49
SDSS J16545079+3747146	J16545079+3747146	L2	...	L0.7	15.01	1.35	2013 Apr 26	120	60; 60
VB 8	J16553529−0823401	M7 V	...	M7.0	9.780	0.96	2007 Jul 04	120	... ; ...
2MASS J16573454+1054233	J16573454+1054233	L2	...	L1.4	14.15	1.35	2009 Jun 29	120	49; 49
WISE J165842.56+510335.0	J16584256+5103350	...	L6pec	L5.5:	15.06	1.40	2013 Oct 23	120	69; 69
SDSS J16585026+1820006	J16585026+1820006	L0	...	L0.9	15.48	0.91	2010 Jul 07	120	... ; ...
SDSS J17031670+19063603	J17031670+19063603	L0	...	M8.9	14.92	1.27	2012 Jul 09	120	48; 48
2MASS J17072343−0558249B	J17072343−05582489	...	L3	L0.0	12.26	1.23	2006 Aug 28	120	41; 41
DENIS J1707252−013809	J17072529−0138093	L0.5	L2	L1.0	14.29	1.22	2006 Aug 28	120	59; 59, 64
2MASSI J1707333+430130	J17073334+4301304	L0.5	...	M8.7	13.97	1.35	2008 Sep 08	120	27; 27

Table 3.2 Continued

Source	Designation	Spectral Type			2MASS		Date	$\lambda/\Delta\lambda$	Ref[b]
		Opt	NIR	SpeX[a]	J	J-K_s			
SDSS J17104934+33232518	J17104934+33232518	L0	···	M9.4	15.13	1.05	2011 Apr 19	120	48; 48
2MASS J17111353+2326333	J17111353+2326333	L0:	···	L0.5:	14.50	1.44	2008 Jul 13	120	44; 44
G 203−50 B	J17114530+4029021	···	L5+2−1.5	L5.0	15.00	1.20	2008 Sep 09	120	86; 86
···	···	···	···	···	···	···	··· 2010 Jul 07	120	86; 86
2MASS J10511900+5613086	J17170450+1509530	M7	···	M7.9	13.61	1.11	2012 May 30	75	··· ; ···
SDSS J171714.10+652622.2	J17171408+6526221	L4	···	L6.2	14.95	1.77	2009 Jun 30	120	20; 20
SDSS J17175402+64274503	J17175402+64274503	M8	···	M8.8	14.41	1.03	2013 Oct 22	120	48; 48
2MASSI J1721039+334415	J17210390+3344160	L3	L5±1	L5.3:	13.63	1.14	2008 Sep 08	120	27; 27, 50
SDSS J172244.32+632946.8	J17224432+6329470	L0	···	L0.7	15.37	1.29	2009 Jun 30	120	20; 20
SDSS J17254384+5325349	J17254384+5325349	L1	···	M8.0	15.16	0.95	2010 Jul 07	120	··· ; ···
2MASSI J1726000+153819	J17260007+1538190	L3β	···	L3.6::	15.67	2.01	2008 May 11	120	13; 56
···	···	···	···	···	···	···	··· 2008 Jul 13	120	13; 56
2MASS J17281134+0839590	J17281134+0839590	M9 pec	···	M9.8	13.63	1.13	2009 Jun 29	120	··· ; ···
DENIS−P J1733423−165449	J17334227−1654500	L0.5±1	···	L0.9	13.53	1.18	2006 Apr 11	120	53; 53
2MASSW J1743415+212707	J17434148+2127069	L2.5	···	L2.4	15.83	1.51	2009 Jun 30	120	13; 13
DENIS−P J1745346−164053	J17453466−1640538	L1.5±1	···	L1.3	13.65	1.24	2008 Sep 08	120	53; 53
2MASS J17461199+5034036	J17461199+50340362	L5	···	L5.7	15.10	1.57	2012 Jul 09	120	49; 49
2MASS J18000116−1559235	J18000116−1559235	L5.5	···	L4.3	13.30	···	2012 Jul 09	120	68; 68

Table 3.2 Continued

Source	Designation	Spectral Type			2MASS		Date	λ/Δλ	Ref[b]
		Opt	NIR	SpeX[a]	J	J-K_s			
2MASS J18064570+2923591	J18064570+2923591	M8:	···	M8.3	14.20	1.26	2010 Jul 07	120	··· ; ···
LSR 1826+3014	J18261131+3014201	M8.5	d/sdM8.5	M9.9	11.66	0.85	2004 Sep 09	120	23; 23, 75
SDSS J183929.17+442438	J18392917+442438	M9	···	M8.9	13.43	1.08	2008 Nov 04	120	48; 48
DENIS J19013910−3700170	J19013910−3700170	M8	···	L0.1::	14.26	1.96	2013 Apr 24	120	59; 59
DENIS−P J1909081−193748	J19090821−1937479	L1±1	···	L1.4	14.52	1.61	2008 Sep 08	120	53; 53
VB 10	J19165762+0509021	M8 V	···	M8.0	9.910	1.14	2007 Jul 04	120	90; 73
2MASS J19233810−3308410	J19233810−3308410	M7	···	M8.5	13.27	1.04	2012 Sep 27	120	··· ; ···
DENIS JJ1934511−184134	J1934511−184134	M8.5	···	M8.5	14.28	1.15	2013 Oct 23	120	59; 59
LEHPM 2−90	J19453495−2557190	···	M9	M8.9	12.35	0.84	2006 Sep 02	120	32; 75
2MASS J19561542−1754252	J19561542−1754252	M8	L0±1	M8.5	13.75	1.10	2007 Sep 16	120	47; 49, 82
2MASS J20025073−0521524	J200250732−05215242	L6	···	L6.8::	15.32	1.90	2007 Jul 04	120	44; 44
DENIS J2013108−124244	J2013108−124244	L1.5	···	L0.7	14.52	1.21	2013 Oct 22	120	59; 59
2MASS J20263647+0439400	J20263647+0439400	M9:	···	M8.5	14.16	1.23	2009 Jun 28	120	··· ; ···
2MASS J2035203−311008	J2035203−311008	M7	···	M7.9	13.19	1.03	2010 Jul 07	120	··· ; ···
2MASS J20414283−3506442	J20414283−3506442	L2:	···	L1.9	14.89	1.49	2008 Sep 08	120	44; 44
SDSS J204724.7+142152	J2047247+142152	M7.5	···	M8.9	13.04	1.16	2008 Nov 03	120	48; 48
LEHPM 2−381	J20522811−4758362	M8	M8	M8.1	12.94	1.06	2004 Sep 06	120	32; 75
2MASSI J2054358+151904	J20543585+1519043	L1:	···	L0.3	16.37	1.39	2009 Jun 28	120	13; 13

Table 3.2 Continued

Source	Designation	Spectral Type			2MASS		Date	λ/Δλ	Ref[b]
		Opt	NIR	SpeX[a]	J	J-K_s			
2MASSI J2057153+171515	J20571538+1715154	L1.5	···	M9.9	15.97	1.47	2009 Jun 28	120	13; 13
2MASS J20575592−0050060	J20575592−0050060	M9	···	M9.3	14.97	1.20	2009 Jun 29	120	··· ; ···
2MASS J21075409−4544064	J21075409−45440639	L0:	···	L2.6	14.92	1.53	2013 Aug 14	120	49; 49
HB 2115−4518	J2118317−450552	M8.5	···	M8.6	13.43	1.06	2008 Jul 14	120	··· ; ···
SDSS J211846.77−001044.6	J21184677−00104469	L1	···	L2.2:	16.20	1.13	2012 Sep 27	120	54; 54
SDSS J212033.89+102159	J21203389+102159	M8	···	M9.0	13.54	1.12	2008 Nov 03	120	48; 48
2MASS J21233110−2345180	J21233110−2345180	M7.5	···	M8.2	13.58	1.04	2013 Jul 17	75	44; 44
2MASS J21263403−3143220	J21263403−3143220	M9	···	M9.2	13.47	1.10	2009 Jun 28	120	··· ; ···
HB 2124−4228	J2127261−421518	M7.5	···	M8.9	13.32	1.14	2008 Jul 14	120	··· ; ···
HB 2126−4459	J2130086−444627	M8.5	···	M8.2	14.32	1.15	2008 Jul 14	120	··· ; ···
2MASSW J2130446−084520	J21304463−08452049	L1.5	···	M8.3	14.14	1.32	2006 Sep 01	120	52; 52
···	···	···	···	···	···	···	··· 2006 Sep 02	120	52; 52
···	···	···	···	···	···	···	··· 2008 Jul 13	120	52; 52
···	···	···	···	···	···	···	··· 2008 Sep 09	120	52; 52
···	···	···	···	···	···	···	··· 2012 Sep 27	120	52; 52
···	···	···	···	···	···	···	··· 2012 Oct 27	120	52; 52
SDSS J213240.36+102949.4	J21324035+10294940	···	L4.5±1	L4.8::	16.59	1.96	2012 Oct 27	120	40; 40
SDSS J213307.94+232159	J21330794+232159	M9.5	···	M9.6	13.74	1.18	2008 Nov 04	120	48; 48

Table 3.2 Continued

Source	Designation	Spectral Type			2MASS		Date	λ/Δλ	Ref[b]
		Opt	NIR	SpeX[a]	J	J-K_s			
SDSS J213435.61+240408	J21343561+240408	M8	···	M9.2	13.57	1.17	2008 Nov 04	120	48; 48
2MASS J21371044+1450475	J21371044+1450475	L2	···	L0.8	14.13	1.32	2008 Sep 08	120	49; 49
DENIS J21391360−3529500	J21391360−3529500	L0	···	L2.1:	14.47	1.11	2013 Aug 14	120	59; 59
SDSS J214046.55+011259.7	J21404654+0112594	L3	···	L4.4	15.89	1.47	2008 Sep 08	120	20; 20
2MASS J21420580−3101162	J21420580−3101162	L3	···	L2.9	15.84	1.88	2010 Jul 07	120	43; 43
SDSS J214527.82−073434.2	J21452782−0734342	M9	···	M8.7	15.59	1.28	2009 Nov 04	120	48; 48
2MASS J21472764+0101040	J21472764+0101040	M9	···	M9.1	14.57	1.10	2009 Jun 28	120	··· ; ···
2MASS J21481628+4003593	J21481633+4003594	L6	L6.5pec	L4.0	14.15	2.38	2005 Sep 09	120	51; 51
2MASS J21483083+0020540	J21483083+0020540	M9	···	M8.5	15.46	1.15	2009 Jun 28	120	··· ; ···
SDSS J214956.55+060334	J21495655+060334	M9	···	M8.1	13.34	1.17	2008 Nov 03	120	48; 48
SDSS J215339.77+295005	J21533977+295005	M9	···	M8.8	13.94	1.17	2008 Nov 03	120	48; 48
2MASS J21580457−1550098	J21580456−15500980	L4:	···	L4.3:	15.04	1.85	2006 Sep 01	120	52; 52
2MASS J22044198−0036510	J22044198−0036510	M9	···	M8.5	15.73	1.24	2009 Jun 29	120	··· ; ···
2MASSW J2206450−421721	J22064498−4217208	L2	···	L4.2::	15.56	1.95	2008 Jul 14	120	13; 13
GRH 2208−2007	J2210499−195224	M7.5	···	M8.8	14.00	0.85	2008 Jul 14	120	··· ; ···
2MASS J22114470+6856262	J22114470+6856262	···	L2	L2.2	15.67	1.65	2005 Sep 08	120	61; 61
2MASS J22134491−2136079	J22134491−21360789	L0γ	···	L1.9:	15.38	1.62	2006 Sep 02	120	44; 56
···	···	···	···	···	···	···	··· 2008 Aug 29	120	44; 56

Table 3.2 Continued

Source	Designation	Spectral Type			2MASS		Date	$\lambda/\Delta\lambda$	Ref[b]
		Opt	NIR	SpeX[a]	J	J-K_s			
WISE J222219.93+302601.4	J22221993+3026014	···	L9	L6.7:	16.55	1.37	2013 Oct 23	120	69; 69
LHS 523	J22285440−1325178	M6.5	···	M7.7	10.77	0.92	2007 Sep 16	120	··· ; ···
2MASPJ2234330+291850	J2234331+291849	M8:	···	M7.9	14.04	1.08	2008 Jul 12	120	··· ; ···
2MASS J22355013+1227370	J22355013+1227370	M9	···	M9.2	15.21	1.17	2009 Jun 30	120	··· ; ···
2MASSI J2238074+435317	J22380742+4353179	L1.5	···	L0.6	13.84	1.32	2009 Nov 07	120	27; 27
···	···	···	···	···	···	···	··· 2010 Jul 07	120	27; 27
SDSS J22434553−08215302	J22434553−08215302	M8	···	M8.4	15.43	1.14	2013 Jul 17	75	48; 48
SDSS J225003.72+143046.7	J22500372+1430467	M9	···	M8.7	14.94	1.22	2009 Nov 04	120	48; 48
···	···	···	···	···	···	···	··· 2009 Nov 07	120	48; 48
2MASSI J2254519−284025	J22545194−2840253	L0.5	L0.5	L0.2	14.13	1.18	2008 Jul 14	120	27; 27, 31
SDSSp J225529.09−003433.4	J22552907−0034336	L0:	···	M8.6	15.65	1.21	2008 Sep 07	120	19; 19
ULAS J22585405+0113512	J22585405+0113512	M9	···	M8.8	13.91	1.00	2013 Aug 14	120	62; 62
SDSS J225913.88−005158.2	J22591388−0051581	L2	···	L1.6	16.36	1.71	2009 Jun 29	120	20; 20
SDSS J230809.9−313122	J2308099−313122	M7	···	M7.5	13.62	1.04	2008 Nov 04	120	48; 48
DENIS J2308113−272200	J2308113−272200	L1.5	···	L1.4	14.58	1.40	2013 Sep 03	120	59; 59
SSSPM J2310−1759	J23101846−1759090	L0:	L1	M9.9	14.38	1.41	2008 Jul 14	120	83; 44, 37
SDSS J23172515−00543358	J23172515−00543358	M9	···	M8.7	15.68	0.94	2012 Sep 27	120	48; 48
2MASS J2320292+412341	J2320292+412341	L1:	···	M9.8	14.59	1.39	2003 Aug 12	75	76; ···

Table 3.2 Continued

Source	Designation	Spectral Type			2MASS		Date	λ/Δλ	Ref[b]
		Opt	NIR	SpeX[a]	J	J-K_s			
···	···	···	···	···	···	···	··· 2008 Sep 08	120	··· ; ···
2MASS J23211254−1326282	J23211254−1326282	···	L1	L0.4	14.50	1.36	2003 Sep 04	75	47; 47
···	···	···	···	···	···	···	··· 2008 Jul 12	120	47; 47
···	···	···	···	···	···	···	··· 2008 Sep 08	120	47; 47
SDSS J232136.11−002819.1	J23213611−0028191	M9	···	M8.3	15.48	1.04	2009 Nov 04	120	48; 48
SDSS J232246.84−313323	J23224684−313323	L0:	···	L1.6:	13.58	1.25	2006 Aug 28	120	48; 48
···	···	···	···	···	···	···	··· 2008 Nov 04	120	48; 48
SDSS J232313.4−024435	J2323134−024435	M8.5	···	M8.0	13.58	1.10	2008 Nov 03	120	48; 48
2MASS J23302258−0347189	J23302258−0347189	L1:	···	L0.5	14.48	1.35	2008 Jul 14	120	44; 44
HD 221356BC	J23310217−0406248	M9+L3	···	M8.7	12.94	0.98	2013 Dec 05	120	14; 46
LSPM J2331+4607N	J23311807+4607310	···	d/sdM7	M7.4	15.92	0.74	2005 Sep 07	120	··· ; 75
2MASS J23312935+1552220	J23312935+1552220	L0	···	M9.5	15.06	1.06	2009 Jun 30	120	··· ; ···
SDSS J233224.38−005025	J23322438−005025	M8	···	M7.7	13.65	1.04	2008 Nov 03	120	48; 48
SDSS J233350.76−000011.3	J23335076−0000113	M9	···	M8.6	15.52	0.98	2009 Nov 07	120	48; 48
2MASS J23335838+0050110	J23335838+0050110	M9	···	M9.3	15.01	1.17	2009 Jul 01	120	··· ; ···
SDSS J23352642+0817213	J23352642+0817213	L0	···	M9.5	14.72	1.34	2012 Oct 24	120	60; 60
SDSS J23371664−09332480	J23371664−09332480	M8	···	M7.6	13.41	1.13	2013 Aug 14	120	48; 48
2MASS J2341286−113335	J2341286−113335	M8	···	M7.9	13.55	1.00	2010 Jul 07	120	··· ; ···

Table 3.2 Continued

Source	Designation	Spectral Type			2MASS		Date	λ/Δλ	Ref[b]
		Opt	NIR	SpeX[a]	J	J-K_s			
2MASS J23440624−0733282	J23440624−0733282	L4.5	···	L6.0	14.80	1.57	2009 Jun 29	120	52; 52
2MASS J23453903+0055137	J23453903+0055137	M9	···	M9.2	13.77	1.19	2008 Jul 14	120	49; 49
SDSS J234654.7−315353	J2346547−315353	M8	···	M8.7	13.28	1.08	2008 Nov 04	120	48; 48
2MASS J2352050−110043	J2352050−110043	M7	···	M8.0	12.84	1.10	2010 Jul 07	120	··· ; ···
DENIS−P J2353−0833	J2353594−083331	M8.5	···	M8.6	13.03	1.10	2010 Jul 07	120	··· ; ···
DENIS J23545990−1852210	J23545990−1852210	L2	···	L2.6:	14.22	1.39	2013 Aug 14	120	59; 59
SSSPM J2356−3426	J23561081−3426044	M9.0	L0.5	M9.3	12.95	0.98	2007 Sep 16	120	37; 37
SSSPM J2400−2008	J23595762−2007394	M9.5	L1	M8.9	14.38	1.13	2008 Jul 14	120	37; 37

[a]Near-infrared classification from SpeX data based on index method described in Burgasser (2007a).

[b]First citation is the discovery reference; next citation(s) are classification references (optical and near-infrared).

References. — (1) Haro & Chavira (1966); (2) Liebert (1976); (3) Becklin & Zuckerman (1988); (4) Bessell (1991); (5) Kirkpatrick et al. (1995); (6) Tinney et al. (1998); (7) Rebolo et al. (1998); (8) EROS Collaboration et al. (1999); (9) Delfosse et al. (1999); (10) Martín et al. (1999); (11) Kirkpatrick et al. (1999b); (12) Fan et al. (2000); (13) Kirkpatrick et al. (2000); (14) Gizis et al. (2000b); (15) Basri et al. (2000); (16) Gizis et al. (2000a); (17) Scholz et al. (2001); (18) Wilson et al. (2001); (19) Schneider et al. (2002); (20) Hawley et al. (2002); (21) Geballe et al. (2002); (22) Gizis (2002); (23) Lépine et al. (2002a); (24) Phan-Bao et al. (2003); (25) Kendall et al. (2003); (26) Lépine et al. (2003); (27) Cruz et al. (2003); (28) Cruz et al. (2003); (29) Berriman et al. (2003); (30) Wilson et al. (2003); (31) Kendall et al. (2004); (32) Pokorny et al. (2004); (33) Scholz et al. (2004b); (34) Knapp et al. (2004); (35) Golimowski et al. (2004b); (36) Deacon et al. (2005); (37) Lodieu et al. (2005); (38) Billères et al. (2005); (39) Reid & Gizis (2005); (40) Chiu et al. (2006); (41) McElwain & Burgasser (2006); (42) Cushing et al. (2006); (43) Liebert & Gizis (2006); (44) Cruz et al. (2007); (45) Burgasser et al. (2007a); (46) Caballero (2007); (47) Kendall et al. (2007); (48) West et al. (2008); (49) Reid et al. (2008b); (50) Burgasser et al. (2008b); (51) Looper et al. (2008b); (52) Kirkpatrick et al. (2008); (53) Phan-Bao et al. (2008); (54) Zhang et al. (2009); (55) Faherty et al. (2009); (56) Cruz et al. (2009); (57) Shkolnik et al. (2009); (58) Jenkins et al. (2009); (59) Martín et al. (2010); (60) Schmidt et al. (2010); (61) Kirkpatrick et al. (2010); (62) Zhang et al. (2010); (63) Bochanski et al. (2011); (64) Phan-Bao (2011); (65) Geißler et al. (2011); (66) Kirkpatrick et al. (2011); (67) Shkolnik et al. (2012); (68) Folkes et al. (2012); (69) Thompson et al. (2013); (70) Scholz (2013); (71) Allers & Liu (2013); (72) Andrei et al. (2011); (73) Boeshaar & Tyson (1985); (74) Schmidt et al. (in prep); (75) This paper; (76) Cruz et al. (2013); (77) Deacon et al. (2009); (78) Forveille et al. (2004); (79) Hall (2002); (80) Irwin et al. (1991); (81) Kirkpatrick (priv. comm.); (82) Kendall et al. (2007); (83) Lodieu et al. (2002); (84) Looper et al. (in prep); (85) Phan-Bao (2011); (86) Radigan et al. (2008); (87) Ruiz & Takamiya (1995); (88) Salim et al. (2003); (89) Tinney et al. (1993); (90) van Biesbroeck (1961).

The sources observed have optical and/or near-infrared spectral classifications reported in the literature. To obtain a self-consistent set of spectral types, we computed SpeX spectral types based on spectral indices, following the method described in Burgasser (2007a). From these, we selected two samples: the "candidate" sample which has been purged of spectral types outside the M7-L7 range, optical subdwarfs, giants, and poor quality spectra, but keeping binaries, objects suspected of being binaries from previous studies, young objects and unusually red and blue dwarfs, and the "template" sample which has been purged of binaries, candidate binaries and poor quality spectra (as determined by visual inspection). The "candidate" sample contains 815 spectra of 738 objects with SpeX spectral types between M7-L7, as those would be the potential primaries for late-M/early-L plus T binaries. The "template" sample comprise 1110 spectra of 992 single sources whose spectral types range between M7-L7 for primaries and T1-T8 for secondaries used in spectral fitting.

The distribution of spectral types for both samples is shown in Figure 3.1. In both samples, the number of spectra decreases toward later spectral types due to declining space densities for L dwarfs (Cruz et al. 2003) and sensitivity limits for late L and T dwarfs. Since there are significantly more sources with late-M spectral types in our samples, it is more likely to find binaries with a late-M primary. The sources included were observed as part of several different programs, including our ongoing program to compile a magnitude-limited sample of L dwarfs (Burgasser et al. in prep.). As such, we do not claim the sample to be complete or unbiased.

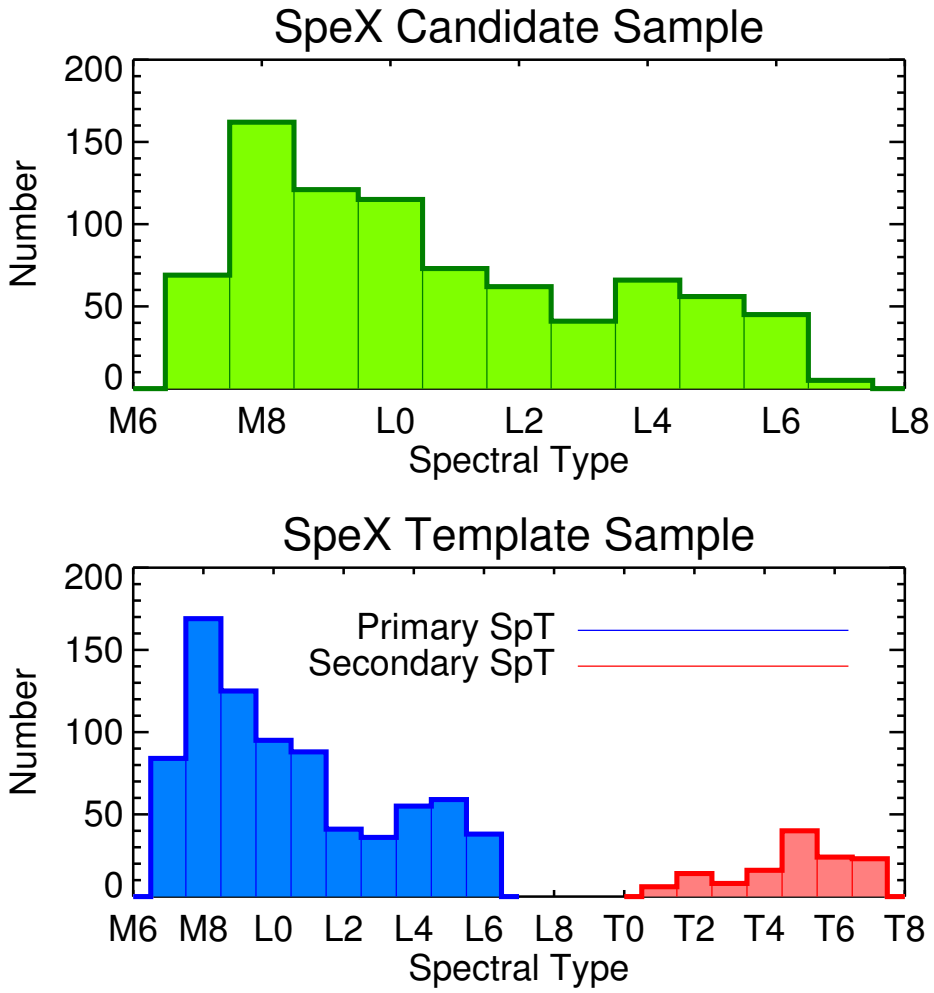

Figure 3.1 Distribution of SpeX spectral types in the samples used for selecting candidates (top) and template fitting (bottom).

3.3 Identification of spectral binaries

3.3.1 Visual inspection

The spectral morphology of unresolved late-M/early-L plus T dwarf binary systems gives rise to a distinctive feature in blended-light spectra: a small "dip" centered at 1.63 μm, which is the combination of CH_4 absorption from the secondary and FeH from the primary (Cushing et al. 2003; Burgasser 2007b). Methane does not exist in

the spectra of late-M/early-L dwarfs, so its presence indicates a T dwarf companion. However, this feature is very weak in blended-light spectra since a T dwarf is significantly fainter than the M/L primary (e.g. $\Delta J \sim 3.5$ mag between an M8 and a T5, which is the case for 2MASS J03202839−0446358). Moreover, variations in the spectral slope for a blue or red L dwarf, can make this feature ambiguous, as can poor correction of Hydrogen lines in the A0V calibrators. Alternative indicators such as a relatively higher flux around the 1.25 μm peak and inflated bump short ward of 2.2 μm, may also reveal the presence of a T dwarf companion, or that the spectrum of the source is unusually blue.

To facilitate our visual inspection, we fit the candidate sample to templates of single objects, following the same chi-squared minimization routine as in Section 3.3.3, and then subtracted the median combination of the ten best fitting single sources from each spectrum. The objects with residuals consistent with a T dwarf spectrum were selected as visual candidates. To validate this procedure, we also performed the same template subtraction on four confirmed spectral binaries: SDSS J000649.16−085246.3, 2MASS J03202839−0446358, SDSS J080531.89+481233.0, and 2MASS J13153094−2649513 (see Table 5.9). The residuals from these subtractions clearly exhibited T dwarf-like morphologies. Twelve sources were selected as visual candidates.

3.3.2 Spectral indices

In addition to visual inspection, we also used spectral indices to identify additional candidate binaries due to the subtlety of T dwarf features in combined-light spectra (Burgasser et al. 2010a). We initially examined standard classification indices from Burgasser et al. (2006b), as well as the "H-dip" index from Burgasser et al. (2010a), and further defined five new indices. The new indices were designed by comparing the residuals of the four known binary spectra after subtracting their best single template

fits. As a control sample, we also examined single templates subtracted from each other, which showed no evidence for a T dwarf companion.

The new spectral indices specifically designed in this paper are:

- H-bump: measures the peak in the continuum from the T dwarf in the H band relative to the dip centered around 1.63 μm seen in M+T binaries, making this index complimentary to H-dip. A higher value of H-bump implies a larger flux at 1.55 μm, possibly caused by the presence of a T dwarf.

- J-curve: designed to detect the flux coming from both the 1.05 μm and 1.27 μm peaks of a T dwarf, as compared to the deep methane absorption at 1.12 μm.

- J-slope and K_s-slope: measure the slope of the peaks in the J and K_s bands at 1.27 μm and 2.10 μm. In both cases, the peaks in a single late-M/early-L should look somewhat flat, giving values close to one, whereas in a late-M/early-L plus T dwarf binary the slope of the J and K_s band peaks are slightly negative and positive, respectively.

- H_2O-Y: measures the prominence of the Y-band peak of the T dwarf at $\sim$ 1.05 μm compared to the water and methane absorption around $\sim$ 1.15 μm. M and L dwarfs do not present peaks in the Y-band.

The thirteen indices examined are described in Table 3.3. We also used J-K_s, J-H and H-K_s colors synthesized from the spectra themselves, and the source spectral type, for a total of seventeen parameters.

Comparing all seventeen parameters against each other yielded 136 pairings. After visual examination to determine which pairings best segregated the four known M/L+T binaries, twelve combinations were selected (Figure 3.2). We then used two techniques to define regions of interest in each combination for candidate selection. If a

Table 3.3 Spectral indices

Spectral Index	Numerator Range (μm)	Denominator Range (μm)	Feature	Ref.
H_2O-*J*	1.14-1.165	1.26-1.285	1.15 μm H_2O	1
CH_4-*J*	1.315-1.335	1.26-1.285	1.32 μm CH_4	1
H_2O-*H*	1.48-1.52	1.56-1.60	1.40 μm H_2O	1
CH_4-*H*	1.635-1.675	1.56-1.60	1.65 μm CH_4	1
H_2O-*K*	1.975-1.995	2.08-2.10	1.90 μm H_2O	1
CH_4-*K*	2.215-2.255	2.08-2.12	2.20 μm CH_4	1
K/*J*	2.06-2.10	1.25-1.29	$J-K$ color	1
H-dip	1.61-1.64	1.56-1.59 + 1.66-1.69[a]	1.63 μm FeH/CH_4	2
K-slope	2.06-2.10	2.10-2.14	*K*-band shape/CIA H_2	3
J-slope	1.27-1.30	1.30-1.33	1.28 μm flux peak shape	4
J-curve	1.04-1.07 + 1.26-1.29[b]	1.14-1.17	Curvature across *J*-band	4
H-bump	1.54-1.57	1.66-1.69	Slope across *H*-band peak	4
H_2O-*Y*	1.04-1.07	1.14-1.17	1.15 μm H_2O	4

[a]Denominator is average of these two wavelength ranges.

[b]Numerator is average of these two wavelength ranges.

Note. — Indices were calculated by integrating flux between the specified wavelength ranges.

References. — (1) Burgasser et al. (2006b); (2) Burgasser et al. (2010a); (3) Burgasser et al. (2002b); (4) This paper.

trend among all sources was clear, we fit the points to a second order polynomial and defined a region demarcated in the y-axis by the +1σ or -1σ curves from the fit function, and in the x-axis by the horizontal spread of the binary benchmarks. Conversely, if the points did not indicate any trends, then the region was demarcated such that it included the four binary benchmarks. The limits to these regions are described in Table 3.4.

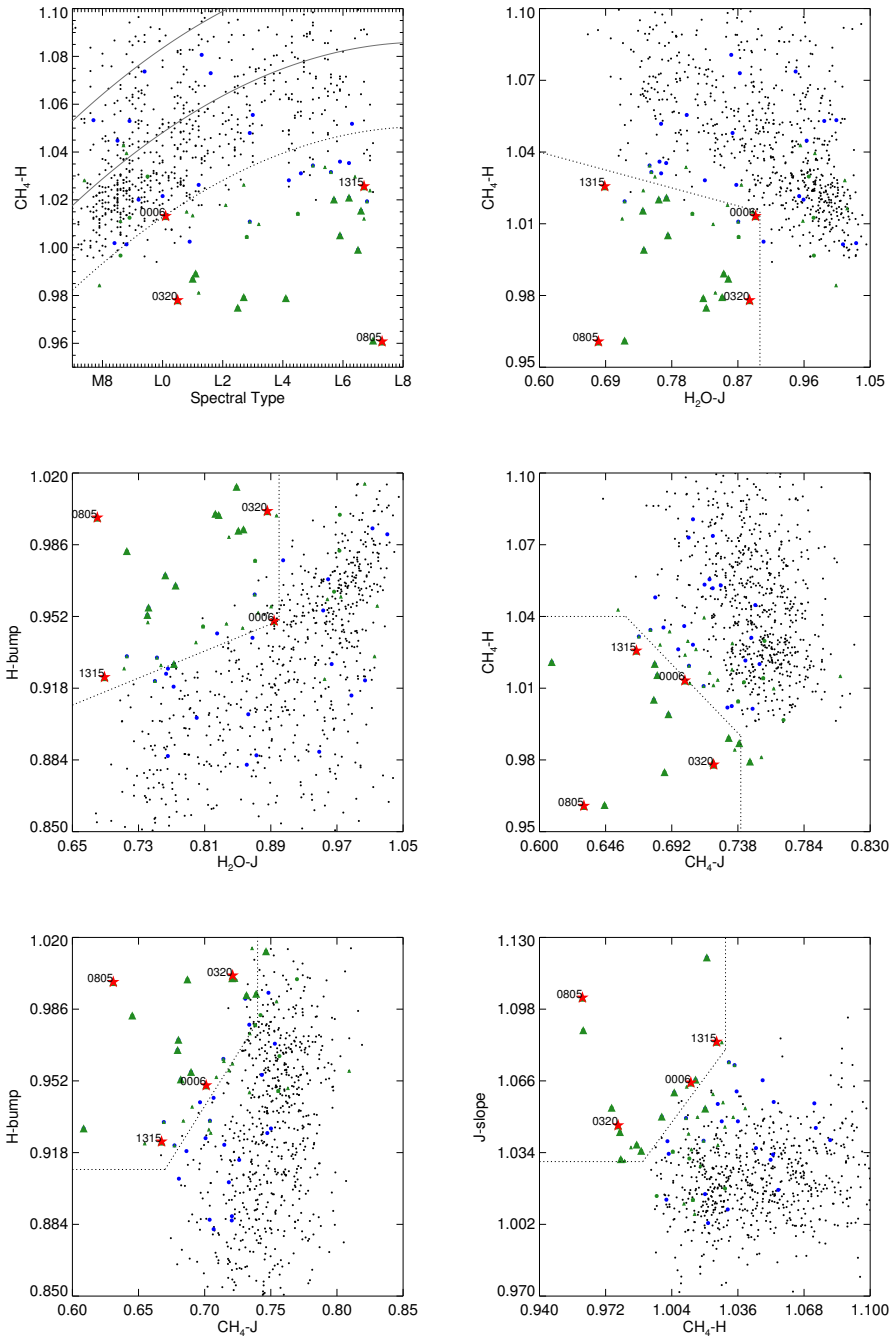

Figure 3.2 Index selection of spectral binary candidates. The indices calculated from the candidate sample of SpeX spectra are shown in black. The labeled red stars represent the four binary benchmarks. Unusually blue sources are plotted as blue circles, while the large and small green triangles show the strong and weak candidates, respectively. The green circles represent the visual candidates.

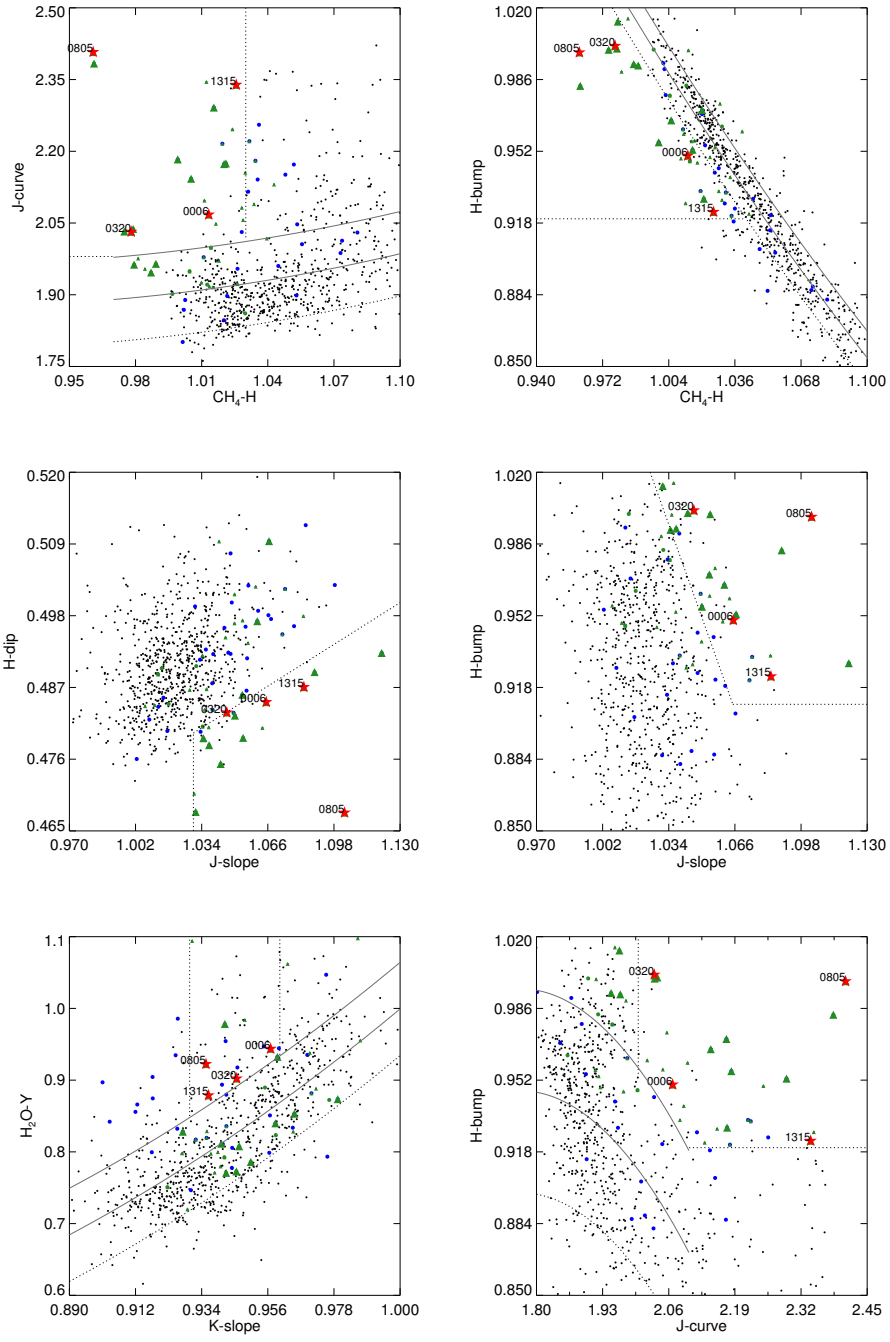

Figure 3.2 Continued.

Table 3.4 Delimiters for selection regions in parameter spaces.

x vs. y	Limits
SpT vs. CH_4-*H*	Best fit curve: $y = -4.3 \times 10^{-4}x^2 + 0.0253x + 0.7178$, σ = 0.0354. Select points below the -1σ curve.
H_2O-*J* vs. CH_4-*H*	Intersection of: $y = -0.08x + 1.09$ and $x = 0.90$. Select points on lower left corner.
H_2O-*J* vs. *H*-bump	Intersection of: $y = 0.16x + 0.806$ and $x = 0.90$. Select points on upper left corner.
CH_4-*J* vs. CH_4-*H*	Intersection of: $y = -0.56x + 1.41$ and $y = 1.04$. Select points on lower left corner.
CH_4-*J* vs. *H*-bump	Intersection of: $y = 1.00x + 0.24$, $x = 0.74$, and $y = 0.91$. Select points on upper left corner.
CH_4-*H* vs. *J*-slope	Intersection of: $y = 1.250x - 0.207$, $x = 1.03$, and $y = 1.03$. Select points on upper left corner.
CH_4-*H* vs. *J*-curve	Best fit curve: $y = 1.245x^2 - 1.565x + 2.224$, σ = 0.088. Select points above the 1σ curve, up to CH_4-*H* = 1.03.
CH_4-*H* vs. *H*-bump	Best fit curve: $y = 1.36x^2 - 4.26x + 3.89$, σ = 0.013. Select points below the -1σ curve, down to *H*-bump = 0.92.
J-slope vs. *H*-dip	Intersection of $y = 0.20x + 0.27$ and $x = 1.03$. Select points on lower right corner.
J-slope vs. *H*-bump	Intersection of: $y = -2.75x + 3.84$ and $y = 0.91$. Select points on upper right corner.
K-slope vs. H_2O-*Y*	Best fit curve: $y = 12.036x^2 - 20.000x + 8.973$, σ = 0.064. Select points above the 1σ curve and between *K*-slope = 0.93-0.96.
J-curve vs. *H*-bump	Best fit curve: $y = 0.269x^2 - 1.326x + 2.479$, σ = 0.048. Select points above the 1σ and greater than *J*-curve = 2.00 and *H*-bump = 0.92.

Objects falling in eight or more selection regions were considered strong index candidates, those falling in four to eight regions were considered weak index candidates (Figure 3.3). The number of selected sources rises sharply below four combinations, suggesting that sources selected fewer than four times are spurious. Three of our benchmarks were selected by all twelve combinations, while SDSS J0006−0852 missed only the SpT/CH_4-H cut, since it falls within one standard deviation from the fitting curve.

In total, nine strong and twenty-one weak candidates were selected, including the previously identified spectral binaries 2MASS J20261584−2943124 (Gelino & Burgasser 2010) and 2MASS J13114227+3629235 (Kirkpatrick et al. 2011). Seven visual candidates overlapped with the index candidates: five as strong and two as weak.

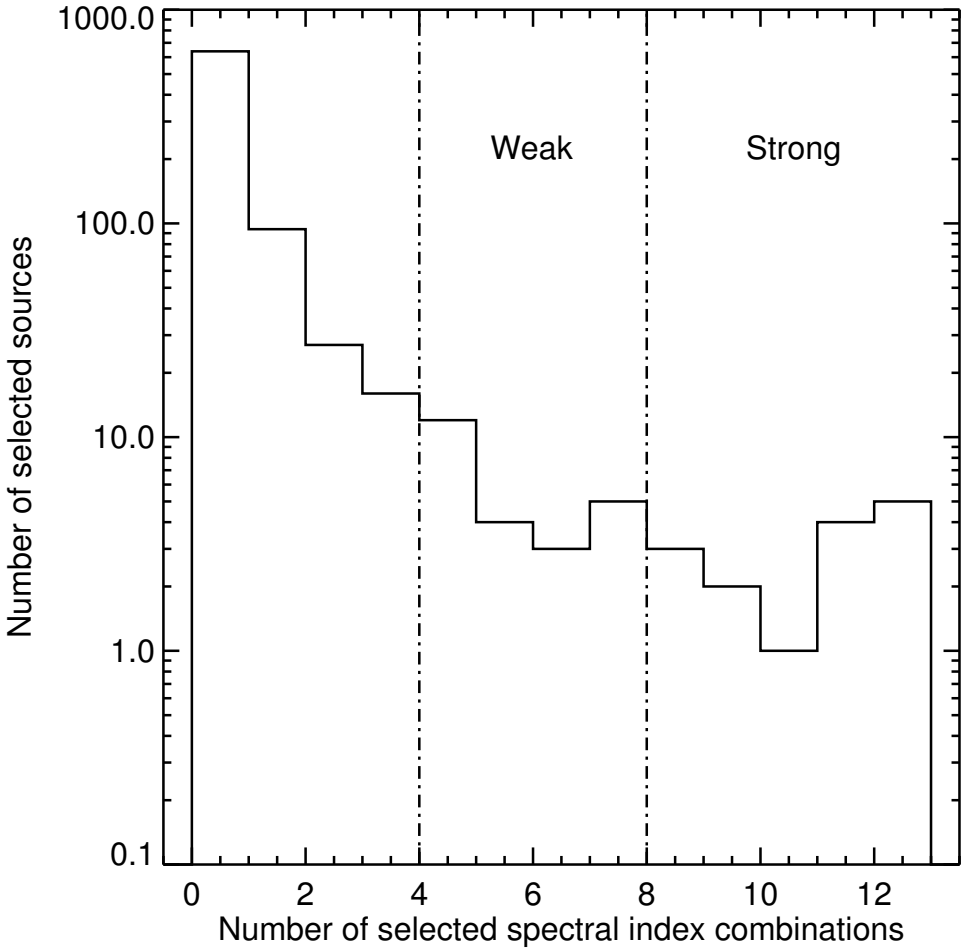

Figure 3.3 The number of sources satisfying index combinations versus total number of combinations. Sources selected 8 or more times are considered *strong* candidates. Sources selected between 4 and 8 times are considered *weak* candidates.

3.3.3 Spectral template fitting

To statistically test the binary hypothesis for our visual and index-selected candidates, we compared each spectrum to templates of both single sources and binary systems, using the method described in Burgasser et al. (2010a). The candidates determined by visual inspection or spectral index selection were first rejected from the template pool. Then, all spectra were interpolated onto a common wavelength scale from 0.8 to 2.4 μm and normalized to the peak flux between $1.2-1.3$ μm. Each candidate spectrum $C[\lambda]$

was directly compared to all single templates $T[\lambda]$ and ranked by a weighted chi-squared statistic.

$$\chi^2 \equiv \sum_{\lambda} w[\lambda] \left[\frac{C[\lambda] - \alpha T[\lambda]}{\sigma_c[\lambda]} \right]^2 \tag{3.1}$$

where $w[\lambda]$ is a vector of weights proportional to the wave band size of each pixel (see Cushing et al. 2008), α is a scaling factor minimizing χ^2 and $\sigma_c[\lambda]$ is the noise spectrum for each candidate. The statistic was computed over the wavelength range: $\{\lambda\} = 0.95 - 1.35$ μm, $1.45 - 1.80$ μm and $2.00 - 2.35$ μm, avoiding regions of strong telluric absorption.

Binary templates were constructed by first scaling each template spectrum to absolute fluxes using the 2MASS M_{Ks} versus spectral type relation of Looper et al. (2008a), and then combining all pairs of single templates, such that the spectral type of the primary was earlier than that of the secondary resulting in a total of $638,686$ binary templates. More specifically, the primary spectral type was fixed to lie between M7$-$L7 while the secondary spectral type ranged between T1$-$T8, since types earlier than T1 do not evidence strong methane features yet. The best binary fits were ranked using a chi-squared minimization routine. We determined the true significance that a binary template is superior to a single template by comparing the χ^2 distributions of the binary and single fits using the one-sided F-test statistic $\eta_{\rm SB}$:

$$\eta_{\rm SB} \equiv \frac{\min(\{\chi^2_{\rm single}\})}{\min(\{\chi^2_{\rm binary}\})} \frac{\rm dof_{binary}}{\rm dof_{single}}. \tag{3.2}$$

Here, dof is the degrees of freedom for each fit (Equation 2 in Burgasser et al. (2010a)). Candidates with an F-statistic falling under the 90% confidence level were rejected, including five visual candidates. In particular, 2MASS J14493784+2355378 and 2MASS J14232186+6154005 (also a weak index-selected candidate), two previously

identified spectral binary candidates from Gizis et al. (2003) and Geißler et al. (2011) were rejected due to their low confidence level that the binary fit was statistically better than the single fit. Since our template sample includes a wide range of objects such as young and unusually blue and red dwarfs, the peculiarities of these candidates may be better explained by factors other than unresolved binarity. One exception to the index selection was 2MASSI J1711457+223204 whose SpeX spectral type was too late to be included in the candidate sample, yet it was a visual candidate and passed the binary fit F-test. Figures 3.4 and 3.5 show the best single (left) and binary (right) template fits to our strong and weak candidates. Table 3.5 summarizes the results of these fits.

Upon further examination, some binary fits still proved unsatisfactory. This was the case for the following objects: the blue L dwarfs 2MASS J1118−0856, 2MASS J1416+1348, 2MASS J1515+4847, 2MASS J1711+40285, and the subdwarfs 2MASS J0330−2348, 2MASS J0330+3505, 2MASS J0402+1730, 2MASS J1541+5425 and 2MASS J2331+4607. Section 3.5.1 discusses these issues in more detail. As a result, fourteen candidates have been recognized, of which twelve are newly identified.

In an effort to balance the tradeoff between fidelity of binary candidates and completeness, we are leaning towards the former. Our binary selection criteria are conservative and it is likely that other spectral binaries may be identified with slightly looser constraints.

Table 3.5 Binary candidates resulting from spectral fitting

Source	Primary SpT [a]	Secondary SpT [a]	Confidence[b]	ΔJ	ΔK	SB Ref.	Comments[c]
Strong Candidates							
2MASS J02361794+0048548	L5.0±0.6	T1.9±1.1	97%	1.05±0.48	1.80±0.55	1	···
SDSS J093113.23+280227.1	L1.4±0.1	T2.6±0.9	> 99%	2.22±0.23	2.74±0.25	1	V, B
2MASS J13114227+3629235	L4.8±0.6	T4.1±2.7	> 99%	2.19±1.02	3.14±1.33	5	V
2MASS J13411160−30525049	L1.2±0.3	T6.3±1.0	98%	3.28±0.53	4.82±0.63	1	V
2MASS J14532589+1420418	L1.1±0.0	T6.0±1.1	> 99%	3.27±0.46	4.42±0.63	1	V, (B)
2MASS J20261584−2943124	L0.1±0.5	T5.8±1.0	> 99%	3.42±0.40	4.82±0.57	4	V
Weak Candidates							
2MASS J02060879+22355930	L5.1±0.5	T3.2±2.3	95%	1.61±0.89	2.36±1.25	1	···
DENIS−P J04272708−1127143	M7.4±0.2	T5.1±1.5	92%	4.13±0.62	4.98±0.84	1	···
2MASS J10365305−3441380	L5.2±0.4	T1.4±0.4	> 99%	0.51±0.32	1.41±0.24	1	···
2MASS J10595138−2113082	L0.6±0.4	T3.4±1.3	> 99%	2.58±0.32	3.30±0.64	1	V
SDSS J142227.20+221557.5	L4.2±0.6	T4.1±2.3	96%	2.36±0.78	3.22±1.18	1	B
WISE J16235970−0508114	L0.6±0.3	T6.0±0.8	> 99%	3.39±0.40	4.80±0.53	1	···
2MASS J17072529−0138093	L0.7±0.5	T4.3±2.0	97%	2.87±0.75	3.75±1.01	1	···
Visual Candidates							
2MASSI J1711457+223204	L1.5±0.6	T2.5±1.0	> 99%	1.20±0.40	3.08±0.64	6	V
Rejected Blue L dwarfs[d]							
2MASS J11181292−0856106	L1.4±0.7	T2.3±2.3	93%	1.50±0.82	2.42±1.11	···	B
SDSS J141624.09+134826.7	L4.4±1.1	T3.9±1.4	> 99%	2.12±0.42	2.99±0.67	···	B
2MASS J15150083+4847416	L5.0±0.6	T2.7±1.9	93%	1.32±0.61	2.17±0.84	1	B
2MASS J17114559+4028578	L4.4±0.3	T2.7±0.8	> 99%	1.60±0.18	2.32±0.33	···	B
Rejected Candidates							
2MASS J03205965+1854233	M7.8±0.1	T6.0±1.5	58%	4.43±0.73	5.47±0.92	···	V
2MASS J03264453+1919309	M8.5±0.0	T6.7±0.8	87%	4.66±0.50	5.91±0.58	···	V
2MASS J03303847−2348463	M7.7±0.3	T5.6±1.6	49%	3.97±0.85	4.58±1.05	···	···
2MASS J03301720+3505001	M7.7±0.5	T5.3±1.7	55%	4.27±0.81	5.08±1.03	···	···
2MASS J03440891+0111249	L0.6±0.5	T4.8±2.1	56%	3.34±0.88	4.14±1.19	···	···
2MASS J04024315+1730136	M7.5±0.2	T5.4±1.7	48%	4.59±0.78	5.29±1.01	···	···
2MASS J04430581−3202090	L4.5±0.3	T1.7±1.0	85%	1.41±0.34	2.05±0.39	1	B
2MASS J08433328+1024435	L0.9±0.3	T4.9±2.0	80%	3.01±0.75	3.99±1.03	···	···

Table 3.5 Continued

Source	Primary SpT [a]	Secondary SpT [a]	Confidence[b]	ΔJ	ΔK	SB Ref.	Comments[c]
2MASS J08475148+0138110	L2.0±0.7	T5.7±2.1	59%	3.19±0.74	4.61±1.07	···	···
2MASS J14232186+6154005	L1.9±0.8	T4.6±1.9	72%	2.63±0.67	3.78±0.97	3	V
2MASS J14493784+2355378	M9.4±0.3	T6.2±1.7	51%	4.22±0.69	5.39±1.00	2	V
2MASS J15412408+5425598	M7.6±0.3	T5.4±1.6	55%	4.53±0.75	5.22±0.99	···	···
2MASS J16403561+2922225	M8.1±0.7	T5.3±1.7	51%	4.38±0.77	5.09±1.00	···	···
2MASS J17175402+64274503	M8.5±0.1	T4.6±1.8	86%	4.18±0.70	4.93±1.02	···	···
2MASS J19064847+4011068	L0.0±0.4	T5.9±1.8	74%	3.68±0.75	4.85±1.01	···	···
2MASS J20472471+1421526	M8.4±0.2	T5.7±1.6	81%	4.10±0.70	5.13±0.95	···	V
2MASS J23311807+4607310	M7.5±0.0	T5.7±1.5	53%	4.60±0.75	5.30±0.95	···	···

[a]Uncertainties include systematics from spectral classification of Burgasser (2007a).

[b]Confidence that the source fits the binary template better than the single template based on a one-sided F-test. See Section 3.3.3.

[c]B = Unusually blue L dwarf, (B) = From this paper; V = Also a visual candidate.

[d]See Section 3.5.1.

References. — (1) This paper; (2) Bouy et al. (2003); (3) Geißler et al. (2011); (4) Gelino & Burgasser (2010); (5) Kirkpatrick et al. (2011); (6) Burgasser et al. (2010a).

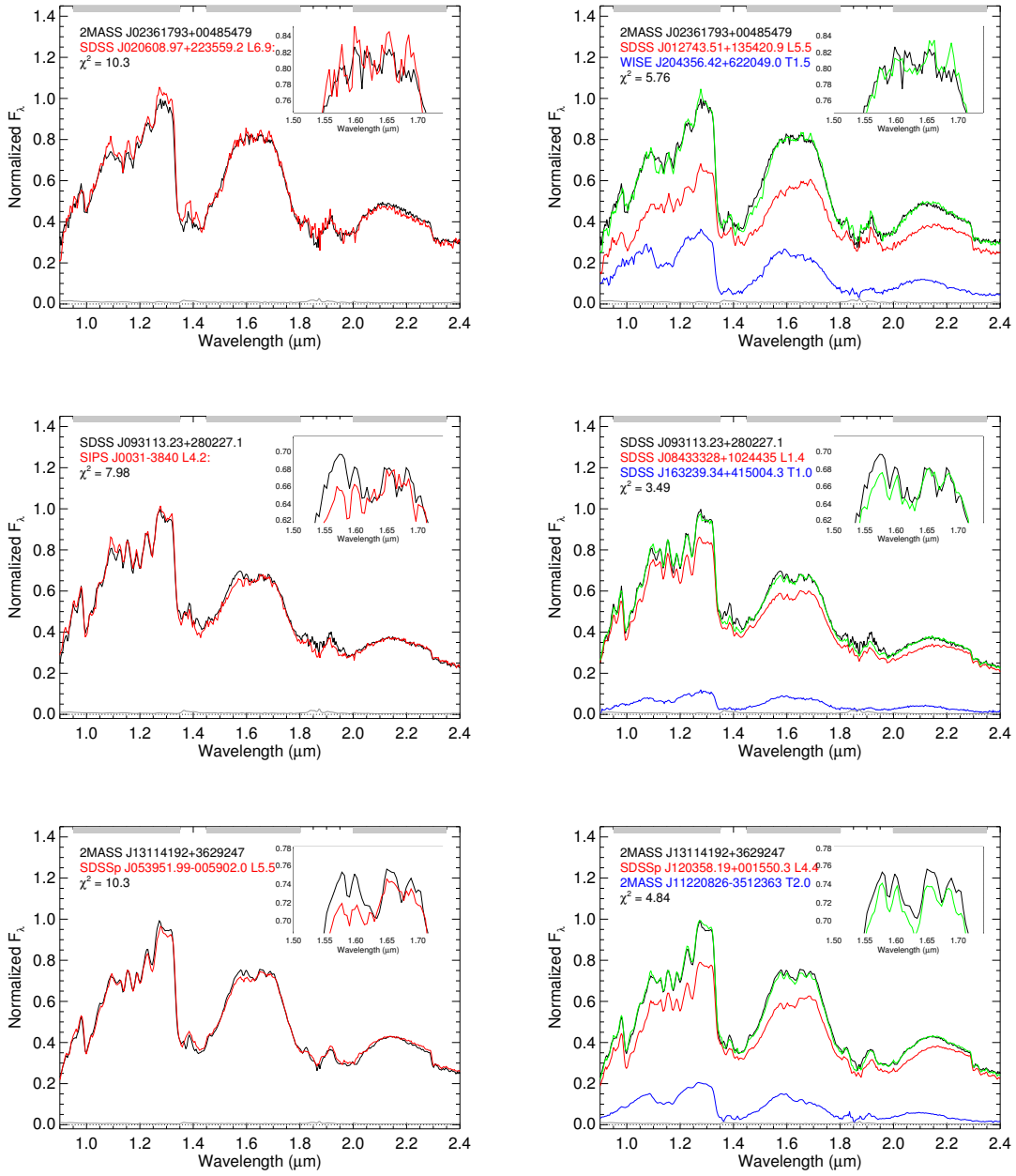

Figure 3.4 Best fits to single (left) and binary (right) templates for our strong candidates. The black line shows the candidate spectrum. For the single fits, the red line is the best single template. For the binary fits, the green line is the best binary template, which is the addition of the red (primary) and blue (secondary) lines. The gray line represents the uncertainty in the candidate spectrum. The gray horizontal bars at the top of the figures mark the parts of the spectrum being fit, while water absorption dominates the gaps. Notice the significant fitting improvement on the binary fits as compared to the single fits, particularly around the methane absorption feature centered at 1.63 μm (see inset).

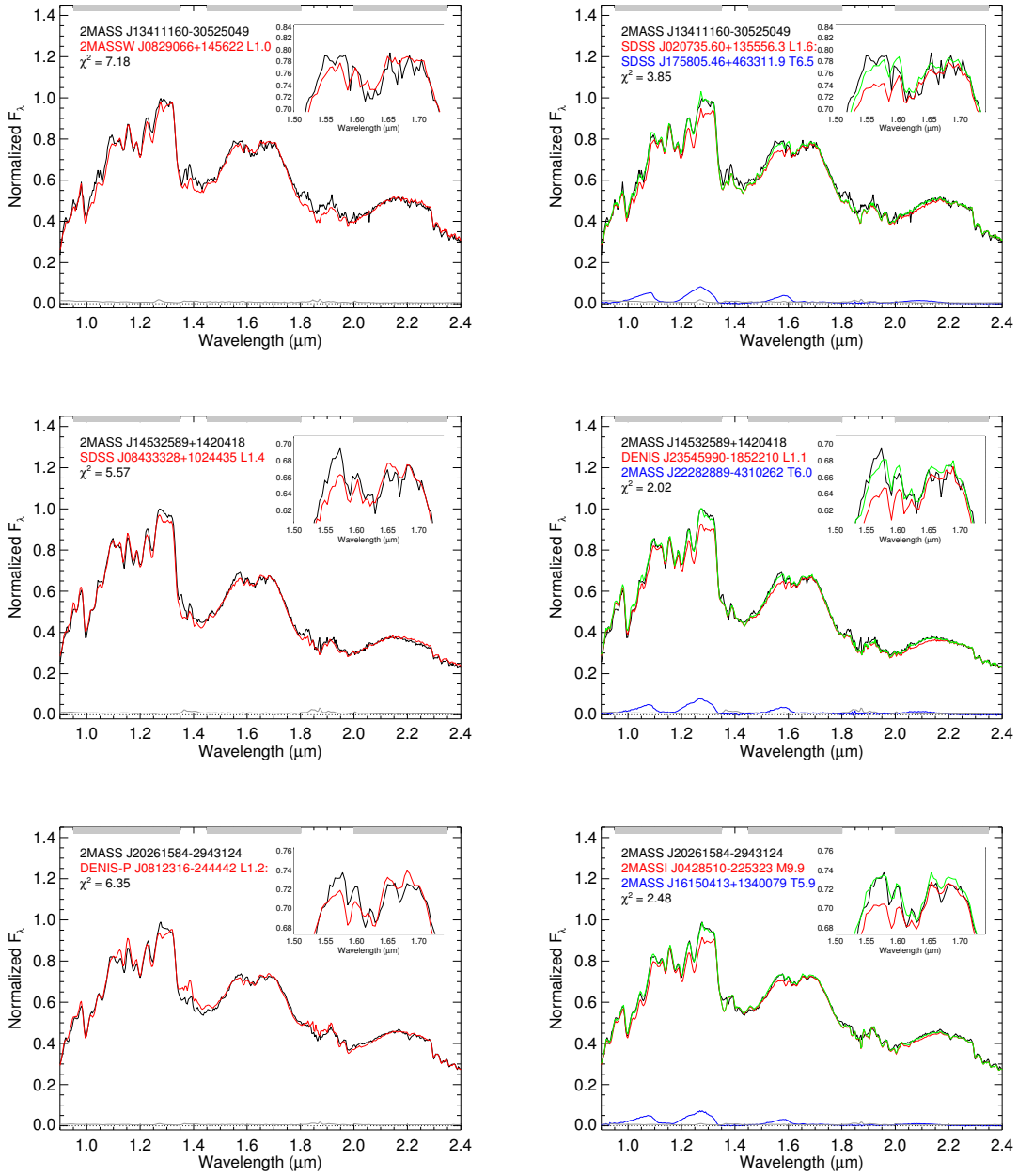

Figure 3.4 Continued.

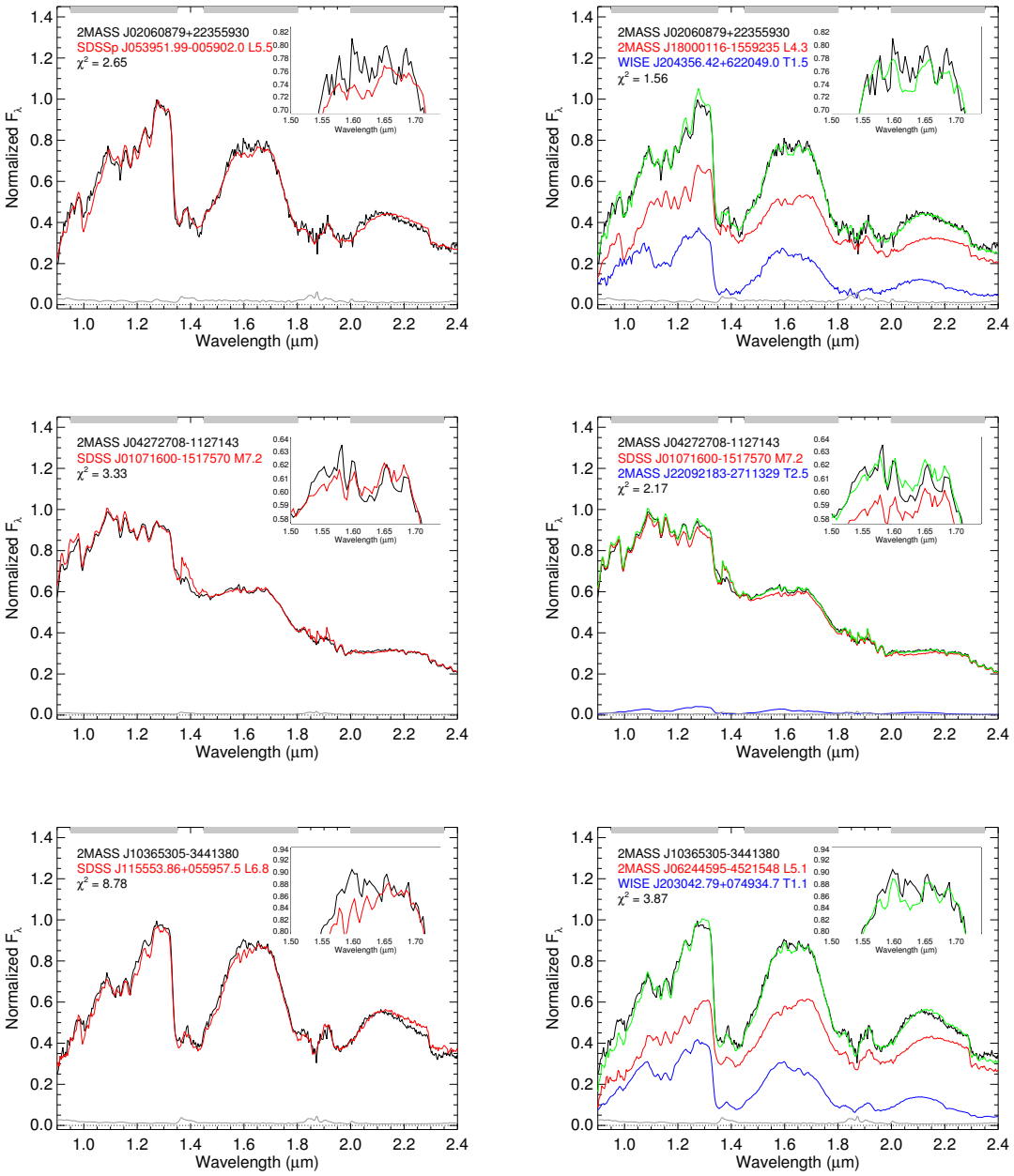

Figure 3.5 Best fits to single (left) and binary (right) templates for our weak candidates. Same color code as for Figure 3.4.

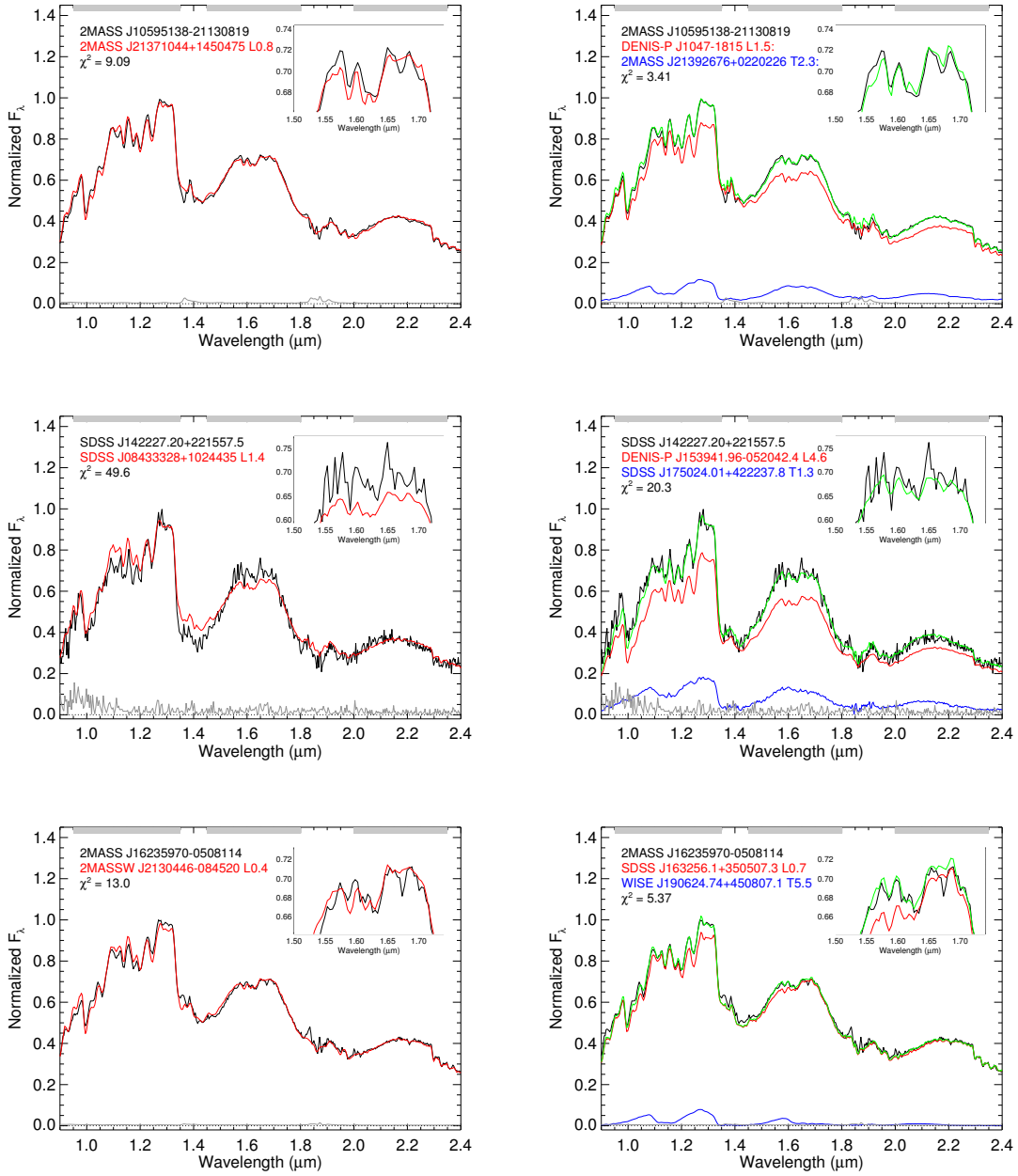

Figure 3.5 Continued.

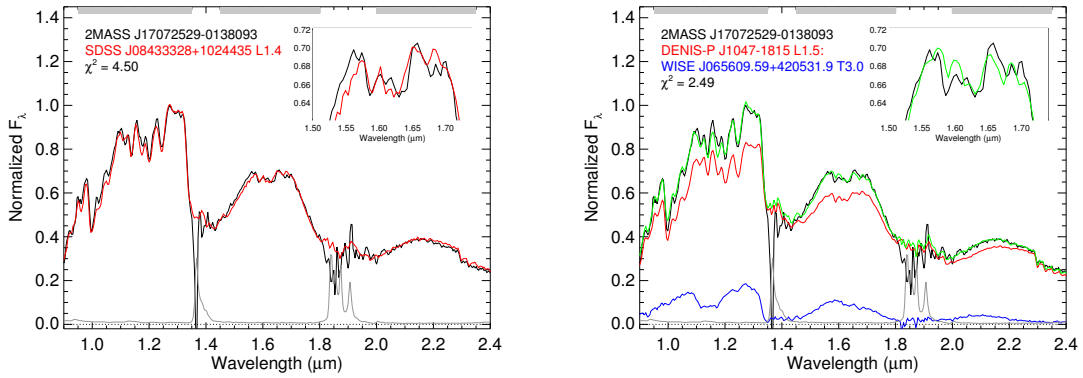

Figure 3.5 Continued.

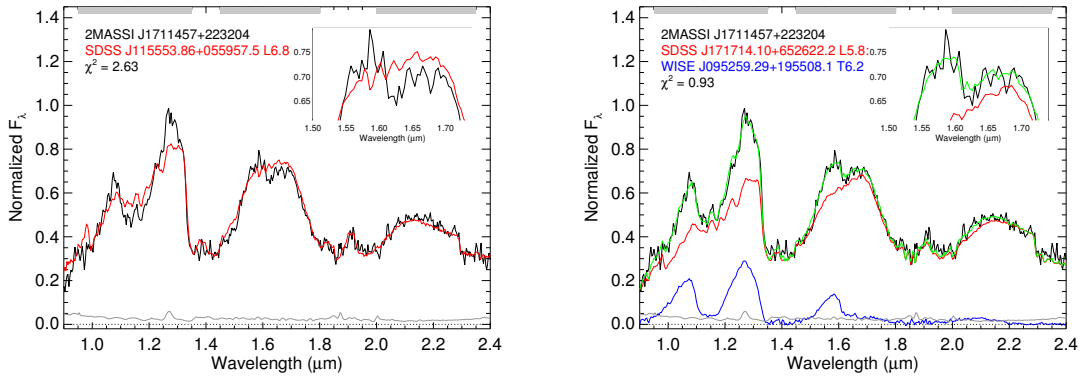

Figure 3.6 Best fits to single (left) and binary (right) templates for the only visual candidate not selected by indices. Same color code as for Figure 3.4.

3.4 Individual candidates

In summary, from the ∼800 sources compiled in the candidate sample, twelve were selected by visual inspection and thirty were selected by spectral indices. Seven sources overlapped the results of these selection methods. After fitting all thirty-five candidates, seventeen were rejected due to their confidence level lower than 90%, and four more due to their unusually blue colors (See Section 3.5.1), leading to a final count of fourteen. Labels of strong and weak candidates come from index selection.

3.4.1 Strong candidates

3.4.1.1 2MASS J02361794+0048548

Originally discovered by Geballe et al. (2002), 2MASS J0236+0048 was classified as an L6 in the optical and L6.5 in the infrared by Casewell et al. (2008). In their study, Casewell et al. (2008) comment that this object may belong to the Pleiades moving group, given its proper motion of $[\mu_\alpha cos\delta, \mu_\delta] = [161.33 \pm 10.10, 176.33 \pm 19.16]$ mas yr^{-1} and agreement between photometric and moving group distances at d = 26 pc. However, Scholz et al. (2009) reclassified this object as an L9, reducing its spectroscopic distance to 18 pc while its strong FeH band at 0.99 μm argues against low surface gravity (Allers et al. 2007). Nevertheless, the spectrum of this source does not show any signs of youth (Allers et al. 2007). 2MASS J0236+0048 is selected by eleven out of twelve spectral index combinations, and its binary fit is significantly better than its single fit, making this a strong binary candidate with L5.0±0.6 and T1.9±1.1 components.

3.4.1.2 SDSS J093113.09+280228.9

Schmidt et al. (2010) discovered SDSS J0931+2802 in the SDSS catalog and classified it as an L3 at a mean distance of 29±9 pc. Its spectrum shows excess flux in

the J-band at $\sim 1.27\mu$m and a noticeable dip in the H-band in the vicinity of 1.63μm, as expected for a T dwarf component. This source was selected as a visual candidate, and by eleven out of twelve spectral index combinations, and our spectral fitting predicts component types of L1.4±0.1 and T2.6±0.9.

3.4.1.3 2MASS J13114227+3629235

Identified as a brown dwarf candidate by Zhang et al. (2009), 2MASS J1311+3629 is a peculiar L5. While also classified as unusually blue in wavelengths longer than J band (Mace et al. 2013), it lacks evidence of low metallicity or H_2 collision-induced absorption (CIA) in H and K bands. Kirkpatrick et al. (2011) identified the methane feature in the H band centered around 1.63 μm suggesting unresolved binarity. In this study, it was selected by eleven spectral index combinations and also as a visual candidate due to its methane absorption band starting at 1.60 μm. Template fitting gives spectral types of L4.8±0.6 and T4.1±2.7.

3.4.1.4 2MASS J13411160−30525049

2MASS J1341−3052 was discovered by Reid et al. (2008b) and classified as an L3 in the optical by Faherty et al. (2009), who also measured its parallax and distance (24 ± 2 pc). 2MASS J1341−3052 was selected by eight spectral indices, and its spectral fitting suggests component spectral types of L1.2±0.3 and T6.3±1.0.

3.4.1.5 SDSS J142227.20+221557.5

SDSS J1422+2215 was identified and classified as an L6 in the NIR by Chiu et al. (2006) and also as an unusually blue L dwarf, showing strong H_2O and FeH absorption bands, which may be due to subsolar metallicity and/or thinner condensate cloud decks. It was selected by eight out of twelve spectral index combinations with most likely

component spectral types of L3.6±1.2 and T2.7±1.7.

3.4.1.6 2MASS J14532589+1420418

2MASS J1453+1420 was classified as an L1 in both the infrared (Kirkpatrick et al. 2010) and the optical (Schmidt et al. 2010), where it clearly shows excess flux in the *J* band and a dip in the *H* band. It is selected by eleven out of twelve spectral index combinations, and it is slightly blue with a J-K_s color of 1.18±0.05 as compared to the median for L1 spectral type 1.34±0.19 (Schmidt et al. 2010). It is best fit by L1.1±0.0 and T6.0±1.1 components.

3.4.1.7 2MASS J20261584−2943124

2MASS J2026−2943 had already been identified as a spectral binary candidate by Gelino & Burgasser (2010), but it failed to be resolved by Keck AO, thus setting an upper limit in separation of 0.″25 or a projected separation of 9 AU at a distance of 36±5 pc (Gelino & Burgasser 2010). This source clearly shows a dip in its spectrum centered at 1.63 μm, and it is best fit by a combination of L1.0±0.5 and T5.8±1.0 components.

3.4.2 Weak Candidates

3.4.2.1 2MASS J02060879+22355930

2MASS J0206+2235 was discovered and classified as an L5.5 by Chiu et al. (2006), and characterized as a blue L dwarf by Schneider et al. (2014). It was selected by seven spectral index combinations and fit to L5.1±0.5 and T3.2±2.3 components.

3.4.2.2 2MASS J04272708−1127143

2MASS J0427−1127 was discovered and classified as an M7 by Martín et al. (2010). It was selected by five spectral index combinations and best fit by M7.4±0.2 and T5.1±1.5 components.

3.4.2.3 2MASS J10365305−3441380

2MASS J1036−3441 was classified as an L6 (Gizis 2002) at a distance of 21±3 pc. It almost made the cut for a strong candidate, since it was selected by seven spectral index combinations. This source was best fit by components with L5.2±0.4 and T1.4±0.4 spectral types. Despite not having a pronounced methane absorption feature centered at 1.63 μm, the binary fit is significantly better than the single fit, especially at the *J* band peak.

3.4.2.4 2MASS J10595138−2113082

2MASS J1059−2113 is an L1 (Cruz et al. 2003) at a distance of 32.1 ±2.2 pc. This source was selected by four spectral index combinations and its best binary fit yields components with L0.6±0.4 and T3.4±1.3 spectral types. Its spectrum shows a strong absorption feature centered at 1.63 μm, as well as a flux excess at 1.23 μm and 2.20 μm.

3.4.2.5 WISE J16235970−0508114

WISE J1623−0508 was classified as an L1 in the NIR (Thompson et al. 2013). This source was selected by four spectral index combinations and best fit by L0.6±0.3 and T6.0±0.3 components.

3.4.2.6 2MASS J17072529−0138093

2MASS J1707−0138 was discovered and classified as an L2 by Martín et al. (2010). Selected by five spectral index combinations, its spectrum is best fit by components with L0.7±0.5 and T4.3±2.0 spectral types. Its spectrum shows a strong absorption feature centered at 1.63 μm.

3.4.3 Visual Candidates

3.4.3.1 2MASSI J1711457+223204

2MASS J1711+2232 was first identified and classified as an L6.5 in the optical by Kirkpatrick et al. (2000). Due to its FeH and CH_4 absorption features in the *H* band, Burgasser et al. (2010a) suggested it could be a spectral binary with L5.0 and T5.5 components. We find slightly different component spectral types of L1.5±0.6 and T2.5±1.0, yet this source was not selected by spectral indices because of its late SpeX spectral type of L8.8. Despite having been imaged with HST/WFPC, it remains unresolved (Gizis et al. 2003).

3.5 Discussion

3.5.1 Blue L dwarfs as contaminants

Four of the candidates selected by spectral indices were rejected after spectral fitting due to their poor binary fits. When we investigated these sources in detail, we found they were classified as blue objects in the literature and/or showed an unusually blue spectrum. 2MASS J11181292−0856106 was classified as a metal-poor subdwarf by Kirkpatrick et al. (2010). SDSS J141624.09+134826.7 is part of a resolved binary system with a T7.5 companion (Burningham et al. 2010; Burgasser et al. 2010b; Scholz

2010) that is itself a blue outlier. Bowler et al. (2010) rejected unresolved binarity for the primary based on a qualitative comparison to the unusually blue L dwarf 2MASS J11263991−5003550. The L6 2MASS J15150083+4847416 shows a stable RV of -29.97 ± 0.14 km s^{-1} (Wilson et al. 2003) and no signs of binarity from its spectrum. Finally, 2MASS J17114558+40285779 was discovered by Radigan et al. (2008) as an unusually blue wide companion to the K star G203-50. They discuss the possibility that the object may be unusual due to unresolved binarity, but argue in favor of low metallicity. For all of these sources, the lack of single templates akin to blue objects resulted in statistically better binary fits, yet the match is still relatively poor around the 1.63 μm methane absorption feature.

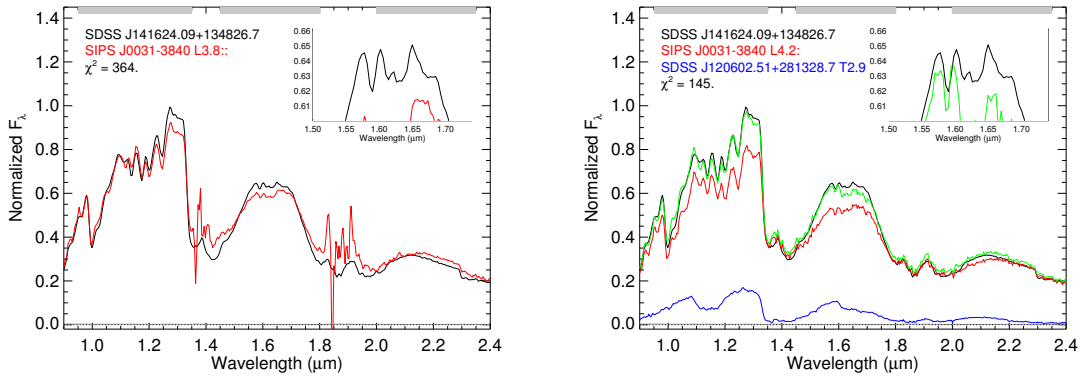

Figure 3.7 Example of binary fits to the blue L dwarf SDSS J141624.09+134826.7.

A few more previously unidentified NIR subdwarfs were also selected as weak candidates and subsequently rejected due to their poor binary fits. The best binary fits for 2MASS J0330384−234846, 2MASS J0330172+350500, 2MASS J0402431+173013, 2MASS J1541240+542559, and 2MASS J2331180+460731 use another subdwarf as a primary, which again indicates that they are part of a rare blue population that has a short supply of examples in this sample.

M+T binaries have slightly bluer spectra caused by the extra flux in the *J* band cor-

responding to the peak in the T dwarfs. Particularly, some sources originally classified as unusually blue have been later identified as spectral binaries (e.g. SDSS J0805+4812 Burgasser 2007b; Dupuy & Liu 2012). In contrast, intrinsically blue L dwarfs have low metallicity, thin cloud coverage, large-grain clouds or a combination of these, causing a blue tilt to the NIR spectrum (Schmidt et al. 2010; Burgasser et al. 2008b; Cruz et al. 2007). Faherty et al. (2009) have defined red and blue photometric outliers as the objects whose J-K_s color placed them 2σ or 0.4 mag away from the average for their spectral type, while pointing out the difficulty to distinguish outliers beyond a spectral type of L9 due to the small sample of objects. Figure 3.8 shows the J-K colors for our sample as compared to their spectral types, including the median and $\pm 2\sigma$ lines as calculated from the sample (solid lines) and reported in the literature (dashed lines) by West et al. (2011) and Schmidt et al. (2010) for samples of M and L dwarfs, respectively. Figure 3.8 suggests that blue L dwarfs are a major contaminant in our sample since a significant fraction of both known binaries and candidates have similar colors and thus lie in the same region as blue sources. We conclude that the blue L dwarf contaminants can be recognized if rejected due to their poor fits to binary template spectra.

3.5.2 Separation distribution of binary systems

True confirmation of our candidates requires observational follow-up to either resolve the systems or measure RV or astrometric variability. As noted in the introduction, spectral binaries can be used to devise an unbiased method to measure the VLM binary separation distribution. Therefore, it is worth examining the separation distribution of VLM and brown dwarf spectral binaries confirmed to date, to see if there are any differences compared to the resolved population.

Figure 3.9 shows the distribution of projected separations from 122 confirmed

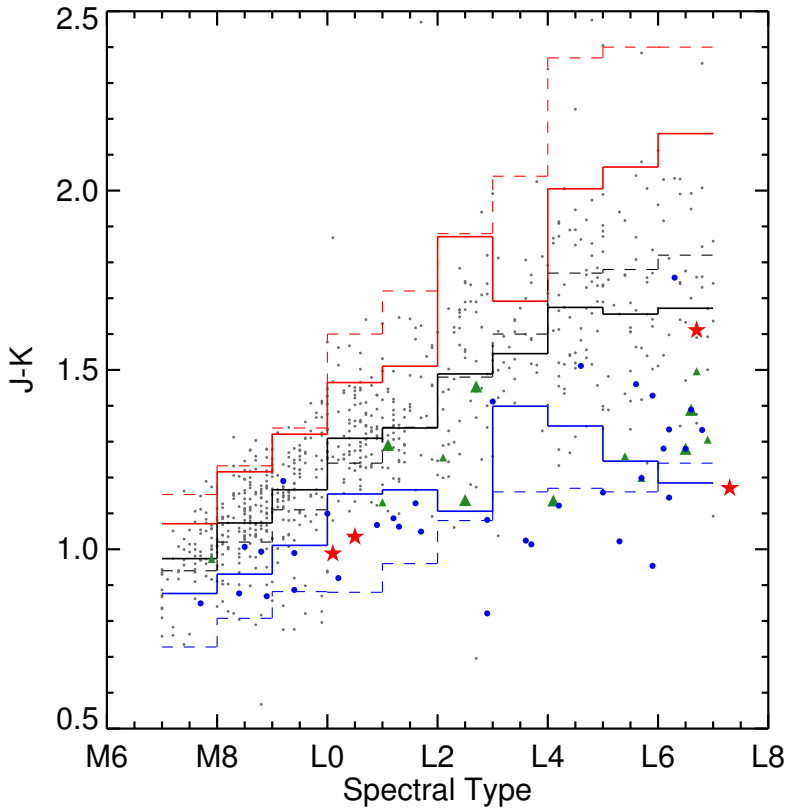

Figure 3.8 Comparison of spectrophotometric J-K_s colors of the "candidate" sample as a function of spectral type. The solid black line shows the median J-K colors from the sample, while the dashed black line represents the median J-K colors as calculated by West et al. (2011) and Schmidt et al. (2010) from samples of M and L dwarfs. The +2σ and -2σ boundaries are indicated in red and blue, respectively. The dashed lines indicate the +2σ and -2σ boundaries from West et al. (2011) and Schmidt et al. (2010) . Outliers to these regions indicate unusually red and blue dwarfs as described by Faherty et al. (2009). Red stars indicate confirmed M/L+T binaries, while large and small green triangles are strong and weak binary candidates as selected by spectral indices. Blue circles represent unusually blue sources as listed in the literature.

VLM binaries[3]. Among the observational methods for detecting binaries, such as direct imaging, radial velocity variations, astrometric variations, and microlensing, direct

[3]Based on the compilation at the Very-Low-Mass Binaries Archive, http://www.vlmbinaries.org, and more recent discoveries by Choi et al. (2013); Duchêne et al. (2013); Luhman (2013); Radigan et al. (2013); Sahlmann et al. (2013); Burgasser et al. (2012); Liu et al. (2012); Artigau et al. (2011); Burgasser et al. (2011b); Dhital et al. (2011); Gelino et al. (2011); Geißler et al. (2011); Liu et al. (2011); Allers et al. (2010); Burgasser et al. (2010a); Hwang et al. (2010); Stumpf et al. (2010); Allers et al. (2009); Luhman et al. (2009).

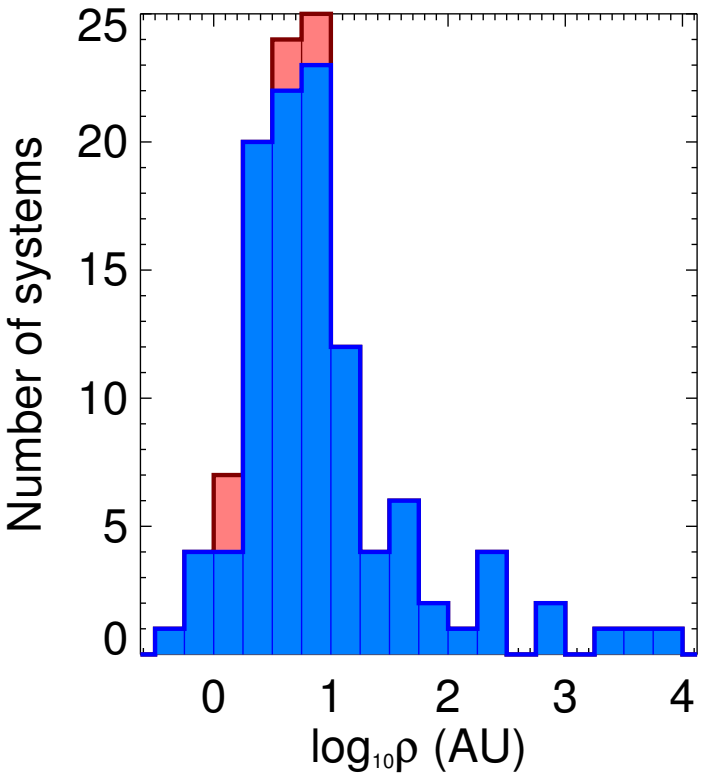

Figure 3.9 Projected separation (ρ) distribution of 122 confirmed brown dwarf and VLM binary systems from the Very Low Mass Binaries Archive. Spectral binaries are shown in red. Binary systems with only upper limits in separation have been excluded.

imaging has proven to be the most successful so far (68% of confirmed VLM binaries), but its biggest drawback is its limit in resolution. At minimum angular scales of 0.″1-0.″2 for AO and HST programs, and typical distances of field brown dwarfs of 20-30 pc, telescope sensitivity reaches its limit at separations of around 2-6 AU. At 2.90 AU, the mean projected separation of eight independently-confirmed spectral binaries plotted in Figure 3.9 falls at the lower end of this sensitivity limit, at less than the mean of known VLM binaries excluding the spectral binaries (3.75 AU), raising the possibility that there may be significantly more tightly bound systems.

To assess whether this is a significant difference, we performed a two-sample

Kolmogorov-Smirnov test comparing the projected separation distributions of all binary systems to the confirmed spectral binaries. Specifically, the distributions were constrained in angular separation to 50-500 mas, where the lower limit corresponds to the smallest possible imaging resolution in good seeing, while the upper limit restricts the maximum size of the slit. In addition, the distance was constrained to less than 30 pc, since objects that are farther away would be more difficult to confirm as binaries. In this way, we intend to fairly compare the spectral binary method to the other available methods for binary detection. These constraints reduced the number of spectral binaries to six. The result was a D statistic of 0.41 and a probability of 25%. While the low probability is indicative of a difference between the samples, the small sample size makes this statistic inconclusive. Many more of the existing spectral binaries need to be characterized before a significant difference can be confirmed or ruled out.

3.6 Summary

We have identified foureen brown dwarf binary candidates with late-M/early-L plus T dwarf components based on visual inspection of low resolution data, and analysis with spectral indices and template fitting. We combined five new spectral indices, with previously defined ones, spectral type, and J-H, H-K_s, and J-K_s colors to define pairings that effectively select spectral binary candidates, and confirmed them by comparison to both single and binary template spectra from the SpeX Prism Library. Unusually blue L dwarfs were the main contaminant of this analysis, with four candidates classified as unusually blue but nonetheless being poorly matched to binary spectra. Exploring the separation distribution of binary systems we find suggestive evidence that spectral binaries are more closely separated than other binaries, but the confirmed sample is too small to be conclusive. We are now undertaking follow-up AO imaging and RV

monitoring of these candidates to confirm them and measure orbital properties.

Acknowledgments

The authors thank telescope operators for their assistance during our observations. DBG would like to thank the Friends of the International Center at UCSD for their generous scholarship as well as Davy Kirkpatrick and fellow graduate students Alex Mendez and David Vidmar for their helpful discussion and coding tips. This publication makes use of data from the SpeX Prism Spectral Libraries, maintained by Adam Burgasser at http://www.browndwarfs.org/spexprism; the Dwarf Archives Compendium, maintained by Chris Gelino at http://DwarfArchives.org; and the VLM Binaries Archive maintained by Nick Siegler at http://vlmbinaries.org. The authors wish to recognize and acknowledge the very significant cultural role and reverence that the summit of Mauna Kea has always had within the indigenous Hawaiian community. We are most fortunate to have the opportunity to conduct observations from this mountain.

Facilities: IRTF (SpeX).

This Chapter, in full, is a reprint of the material as it appears in the Astrophysical Journal 2014, Vol. 794, Num. 143. Bardalez Gagliuffi, Daniella; Burgasser, Adam; Gelino, Christopher; Looper, Dagny; Nicholls, Christine; Schmidt, Sarah; Cruz, Kelle; West, Andrew; Gizis, John; Metchev, Stanimir. The dissertation author was the primary investigator and author of this paper.

Chapter 4

High Resolution Imaging Follow-up

4.1 Laser Guide Star Adaptive Optics Imaging

Observational studies of field brown dwarfs indicate that only $\sim 10-20\%$ are found in very low mass (VLM) binary systems (Bouy et al. 2003; Close et al. 2003; Basri & Reiners 2006; Allen 2007; Burgasser 2007a; Kraus & Hillenbrand 2012). In contrast, the binary fraction for G stars is $\sim 40\%$ (Duquennoy & Mayor 1991) and $\sim 30\%$ for M dwarfs (Fischer & Marcy 1992). These statistics suggest a steady decline of binary fraction with mass. The peak in the observed projected separation distribution also decreases with mass, going from 30AU for G dwarfs (Duquennoy & Mayor 1991), $4-30$AU for M dwarfs (Raghavan et al. 2010; Fischer & Marcy 1992) to $6-8$AU for VLM stars and brown dwarfs (Allen 2007; Burgasser et al. 2007c; Kraus & Hillenbrand 2012).

The observed peak in the projected separation distribution for VLM dwarfs is largely based on direct imaging studies, which have discovered $> 80\%$ of the VLM binary systems to date (Burgasser et al. 2007c; Bardalez Gagliuffi et al. 2014 [hereafter: BG14]). Angular resolution limits impose a bias on the separations observed. For ground-

based telescopes with Adaptive Optics (AO) and the Hubble Space Telescope (HST), this resolution limit is roughly $0\farcs05 - 0\farcs1$, which at the typical distances of known VLM dwarfs, $20 - 40$pc[1], corresponds to the observed peak in the projected separation distribution. Tighter systems are unresolvable. Measurements of radial velocity (RV) and astrometric variability more adequately probe the small projected separation regime, but such measurements are resource-intensive and introduce their own set of geometric biases. An alternative approach to identifying closely-separated VLM binaries is as *spectral binary* systems. Spectral binaries exhibit peculiarities in blended-light spectra that arise from the superposition of two components with distinct spectral morphologies. This method has been used to disentangle the spectra of white dwarf/M dwarf binaries (Silvestri et al. 2007) and more recently, VLM stars and brown dwarfs, especially those with a T dwarf component (e.g. Cruz et al. 2004; Metchev et al. 2008; Burgasser et al. 2010a [hereafter: B10]; Geißler et al. 2011; Day-Jones et al. 2013; BG14). The identification of spectral binaries is independent of their projected separation, allowing the identification of binaries with very tight separations. The selection biases for this method (small separation, distinct component masses) are different from those of direct imaging, RV and astrometric variability, and overluminosity, providing a complementary approach to finding VLM binary systems.

Many brown dwarf spectral binaries have been discovered serendipitously (Cruz et al. 2004; Burgasser 2007b; Gelino & Burgasser 2010), yet recent systematic searches (B10, BG14) have increased the number of known spectral binaries to $\sim$50. Follow-up of candidates is necessary to confirm their binary nature since the spectral peculiarities that signal binarity may instead be the result of atmospheric variability, as in the case of the T1.5 2MASS J21392676+0220226[2] (Radigan et al. 2012; Khandrika

[1] In order to achieve S/N$\gtrsim$25 with low and high resolution spectroscopy.

[2] Hereafter targets observed in this study are referred to by shorthand notation: J*hhmm* + *ddmm*, where *h* is hour, *d* is degree and *m* is minute. Full coordinates are listed in Table 4.2.

et al. 2013). Only 12 spectral binaries have been confirmed by direct imaging, radial velocity, astrometric variability or overluminosity (See Table 4.8; Burgasser et al. 2006c; Blake et al. 2008; Gelino & Burgasser 2010; Burgasser et al. 2011b; Stumpf et al. 2011; Burgasser et al. 2012; Dupuy & Liu 2012; Faherty et al. 2012; Manjavacas et al. 2013) and many of these have turned out to be close separation systems. The M9 dwarf SDSS J0006−0852AB (Burgasser et al. 2012) and the M8.5 dwarf 2MASS J0320−0446AB (Blake et al. 2008; Burgasser et al. 2008a) were confirmed as binaries by RV variability and found to have projected separations < 1 AU. The L4 dwarf SDSS J0805+4812 (Burgasser 2007b), confirmed as a binary through astrometric variability, has a semi-major axis $0.9 - 2.3$ AU (Dupuy & Liu 2012). Even with the high resolution images provided by the Keck II Laser Guide Star Adaptive Optics (LGS-AO) system, none of these binaries can be resolved.

Nevertheless, high resolution imaging remains an efficient first test for binarity. In this article, we present high resolution LGS-AO observations of 43 late-M, L and T dwarfs, 17 of which are spectral binary candidates. Section 4.2 describes the target selection and observation procedures using the LGS-AO system and Keck II/NIRC2 (van Dam et al. 2006; Wizinowich et al. 2006). For the unresolved spectral binaries (visual and index-selected) we determine detection and separation limits in Section 4.3.1. We discuss in detail each of the known, unresolved binaries in Section 4.3.2.1. We report three resolved sources and describe their properties in Section 4.3.2.2. In Section 4.3.3.1 we analyze multi-epoch AO images of SDSS J2052−1609 and determine a first astrometric orbit for this L/T transition system. For the other two resolved systems, we estimate orbital parameters with Monte Carlo methods in Section 4.3.4. We discuss the broader implications of our results in the context of small separation VLM binaries in Section 4.3.5. Our results are summarized in Section 4.4.

4.2 Target Selection and Observations

4.2.1 Spectral Binary Identification

The 43 sources observed in our study (Table 4.2) were selected from known late-M, L and T dwarfs in the vicinity of the Sun with a suitable tip-tilt star for LGS-AO correction. These include 33 M9−T3 dwarfs initially classified as spectral binaries by visual inspection, before the B10 and BG14 selection criteria had been defined. We re-examined their binary candidacy by dividing them into two groups according to spectral type: 15 objects in the M7−L7 range analyzed with the BG14 method, and 22 objects in the L5−T3 range, analyzed with the B10 method. The four objects overlapping in these spectral type ranges were analyzed by both methods. Ten other low mass stars and brown dwarfs were also observed as back-up targets, but were excluded from the analysis because visual inspection rejected them as spectral binary candidates.

Indices were measured from low resolution ($\lambda/\Delta\lambda = 75 - 120$), near-infrared IRTF/SpeX spectra (Rayner et al. 2003) covering $0.9 - 2.4\mu$m, accessed from the SpeX Prism Libraries (Burgasser 2014). One of our targets, 2MASS J2126+7617, has a declination outside the observable range of SpeX/IRTF ($-50^\circ < \delta < +67^\circ$), so a smoothed Keck/NIRSPEC spectrum was used instead (Kirkpatrick et al. 2010). Spectral indices given in B10 and BG14 were calculated for each spectrum, and regions of interest (ROI) in index-index spaces were delineated using confirmed binaries. Slight modifications to the limits of some ROIs in both B10 and BG14 were made to include known binaries WISEP J0720−0846 and 2MASS J1209−1004 (Burgasser et al. 2015b; Liu et al. 2010, respectively), which had not been detected at the time the index selection criteria were defined. Table 4.1 shows the updated limits of the index selection ROIs for both sets of criteria. Strong and weak candidates are selected by the number of times they fall within the ROIs, as described in B10 and BG14.

Table 4.1 Updated index selection criteria for B10 and BG14

x	y	Limits
Burgasser et al. (2010a) Indices		
H_2O-J	H_2O-K	$0.325 < x < 0.65$ and $y > 0.615x + 0.300$
CH_4-H	CH_4-K	$0.6 < x < 1.0$ and $y > 1.063x - 0.288$
CH_4-H	K/J	$0.65 < x < 1.00$ and $y > 0.471x - 0.096$
H_2O-H	H-dip	$0.44 < x < 0.68$ and $y < 0.49$
SpT	H_2O-J/H_2O-H	L8.5$< x <$T3.5, $y < 0.925$ and $y < -0.037x + 2.106$
SpT	H_2O-J/CH_4-K	L8$< x <$T4.5 and $y < 0.041x - 0.517$
Bardalez Gagliuffi et al. (2014) Indices		
SpT	CH_4-H	$M7.5 < x < L8$ and $y < -4.3 \times 10^{-4}x^2 + 0.0253x + 0.6824$
H_2O-J	CH_4-H	$0.60 < x < 0.92$ and $y < -0.094x + 1.096$.
H_2O-J	H-bump	$0.65 < x < 0.90$ and $y > 0.16x + 0.806$.
CH_4-J	CH_4-H	$0.6 < x < 1.04$, $y < 1.04$ and $y < -0.562x + 1.417$.
CH_4-J	H-bump	$0.60 < x < 0.74$, $y > 0.91$ and $y > 1.00x + 0.24$.
CH_4-H	J-slope	$0.94 < x < 1.03$, $y > 1.03$ and $y > 1.250x - 0.207$.
CH_4-H	J-curve	$0.95 < x < 1.03$ and $y > 1.245x^2 - 1.565x + 2.312$.
CH_4-H	H-bump	$0.94 < x < 1.04$, $y > 0.92$ and $y < 1.36x^2 - 4.26x + 3.877$.
J-slope	H-dip	$1.03 < x < 1.13$ and $y < 0.20x + 0.27$.
J-slope	H-bump	$1.025 < x < 1.130$, $y > -2.75x + 3.84$ and $y > 0.91$.
K-slope	H_2O-Y	$0.93 < x < 0.96$ and $y > 12.036x^2 - 20.000x + 9.037$.
J-curve	H-bump	$2.00 < x < 2.45$, $y > 0.92$ and $y > 0.269x^2 - 1.326x + 2.527$.

From the BG14 set, 8 sources were selected as candidates from spectral indices (4 as strong, 4 as weak). Single and binary templates were fit to these index-selected sources, ranked by a χ^2 statistic. The best fit single and binary templates were compared to each other with an F-test to assess the percentage confidence that the binary fit is statistically better than the single fit. The primary types were constrained to ± 3 subtypes from the combined optical spectral type or, in its absence, near infrared type, and the secondary types were allowed to vary between T1 and T8. After template fitting, 6 sources remained as candidates. From the B10 set, 16 sources were selected as index candidates (11 as strong, 5 as weak) and after fitting, 12 sources remained as candidates. 2MASS J1711+2232 was selected as a candidate on both sets. In all, we classify 17 sources as true spectral binary candidates (Table 4.2), close to half of the visually-selected spectral binaries.

4.2.2 NIRC2 High Resolution Imaging and Reduction

High angular resolution images of our targets were obtained using the Keck II LGS-AO system with NIRC2 on nine nights between August 2009 and January 2014. Tip-tilt reference stars within $60''$ of the targets were selected from the USNO-B catalog (Monet et al. 2003). A 3-point dither pattern was used to avoid the noisy lower left quadrant of the array, and was repeated as needed with different dither offsets to build up long exposures. Total integration times were between 60s and 720s, depending on the brightness of the source and the atmospheric conditions. All objects were observed with the Mauna Kea Observatories (MKO) *H* filter (Simons & Tokunaga 2002; Tokunaga et al. 2002) and narrow plate scale (9.970 ± 0.012 *mas*/pixel for a single-frame field-of-view of $10'' \times 10''$; Pravdo et al. 2006). The MKO *J* and/or K_s filters were also used for targets with apparent companions.

Table 4.2 NIRC2 Observation Log

Name	SpT	2MASS H	Date	Reference Star	Filter	t_{exp}(s)	Airmass	Strehl Ratio	S/N
Spectral Binaries from B10 and BG14									
SDSS J011912.22+240331.6	T2	16.46 ± 0.03	2009 Aug 15	1140-0016097	H	720	1.02	0.25	717
			2013 Sep 22	1140-0016097	H	120	1.01	0.01	103
			2013 Sep 23	1140-0016097	H	120	1.05	0.23	897
SDSS J024749.90−163112.6	T2	16.31 ± 0.03	2009 Aug 15	0734-0037544	H	720	1.32	0.11	764
2MASS J03440892+0111251	L0.5	13.91 ± 0.04	2013 Sep 22	0911-0037820	H	175	1.07	0.15	3043
SDSS J035104.37+481046.8	T1	15.57 ± 0.14	2009 Aug 15	1381-0118655	H	720	1.38	0.14	894
2MASS J05185995−2828372	T1	14.83 ± 0.07	2013 Sep 23	0615-0055796	H	120	1.63	0.12	1718
WISE J07200320−0846513	M9.5	9.92 ± 0.02	2014 Jan 19	0812-0137371	H	60	1.28	0.02	1638
SDSS J080531.84+481233.0	L9	13.92 ± 0.04	2010 Mar 24	1382-0223846	K_s	540	1.21	0.12	2624
			2013 Sep 23	1382-0223846	H	120	1.61	0.09	3029
2MASS J11061197+2754225	T2.5	14.15 ± 0.05	2010 Mar 24	1179-0233699	H	720	1.03	0.07	2559
2MASS J12095613−1004008	T3	15.33 ± 0.09	2014 Jan 13	0799-0230529	H	120	1.15	0.04	1146
2MASS J13411160−3052505	L3	13.72 ± 0.03	2014 Jan 13	0591-0304901	J	120	1.61	0.02	807
			2014 Jan 13	0591-0304901	H	120	1.65	0.04	1508
			2014 Jan 19	0591-0304901	H	120	1.59	0.04	1845
			2014 Jan 13	0591-0304901	K_s	180	1.59	0.05	1861
SDSS J143553.25+112948.6	T2	16.52 ± 0.04	2009 Aug 15	1014-0229971	H	360	1.25	0.05	373
			2009 Aug 15	1014-0229971	K_s	360	1.30	0.08	268
SDSS J151114.66+060742.9	T0	14.96 ± 0.08	2009 Aug 15	0961-0243717	J	360	1.36	0.01	560

Table 4.2 Continued

Name	SpT	2MASS H	Date	Reference Star	Filter	t_{exp}(s)	Airmass	Strehl Ratio	S/N
			2009 Aug 15	0961-0243717	H	360	1.27	0.09	1078
			2009 Aug 15	0961-0243717	K_s	720	1.32	0.13	1101
			2010 May 19	0961-0243717	H	120	1.03	0.09	94
SDSS J151643.01+305344.4	T0.5	15.87 ± 0.16	2010 Mar 24	0930-0297471	H	720	1.04	0.06	1007
SDSS J154727.23+033636.3	L2	15.07 ± 0.06	2009 Aug 15	0936-0258682	H	720	1.40	0.01	805
2MASS J1711457+223204	L6.5	15.80 ± 0.11	2010 May 13	1125-0317350	J	720	1.22	0.05	381
			2010 May 13	1125-0317350	H	720	1.27	0.07	844
2MASS J1733423−165449	L0.5	12.81 ± 0.06	2009 Aug 15	0730-0518366	J	720	1.39	0.08	2324
			2009 Aug 15	0730-0518366	H	720	1.36	0.10	2748
SDSS J205235.31−160929.8	T1	15.45 ± 0.03	2009 Aug 15	0738-0802833	J	360	1.30	0.06	543
			2009 Aug 15	0738-0802833	H	360	1.27	0.00	1003
			2009 Aug 15	0738-0802833	K_s	360	1.28	0.17	729
Visually Selected Spectral Binary Candidates									
2MASS J0019457+521317	M9	12.07 ± 0.02	2009 Aug 15	1422-0011510	J	360	1.30	0.09	2502
			2009 Aug 15	1422-0011510	H	720	1.28	0.25	5028
2MASS J00320509+0219017	L1.5	13.39 ± 0.02	2009 Aug 15	0923-0006944	H	720	1.10	0.11	2811
SDSS J003259.36+141036.6	L8	15.65 ± 0.14	2009 Aug 15	1041-0005438	H	720	1.02	0.10	1112
			2009 Aug 15	1041-0005438	K_s	360	1.02	0.11	721
2MASS J02361794+0048548	L6.5	15.27 ± 0.07	2013 Sep 22	0908-0027044	H	180	1.06	0.14	1959
SDSS J075840.33+324723.4	T2	14.11 ± 0.04	2010 Mar 24	1227-0198441	H	720	1.06	0.05	2333

Table 4.2 Continued

Name	SpT	2MASS H	Date	Reference Star	Filter	t_{exp}(s)	Airmass	Strehl Ratio	S/N
SDSS J093109.56+032732.5	L7.5	16.27 ± 0.24	2010 Mar 24	0934-0195871	H	720	1.18	0.03	611
2MASS J09490860−1545485	T2	15.26 ± 0.11	2010 Mar 24	0742-0216967	H	720	1.24	0.05	1399
SDSS J103321.92+400549.5	L6	16.05 ± 0.04	2010 Mar 24	1300-0206652	H	720	1.07	0.06	828
SDSS J112118.57+433246.5	L7.5	16.56 ± 0.04	2010 Mar 24	3015-00408-1	H	720	1.16	0.08	674
2MASS J11582073+0435022	sdL7	14.68 ± 0.06	2010 May 13	0945-0201532	H	720	1.04	0.15	1776
			2010 May 13	0945-0201532	K_s	720	1.04	0.23	1882
SDSS J120602.51+281328.7	T3	15.83 ± 0.03	2010 Mar 24	1182-0220446	H	720	1.11	0.10	197
2MASS J14283132+5923354	L4	13.88 ± 0.04	2010 May 19	1493-0219430	H	720	1.29	0.10	3219
2MASS J1707333+430130	L0.5	13.18 ± 0.03	2009 Aug 15	1330-0334426	H	720	1.41	0.08	2425
2MASS J1721039+334415	L3	12.95 ± 0.03	2009 Aug 15	1237-0272128	H	720	1.21	0.11	953
			2010 Mar 24	1237-0272128	H	720	1.03	0.07	2721
2MASS J21265916+7617440	T0	13.59 ± 0.04	2013 Sep 23	1662-0097897	H	120	2.16	0.08	79
SDSS J214956.55+060334	M9	12.63 ± 0.03	2009 Aug 15	0960-0568745	H	720	1.08	0.09	2670
Additional Targets									
WISEP J004701.06+680352.1	L7.5	13.97 ± 0.04	2013 Sep 23	1580-0021858	H	90	1.56	0.28	2410
2MASS J03001631+2130205	L6p	14.73 ± 0.07	2013 Sep 22	1115-0038422	H	120	1.06	0.13	1583
2MASS J03020122+1358142	L3	15.43 ± 0.09	2013 Sep 23	1039-0030470	H	120	1.01	0.05	944
HYT0429+1535	···	···	2013 Sep 22	1031-0059287	CH_4	120	1.01	0.16	131
			2013 Sep 22	1031-0059287	H	120	1.00	0.17	88
2MASSI J0443058−320209	L5	14.35 ± 0.06	2013 Sep 22	0579-0075735	H	120	1.67	0.07	2206

Table 4.2 Continued

Name	SpT	2MASS H	Date	Reference Star	Filter	t_{exp}(s)	Airmass	Strehl Ratio	S/N
WISE J052857.69+090104.4	M9.5p	15.44 ± 0.12	2014 Jan 19	0990-0058827	H	135	1.40	0.07	99
SDSS J115013.17+052012.3	L6	15.46 ± 0.14	2014 Jan 13	0279-01016-1	H	60	1.03	0.17	993
ULAS J132605.18+120009.9	T6p	17.93 ± 0.09	2010 May 19	1019-0249297	H	720	1.02	0.24	371
2MASS J14140586+0107102	L4.8:	15.73 ± 0.19	2010 May 13	0317-00292-1	H	720	1.07	0.20	1168
2MASS J20025073−0521524	L6	14.28 ± 0.05	2009 Aug 15	0846-0581639	H	360	1.35	0.12	1709

The images were reduced in a standard fashion using Interactive Data Language (IDL) scripts. First, a dark frame was subtracted from each science frame. For each science exposure a sky frame was constructed from the median average of all images acquired for the target, exclusive of the frame being reduced. The sky-subtracted frames were then divided by a normalized dome flat. A bad pixel mask was applied to smooth over bad pixels using the average of the neighboring pixels. All images in a given epoch and common filter were shifted to align the target to a common location, and the stack was median-combined to create the final mosaics.

4.3 Analysis

4.3.1 Image Characterization and Companion Detection Limits for Unresolved Sources

The reduced image mosaics around each target are shown in Figures 4.1 and 4.2. Strehl and signal-to-noise ratios (S/N) are reported in Table 4.2. The Strehl ratio was calculated by comparing each point source to a theoretical, diffraction-limited, monochromatic, NIRC2 point spread function (PSF) with the `NIRC2Strehl` IDL routine[3]. The S/N was computed assuming Poisson statistics:

$$S/N = \frac{N_{star}}{\sqrt{n_{sky}\,\sigma_{sky}^2 + \frac{N_{star}}{g}}} \tag{4.1}$$

where N_{star} is the total counts from the star at a radius of 1.5 times the full width at half maximum, n_{sky} is the number of pixels used for the standard deviation of the sky counts, σ_{sky}, which encompasses noise from several sources (read out, dark current, image reduction, etc.) and g is the gain in DN/e^- (data number per electron).

[3]Retrieved from https://www2.keck.hawaii.edu/optics/lgsao/software/

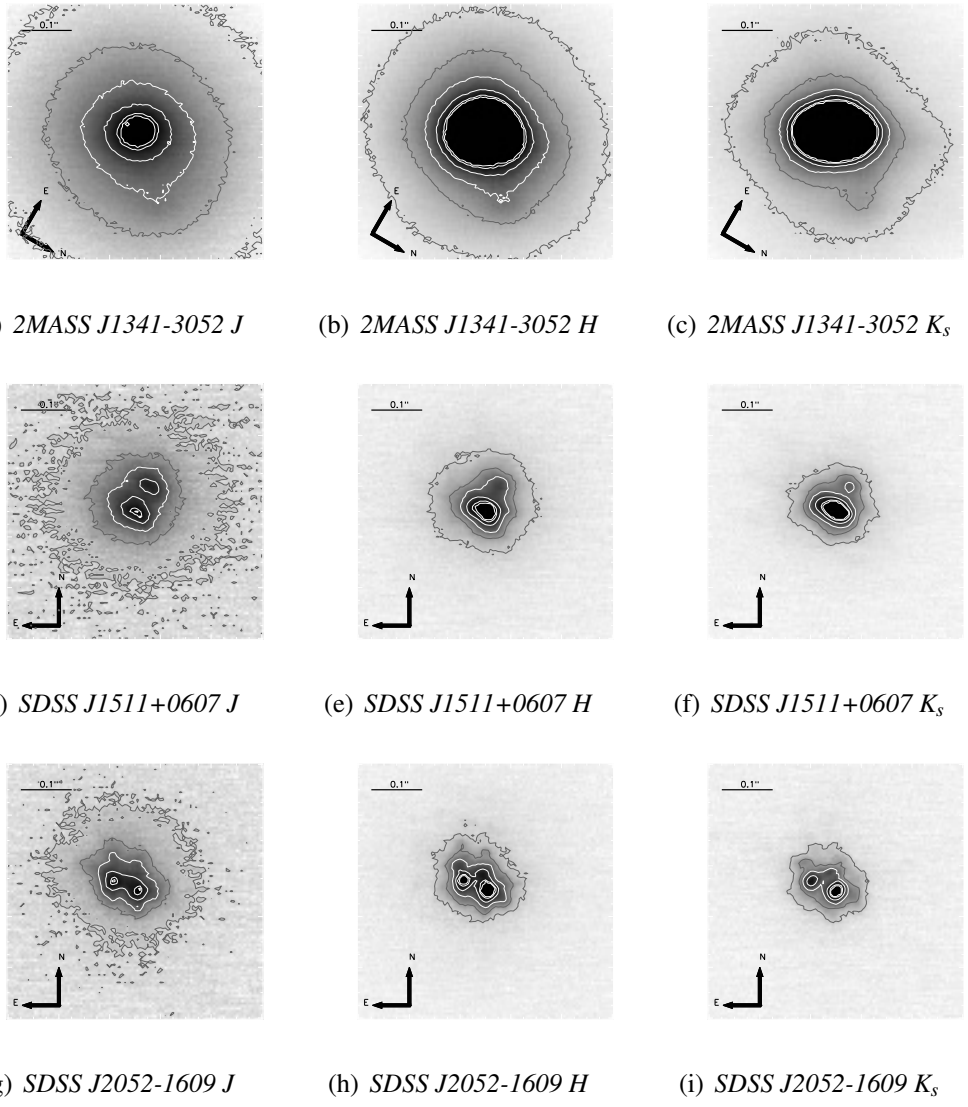

(a) *2MASS J1341-3052 J* (b) *2MASS J1341-3052 H* (c) *2MASS J1341-3052 K_s*

(d) *SDSS J1511+0607 J* (e) *SDSS J1511+0607 H* (f) *SDSS J1511+0607 K_s*

(g) *SDSS J2052-1609 J* (h) *SDSS J2052-1609 H* (i) *SDSS J2052-1609 K_s*

Figure 4.1 Keck NIRC2 LGS-AO images of the three binaries resolved in this sample in JHK_s bands.

Three of our sources are resolved: 2MASS 1341−3052, SDSS 1511+0607 and SDSS 2052−1609; these are shown in Figure 4.1 and discussed further in Section 4.3.2.2. One source, 2MASS J1733−1654, has a feature that we cannot distinguish between bona fide source and PSF structure, so we consider this to be a "source of interest". The remaining sources are unresolved at the limits of our sensitivity and image quality. Because the PSF of the images vary considerably, we determined detection limits through

a source implantation simulation of representative images. We organized the targets by Strehl and S/N and selected two representative sources of high Strehl (WISE J0047+6308) and low Strehl (2MASS J0032+0219), as shown in Figure 4.3. For these sources, we simulated binary companions by scaling down the brightness of each image, and then shifting and superimposing it onto the original image. The implanted image was scaled down by a maximum of 6 magnitudes, which was the largest magnitude difference inferred from the template fitting of spectral binary candidates, and shifted by up to 50 pixels or $\sim 0\farcs5$ in any angle. Magnitude difference, separation and position angle were all drawn from a uniform random distribution.

We visually examined each image at multiple contrast ratios to search for the implanted companion. This experiment was performed N$\gtrsim$12,000 times per source, varying the target, scale factor and offset. A "detection" required clicking within 15 pixels of the implanted secondary, with the option to decide if an implanted companion was visually undetectable. We determined the maximum relative magnitude as a function of separation for which the detection fraction exceeded 50%. The detection fraction was calculated in steps of 0.5 mag and $0\farcs05$, sliding by half a step along both axes for a total of $\sim$400 overlapping bins. Figure 4.4 shows that the PSF dominates the sensitivity close to the star centroid. For the case of low Strehl ratio, detections reach a minimum at $\Delta H \approx 5$ mag, $0\farcs3$ away from the center of the PSF, beyond which our sensitivity is limited by sky noise. For the high Strehl ratio case the floor lies around 5.5 magnitude difference at radii greater than $0\farcs4$.

We applied the sensitivity curves of our representative sources to systems with similar Strehl ratios. For the 30 unresolved spectral binary candidates, we compared these sensitivity limits to the magnitude differences predicted from template fitting to determine separation limits (Table 4.3). Figure 4.5 shows an example of the sensitivity curve and separation constraint for the spectral binary candidate 2MASS J1711+2232.

Five of our unresolved spectral binaries have been previously confirmed as true binaries (See Section 4.3.2.1), but our separation limits are up to 40% greater, i.e. these binaries can not be resolved with our observations. For the case of 2MASS J1209-1004, our estimated separation limit is smaller than the measured separation, suggesting that the secondary has moved to a closer configuration. Similarly, for our three resolved systems the calculated separation limit is always smaller than the measured separation, which means that our separation limits correctly constrain the PSF of the primary. The remaining 9 unresolved spectral binaries have angular separation limits between $0\farcs04 - 0\farcs28$.

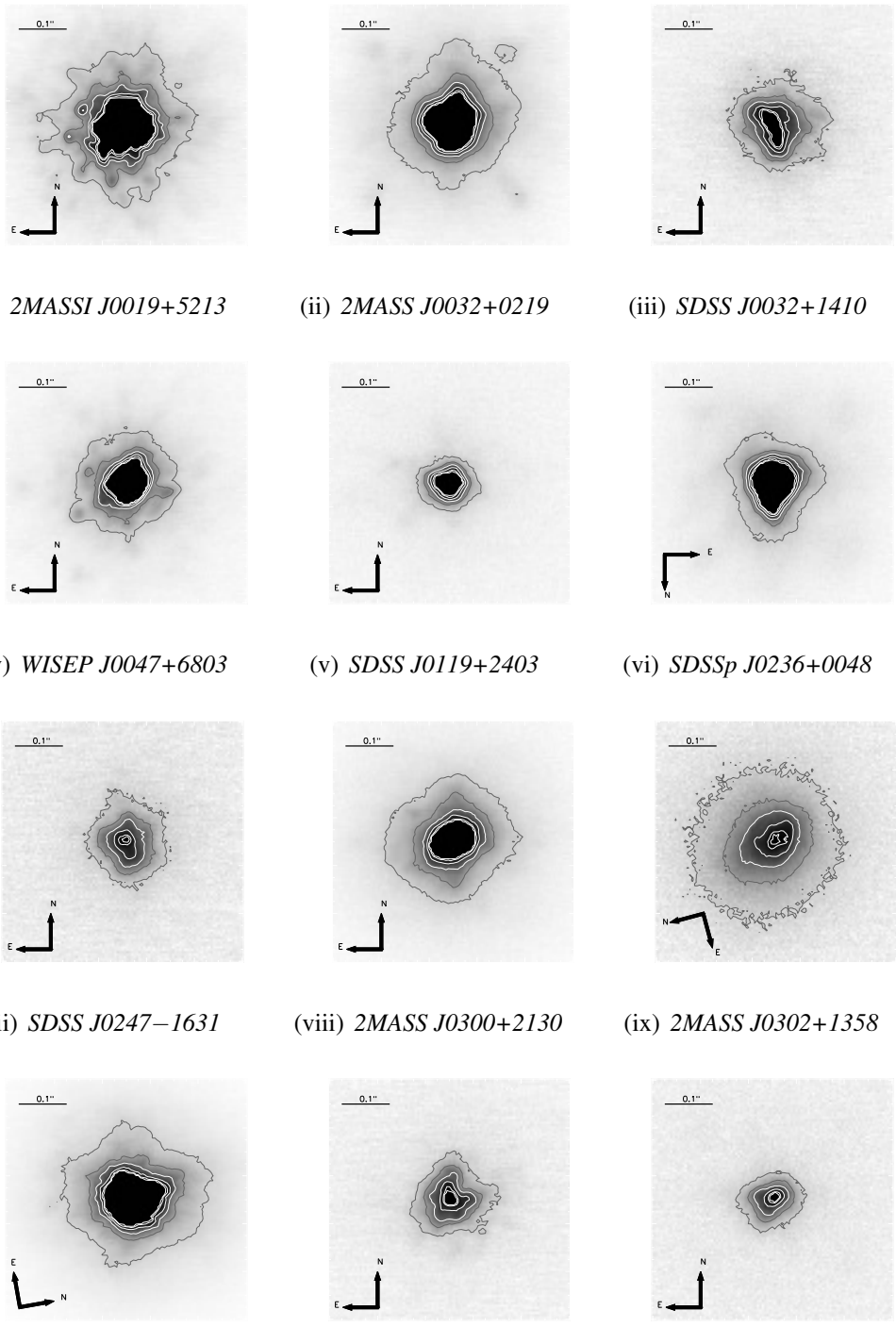

(i) *2MASSI J0019+5213* (ii) *2MASS J0032+0219* (iii) *SDSS J0032+1410*

(iv) *WISEP J0047+6803* (v) *SDSS J0119+2403* (vi) *SDSSp J0236+0048*

(vii) *SDSS J0247−1631* (viii) *2MASS J0300+2130* (ix) *2MASS J0302+1358*

(x) *2MASS J0344+0110* (xi) *SDSS J0351+4810* (xii) *HTY J0429+1535*

Figure 4.2 Keck NIRC2 LGS-AO images in the *H* band of all targets. Contours are drawn at 20, 40, 60, 80, 95 and 99% of the image minimum.

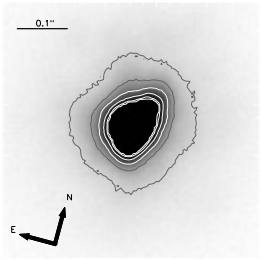

(xiii) *2MASS J0443-3202*

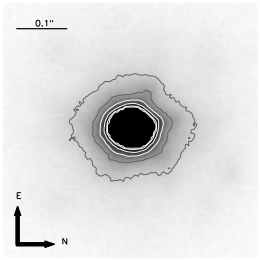

(xiv) *2MASS J0518−2828*

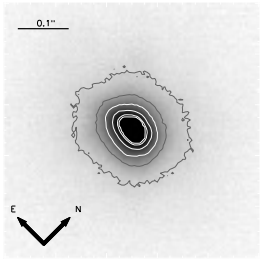

(xv) *WISE J0528+0901*

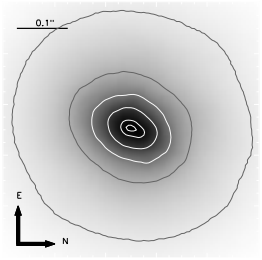

(xvi) *WISE J0720−0846*

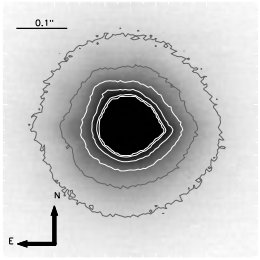

(xvii) *SDSS J0758+3247*

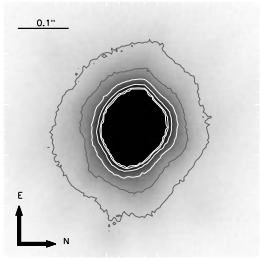

(xviii) *SDSS J0805+4812*

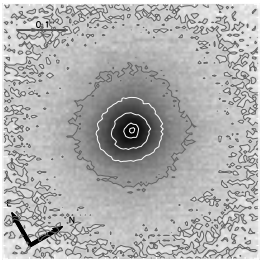

(xix) *SDSS J0931+0327*

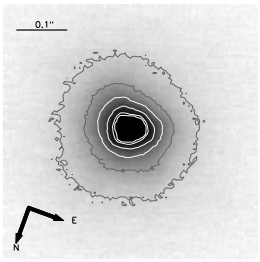

(xx) *2MASS J0949−1545*

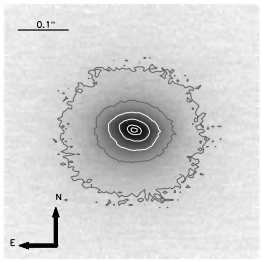

(xxi) *SDSS J1033+4005*

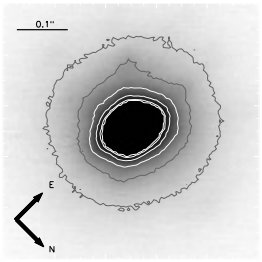

(xxii) *2MASS J1106+2754*

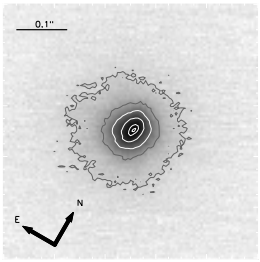

(xxiii) *SDSS J1121+4332*

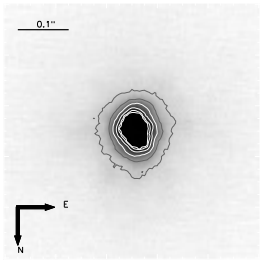

(xxiv) *2MASS J1150+0520*

Figure 4.2 Continued.

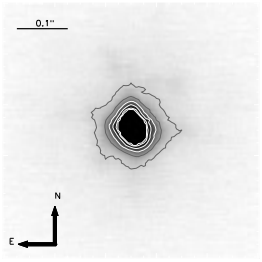

(xiii) *2MASS J1158+0435*

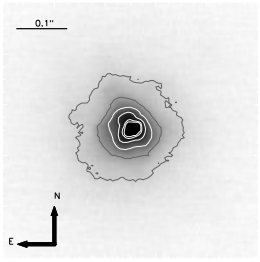

(xiv) *SDSS J1206+2813*

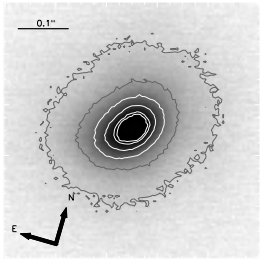

(xv) *2MASS J1209−1004*

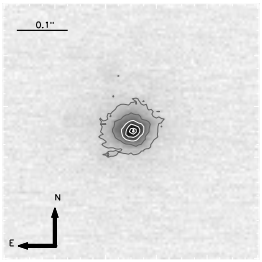

(xvi) *ULAS J1326+1200*

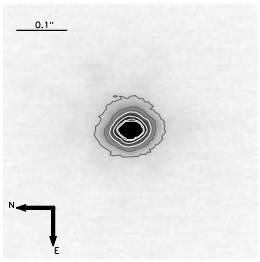

(xvii) *2MASS J1414+0107*

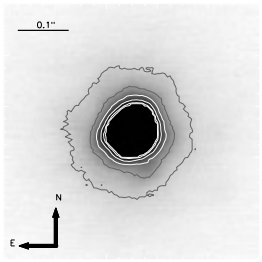

(xviii) *2MASS J1428+5923*

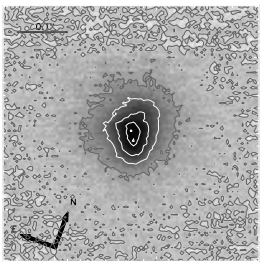

(xix) *SDSS J1435+1129*

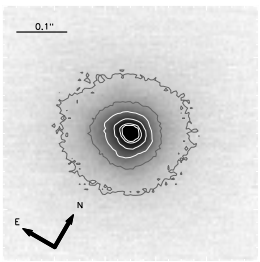

(xx) *SDSS J1516+3053*

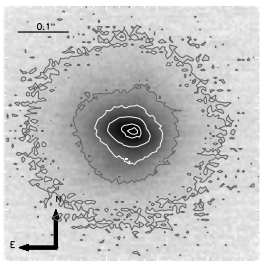

(xxi) *SDSS J1547+0336*

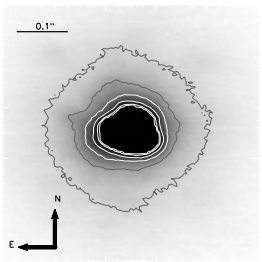

(xxii) *2MASS J1707+4301*

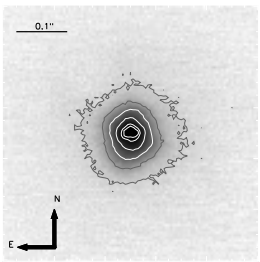

(xxiii) *2MASS J1711+2232*

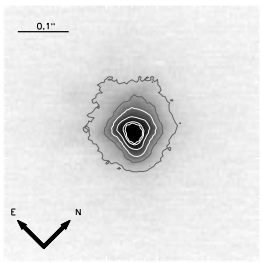

(xxiv) *2MASS J1721+3344*

Figure 4.2 Continued.

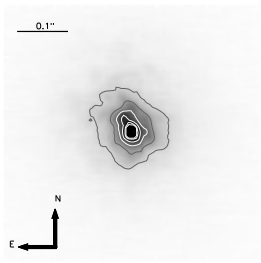

(xiii) *2MASS J1733−1654*

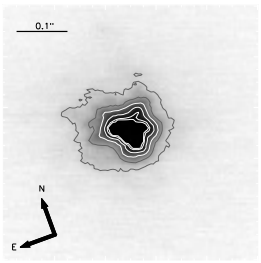

(xiv) *2MASS J2002−0521*

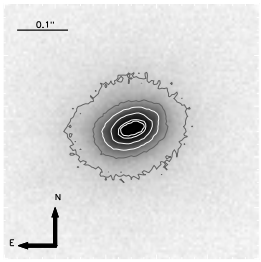

(xv) *2MASS J2126+7617*

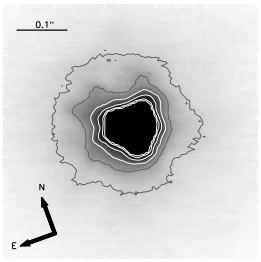

(xvi) *2MASS J2149+0603*

Figure 4.2 Continued.

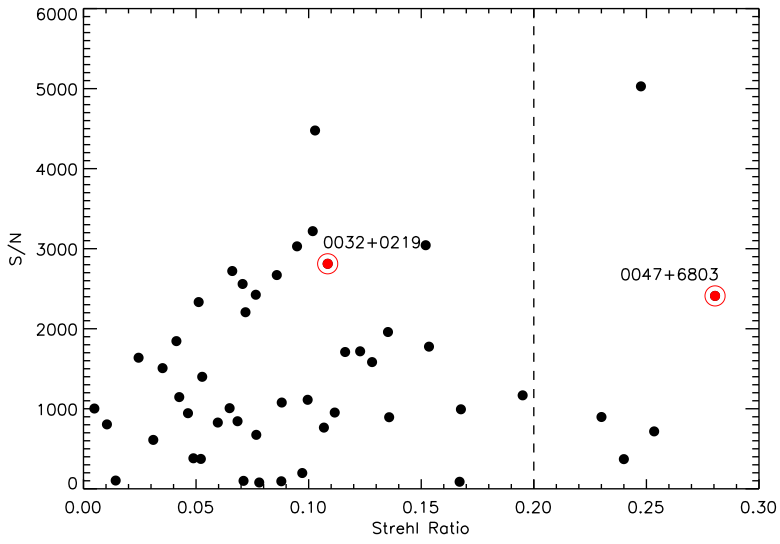

Figure 4.3 Strehl ratio vs. signal-to-noise ratio of all *H* band observations (black dots). The two representative sources used in the empirical sensitivity curves are marked in red. The two groups are separated by the dashed lines. See Table 4.2 for the list of objects.

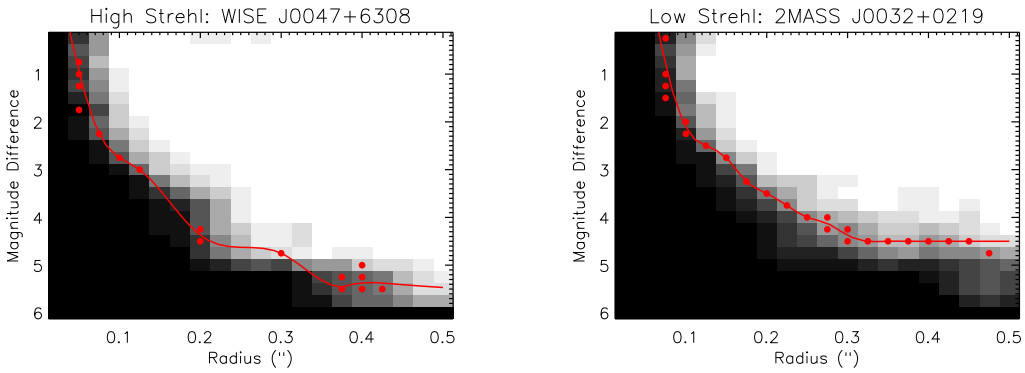

Figure 4.4 Empirical sensitivity curves from simulated binaries for two representative sources based on their Strehl and signal-to-noise ratios (see Table 4.2). The red line delimits the detections of secondaries (white) from non-detections (black).

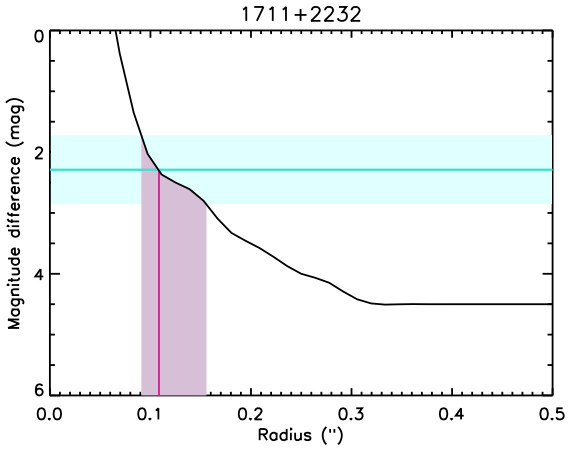

Figure 4.5 Example separation constraint for 2MASS J1711+2232. Given the empirical sensitivity curve for its Strehl ratio vs. S/N group (low Strehl-low S/N, representative source: 2MASS J0032+0219) in black, and the estimated magnitude difference in cyan (uncertainties are shown as the shaded region), we can set an upper limit for an undetected secondary at the intersection (magenta line). The values for the separation constraints for all observations are reported in Table 4.3.

Table 4.3 Projected separation constraints for spectral binaries and all targets

Source	Spectral Type			2MASS ΔJ	2MASS ΔH	2MASS ΔK	Confidence	Distance (pc)	Ref.	Separation	
	Optical[a]	Primary	Secondary							Angular (*mas*)	Projected (AU)
Spectral Binaries											
SDSS J011912.22+240331.6	T2.0	T0.3±0.7	T3.7±0.5	-0.28±0.13	0.30±0.11	0.82±0.20	> 99%	43±3	1	< 43	< 1.9
SDSS J024749.90−163112.6	T2.0	L8.4±0.6	T5.7±0.5	0.57±0.30	1.62±0.33	2.10±0.30	100%	40±3	1	< 96	< 3.8
2MASS J03440892+0111251	L0.5	L0.3±0.4	T3.8±1.5	2.77±0.38	3.10±0.65	3.50±0.70	98%	41±4	1	< 226	< 9.2
SDSS J035104.37+481046.8	T1.0	L6.3±0.7	T5.4±0.9	0.45±0.47	1.62±0.51	2.45±0.52	> 99%	37±4	1	< 102	<3.8
2MASS J05185995−2828372	···	L6.4±0.4	T5.6±0.5	0.54±0.25	1.75±0.27	2.48±0.28	100%	23±1[c]	4	< 98	< 2.2
WISE J07200320−0846513	···	M8.9±0.0	T5.2±0.7	3.50±0.24	4.15±0.36	4.57±0.41	100%	6±1[c]	2	< 500	< 3.0
SDSS J080531.84+481233.0	L9.0	L5.3±0.1	T5.8±0.4	1.92±0.17	2.85±0.18	3.49±0.30	100%	23±1[c]	4	< 164	< 3.8
2MASS J11061197+2754225	T2.5	L8.9±0.5	T4.2±0.4	-0.24±0.14	0.49±0.17	1.03±0.16	100%	21±1[c]	3	< 74	< 1.5
2MASS J12095613−1004008	···	T1.1±0.0	T6.0±0.4	0.95±0.11	1.77±0.15	2.10±0.28	> 99%	22±1[c]	4	< 100	< 2.1
2MASS J13411160−30525049[b]	L3.0	L2.3±0.6	T6.0±1.0	2.68±0.08	4.03±0.12	4.23±0.07	96%	29±3	1	279±17	8.9 ± 0.4
SDSS J143553.25+112948.6	T2.0	L8.9±0.7	T5.6±0.5	0.28±0.24	1.38±0.28	2.11±0.37	> 99%	44±4	1	< 90	< 4.0
SDSS J151114.66+060742.9[b]	T0.0	L5.2±0.9	T4.9±0.4	0.25±0.13	1.41±0.13	2.38±0.30	> 99%	28±5[c]	5	108±11	2.9±0.3
SDSS J151643.01+305344.4	T0.5	L7.6±0.8	T2.3±0.3	-0.36±0.24	0.21±0.21	0.80±0.27	99%	39±4	1	< 70	< 2.7
SDSS J154727.23+033636.3	L2.0	L1.8±0.2	T6.6±1.0	3.32±0.53	4.38±0.60	4.98±0.65	90%	53±6	1	Unconstrained	Unconstrained
2MASS J1711457+223204	L6.5	L5.5±0.5	T5.3±1.0	1.21±0.41	2.29±0.56	3.08±0.64	> 99%	30±4[c]	4	< 156	< 4.7
2MASS J1733423−165449	L0.5	L0.1±0.2	T4.0±1.3	2.76±0.30	3.14±0.54	3.59±0.60	98%	24±2	1	< 219	< 5.3
SDSS J205235.31−160929.8[b]	T1.0	L5.9±1.6	T2.1±0.5	0.03±0.25	0.44±0.30	1.12±0.40	> 99%	30±1[c]	4	103±2	3.2±0.5

Table 4.3 Continued

Source	Spectral Type			2MASS ΔJ	2MASS ΔH	2MASS ΔK	Confidence	Distance (pc)	Ref.	Separation	
	Optical[a]	Primary	Secondary							Angular (*mas*)	Projected (AU)
Visual Spectral Binaries											
2MASSI J0019457+521317	M9.0	M8.5±0.2	T6.9±1.1	4.82±0.54	5.53±0.65	5.91±0.71	50%	20±2	1	Unconstrained	Unconstrained
2MASS J00320509+0219017	L1.5	L0.1±0.3	T6.4±1.4	4.06±0.68	4.87±0.83	5.36±0.85	49%	33±4	1	Unconstrained	Unconstrained
SDSS J003259.36+141036.6	L8.0	L6.2±0.7	T2.4±1.9	0.55±0.70	1.03±0.95	1.54±0.97	50%	33±6[c]	4	< 96	< 3.2
SDSSp J023617.93+004855.0	L6.5	L5.1±0.5	T1.9±1.2	1.04±0.49	1.33±0.59	1.81±0.58	7%	39±4	1	< 95	< 3.7
SDSS J075840.33+324723.4	T2.0	T2.3±0.0	T2.2±0.0	-0.28±0.0	-0.07±0.0	0.193±0.0	92%	16±2	1	< 65	< 1.0
SDSS J093109.56+032732.5	L7.5	L7.2±0.3	T6.6±1.8	2.66±0.49	3.45±0.78	3.87±0.91	90%	37±4	1	< 288	< 10.7
2MASS J09490860−1545485	T2.0	T1.1±0.2	T3.5±2.0	0.54±1.01	0.83±1.28	0.83±1.26	95%	18±2[c]	5	< 101	< 1.8
SDSS J103321.92+400549.5	L6.0	L4.9±0.6	T4.4±2.2	1.96±0.72	2.52±1.02	2.99±1.07	84%	54±6	1	< 206	< 11.2
SDSS J112118.57+433246.5	L7.5	L6.8±0.5	T5.0±1.5	1.52±0.64	2.21±0.80	2.74±0.84	95%	52±6	1	< 164	< 8.4
2MASS J11582077+0435014	sdL7	L6.4±0.0	T2.6±0.8	1.42±0.12	1.57±0.22	1.98±0.26	100%	28±2	1	< 93	< 2.5
SDSS J120602.51+281328.7	T3.0	T2.0±0.4	T5.0±0.8	0.46±0.35	1.05±0.49	1.26±0.50	74%	29±3	1	< 87	< 2.5
2MASS J14283132+5923354	L4.0	L4.4±0.7	T6.4±2.0	3.30±0.72	4.24±1.00	4.77±1.06	68%	21±3	1	Unconstrained	Unconstrained
2MASS J17073334+4301304	L0.5	M8.7±0.1	T6.9±0.7	4.41±0.47	5.28±0.51	5.75±0.53	60%	35±3	1	Unconstrained	Unconstrained
2MASS J1721039+334415	L3.0	L2.5±0.0	T3.8±2.0	2.91±0.62	3.10±0.99	3.32±1.09	99%	19±2	1	< 270	< 5.1
2MASS J21265916+7617440	T0.0	L8.5±1.0	T4.5±2.0	0.42±0.82	1.21±1.01	1.75±1.03	63%	12±2	1	< 106	< 1.3
SDSS J214956.55+060334	M9.0	M8.2±0.0	T6.6±1.2	4.83±0.59	5.53±0.70	5.91±0.74	58%	29±3	1	Unconstrained	Unconstrained

[a]Unresolved or combined optical spectral type.

[b]Resolved binary with *measured* delta magnitudes.

[c]Parallactic distance. Otherwise, spectrophotometric distance, assuming relative magnitudes from template fitting.

References. — (1) This paper; (2) Burgasser et al. (2015b); (3) Manjavacas et al. (2013); (4) Dupuy & Liu (2012); (5) Faherty et al. (2012).

4.3.2 Binaries

4.3.2.1 Unresolved Known Binaries

4.3.2.1.1 2MASS J05185995-2828372 2MASS J0518−2828 was the first source to be identified as a spectral binary of L6 and T4 components (Cruz et al. 2004) and was marginally resolved with HST (Burgasser et al. 2006c) with an angular separation of $0\farcs051 \pm 0\farcs012$. Dupuy & Liu (2012) find a small astrometric perturbation for this source that cannot be clearly attributed to orbital motion. Konopacky et al. (2010) observed this source with LGS-AO at Keck in 2006 and were not able to resolve it. Its parallactic distance has been measured to be 22.9±0.4 pc (Dupuy & Liu 2012), implying a projected separation of 1.17±0.28 AU from the HST measurement. Our LGS-AO observations also fail to resolve this system to a limit of 98 *mas* or 2.2 AU, which is consistent with the HST observations. This system appears to be a very tight binary whose separation is just below the limits of ground-based AO imaging.

4.3.2.1.2 WISEP J072003.20−084651.2 WISEP J0720−0846 was discovered by Scholz (2014) and confirmed by Burgasser et al. (2015b) as an M9 at a distance of 6.0±1.0 pc. The latter study identified a candidate companion at an angular separation of 139±14 *mas* in NIRC2 LGS-AO observations, which has been confirmed at a slightly wider offset (angular separation 197 ± 3 *mas*, projected separation 1.18 ± 0.21AU) with ΔH = 3.85±0.11 mag in follow-up observations (Burgasser et al. 2015a). Our analysis does not resolve the companion to limits of 500 *mas* and 3 AU, beyond the separation reported in that study.

4.3.2.1.3 SDSS J080531.84+481233.0 SDSS J0805+4812 is a blue L dwarf discovered by Hawley et al. (2002), and a spectral binary of L4.5 and T5 components (Burgasser 2007b). This source shows astrometric variability with an amplitude of 15 *mas* (Dupuy &

Liu 2012). Our LGS-AO observations show an elongated PSF that we attribute to tip-tilt correction errors, but no resolved companion. Dupuy & Liu (2012) estimate a semi-major axis of $40-100$ *mas* assuming a mass ratio $q = 0.55-0.88$ and from the measured parallactic distance of 22.9 ± 0.6pc, they infer a projected separation of $0.9-2.3$AU. Our observations do not resolve this system to limits of 164 *mas* and 3.8 AU, both consistent with the Dupuy & Liu (2012) estimates.

4.3.2.1.4 2MASS J11061197+2754225 The T2.5 2MASS J1106+2754 was first discovered by Looper et al. (2007) and later observed with NIRC2 with LGS-AO in June 2006, but was unresolved (Looper et al. 2008b). B10 identified it as a spectral binary of T0.0±0.2 and T4.5±0.2 components due to its CH_4 absorption feature in the *H* band, and ruled out a separation greater than 1.5 AU based on Keck imaging. Manjavacas et al. (2013) finds that this source is $\sim$1 mag overluminous and determined a parallactic distance of $20.6^{+1.0}_{-1.2}$ pc. Our LGS-AO observations were unable to resolve this source, implying upper limits of 74 *mas* and 1.5 AU, the same constraint as that reported by Burgasser et al. (2010a).

4.3.2.1.5 2MASS J12095613-1004008 2MASS J1209−1004 was first discovered by Burgasser et al. (2004) and is the T3 spectral standard (Burgasser et al. 2006a). Liu et al. (2010) resolved the system with NIRC2 and LGS-AO in the *J* band, and estimated component types of T2.0±0.5 and T7.5±0.5 based on photometry. The mass ratio of this binary is estimated to be $q = 0.5$, which is unusually small for brown dwarf binaries (Bouy et al. 2003; Burgasser 2007a). Liu et al. (2010) found an angular separation of 151 ± 13 *mas* at a position angle of $314^\circ \pm 5^\circ$ with a magnitude difference of $\Delta H = 2.8 \pm 0.3$ mag. Its parallactic distance $d = 21.8$±0.5 pc (Dupuy & Liu 2012) leads to a projected separation of 3.3±0.3 AU. This source was not resolved in our *H* band LGS-AO image, with limits of 95 *mas* and 2.1 AU. In this case, our observation should

have detected the companion, suggesting that orbital motion may have moved into closer projected alignment, or that the companion could be the source of the elongation of the PSF to the South East.

4.3.2.2 Resolved Binaries

4.3.2.2.1 2MASS J13411160−30525049 The L3 2MASS 1341−3052 was first discovered by Reid et al. (2008b) in the Two Micron All Sky Survey (2MASS; Cutri et al. 2003) and later identified as a spectral binary candidate with L1.0±0.5 and T6.0±1.0 components (BG14). Our NIRC2 observations resolve the source with an angular separation of 279 ± 17 *mas* at a position angle of $317.9^\circ \pm 0.6^\circ$. The original template matching analysis assumed relative spectral fluxes on the Looper et al. (2008a) absolute magnitude to spectral type relation. We repeated this analysis using the relative photometry in all three JHK_s bands to scale and select binary templates in a similar fashion as described in Burgasser et al. (2011a). Our revised template fit analysis resulted in component spectral types of L2.5±1.0 and T6.0±1.0; i.e. we infer a primary classification more consistent with the combined-light optical classification.

2MASS J1341−3052 is the only one of the three resolved systems that does not have a parallax measurement. We estimated its distance using the calculated component apparent magnitudes with the Dupuy & Liu (2012) spectral type to absolute magnitude relation and component spectral types from template fitting. Uncertainties were propagated from spectral type, apparent magnitudes and spectral type relation, accordingly. We calculated one distance per filter and then obtained the weighted average distance from the MKO JHK_s filters. The distances for both components (29±3 pc for the primary and 31±6 pc for the secondary were consistent across filters. The uncertainty-weighted average yields a distance estimate of 29±3 pc. From this we infer a projected separation of 8.1 ± 0.5 AU.

A spectral type versus absolute magnitude plot is shown in Figure 4.6, using the Dupuy & Liu (2012) parallax sample of 259 objects as a reference. The primary absolute magnitude is anchored to the Dupuy & Liu (2012) relation due to the lack of a trigonometric distance, while the secondary absolute magnitude was derived from the primary's using the measured relative magnitude. In the *J* band, the secondary adds 0.09 mags to the primary, barely enough to make the combined absolute magnitude look like an outlier. In the *K* band, the secondary adds 0.02 mags to the primary, so it appears as if the secondary absolute magnitude also falls on the relation and the combined magnitude is within the $+1\sigma$ curve. This source could not have been detected as an overluminous binary candidate because of the late type of the secondary.

4.3.2.2.2 SDSS J151114.66+060742.9 The T0 SDSS J1511+0607 was discovered by Chiu et al. (2006) in the Sloan Digital Sky Survey (SDSS; Adelman-McCarthy et al. 2007). This source was identified as a "strong" binary candidate in B10, and found to be 1 mag overluminous for its spectral type in M_{JHK} by Faherty et al. (2012). Multi-band imaging with NIRC2 on 2009 Aug 15 resolved the system into two components separated by 108 ± 11 *mas* at a position angle of $335^\circ \pm 4^\circ$. The parallax measurement of 37 ± 7 *mas* by Faherty et al. (2012) implies a distance of 28 ± 5 pc, which in turn corresponds to a projected separation of 2.9 ± 0.3 AU. Including the measured relative JHK_s magnitudes in our template fitting gives updated component spectral types of L5.0$\pm$1.0 and T5.0$\pm$0.5.

Using the combined light magnitude, the relative magnitudes and the parallactic distance, we determined the absolute magnitudes for the components (Figure 4.6). While the combined absolute magnitude of SDSS J1511+0607 clearly stands out as an outlier in spectral type to absolute magnitude plots, its components look typical. Indeed, its primary lies slightly below the Dupuy & Liu (2012) spectral type to absolute magnitude relation.

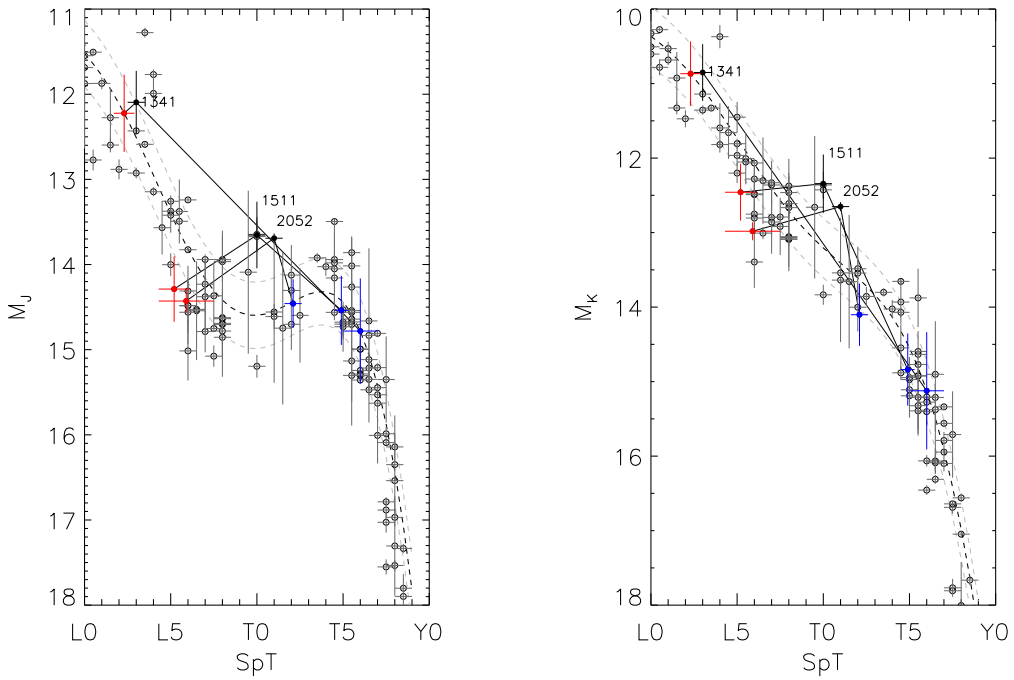

Figure 4.6 Absolute magnitudes in J and K_s for the three resolved binaries (black dots) and the Dupuy & Liu (2012) parallax sample (grey circles) shown with the Dupuy & Liu (2012) spectral type to absolute magnitude relation (black dashed line) and its 1-σ outliers (grey dashed lines). Only SDSS J1511+0607 and SDSS J2052−1609 have parallaxes reported in the literature. The three binaries are split into component spectral types, where the primaries for the two objects with parallaxes lie on the faint end of the absolute magnitude relation for their spectral type (red dots) , and the secondaries (blue dots) are all within 1-σ from the relation.

4.3.2.2.3 SDSS J205235.31−160929.8 Also discovered by Chiu et al. (2006), SDSS 2052−1609 was classified as an T1±1 brown dwarf. B10 identified it as a spectral binary candidate with component types of L7.5±1.0 and T2±0.5, noting that the best fit primary was unusually blue when compared to the median $J-K_s$ colors of Faherty et al. (2009). Stumpf et al. (2011) was able to resolve the components with VLT/NACO, and also reported archival HST/NICMOS data which confirmed common proper motion and indicated some orbital motion. Stumpf et al. (2011) determined component spectral

Table 4.4 Properties of three resolved binary systems.

Parameter	2MASS J1341−3052	SDSS J1511+0607	SDSS J2052−1609
Primary SpT	L2.5±1.0	L5.5±1.0	L6.0±2.0
Secondary SpT	T6.0±1.0	T5.0±0.5	T2.0±0.5
ΔJ	2.68±0.08	0.25±0.13	0.03±0.25
ΔH	4.03±0.12	1.41±0.13	0.44±0.30
ΔK_s	4.23±0.07	2.38±0.30	1.12±0.40
Distance (pc)	29±3[1]	28±5[2]	30±1[3]
Ang. Sep. (*mas*)	279±17	108±11	103±2
Proj. Sep. (AU)	8.1±0.5	2.9±0.3	3.0±0.1
PA (°)	317.9±0.6	335.0±4.3	68.4±1.1
Epoch (JD)	2456671.15	2455058.77	2455058.94

References. — (1) This paper; (2) Faherty et al. (2012); (3) Dupuy & Liu (2012)

types by comparing the objects' JHK_s colors to mean colors from Dwarf Archives[4] and obtained divergent results for the primary component (T0.5±0.5 and T2.5±0.5) as compared to those from B10. Using our NIRC2 photometry to constrain spectral template fitting, we find component spectral types of L6.0±2.0 and T2.0±0.5. Dupuy & Liu (2012) find a parallactic distance of 29.5±0.7 pc. The angular separation between the components was measured to be 103±2 *mas*, leading to a projected separation of 3.0±0.1 AU.

Absolute magnitudes of this source and its components were calculated from its parallactic distance and measured magnitude differences. As for the case of SDSS J1511+0607, the primary of SDSS J2052−1609 appears to be underluminous, while its secondary falls comfortably within 1σ from the Dupuy & Liu (2012) relation (Figure 4.6).

4.3.3 Orbital Parameters

4.3.3.1 Preliminary Orbit for SDSS J2052−1609

Our observations of SDSS J2052−1609AB confirm prior results by Stumpf et al. (2011) and adds to coverage of its orbital motion first detected in that study. We identified

[4]http://www.dwarfarchives.org

Table 4.5 Resolved Separation Measurements for SDSS J2052−1609AB

UT Date	JD	Instrument	Δα (mas)	Δδ (mas)	Ref
2005 Oct 11	2453654	Keck/NIRC2	25.4±1.2	114.3±1.4	1,2
2007 Apr 23	2454213	Keck/NIRC2	54.6±2.1	88.8±1.5	1,2
2008 Jun 24	2454642	HST/NICMOS	79.2±0.9	65.6±0.8	3
2009 Jun 19	2455002	VLT/NACO	93.1±1.0	38.9±0.9	3
2009 Aug 15	2455058	Keck/NIRC2	95.7±0.7	38.1±0.7	1
2010 May 01	2455317	Keck/NIRC2	103.4±1.7	20.6±1.5	1,4

References. — (1) This paper; (2) NIRC2 PI M. Liu; (3) Stumpf et al. (2011); (4) NIRC2 PI B. Biller.

additional archival NIRC2 + LGSAO images of the system taken on 2005 October 11, 2007 April 23 (PI M. Liu) and 2010 May 1 (PI B. Biller), and analyzed these data in the same manner as described above. The resulting six epochs of relative astrometry spanning just over 4.5 yr are listed in Table 4.5 and displayed in Figure 4.8. These measurements confirm the direction of motion previously identified and cover a significant fraction of the system's orbit.

To more tightly constrain the orbit of this system, we used an Markov Chain Monte Carlo (MCMC) routine with Metropolis-Hasting algorithm (Metropolis et al. 1953; Hastings 1970) to iteratively fit a seven-parameter orbit model to the twelve astrometric measurements (six each in relative Right Ascension and declination) and parallax distance measurement (d = 29.5±0.7 pc; Dupuy & Liu 2012). The methodology used is described in detail in Burgasser et al. (2015a). The parameter vector is

$$\vec{\theta} = (P, a, e, i, \omega, \Omega, M_0, d) \tag{4.2}$$

where P is the period of the orbit in years, a the semi-major axis in AU, e the eccentricity, i the inclination, ω the argument of periastron, Ω the longitude of nodes, M_0 the mean anomaly at epoch τ_0 = 2453654.31 (Julian Date), and d is the distance in pc. We computed an MCMC chain of 10^7 parameter sets, at each step varying parameters using

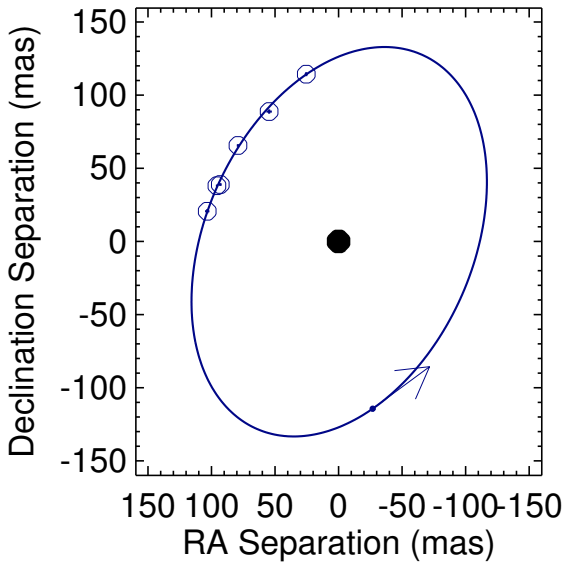

Figure 4.7 Parameter distributions and correlations (triangle plot) for period (P), semi-major axis (a), eccentricity (e), inclination (i), and total system mass (M_{tot}) based on our MCMC orbital analysis of SDSS J2052−1609AB. Contour plots show χ^2 distributions as a function of parameter pairs, highlighting correlations. Normalized histograms at the ends of rows are marginalized over all other parameters. Median values are indicated by solid lines in all panels, and 16% and 84% quantiles are indicated by dashed lines in the histograms.

a normal distribution with scale factors that were allowed to vary dynamically to improve convergence.[5] We applied additional constraints of 1 yr $< P <$ 100 yr and $0 < e < 0.6$ to eliminate improbable regions of parameter space, and constained the distance to lie within 28 pc $< d <$ 31 pc; our parameter chain was largely insensitive to these limits. Convergence of the chain was monitored through autocorrelation of parameters and evolution of divergence in sequential subchains, and acceptance rates were typically $0.5 - 1\%$. The first 10% of the MCMC chain was removed from subsequent analysis.

Figure 4.8 shows the best-fit relative visual orbit compared to the measurements,

[5] We used an initial scale factor set $\vec{\beta}$ = (5 yr, 0.5 AU, 0.2, 20°, 20°, 20°, 20°, 0.7 pc), but if a parameter θ_j did not change in 1000 iterations, β_j was changed to 3 times the standard deviation of the previous (up to 100) changed values.

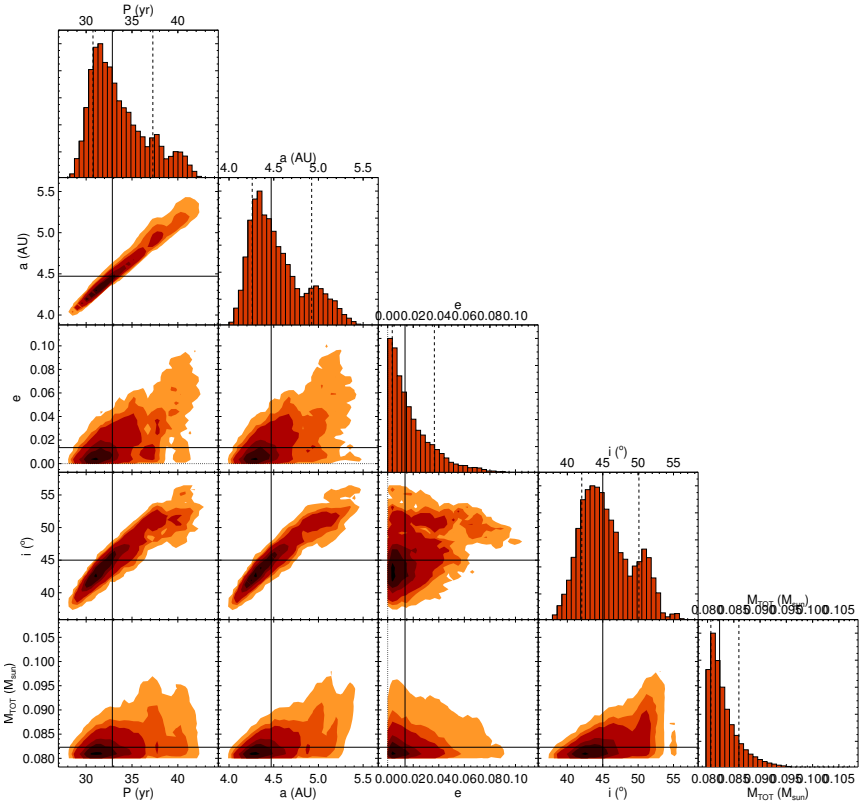

Figure 4.8 Visual orbit of SDSS J2052−1609AB based on MCMC analysis of separation measurements reported here and in Stumpf et al. (2011) (open circles). The orbital motion of the secondary (blue line) relative to the primary (black dot at the origin) is shown projected on the sky, with the arrow indicating the direction of orbital motion at periapse ($M = 0°$). Error bars are plotted but indiscernible on this scale.

which is an acceptable fit ($\chi^2 = 12.05$ for 6 degrees of freedom). Table 4.6 lists the best-fit orbital parameters, as well as median values and 16% and 84% quartiles, while Figure 4.7 displays the distributions and correlations of P, a, e, i and $M_{tot} = a^3/P^2$, the total system mass in Solar units. All of the parameters are reasonably well-determined despite the limited phase coverage, although there are strong correlations between P, a, i and e and a hint of a secondary solution (double-peaked distributions). From the primary solution, we estimate an orbit period of 33^{+4}_{-2} yr and total system mass of $0.0823^{+0.0037}_{-0.0017}$ $M_\odot$, which

Table 4.6 Orbital Analysis of SDSS J2052−1609AB Relative Astrometry

Parameter	Best	Median
Best χ^2 (DOF)	12.05 (6)	···
P^a(yr)	32	33^{+4}_{-2}
a (AU)	4.4	$4.5^{+0.5}_{-0.2}$
e^a	0.005	$0.014^{+0.023}_{-0.010}$
i (°)	45	45^{+5}_{-3}
ω (°)	98	100^{+15}_{-13}
Ω (°)	327	327^{+3}_{-4}
M_0 (°)	318	313^{+15}_{-8}
d^a(pc)	30.5	$30.7^{+0.2}_{-0.4}$
M_{tot} ($M_\odot$)	0.081	$0.0823^{+0.0037}_{-0.0017}$

[a]Parameter was constrained to a limited value range in MCMC analysis.

is consistent with the lower limit of 0.074 $M_\odot$ proposed by Stumpf et al. (2011) assuming a circular orbit. Indeed, the orbit of SDSS J2052−1609AB appears to be fairly circular ($0.014^{+0.023}_{-0.010}$) and significantly inclined to the line of sight ($45^\circ\,^{+4^\circ}_{-2^\circ}$). The best fit template fitting results suggest component spectral types of L5.8±1.8 and T2.1±0.5. Assuming effective temperatures corresponding to these spectral types (1544±181K for the primary and 1248±101K for the secondary; Stephens et al. 2009), and using the evolutionary models of Saumon & Marley (2008) to estimate age-dependent component masses, we estimate an age of 0.4–1.4 Gyr for this system, where the range accounts for the total mass uncertainty, effective temperature uncertainties, and cloud effects on brown dwarf evolution. Observations over the next decade should greatly improve the mass and orbit constraints on this system, and resolved spectroscopy should make it possible to critically test evolutionary models (e.g., Konopacky et al. 2010; Dupuy et al. 2014).

4.3.4 Estimated orbital parameters for 2MASS J1341−3052 and SDSS J1511+0607

For 2MASS J1341−3052 and SDSS J1511+0607 only a single epoch of astrometry is available. Hence, we performed a simple Monte Carlo simulation to find the

distributions of likely semi-major axes and periods for these systems. Following the procedure described in Burgasser et al. (2015b), we created random uniformly-distributed vectors for eccentricity $0 < \varepsilon < 0.6$ (Dupuy & Liu 2011), inclination $0 < \sin i < 1$, longitude of ascending node $0 < \Omega < 2\pi$, argument of periapse $0 < \omega < 2\pi$, and mean anomaly angle $0 < M < 2\pi$ for 10^5 hypothetical orbits with a fixed semi-major axis of $a = 1$ AU. We numerically solved the Kepler equation to find the eccentric anomaly, calculated the Thiele-Innes constants (Innes 1907; van den Bos 1927), and found the x and y projected positions on the sky leading to the total projected separation, r_{tot}. The distributions of semi-major axes for the resolved systems were inferred by transforming variables:

$$a = (1\text{AU}) \times \frac{\rho d}{r_{tot}} \tag{4.3}$$

where a is the semi-major axis in AU, ρ is the angular separation in arc seconds, d is the distance to the system in parsecs and r_{tot} is in AU. The observed projected separation, $r_{obs} = \rho d$, constrains the array of allowed orbits, r_{tot}, and as a result we arrive at a distribution of probable semi-major axes, a.

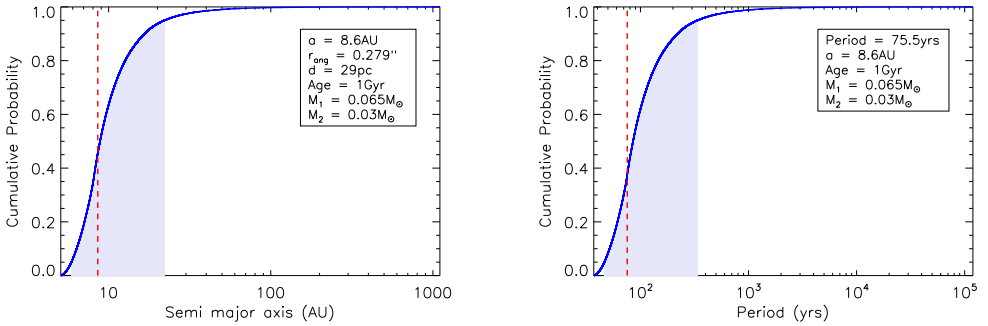

(a) *2MASS J1341−3052*.

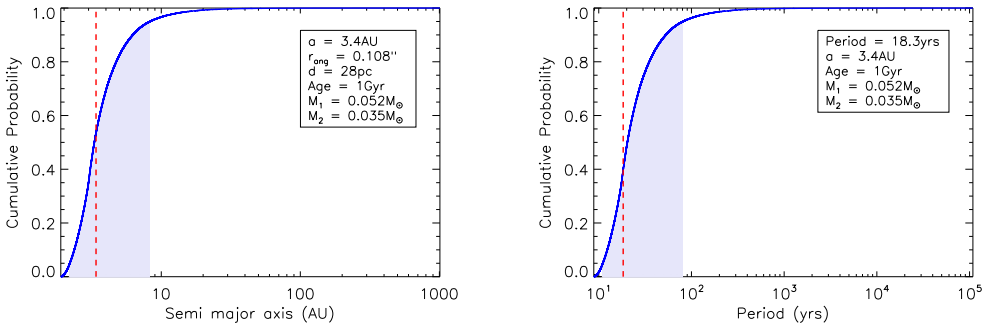

(b) *SDSS J1511+0607*.

Figure 4.9 Cumulative probability distribution of possible semi-major axes and periods for two of the resolved sources from a Monte Carlo simulation for an age of 1Gyr, using one single observation for projected separation from the LGS-AO images in each case. The simulation parameters are shown on the box in the upper right corner. The most likely semi-major axis and period is represented by the dotted red line. The shaded regions indicate the central 68% ($\pm 1\sigma$ equivalent) of data points.

Table 4.7 Estimated masses and orbit results from Monte Carlo simulation.

System	Age (Gyr)	Primary Mass ($M_\odot$)	Secondary Mass ($M_\odot$)	Semi-major Axis (AU)	Period (years)
2MASS J1341−3052AB	0.5	0.052±0.005	0.022±0.005	$8.6^{+5.2}_{-1.8}$	85^{+104}_{-20}
SpT = L2.5±1.0 and T6.0±1.0	1.0	0.065±0.004	0.030±0.007	$8.6^{+5.3}_{-1.8}$	71^{+91}_{-18}
Primary T_{eff} = 1904±165K	5.0	0.075±0.002	0.054±0.007	$8.6^{+5.3}_{-1.8}$	64^{+79}_{-15}
Secondary T_{eff} =1027±144K	10	0.075±0.001	0.061±0.006	$8.6^{+5.2}_{-1.8}$	63^{+76}_{-14}
SDSS J1511+0607AB	0.5	0.041±0.004	0.026±0.003	$3.4^{+1.8}_{-0.8}$	21^{+25}_{-5}
SpT = L5.0±1.0 and T5.0±0.5	1.0	0.052±0.005	0.035±0.004	$3.4^{+1.8}_{-0.9}$	18^{+22}_{-5}
Primary T_{eff} = 1617±139K	5.0	0.070±0.002	0.059±0.004	$3.4^{+1.7}_{-0.9}$	15^{+18}_{-3}
Secondary T_{eff} = 1115±107K	10	0.072±0.001	0.065±0.003	$3.4^{+1.8}_{-0.9}$	15^{+17}_{-4}

The cumulative probability distributions for the semi-major axes of 2MASS J1341−3052 and SDSS J1511+0607 are shown in Figure 4.9. The most likely semi-major axes are demarcated by a dashed red line and the central 68% ($\pm1\sigma$ equivalent) of the data are shaded in lavender. We estimated the periods for these orbits in years assuming $P^2 = a^3/M_{tot}$, with $M_{tot} = M_1 + M_2$ in Solar masses estimated from the models of Baraffe et al. (2003) for ages of 0.5, 1, 5 and 10 Gyr (Table 4.7). For 2MASS J1341−3052, we obtain most likely semi-major axis and period of $8.6^{+5.2}_{-1.8}$ AU and 63−85 years for decreasing ages, while for SDSS J1511+0607 the most likely semi-major axis and periods are $3.4^{+1.8}_{-0.8}$ AU and 15−21 years.

4.3.5 On the frequency of short period VLM binaries

Starting from a sample of LGS-AO observations of 43 brown dwarfs, we resolved 3 of 17 spectral binary candidates and none of the other targets. 2MASS J1733−1654 has a particularly asymmetrical PSF shape which could indicate the presence of a marginally resolved companion NE of the primary, but this is inconclusive from our images. The fraction of resolved systems from the spectral binary sample is $3/17 = 18^{+13}_{-6}$% (binomial uncertainties), which is consistent with the observed binary fractions reported in the literature from imaging programs ($10-20$%; Bouy et al. 2003; Close et al. 2003; Basri & Reiners 2006; Allen 2007; Burgasser 2007a; Kraus & Hillenbrand 2012). Among

the spectral binaries, 2MASS J0518−2828, WISEP J0720−0846, SDSS J0805+4812, 2MASS J1106+2754 and 2MASS J1209−1004 are known binaries unresolved in our images. This indicates a minimum binary fraction for spectral binaries in this sample of $(3+5)/17 = 47^{+12}_{-11}\%$. This is considerably higher than typical VLM binary search samples and indicates that the spectral binary sample is positively biased towards binaries. The fact that over half of the known binaries in this sample are not resolved suggests that imaging programs are similarly missing binaries, and that the true binary fraction may be significantly higher than what is currently reported. Note that the fraction reported here remains a lower limit; an unknown number of the 9 unresolved and unconfirmed spectral binaries may be true binaries with separations $\lesssim 1.5-9.2$ AU.

Of the 12 confirmed spectral binaries to date (Table 4.8), about half have been unresolved in reported LGS-AO imaging, which is roughly consistent with the 3 resolved and 5 unresolved binaries in our sample. While follow-up of unresolved systems is more time-consuming and resource-intensive (radial velocity and astrometric monitoring), we speculate that the number of unresolved but confirmed spectral binaries will increase as follow-up is completed.

A high incidence of unresolved but confirmed spectral binaries implies a high incidence of currently unresolved binaries in general. For example, if all of the unresolved spectral binaries in our sample actually are binaries, this would indicate a ratio of unresolved-to-resolved systems of 4.7:1. Given that the resolved binary fraction is roughly 15%, this rate of unresolved pairs would imply an overall binary fraction of over 60%. It is more likely that the current pool of spectral binary candidates contains some number of contaminants, such as blue L dwarfs (BG14) and variable brown dwarfs (Khandrika et al. 2013; Radigan et al. 2012) which will need to be identified through more detailed spectral and photometric variability analysis. Nevertheless, it is important to note that all 17 spectral binary systems studied here have resolved or

Table 4.8 Confirmed Spectral Binaries

Name	Spectral Type				2MASS-J	$J-K_s$	ΔJ	Separations (AU)	Confirmation method[a]	Ref. SB;Conf.
	Combined Optical	Combined NIR	Primary	Secondary						
SDSS J000649.16−085246.3	M9	···	M8.5±0.5	T5±1	14.14±0.04	1.01±0.05	3.15±0.31	0.29±0.01	RV	5; 5
2MASS J03202839−0446358	M8:	L1	M8.5±0.3	T5±0.9	12.13±0.03	1.13±0.04	3.50±0.20	0.404±0.042	RV	8; 3
2MASS J05185995−2828372	···	···	L8.6±0.3	T6.4±1.0	15.98±0.10	1.82±0.12	0.13±0.19	1.8±0.5	DI	12; 10
WISEP J072003.20−084651.2	M9.5	···	M8.9±0.0	T5.2±0.7	10.63±0.02	1.16±0.03	3.30±0.20	0.84±0.17	DI	4; 4
SDSS J080531.84+481233.0	L4	L9.5	L5.1±0.4	T5.7±0.5	14.73±0.04	1.46±0.05	1.50±0.09	0.9-2.3	AV	9; 13
SDSS J092615.38+584720.9	T4.5	···	T4.0±0.1	T5.3±0.7	16.77±0.14	<1.57	0.40±0.20	2.6±0.5	DI	16; 10, 11
2MASS J11061197+2754225	···	T2.5	T0.4±0.3	T4.0±0.8	14.82±0.04	1.02±0.07	-0.37±0.06	<2.67	OL	7, 14; 15
2MASS J12095613−1004008	···	T3	T1.2±0.3	T5.9±0.6	15.91±0.08	0.85±0.16	1.50±0.20	4.8±0.2	DI	1; 18
2MASS J13153094−2649513	L5	···	L4.9±0.5	T6.1±2.1	15.07±0.05	1.63±0.07	3.03±0.03	6.6±0.9	DI	6; 6
2MASS J13411160−30525049	L3	···	L2.3±0.6	T6.0±1.0	14.61±0.03	1.53±0.04	3.28±0.53	7.8±0.5	DI	2; 1
SDSS J151114.66+060742.9	···	T0±2	L5.2±0.9	T4.9±0.5	16.02±0.08	1.47±0.13	0.54±0.32	2.9±0.3	DI	7; 1
SDSS J205235.31−160929.8	···	T1±1	L5.8±1.8	T2.1±0.5	16.33±0.12	1.21±0.19	0.04±0.18	3.0±0.1	DI	7; 17

[a]RV = Radial velocity variability, DI = Direct imaging, AV = Astrometric variability, OL = Overluminosity.

References. — (1) This paper; (2) Bardalez Gagliuffi et al. (2014); (3) Blake et al. (2008); (4) Burgasser et al. (2015b); (5) Burgasser et al. (2012); (6) Burgasser et al. (2011b); (7) Burgasser et al. (2010a); (8) Burgasser et al. (2008a); (9) Burgasser (2007b); (10) Burgasser et al. (2006c); (11) Carson et al. (2011); (12) Cruz et al. (2004); (13) Dupuy & Liu (2012); (14) Looper et al. (2008a); (15) Manjavacas et al. (2013); (16) Metchev et al. (2008); (17) Stumpf et al. (2011); (18) Liu et al. (2010).

upper limit separations near or below the peak of the resolved binary separation of VLM dwarfs (Allen 2007). This is strong evidence that a large number of VLM binaries are being missed in current imaging surveys.

4.4 Summary

We have observed 43 late-M, L and T dwarfs with Keck/NIRC2 LGS-AO, including 17 spectral binary candidates with high resolution Keck/NIRC2 LGS-AO imaging. Three sources were resolved: 2MASS J1341−3052, SDSS J1511+0607 and SDSS J2052−1609, while five other confirmed binaries were unresolved. Only one of our spectral binary candidates, 2MASS J1733−1654, has a candidate faint companion on the images, requiring confirmation. We used relative photometry to update the estimated component spectral types of our resolved systems. For SDSS J2052−1609, we combined our observations with those of Stumpf et al. (2011) and archival data to make a preliminary determination of orbital parameters, finding a period of 33^{+4}_{-2} years and system mass of $0.0823^{+0.0037}_{-0.0017}M_{\odot}$ consistent with a relatively young system (0.4−1.4 Gyr). For 2MASS J1341−3052 and SDSS J1511+0607, we estimated their most likely semi-major axes and periods based on their observed angular separations, distances and estimated masses. 2MASS J1341−3052 has a projected separation of 8.1±0.5 AU and a period in the range of $63-85$ years depending on the ages. For SDSS J1511+0607, we estimate a projected separation of 2.9±0.3 AU and a period in the $17-25$ years range.

For the remaining 14 unresolved spectral binaries we calculated separation limits based on their estimated component magnitude differences from template fitting and empirical sensitivity curves. Five of these unresolved systems are confirmed binaries with measured angular separations smaller than our upper limits, and therefore consistent. The other 9 unresolved systems have upper limits in angular separation of $0\farcs04-0\farcs28$,

corresponding to projected separations limits of $1.5-9.2$AU.

The binary fraction of the spectral binary candidates in this sample is $47^{+12}_{-11}\%$, significantly higher than those from prior imaging surveys ($10-20\%$; Bouy et al. 2003; Burgasser et al. 2003b; Cruz et al. 2003) and the overall binary fraction ($20-25\%$; Basri & Reiners 2006; Burgasser 2007a; Joergens 2008). While this sample is clearly biased towards binary systems, the high percentage of unresolved systems suggests that there may exist a large population of very tight brown dwarf binaries that cannot be confirmed with high resolution imaging. Confirmation of the 9 remaining unresolved spectral binaries depends on high resolution radial velocity or astrometric variability measurements that are currently ongoing. If these unresolved sources turn out to be binaries, a great advantage of their short projected separation is the high likelihood for full orbit and dynamical mass determinations. In any case, an unbiased, volume-limited sample of spectral binaries with complete follow-up is required in order to find the true underlying binary fraction.

Acknowledgements

We would like to thank our referee Sandy Leggett for her helpful comments. The authors thank observing assistants Jason McIlroy, Heather Hershley, Terry Stickel, and Gary Puniwai and support astronomers Hien Tran, Luca Rizzi, Marc Kassis, and Al Conrad for their assistance during our observations. DBG acknowledges funding support from the IPAC graduate fellowship. DBG and AJB acknowledge support from the National Aeronautics and Space Administration under Grant No. NNX15AI75G. CRG was partially supported by a NASA Keck PI Data Award, administered by the NASA Exoplanet Science Institute. This research has made use of the Keck Observatory Archive (KOA), which is operated by the W. M. Keck Observatory and the NASA Exoplanet Science Institute (NExScI), under contract with the National Aeronautics and

Space Administration. This publication makes use of data from the SpeX Prism Spectral Libraries, maintained by Adam Burgasser at http://www.browndwarfs.org/spexprism; the Dwarf Archives Compendium, maintained by Chris Gelino, Davy Kirkpatrick, Mike Cushing, David Kinder and Adam Burgasser at http://DwarfArchives.org; and the VLM Binaries Archive maintained by Nick Siegler at http://vlmbinaries.org. The authors wish to recognize and acknowledge the very significant cultural role and reverence that the summit of Mauna Kea has always had within the indigenous Hawaiian community. We are most fortunate to have the opportunity to conduct observations from this mountain.

Facilities: Keck NIRC2.

This Chapter, in full, is a reprint of the material as it appears in the Astronomical Journal 2015, Vol. 150, Num. 163. Bardalez Gagliuffi, Daniella; Gelino, Christopher; Burgasser, Adam; Looper. The dissertation author was the primary investigator and author of this paper.

Chapter 5

Volume-Limited SpeXtroscopic Sample of M7−L5 Ultracool Dwarfs up to 25 pc

5.1 Ultracool Dwarfs in the Solar Neighborhood

Brown dwarfs are the lowest mass products of star formation, lacking enough mass to sustain the core nuclear fusion reactions that power stars ($\lesssim 0.08 M_{\odot}$; Kumar 1963). Their atmospheres resemble those of giant planets and their spectra differ greatly from the black body spectral energy distributions of hydrogen-burning stars due to strong molecular absorption. Without an internal energy generation mechanism, brown dwarfs are supported by degeneracy pressure, and become cooler as they age, slowly releasing the leftover thermal energy from their initial collapse. These objects can be classified in temperature-based spectral classes of M, L, T and Y dwarfs (Kirkpatrick et al. 1999b; Burgasser 2002; Cushing et al. 2011) with transitions determined by the appearance and disappearance of atomic and molecular species in their near infrared spectra.

Since their initial discovery in 1995 (Rebolo et al. 1995; Nakajima et al. 1995), roughly 10,000 very low mass (VLM) stars and brown dwarfs have been identified (e.g.

Best et al. 2017). Collectively called ultracool dwarfs[1], these objects are diverse in their masses, ages, temperatures, colors, composition, kinematics, and rotation rates, to name a few properties. In order to understand the extent and origins of this diversity, we need to analyze a well-characterized, representative sample.

The Solar neighborhood presents an opportunity to compile such sample. Bearing in mind the location and motion of the Sun with respect to the galactic center and the distinct kinematics and metallicity distributions of the thin disk, thick disk and halo population, a small volume near the Sun can be treated as representative of the Milky Way. Since brown dwarfs are intrinsically faint, collecting data in the Solar Neighborhood yields the highest signal-to-noise ratios.

The diversity of brown dwarfs encompasses those hosting disks (e.g. Ricci et al. 2014; Testi et al. 2016) or exoplanets (e.g. Chauvin et al. 2004; Han et al. 2013), isolated objects and those found in binary or higher-order multiple systems (e.g. Liu et al. 2010; Radigan et al. 2013; Burgasser et al. 2015b), red or blue color outliers (e.g. Liu et al. 2013; Burgasser 2007b) with varied atmospheres and compositions (e.g. Burgasser et al. 2003c), radio quiescent or active (e.g. Burgasser et al. 2013), among other examples. Understanding this diversity can provide the tools to answer fundamental questions about brown dwarf formation mechanisms and evolution processes.

Large area surveys in optical, near-infrared and mid-infrared bands have provided extensive knowledge of the population characteristics of ultracool dwarfs. Some notable examples include the Sloan Digital Sky Survey (SDSS; York et al. 2000), the Two-Micron All Sky Survey (2MASS; Cutri et al. 2003), the UKIRT Infrared Deep Sky Survey (UKIDSS;) and more recently, the Wide Field Infrared Survey Explorer (WISE; Wright et al. 2010) whose mid-infrared filters were designed to encompass the flux peak of the coldest brown dwarfs. Previous studies have built upon these surveys to

[1] $M \lesssim 0.1\ M_{\odot}$

discover new ultracool dwarfs by exploring the locus of these objects in color-magnitude diagrams (Kirkpatrick et al. 1999b; Burgasser 2002; Cruz et al. 2003; Metchev et al. 2008; Reid et al. 2008b; Kirkpatrick et al. 2011). However, new discoveries of nearby brown dwarfs, in particular the L/T transition binary WISE J104915.57?531906.1 (Luhman 2013), the 250 K WISE J085510.83?071442.5 (Luhman 2014) and the M9.5+T5 binary system WISE J072003.20−084651.2Scholz 2014; Burgasser et al. 2015b, all at distances of 6 pc or less, show that the nearby sample is incomplete.

Cruz et al. (2003) discovered 186 M7−L6 dwarfs from photometric selections starting from a 2MASS sample of $\sim$ 11 million infrared sources. Candidates were followed up and confirmed with far-red optical spectroscopy at four different telescopes. Skrzypek et al. (2015) designed a *photo-type* method to accurately determine the spectral type of ultracool dwarfs through high quality UKIDSS photometry alone and a χ^2 minimization routine. However, only 19 out of 1187 L and T dwarfs photo-typed in their paper were spectroscopically confirmed for consistency (Skrzypek et al. 2016). SDSS discovered brown dwarfs from their optical spectra, but obtained spectra by random pointing for roughly $1/4$ of the SDSS footprint. WISE focused on the photometry of the coolest T and Y-type brown dwarfs, providing the coolest brown dwarf known (WISE J085510.83−071442.5 at 250 K, 2 pc away from the Sun; Luhman 2014). The aim of the REsearch Consortium On Nearby Stars (RECONS; Winters et al. 2015) is to discover and characterize the Sun's stellar neighbors up to 25 pc, which expressly misses fainter targets. This variety of approaches and observational designs translates into a variety of biases which are difficult to homogenize and analyze statistically if we were to consolidate these objects into one sample. This is why it is important to compile a uniform, volume-complete sample.

With a focus on spectral binary systems as a means to find the true ultracool binary fraction, we are interested in compiling a uniform sample of late-M and early-L

dwarfs that could act as primaries to T dwarfs. Observationally, the transition from M to L dwarfs is characterized by the formation of condensate species leading to the evolution from clear to dusty or cloudy atmospheres. The spectral absorption features of late-M dwarfs caused by molecular transitions of VO, TiO, H_2O, CO, FeH and CaH mark a clear departure from the smoother black body spectra of hotter stars. L dwarfs were designated as a new spectral class by Kirkpatrick et al. (1999b) based on weakening VO and TiO and strengthening of alkalis and metal hydrides compared to late-M dwarfs (e.g. Lodders 2002). As the effective temperatures of these objects drop below 2000 K, some of the gaseous phases will condense into liquids or solids (e.g. TiO becomes perovskite, $CaTiO_3$), partially depleting the atmosphere of gas molecules and introducing green house effect from the dust grain opacity (Allard et al. 1997). This transition has an observable effect not only on the absorption lines and bands identified in the near-infrared spectra of these objects, but also on the overall shape and $J-K$ colors of their spectra.

In this paper, we present a complete, volume-limited, near-infrared, spectroscopic sample of M7−L5 dwarfs up to 25 pc, homogeneously acquired with IRTF/SpeX (Rayner et al. 2003). Section 5.2 describes the sample selection from previous surveys, synthesis and assembly into a clean database. Section 5.3 recounts the new SpeX observations. Section 5.4 characterizes the sample with spectral type and gravity classifications, estimate spectrophotometric distances and compare to parallaxes when available, calculate completeness and present new binary discoveries, along with other subpopulations such as red/blue dwarfs, subdwarfs, and low-gravity sources. Finally, we summarize our findings in Section 5.5.

5.2 Sample Construction

5.2.1 Summary

The sample we present is a multi-wavelength photometric compilation of ultracool sources accompanied by near infrared, low resolution, spectroscopic observations carried out in their entirety with the SpeX spectrograph. The spectral types reported here are homogeneous to the same instrument.

The final sample contains 443 ultracool dwarfs with spectral types spanning M7−L5, listed in Table 5.1. Photometry is available for *riz* bands from SDSS, *JHK* and K_s from 2MASS, UKIDSS and MKO, $W1W2W3$ from WISE, and *G* from GAIA where applicable. About 29% of the sample has trigonometric parallaxes. Spectrophotometric distances for the remaining sources were calculated for all the magnitudes or colors available. Near infrared, low resolution spectra from IRTF/SpeX were obtained for 92% of the observable sample, i.e. whose declinations were accessible by IRTF ($-50^\circ < \delta < +67^\circ$). The spectral sample comprises 85% of the total number of sources.

Table 5.1 Sample of M7−L5 ultracool dwarfs in the 25 pc volume

Designation	Adopted SpT	SpT Flag	J (mag)	$J-K$	Distance (pc)	Distance Type	Ref.
J00043484−4044058B	L5.0	OPT	13.76±0.04	1.7±0.06	13.01±0.67	Trig	12
J00043484−4044058C	L5.0	OPT	>13.9	>1.6	13.01±0.67	Trig	13
J00065794−6436542	L0.0	OPT	13.38±0.03	1.22±0.04	23±3	NIR	12
J00130931−0025521	M7.0	OPT	12.17±0.02	0.85±0.04	21±3	NIR	12
J00145575−4844171	L2.5	OPT	14.05±0.04	1.33±0.05	20±2	NIR	20
J00154476+3516026	L2.0	OPT	13.88±0.03	1.61±0.04	18±2	WISE	21
J00192626+4614078	M8.0	OPT	12.6±0.02	1.1±0.02	21±2	NIR	12
J00194579+5213179	M9.0	OPT	12.79±0.02	1.17±0.03	20±2	NIR	2
J00242463−0158201	M9.5	OPT	11.99±0.04	1.45±0.04	12.5±0.53	Trig	22
J00265632−5428530	M8.0	OPT	12.46±0.02	1.12±0.04	20±2	NIR	12
J00275592+2219328A	M7.5	OPT	10.61±0.02	1.04±0.03	15.27±0.89	Trig	12
J00275592+2219328B	M8.0	OPT	10.61±0.02	1.04±0.03	15.27±0.89	Trig	12
J0028208+224905	L7.0	SIMBAD	15.61±0.07	1.83±0.1	19±2	NIR	23
J00311925−3840356	L2.5	OPT	14.1±0.03	1.18±0.05	22±3	NIR	24
J003154778+06494639	M8.0	NIR	12.82±0.02	1.1±0.03	21±2	Color	12
J00332386−1521309	L4.0	SIMBAD	15.29±0.06	1.88±0.07	23±3	WISE	25
J00361617+1821104	L3.5	OPT	12.47±0.03	1.41±0.03	8.76±0.06	Trig	26
J00413538−5621127	M6.5	OPT	11.96±0.02	1.1±0.03	19±2	WISE	12
J00452143+1634446	L3.5	SIMBAD	13.06±0.02	1.69±0.03	9±1	WISE	17
J00464841+0715177	L0.0	OPT	13.88±0.03	1.34±0.04	18±2	Color	17
J004926771−06354671	M9.0	NIR	13.34±0.02	1.24±0.03	22±2	Color	12
J00525468−2705597	M7.5	OPT	13.61±0.03	1.07±0.04	21.74±4.73	Trig	12
J00531899−3631102	L3.5	OPT	14.44±0.03	1.51±0.04	20±2	NIR	20
J01004911−1933398	L3.0	OPT	13.49±0.03	0.73±0.04	16±2	NIR	12
J01025100−3737438	M8.0	OPT	11.13±0.02	1.06±0.03	12.2±0.41	Trig	27
J01090150−5100494	M8.5	OPT	12.23±0.02	1.14±0.03	17.3±1.05	Trig	28
J01095117−0343264	M9.0	OPT	11.69±0.02	1.27±0.03	9.59±0.21	Trig	2
J01231125−6921379	M7.5	OPT	12.32±0.02	1.0±0.04	20±2	NIR	12
J01243124−0027556	M7.0	OPT	12.11±0.02	0.98±0.03	20±2	NIR	12
J01282664−5545343	L2.0	OPT	13.78±0.03	1.44±0.04	19±2	NIR	12
J01311838+3801554	L4.0	OPT	14.68±0.03	1.62±0.05	20±2	NIR	29
J01410321+1804502	L1.0	OPT	13.88±0.02	1.38±0.04	23±3	Color	17

Table 5.1 Continued

Designation	Adopted SpT	SpT Flag	J (mag)	$J-K$	Distance (pc)	Distance Type	Ref.
J01443536−0716142	L5.0	OPT	14.19±0.03	1.92±0.04	13±1	NIR	30
J01483864−3024396	M7.5	OPT	12.3±0.02	1.08±0.03	20±2	NIR	2
J01490895+2956131	M9.5	OPT	13.45±0.02	1.47±0.03	22.52±0.36	Trig	12
J01550354+0950003	L4.0	SIMBAD	14.82±0.04	1.69±0.05	21±2	NIR	23
J02050344+1251422	L5.0	OPT	15.68±0.06	2.01±0.07	22±3	WISE	21
J02052940−1159296	L5.0	OPT	14.59±0.03	1.59±0.04	19.76±0.59	Trig	12
J02081833+2542533	L1.0	OPT	13.99±0.03	1.4±0.04	25±3	Color	21
J02115089+4728300	M8.0	NIR	12.84±0.02	1.01±0.03	23±2	Color	12
J02132880+4444453	L1.5	OPT	13.49±0.02	1.28±0.03	19±2	NIR	2
J02150802−3040011	M8.0	OPT	11.62±0.03	1.08±0.04	14±2	NIR	12
J02182913−3133230	L3.0	OPT	14.73±0.04	1.57±0.05	23±3	WISE	2
J02192210−3925225	L4.0	NIR	15.54±0.1	1.72±0.14	7±1	WISE	12
J02271036−1624479	L1.5	OPT	13.57±0.02	1.43±0.04	19±2	NIR	23
J02284243+1639329	L0.0	OPT	13.17±0.03	1.35±0.04	20±2	NIR	23
J02284355−6325052	L1.0	OPT	13.56±0.03	1.31±0.04	21±2	NIR	12
J02354955−0711214	M7.0	OPT	12.45±0.03	1.02±0.04	25±3	Color	12
J02355993−2331205	L1.5	OPT	13.67±0.15	1.48±0.17	21.21±0.12	Trig	31
J024029501+28325766	M7.5	OPT	12.67±0.02	1.04±0.03	21±2	Color	1
J02484100−1651216	M8.0	OPT	12.55±0.02	1.13±0.03	16.23±1.42	Trig	12
J0251148−035245	L3.0	OPT	13.06±0.03	1.4±0.04	12±1	NIR	2
J02530084+1652532	M6.5	OPT	8.39±0.03	0.81±0.05	3.84±0.04	Trig	32
J0253202+271333	M8.0	OPT	12.5±0.02	1.01±0.03	21±2	NIR	2
J02540582−1934523	M9.0	OPT	13.08±0.03	1.17±0.04	23±3	NIR	2
J03061159−3647528	M8.0	OPT	11.69±0.02	1.06±0.03	13.08±0.24	Trig	33
J03122509+0021585	M7.0	OPT	12.23±0.02	1.01±0.04	21±3	NIR	12
J03140344+1603056	L0.0	OPT	12.53±0.02	1.29±0.03	15±2	NIR	23
J03144011−0450316	M7.5	OPT	12.64±0.02	1.04±0.04	24±3	NIR	12
J03205965+1854233	M8.0	OPT	11.76±0.02	1.12±0.03	14.64±0.13	Trig	12
J03264453+1919309	M8.5	OPT	13.12±0.02	1.18±0.03	25±3	NIR	23
J03283463+1129515	M8.0	OPT	12.46±0.02	1.13±0.03	20±2	NIR	12
J03300506+2405281	M7.0	OPT	12.39±0.02	1.0±0.03	23±3	NIR	12
J03313025−3042383	M7.5	OPT	11.36±0.02	1.1±0.03	13±2	NIR	12

Table 5.1 Continued

Designation	Adopted SpT	SpT Flag	J (mag)	$J-K$	Distance (pc)	Distance Type	Ref.
J03341218−4953322	M9.0	OPT	11.38±0.02	0.98±0.03	8.29±0.25	Trig	34
J03393521−3525440	M9.5	OPT	10.72±0.02	1.18±0.03	6.41±0.04	Trig	12
J03395284+2457273	M8.0	OPT	12.84±0.02	1.1±0.03	19.27±1.93	Trig	12
J03442102+3206158	M8.0	OPT	>15.28	>1.37	20±3	WISE	12
J03442694+3203494	M9.0	OPT	>17.29	···	13±2	WISE	12
J034429979+32192276	L0.0	NIR	12.44±0.02	1.26±0.02	14±2	NIR	35
J03505737+1818069	M9.0	OPT	12.97±0.02	1.19±0.03	23±2	Color	12
J03510004−0052452	M8.0	OPT	11.3±0.02	1.07±0.03	14.68±0.41	Trig	36
J03521086+0210479	M9.0	OPT	13.08±0.03	1.12±0.04	23±3	NIR	18
J03550477−1032415	M8.5	OPT	13.08±0.03	1.1±0.04	25±3	NIR	12
J03552337+1133437	L3.0	SIMBAD	14.05±0.02	2.52±0.03	8±1	WISE	23
J04013766+2849529	L3.0	SIMBAD	13.41±0.02	1.6±0.03	13±2	NIR	37
J04041807+4127398	L2.0	OPT	14.15±0.03	1.73±0.04	18±2	WISE	37
J04082905−1450334	L2.0	OPT	14.22±0.03	1.4±0.04	24±3	NIR	17
J041539163+28185862	M9.0	NIR	10.55±0.02	1.32±0.03	6±1	WISE	12
J04173745−0800007	M7.5	OPT	12.18±0.03	1.09±0.04	19±2	NIR	38
J041807965+28260370	M8.0	NIR	11.54±0.02	1.1±0.03	13±1	Color	12
J04210718−6306022	L5.0	OPT	15.56±0.05	2.12±0.06	19±2	WISE	12
J042154823+26423722	M8.0	NIR	12.32±0.02	1.1±0.03	18±2	NIR	12
J042353227−00065872	···	···	13.65±0.02	1.17±0.04	23±3	Color	39
J042450211+26410066	M8.0	NIR	12.41±0.02	1.13±0.03	19±2	NIR	12
J04270723+0859027	M8.0	OPT	12.92±0.03	1.19±0.04	19±2	Color	12
J042724678+26241993	M8.0	NIR	11.36±0.02	1.18±0.03	11±1	NIR	12
J04291842−3123568	M7.5	OPT	10.87±0.02	1.1±0.03	10±1	NIR	38
J04305157−0849007	M8.0	OPT	12.9±0.02	1.12±0.03	24±3	NIR	2
J04351455−1414468	M8.0	OPT	11.88±0.03	1.93±0.04	10±1	WISE	40
J04351612−1606574	M8.0	OPT	10.41±0.03	1.05±0.03	10.49±0.12	Trig	12
J04390101−2353083	L6.5	OPT	14.41±0.03	1.59±0.04	9.06±0.33	Trig	12
J04402325−0530082	M7.0	OPT	10.66±0.02	1.11±0.03	9.48±0.29	Trig	12
J044104244+25575612	M7.0	NIR	10.95±0.02	1.0±0.03	12±1	NIR	12
J04430581−3202090	L5.0	OPT	15.27±0.05	1.4±0.08	23±3	NIR	12
J04433761+0002051	M9.0	OPT	12.51±0.03	1.29±0.03	11±1	Color	41

Table 5.1 Continued

Designation	Adopted SpT	SpT Flag	J (mag)	$J-K$	Distance (pc)	Distance Type	Ref.
J04455387−3048204	L2.0	OPT	13.39±0.03	1.42±0.03	12.74±0.8	Trig	2
J044806329+15512512	L2.0	NIR	13.71±0.02	1.73±0.03	14±2	WISE	12
J04510093−3402150	L0.5	OPT	13.54±0.02	1.25±0.04	21.07±0.67	Trig	2
J05002100+0330501	L4.0	OPT	13.67±0.02	1.61±0.03	13.54±0.36	Trig	23
J05004808+0442143	L1.0	NIR	13.8±0.03	1.29±0.04	24±3	NIR	42
J05012406−0010452	L4.0	SIMBAD	14.98±0.04	2.02±0.05	13.09±0.82	Trig	23
J050441399+25095440	M9.0	NIR	10.91±0.02	1.32±0.03	7±1	WISE	12
J05061292+0439272	M7.0	OPT	8.91±0.02	0.84±0.03	5±1	NIR	43
J050855063+33192721	L2.0	NIR	14.22±0.03	1.59±0.04	21±3	WISE	12
J05102012+2714032	M8.0	OPT	10.7±0.02	1.14±0.03	9.93±0.16	Trig	3
J05120636−29495400	L4.5	OPT	15.46±0.06	2.18±0.07	18±2	WISE	2
J05153094+5911185	M7.5	OPT	11.32±0.03	1.0±0.04	15.22±0.3	Trig	4
J05173766−3349027	M8.0	OPT	12.0±0.02	1.17±0.03	16±2	NIR	44
J05181131−3101529	M6.5	OPT	11.88±0.03	0.98±0.04	19±2	WISE	12
J05233822−1403022	L2.5	OPT	13.08±0.02	1.45±0.04	12.35±0.27	Trig	2
J05264316−1824315	M7.0	NIR	12.36±0.02	0.91±0.03	23±3	NIR	12
J05301261+6253254	L1.0	OPT	14.05±0.03	1.34±0.04	23±3	Color	23
J05345844−1511439	M9.0	OPT	13.19±0.03	1.22±0.04	24±3	NIR	29
J05372332−0816055	M7.0	NIR	12.3±0.02	0.95±0.03	22±3	NIR	12
J05392474+4038437	M8.0	OPT	11.11±0.02	1.06±0.03	11±1	NIR	12
J05394952+5253597	L5.0	NIR	14.76±0.04	1.43±0.05	18±2	NIR	45
J05395200−0059019	L5.0	OPT	14.03±0.03	1.51±0.04	13.14±0.37	Trig	2
J05431887+6422528	L1.0	OPT	13.57±0.03	1.52±0.04	19±2	WISE	23
J05441150−2433018	M8.0	OPT	12.53±0.02	1.07±0.03	21±2	NIR	12
J05480722+0033588	M7.0	OPT	13.21±0.03	1.99±0.04	13±2	Color	46
J05500794+1610519	L2.0	NIR	14.44±0.03	1.6±0.04	23±3	WISE	6
J06022216+6336391	L1.0	OPT	14.27±0.03	1.58±0.04	24±3	WISE	23
J06023045+3910592	L1.0	OPT	12.3±0.02	1.44±0.03	10±1	WISE	47
J06091922−3549311	L3.0	NIR	13.63±0.11	1.62±0.13	22.14±0.17	Trig	43
J06145280+4536556	M9.0	OPT	13.02±0.02	>1.18	22±3	WISE	12
J06154934−01004158	L2.0	OPT	13.75±0.03	1.21±0.04	20±2	NIR	48
J06244172+6626309	L1.0	SIMBAD	13.41±0.05	1.14±0.06	20±2	NIR	12

Table 5.1 Continued

Designation	Adopted SpT	SpT Flag	J (mag)	$J-K$	Distance (pc)	Distance Type	Ref.
J06244595−4521548	L5.0	OPT	14.48±0.03	1.88±0.04	11.92±0.64	Trig	23
J06300140−1840143	M8.5	OPT	12.68±0.03	1.22±0.04	19.52±0.03	Trig	12
J06320617+8305014	L0.5	OPT	13.75±0.03	1.35±0.04	21±2	Color	12
J06411840−4322329	L1.5	OPT	13.75±0.03	1.3±0.04	17.95±1.84	Trig	23
J06431685−1843375	M8.0	OPT	13.01±0.02	1.21±0.03	25±3	NIR	12
J06521977−2534505	L0.0	OPT	12.76±0.02	1.24±0.03	15.68±0.23	Trig	49
J06523073+4710348	L4.5	OPT	13.51±0.02	1.82±0.03	9±1	WISE	12
J06572547−4019134	M7.5	OPT	12.73±0.02	1.06±0.03	25±3	NIR	12
J07003664+3157266	L3.5	OPT	12.92±0.02	1.61±0.03	12.2±0.3	Trig	12
J07025026−6102482	M7.0	SIMBAD	10.36±0.02	0.84±0.03	9±1	NIR	12
J07075327−4900503	M8.5	OPT	13.23±0.03	1.12±0.04	14.29±0.82	Trig	50
J07111138+4329590	M7.0	OPT	9.98±0.02	0.85±0.03	12.85±0.5	Trig	5
J07140394+3702459	M8.0	OPT	11.98±0.02	1.14±0.03	16±2	NIR	12
J071551828−11452847	L4.0	NIR	14.3±0.04	1.49±0.06	18±2	NIR	6
J07164790−0630369	L1.0	OPT	13.9±0.04	1.33±0.05	24±3	NIR	48
J07171626+5705430	L3.0	OPT	14.64±0.03	1.69±0.04	20±3	WISE	17
J07200325−0846499	M9.0	OPT	10.63±0.02	1.16±0.03	6.02±1.02	Trig	51
J07231462+5727081	L1.0	OPT	13.97±0.03	1.36±0.04	25±3	NIR	23
J07235262−3309435	L5.0	NIR	15.74±0.06	2.03±0.08	24±3	WISE	52
J07410681+1738459	M7.0	OPT	12.01±0.02	1.07±0.03	17±2	Color	12
J07421169−1211516	L4.8	SPEX	12.63±0.03	0.72±0.04	8±1	NIR	6
J07464256+2000321	L0.5	OPT	11.76±0.02	1.29±0.03	11.6±0.62	Trig	26
J07511645−2530432	L2.5	OPT	13.16±0.02	1.17±0.03	16.91±0.24	Trig	48
J07522390+1612157	M7.0	OPT	10.88±0.02	1.03±0.03	18.62±1.14	Trig	12
J08040580+6153336	M9.0	OPT	12.74±0.02	1.29±0.03	19±2	NIR	12
J08053189+4812330	L4.0	OPT	14.73±0.04	1.29±0.06	22±3	NIR	12
J08072607+3213101	M8.0	OPT	12.17±0.02	1.12±0.04	14±2	Color	48
J08105865+1420390	M8.0	OPT	12.73±0.02	1.14±0.03	19±2	Color	27
J08123170−2444423	L2.5	OPT	13.82±0.03	1.43±0.04	21.99±0.46	Trig	48
J08151407+1030117	M7.0	OPT	12.42±0.02	1.09±0.03	23±3	NIR	12
J08185804+2333522	M7.0	OPT	12.18±0.02	1.03±0.03	19±2	Color	12
J08230313−4912012	L1.5	OPT	13.55±0.03	1.48±0.04	16±2	WISE	48

Table 5.1 Continued

Designation	Adopted SpT	SpT Flag	J (mag)	$J-K$	Distance (pc)	Distance Type	Ref.
J08283419−1309198	L2.0	OPT	12.8±0.03	1.51±0.04	11.37±0.1	Trig	53
J08294949+2646348	M6.5	OPT	8.24±0.02	0.98±0.03	3.63±0.04	Trig	54
J08303256+0947153	M8.0	OPT	11.89±0.02	1.13±0.03	16.72±1.26	Trig	12
J08352366+1029318	M9.0	OPT	13.14±0.02	1.09±0.03	23±2	Color	27
J08354256−0819237	L6.5	OPT	13.17±0.02	2.03±0.03	8.53±0.81	Trig	2
J08355829+05483080	L3.0	OPT	14.53±0.04	1.36±0.05	23±3	NIR	23
J08402975+1824091	M6.0	OPT	11.05±0.02	1.01±0.03	14.03±0.22	Trig	55
J08472872−1532372	L2.0	OPT	13.51±0.03	1.45±0.04	13.07±0.6	Trig	2
J08500174−1924184	M8.0	OPT	12.76±0.02	1.13±0.03	23±3	NIR	12
J08513558+7727182	M8.0	OPT	12.93±0.03	1.1±0.04	25±3	NIR	12
J08522464+2540591	M6.0	OPT	12.19±0.02	1.0±0.03	26±2	Color	12
J08533619−0329321	M9.0	OPT	11.21±0.03	1.27±0.04	8.48±0.05	Trig	28
J08581519+1945470A	M7.0	OPT	7.79±0.02	0.9±0.03	5.66±0.09	Trig	12
J08581519+1945470B	M7.0	NIR	···	···	5.26±0.08	Trig	12
J08593854+6341355	L0.0	OPT	13.7±0.03	1.31±0.04	23±3	Color	23
J08594029+1145325	M8.0	OPT	12.74±0.02	1.25±0.03	15±2	Color	12
J09002359+2150054	M6.0	OPT	9.44±0.02	1.0±0.03	6.37±0.11	Trig	56
J09020690+0033195	M7.0	OPT	12.11±0.02	0.94±0.03	19.96±1.51	Trig	57
J09054654+5623117	L5.0	OPT	15.4±0.05	1.66±0.06	23±3	NIR	12
J09083803+5032088	L5.0	OPT	14.55±0.02	1.6±0.04	11±2	Color	12
J09095749−0658186	L0.0	OPT	13.89±0.02	1.35±0.04	23.53±2.33	Trig	2
J09111297+7401081	L0.0	OPT	12.92±0.03	1.17±0.04	19±2	NIR	12
J09113059+2248111	M7.0	OPT	11.74±0.02	0.98±0.03	17±2	NIR	12
J09161504+2139512	M9.0	OPT	13.22±0.02	1.15±0.04	17±2	Color	58
J09211410−2104446	L1.0	OPT	12.78±0.02	1.09±0.03	15±2	NIR	23
J09230296−2300415	M8.2	SPEX	10.9±0.02	0.55±0.03	10±1	NIR	12
J09282562+4230545	M8.5	OPT	13.08±0.02	1.14±0.03	20±2	Color	12
J09424604+5531025	M8.0	OPT	12.92±0.02	1.12±0.03	17±2	Color	12
J09473829+3710178	M7.0	OPT	12.19±0.02	0.85±0.03	22±3	NIR	12
J09492223+0806450	M8.5	OPT	12.3±0.02	1.1±0.04	16.58±0.46	Trig	23
J09524622+0620410	M8.0	OPT	12.45±0.02	1.0±0.03	20±2	Color	58
J09532126−1014205	L0.0	OPT	13.47±0.03	1.33±0.04	23±3	NIR	29

Table 5.1 Continued

Designation	Adopted SpT	SpT Flag	J (mag)	$J-K$	Distance (pc)	Distance Type	Ref.
J10031918−0105079	M7.0	OPT	12.33±0.02	1.09±0.03	17±2	Color	57
J10042066+5022596	L2.0	SIMBAD	14.83±0.05	2.05±0.06	16±2	WISE	59
J10043929−33351889	L4.0	OPT	14.48±0.04	1.56±0.04	18.25±1.86	Trig	60
J10063197−1653266	M7.5	OPT	12.04±0.02	1.04±0.03	18±2	NIR	2
J10163470+2751497	M8.0	OPT	11.99±0.02	1.03±0.03	17.24±0.86	Trig	61
J10170754+1308398	L2.0	OPT	14.1±0.02	1.39±0.03	23±3	NIR	2
J101726800+07192609	M8.0	NIR	12.5±0.03	1.02±0.04	23±2	Color	7
J10192447−2707171	L0.5	OPT	13.53±0.03	1.06±0.04	24±3	NIR	18
J10195684+7324087	M8.5	OPT	12.92±0.02	1.1±0.03	23±3	NIR	27
J10213232−2044069	M9.0	OPT	13.19±0.02	1.12±0.04	24±3	NIR	23
J10224821+5825453	L1.0	SIMBAD	13.5±0.03	1.34±0.04	20±2	NIR	23
J10240997+1815533	M8.0	OPT	12.28±0.02	1.04±0.03	21±2	Color	23
J10292165+1626526	L2.5	OPT	14.29±0.03	1.67±0.03	19±2	WISE	21
J10451718−2607249	M8.0	OPT	12.79±0.02	1.16±0.03	23±3	NIR	23
J10452400−0149576	L1.0	OPT	13.16±0.02	1.38±0.03	17±2	NIR	60
J10471381+4026493A	M8.0	NIR	11.7±0.02	0.44±0.03	14±2	Color	14
J10471381+4026493B	L0.0	NIR	13.0±0.21	0.69±0.26	14±2	Color	12
J10473108−18155739	L2.5	OPT	14.2±0.03	1.31±0.04	22±3	NIR	62
J10481258−1120082	M7.0	OPT	8.86±0.02	0.93±0.04	4.52±0.07	Trig	63
J10481463−3956062	M9.0	OPT	9.54±0.02	1.09±0.03	4.03±0.01	Trig	23
J10482788−5254180	L1.5	OPT	14.02±0.03	1.35±0.04	24±3	NIR	48
J10484281+0111580	L1.0	OPT	12.92±0.02	1.3±0.03	16±2	Color	41
J10511900+5613086	L2.0	OPT	13.24±0.03	1.34±0.04	15±2	NIR	23
J10541102−8505023	M8.0	SIMBAD	12.7±0.02	1.04±0.03	22±3	NIR	60
J10544168+1214084	M7.5	OPT	12.46±0.02	1.01±0.03	22±2	Color	39
J10554733+0808427	M9.0	OPT	12.55±0.03	1.18±0.04	14±2	Color	57
J10584787−1548172	L3.0	OPT	14.12±0.05	1.57±0.07	15.04±0.99	Trig	64
J11040127+1959217	L4.0	OPT	14.38±0.03	1.43±0.04	18±2	NIR	2
J11061897+0428327	M7.0	OPT	12.33±0.02	1.0±0.03	20.79±1.34	Trig	8
J11073750−2759385	M7.0	NIR	12.34±0.03	1.03±0.04	22±3	NIR	65
J11083081+6830169	L1.0	OPT	13.12±0.02	1.54±0.03	14±2	WISE	66
J11122567+3548131	L4.5	OPT	14.58±0.03	1.86±0.04	21.72±0.42	Trig	21

Table 5.1 Continued

Designation	Adopted SpT	SpT Flag	J (mag)	$J-K$	Distance (pc)	Distance Type	Ref.
J11214924−1313084	M8.0	OPT	12.11±0.02	1.28±0.03	15.19±0.47	Trig	15
J11232934+0154040	M7.0	OPT	12.36±0.03	1.01±0.04	20±2	Color	67
J11240487+3808054	M8.5	OPT	12.71±0.02	1.14±0.03	21±2	NIR	2
J11263991−5003550	L5.0	OPT	14.0±0.03	1.17±0.04	16.84±0.47	Trig	58
J11345493+0022541	M9.0	OPT	12.85±0.02	1.18±0.03	18±2	Color	23
J113911077+0841121	M8.0	NIR	12.92±0.03	1.09±0.04	19±2	Color	23
J11414406−2232156	M7.5	OPT	12.63±0.02	1.06±0.03	23±3	NIR	68
J11524266+2438079	M9.0	OPT	13.03±0.02	1.25±0.03	18±2	Color	12
J11535267+0659561	M8.0	OPT	11.26±0.02	0.99±0.03	14.22±0.55	Trig	8
J11543399+0135545	M9.0	OPT	13.16±0.03	1.17±0.04	24±3	NIR	23
J11553952−3727350	L2.0	OPT	12.81±0.02	1.35±0.03	9.58±0.43	Trig	60
J11554286−2224586	M7.5	OPT	10.93±0.02	1.05±0.03	11.17±0.22	Trig	70
J11555389+0559577	L6.0	OPT	15.66±0.08	1.54±0.11	17.27±3.04	Trig	69
J11592743−5247188	M9.0	OPT	11.43±0.03	1.11±0.03	9.48±0.01	Trig	33
J120032924+2048513	···	···	12.86±0.02	1.0±0.03	24±2	Color	71
J12035812+0015500	L3.0	OPT	14.01±0.03	1.53±0.04	18±2	NIR	72
J12130336−0432437	L5.0	OPT	14.68±0.04	1.67±0.05	17±2	NIR	2
J12210359+0857217	M7.0	NIR	12.24±0.02	1.02±0.03	24±2	Color	8
J12212770+0257198	L0.5	OPT	13.17±0.02	1.22±0.04	18±2	Color	23
J12245222−1238352	M9.0	OPT	12.57±0.02	1.22±0.04	17.06±1.11	Trig	73
J12281523−1547342	L5.0	OPT	14.38±0.03	1.61±0.04	20.24±0.78	Trig	74
J12321772−6856005	M8.0	OPT	12.42±0.02	1.1±0.03	19±2	NIR	48
J12392727+5515371	L5.0	OPT	14.71±0.03	1.92±0.04	15±2	WISE	21
J12405273+1129387	L1.0	OPT	11.83±0.03	0.84±0.04	10±1	NIR	75
J12464678+4027150	L4.0	OPT	15.09±0.05	1.81±0.06	21±3	WISE	21
J12465176+3148104	M7.0	OPT	12.23±0.02	1.02±0.03	21±3	NIR	27
J12505265−2121136	M6.5	OPT	11.16±0.02	1.03±0.03	17.31±0.52	Trig	76
J12522264+0252058	M8.0	OPT	12.5±0.02	0.99±0.04	20±2	Color	57
J12531092−5709248	L0.5	OPT	13.45±0.02	1.4±0.03	21±2	NIR	48
J12531240+4034038	M7.5	OPT	12.18±0.02	1.02±0.03	21±2	Color	77
J12560215−1257217	M7.5	OPT	11.02±0.02	0.97±0.03	11±1	NIR	78
J12565688+0146163	L2.0	OPT	14.48±0.03	1.69±0.04	23±3	WISE	76

Table 5.1 Continued

Designation	Adopted SpT	SpT Flag	J (mag)	$J-K$	Distance (pc)	Distance Type	Ref.
J12590470−4336243	M8.0	SIMBAD	10.53±0.02	1.01±0.03	···	Trig	79
J13004255+1912354	L1.0	OPT	12.72±0.02	1.09±0.03	12±1	Color	49
J13054019−2541059A	L2.0	OPT	13.83±0.08	2.41±0.17	18.66±0.7	Trig	12
J13054019−2541059B	L3.5	OPT	14.65±0.12	1.93±0.12	12±1	WISE	16
J13054106+2046394	L4.0	OPT	15.2±0.05	1.83±0.07	21±3	WISE	2
J13082507+0725512	M9.0	OPT	13.18±0.03	1.18±0.04	19±2	Color	23
J13092185−2330350	M8.0	OPT	11.78±0.02	1.12±0.03	14.42±0.28	Trig	48
J13113921+8032219	M8.0	OPT	12.76±0.02	1.08±0.03	23±3	NIR	39
J13142039+1320012	M7.0	OPT	9.75±0.02	0.96±0.03	16.39±0.75	Trig	7
J13153094−2649513	L5.5	OPT	15.2±0.05	1.73±0.07	19±2	NIR	20
J13171150+1849232	M9.0	OPT	12.42±0.02	1.1±0.03	17±2	NIR	71
J13261625+5640448	M7.0	OPT	11.82±0.02	0.95±0.03	18±2	Color	57
J13314894−0116500	L6.0	OPT	15.46±0.04	1.39±0.08	14.86±2.78	Trig	41
J13322442−0441126	M7.5	OPT	12.37±0.03	1.09±0.03	21±2	NIR	12
J13365044+4751321	M8.0	OPT	12.66±0.02	0.99±0.03	22±2	Color	71
J13382615+4140342	L2.5	OPT	14.22±0.02	1.45±0.04	22±3	NIR	21
J13564148+4342587	M7.0	OPT	11.71±0.02	1.06±0.03	15±2	Color	80
J13595510−4034582	L1.0	OPT	13.64±0.03	1.08±0.04	15.58±1.33	Trig	23
J14032232+3007547	M9.0	OPT	12.68±0.02	1.08±0.03	18±2	Color	71
J14112131−2119503	M9.0	OPT	12.44±0.02	1.11±0.03	17±2	NIR	2
J14122449+1633115	L0.5	OPT	13.89±0.03	1.37±0.04	25±3	Color	21
J14162408+1348263	L5.0	OPT	13.15±0.02	1.03±0.03	9.1±0.15	Trig	58
J14211873−1618201	M7.5	OPT	12.76±0.02	1.08±0.04	24±3	NIR	39
J14213145+1827407	L0.0	OPT	13.23±0.02	1.29±0.03	19±2	Color	49
J14222424+2116076	M8.0	OPT	12.44±0.03	0.99±0.03	18±2	Color	71
J14252798−3650229	L3.0	OPT	13.75±0.03	1.94±0.04	11.57±0.11	Trig	81
J1426316+155701	M9.0	OPT	12.91±0.02	1.18±0.03	19±2	Color	2
J14280420+1356137	M7.5	OPT	11.01±0.02	0.98±0.03	12.08±0.6	Trig	5
J14283132+5923354	L4.0	OPT	14.78±0.04	1.52±0.05	22±3	NIR	23
J14284323+3310391	M9.0	OPT	11.99±0.02	1.25±0.03	11.01±0.16	Trig	82
J14304358+2915405A	L2.0	OPT	14.27±0.03	1.5±0.04	24±3	NIR	17
J14304358+2915405B	L2.0	OPT	···	···	37±6	Color	2

Table 5.1 Continued

Designation	Adopted SpT	SpT Flag	J (mag)	$J-K$	Distance (pc)	Distance Type	Ref.
J14343616+2202463	L5.5	SDSS	14.52±0.04	0.97±0.06	16±2	NIR	83
J14380829+6408363	L0.0	OPT	12.98±0.02	1.34±0.03	17±2	Color	57
J14392836+1929149	L1.0	OPT	12.76±0.02	1.21±0.03	14.37±0.1	Trig	74
J14402293+1339230	M8.0	OPT	12.4±0.02	1.06±0.03	22.22±0.55	Trig	29
J14422164+6603208	L0.0	OPT	11.44±0.03	1.14±0.08	10.97±0.04	Trig	84
J14442067−2019222	M9.0	OPT	12.55±0.03	0.61±0.04	16.34±1.36	Trig	85
J144506278+4409393	M8.0	NIR	12.45±0.02	1.02±0.03	23±2	Color	86
J14460061+0024519	L6.0	OPT	15.89±0.08	1.96±0.1	21.41±6.69	Trig	41
J14480337+1554149	M7.0	OPT	12.48±0.02	1.01±0.03	26±3	Color	87
J14482563+1031590	L4.0	OPT	14.56±0.03	1.87±0.05	15±2	WISE	12
J14501581+2354424	L4.0	OPT	13.8±0.5	1.54±0.71	18.17±0.11	Trig	88
J14540797−6604476	L3.5	OPT	13.06±0.02	1.34±0.04	11.78±0.24	Trig	48
J14562776+1755090	M7.0	OPT	11.98±0.02	1.06±0.03	17±2	Color	2
J14563831−2809473	M7.0	OPT	9.96±0.03	1.04±0.04	6.88±0.15	Trig	63
J145638314−28094738	M7.0	OPT	9.97±0.03	1.04±0.04	6.88±0.15	Trig	8
J14573965+4517167	M9.0	OPT	13.12±0.02	1.19±0.03	19±2	Color	29
J14582453+2839580	M8.5	OPT	13.08±0.02	1.23±0.03	19±2	Color	89
J15002635−0039281	M7.0	OPT	11.59±0.03	0.95±0.04	20±2	Color	71
J15010818+2250020	M8.5	OPT	11.87±0.02	1.16±0.03	10.59±0.07	Trig	89
J15041621−2355564	M7.5	OPT	12.01±0.03	0.98±0.04	18±2	NIR	48
J15065441+1321060	L3.0	OPT	13.36±0.02	1.62±0.03	13±2	NIR	49
J15072779−2000431	M7.5	OPT	11.71±0.02	1.05±0.03	15±2	NIR	80
J15074769−1627386	L5.0	OPT	12.83±0.03	1.52±0.04	7.33±0.03	Trig	86
J15101685−0241078	M9.0	OPT	12.61±0.02	1.27±0.03	16.34±1.25	Trig	89
J15104786−2818174	M9.0	OPT	12.84±0.03	1.15±0.04	20±2	NIR	12
J15150083+4847416	L6.0	OPT	14.11±0.03	1.61±0.04	11±1	NIR	69
J15200224−4422419B	L4.5	SIMBAD	14.7±0.07	1.48±0.08	19±2	NIR	18
J15210103+5053230	M7.5	OPT	12.01±0.02	1.09±0.03	13±1	Color	80
J15230657−2347526	L2.5	SIMBAD	14.2±0.03	1.3±0.05	21±3	WISE	18
J15242475+2925318	M7.5	OPT	11.21±0.02	1.05±0.03	12±1	NIR	89
J15261405+2043414	L7.0	OPT	15.59±0.06	1.66±0.08	20.62±3.7	Trig	21
J15291017+6312539	M8.0	NIR	11.64±0.02	1.09±0.03	14±2	NIR	66

Table 5.1 Continued

Designation	Adopted SpT	SpT Flag	J (mag)	$J-K$	Distance (pc)	Distance Type	Ref.
J15345325+1219495	L6.0	OPT	15.33±0.05	1.5±0.06	20±2	NIR	27
J15345704−1418486	M7.0	OPT	11.38±0.02	1.08±0.03	14±2	NIR	80
J153824172−19531162	L6.0	SIMBAD	15.93±0.06	1.93±0.08	22±3	WISE	9
J15394189−0520428	L4.0	OPT	13.92±0.03	1.35±0.04	15.5±0.82	Trig	81
J15394442+7437273	M9.0	OPT	12.93±0.02	1.2±0.03	21±2	NIR	23
J15404341−5101357	M7.0	OPT	8.96±0.02	1.02±0.05	4.39±0.46	Trig	90
J15445518+3301447	L6.0	OPT	15.55±0.06	1.6±0.07	22±3	NIR	91
J15460540+3749458	M7.5	OPT	12.44±0.02	1.03±0.03	21±2	Color	29
J15464185−5534468	M7.5	OPT	10.21±0.02	1.1±0.03	6.71±1.8	Trig	92
J15485834−1636018	L2.0	OPT	13.89±0.03	1.26±0.04	21±2	NIR	80
J15510662+6457047	M8.0	OPT	12.89±0.02	1.17±0.03	24±3	NIR	29
J15525906+2948485	L1.0	SIMBAD	13.48±0.03	1.46±0.04	17±2	Color	17
J15531993+1400337	M9.0	OPT	13.05±0.02	1.23±0.03	17±2	Color	29
J15551573−0956055	L1.0	OPT	12.56±0.02	1.11±0.03	13.42±0.22	Trig	60
J16073123−0442091	M8.0	OPT	11.9±0.02	1.18±0.03	15.65±0.36	Trig	93
J16081603−3903042	M7.5	SIMBAD	12.52±0.02	1.26±0.03	21±2	NIR	94
J16095217−2136277	M7.0	OPT	12.57±0.03	1.0±0.04	25±3	NIR	95
J16134550+1708270	M9.5	OPT	13.47±0.02	1.28±0.03	23±3	Color	67
J16141484−2427081	M7.0	OPT	12.47±0.03	0.99±0.04	24±3	NIR	96
J16154245+0546400	M9.0	OPT	12.88±0.02	1.14±0.03	16±2	Color	23
J16154416+3559005	L4.0	OPT	14.54±0.03	1.6±0.04	19±2	NIR	21
J16271142−2348505	M8.8	SPEX	13.32±0.03	1.36±0.04	25±3	NIR	65
J16272794+8105075	M9.0	OPT	13.03±0.02	1.15±0.03	18±2	Color	29
J16325882−0631481	M7.0	OPT	12.74±0.02	1.12±0.03	18.76±0.52	Trig	23
J16331306−7553232	M9.5	OPT	13.15±0.02	1.03±0.03	23±3	NIR	98
J16334908−6808480	M8.0	NIR	11.19±0.06	1.12±0.08	8±1	WISE	97
J16351919+4223053	M9.0	OPT	12.88±0.02	1.09±0.03	17±2	Color	57
J16452211−1319516	L1.5	OPT	12.45±0.03	1.31±0.04	9.1±0.51	Trig	60
J16553529−0823401	M7.0	OPT	9.78±0.03	0.96±0.04	6.47±0.03	Trig	99
J16573454+1054233	L2.0	OPT	14.15±0.04	1.35±0.05	23±3	NIR	23
J16580380+7027015	L1.0	OPT	13.29±0.02	1.37±0.03	18.55±0.24	Trig	49
J17054834−0516462	L0.5	OPT	13.31±0.03	1.28±0.04	22.47±6.06	Trig	81

Table 5.1 Continued

Designation	Adopted SpT	SpT Flag	J (mag)	$J-K$	Distance (pc)	Distance Type	Ref.
J17065487−1314396	L5.0	SIMBAD	14.52±0.04	1.42±0.05	16±2	NIR	66
J17071830+6439331	M9.0	OPT	12.54±0.02	1.16±0.03	16±2	Color	12
J17072343−0558249A	M9.0	SIMBAD	12.26±0.11	1.23±0.14	12±1	WISE	19
J17072343−0558249B	L3.0	SIMBAD	13.96±0.11	1.76±0.14	16±2	NIR	19
J17114559+4028578	L5.0	SIMBAD	15.0±0.06	1.2±0.08	13.55±0.94	Trig	100
J17125121−0507249	M9.5	SPEX	13.05±0.04	0.82±0.05	19.96±1.44	Trig	101
J17163523−0315431	L0.0	OPT	11.05±0.02	1.84±0.03	6±1	NIR	98
J17171408+6526221	L4.0	OPT	14.95±0.04	1.77±0.05	21±3	WISE	41
J17210390+3344160	L3.0	OPT	13.62±0.02	1.14±0.03	16±2	NIR	102
J17264070−2737593	L5.0	OPT	13.4±0.03	1.18±0.04	10±1	NIR	103
J17312974+2721233	L0.0	OPT	12.09±0.03	1.18±0.03	8.79±0.54	Trig	23
J17331893+4633593	M9.5	OPT	13.24±0.02	1.35±0.03	22±3	NIR	29
J17334227−1654500	L0.5	OPT	13.53±0.05	1.18±0.06	18±2	WISE	48
J17335314+1655129	M7.0	OPT	8.9±0.03	0.9±0.04	5±1	NIR	104
J17343053−1151388	M8.5	OPT	13.11±0.03	1.23±0.04	24±3	NIR	11
J17351296+2634475	M7.5	OPT	11.25±0.03	1.1±0.03	9±1	Color	23
J17395322+5532451	M7.5	NIR	12.16±0.02	1.03±0.03	20±2	Color	105
J17410280−4642218	L7.0	SIMBAD	15.79±0.08	2.35±0.08	13±2	WISE	58
J17430860+8526594	L5.0	SIMBAD	14.56±0.04	1.09±0.06	18±2	NIR	10
J17453466−1640538	L1.5	OPT	13.65±0.03	1.24±0.04	20±2	NIR	48
J17461199+5034036	L5.0	OPT	15.1±0.06	1.57±0.07	21±2	NIR	23
J17502484−0016151	L4.5	OPT	13.29±0.02	1.44±0.03	9.22±0.22	Trig	58
J17534518−6559559	L4.0	OPT	14.1±0.03	1.67±0.04	17.24±1.46	Trig	23
J17562963−4518224	M9.0	OPT	12.39±0.02	1.13±0.03	17±2	NIR	48
J17565620−4805096	L0.0	OPT	13.41±0.02	1.22±0.03	23±3	NIR	48
J17571539+7042011	M7.5	OPT	11.45±0.02	1.06±0.03	19.08±0.4	Trig	49
J18000116−1559235	L5.5	OPT	13.43±0.02	1.45±0.04	9±1	NIR	106
J18071593+5015316	L1.5	OPT	12.93±0.02	1.33±0.04	14±2	NIR	2
J18212815+1414010	L4.5	OPT	13.43±0.02	1.78±0.03	9.39±0.02	Trig	68
J18261131+3014201	M8.5	OPT	11.66±0.02	0.85±0.03	14±2	NIR	107
J18300760−1842361	M7.5	OPT	10.43±0.03	1.61±0.03	6±1	WISE	106
J18353790+3259545	M8.5	OPT	10.27±0.02	1.1±0.03	5.67±0.02	Trig	108

Table 5.1 Continued

Designation	Adopted SpT	SpT Flag	J (mag)	$J-K$	Distance (pc)	Distance Type	Ref.
J18393308+2952164	M6.5	OPT	11.01±0.02	1.01±0.03	12.61±0.32	Trig	75
J18432213+4040209	M8.0	OPT	11.31±0.02	1.0±0.03	14.14±0.16	Trig	2
J18450541−6357475	M8.5	OPT	9.54±0.02	1.04±0.03	3.85±0.02	Trig	79
J18451889+3853248	M8.0	OPT	12.21±0.02	1.17±0.03	17±2	NIR	68
J18470342+5522433	M6.5	OPT	11.92±0.02	1.02±0.03	20±2	NIR	2
J19064801+4011089	L1.0	OPT	13.08±0.02	1.31±0.03	16±2	Color	109
J19165762+0509021	M8.0	OPT	9.91±0.02	1.14±0.03	5.88±0.03	Trig	110
J19285196−4356256	L4.0	OPT	15.2±0.04	1.74±0.06	25±3	NIR	23
J19360187−5502322	L5.0	OPT	14.49±0.04	1.44±0.05	15.08±1.23	Trig	23
J19453551−2557215	M9.0	NIR	12.35±0.02	0.84±0.04	17±2	NIR	44
J20004841−7523070	M9.0	OPT	12.73±0.03	1.22±0.04	19±2	NIR	80
J20025073−0521524	L6.0	OPT	15.32±0.05	1.9±0.06	17±2	WISE	29
J20040620+1704125	L4.5	NIR	···	···	17.24±0.27	Trig	111
J201035392+06343676	M8.5	SIMBAD	12.53±0.02	1.1±0.03	19±2	NIR	10
J20140359−2016217	M7.5	OPT	12.54±0.02	1.09±0.04	22±3	NIR	2
J20282035+0052265	L3.0	OPT	14.3±0.04	1.5±0.05	20±2	NIR	41
J20360316+1051295	L2.0	OPT	13.95±0.03	1.5±0.04	19±2	WISE	76
J20370715−1137569	M8.0	OPT	12.27±0.03	1.01±0.03	18±2	NIR	80
J20575409−0252302	L1.5	OPT	13.12±0.02	1.4±0.04	14.27±0.75	Trig	2
J21041491−1037369	L2.0	OPT	13.84±0.03	1.47±0.04	18.87±0.61	Trig	2
J21183174−4505522	M8.5	OPT	13.42±0.02	1.06±0.04	21.41±3.62	Trig	33
J213630294+05153290	M8.5	OPT	13.35±0.03	1.1±0.04	24±3	Color	23
J21371044+1450475	L2.0	OPT	14.13±0.03	1.32±0.04	23±3	NIR	23
J21373742+0808463	L5.0	OPT	14.77±0.03	1.76±0.04	17±2	NIR	23
J21402931+1625183	M8.5	OPT	12.94±0.03	1.11±0.04	21±2	Color	49
J21580457−1550098	L4.0	OPT	15.04±0.04	1.86±0.05	21±3	WISE	20
J22000201−3038327	L0.0	OPT	13.44±0.03	1.24±0.04	23±3	NIR	81
J22021125−1109461	M6.5	OPT	12.36±0.02	0.99±0.04	24±3	WISE	75
J22062280−2047058	M8.0	OPT	12.37±0.02	1.06±0.04	19±2	NIR	112
J22244381−0158521	L4.5	OPT	14.07±0.03	2.05±0.04	11.35±0.14	Trig	21
J22264440−7503425	M8.0	OPT	12.35±0.02	1.11±0.03	19±2	NIR	23
J22285440−1325178	M6.5	OPT	10.77±0.02	0.92±0.03	11.11±0.6	Trig	8

Table 5.1 Continued

Designation	Adopted SpT	SpT Flag	J (mag)	$J-K$	Distance (pc)	Distance Type	Ref.
J22341394+2359559	M9.5	OPT	13.14±0.02	1.31±0.03	18±2	Color	2
J22354905+1840298	M7.0	OPT	12.39±0.02	1.03±0.03	21±2	Color	29
J22373255+3922398	M9.5	OPT	13.34±0.02	1.16±0.03	20±3	WISE	113
J22380742+4353179	L1.5	OPT	13.84±0.03	1.32±0.04	22±3	NIR	87
J22425317+2542573	L3.0	OPT	14.81±0.04	1.76±0.05	22±3	WISE	25
J22490917+3205489	L5.0	OPT	15.48±0.06	1.89±0.08	23±3	NIR	29
J23062928−0502285	M8.0	OPT	11.35±0.02	1.06±0.03	12.11±0.38	Trig	49
J23065876−5008589	M9.0	OPT	13.39±0.02	1.15±0.04	21.46±0.72	Trig	76
J23072655+8753294	L3.0	OPT	14.69±0.04	1.52±0.06	23±3	WISE	23
J23081874+0629514	L0.5	PHOT	13.49±0.0	1.14±0.0	18±3	Color	114
J23081888+0629551	M8.0	NIR	10.62±0.02	0.86±0.03	9±1	NIR	115
J23174712−4838501	L5.0	SIMBAD	15.15±0.04	1.97±0.05	17±2	WISE	58
J23224684−3133231	L0.0	OPT	13.58±0.03	1.25±0.04	17.06±1.63	Trig	57
J23272645−1741329	M7.0	SIMBAD	11.75±0.02	0.92±0.03	17±2	NIR	82
J23294790−1607551	M9.5	OPT	13.37±0.03	1.06±0.04	25±3	NIR	11
J23312174−2749500	M7.5	OPT	11.65±0.02	1.0±0.04	14.46±0.43	Trig	112
J23343945+1933041	M8.0	OPT	12.78±0.02	1.16±0.03	21±2	Color	29
J23371491−0838084	M7.0	OPT	12.19±0.03	1.0±0.04	16±2	Color	2
J23440624−0733282	L4.5	OPT	14.8±0.04	1.57±0.05	20±2	NIR	20
J23464599+1129094	M9.0	OPT	12.8±0.02	1.19±0.03	17±2	Color	23
J23473680+2702068	M9.0	OPT	13.19±0.02	1.21±0.03	24±3	NIR	116
J23494899+1224386	M8.0	OPT	12.6±0.02	1.04±0.03	18±2	Color	29
J235122005+30105400	L5.5	OPT	15.85±0.1	1.83±0.12	25±3	NIR	11
J23515044−2537367	M8.0	OPT	12.47±0.03	1.2±0.04	19±2	NIR	29
J23520481−2208032	M9.5	NIR	12.71±0.02	0.75±0.03	20±2	NIR	117
J23535946−0833311	M8.5	OPT	13.03±0.03	1.1±0.04	19±2	Color	118
J23540928−3316266	M9.0	OPT	13.05±0.02	1.17±0.03	22.53±1.06	Trig	93
J23561081−3426044	M9.0	OPT	12.95±0.02	0.98±0.03	19.09±0.62	Trig	33

References. — (1) Luyten (1979); (2) Cruz et al. (2003); (3) Reid et al. (2004); (4) Lépine et al. (2002b); (5) Reid et al. (2003); (6) Kirkpatrick et al. (2014); (7) Lépine & Shara (2005); (8) Bessell (1991); (9) Reid et al. (2008a); (10) Luhman et al. (2012); (11) Kirkpatrick et al. (2010); (12) Cutri et al. (2003); (13) Leggett et al. (2002); (14) Close et al. (2003); (15) Koerner et al. (1999); (16) Liu & Leggett (2005); (17) Wilson et al. (2003); (18) Kendall et al. (2007); (19) McElwain & Burgasser (2006); (20) Kirkpatrick et al. (2008); (21) Kirkpatrick et al. (2000); (22) Irwin et al. (1991); (23) Reid et al. (2008b); (24) Deacon et al. (2005); (25) Gizis et al. (2003); (26) Reid et al. (2000); (27) SCH-NP; (28) Crifo et al. (2005); (29) Cruz et al. (2007); (30) Liebert et al. (2003); (31) Gizis et al. (2001); (32) Basri et al. (2000); (33) Lodieu et al. (2005); (34) Phan-Bao et al. (2006); (35) Luhman et al. (2016); (36) Kirkpatrick et al. (1997); (37) Castro et al. (2013); (38) CRUZ-NP; (39) Faherty et al. (2009); (40) Kendall et al. (2003); (41) Hawley et al. (2002); (42) Kirkpatrick et al. (2016); (43) Zacharias et al. (2012); (44) Pokorny et al. (2004); (45) Deacon et al. (2014); (46) Kang et al. (2015); (47) Salim et al. (2003); (48) Phan-Bao et al. (2008); (49) Gizis et al. (2000b); (50) Reylé et al. (2006); (51) Scholz (2014); (52) Schneider et al. (2017); (53) Scholz & Meusinger (2002); (54) Liebert (1976); (55) Haro & Chavira (1966); (56) Shkolnik et al. (2009); (57) West et al. (2008); (58) Schneider et al. (2014); (59) Rebolo et al. (1998); (60) Gizis (2002); (61) Kirkpatrick et al. (1995); (62) Martín et al. (1999); (63) Davison et al. (2015); (64) Delfosse et al. (1997); (65) LOOPER-NP; (66) Gagné et al. (2015c); (67) Schmidt et al. (2014); (68) Looper et al. (2008b); (69) Schmidt et al. (2010); (70) Phan-Bao et al. (2003); (71) West et al. (2011); (72) Fan et al. (2000); (73) Tinney et al. (1993); (74) Kirkpatrick et al. (1999b); (75) Marocco et al. (2015); (76) Jenkins et al. (2009); (77) Kirkpatrick et al. (1993); (78) Gauza et al. (2015); (79) Burgasser et al. (2015b); (80) Schmidt et al. (2007); (81) Kendall et al. (2004); (82) Reid & Gizis (2005); (83) Sheppard & Cushing (2009b); (84) Faherty et al. (2012); (85) Scholz et al. (2004b); (86) Reid et al. (2007); (87) Dahn et al. (2002); (88) Goto et al. (2002); (89) Kirkpatrick et al. (2011); (90) Pérez Garrido et al. (2014); (91) Zhang et al. (2009); (92) Rajpurohit et al. (2013); (93) Gizis et al. (2002); (94) Comerón et al. (2003); (95) Lodieu et al. (2007); (96) Slesnick et al. (2008); (97) Luhman & Sheppard (2014); (98) Martín et al. (2010); (99) Alonso-Floriano et al. (2015); (100) Radigan et al. (2008); (101) MEL-NP; (102) Costa et al. (2005); (103) Beamín et al. (2013); (104) Newton et al. (2014); (105) GIZ-NP; (106) Folkes et al. (2012); (107) Lépine et al. (2002a); (108) Lépine et al. (2003); (109) Gizis et al. (2011); (110) Herbig (1956); (111) Gray et al. (2006); (112) Deshpande et al. (2012); (113) Kirkpatrick et al. (2001); (114) Skrzypek et al. (2015); (115) SpeX Prism Library; (116) Allen et al. (2007); (117) Pokorny et al. (2003); (118) Phan-Bao & Bessell (2006)

5.2.2 Surveys overview

The sources in this compilation are drawn from several surveys and databases, each one compiled for its own scientific purposes. Jonathan Gagne's "List of All Ultracool Dwarfs"[2] includes 10,728 dwarfs with spectral types between M6−Y2 and a few planetary-mass objects drawn from the Dwarf Archives[3] and more recent publications. These sources were complemented with other late-M, L and T dwarfs from Skrzypek et al. (2015) providing 1157 L0−T8 *photo-typed* dwarfs from UKIDSS, Schmidt et al. (2015) adding 484 L0−L8 dwarfs from SDSS, Marocco et al. (2015) supplying 195 M8−T6 dwarfs from UKIDSS, Winters et al. (2015) photometrically-selected 137 ∼M0−L1 from RECONS, Dieterich et al. (2014) with 64 M6−L4 dwarfs, 38 M6−M9 within 30 pc from West et al. (2011), 11 M6−M7 from Gaidos et al. (2014), 732 M3-L9 dwarfs from the SPECULOOS target list (Gillon et al. 2013) and 1484 M7-L5 dwarfs from the PanSTARRS release of Best et al. (2017) amounting to $> 15,000$ entries. This initial compilation was trimmed down to the final 443 by spectral type, distance, duplicate and non-stellar object cuts (see Section 5.2.4).

5.2.3 SpeX Prism Library

Additionally, a number of M7−L5 dwarfs with SpeX spectra were already in the SpeX Prism Library (SPL; Burgasser 2014), a repository of more than 2000 low-resolution ($\Delta\lambda/\lambda \sim 75 - 120$), near-infrared spectra of M, L and T dwarfs. The spectra in the library has been continuously collected over the last 12 years, and it includes 2932 spectra of 951 M dwarfs, 897 L dwarfs, and 230 T dwarfs, among other sources, including a few white dwarfs, FGK stars, giants and galaxies.

[2] Available at: https://jgagneastro.wordpress.com/list-of-ultracool-dwarfs/
[3] http://spider.ipac.caltech.edu/staff/davy/ARCHIVE/index.shtml

5.2.4 Database clean-up

Building a complete sample of M7−L5 dwarfs from a handful of surveys entails careful consolidation of data stemming from a variety of instruments with different calibrations. After stitching together all the surveys, the sample contained $\sim 15,000$ entries. In order to collect as much information as possible on these sources, we also downloaded photometry, proper motions, and parallaxes from the 2MASS, SDSS DR9, AllWISE, ULAS, GAIA and PPMXL catalogs through the Vizier interface, using the `Astroquery` Python package[4] for all coordinate pairs and selecting the closest match up to $15''$. We downloaded coordinates, epochs, identifiers, *rizJHKW*1*W*2 magnitudes and uncertainties from SDSS, 2MASS, WISE; *YJHK* magnitudes and uncertainties from UKIDSS and proper motions from PPMXL, including the corresponding 2MASS *JHK* magnitudes provided as products from catalog crossmatching. Spectral types from SDSS were obtained when available. In addition to these surveys, we also downloaded *rizJHK* magnitudes and uncertainties, spectral type, object type, parallaxes, proper motions and radial velocities when available from SIMBAD with the same search radius, also through `Astroquery`.

The clean-up process was iterative in nature. First, we removed duplicates with TOPCAT (Taylor 2005) through an internal match which organized the sources in near-neighbor groups by marking the rows with the same group identifier. The internal match was done for a radius of $15''$, thus matching the data retrieval radius. Given this relatively large radius, objects with the same group ID were manually checked to avoid deleting two components of a binary system. This step reduced the number of entries to $\sim 12,000$.

[4] https://astroquery.readthedocs.io/en/latest/

5.2.4.1 Spectral Types

From the surveys and downloads, there were five sources of spectral types: optical, optical from SDSS, near-infrared, "literature" as downloaded from SIMBAD (without specifying whether it was optical or near-infrared), and photo-type from Skrzypek et al. (2015). A first cut in spectral types was done by requiring that any of the five spectral types be within M7−L5, reducing the sample size to $\sim 8,900$. An adopted spectral type was chosen by availability by following this preference: optical, SDSS optical, literature, near-infrared, and photo-type.

5.2.4.2 Preliminary Distance Cut

Trigonometric distances were calculated for the objects with measured parallaxes. A handful of parallaxes came from GAIA, while most came from the literature through SIMBAD. Spectrophotometric distances for JHK_sW1W2 filters were calculated using the adopted spectral type, the 2MASS and WISE magnitudes and the absolute magnitude relations of Dupuy & Liu (2012), valid for M6−T9 dwarfs. Additionally, photometric distances using $i-z$, $i-J$ and $i-K_s$ colors were estimated with the linear relations of Schmidt et al. (in prep.). We performed a preliminary distance cut by keeping entries where any of the trigonometric or spectrophotometric distances were within 30 pc. This reduced the number of entries significantly to $\sim 1,200$.

5.2.4.3 Magnitudes

With this manageable sample size, we organized the photometry. Part of the WISE and PPMXL products are crossmatches with the 2MASS catalog. We compared the JHK_s magnitudes from the 2MASS and WISE catalogs and kept the 2MASS magnitudes when the difference was within 0.05 mag, accounting for rounding errors. Separately, we did the same comparison between the JHK_s magnitudes from 2MASS and the PPMXL

crossmatch. The objects whose magnitude difference was larger than $0.05\,mag$ were flagged for visual checks in multi-wavelength finder chart images, and SIMBAD and Vizier tables. The WISE-2MASS and PPMXL-2MASS JHK_s matches were consolidated onto one 2MASS column per filter following the same difference requirement, with minor discrepancies fixed by visual inspection. The same procedure was followed to consolidate JHK magnitudes from UKIDSS from the literature and our Vizier download, with a majority of agreements. The MKO JHK magnitudes from the Gagné list were unmatched. While UKIDSS uses MKO filters, we keep these columns separate because the quantum efficiency of the UKIDSS and Keck detectors differ.

The mismatches between WISE and 2MASS JHK_s magnitudes typically happened when two nearby stars with a large magnitude difference (~ 3 mag) were alternatively picked up by one of the surveys. The larger WISE pixels would pick up on the bright source and crossmatch it to the brighter 2MASS source, yet we were looking for the fainter 2MASS source. In these cases, we assigned the 2MASS JHK_s magnitudes to the source, and replaced the WISE $W1W2W3$ entries with NaN.

For convenience, we assigned adopted JHK magnitudes where more than one near-infrared survey was available. We prioritized reported MKO JHK magnitudes since that was the only magnitude information available for many faint secondaries of binary systems. If no MKO was available, we used 2MASS magnitudes. UKIDSS JHK were compared to 2MASS JHK to make sure they were properly matched and corresponded to the same object. If a source was detected in UKIDSS but not in 2MASS, we adopted the UKIDSS JHK magnitudes, if it was detected in both, we adopted the 2MASS JHK_s magnitudes. All sources in the final sample have near-infrared magnitudes, 92% have mid-infrared magnitudes and only 41% have optical magnitudes.

Figure 5.1 shows the color locii of M7−L5 dwarfs as described by Davenport et al. (2014). The main advantage of these color combinations is the use of filters from

all three sky surveys. Mismatches between SDSS and 2MASS were identified as outliers in these plots and manually corrected after visual inspection with finder charts.

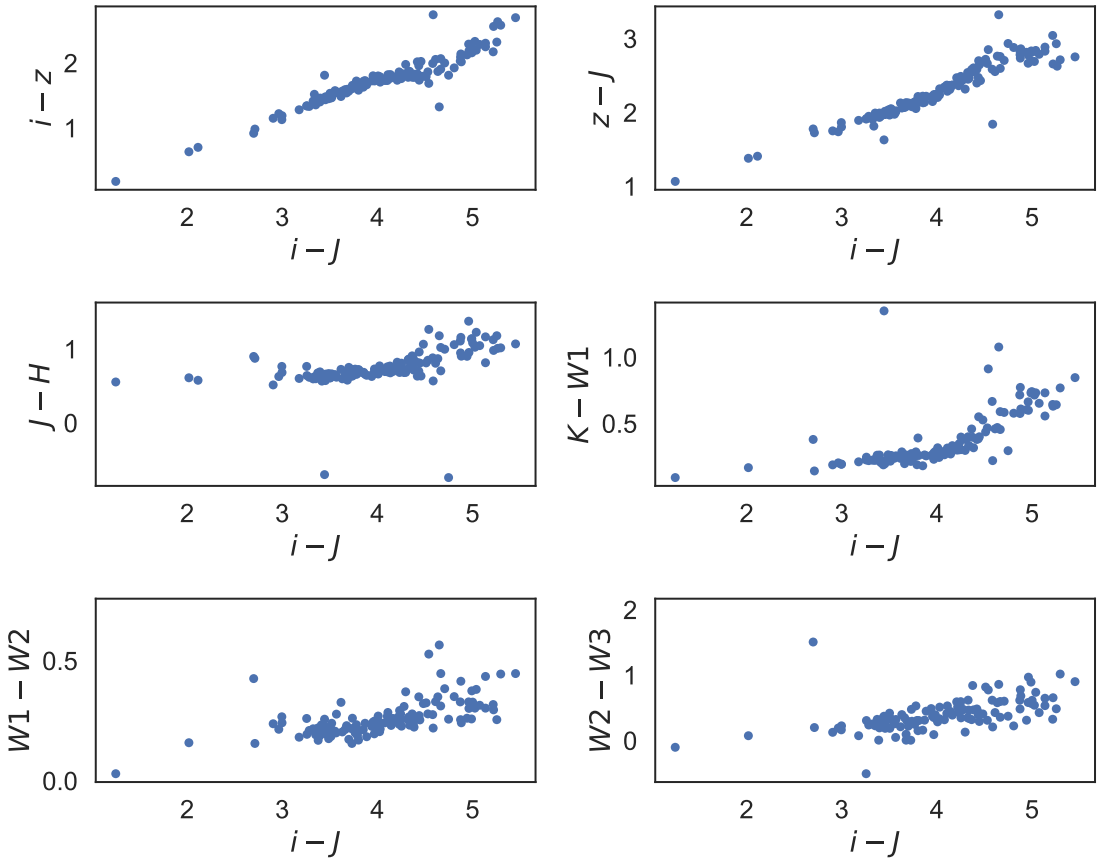

Figure 5.1 Color locus of the known M7−L5 25 pc sample in SDSS, 2MASS, and WISE colors as a function of $i-J$ (Davenport et al. 2014).

Finally, roughly a dozen galaxies, supernovae, white dwarfs and giant stars were identified by their SIMBAD object type, SDSS shape or SIMBAD literature spectral type (containing roman numerals other than "V" or "VI" for dwarfs and subdwarfs). These objects were eliminated from the sample.

5.2.4.4 Distances

After all the magnitudes had been checked and/or corrected, we recalculated distances following the same procedure as before. Additionally, we calculated average distances, weighted by their uncertainties, packing together the "color" distances ($i-z$, $i-J$, $i-K_s$), the near-infrared distances (J, H, K_s) and the mid-infrared distances ($W1$, $W2$).

In order to select sources within 25 pc, we designed a tiered selection process. First, sources whose trigonometric distance was outside 25 pc were rejected from the sample. Sources lacking parallaxes could fall under four categories, depending on the amount of distance information they had. If all three average distances were real and not missing, we rejected the case where all three were greater than 25 pc, and kept those sources where two or three distances were lower than 25 pc. Objects with two distances outside 25 pc and one inside 25 pc were placed on a separate peripheral sample. For the case of two real average distances and one missing, sources were kept in the sample if both distances were within 25 pc, rejected if both were outside 25 pc, and saved for further checks on the peripheral sample if one distance was below and the other one above 25 pc. If only one piece of spectrophotometric distance information was available, the source was kept if its distance was within 25 pc and rejected if above 25 pc. Finally, if there was no distance information at all, the source would be included in the peripheral sample for further checks.

5.3 Observations

In addition to the 206 spectra of M7-L5 dwarfs already contained in the SpeX Prism Library, 289 sources were newly observed with SpeX between UT 2015 February 24 and 2017 May 7 as part of IRTF programs: 2015A074, 2015B087, 2016A079,

2016B114, 2017A102 (PI: Bardalez Gagliuffi), and 2016A038 (PI: Burgasser), over a total of 15 nights. The latitude, equatorial mount and location of SpeX within the IRTF allow for observation of declinations in the $-50^\circ < \delta < +67^\circ$ range. 92% of the M7$-$L5 sample lies within these declinations, and we have obtained spectra for 89.3% of these sources observable by SpeX. Sources were observed in prism mode, which continuously samples wavelengths between $0.75-2.5\mu$m at a dispersion of $20-30$Å pixel^{-1}. Starlight was dispersed with the $0\farcs5$ slit, only resorting to the $0\farcs8$ slit if the seeing rose above $1\farcs2$, and always keeping the slit aligned with the parallactic angle. Integration times ranged between $60-150$ s per exposure, depending on the brightness of the source and atmospheric conditions. Observations were carried out in an ABBA dither pattern along the slit, with an additional AB cycle if more counts were needed to achieve S/N$\sim$ 100. Immediately after acquiring spectra for our science targets, bright A0 stars were observed at a similar airmass and used for flux calibration of the raw science spectra and correction for telluric absorption. Internal flat fields and Ar arc lamps were observed with each flux standard for pixel response and wavelength calibration. All data were reduced with the SpeXtool package v4.1 (Cushing et al. 2004; Vacca et al. 2003) using standard settings. The observations log is summarized in Table 5.2.

Table 5.2 SpeX observing log

Designation	2MASS J	2MASS K_s	Slit	Total t_{exp} (s)	Airmass	Observation Date	Median S/N	A0 Standard
Within 25 pc								
J00130931−0025521	12.167	11.319	0.5x15″	539	1.098	20151006	379.34	HD 1154
J00192626+4614078	12.603	11.502	0.5x15″	539	1.127	20151117	296.67	HD 222749
J00525468−2705597	13.611	12.54	0.5x15″	719	1.461	20150804	186.29	HD 222332
...	...	...	0.5x15″	717	1.474	20151116	163.85	HD 225200
J01004911−1933398	13.487	12.755	0.5x15″	478	1.348	20161007	85.90	HD 13433
J01243060−3355014	10.555	9.682	0.5x15″	119	1.767	20161007	301.30	HD 17224
J01243124−0027556	12.107	11.125	0.5x15″	719	1.075	20151006	453.78	HD 13936
J02150802−3040011	11.617	10.542	0.5x15″	359	1.626	20150804	378.88	HD 18735
J02192210−3925225	11.381	10.404	0.5x15″	358	1.946	20151116	438.33	HD 17864
J02354955−0711214	12.452	11.43	0.5x15″	539	1.122	20151006	339.91	HD 13936
J03122509+0021585	12.228	11.222	0.5x15″	539	1.062	20151006	370.59	HD 18571
J03144011−0450316	12.64	11.602	0.5x15″	717	1.101	20151006	348.09	HD 18571
J03283463+1129515	12.463	11.33	0.5x15″	539	1.012	20151003	252.70	HD 21379
...	...	...	0.5x15″	539	1.013	20151006	339.37	HD 21686
J03300506+2405281	12.386	11.385	0.5x15″	359	1.021	20161007	288.20	HD 23258
J03304458+0108263	13.229	12.277	0.5x15″	717	1.109	20160219	253.09	HD 18571
J03505737+1818069	12.967	11.779	0.5x15″	717	1.021	20151003	287.53	HD 23258
...	...	...	0.5x15″	717	1.003	20151006	306.47	HD 21686
J03550477−1032415	13.08	11.975	0.5x15″	717	1.171	20151006	220.41	HD 25792

Table 5.2 Continued

Designation	2MASS J	2MASS K_s	Slit	Total t_{exp} (s)	Airmass	Observation Date	Median S/N	A0 Standard
J04291842−3123568	10.874	9.77	0.5x15″	239	1.663	20161129	456.30	HD 31506
J04350850+2311398	12.528	11.592	0.5x15″	359	1.058	20161007	247.24	HD 27761
J04411078+2555116	13.193	11.445	0.5x15″	717	1.071	20151117	215.61	HD 23258
J05061292+0439272	8.909	8.067	0.5x15″	719	1.042	20160219	408.95	HD 31411
J05181131−3101529	11.878	10.9	0.5x15″	478	1.618	20161007	60.53	HD 31506
...	...	...	0.5x15″	239	1.595	20161129	321.79	HD 31506
J05264316−1824315	12.358	11.448	0.5x15″	717	1.308	20160218	236.69	HD 38206
J05392474+4038437	11.109	10.044	0.5x15″	239	1.070	20161007	398.46	HD31069
J05394952+5253597	14.756	13.322	0.5x15″	717	1.198	20161007	101.46	HD31069
J05480722+0033588	13.213	11.22	0.5x15″	717	1.062	20151006	241.79	HD 34317
J06145280+4536556	13.022	11.837	0.5x15″	717	1.136	20160218	324.04	HD 45105
...	...	...	0.5x15″	478	1.121	20161129	208.11	HD 39250
J06300140−1840143	12.681	11.461	0.5x15″	717	1.334	20161007	279.22	HD 49529
J06431685−1843375	13.009	11.803	0.5x15″	478	1.444	20161007	173.87	HD 49529
J06572547−4019134	12.728	11.667	0.5x15″	717	2.009	20160219	210.50	HD 42426
J07140394+3702459	11.976	10.838	0.5x15″	539	1.061	20160218	421.38	HD 56386
J07410681+1738459	12.011	10.942	0.5x15″	239	1.035	20161129	266.63	HD 57208
J08040580+6153336	12.74	11.454	0.5x15″	717	1.346	20160218	323.68	HD 63586
J08072607+3213101	12.168	11.051	0.5x15″	539	1.074	20160218	371.70	HD 71906
J08081359+2106094	7.336	6.522	0.5x15″	79	1.016	20161129	484.72	HD 74721

Table 5.2 Continued

Designation	2MASS J	2MASS K_s	Slit	Total t_{exp} (s)	Airmass	Observation Date	Median S/N	A0 Standard
J08151407+1030117	12.423	11.334	0.5x15″	359	1.114	20161129	281.16	HD 74721
J08185804+2333522	12.175	11.149	0.5x15″	539	1.027	20160218	326.48	HD 64648
J08500174−1924184	12.765	11.633	0.5x15″	717	1.291	20160218	245.18	HD 69589
J08581519+1945470A[1]	7.791	6.889	0.5x15″	118	1.005	20160219	808.19	HD 74721
J08581519+1945470B[1]	7.791	6.889	0.5x15″	118	1.008	20160219	1560.42	HD 74721
J08593854+6341355	13.701	12.387	0.5x15″	717	1.596	20150224	161.43	HD 63586
J09113059+2248111	11.745	10.765	0.5x15″	179	1.014	20160219	340.84	HD 74721
J09282562+4230545	13.082	11.943	0.5x15″	478	1.090	20160219	279.97	HD 71906
J09424604+5531025	12.921	11.801	0.5x15″	539	1.385	20150224	198.57	HD 92728
J09473829+3710178	12.189	11.338	0.5x15″	1195	1.055	20150512	85.68	HD 88960
J10063197−1653266	12.036	10.992	0.5x15″	719	1.249	20160218	226.45	HD 86593
J10240997+1815533	12.275	11.239	0.5x15″	539	1.032	20150511	111.06	HD 89239
J10452400−0149576	13.16	11.78	0.5x15″	717	1.023	20160530	313.66	HD 97585
J10471381+4026493	12.436	11.254	0.5x15″	539	1.123	20160530	245.74	HD 5126
J10481463−3956062	9.538	8.447	0.5x15″	717	2.020	20150512	42.36	HD 98176
J10544168+1214084	12.46	11.446	0.5x15″	359	1.009	20160219	284.35	HD 101060
...	...	...	0.5x15″	478	1.018	20160528	128.64	HD 99966
J11061897+0428327	12.329	11.332	0.5x15″	359	1.136	20160528	262.36	HD 97585
J11122567+3548131	14.584	12.721	0.5x15″	717	1.149	20160530	112.02	HD 98152
J11214924−1313084	12.11	10.83	0.5x15″	359	1.207	20160528	175.79	HD 97516

Table 5.2 Continued

Designation	2MASS J	2MASS K_s	Slit	Total t_{exp} (s)	Airmass	Observation Date	Median S/N	A0 Standard
J11232934+0154040	12.365	11.355	0.5x15″	539	1.129	20170506	288.90	HD 109615
J11331404+0636474	11.782	10.898	0.5x15″	358	1.107	20170506	344.84	HD 109615
J11345493+0022541	12.853	11.672	0.5x15″	478	1.172	20160219	280.78	HD 97585
J11524266+2438079	13.027	11.776	0.5x15″	956	1.012	20150512	109.76	HD 105388
J12465176+3148104	12.227	11.209	0.5x15″	358	1.041	20170506	180.43	HD 109691
J12505265−2121136	11.16	10.128	0.5x15″	358	1.337	20170506	300.61	HD 110902
J12522264+0252058	12.495	11.502	0.5x15″	956	1.049	20150512	33.10	HD 109309
J12531240+4034038	12.185	11.162	0.5x15″	539	1.093	20150511	155.75	HD 89239
J12560215−1257217	11.018	10.044	0.5x15″	358	1.191	20160218	435.69	HD 112304
J13082507+0725512	13.185	12.004	0.5x15″	956	1.110	20150701	296.77	HD 116960
J13092185−2330350	11.785	10.669	0.5x15″	359	1.381	20150224	191.79	HD 110902
...	...	...	0.5x15″	358	1.384	20150225	215.68	HD 114345
J13171150+1849232	12.424	11.326	0.5x15″	539	1.010	20160218	262.79	HD 111744
J13261625+5640448	11.825	10.871	0.5x15″	717	1.266	20150511	37.67	HD 125299
J13322442−0441126	12.369	11.283	0.5x15″	956	1.103	20150512	112.75	HD 109309
J13365044+4751321	12.659	11.668	0.5x15″	836	1.132	20150511	182.19	HD 89239
J13564148+4342587	11.709	10.65	0.5x15″	717	1.120	20150511	236.37	HD 89239
J14032232+3007547	12.684	11.602	0.5x15″	359	1.059	20150224	162.18	HD 121880
J14112131−2119503	12.437	11.33	0.5x15″	717	1.329	20150511	124.28	HD 125299
J14211873−1618201	12.755	11.67	0.5x15″	717	1.241	20160218	222.44	HD 126818

Table 5.2 Continued

Designation	2MASS J	2MASS K_s	Slit	Total t_{exp} (s)	Airmass	Observation Date	Median S/N	A0 Standard
J14222424+2116076	12.435	11.445	0.5x15″	539	1.002	20160219	377.68	HD 121880
...	...	...	0.5x15″	539	1.002	20160530	350.21	HD 124773
J14480337+1554149	12.483	11.475	0.5x15″	719	1.033	20150701	312.31	HD 131951
J14482563+1031590	14.556	12.683	0.5x15″	717	1.015	20160528	78.13	HD 136831
J14562776+1755090	11.981	10.919	0.5x15″	956	1.103	20150512	111.16	HD 136831
...	...	...	0.5x15″	119	1.008	20170506	163.99	HD 136831
J14563831−2809473	9.965	8.928	0.5x15″	177	1.495	20160528	87.18	HD 138295
J14573965+4517167	13.119	11.927	0.5x15″	478	1.132	20160528	139.64	HD 121409
J15002635−0039281	11.593	10.647	0.5x15″	239	1.125	20160530	386.88	HD 140729
J15010818+2250020	11.866	10.706	0.5x15″	358	1.001	20160530	372.69	HD 140729
J15041621−2355564	12.011	11.032	0.5x15″	717	1.393	20150511	76.07	HD 125299
J15072779−2000431	11.713	10.661	0.5x15″	478	1.303	20150511	106.69	HD 125299
J15104786−2818174	12.838	11.687	0.5x15″	478	1.517	20150701	279.64	HD 131885
...	...	...	0.5x15″	358	1.502	20160528	42.14	HD 138295
J15210103+5053230	12.014	10.922	0.5x15″	358	1.166	20160218	304.61	HD 121409
J15242475+2925318	11.206	10.155	0.5x15″	358	1.015	20170506	444.85	HD 140729
J15291017+6312539	11.643	10.554	0.5x15″	239	1.374	20160218	275.54	HD 143187
J15404341−5101357	8.961	7.943	0.5x15″	133	3.040	20150224	48.57	HD 126561
...	...	...	0.5x15″	119	3.054	20150224	40.34	HD 126561
J15460540+3749458	12.435	11.407	0.5x15″	359	1.051	20160530	276.57	HD 140729

Table 5.2 Continued

Designation	2MASS J	2MASS K_s	Slit	Total t_{exp} (s)	Airmass	Observation Date	Median S/N	A0 Standard
J15510662+6457047	12.887	11.719	0.5x15″	956	1.415	20160218	160.29	HD 143187
J15531993+1400337	13.05	11.823	0.5x15″	539	1.017	20160530	250.19	HD 140729
J16073123−0442091	11.896	10.717	0.5x15″	478	1.099	20150225	255.86	HD 136831
J16154245+0546400	12.88	11.741	0.5x15″	359	1.033	20160530	223.77	HD 140729
J16325882−0631481	12.742	11.621	0.5x15″	539	1.120	20170506	255.04	HD 148968
J17071830+6439331	12.539	11.375	0.8x15″	1795	1.416	20160702	92.41	HD 143187
J17331893+4633593	13.242	11.889	0.5x15″	717	1.341	20161007	85.61	HD 172728
J17335314+1655129	8.895	7.995	0.5x15″	177	1.058	20160528	318.79	HD 165029
J17351296+2634475	11.252	10.157	0.5x15″	239	1.129	20150916	429.44	HD 165029
J17562963−4518224	12.386	11.259	0.5x15″	539	2.368	20170506	190.75	HD 182328
J17565620−4805096	13.409	12.19	0.5x15″	717	2.656	20170506	155.25	HD 163761
J18300760−1842361	10.427	8.818	0.5x15″	119	1.549	20161007	262.82	HD 169961
J18393308+2952164	11.011	10.005	0.8x15″	389	1.018	20160702	503.00	HD 182761
...	...	...	0.5x15″	79	1.200	20161007	169.90	HD 174567
J18451889+3853248	12.214	11.047	0.5x15″	539	1.103	20150916	427.81	HD 174567
J18470342+5522433	11.92	10.901	0.8x15″	478	1.238	20160702	374.60	HD 178207
...	...	...	0.5x15″	239	1.412	20161007	228.14	HD 178207
J20140359−2016217	12.537	11.447	0.5x15″	796	1.310	20150701	416.73	HD 185533
J20370715−1137569	12.272	11.257	0.5x15″	719	1.172	20150701	465.60	HD 190454
J21373742+0808463	14.774	13.019	0.5x15″	717	1.049	20151116	81.79	HD 208108

Table 5.2 Continued

Designation	2MASS J	2MASS K_s	Slit	Total t_{exp} (s)	Airmass	Observation Date	Median S/N	A0 Standard
J21580457−1550098	15.04	13.185	0.5x15″	1496	1.369	20151006	62.18	HD 202990
J22021125−1109461	12.361	11.374	0.5x15″	796	1.165	20150701	528.31	HD 215143
J22062280−2047058	12.37	11.315	0.5x15″	359	1.315	20161007	159.80	HD 208087
J22354905+1840298	12.393	11.365	0.5x15″	717	1.189	20150804	439.08	HD 210501
J23081888+0629551	10.615	9.754	0.5x15″	657	1.102	20150916	198.55	HD 210501
J23272645−1741329	11.752	10.835	0.5x15″	358	1.265	20151116	337.81	HD 218639
J23312174−2749500	11.646	10.651	0.5x15″	478	1.492	20150701	516.29	HD 225200
J23343945+1933041	12.776	11.618	0.5x15″	657	1.210	20150804	388.67	HD 210501
J23371491−0838084	12.189	11.189	0.5x15″	719	1.137	20150701	459.67	HD 219833
J23464599+1129094	12.798	11.605	0.5x15″	478	1.074	20150804	311.73	HD 210501
J23473680+2702068	13.193	11.983	0.5x15″	239	1.026	20161007	155.84	HD 222749
J23494899+1224386	12.601	11.557	0.5x15″	478	1.054	20150804	372.19	HD 210501
Outside 25 pc								
J00202316−2346054	12.345	11.335	0.5x15″	478	1.387	20150804	347.80	HD 222332
J00512264−2251318	13.019	11.961	0.5x15″	478	1.409	20161129	169.80	HD 9132
J005349112−01135447	···	···	0.5x15″	719	1.090	20151006	428.37	HD 1154
J012942560−08235809	10.655	9.771	0.5x15″	79	1.138	20161007	294.78	HD 13936
J024029501+28325766	12.674	11.633	0.5x15″	478	1.059	20161007	309.50	HD 13869
J034848823+24203233	11.995	11.29	0.5x15″	539	1.008	20151003	229.66	HD 23258
···	···	···	0.5x15″	539	1.031	20151117	400.47	HD 23258

Table 5.2 Continued

Designation	2MASS J	2MASS K_s	Slit	Total t_{exp} (s)	Airmass	Observation Date	Median S/N	A0 Standard
J05004808+0442143	13.8	12.513	0.5x15″	478	1.066	20161129	178.46	HD 34369
J05075070−0342427	15.502	14.724	0.5x15″	1197	1.123	20160219	61.06	HD 31411
J050855063+33192721	14.217	12.623	0.5x15″	478	1.077	20161129	120.65	HD 39250
J05372332−0816055	12.299	11.348	0.5x15″	717	1.133	20151003	299.66	HD 37887
J05382666−0222503	14.479	13.474	0.5x15″	956	1.085	20151003	84.92	HD 37887
J06502626−2135361	16.173	15.277	0.5x15″	239	1.381	20161129	333.99	HD 56341
J070541584+27282445	7.596	6.781	0.5x15″	79	1.040	20161129	360.10	HD 57208
J093349.13−160325.9	12.720	11.890	0.8x15″	717	1.255	20150511	73.17	HD 79752
J09401610+4017365	13.563	12.473	0.5x15″	478	1.074	20160219	220.67	HD 71906
J110531332+43311705	8.742	7.839	0.5x15″	79	1.279	20160530	862.74	HD 98152
J11131089+2110086	13.865	12.885	0.5x15″	717	1.001	20170506	118.98	HD 101060
J114805021+02035097	15.517	14.509	0.5x15″	1197	1.055	20150225	58.45	HD 101122
J125214122+14223980	16.001	14.487	0.5x15″	1197	1.005	20150225	42.45	HD 116960
J134148910+55104587	15.209	14.042	0.5x15″	897	1.231	20150224	60.85	HD 116405
J15400513+0102087	15.212	14.083	0.5x15″	1197	1.057	20150225	71.93	HD 136831
J154028.73−261354.6	11.646	10.730	0.5x15″	478	1.465	20150701	527.74	HD 131885
J155306.00+064228.7	10.954	10.370	0.5x15″	358	1.055	20170506	307.97	HD 136831
J16094592−3431297	13.72	13.027	0.5x15″	478	1.724	20150701	480.81	HD 138575
J162651682−38123263	10.365	9.443	0.5x15″	159	1.922	20150701	499.26	HD 150641
J165633622−20463730	11.299	10.368	0.5x15″	358	1.324	20170506	359.62	HD 44925

Table 5.2 Continued

Designation	2MASS J	2MASS K_s	Slit	Total t_{exp} (s)	Airmass	Observation Date	Median S/N	A0 Standard
J17075766−1928030	16.557	15.734	0.5x15″	159	1.299	20150701	580.14	HD 157170
J171226032−19070389	10.716	9.895	0.5x15″	478	1.313	20150701	893.98	HD 157170
J175530638−04554242	14.265	14.091	0.5x15″	159	1.129	20150701	565.49	HD 171149
J1803360469−185850566	9.131	8.275	0.5x15″	119	1.284	20150701	1119.56	HD 157170
J18094366−0219347	16.149	14.826	0.5x15″	159	1.122	20150701	773.77	HD 171149
J18094860−0247405	16.182	15.224	0.5x15″	478	1.139	20150701	661.88	HD 171149
J18455806−2856018	13.997	13.676	0.5x15″	58	1.521	20150701	790.49	HD 178252
J193104582−03061865	11.147	10.228	0.5x15″	79	1.259	20161007	198.10	HD 190454
J19535448+4424533A[1]	8.275	7.387	0.8x15″	66	1.101	20160702	894.18	HD 165029
J1953552460+442452642B[1]	8.275	7.387	0.8x15″	66	1.100	20160702	1108.37	HD 165029
J20025208−4433130	13.528	12.586	0.5x15″	717	2.305	20170506	122.25	HD 186216
J202614.60−294323.0	14.802	13.360	0.5x15″	1137	1.671	20150804	109.39	HD 190285
J21144103−4339531	13.016	11.953	0.5x15″	478	2.236	20151006	638.82	HD 196212
J213630294+05153290	13.353	12.248	0.8x15″	719	1.033	20160702	222.86	HD 210501
J22200100+1214368	14.269	13.811	0.5x15″	956	1.122	20150916	174.53	HD 210501
J22410525+0230567	14.703	14.265	0.5x15″	956	1.056	20160814	99.31	HD 210501
J22550604+0018475	11.458	11.097	0.5x15″	358	1.176	20150916	472.77	HD 210501
J22593244+4450284	13.336	12.326	0.5x15″	717	1.116	20160814	134.51	HD 222749
J233015.57−473655.4	11.229	10.279	0.5x15″	358	2.595	20151116	287.89	HD 216923
J23305124−0844546	17.288	15.369	0.8x15″	4894	1.157	20161129	26.51	HD 219833

Table 5.2 Continued

Designation	2MASS J	2MASS K_s	Slit	Total t_{exp} (s)	Airmass	Observation Date	Median S/N	A0 Standard
J00044144−2058298	12.404	11.396	0.5x15″	478	1.324	20150804	319.47	HD 222332
J00045618+0451168	14.301	13.381	0.5x15″	956	1.075	20160814	66.09	HD 7215
J00165953−4056541	15.316	13.432	0.5x15″	1496	2.090	20150804	85.64	HD 224622
J00315477+0649463	12.82	11.718	0.5x15″	717	1.038	20151117	302.32	HD 1154
J00492677−0635467	13.342	12.103	0.5x15″	717	1.116	20151116	212.33	HD 1154
...	...	...	0.5x15″	478	1.127	20160817	221.03	HD 1154
J01070426+2435279	13.484	12.228	0.5x15″	717	1.039	20151117	244.23	HD 7215
J01092170+2949255	12.912	11.681	0.5x15″	478	1.084	20161007	162.54	HD 222749
J01204916−0741036	12.988	11.853	0.5x15″	717	1.127	20151116	271.44	HD 13936
J01245988+2847587	13.378	12.25	0.5x15″	717	1.051	20151117	228.95	HD 7215
J02115089+4728300	12.836	11.822	0.5x15″	717	1.137	20151116	179.44	HD 21038
...	...	...	0.5x15″	539	1.304	20151230	218.62	HD 15090
J02185792−0617499	12.85	11.837	0.5x15″	717	1.113	20151006	279.86	HD 13936
J04235322−0006587	13.648	12.475	0.5x15″	717	1.087	20161007	140.22	HD 31411
J07062855+3858247	12.859	11.897	0.5x15″	717	1.091	20160218	272.69	HD 56386
J08215010+4532019	13.464	12.378	0.5x15″	717	1.109	20160219	263.83	HD 71906
J11062352+5259317	13.371	12.263	0.5x15″	717	1.213	20160218	268.24	HD 95126
J11301367+1937346	13.381	12.286	0.5x15″	717	1.050	20160218	181.50	HD 105388
J11391107+0841121	12.922	11.836	0.5x15″	478	1.090	20160219	256.99	HD 97585
J11582484+1354456	13.926	12.762	0.5x15″	478	1.035	20160528	107.37	HD 97585

Table 5.2 Continued

Designation	2MASS J	2MASS K_s	Slit	Total t_{exp} (s)	Airmass	Observation Date	Median S/N	A0 Standard
J12003292+2048513	12.862	11.861	0.5x15″	717	1.068	20160219	322.35	HD 105388
J12172935+0035326	13.085	12.046	0.5x15″	717	1.106	20160218	171.07	HD 111744
J14360977+2900350	13.299	12.173	0.5x15″	717	1.013	20160219	263.57	HD 122945
...	...	...	0.5x15″	539	1.023	20160530	216.34	HD 124773
J14432796+0316543	13.298	12.176	0.5x15″	717	1.044	20160218	171.88	HD 123233
J14450627+4409393	12.446	11.429	0.5x15″	539	1.105	20160528	130.66	HD 121409
J14521846+4826214	13.353	12.31	0.5x15″	717	1.174	20160528	145.25	HD 121409
J16272658−2425543	13	11.839	0.5x15″	717	1.406	20170506	211.97	HD 144254
J17433487+5844110	14.01	12.681	0.5x15″	717	1.315	20170506	141.54	HD 44925
J21363029+0515329	13.353	12.248	0.5x15″	478	1.033	20161007	103.11	HD 210501
J233110.53−040621.1	10.205	9.702	0.5x15″	956	1.127	20150701	220.98	HD 219833
J23590836+2338311	13.576	12.296	0.5x15″	719	1.038	20150804	278.09	HD 210501
J00133470+1109403	15.721	14.225	0.5x15″	1197	1.059	20151117	61.96	HD 7215
J00320509+0219017	14.324	12.802	0.5x15″	717	1.048	20151117	147.10	HD 1154
J01090918−4954532	13.546	12.45	0.5x15″	717	3.054	20161129	82.34	HD 15911
J01473282−4954478	13.058	11.916	0.5x15″	956	2.861	20151117	25.00	HD 20686
...	...	...	0.5x15″	717	2.998	20161129	135.63	HD 15911
J01514102−0051564	15.096	13.587	0.5x15″	897	1.266	20151230	80.41	HD 13936
J02501167−0151295	12.886	11.909	0.5x15″	478	1.097	20161007	224.98	HD 18571
J02575455+4111324	13.95	12.721	0.5x15″	478	1.118	20161007	140.24	HD 21038

Table 5.2 Continued

Designation	2MASS J	2MASS K_s	Slit	Total t_{exp} (s)	Airmass	Observation Date	Median S/N	A0 Standard
J03100053+0726506	12.85	11.775	0.5x15″	478	1.040	20161007	211.64	HD 18571
J04221644+2549118	13.059	11.936	0.5x15″	478	1.065	20161007	233.60	HD 23258
J04453237−3642258	13.358	12.255	0.5x15″	717	1.812	20151003	122.90	HD 25536
...	...	...	0.5x15″	956	1.810	20151006	130.46	HD 25536
J05383888−0228016	15.272	14.431	0.5x15″	897	1.189	20161007	44.02	HD 39953
J06003375−3314268	13.205	12.012	0.5x15″	956	1.661	20151006	177.11	HD 36517
J06575576+4029420	13.295	12.254	0.5x15″	717	1.111	20160218	225.97	HD 45105
J06595849+1717162	14.841	13.021	0.5x15″	478	1.068	20161129	85.14	HD 57208
J07214625+1937444	12.976	11.936	0.5x15″	717	1.023	20160219	332.32	HD 64648
J07465323+3945098	12.572	11.617	0.5x15″	359	1.126	20161129	192.39	HD 71906
J08002758+5511346	14.623	13.36	0.5x15″	717	1.501	20150224	89.05	HD 63586
J08051104−3158115	13.113	12.113	0.5x15″	478	1.653	20161129	151.23	HD 61943
J08272028+4502043	13.381	12.338	0.5x15″	478	1.109	20160219	234.72	HD 71906
J08294908−0012241	13.488	12.465	0.5x15″	717	1.066	20160218	175.64	HD 65158
J08355736+4318310	13.047	11.965	0.5x15″	478	1.113	20161129	225.81	HD 71906
J08404912+4827404	13.464	12.442	0.5x15″	478	1.169	20161129	184.72	HD 71906
J08481673+3309088	12.324	11.416	0.5x15″	539	1.109	20160218	317.61	HD 71906
J09130443−0733042	13.398	12.143	0.5x15″	956	1.126	20160218	230.44	HD 73687
J09261233+5309390	13.51	12.514	0.5x15″	478	1.239	20160219	217.23	HD 71906
J09411150+3940530	13.427	12.113	0.5x15″	478	1.077	20160219	247.96	HD 71906

Table 5.2 Continued

Designation	2MASS J	2MASS K_s	Slit	Total t_{exp} (s)	Airmass	Observation Date	Median S/N	A0 Standard
J09472006−0020093	12.255	11.349	0.5x15″	539	1.066	20160218	339.03	HD 79108
J10021216+6349262	12.905	11.979	0.5x15″	717	1.405	20160218	176.36	HD 63586
J10110024+4245035	13.363	12.316	0.5x15″	717	1.121	20160218	195.99	HD 95126
J10503222+4907423	12.989	11.968	0.5x15″	717	1.165	20160218	309.42	HD 95126
J11000965+4957470	15.282	13.474	0.5x15″	1197	1.222	20160530	96.00	HD 5126
J11092745−1606515	14.97	13.892	0.5x15″	1197	1.237	20150225	71.53	HD 101122
J11173691+3609359	14.269	12.963	0.5x15″	717	1.043	20170506	98.95	HD 89239
J11194647+0820356	12.767	11.899	0.5x15″	478	1.096	20160219	281.20	HD 97585
...	...	...	0.5x15″	717	1.057	20160528	265.49	HD 97585
J11230019+0400587	13.28	12.252	0.5x15″	539	1.084	20170506	564.91	HD 97585
J11294321+3201511	12.802	11.883	0.5x15″	717	1.045	20160218	303.64	HD 105388
...	...	...	0.5x15″	29	1.027	20160219	237.94	HD 105388
J11394192−0310039	14.403	13.203	0.5x15″	717	1.131	20150224	104.72	HD 101060
J11583344+3953064	12.934	11.922	0.5x15″	539	1.064	20170506	193.53	HD 109615
J12013372+4046472	12.636	11.735	0.5x15″	539	1.161	20160219	334.34	HD 105388
J12080810+3520281	12.367	11.419	0.5x15″	359	1.067	20160528	259.03	HD 109615
J13032398+3602486	13.638	12.463	0.5x15″	539	1.051	20160530	162.03	HD 109691
J13480100−0304328	12.741	11.656	0.5x15″	539	1.088	20170506	185.16	HD 123233
J13484591+0353545	14.628	13.229	0.5x15″	1049	1.041	20150225	70.48	HD 116960
J13543964+5044510	14.353	13.157	0.5x15″	478	1.192	20150224	101.04	HD 116405

Table 5.2 Continued

Designation	2MASS J	2MASS K_s	Slit	Total t_{exp} (s)	Airmass	Observation Date	Median S/N	A0 Standard
J14325112+3636440	14.304	13.069	0.5x15″	717	1.046	20150225	39.04	HD 116405
J14345819−2335572	12.93	11.87	0.5x15″	717	1.377	20160218	179.15	HD 126818
J14532303+1543081	13.255	12.208	0.5x15″	717	1.019	20160219	202.99	HD 131951
J14534847+3733165	13.172	12.123	0.5x15″	359	1.112	20160528	162.44	HD 121409
J14591936+0604535	13.154	12.192	0.5x15″	717	1.033	20170506	199.54	HD 136831
J15123329−1032414	13.156	12.021	0.5x15″	717	1.159	20170506	184.20	HD 133772
J15435815+3206420	12.73	11.739	0.5x15″	359	1.023	20160530	243.59	HD 140729
J15503820+3041038	13.003	11.949	0.5x15″	359	1.021	20160530	219.19	HD 140729
J16271825+3538347	12.346	11.352	0.5x15″	239	1.039	20160530	260.59	HD 145647
J17031418+5910480	12.805	11.859	0.8x15″	956	1.292	20160702	99.93	HD 143187
J19223062+6610194	14.571	13.162	0.5x15″	717	1.448	20170506	96.21	HD 44925
J20045369−1416231	13.129	12.045	0.5x15″	598	1.224	20150804	254.85	HD 190454
J20364425−0847138	13.423	12.434	0.5x15″	717	1.159	20150804	236.55	HD 190454
J21254581−0018340	13.137	12.118	0.5x15″	956	1.072	20150701	352.79	HD 198070
J21304464−0845205	14.137	12.815	0.5x15″	956	1.290	20151006	73.98	HD 202990
J22355244+0418563	15.371	13.786	0.5x15″	1197	1.080	20150701	120.11	HD 215143
J22470170+1955286	13.791	12.648	0.5x15″	717	1.000	20160814	110.31	HD 210501
J22520151−1815594	13.521	12.369	0.5x15″	478	1.278	20161007	114.62	HD 208087
J22574047−0106465	12.67	11.718	0.5x15″	539	1.277	20150804	346.84	HD 215143
J23081888+0629551[2]	10.615	9.754	0.5x15″	358	1.122	20150916	721.29	HD 210501

Table 5.2 Continued

Designation	2MASS J	2MASS K_s	Slit	Total t_{exp} (s)	Airmass	Observation Date	Median S/N	A0 Standard
J23291290+2704152	13.576	12.557	0.5x15″	717	1.019	20160814	80.94	HD 222749
J23361644+1835004	13.659	12.464	0.8x15″	717	1.003	20160702	186.96	HD 210501
...	...	...	0.5x15″	717	1.022	20160814	65.81	HD 7215
J23364395+2153388	12.709	11.719	0.5x15″	478	1.028	20161007	221.84	HD 222749
J23381868−4726132	13.25	12.072	0.5x15″	478	2.561	20161110	92.48	HD 216009

[1]Serendipitous binary discovery, magnitudes are for combined system.

[2]Background source.

5.4 Sample Characterization

5.4.1 Spatial Distribution and Density

Since 25 pc is a relatively small radius compared to the radius of the Milky Way ($R_{MW} \sim 25$ kpc), we are safe to assume a priori an isotropic distribution of sources within this volume. From our literature research, we found 443 M7−L5 sources confidently within 25 pc, distributed at all hour angles and declinations, except for the galactic plane ($-15^\circ < b < +15^\circ$) which remains largely unexplored. Taking into account the declinations accessible by SpeX, our sample is reduced to an observable sample of 408 sources. Over the course of 3 years and supplemented by previous SpeX observations in the SpeX Prism Library, we were able to compile near-infrared spectra for 370 objects, amounting to 91% of the observable sample and 84% of the full sample. Figure 5.2 shows the spatial distribution of all our targets as black dots, and the ones with an observed SpeX spectrum are shown in red. The regions inaccessible by SpeX are shaded in gray.

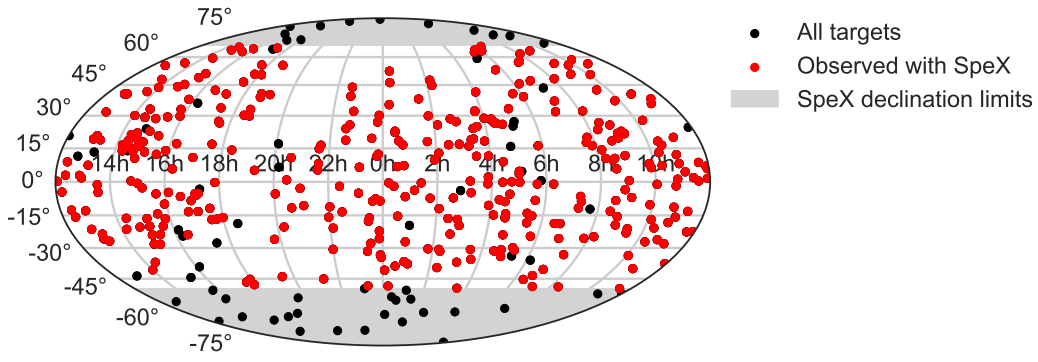

Figure 5.2 Spatial distribution of targets in the M7−L5 25 pc sample. The sample is shown as black dots, objects for which we have spectra are shown as red dots. The sky regions inaccessible by SpeX are shaded in gray.

We estimated the total angular area covered by our observations by creating a 360 by 180 grid, representing the full sky in equatorial coordinates with cells spaced by one degree. Areas to each cell were assigned as the area between consecutive right ascensions

and declinations times the cosine of the middle declination, $A = \Delta\alpha\Delta\delta cos(\frac{\delta_x+\delta_{x+1}}{2})$, where δ_x and δ_{x+1} are the declinations of the top and bottom edges of the cell. The total area added up to 4π radians or 41,253 deg^2. We blocked the areas inaccessible by SpeX, and the cells with galactic declinations in the $-15^\circ < b < +15^\circ$ range. The new sum of individual areas added up to 26,210 deg^2 or 64% of the full surface area of a sphere. The number of sources within that area is 361. The surface density of the M7−L5 25 pc sample is 0.014 deg^2. In order to find a volume density, we divide the number of sources over the surveyed volume, which is the fraction of angular area times $4\pi R^3/3$, where $R = 25$ pc. We find that the volume density of the sample is 0.009 pc^{-3}. This density implies that the total number of sources expected in 25 pc within the studied spectral type range should be 568.

5.4.2 Spectral Type Classification and Analysis

Optical and near-infrared spectral types for the sample were obtained from the literature. Out of the full 443 objects in the sample, 381 have a measured optical spectral type, and 264 have a near-infrared type. The distribution of spectral types is shown in Figure 5.3.

Figure 5.4 shows a comparison between these values per source. The size of the circles is proportional to the frequency of occurrence of a given spectral type pair. The scatter between spectral types is 0.76; the 3σ boundaries are delineated by the dashed blue lines. The outliers must be carefully examined to determine either misclassification or peculiarity

The SpeX spectra was classified by near-infrared spectral standards from Kirkpatrick et al. (2010), following the method describe therein which compares the *J* bands of the spectrum and spectral standard by a χ^2 minimization routine. The distribution of spectral types is shown in Figure 5.5 with the adopted spectral types as a backdrop.

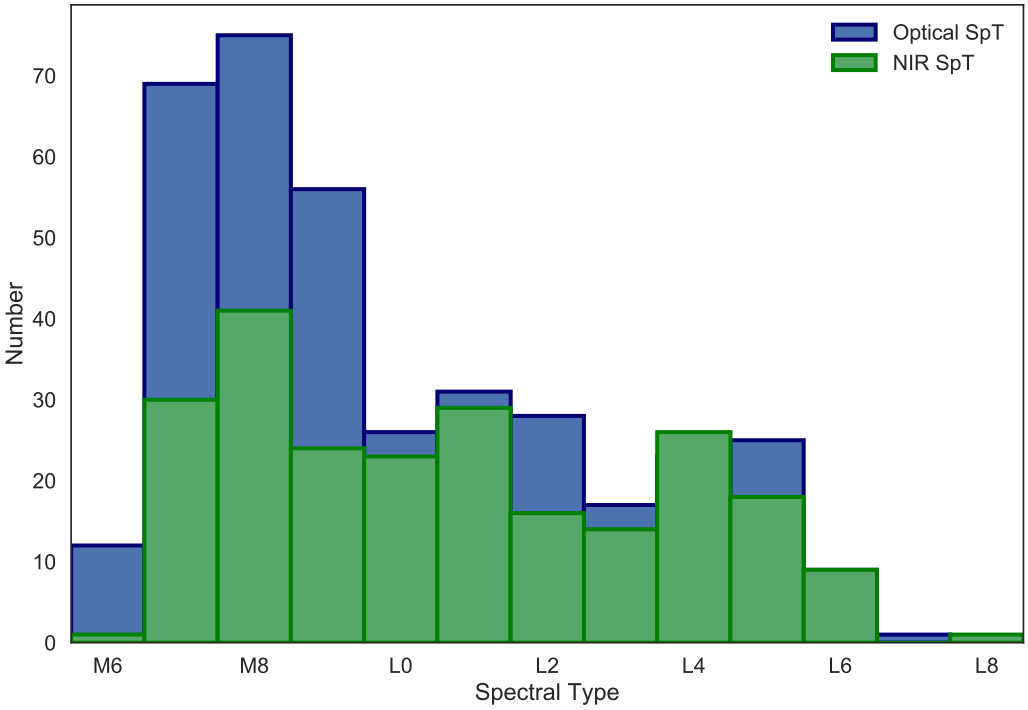

Figure 5.3 Histogram of optical and near-infrared spectral types as reported in the literature for the M7−L5 25 pc sample. Optical spectral types are shown in blue and near-infrared types are shown in green.

Figure 5.6 shows the comparison between the literature optical or near-infrared classifications compared to the classification by standard. The scatter for the optical-NIR standard comparison is 1.0 subtype, while the scatter for the NIR-NIR standard comparison is only slightly smaller at 1.1 subtypes. For the adopted spectral type, the scatter is 1.16 when compared to the SpeX spectral type compared to near-infrared spectral standards.

Additionally, the SpeX spectra was classified using spectral indices from Burgasser (2007a), Allers et al. (2007), and Reid et al. (2001a). These indices are applicable in the L0−T8, M5−L5, and M7−L8 spectral type ranges, respectively. The indices from Burgasser (2007a) tend to predict a later classification for both optical and near-

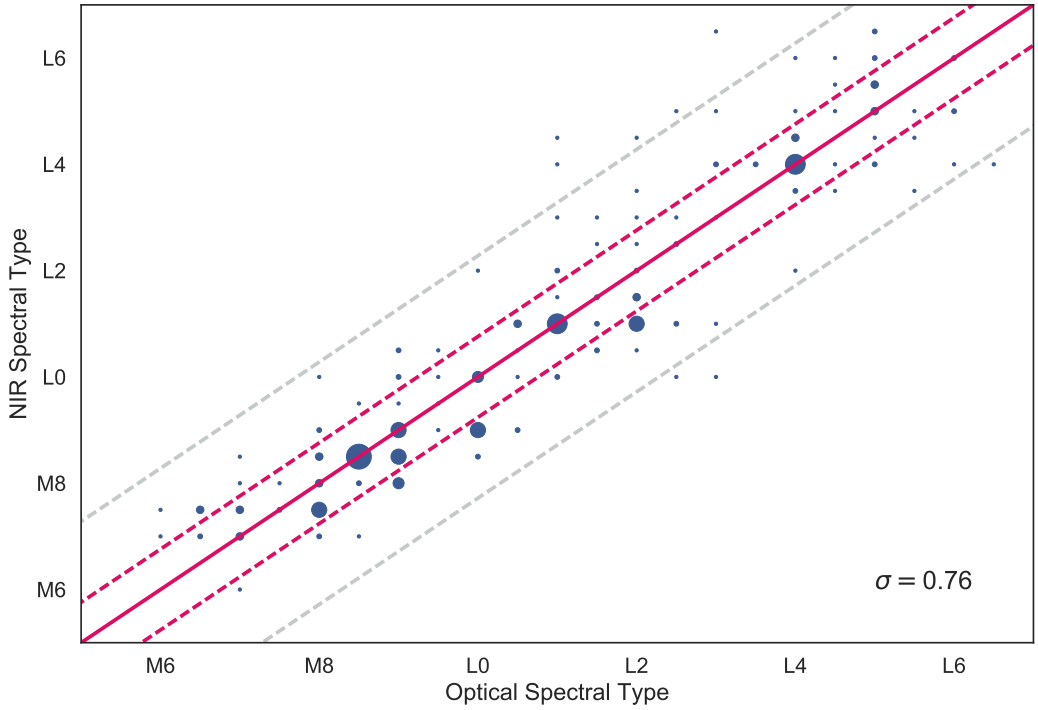

Figure 5.4 Comparison of optical and near-infrared spectral types from the literature for the M7−L5 25 pc sample. The size of the circles scales as the cube of the number of repeated points. The solid line marks where the slope equals one, while the dashed lines encompass the 1σ and 3σ limits in pink and silver, respectively.

infrared spectral types. The Allers et al. (2007) indices are the best at predicting optical spectral types within $\sigma = 0.67$ types. The scatter is larger for near-infrared types, with a tendency to predict spectral types earlier than measured in the literature. For both optical and near-infrared types, the Reid et al. (2001a) indices predict spectral types within a subtype. All spectral types for sample sources are summarized in Table 5.3.

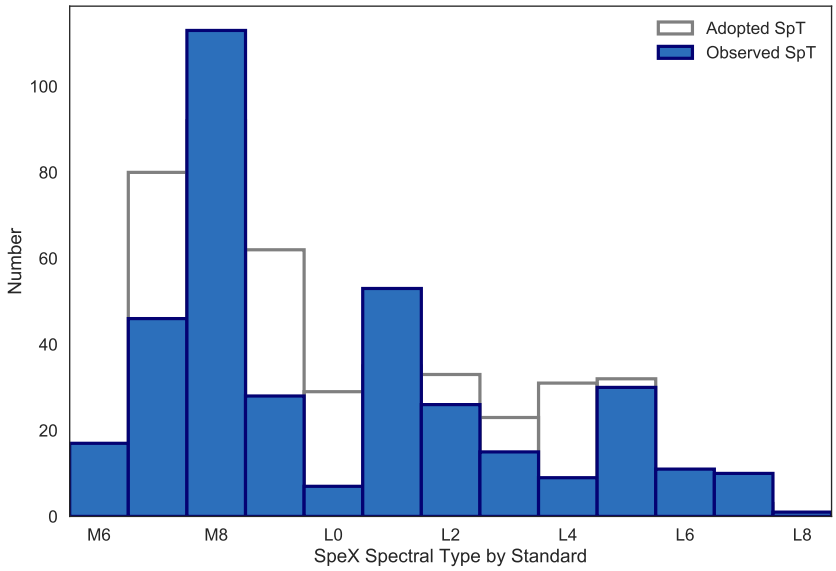

Figure 5.5 Distribution of observed SpeX spectral type as classified by Kirkpatrick et al. (2010) near-infrared standards.

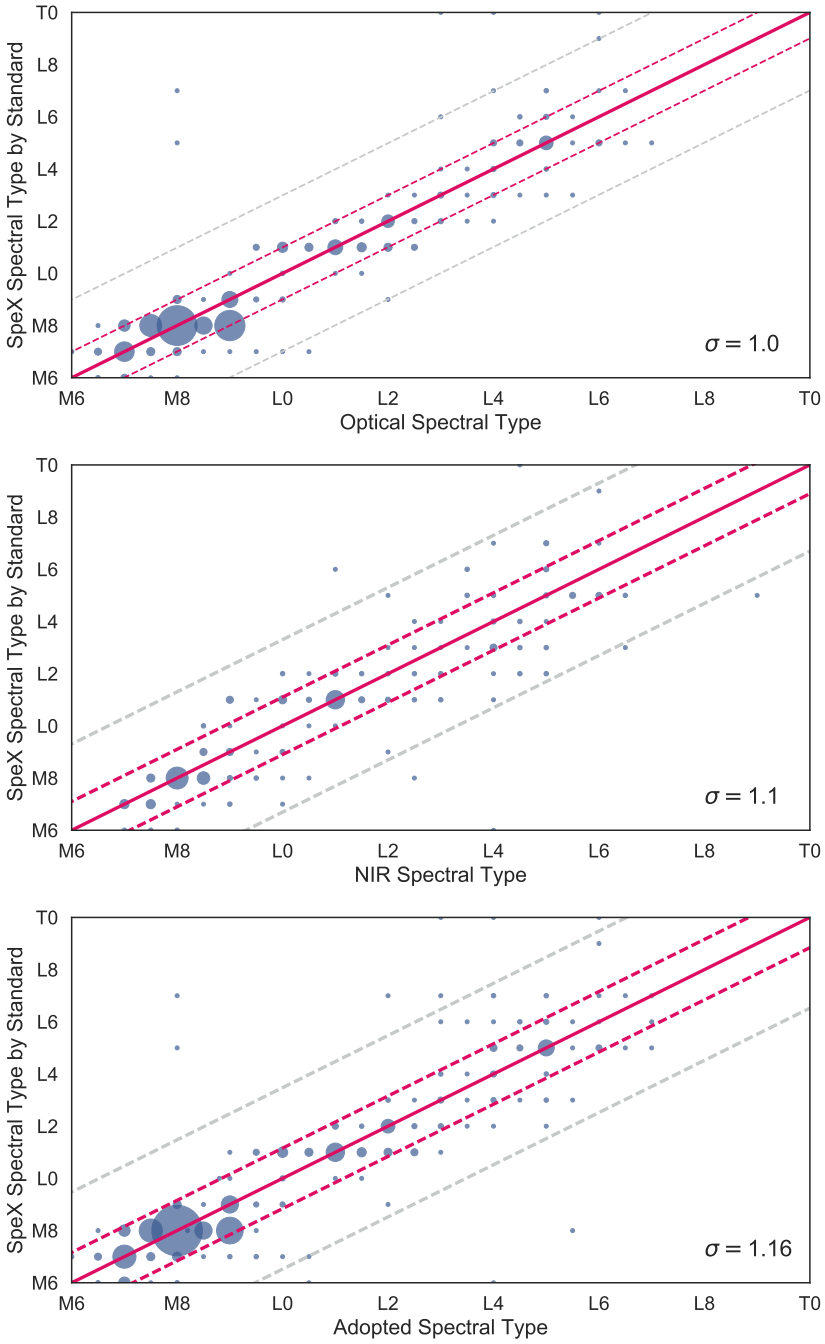

Figure 5.6 Literature optical and near-infrared spectral types compared against measured spectral types with Kirkpatrick et al. (2010) near-infrared standards. Circle sizes are proportional to the frequency of a given optical-NIR spectral type pair. The solid line has a slope of one, and the dashed lines are the 3σ limits.

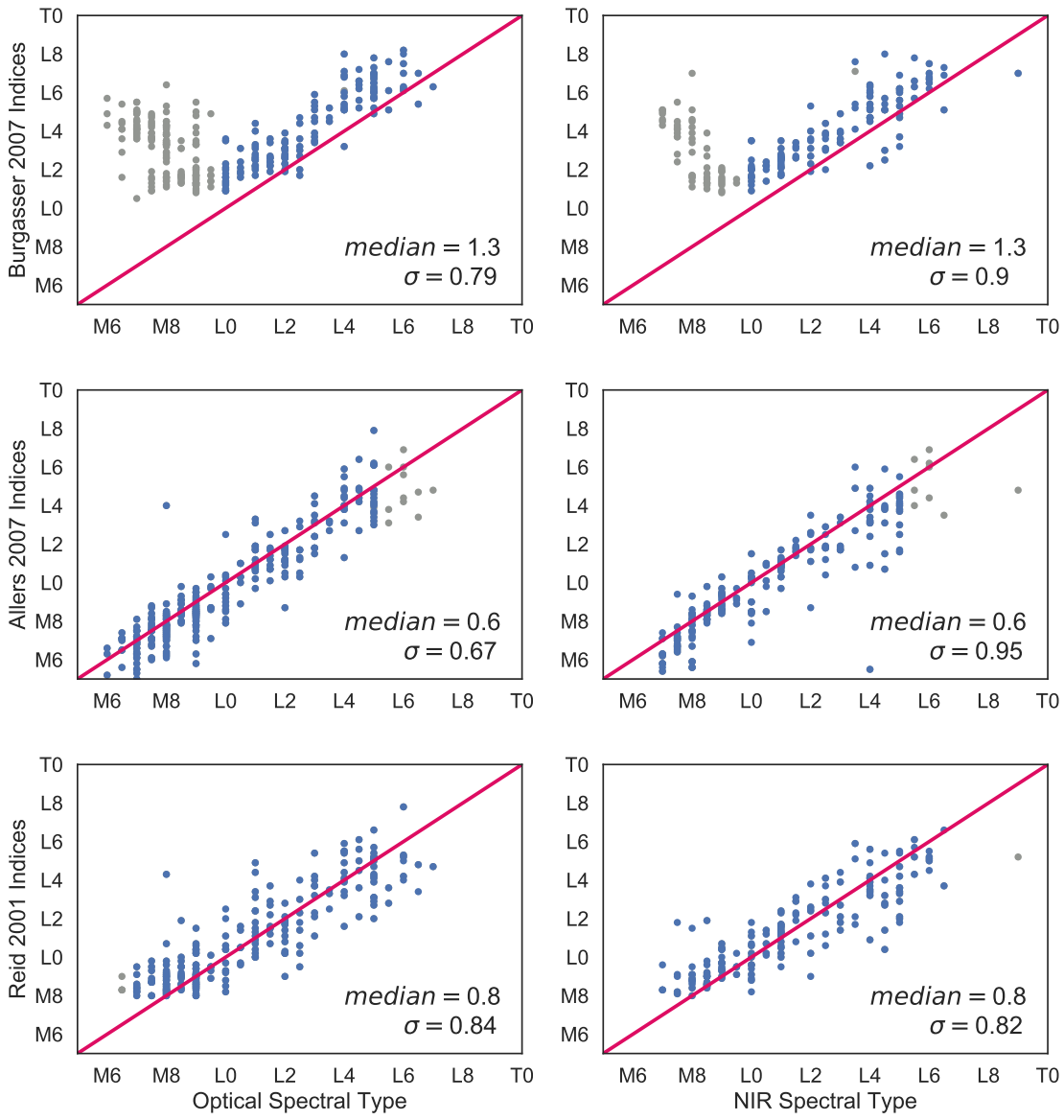

Figure 5.7 Literature optical and near-infrared spectral types compared against measured spectral types with the index sets of Burgasser (2007a), Allers et al. (2007) and Reid et al. (2001a). Points outside the spectral type ranges defined for each index classification are plotted in gray and do not enter the σ calculation.

Table 5.3 Spectral type classification for M7−L5 25 pc Sample

Designation	Literature Spectral Type					NIR Standard	Classification by Indices			References
	Adopted	Optical	NIR	SIMBAD	SDSS		Burgasser (2007a)	Allers et al. (2007)	Reid et al. (2001a)	
J00043484−4044058B	L5.0	L5	L4.5	L5+L5	···	L4.0	L5.7±0.6	L3.9±0.3	L2.7±0.8	113;143;23
J00043484−4044058C	L5.0	L5	···	L5+L5	···	···	···	···	···	23; ··· ;23
J00065794−6436542	L0.0	L0	M8γ	M9:	···	···	···	···	···	98;66;23
J00130931−0025521	M7.0	M7	···	M6.0V	···	M6.0	L4.2:±1.1	M6.1±0.3	···	57; ··· ;112
J00145575−4844171	L2.5	L2.5 p	L2.5:	L2.5	···	L3.0	L4.4±0.6	L2.9±0.4	L3.0±0.8	20;147;39
J00154476+3516026	L2.0	L2	L1	L2V	···	L2.0	L2.8±0.6	L0.9±0.3	L0.8±0.8	21;129;21
J00192626+4614078	M8.0	M8	M8γ	M8	···	M8.0	L3.3:±1.1	M7.2±0.3	M8.1:±1.2	2;66;80
J00194579+5213179	M9.0	M9	···	M9	···	M8.0	L1.2±0.8	M8.4±0.4	M9.1±0.8	80; ··· ;80
J00242463−0158201	M9.5	M9.5	L0.5	M9.5V	···	L1.0	L2.0±0.6	M9.8±0.3	L0.1±0.8	29;129;170
J00265632−5428530	M8.0	M8	···	···	···	···	···	···	···	97; ··· ; ···
J00275592+2219328A	M7.5	M7.5 + M8	···	M8Ve	···	M8.0	L2.6:±1.4	M7.6±0.4	M8.4±0.8	122; ··· ;5
J00275592+2219328B	M8.0	M8	···	M8Ve	···	···	···	···	···	5; ··· ;5
J0028208+224905	L7.0	···	L5 β	L7:	···	L6.0	L5.9±0.9	L2.7±0.7	L3.0±0.9	··· ;66;158
J00311925−3840356	L2.5	L2.5	L2 p(blue)	L2pec	···	L1.0	L4.7±0.6	L3.2±0.5	L4.0±0.8	98;89;89
J003154778+06494639	M8.0	···	M8.0	M7	···	M8.0	L3.6:±1.1	M7.4±0.3	···	··· ;115;23
J00332386−1521309	L4.0	L4β	L1	L4	···	L6.0	L3.5±0.6	L1.1±0.4	L1.7:±1.1	125;148;39
J00361617+1821104	L3.5	L3.5	L4	L3.5	···	L2.0	L4.7±0.5	L3.1±0.3	L3.5±0.8	21;143;26
J00413538−5621127	M6.5	M6.5 + M9	M7.5	M7.5e	···	···	···	···	···	126;66;118
J00452143+1634446	L3.5	L2β	L3.5	L3.5	···	L6.0	L4.1±0.6	L0.8±0.4	L1.7±0.8	125;17;39

Table 5.3 Continued

Designation	Literature Spectral Type					NIR Standard	Classification by Indices			References
	Adopted	Optical	NIR	SIMBAD	SDSS		Burgasser (2007a)	Allers et al. (2007)	Reid et al. (2001a)	
J00464841+0715177	L0.0	L0::	L0 γ	L0	···	L1.0	L1.8±0.6	L0.1±0.3	L2.0±0.8	23;66;66
J004926771−06354671	M9.0	···	M9.0	M8.5	···	M9.0	L1.6±0.6	M9.1±0.3	M10.0±0.8	··· ;115;39
J00525468−2705597	M7.5	M7.5:	···	M7.5:V	···	M8.0	L0.9±0.6	M8.7±0.4	M9.5±0.8	127; ··· ;127
J00531899−3631102	L3.5	L3.5	L4:	L4	···	L4.0	L5.2±0.6	L3.2±0.4	L3.3±0.8	20;147;58
J01004911−1933398	L3.0	L3.0	···	L3.0	···	···	···	···	···	128; ··· ;128
J01025100−3737438	M8.0	M8	M8	M8.0V	···	M8.0	L2.9:±1.1	M7.8±0.3	M8.6±0.8	29;129;136
J01090150−5100494	M8.5	M8.5	M7	M8.5e	···	···	···	···	···	33;147;33
J01095117−0343264	M9.0	M9	···	M9Ve	···	M9.0	L2.5:±1.2	M8.0±0.3	M8.0:±1.0	112; ··· ;5
J01231125−6921379	M7.5	M7.5	···	M8	···	···	···	···	···	80; ··· ;80
J01243124−0027556	M7.0	M7	···	M7V	···	M7.0	L5.1:±1.1	M6.0±0.3	···	··· ; ··· ;71
J01282664−5545343	L2.0	L2	L1	L1	···	···	···	···	···	23;18;39
J01311838+3801554	L4.0	L4:	···	L4	···	L2.0	L3.2±0.6	L1.3±0.4	L1.6±0.8	29; ··· ;39
J01410321+1804502	L1.0	L1	L4.5	L4.5	···	L2.0	L2.5±0.6	L0.7±0.3	L0.4±0.8	29;39;39
J01443536−0716142	L5.0	L5	L5	L6.5	···	L6.0	L4.9±0.6	L3.0±0.4	L2.0±0.8	30;147;58
J01483864−3024396	M7.5	M7.5	···	M7.5	···	M8.0	L3.7:±1.3	M7.7±0.4	M8.7:±1.3	2; ··· ;80
J01490895+2956131	M9.5	M9.5	M9.5	M9.5V	···	L1.0	L1.7±0.6	M9.7±0.3	M9.5±0.8	129;129;171
J01550354+0950003	L4.0	L5	L4 β	L4	···	L4.0	L5.2±0.7	L3.4±0.5	L3.1±0.9	23;66;66
J02050344+1251422	L5.0	L5	···	L5V	···	L6.0	L6.0±0.6	L3.6±0.4	L3.9±0.8	21; ··· ;21
J02081833+2542533	L1.0	L1	···	L1V	···	L2.0	L2.8±0.6	L0.7±0.3	L0.7±0.8	21; ··· ;21

Table 5.3 Continued

Designation	Literature Spectral Type					NIR Standard	Classification by Indices			References
	Adopted	Optical	NIR	SIMBAD	SDSS		Burgasser (2007a)	Allers et al. (2007)	Reid et al. (2001a)	
J02115089+4728300	M8.0	···	M8.0	M7	···	M8.0	L3.9:±1.2	M7.8±0.3	M9.1±0.8	··· ;115; ···
J02132880+4444453	L1.5	L1.5	···	L1.5	···	L1.0	L1.9±0.6	L0.7±0.3	L1.5±0.8	2; ··· ;80
J02150802−3040011	M8.0	M8	···	M8	···	M8.0	L3.5:±1.1	M7.4±0.3	M8.6±0.8	29; ··· ;80
J02182913−3133230	L3.0	L3	L4	L3	···	L3.0	L4.7±0.6	L3.2±0.5	L3.7±0.8	2;129;39
J02192210−3925225	L4.0	···	L4	M6+L4	···	M6.0	L4.7:±1.1	M5.5±0.3	···	··· ;149;149
J02271036−1624479	L1.5	L1.5	L0.5:	L1.5	···	L0.0	L2.2±0.6	L0.1±0.3	L0.7:±1.0	58;147;58
J02284243+1639329	L0.0	L0:	M8.5	L0	···	M9.0	L1.0±0.6	M8.1±0.3	M8.5:±1.0	23;129;80
J02284355−6325052	L1.0	L1	L0	L0.5	···	···	···	···	···	23;18;11
J02354955−0711214	M7.0	M7	···	M7V	···	M7.0	L4.2:±1.1	M6.6±0.3	···	57; ··· ;71
J02355993−2331205	L1.5	L1.5	L1	L1.5	···	L2.0	L2.4±0.6	L0.7±0.3	L0.5±0.8	58;31;58
J024029501+28325766	M7.5	M7.5	···	M7.5	···	M7.0	L4.0:±1.1	M6.9±0.3	M8.4:±1.2	119; ··· ;116
J02484100−1651216	M8.0	M8	···	M8e	···	M8.0	L5.3:±1.5	M6.3±0.4	···	79; ··· ;3
J0251148−035245	L3.0	L3	L1	···	···	···	···	···	···	2;17; ···
J02530084+1652532	M6.5	M6.5	M7.5	M7	···	M6.0	L2.9:±1.1	M7.4±0.3	M9.0±0.8	130;150;99
J0253202+271333	M8.0	M8	···	M8.0V	···	M8.0	L3.4:±1.2	M7.9±0.3	M9.3:±1.2	2; ··· ;112
J02540582−1934523	M9.0	M9	M9	M9	···	M8.0	L1.9±0.8	M8.6±0.3	M9.4±0.8	23;151;23
J03061159−3647528	M8.0	M8	L0	M7/8.5e	···	M8.0	L1.6±0.8	M8.4±0.3	M9.1±0.8	33;33;28
J03122509+0021585	M7.0	M7	···	M7V	···	M7.0	L4.6:±1.1	M6.6±0.3	···	··· ; ··· ;71
J03140344+1603056	L0.0	L0	M9 p	L0	···	L1.0	L1.3±0.5	M9.2±0.3	M9.5±0.8	80;66;39

Table 5.3 Continued

Designation	Literature Spectral Type					NIR Standard	Classification by Indices			References
	Adopted	Optical	NIR	SIMBAD	SDSS		Burgasser (2007a)	Allers et al. (2007)	Reid et al. (2001a)	
J03144011−0450316	M7.5	M7.5	···	M7.5	···	M8.0	L3.9:±1.1	M7.5±0.3	···	2; ··· ;2
J03205965+1854233	M8.0	M8	···	M8V	···	M8.0	L4.2:±1.4	M7.5±0.3	···	2; ··· ;89
J03264453+1919309	M8.5	M8.5	M8.5	M8.5	···	M8.0	L1.9±0.8	M7.9±0.3	M8.6:±1.0	23;129;23
J03283463+1129515	M8.0	M8	···	M8	···	M8.0	L1.8±0.8	M8.4±0.3	M9.1±0.8	29; ··· ;80
J03300506+2405281	M7.0	M7	···	M7	···	M7.0	L4.5:±1.1	M6.3±0.3	···	39; ··· ;39
J03313025−3042383	M7.5	M7.5	···	M7.5V	···	M8.0	L3.5:±1.2	M7.5±0.3	M8.7:±1.2	2; ··· ;2
J03341218−4953322	M9.0	M9	M8	M9	···	M8.0	L1.7±0.5	M9.3±0.3	L1.5±0.8	34;152;39
J03393521−3525440	M9.5	M9.5	L0	M9.5Ve	···	L1.0	L1.4±0.6	L0.3±0.3	L1.8±0.8	131;153;131
J03395284+2457273	M8.0	M8	M7.5	M8V	···	M8.0	L3.9:±1.1	M7.1±0.3	···	129;129; ···
J03442102+3206158	M8.0	M8	···	M2.75	···	M9.0	L1.4±0.6	M8.2±0.3	M9.5±0.8	··· ; ··· ;172
J03442694+3203494	M9.0	M9	···	M4.75	···	M8.0	L5.5:±1.1	M5.8±0.3	···	··· ; ··· ;172
J034429979+32192276	L0.0	···	L0.0	···	···	L0.0	L2.5:±1.1	M6.9±0.9	L0.7:±1.7	··· ;115; ···
J03505737+1818069	M9.0	M9.0	···	M9.0V	···	M8.0	L5.0:±1.1	M7.0±0.3	···	112; ··· ;112
J03510004−0052452	M8.0	M8	M7.5	M8.0V	···	M7.0	L4.5:±1.1	M6.4±0.3	···	57;129;112
J03521086+0210479	M9.0	M9	L0:	M9	···	M9.0	L1.7±0.8	M8.5±0.3	M8.9±0.8	23;18;23
J03550477−1032415	M8.5	M8.5	M8.5γ	M8.5	···	M8.0	L1.7±0.8	M8.3±0.3	M9.2±0.8	39;66;39
J03552337+1133437	L3.0	L5γ	L3 γ	L3−L6	···	L7.0	L6.6±0.6	L1.5±0.3	L2.6±0.8	125;66;66
J04013766+2849529	L3.0	···	L2.5	L3	···	L4.0	L3.8±0.6	L1.9±0.3	L2.3±0.8	··· ;37;37
J04041807+4127398	L2.0	L2	L3 p(red)	L2	···	L3.0	L3.4±0.6	L1.9±0.3	L1.8±0.8	37;6;37

Table 5.3 Continued

Designation	Literature Spectral Type					NIR Standard	Classification by Indices			References
	Adopted	Optical	NIR	SIMBAD	SDSS		Burgasser (2007a)	Allers et al. (2007)	Reid et al. (2001a)	
J04082905−1450334	L2.0	L2	L4.5	L4.5	···	L2.0	L3.0±0.6	L1.5±0.3	L1.4±0.8	2;17;39
J041539163+28185862	M9.0	···	M9.0	M3.75	···	···	···	···	···	··· ;115;173
J04173745−0800007	M7.5	M7.5	···	M7.5V	···	M8.0	L3.7:±1.2	M7.5±0.3	M8.7:±1.2	2; ··· ;112
J041807965+28260370	M8.0	···	M8.0	M6	···	M8.0	L1.4:±1.3	M7.2±0.4	M8.8±0.8	··· ;115;174
J04210718−6306022	L5.0	L5 β	L5 γ	L5	···	···	···	···	···	125;121;23
J042154823+26423722	M8.0	···	M8.0	···	···	M6.0	L4.5:±1.1	M5.6±0.3	···	··· ;115; ···
J042353227−00065872	···	···	···	M8.5	···	M8.0	L1.0±0.6	M8.9±0.4	L0.0±0.8	··· ; ··· ;39
J042450211+26410066	M8.0	···	M8.0	···	···	M8.0	L4.2:±1.2	M5.9±0.3	···	··· ;115; ···
J04270723+0859027	M8.0	M8	M9	M8	···	M8.0	L0.8±0.5	M8.5±0.3	M9.2±0.8	23;129;23
J042724678+26241993	M8.0	···	M8.0	···	···	M6.0	L7.0:±1.1	M5.9±0.4	···	··· ;115; ···
J04291842−3123568	M7.5	M7.5	···	M7.5:	···	M8.0	L4.9:±1.1	M6.1±0.3	···	2; ··· ;80
J04305157−0849007	M8.0	M8	M8.5	M8V	···	M8.0	L1.5±0.8	M8.3±0.3	M8.5±0.8	132;129;2
J04351455−1414468	M8.0	M8	young M	M8	···	L7.0	L2.6±0.5	M7.8±0.3	L0.7:±1.0	39;154;39
J04351612−1606574	M8.0	M8	M7	M8Ve	···	M7.0	L4.3::±2.2	M7.4±0.5	M9.6:±1.4	131;129;131
J04390101−2353083	L6.5	L6.5	···	L4.5	···	L5.0	L7.0±0.6	L4.7±0.4	L4.8±0.8	2; ··· ;58
J04402325−0530082	M7.0	M7	···	M7.5Ve	···	M8.0	L3.6:±1.5	M7.2±0.4	···	131; ··· ;131
J044104244+25575612	M7.0	···	M7.0	···	···	M6.0	L4.1:±1.1	M5.6±0.3	···	··· ;115; ···
J04430581−3202090	L5.0	L5	L6.5:	L5	···	L5.0	L6.9±0.6	L6.1±0.9	L5.4±0.8	40;129;39
J04433761+0002051	M9.0	M9	L0 γ	M9.0V	···	M9.0	L1.3±0.6	M9.5±0.3	L0.4±0.8	29;66;112

Table 5.3 Continued

Designation	Literature Spectral Type					NIR Standard	Classification by Indices			References
	Adopted	Optical	NIR	SIMBAD	SDSS		Burgasser (2007a)	Allers et al. (2007)	Reid et al. (2001a)	
J04455387−3048204	L2.0	L2	···	L2	···	L1.0	L2.0±0.6	L0.3±0.3	L0.2±0.8	2; ··· ;80
J044806329+15512512	L2.0	···	L2.0	M4.5	···	···	···	···	···	··· ;115;175
J04510093−3402150	L0.5	L0.5	L0.5	L0.5	···	L1.0	L2.4±0.6	L1.0±0.3	L1.4±0.8	2;129;2
J05002100+0330501	L4.0	L4	L4	L4	···	L3.0	L5.1±0.6	L4.0±0.3	L4.1±0.8	23;66;23
J05004808+0442143	L1.0	···	L1.0	···	···	L1.0	L2.5±0.6	L0.9±0.3	L1.2±0.8	··· ;115; ···
J05012406−0010452	L4.0	L4γ	L3 γ	L4	···	L7.0	L5.7±0.6	L1.9±0.4	L3.8±0.8	125;66;66
J050441399+25095440	M9.0	···	M9.0	M3.5	···	···	···	···	···	··· ;115; ···
J05061292+0439272	M7.0	M7	···	M3	···	···	···	···	···	··· ; ··· ; ···
J050855063+33192721	L2.0	···	L2.0	···	···	L2.0	L3.5±0.6	L1.4±0.3	L1.8±0.8	··· ;115; ···
J05102012+2714032	M8.0	M8	···	M7V	···	···	···	···	···	120; ··· ;104
J05120636−29495400	L4.5	L4.5	L5 γ	L5	···	L6.0	L7.2±0.7	L3.9±0.7	L5.2±0.9	20;66;66
J05153094+5911185	M7.5	M7.5	···	M7V	···	···	···	···	···	120; ··· ; ···
J05173766−3349027	M8.0	M8.0	M9	M8.0V	···	···	···	···	···	112;129;112
J05181131−3101529	M6.5	M6.5	M7γ	M6.5	···	M7.0	L3.6:±1.1	M6.5±0.3	···	28;66;92
J05233822−1403022	L2.5	L2.5	L5	L2.5	···	L2.0	L3.2±0.6	L1.7±0.3	L1.8±0.8	2;17;80
J05264316−1824315	M7.0	···	M7β	···	···	M7.0	L3.8:±1.1	M6.5±0.3	···	··· ;66; ···
J05301261+6253254	L1.0	L1	L1	L1	···	L1.0	L2.6±0.6	L1.7±0.4	L2.4±0.8	23;129;23
J05345844−1511439	M9.0	M9	M9	M9	···	M9.0	L2.0±0.8	M8.8±0.3	M9.0±0.8	39;129;39
J05372332−0816055	M7.0	···	M7.0	M6.5	···	M6.0	L5.0:±1.1	M5.8±0.3	···	··· ;115;3

Table 5.3 Continued

Designation	Literature Spectral Type					NIR Standard	Classification by Indices			References
	Adopted	Optical	NIR	SIMBAD	SDSS		Burgasser (2007a)	Allers et al. (2007)	Reid et al. (2001a)	
J05392474+4038437	M8.0	M8	···	M8	···	M8.0	L3.6:±1.1	M7.4±0.3	M8.1±0.8	39; ··· ;39
J05394952+5253597	L5.0	···	L5	···	···	L2.0	L3.7±0.6	L1.6±0.3	L2.1±0.8	··· ;45; ···
J05395200−0059019	L5.0	L5	L5	L5	···	L5.0	L6.2±0.6	L4.6±0.4	L4.7±0.8	72;143;58
J05431887+6422528	L1.0	L1	L2	L1	···	L1.0	L2.7±0.6	L1.8±0.3	L2.4±0.8	23;66;23
J05441150−2433018	M8.0	M8	M7.5	M8	···	M8.0	L2.4:±1.1	M7.7±0.3	M8.1±0.8	80;129;80
J05480722+0033588	M7.0	M7	···	···	···	···	···	···	···	··· ; ··· ; ···
J05500794+1610519	L2.0	···	L2	···	···	L3.0	L4.0±0.6	L2.6±0.3	L2.6±0.8	··· ;6; ···
J06022216+6336391	L1.0	L1:	L2	L2	···	L2.0	L3.1±0.6	L1.7±0.3	L1.1±0.8	23;129;66
J06023045+3910592	L1.0	L1	L1	L1V	···	L1.0	L2.5±0.5	L1.0±0.3	L1.5±0.8	133;153;47
J06091922−3549311	L3.0	···	L3γ	···	···	···	···	···	···	··· ;153; ···
J06145280+4536556	M9.0	M9	···	M9	···	M8.0	L3.3:±1.1	M7.8±0.3	M8.5:±1.0	2; ··· ; ···
J06154934−01004158	L2.0	L2+/−1	···	L2.5	···	L1.0	L2.6±0.6	L1.2±0.3	L1.7±0.8	48; ··· ;48
J06244172+6626309	L1.0	···	L1	L1	···	L1.0	L2.1±0.6	L1.0±0.4	L1.3±0.8	··· ;37;37
J06244595−4521548	L5.0	L5:	L5	L6.5	···	L7.0	L6.0±0.7	L3.7±0.6	L2.9±0.9	23;129;58
J06300140−1840143	M8.5	M8.5	···	M8.5	···	M8.0	L1.7±0.5	M9.3±0.3	L0.0±0.8	48; ··· ;48
J06320617+8305014	L0.5	L0.5	···	L0.5	···	···	···	···	···	23; ··· ;23
J06411840−4322329	L1.5	L1.5	L2.5:	L1.5	···	L1.0	L3.6±0.6	L2.5±0.4	L3.7±0.8	23;129;23
J06431685−1843375	M8.0	M8.0	···	M8.0V	···	M9.0	L1.6±0.6	M8.3±0.3	M8.9±0.8	106; ··· ;106
J06521977−2534505	L0.0	L0	M9	L0	···	L1.0	L1.6±0.6	M9.4±0.3	L0.4±0.8	39;129;39

Table 5.3 Continued

Designation	Literature Spectral Type					NIR Standard	Classification by Indices			References
	Adopted	Optical	NIR	SIMBAD	SDSS		Burgasser (2007a)	Allers et al. (2007)	Reid et al. (2001a)	
J06523073+4710348	L4.5	L4.5	···	L3.5+L6.5	···	L5.0	L6.6±0.6	L4.8±0.4	L5.0±0.8	2; ··· ;138
J06572547−4019134	M7.5	M7.5	···	M7.5	···	M6.0	L4.8:±1.1	M6.0±0.3	···	39; ··· ;39
J07003664+3157266	L3.5	L3.5	···	L3.5+L6	···	L3.0	L4.5±0.6	L2.7±0.4	L2.5±0.8	134; ··· ;138
J07025026−6102482	M7.0	···	···	M7.0	···	···	···	···	···	··· ; ··· ;86
J07075327−4900503	M8.5	M8.5	M8	M8.5e	···	M8.0	L1.3±0.6	M8.6±0.3	M9.5±0.8	44;129;33
J07111138+4329590	M7.0	M7	M7	M5.5V	···	···	···	···	···	120; ··· ;99
J07140394+3702459	M8.0	M8	···	M8	···	M8.0	L3.5:±1.2	M7.5±0.3	M8.8:±1.2	80; ··· ;80
J071551828−11452847	L4.0	···	L4pec(blue)	···	···	L5.0	L6.1±0.6	L5.3±0.8	L6.1:±1.0	6; ··· ; ···
J07164790−0630369	L1.0	L1:	L1	L1	···	L1.0	L1.7±0.6	M9.7±0.4	L0.2±0.8	48;129;48
J07171626+5705430	L3.0	L3	L6.5	L3	···	L3.0	L5.1±0.6	L3.5±0.4	L3.7±0.8	23;17;58
J07200325−0846499	M9.0	M9:	L0 p	M9.5+T5	···	M9.0	L2.1±0.5	M9.0±0.3	M9.6±0.8	51;129;79
J07231462+5727081	L1.0	L1	L0	L1	···	L1.0	L2.0±0.6	L0.2±0.3	M10.0±0.8	23;129;23
J07235262−3309435	L5.0	···	L5 red	···	···	L3.0	L4.7±0.7	L2.5±0.6	L3.4±0.9	··· ;155; ···
J07410681+1738459	M7.0	M7	···	M7.0V	···	M8.0	L4.7:±1.1	M6.8±0.3	···	29; ··· ;112
J07421169−1211516	L4.8	···	WD?	···	···	···	···	···	···	··· ;6; ···
J07464256+2000321	L0.5	L0.5	L1	L0.5V	···	L1.0	L1.8±0.6	L0.3±0.3	L0.5±0.8	21;143;21
J07511645−2530432	L2.5	L2.5	L1	L1.5	···	L1.0	L2.7±0.6	L1.3±0.3	L2.3±0.8	48;129;48
J07522390+1612157	M7.0	M7	···	M7.0V	···	M7.0	L5.5:±1.1	M5.3±0.3	···	2; ··· ;56
J08040580+6153336	M9.0	M9:	···	M9	···	M9.0	L4.2:±1.1	M7.7±0.3	M8.1:±1.0	23; ··· ;80

Table 5.3 Continued

Designation	Literature Spectral Type					NIR Standard	Classification by Indices			References
	Adopted	Optical	NIR	SIMBAD	SDSS		Burgasser (2007a)	Allers et al. (2007)	Reid et al. (2001a)	
J08053189+4812330	L4.0	L4	L4.5 + T5	L5	···	T0.0	L8.0±0.6	L5.9±0.9	L5.4:±1.1	41;156;58
J08072607+3213101	M8.0	M8	···	M8	···	M8.0	L3.8:±1.1	M7.6±0.3	M8.0:±1.2	29; ··· ;80
J08105865+1420390	M8.0	M8	···	M8V	···	M8.0	L3.4:±1.1	M7.3±0.3	···	29; ··· ;71
J08123170−2444423	L2.5	L2.5:	L1	L1.5	···	L1.0	L1.7±0.6	L0.3±0.3	M9.5±0.8	48;129;48
J08151407+1030117	M7.0	M7	···	M7	···	M7.0	L4.1:±1.1	M7.1±0.3	M8.2:±1.2	23; ··· ;23
J08185804+2333522	M7.0	M7	···	M7	···	M8.0	L4.9:±1.1	M6.3±0.3	···	29; ··· ;80
J08230313−4912012	L1.5	L1.5	L3	L1.5	···	L2.0	L3.4±0.6	L1.7±0.3	L2.7±0.8	48;106;48
J08283419−1309198	L2.0	L2	L2:	L2	···	L1.0	L2.3±0.5	L1.1±0.3	L0.2±0.8	33;147;53
J08294949+2646348	M6.5	M6.5	···	···	···	M7.0	L4.4:±1.1	M6.5±0.3	···	76; ··· ; ···
J08303256+0947153	M8.0	M8	M8	M7.5Ve	M8	M8.0	L3.9:±1.1	M7.1±0.3	···	129;129;176
J08352366+1029318	M9.0	M9	M8	M7	···	M8.0	L3.9:±1.1	M7.5±0.3	···	23;129;23
J08354256−0819237	L6.5	L6.5	L4	L6.5	···	L7.0	L5.4±0.6	L3.4±0.3	L3.4±0.8	58;147;58
J08355829+05483080	L3.0	L3	···	L3	Ldwarf	L2.0	L3.4±0.6	L1.8±0.3	L2.3±0.8	39; ··· ;39
J08402975+1824091	M6.0	M6	M7	M6.0V	···	M7.0	L4.9:±1.1	M6.3±0.3	···	56;129;56
J08472872−1532372	L2.0	L2	···	L1.5	···	L2.0	L2.7±0.6	L0.5±0.3	L0.3±0.8	2; ··· ;58
J08500174−1924184	M8.0	M8	···	M8	···	M8.0	L1.4±0.8	M7.8±0.3	M8.8±0.8	39; ··· ;39
J08513558+7727182	M8.0	M8:	···	M8:	···	···	···	···	···	23; ··· ;23
J08522464+2540591	M6.0	M6	···	M7V	M6	M6.0	L5.7:±1.1	M5.2±0.3	···	57; ··· ;71
J08533619−0329321	M9.0	M9	M8.5	M9Ve	···	L0.0	L1.3±0.8	M8.3±0.3	M9.0:±1.0	82;129;82

Table 5.3 Continued

Designation	Literature Spectral Type					NIR Standard	Classification by Indices			References
	Adopted	Optical	NIR	SIMBAD	SDSS		Burgasser (2007a)	Allers et al. (2007)	Reid et al. (2001a)	
J08581519+1945470A	M7.0	M8	···	···	···	M6.0	L4.6:±1.1	M6.1±0.3	···	123; ··· ; ···
J08581519+1945470B	M7.0	···	M7	M7V	···	M5.0	L5.1:±1.1	M5.4±0.3	···	··· ;104;104
J08593854+6341355	L0.0	L0	M8.5	L0	M9	L0.0	L2.1±0.8	M8.8±0.4	M9.2:±1.0	23;129;23
J08594029+1145325	M8.0	M8	M8.5	M8	···	M9.0	L2.7:±1.1	M8.1±0.3	M8.5:±1.0	129;129;23
J09002359+2150054	M6.0	M6.0	M7.5	M6.5V	···	M7.0	L4.3:±1.1	M6.6±0.3	···	63;129;63
J09020690+0033195	M7.0	M7	M7.5	M6V	···	M7.0	L4.1:±1.1	M6.8±0.3	···	57;129;89
J09054654+5623117	L5.0	L5	···	L5	···	L5.0	L7.0:±1.7	L4.8:±1.5	L5.1:±1.6	23; ··· ;58
J09083803+5032088	L5.0	L5	L9	L8	···	L5.0	L7.0±0.6	L4.8±0.4	L5.2±0.8	2;143;58
J09095749−0658186	L0.0	L0	L0	L0	···	L1.0	L2.0±0.6	L0.3±0.3	L0.6±0.8	20;129;116
J09111297+7401081	L0.0	L0	···	L0	···	···	···	···	···	23; ··· ;80
J09113059+2248111	M7.0	M7	···	M7V	M6	M6.0	L5.0:±1.1	M5.5±0.3	···	··· ; ··· ;71
J09161504+2139512	M9.0	M9	···	M9V	M9	M8.0	L2.0±0.6	M9.7±0.3	L0.4±0.8	71; ··· ;71
J09211410−2104446	L1.0	L1	L4 p(blue)	L1	···	L1.0	L4.4±0.6	L3.3±0.4	L4.9±0.8	58;157;58
J09230296−2300415	M8.2	···	···	···	···	M8.0	L1.1±1.0	M8.7±0.5	M9.2±0.8	··· ; ··· ; ···
J09282562+4230545	M8.5	M8.5	···	M8	···	M8.0	L1.5±0.8	M8.4±0.3	M8.9±0.8	2; ··· ;71
J09424604+5531025	M8.0	M8	···	M8V	···	M8.0	L1.1±0.6	M8.3±0.3	M9.0±0.8	57; ··· ;71
J09473829+3710178	M7.0	M7	···	M7.0V	···	M6.0	L4.5:±1.3	M6.1±0.4	M8.4:±1.2	57; ··· ; ···
J09492223+0806450	M8.5	M8.5	M8.5	M8.5	···	M8.0	L3.1:±1.1	M8.3±0.3	M8.4±0.8	23;129;23
J09524622+0620410	M8.0	M8	M7.5	M8	···	M7.0	L2.8:±1.1	M7.0±0.3	M8.2±0.8	129;129;67

Table 5.3 Continued

Designation	Literature Spectral Type					NIR Standard	Classification by Indices			References
	Adopted	Optical	NIR	SIMBAD	SDSS		Burgasser (2007a)	Allers et al. (2007)	Reid et al. (2001a)	
J09532126−1014205	L0.0	L0	M9	L0	···	L1.0	L1.4±0.6	M9.7±0.3	L0.4±0.8	29;66;39
J10031918−0105079	M7.0	M7	M8	M7Ve	···	M8.0	L3.6:±1.1	M7.5±0.3	M8.0:±1.2	57;129;60
J10042066+5022596	L2.0	L3β	L4 γ	L2	···	L7.0	L8.0±0.7	L3.2±0.5	L4.9±0.8	125;66;39
J10043929−33351889	L4.0	L4	L4.5:	L4	···	L3.0	L5.4±0.6	L4.0±0.4	L4.0±0.8	60;129;39
J10063197−1653266	M7.5	M7.5	···	M7.5	···	M8.0	L3.6:±1.1	M7.1±0.3	···	2; ··· ;80
J10163470+2751497	M8.0	M8	M7.5	M8V	M7	M8.0	L4.1:±1.1	M6.7±0.3	···	89;129;89
J10170754+1308398	L2.0	L2:	L1	L3	L0	L2.0	L2.7±0.6	L1.1±0.3	L1.2±0.8	2;17;177
J101726800+07192609	M8.0	···	M8.0	···	···	M7.0	L4.6:±1.1	M6.7±0.3	···	··· ;115; ···
J10192447−2707171	L0.5	L0.5	M9	M9.5	···	M7.0	L1.9±0.8	M8.9±0.4	L0.5±0.8	98;129;18
J10195684+7324087	M8.5	M8.5	···	M8.5	···	···	···	···	···	2; ··· ; ···
J10213232−2044069	M9.0	M9	M8.5	M9	···	M8.0	L1.3±0.8	M8.5±0.3	M8.7±0.8	23;129;23
J10224821+5825453	L1.0	L1β	L1	L1	···	L1.0	L2.2±0.6	L0.8±0.3	L1.4±0.8	125;153;39
J10240997+1815533	M8.0	M8	···	M8	···	M7.0	L4.2:±1.2	M6.7±0.4	···	23; ··· ;80
J10292165+1626526	L2.5	L2.5	L3	L2.5	L2	L2.0	L3.6±0.6	L1.7±0.3	L1.4±0.8	21;129;21
J10451718−2607249	M8.0	M8	···	M8	···	M8.0	L3.4:±1.1	M8.1±0.3	M8.3±0.8	23; ··· ;23
J10452400−0149576	L1.0	L1	L1	L1	···	L1.0	L2.1±0.6	L0.6±0.3	L0.0±0.8	60;153;80
J10471381+4026493A	M8.0	M9	M8	M9V	···	M8.0	L1.6±0.8	M8.0±0.3	M8.6±0.8	71;14;71
J10471381+4026493B	L0.0	···	L0	M9V	···	···	···	···	···	··· ;14;71
J10473108−18155739	L2.5	L2.5	L0	L2.5	···	L1.0	L2.0±0.6	L0.5±0.3	L0.2±0.8	62;153;116

Table 5.3 Continued

Designation	Literature Spectral Type					NIR Standard	Classification by Indices			References
	Adopted	Optical	NIR	SIMBAD	SDSS		Burgasser (2007a)	Allers et al. (2007)	Reid et al. (2001a)	
J10481258−1120082	M7.0	M7	···	M6.0V	···	M7.0	L4.0:±1.1	M6.9±0.3	M8.5:±1.2	63; ··· ;63
J10481463−3956062	M9.0	M9	···	M9V	···	M8.0	L0.8±0.8	M9.1±0.7	L0.2±0.9	23; ··· ; ···
J10482788−5254180	L1.5	L1.5	···	L1.5	···	···	···	···	···	48; ··· ;48
J10484281+0111580	L1.0	L1	L4	L1	···	L1.0	L2.2±0.6	L0.9±0.3	L0.9±0.8	41;81;58
J10511900+5613086	L2.0	L2	L1	L2	···	L1.0	L2.3±0.6	L1.2±0.3	L0.6±0.8	23;129;80
J10541102−8505023	M8.0	···	···	M8	···	···	···	···	···	··· ; ··· ; ···
J10544168+1214084	M7.5	M7.5	···	M7.5	···	M7.0	L3.9:±1.1	M6.8±0.3	···	39; ··· ;39
J10554733+0808427	M9.0	M9	M8.5	M9V	M9	M8.0	L1.2±0.8	M8.4±0.3	M8.6±0.8	57;129;71
J10584787−1548172	L3.0	L3	L3	L2.5	···	L4.0	L3.9±0.6	L1.8±0.3	L2.1±0.8	74;66;58
J11040127+1959217	L4.0	L4	···	L4	L4	L5.0	L5.8±0.6	L4.4±0.4	L4.4±0.8	2; ··· ;58
J11061897+0428327	M7.0	M7	M7.5	M6.5V	···	M7.0	L3.7:±1.1	M7.2±0.3	M9.1:±1.2	82;129;8
J11073750−2759385	M7.0	···	M7	···	···	M7.0	L4.6:±1.2	M6.3±0.4	···	··· ;65; ···
J11083081+6830169	L1.0	L1	L1γ	L0.5	···	···	···	···	···	66;66;80
J11122567+3548131	L4.5	L4.5	L5	L4.5+L6:	···	L6.0	L5.6±0.6	L4.2±0.4	L3.6±0.8	21;158;178
J11214924−1313084	M8.0	M8	M8.5	M8+L7.5	···	M9.0	L1.0±0.6	M8.5±0.3	M9.0±0.8	··· ;129; ···
J11232934+0154040	M7.0	M7	···	M7	M6III	M7.0	L4.3:±1.1	M7.5±0.3	M8.3±0.8	··· ; ··· ;67
J11240487+3808054	M8.5	M8.5	···	M8.5V	···	M8.0	L1.6±0.8	M8.9±0.3	M9.5±0.8	2; ··· ;2
J11263991−5003550	L5.0	L5	L6.5 p	L5	···	L5.0	L7.3±0.6	L6.1:±1.2	L6.6:±1.1	58;157;58
J11345493+0022541	M9.0	M9	···	M9	···	M8.0	L3.5:±1.1	M7.2±0.3	M8.0:±1.0	23; ··· ;23

Table 5.3 Continued

Designation	Literature Spectral Type					NIR Standard	Classification by Indices			References
	Adopted	Optical	NIR	SIMBAD	SDSS		Burgasser (2007a)	Allers et al. (2007)	Reid et al. (2001a)	
J113911077+0841121	M8.0	···	M8.0	M7.5	···	M8.0	L1.7±0.8	M8.1±0.3	M8.9±0.8	··· ;115;23
J11414406−2232156	M7.5	M7.5	M8	M7.5V	···	M8.0	L1.1±0.6	M8.4±0.3	M8.8±0.8	2;129;2
J11524266+2438079	M9.0	M9	···	M9V	···	···	···	···	···	71; ··· ;71
J11535267+0659561	M8.0	M8	M7	M8V	···	M7.0	L4.3:±1.1	M6.2±0.3	···	135;129;135
J11543399+0135545	M9.0	M9:	···	M9:	···	M8.0	L3.3:±1.1	M8.1±0.3	M8.5±0.8	23; ··· ;23
J11553952−3727350	L2.0	L2	L2.5	L2	···	L2.0	L3.1±0.6	L1.8±0.3	L2.8±0.8	60;129;23
J11554286−2224586	M7.5	M7.5	M7.5	M7.5V	···	M8.0	L3.7:±1.1	M7.1±0.3	···	136;129;136
J11555389+0559577	L6.0	L6	L6−L8 p	L5	···	L9.0	L7.5±0.6	L6.9±0.9	L5.3:±1.1	69;66;58
J11592743−5247188	M9.0	M9	···	M9V	···	···	···	···	···	··· ; ··· ; ···
J120032924+2048513	···	···	···	M8V	···	···	···	···	···	··· ; ··· ;71
J12035812+0015500	L3.0	L3	L5	L4	L2	L3.0	L5.3±0.6	L4.1±0.4	L4.2±0.8	72;129;23
J12130336−0432437	L5.0	L5	L4	L5	···	L3.0	L5.8±0.6	L4.2±0.5	L4.1±0.8	2;129;80
J12210359+0857217	M7.0	···	M7.0	M:	···	M7.0	L5.1:±1.1	M5.8±0.3	···	··· ;115; ···
J12212770+0257198	L0.5	L0.5	M9 p	L0.5	M9	L1.0	L2.1±0.6	L0.3±0.3	M9.7±0.8	58;66;58
J12245222−1238352	M9.0	M9	M8.5	M8Ve	···	M9.0	L1.5±0.8	M8.4±0.3	M9.1:±1.0	60;129;60
J12281523−1547342	L5.0	L5	L6	L5	···	L5.0	L6.5±0.7	L4.4±0.6	L5.0±0.9	74;143;170
J12321772−6856005	M8.0	M8	···	M8	···	···	···	···	···	48; ··· ;48
J12392727+5515371	L5.0	L5	···	L5V	L5	L6.0	L6.5±0.6	L4.6±0.4	L4.9±0.8	21; ··· ;21
J12405273+1129387	L1.0	L1.0	L1:	···	···	···	···	···	···	··· ;75; ···

Table 5.3 Continued

Designation	Literature Spectral Type					NIR Standard	Classification by Indices			References
	Adopted	Optical	NIR	SIMBAD	SDSS		Burgasser (2007a)	Allers et al. (2007)	Reid et al. (2001a)	
J12464678+4027150	L4.0	L4	L4	L4V	···	L4.0	L6.1±0.6	L4.5±0.4	L4.9±0.8	21;129;21
J12465176+3148104	M7.0	M7.0	···	M7.0V	···	M7.0	L5.0:±1.2	M6.3±0.3	···	··· ; ··· ; ···
J12505265−2121136	M6.5	M6.5	···	M7.5e	···	M8.0	L4.1:±1.1	M7.1±0.3	M8.3:±1.2	··· ; ··· ;33
J12522264+0252058	M8.0	M8	···	M8V	M8	M8.0	L3.3::±3.1	M7.2±0.9	M8.3:±1.5	57; ··· ;71
J12531092−5709248	L0.5	L0.5	···	L0.5	···	···	···	···	···	48; ··· ;48
J12531240+4034038	M7.5	M7.5	···	M7.0V	M7	M7.0	L4.5:±1.1	M7.1±0.3	···	29; ··· ; ···
J12560215−1257217	M7.5	M7.5	M7.5	M7.0	···	M7.0	L4.2:±1.1	M6.7±0.3	···	78;78;78
J12565688+0146163	L2.0	L2:	L1.5	L2	···	L2.0	L3.4±0.6	L1.6±0.3	L0.8±0.8	23;129;39
J12590470−4336243	M8.0	···	···	M8:	···	···	···	···	···	··· ; ··· ;79
J13004255+1912354	L1.0	L1	L3 p(blue)	L1	···	L1.0	L3.3±0.6	L1.9±0.4	L3.4±0.8	49;157;80
J13054019−2541059A	L2.0	L2	L1.5	L2+L3.5	···	L2.0	L3.7±0.6	L2.2±0.4	L2.3±0.8	74;144;124
J13054019−2541059B	L3.5	L2+L3.5	L3.5	L2+L3.5	···	···	···	···	···	124; ··· ; ···
J13054106+2046394	L4.0	L4:	L5	L5	L5	L5.0	L6.9±0.6	L5.5±0.8	L5.5±0.8	2;159;159
J13082507+0725512	M9.0	M9	···	M9	M9	M8.0	L1.8±0.8	M8.8±0.3	M8.7±0.8	23; ··· ;23
J13092185−2330350	M8.0	M8	···	M7Ve	···	M8.0	L3.8:±1.1	M7.5±0.3	M8.2:±1.0	2; ··· ;60
J13113921+8032219	M8.0	M8.0	···	···	···	···	···	···	···	··· ; ··· ;39
J13142039+1320012	M7.0	M7	M6:	M6.0V	···	···	···	···	···	120;140;99
J13153094−2649513	L5.5	L5.5	L3.5:: + T7	L3.5+T7	···	L5.0	L7.6±0.6	L6.0±0.8	L5.1±0.8	20;160;160
J13171150+1849232	M9.0	M9	···	M9V	M8	M8.0	L4.8:±1.1	M6.3±0.3	···	71; ··· ;71

Table 5.3 Continued

Designation	Literature Spectral Type					NIR Standard	Classification by Indices			References
	Adopted	Optical	NIR	SIMBAD	SDSS		Burgasser (2007a)	Allers et al. (2007)	Reid et al. (2001a)	
J13261625+5640448	M7.0	M7	···	M7V	M7	M7.0	L0.5±0.8	M7.2±0.8	M8.4:±1.0	57; ··· ;71
J13314894−0116500	L6.0	L6	L8 p(blue)	T0	L5	T0.0	L8.2±0.7	···	L7.8:±1.2	41;75;58
J13322442−0441126	M7.5	M7.5	···	M7.5	···	M8.0	L3.2:±1.3	M7.6±0.4	···	2; ··· ;80
J13365044+4751321	M8.0	M8	···	M8V	M8	M8.0	L3.3:±1.2	M7.7±0.3	···	71; ··· ;71
J13382615+4140342	L2.5	L2.5	L2.5	L2.5V	···	L2.0	L3.0±0.7	L1.2±0.4	L0.6±0.8	21;129;21
J13564148+4342587	M7.0	M7	···	M7	···	M8.0	L4.1:±1.1	M7.7±0.3	M8.2:±1.0	80; ··· ;80
J13595510−4034582	L1.0	L1	L3:	L1	···	L1.0	L4.0±0.6	L3.1±0.4	L4.4:±1.0	23;129;23
J14032232+3007547	M9.0	M9	···	M9V	M8	M8.0	L1.7±0.8	M8.2±0.3	M8.4±0.8	71; ··· ;71
J14112131−2119503	M9.0	M9	M8.5β	M9V	···	M8.0	L1.0±0.6	M8.5±0.3	M9.4±0.8	2;66;2
J14122449+1633115	L0.5	L0.5	L0	L0.5V	···	L1.0	L1.6±0.6	L0.0±0.3	M9.6±0.8	21;129;21
J14162408+1348263	L5.0	L5	L6:: p	L5	L5	L5.0	L6.7±0.5	L6.2±0.8	L5.1:±1.0	58;161;58
J14211873−1618201	M7.5	M7.5	···	M7.5	···	M8.0	L1.3±0.6	M8.8±0.3	M9.8±0.8	39; ··· ;39
J14213145+1827407	L0.0	L0	M9	L0	···	L0.0	L0.9±0.6	M8.6±0.3	M9.3:±1.0	23;129;23
J14222424+2116076	M8.0	M8	···	M8V	M8	M8.0	L3.8:±1.1	M7.6±0.3	M8.4±0.8	71; ··· ;71
J14252798−3650229	L3.0	L3:	L3 β	L4	···	L6.0	L5.5±0.6	L3.1±0.4	L4.0±0.8	23;66;66
J1426316+155701	M9.0	M9	···	M9V	M9	M8.0	L1.6:±1.3	M8.7±0.8	M9.0±1.0	2; ··· ;71
J14280420+1356137	M7.5	M7.5	···	M7V	···	···	···	···	···	120; ··· ;104
J14283132+5923354	L4.0	L4	L4.5	L4	L4	L4.0	L5.1±0.6	L3.8±0.4	L3.2±0.8	23;129;23
J14284323+3310391	M9.0	M9	M9	M9Ve	···	M9.0	L1.5±0.8	M8.4±0.3	M8.9:±1.0	82;11;82

Table 5.3 Continued

Designation	Literature Spectral Type					NIR Standard	Classification by Indices			References
	Adopted	Optical	NIR	SIMBAD	SDSS		Burgasser (2007a)	Allers et al. (2007)	Reid et al. (2001a)	
J14304358+2915405A	L2.0	L2	L0.5	L0.5	···	L2.0	L3.1±0.6	L1.7±0.3	L1.7±0.8	2;17;39
J14304358+2915405B	L2.0	···	L3.5	L0.5	···	···	···	···	···	··· ;145;39
J14343616+2202463	L5.5	···	L2.5	L1	L5.5	M8.0	L3.9±0.6	L1.8±0.3	L4.1±0.8	··· ;162;58
J14380829+6408363	L0.0	L0	L0	M9.5	···	M9.0	L0.9±0.6	M8.5±0.3	M8.8±0.8	57;129;80
J14392836+1929149	L1.0	L1	···	L1	L1	L1.0	L2.2±0.5	L1.2±0.3	L1.8±0.8	58; ··· ;58
J14402293+1339230	M8.0	M8	···	M7V	···	L5.0	L6.4±0.6	L4.0±0.4	L4.3±0.8	29; ··· ;71
J14422164+6603208	L0.0	L0	L0:	M3V	···	M7.0	L3.5:±1.1	M7.9±0.3	M8.2±0.8	84;163;179
J14442067−2019222	M9.0	sdM9	d/sdM7	M9.0VI:	···	M7.0	L2.1±0.6	M8.2±0.3	L0.6±0.8	137;129;137
J144506278+4409393	M8.0	···	M8.0	M7.5	···	M8.0	L5.1:±1.2	M5.6±0.4	···	··· ;115;86
J14460061+0024519	L6.0	L6	L5	L6	···	L5.0	L6.2±0.7	L4.4±0.6	L4.0±0.9	41;75;41
J14480337+1554149	M7.0	M7	···	M7	···	M7.0	L5.0:±1.1	M5.8±0.3	···	39; ··· ;39
J14482563+1031590	L4.0	L4:	L3.5	L5.5	L4	L5.0	L7.1±0.6	L4.9±0.7	L5.9±0.8	23;17;58
J14501581+2354424	L4.0	L4	L4: + L4:	L4	···	···	···	···	···	88;88;88
J14540797−6604476	L3.5	L3.5	···	L3.5	···	···	···	···	···	48; ··· ;48
J14562776+1755090	M7.0	M7	···	M6	···	M7.0	L3.8:±1.1	M7.0±0.3	M8.3:±1.2	2; ··· ; ···
J14563831−2809473	M7.0	M7	M7.5	M7V	···	M8.0	L4.1:±1.1	M7.2±0.3	···	63;129;170
J145638314−28094738	M7.0	M7	M7	M7.0Ve	···	···	···	···	···	61;141;63
J14573965+4517167	M9.0	M9	···	M9	···	M9.0	L1.6±0.8	M8.3±0.3	M8.6:±1.1	29; ··· ;116
J14582453+2839580	M8.5	M8.5	M8.5	M8.5V	M9	M8.0	L3.5:±1.2	M8.0±0.3	M8.6:±1.0	89;129;89

Table 5.3 Continued

Designation	Literature Spectral Type					NIR Standard	Classification by Indices			References
	Adopted	Optical	NIR	SIMBAD	SDSS		Burgasser (2007a)	Allers et al. (2007)	Reid et al. (2001a)	
J15002635−0039281	M7.0	M7	···	M7V	M6	M6.0	L5.5:±1.1	M5.0±0.3	···	71; ··· ;71
J15010818+2250020	M8.5	M8.5	M9.5	M8.5V	M9	M8.0	L1.4±0.5	M9.1±0.3	L0.2±0.8	89;129;89
J15041621−2355564	M7.5	M7.5	···	M7Ve	···	M8.0	L1.9±0.9	M7.8±0.4	···	2; ··· ;60
J15065441+1321060	L3.0	L3	L4	L3	···	L3.0	L4.5±0.6	L2.4±0.4	L3.2±0.8	49;164;58
J15072779−2000431	M7.5	M7.5	···	M7.5	···	M8.0	L1.5±0.8	M7.9±0.4	M8.0:±1.0	80; ··· ;80
J15074769−1627386	L5.0	L5	L5.5	L5V	···	L5.0	L5.7±0.9	L4.0±0.7	L4.3±0.9	21;143;21
J15101685−0241078	M9.0	M9	M9.5	M9V	···	M9.0	L1.3±0.6	M8.9±0.3	M9.1±0.8	89;129;89
J15104786−2818174	M9.0	M9	M9	M9	···	M8.0	L1.3±0.6	M9.5±0.3	L0.7±0.8	23;66;23
J15150083+4847416	L6.0	L6	L6	L6	L5	L5.0	L7.0±0.7	L6.0±0.9	L5.2±0.8	29;17;80
J15200224−4422419B	L4.5	···	L4.5	L4.5	···	···	···	···	···	··· ;146;48
J15210103+5053230	M7.5	M7.5	···	M7.5	···	M8.0	L3.6:±1.1	M7.5±0.3	···	80; ··· ;80
J15230657−2347526	L2.5	···	L2.5	L2.5	···	L1.0	L2.0±0.6	L0.4±0.4	L1.2±0.8	··· ;18;39
J15242475+2925318	M7.5	M7.5	···	M7.5V	···	M7.0	L4.3:±1.1	M7.0±0.3	M8.0:±1.2	89; ··· ;89
J15261405+2043414	L7.0	L7	···	L5	···	L5.0	L6.3±0.6	L4.8±0.5	L4.7±0.8	21; ··· ;58
J15291017+6312539	M8.0	···	M8β	···	···	M8.0	L1.6±0.8	M7.8±0.3	M8.9±0.8	··· ;66; ···
J15345325+1219495	L6.0	L6	L4:	L3	Ldwarf	L5.0	L6.3±0.6	L4.2±0.4	L4.2±0.8	··· ;165;58
J15345704−1418486	M7.0	M7	M8.5	M7	···	M8.0	L3.9:±1.1	M8.1±0.3	M8.6±0.8	80;129;80
J153824172−19531162	L6.0	L4γ	L3.5	L6	···	L6.0	L5.4±0.9	L1.7±0.7	L3.1:±1.1	121;121;39
J15394189−0520428	L4.0	L4:	L2	L3.5	···	L5.0	L5.3±0.6	L3.5±0.4	L3.8±0.8	20;81;80

Table 5.3 Continued

Designation	Literature Spectral Type					NIR Standard	Classification by Indices			References
	Adopted	Optical	NIR	SIMBAD	SDSS		Burgasser (2007a)	Allers et al. (2007)	Reid et al. (2001a)	
J15394442+7437273	M9.0	M9	···	M9	···	···	···	···	···	23; ··· ;80
J15404341−5101357	M7.0	M7	M7	M7	···	···	···	···	···	90;90;79
J15445518+3301447	L6.0	L6	···	···	Ldwarf	L5.0	L6.1±0.6	L5.6±0.9	L5.0±0.8	··· ; ··· ; ···
J15460540+3749458	M7.5	M7.5	···	M7.5V	···	M7.0	L4.7:±1.1	M6.1±0.3	···	29; ··· ;112
J15464185−5534468	M7.5	M7.5	···	M7.5	···	···	···	···	···	92; ··· ;92
J15485834−1636018	L2.0	L2	L2:	L2	···	M9.0	L1.9±0.8	M8.7±0.3	M9.0±0.8	39;18;39
J15510662+6457047	M8.0	M8	···	M8.5	···	M8.0	L4.3:±1.1	M7.8±0.3	M8.3:±1.0	29; ··· ;116
J15525906+2948485	L1.0	L0β	L0	L1	L2	L2.0	L2.2±0.6	L0.3±0.3	L1.3±0.8	125;148;39
J15531993+1400337	M9.0	M9	···	M9	M9	M9.0	L3.3:±1.1	M7.8±0.3	M8.4:±1.0	29; ··· ;2
J15551573−0956055	L1.0	L1	L1.5	L1	···	L1.0	L3.2±0.6	L1.9±0.3	L3.1±0.8	60;129;39
J16073123−0442091	M8.0	M8	···	M8	···	M9.0	L3.2:±1.1	M7.8±0.3	···	23; ··· ;23
J16081603−3903042	M7.5	···	···	M7.5	···	···	···	···	···	··· ; ··· ;94
J16095217−2136277	M7.0	M7	···	M7	···	···	···	···	···	95; ··· ;96
J16134550+1708270	M9.5	M9.5	···	M9	···	L1.0	L1.5±0.6	M9.3±0.3	M9.8±0.8	··· ; ··· ;67
J16141484−2427081	M7.0	M7	···	M7	···	···	···	···	···	96; ··· ;96
J16154245+0546400	M9.0	M9	···	M9	···	M9.0	L1.1±0.6	M9.0±0.3	M9.4±0.8	23; ··· ;80
J16154416+3559005	L4.0	L4	L3.5	L3V	L2	···	···	···	···	21;129;21
J16271142−2348505	M8.8	···	···	···	···	L0.0	L1.3±0.6	M7.6±0.3	M9.6±0.8	··· ; ··· ; ···
J16272794+8105075	M9.0	M9	···	M9	···	···	···	···	···	29; ··· ;39

Table 5.3 Continued

Designation	Literature Spectral Type					NIR Standard	Classification by Indices			References
	Adopted	Optical	NIR	SIMBAD	SDSS		Burgasser (2007a)	Allers et al. (2007)	Reid et al. (2001a)	
J16325882−0631481	M7.0	M7	···	M7	···	M8.0	L3.3:±1.1	M8.0±0.3	M8.6±0.8	23; ··· ;23
J16331306−7553232	M9.5	M9.5	···	···	···	···	···	···	···	··· ; ··· ; ···
J16334908−6808480	M8.0	···	M8 + M8.5	···	···	···	···	···	···	··· ;97; ···
J16351919+4223053	M9.0	M9	M8.5	M9V	M9	M8.0	L0.9±0.6	M8.6±0.3	M9.6±0.8	71;129;71
J16452211−1319516	L1.5	L1.5	···	L1	···	L1.0	L2.4±0.6	L1.2±0.3	L1.5±0.8	60; ··· ;58
J16553529−0823401	M7.0	M7 V	···	M7.0V	···	M7.0	L3.9:±1.1	M7.5±0.3	M9.5:±1.2	··· ; ··· ;99
J16573454+1054233	L2.0	L2	L1.5	L2	···	L1.0	L3.1±0.6	L1.7±0.3	L1.9±0.8	23;129;23
J16580380+7027015	L1.0	L1	···	L1	···	···	···	···	···	49; ··· ;80
J17054834−0516462	L0.5	L0.5	L1	L1	···	L1.0	L2.6±0.6	L1.0±0.3	L1.7±0.8	23;153;58
J17065487−1314396	L5.0	···	L5 p	L5pec	···	L4.0	L5.6±0.6	L4.0±0.5	L3.3±0.8	··· ;66;66
J17071830+6439331	M9.0	M9	···	M8.5	···	···	···	···	···	23; ··· ;169
J17072343−0558249A	M9.0	···	M9	M9+L3	···	L1.0	L1.2±0.6	M9.3±0.3	M9.7±0.8	··· ;19;23
J17072343−0558249B	L3.0	···	L3	M9+L3	···	L1.0	L4.9±0.6	L3.4±0.4	L3.9±0.8	··· ;19;23
J17114559+4028578	L5.0	···	L5 p(blue)	L5	···	L5.0	L6.6±0.6	L6.0±0.9	L5.2:±1.1	··· ;100;100
J17125121−0507249	M9.5	···	M7.5	M1V	···	M7.0	L1.8±0.6	M9.4±0.3	L1.8±0.8	··· ; ··· ;180
J17163523−0315431	L0.0	L0.0	···	···	···	···	···	···	···	··· ; ··· ; ···
J17171408+6526221	L4.0	L4	L6	L4	···	L7.0	L6.8±0.6	L4.8±0.4	L5.5±0.8	41;129;41
J17210390+3344160	L3.0	L3	L5 p(blue)	L3	···	T0.0	L5.9±0.6	L4.5±0.4	L5.4:±1.0	80;157;80
J17264070−2737593	L5.0	L5	L5 p(blue)	L5	···	···	···	···	···	103;103;103

Table 5.3 Continued

Designation	Literature Spectral Type					NIR Standard	Classification by Indices			References
	Adopted	Optical	NIR	SIMBAD	SDSS		Burgasser (2007a)	Allers et al. (2007)	Reid et al. (2001a)	
J17312974+2721233	L0.0	L0	L0	L0	···	L1.0	L1.2±0.5	M9.0±0.3	M9.4±0.8	23;148;23
J17331893+4633593	M9.5	M9.5	···	M9.5V	···	M7.0	L4.9:±1.0	M7.1±0.4	M8.9:±1.2	29; ··· ;112
J17334227−1654500	L0.5	L0.5:	L1	L0.5	···	L1.0	L3.1±0.6	L1.0±0.3	L1.6±0.8	48;129;39
J17335314+1655129	M7.0	M7	···	M6V	···	M6.0	L5.1:±1.1	M5.5±0.3	···	··· ; ··· ;104
J17343053−1151388	M8.5	M8.5	M8.5	M8.5	···	M9.0	L1.6±0.8	M8.6±0.3	M9.0:±1.0	11;11;11
J17351296+2634475	M7.5	M7.5	···	M7.5:	···	M8.0	L1.6±0.7	M8.1±0.3	M9.3±0.8	23; ··· ;80
J17395322+5532451	M7.5	···	M7.5	···	···	M8.0	L5.5:±1.1	M6.5±0.3	···	··· ;115; ···
J17410280−4642218	L7.0	···	L5:−L7: γ	L7	···	L7.0	T1.2±0.3	L4.5±0.5	L5.4±0.8	··· ;66;58
J17430860+8526594	L5.0	···	L5 p(blue)	L5	···	···	···	···	···	··· ;10;10
J17453466−1640538	L1.5	L1.5:	L1.5	L1.5	···	L1.0	L2.6±0.6	L1.8±0.3	L2.9±0.8	48;129;48
J17461199+5034036	L5.0	L5	L5.5	L5	···	L5.0	L6.3±0.6	L4.8±0.5	L5.2±0.8	23;129;23
J17502484−0016151	L4.5	L4.5	L5.5	L4.5	···	L5.0	L6.6±0.6	L6.4±0.8	L6.1:±1.0	58;18;58
J17534518−6559559	L4.0	L4::	L4:	L4	···	···	···	···	···	23;147;80
J17562963−4518224	M9.0	M9	···	M9	···	M8.0	L1.2±0.6	M9.2±0.3	L0.3±0.8	48; ··· ;48
J17565620−4805096	L0.0	L0	···	L0	···	L1.0	L2.3±0.6	L0.4±0.3	L1.1±0.8	48; ··· ;48
J17571539+7042011	M7.5	M7.5	···	M7.5V	···	···	···	···	···	49; ··· ;112
J18000116−1559235	L5.5	L5.5	L4.5	···	···	L3.0	L5.1±0.6	L3.1±0.4	L2.8±0.8	106;129; ···
J18071593+5015316	L1.5	L1.5	L1	L1	···	L1.0	L2.6±0.6	L1.2±0.3	L1.6±0.8	2;17;58
J18212815+1414010	L4.5	L4.5 p	L4 p(red)	L5	···	L5.0	L6.4±0.6	L4.9±0.6	L5.6±0.8	68;66;58

Table 5.3 Continued

Designation	Literature Spectral Type					NIR Standard	Classification by Indices			References
	Adopted	Optical	NIR	SIMBAD	SDSS		Burgasser (2007a)	Allers et al. (2007)	Reid et al. (2001a)	
J18261131+3014201	M8.5	M8.5	M8.5 sd?	M8.5V	···	M7.0	L1.8±0.6	M9.8±0.3	L1.9±0.8	107;129;107
J18300760−1842361	M7.5	M7.5	···	M7.5V	···	···	···	···	···	106; ··· ;106
J18353790+3259545	M8.5	M8.5	···	M8.5V	···	M8.0	L1.7::±2.7	M9.1:±1.3	M9.5:±1.3	2; ··· ;112
J18393308+2952164	M6.5	M6.5	M7	M6.5	···	M7.0	L4.1:±1.1	M7.1±0.3	M8.3:±1.2	5;66; ···
J18432213+4040209	M8.0	M8	···	M7.5Ve	···	M8.0	L3.5:±1.1	M7.3±0.4	M9.8:±1.6	2; ··· ;5
J18450541−6357475	M8.5	M8.5	···	M8.5+T6	···	···	···	···	···	79; ··· ;79
J18451889+3853248	M8.0	M8	···	M8	···	M8.0	L4.5:±1.1	M7.3±0.3	M8.3:±1.2	23; ··· ;80
J18470342+5522433	M6.5	M6.5	···	M7+M7.5	···	M7.0	L5.4:±1.1	M5.6±0.3	···	2; ··· ;138
J19064801+4011089	L1.0	L1	L1	L1	···	L0.0	L2.6±0.6	L0.8±0.3	L1.3:±1.0	109;109;109
J19165762+0509021	M8.0	M8.0	M8	M8Ve	···	M8.0	L2.9:±1.1	M8.1±0.3	M8.4±0.8	63;11;181
J19285196−4356256	L4.0	L4	L4 p	L6	···	L3.0	L6.0±0.7	L3.1±0.5	L3.4±0.8	23;147;58
J19360187−5502322	L5.0	L5:	L4	L5	···	···	···	···	···	23;147;39
J19453551−2557215	M9.0	···	M9	···	···	M7.0	L0.8±0.6	M8.6±0.3	M10.0±0.8	··· ;129; ···
J20004841−7523070	M9.0	M9	M9	M9	···	···	···	···	···	80;66;80
J20025073−0521524	L6.0	L6	L5−L7γ	L5.5	···	L7.0	L8.0±0.8	L4.5±0.8	L5.0±0.9	29;66;58
J20040620+1704125	L4.5	···	L4.5	G0V	···	···	···	···	···	··· ;166;111
J201035392+06343676	M8.5	···	M8.5	M8.5V	···	···	···	···	···	10; ··· ;10
J20140359−2016217	M7.5	M7.5	···	M7.5	···	M8.0	L0.9±0.5	M8.2±0.3	M8.9±0.8	2; ··· ;39
J20282035+0052265	L3.0	L3	···	L2.5	···	L2.0	L3.7±0.6	L2.4±0.4	L2.3±0.8	41; ··· ;58

Table 5.3 Continued

Designation	Literature Spectral Type					NIR Standard	Classification by Indices			References
	Adopted	Optical	NIR	SIMBAD	SDSS		Burgasser (2007a)	Allers et al. (2007)	Reid et al. (2001a)	
J20360316+1051295	L2.0	L2	···	L2	···	L2.0	L3.9±0.6	L2.7±0.4	L2.8±0.8	58; ··· ;58
J20370715−1137569	M8.0	M8	···	M8	···	M7.0	L3.3:±1.1	M7.2±0.3	M8.0:±1.0	80; ··· ;80
J20575409−0252302	L1.5	L1.5	L1.5	L1	···	L1.0	L2.7±0.6	L1.4±0.3	L2.2±0.8	2;81;58
J21041491−1037369	L2.0	L2	···	L2	···	L2.0	L3.5±0.7	L1.8±0.4	L2.1±0.9	58; ··· ;58
J21183174−4505522	M8.5	M8.5	M8.5	M8.5e	···	M8.0	L1.7±0.8	M8.9±0.4	M9.8±0.8	33;129;33
J213630294+05153290	M8.5	M8.5	···	M7.5	···	M8.0	L3.1:±1.1	M8.0±0.3	M8.3±0.8	23; ··· ;23
J21371044+1450475	L2.0	L2	L1	L2	···	L1.0	L2.6±0.6	L1.1±0.3	L1.1±0.8	23;129;23
J21373742+0808463	L5.0	L5:	···	L4	···	L5.0	L6.1±0.6	L4.1±0.5	L4.2±0.8	23; ··· ;39
J21402931+1625183	M8.5	M8.5+L2	M8	M8.5+L2	···	M8.0	L1.6±0.8	M8.4±0.3	M9.1±0.8	138;167; ···
J21580457−1550098	L4.0	L4:	L4	L4	···	L4.0	L5.2±0.5	L3.8±0.3	L3.9±0.8	20;11;58
J22000201−3038327	L0.0	L0	M9	L0	···	M9.0	L1.6±0.6	M9.4±0.4	M9.7±0.8	23;168;39
J22021125−1109461	M6.5	M6.5	M7	M6/6.5e	···	M7.0	L4.5:±1.1	M7.1±0.3	M8.3:±1.0	139;66;28
J22062280−2047058	M8.0	M8.0	···	M8.0V	···	M8.0	L1.6±0.8	M8.2±0.3	M8.6±0.8	112; ··· ; ···
J22244381−0158521	L4.5	L4.5	L3.5	L4.5V	···	L3.0	L5.2±0.6	L2.7±0.4	L2.1±0.8	21;143;21
J22264440−7503425	M8.0	M8	···	M8	···	···	···	···	···	23; ··· ;23
J22285440−1325178	M6.5	M6.5	M7.5	M6Ve	···	M6.0	L1.6:±1.4	M7.0±0.4	···	8;129;8
J22341394+2359559	M9.5	M9.5	···	M9.5V	···	M9.0	L1.7±0.8	M8.7±0.3	M8.9:±1.0	2; ··· ; ···
J22354905+1840298	M7.0	M7	···	M7	···	M7.0	L4.9:±1.1	M6.4±0.3	···	29; ··· ;39
J22373255+3922398	M9.5	M9.5	···	M9.5	···	M9.0	L1.4±0.9	M8.6±0.4	M9.5±0.8	80; ··· ;80

Table 5.3 Continued

Designation	Literature Spectral Type					NIR Standard	Classification by Indices			References
	Adopted	Optical	NIR	SIMBAD	SDSS		Burgasser (2007a)	Allers et al. (2007)	Reid et al. (2001a)	
J22380742+4353179	L1.5	L1.5	L0.5	L1.5	···	L1.0	L2.2±0.6	L0.9±0.3	L1.2±0.8	2;129;39
J22425317+2542573	L3.0	L3	L	L3	···	L2.0	L3.5±0.6	L1.5±0.3	L1.1±0.8	29;25;39
J22490917+3205489	L5.0	L5	···	L5	···	L7.0	L6.8:±1.9	L3.2:±1.5	L3.1:±1.8	29; ··· ; ···
J23062928−0502285	M8.0	M8	···	M8	···	M8.0	L2.6:±1.2	M7.6±0.4	M9.0±0.8	29; ··· ;80
J23065876−5008589	M9.0	M9	L0.5	M9e	···	···	···	···	···	33;33;33
J23072655+8753294	L3.0	L3:	···	L3:	···	···	···	···	···	23; ··· ;23
J23081874+0629514	L0.5	···	···	···	···	M6.0	L5.0:±1.1	M5.8±0.3	···	··· ; ··· ; ···
J23081888+0629551	M8.0	···	M8.0	···	···	M8.0	L1.8±0.8	M8.2±0.3	M8.7±0.8	··· ;115; ···
J23174712−4838501	L5.0	···	L5β	L5	···	L5.0	L6.7±0.6	L4.7±0.5	L5.6±0.8	··· ;11;58
J23224684−3133231	L0.0	L0	L2	L0	···	L1.0	L3.6±0.7	L2.5±0.5	L2.5±0.8	39;153;39
J23272645−1741329	M7.0	···	···	M7V	···	M6.0	L4.2:±1.1	M6.6±0.3	M8.3:±1.2	··· ; ··· ;82
J23294790−1607551	M9.5	M9.5	M9	···	···	M9.0	L1.1±0.6	M8.7±0.3	M9.3±0.8	11;11; ···
J23312174−2749500	M7.5	M7.5	···	M7.0V	···	M8.0	L4.4:±1.1	M8.1±0.3	M8.7±0.8	112; ··· ;112
J23343945+1933041	M8.0	M8	···	M8	···	M8.0	L5.0:±1.1	M7.0±0.3	···	29; ··· ;116
J23371491−0838084	M7.0	M7	···	M7.5Ve	···	M8.0	L4.3:±1.1	M6.9±0.3	···	2; ··· ;5
J23440624−0733282	L4.5	L4.5	L6	L4.5	···	L5.0	L6.2±0.6	L4.4±0.4	L4.5±0.8	20;129;20
J23464599+1129094	M9.0	M9	···	M9	···	M8.0	L1.2±0.5	M8.7±0.3	M9.2:±1.0	23; ··· ;80
J23473680+2702068	M9.0	M9	···	M9	···	M9.0	L1.7±0.8	M8.6±0.3	M8.3±0.8	116; ··· ;116
J23494899+1224386	M8.0	M8	···	M8.0V	···	M8.0	L3.8:±1.1	M7.7±0.3	M8.2:±1.0	29; ··· ;112

Table 5.3 Continued

Designation	Literature Spectral Type					NIR Standard	Classification by Indices			References
	Adopted	Optical	NIR	SIMBAD	SDSS		Burgasser (2007a)	Allers et al. (2007)	Reid et al. (2001a)	
J235122005+30105400	L5.5	L5.5	L5:	L6.5	···	L6.0	L6.1±0.6	L3.8±0.5	L3.6±0.8	11;142;58
J23515044−2537367	M8.0	M8	···	M9e	···	M9.0	L1.2±0.5	M8.9±0.3	M9.2:±1.0	29; ··· ;33
J23520481−2208032	M9.5	···	M9.5	···	···	M8.0	L1.5±0.6	M9.2±0.3	M9.5±0.8	··· ; ··· ; ···
J23535946−0833311	M8.5	M8.5	M8.5	M8.5e	···	M8.0	L1.3±0.8	M8.5±0.3	M9.0±0.8	118;129;118
J23540928−3316266	M9.0	M9	M8	M8.5Ve	···	M8.0	L3.4:±1.1	M8.3±0.3	M8.8±0.8	23;152;182
J23561081−3426044	M9.0	M9.0	L0.5	M9e	···	M8.0	L1.4±0.6	M8.5±0.4	L0.2±0.8	33;33;33

[1]Optical, NIR and SIMBAD spectral type references separated by colons.

References. — (2) Cruz et al. (2003), (3) Reid et al. (2004), (5) Reid et al. (2003), (6) Kirkpatrick et al. (2014), (8) Bessell (1991), (10) Luhman et al. (2012), (11) Kirkpatrick et al. (2010), (14) Close et al. (2003), (17) Wilson et al. (2003), (18) Kendall et al. (2007), (19) McElwain & Burgasser (2006), (20) Kirkpatrick et al. (2008), (21) Kirkpatrick et al. (2000), (23) Reid et al. (2008b), (25) Gizis et al. (2003), (26) Reid et al. (2000), (28) Crifo et al. (2005), (29) Cruz et al. (2007), (30) Liebert et al. (2003), (31) Gizis et al. (2001), (33) Lodieu et al. (2005), (34) Phan-Bao et al. (2006), (37) Castro et al. (2013), (39) Faherty et al. (2009), (40) Kendall et al. (2003), (41) Hawley et al. (2002), (44) Pokorny et al. (2004), (45) Deacon et al. (2014), (47) Salim et al. (2003), (48) Phan-Bao et al. (2008), (49) Gizis et al. (2000b), (51) Scholz (2014), (53) Scholz & Meusinger (2002), (56) Shkolnik et al. (2009), (57) West et al. (2008), (58) Schneider et al. (2014), (60) Gizis (2002), (61) Kirkpatrick et al. (1995), (62) Martín et al. (1999), (63) Davison et al. (2015), (65) Looper et al. (in prep.), (66) Gagné et al. (2015c), (67) Schmidt et al. (2014), (68) Looper et al. (2008b), (69) Schmidt et al. (2010), (71) West et al. (2011), (72) Fan et al. (2000), (74) Kirkpatrick et al. (1999b), (75) Marocco et al. (2015), (76) Jenkins et al. (2009), (78) Gauza et al. (2015), (79) Burgasser et al. (2015b), (80) Schmidt et al. (2007), (81) Kendall et al. (2004), (82) Reid & Gizis (2005), (84) Faherty et al. (2012), (86) Reid et al. (2007), (88) Goto et al. (2002), (89) Kirkpatrick et al. (2011), (90) Pérez Garrido et al. (2014), (92) Rajpurohit et al. (2013), (94) Comerón et al. (2003), (95) Lodieu et al. (2007), (96) Slesnick et al. (2008), (97) Luhman & Sheppard (2014), (98) Martín et al. (2010), (99) Alonso-Floriano et al. (2015), (100) Radigan et al. (2008), (103) Beamín et al. (2013), (104) Newton et al. (2014), (106) Folkes et al. (2012), (107) Lépine et al. (2002a), (109) Gizis et al. (2011), (111) Gray et al. (2006), (112) Deshpande et al. (2012), (113) Kirkpatrick et al. (2001), (115) SpeX Prism Library, (116) Allen et al. (2007), (118) Phan-Bao & Bessell (2006), (119) Allen (2007), (120) Lépine et al. (2009), (121) Faherty et al. (2016), (122) Forveille et al. (2005), (123) Cowley & Hartwick (1982), (124) Koen (2013), (125) Cruz et al. (2009), (126) Liu et al. (2010), (127) Liebert & Ferguson (1982), (128) Testi (2009), (129) Bardalez Gagliuffi et al. (2014), (130) Bouy et al. (2005), (131) Teegarden et al. (2003), (132) McCaughrean et al. (2002), (133) Caballero (2007), (134) Salim & Gould (2003), (135) Thorstensen & Kirkpatrick (2003), (136) Bochanski et al. (2011), (137) Dieterich et al. (2014), (138) Winters et al. (2015), (139) Konopacky et al. (2010), (140) Reid et al. (2002b), (141) Dupuy et al. (2016), (142) Geballe et al. (2002), (143) Liu et al. (2016), (144) Knapp et al. (2004), (145) Stumpf et al. (2008), (146) Radigan et al. (2013), (147) Burgasser et al. (2007b), (148) Marocco et al. (2013), (149) Allers et al. (2010), (150) Artigau et al. (2015), (151) **?**, (152) Phan-Bao (2011), (153) Burgasser et al. (in prep.), (154) Allers & Liu (2013), (155) Kirkpatrick et al. (in prep.), (156) **?**, (157) Burgasser et al. (2007a), (158) Burgasser et al. (2008b), (159) Burgasser et al. (2010a), (160) Gomes et al. (2013), (161) Burgasser et al. (2011b), (162) Bowler et al. (2010), (163) Sheppard & Cushing (2009a), (164) Forveille et al. (2004), (165) Witte et al. (2011), (166) Chiu et al. (2006), (167) Liu et al. (2002), (168) Dupuy & Liu (2012), (169) Burgasser & McElwain (2006), (170) Metodieva et al. (2015), (171) Leggett et al. (2001), (172) Liebert et al. (1999), (173) Reid et al. (2006), (174) Luhman et al. (2003), (175) Furlan et al. (2011), (176) Alves de Oliveira et al. (2012), (177) Esplin et al. (2014), (178) Henry et al. (2004), (179) Zhang et al. (2010), (180) Burgasser et al. (2005), (181) Stephenson (1986), (182) Koen et al. (2010), (183) Tinney et al. (1998), (184) Scholz et al. (2004a).

5.4.3 Gravity Classification

Young brown dwarfs ($\tau \lesssim 200$ Myr) undergo significant contraction and therefore are less dense than their older counterparts. This lower density translates into low surface gravity, whose signatures (i.e. reduced collision induced absorption, narrower alkali lines; Allers et al. 2007; Kirkpatrick et al. 2010) dramatically affect the spectral morphology at near-infrared wavelengths. The young brown dwarf population, due to its low-gravity and dusty atmospheres, shares physical properties with directly-imaged exoplanets, thus aiding in the study of the latter (Faherty et al. 2013b).

We calculated gravity classifications for the SpeX spectra following the near-infrared prescription of Allers & Liu (2013). This technique is defined for the spectral type range M6−L5. From the 350 spectra that fit this criterion according to their SpeX classification by standard, 277 were classified as having field gravity (FLD-G), 63 as intermediate gravity (INT-G) and 10 as very low gravity (VL-G), the latter two listed in Table 5.4. Figure 5.8 shows the distributions of gravity types according to spectral types.

Table 5.4 Intermediate gravity and very low gravity sources in the M7−L5 25 pc Sample

Designation	Spectral Type				Reference	Red/blue
	Optical	NIR	NIR Standard	Gravity		
Very Low Gravity Sources						
J00452143+1634446	L2β	L3.5	L6.0	L1.0	17	···
J00464841+0715177	L0::	L0 γ	L1.0	M9.0	17	···
J03442102+3206158	M8	···	M9.0	M9.0	12	···
J03552337+1133437	L5γ	L3 γ	L7.0	L4.0	23	red
J041807965+28260370	···	M8.0	M8.0	M8.0	12	···
J04351455−1414468	M8	young M	L7.0	L1.0	40	red
J04433761+0002051	M9	L0 γ	M9.0	M9.0	41	···
J16271142−2348505	···	···	L0.0	M9.0	65	···
J034429979+32192276	···	L0.0	L0.0	L1.0	35	···
J10042066+5022596	L3β	L4 γ	L7.0	L2.0	59	red
Intermediate Gravity Sources						
J00275592+2219328B	M8	···	···	M8.0	12	···
J03550477−1032415	M8.5	M8.5γ	M8.0	M8.0	12	···
J03264453+1919309	M8.5	M8.5	M8.0	M8.0	23	···
J02530084+1652532	M6.5	M7.5	M6.0	M8.0	32	···
J02355993−2331205	L1.5	L1	L2.0	L2.0	31	···
J02081833+2542533	L1	···	L2.0	L1.0	21	···
J01025100−3737438	M8	M8	M8.0	M8.0	27	···
J04390101−2353083	L6.5	···	L5.0	L6.0	12	···
J0028208+224905	···	L5 β	L6.0	L6.0	23	···
J00275592+2219328A	M7.5 + M8	···	M8.0	M8.0	12	···
J05264316−1824315	···	M7β	M7.0	M8.0	12	···
J09532126−1014205	L0	M9	L1.0	L2.0	29	···
J09230296−2300415	···	···	M8.0	M8.0	12	blue
J20370715−1137569	M8	···	M7.0	M8.0	80	···
J23294790−1607551	M9.5	M9	M9.0	L2.0	11	···
J15104786−2818174	M9	M9	M8.0	M8.0	12	···
J05012406−0010452	L4γ	L3 γ	L7.0	L3.0	23	red
J05120636−29495400	L4.5	L5 γ	L6.0	L3.0	2	red
J05181131−3101529	M6.5	M7γ	M7.0	M8.0	12	···

Table 5.4 Continued

Designation	Spectral Type				Reference	Red/blue
	Optical	NIR	NIR Standard	Gravity		
J09473829+3710178	M7	···	M6.0	M8.0	12	···
J235122005+30105400	L5.5	L5:	L6.0	L6.0	11	···
J09211410−2104446	L1	L4 p(blue)	L1.0	L2.0	23	···
J09083803+5032088	L5	L9	L5.0	L0.0	12	···
J09020690+0033195	M7	M7.5	M7.0	M8.0	57	···
J08500174−1924184	M8	···	M8.0	M8.0	12	···
J08230313−4912012	L1.5	L3	L2.0	L2.0	48	···
J07235262−3309435	···	L5 red	L3.0	L3.0	52	red
J07171626+5705430	L3	L6.5	L3.0	L3.0	17	···
J07140394+3702459	M8	···	M8.0	M8.0	12	···
J06411840−4322329	L1.5	L2.5:	L1.0	L2.0	23	···
J06023045+3910592	L1	L1	L1.0	L2.0	47	···
J05441150−2433018	M8	M7.5	M8.0	M8.0	12	···
J09524622+0620410	M8	M7.5	M7.0	M8.0	58	···
J05431887+6422528	L1	L2	L1.0	L2.0	23	···
J23272645−1741329	···	···	M6.0	M8.0	82	···
J23224684−3133231	L0	L2	L1.0	L2.0	57	···
J23174712−4838501	···	L5β	L5.0	L3.0	58	···
J23062928−0502285	M8	···	M8.0	M8.0	49	···
J14252798−3650229	L3:	L3 β	L6.0	L3.0	81	red
J1426316+155701	M9	···	M8.0	M8.0	2	···
J15150083+4847416	L6	L6	L5.0	L2.0	69	···
J15261405+2043414	L7	···	L5.0	L6.0	21	···
J17395322+5532451	···	M7.5	M8.0	M8.0	105	···
J14213145+1827407	L0	M9	L0.0	L2.0	49	···
J15291017+6312539	···	M8β	M8.0	M8.0	66	···
J23561081−3426044	M9.0	L0.5	M8.0	M8.0	33	···
J15525906+2948485	L0β	L0	L2.0	L0.0	17	···
J13595510−4034582	L1	L3:	L1.0	L2.0	23	···
J16073123−0442091	M8	···	M9.0	M8.0	93	···
J12464678+4027150	L4	L4	L4.0	L3.0	21	···

Table 5.4 Continued

Designation	Spectral Type				Reference	Red/blue
	Optical	NIR	NIR Standard	Gravity		
J14112131−2119503	M9	M8.5β	M8.0	M8.0	2	···
J16553529−0823401	M7 V	···	M7.0	M8.0	99	···
J16351919+4223053	M9	M8.5	M8.0	M8.0	57	···
J22285440−1325178	M6.5	M7.5	M6.0	M8.0	8	···
J21580457−1550098	L4:	L4	L4.0	L0.0	20	red
J213630294+05153290	M8.5	···	M8.0	M8.0	23	···
J21183174−4505522	M8.5	M8.5	M8.0	M8.0	33	···
J22373255+3922398	M9.5	···	M9.0	M8.0	113	···
J19453551−2557215	···	M9	M7.0	M8.0	44	···
J18432213+4040209	M8	···	M8.0	M8.0	2	···
J18261131+3014201	M8.5	M8.5 sd?	M7.0	M8.0	107	···
J17410280−4642218	···	L5:−L7: γ	L7.0	L3.0	58	···
J153824172−19531162	L4γ	L3.5	L6.0	L3.0	9	···
J10240997+1815533	M8	···	M7.0	M8.0	23	···

References. — (2) Cruz et al. (2003), (8) Bessell (1991), (9) Reid et al. (2008a), (11) Kirkpatrick et al. (2010), (12) Cutri et al. (2003), (17) Wilson et al. (2003), (20) Kirkpatrick et al. (2008), (21) Kirkpatrick et al. (2000), (23) Reid et al. (2008b), (27) Schmidt et al. (in prep.), (29) Cruz et al. (2007), (31) Gizis et al. (2001), (32) Basri et al. (2000), (33) Lodieu et al. (2005), (35) Luhman et al. (2016), (40) Kendall et al. (2003), (41) Hawley et al. (2002), (44) Pokorny et al. (2004), (47) Salim et al. (2003), (48) Phan-Bao et al. (2008), (49) Gizis et al. (2000b), (52) Schneider et al. (2017), (57) West et al. (2008), (58) Schneider et al. (2014), (59) Rebolo et al. (1998), (65) Looper et al. (in prep.), (66) Gagné et al. (2015c), (69) Schmidt et al. (2010), (80) Schmidt et al. (2007), (81) Kendall et al. (2004), (82) Reid & Gizis (2005), (93) Gizis et al. (2002), (99) Alonso-Floriano et al. (2015), (105) Gizis et al. (in prep.), (107) Lépine et al. (2002a), (113) Kirkpatrick et al. (2001).

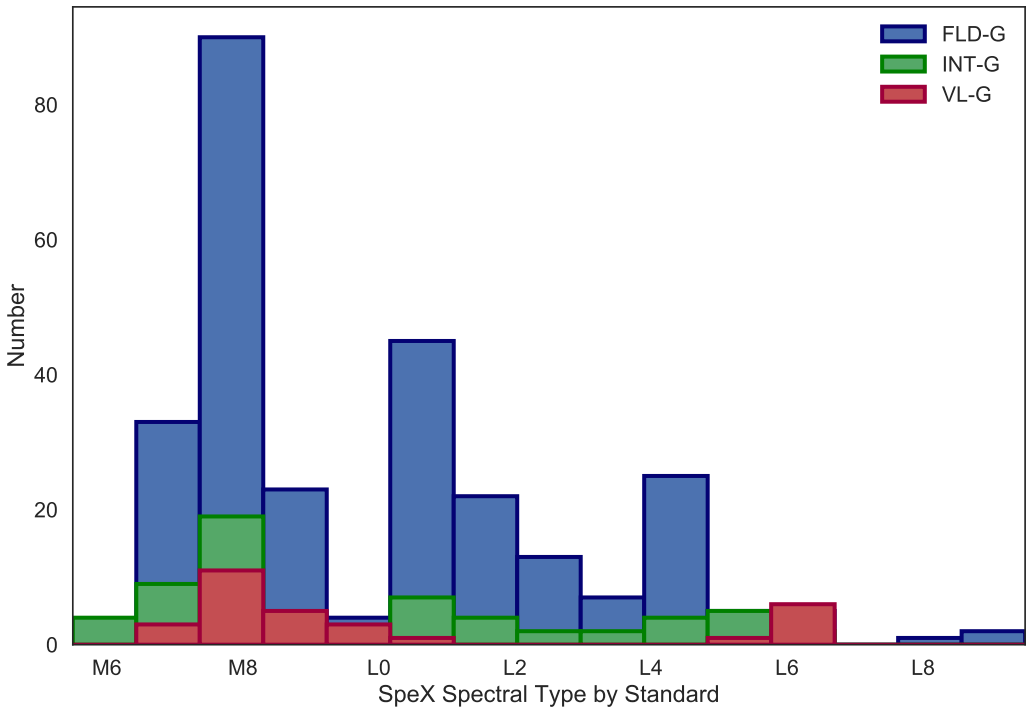

Figure 5.8 Distribution of spectral types as classified by field spectral standard. Objects with gravity classifications of very low gravity (VL-G) or intermediate gravity (INT-G) are plotted in red and green, respectively.

We reclassified the low gravity objects with corresponding VL-G and INT-G spectral standards from Allers & Liu (2013), and show the comparison with field standards on Figure 5.9. While the classification between VL-G and FLD-G standards is fairly consistent up to L2, it diverges significantly for later-type objects, with L6−L8 FLD-G classifications corresponding to the full range of early- to mid-L VL-G classifications. For INT-G sources, a correlation is less clear. FLD-G and INT-G classifications agree fairly well for late-Ms. However, across the L dwarf regime, FLD-G and INT-G classifications differ by a few subtypes. L-type intermediate gravity objects are classified as both earlier-type and later-type field objects. These disagreements reinforce the importance to use gravity classifications to identify the discrepancies caused by low gravity.

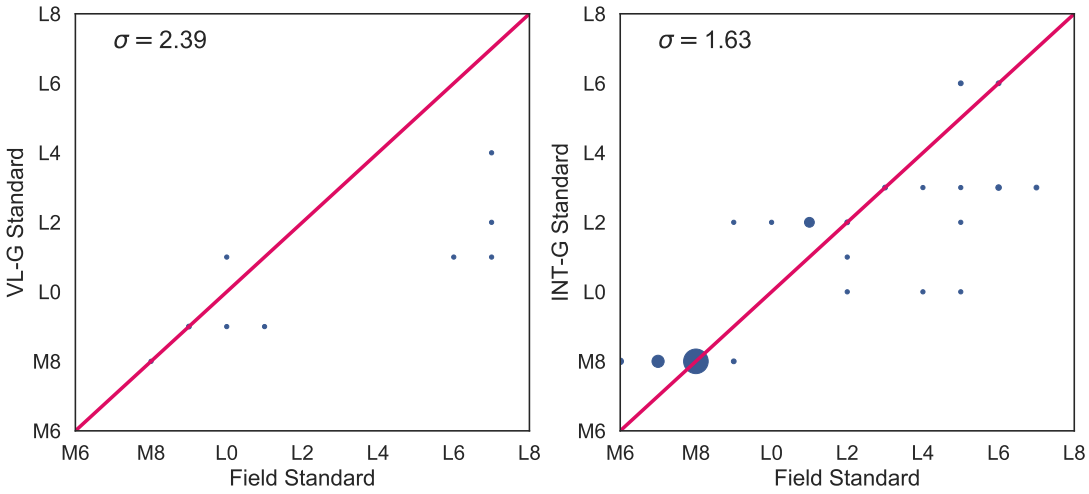

Figure 5.9 Comparison of field and low gravity classifications for objects with a gravity score of VL-G (left) or INT-G (right) according to Allers & Liu (2013). Larger circles indicate a higher incidence of sources.

5.4.4 $J-K_s$ Color Outliers

Of special interest is the identification of red and blue color outliers as ultracool subpopulations. Ultracool dwarfs with red colors are potentially young objects or field dwarfs with thick cloud layers. On the other hand, unusually blue L dwarfs have low metallicity, thin cloud coverage, ages older than the field, and/or halo kinematics (Burgasser et al. 2008b), and they act as contaminants to the spectral binary index selection (Bardalez Gagliuffi et al. 2014). Starting from late-M, ultracool dwarf colors get progressively redder in $J-K$ throughout the L type due to increased opacity originating from dust and possibly cloud formation in the photosphere (e.g. Tsuji et al. 1996b; Lodders & Fegley 2006).

In order to find the color outliers of our sample, we calculated $J-K$ colors using the adopted NIR J and K magnitudes and plotted them against their adopted literature spectral type. We used the median colors and standard deviations of Schmidt et al. (2015) defined for the M7−L6 range to identify outliers at the 2σ level, shown in Figure 5.10.

The individual outliers are listed in Table 5.5. From the total sample of 443 sources, 21 objects were found to have red colors and 11 have blue colors, indicating fractions of 4.7% and 2.5%, respectively. Additionally, we calibrated our SpeX spectra to 2MASS J and K_s magnitudes to find spectrophotometric $J-K_s$ colors. These were compared against literature, purely photometric $J-K_s$ colors. The outliers with large error bars most likely correspond to problems with the reduction or calibration of the spectra. However, the outliers with small error bars may be due to intrinsic atmospheric variability (e.g. Radigan et al. 2012).

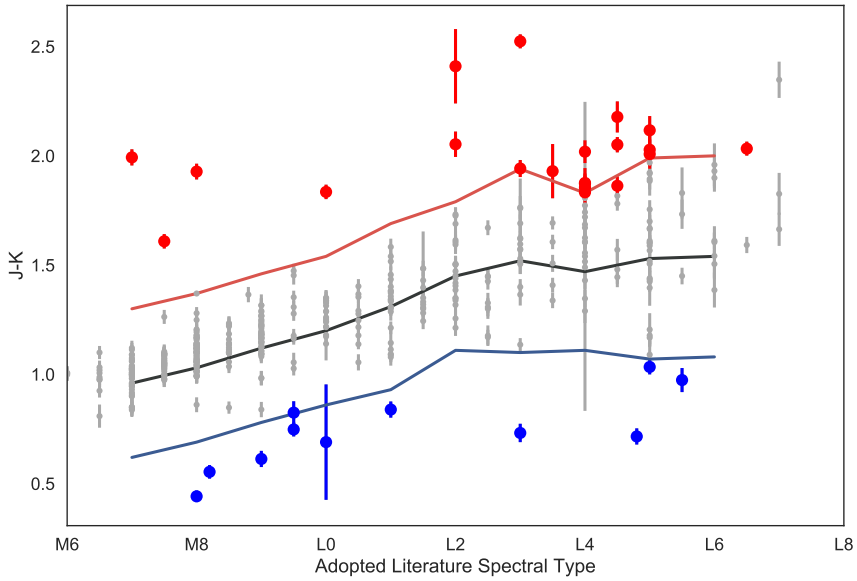

Figure 5.10 $J-K_s$ color outliers. Sample sources are shown in grey, with red and blue color outliers in their corresponding colors. The black solid line corresponds to median $J-K_s$ colors from Schmidt et al. (2015), while the red and blue solid lines mark the 2σ limits.

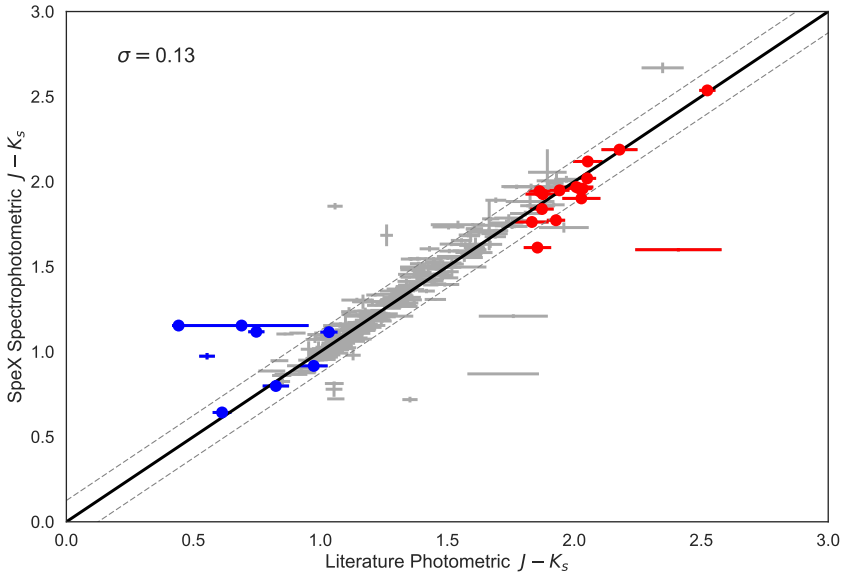

Figure 5.11 Photometric $J - K_s$ color from the literature compared to spectrophotometric $J - K_s$ color from our SpeX observations.

Table 5.5 Red and blue $J - K_s$ color outliers

Designation	Adopted SpT	SpT Flag	$J - K_s$	$J - K_s$ Excess	References
Blue Outliers					
J01004911−1933398	L3.0	OPT	0.73±0.04	-0.79	12
J07421169−1211516	L4.8	SPEX	0.72±0.04	-0.81	6
J09230296−2300415	M8.2	SPEX	0.55±0.03	-0.48	12
J10471381+4026493A	M8.0	NIR	0.44±0.03	-0.59	14
J10471381+4026493B	L0.0	NIR	0.69±0.26	-0.51	12
J12405273+1129387	L1.0	OPT	0.84±0.04	-0.47	75
J14162408+1348263	L5.0	OPT	1.03±0.03	-0.50	58
J14343616+2202463	L5.5	SDSS	0.97±0.06	-0.57	83
J14442067−2019222	M9.0	OPT	0.61±0.04	-0.51	85
J17125121−0507249	M9.5	SPEX	0.82±0.05	-0.38	101
J23520481−2208032	M9.5	NIR	0.75±0.03	-0.45	117
Red Outliers					
J00332386−1521309	L4.0	SIMBAD	1.88±0.07	0.41	25
J02050344+1251422	L5.0	OPT	2.01±0.07	0.48	21
J03552337+1133437	L3.0	SIMBAD	2.52±0.03	1.00	23
J04210718−6306022	L5.0	OPT	2.12±0.06	0.59	12
J04351455−1414468	M8.0	OPT	1.93±0.04	0.90	40
J05012406−0010452	L4.0	SIMBAD	2.02±0.05	0.55	23
J05120636−29495400	L4.5	OPT	2.18±0.07	0.71	2
J05480722+0033588	M7.0	OPT	1.99±0.04	1.03	46
J07235262−3309435	L5.0	NIR	2.03±0.08	0.50	52
J08354256−0819237	L6.5	OPT	2.03±0.03	0.49	2
J10042066+5022596	L2.0	SIMBAD	2.05±0.06	0.60	59
J11122567+3548131	L4.5	OPT	1.86±0.04	0.39	21
J13054019−2541059A	L2.0	OPT	2.41±0.17	0.96	12
J13054019−2541059B	L3.5	OPT	1.93±0.12	0.46	16
J13054106+2046394	L4.0	OPT	1.83±0.07	0.36	2
J14252798−3650229	L3.0	OPT	1.94±0.04	0.42	81
J14482563+1031590	L4.0	OPT	1.87±0.05	0.40	12
J17163523−0315431	L0.0	OPT	1.84±0.03	0.64	98

Table 5.5 Continued

Designation	Adopted SpT	SpT Flag	$J-K_s$	$J-K_s$ Excess	References
J18300760−1842361	M7.5	OPT	1.61±0.03	0.58	106
J21580457−1550098	L4.0	OPT	1.86±0.05	0.38	20
J22244381−0158521	L4.5	OPT	2.05±0.04	0.58	21

References. — (2) Cruz et al. (2003), (6) Kirkpatrick et al. (2014), (12) Cutri et al. (2003), (14) Close et al. (2003), (16) Liu & Leggett (2005), (20) Kirkpatrick et al. (2008), (21) Kirkpatrick et al. (2000), (23) Reid et al. (2008b), (25) Gizis et al. (2003), (40) Kendall et al. (2003), (46) Kang et al. (2015), (52) Schneider et al. (2017), (58) Schneider et al. (2014), (59) Rebolo et al. (1998), (75) Marocco et al. (2015), (81) Kendall et al. (2004), (83) Sheppard & Cushing (2009b), (98) Martín et al. (2010), (101) Melis (in prep.), (106) Folkes et al. (2012), (117) Pokorny et al. (2003).

5.4.5 Distances and Completeness

A crucial part of the construction of a volume-limited sample is to have reliable distances for the determination of the volume itself. Out of the 443 sources in the sample, 30% have parallax measurements. For the remainder of the sample, we used color and spectrophotometric distances, as described in Section 5.2.4.4. Most of the sample has near-infrared and mid-infrared distances, but roughly half has color distances which combine SDSS and 2MASS magnitudes and are independent of spectral type. All distances are listed in Table 5.6. The distributions of the three distance estimates and trigonometric distances are shown in Figure 5.12.

Figure 5.13 compares the trigonometric distances to the spectrophotometric ones. The distances agree until about 20 pc, after which outliers are more prominent. The scatter in the color distance and near-infrared and WISE spectrophotometric distances are σ =0.33, σ =0.23 and σ =0.24, respectively.

Additionally, we compared the spectrophotometric distances to one another in Figure 5.14. We find that the NIR and WISE distances agree for the most part, and this is partly because they both depend on spectral type. Often the disagreement is between color and spectrophotometric distances for this reason. We discarded outliers with a difference between NIR and WISE distances greater than twice the standard deviation of the difference. These objects were either objects blended with a nearby source in the WISE bands or Taurus members, naturally overluminous for their spectral type due to their youth but actually at a distance of 140 pc.

Table 5.6 Trigonometric and spectrophotometric distances for the M7−L5 25 pc sample

Designation	Spectral Type		Parallax (*mas*)	Distance Type (pc)				Parallax Ref.
	Adopted	Flag		*Trigonometric*	*Color*	*NIR*	*WISE*	
J00043484−4044058B	L5.0	OPT	76.86±3.97	13.01±0.67	···	11±1	···	84
J00043484−4044058C	L5.0	OPT	76.86±3.97	13.01±0.67	···	···	···	84
J00065794−6436542	L0.0	OPT	···	···	···	23±3	21±3	···
J00130931−0025521	M7.0	OPT	···	···	27±3	21±3	22±3	···
J00145575−4844171	L2.5	OPT	···	···	···	20±2	21±3	···
J00154476+3516026	L2.0	OPT	···	···	23±3	19±2	18±2	···
J00192626+4614078	M8.0	OPT	···	···	···	21±2	22±3	···
J00194579+5213179	M9.0	OPT	···	···	···	20±2	20±3	···
J00242463−0158201	M9.5	OPT	80.0±3.4	12.5±0.53	10±1	12±1	11±1	76
J00265632−5428530	M8.0	OPT	···	···	···	20±2	20±3	···
J00275592+2219328A	M7.5	OPT	65.5±3.8	15.27±0.89	7±1	9±1	9±1	183
J00275592+2219328B	M8.0	OPT	65.5±3.8	15.27±0.89	···	9±1	9±1	183
J0028208+224905	L7.0	SIMBAD	···	···	27±4	19±2	20±3	···
J00311925−3840356	L2.5	OPT	···	···	···	22±3	22±3	···
J003154778+06494639	M8.0	NIR	···	···	21±2	24±3	24±3	···
J00332386−1521309	L4.0	SIMBAD	···	···	···	25±3	23±3	···
J00361617+1821104	L3.5	OPT	114.2±0.8	8.76±0.06	10±1	8±1	9±1	84
J00413538−5621127	M6.5	OPT	···	···	···	20±2	19±2	···
J00452143+1634446	L3.5	SIMBAD	···	···	12±1	10±1	9±1	···

Table 5.6 Continued

Designation	Spectral Type		Parallax (*mas*)	Distance Type (pc)				Parallax Ref.
	Adopted	Flag		*Trigonometric*	*Color*	*NIR*	*WISE*	
J00464841+0715177	L0.0	OPT	···	···	18±2	28±3	24±3	···
J004926771−06354671	M9.0	NIR	···	···	22±2	25±3	25±3	···
J00525468−2705597	M7.5	OPT	46.0±10.0	21.74±4.73	···	37±4	34±4	185
J00531899−3631102	L3.5	OPT	···	···	···	20±2	20±2	···
J01004911−1933398	L3.0	OPT	···	···	···	16±2	23±3	···
J01025100−3737438	M8.0	OPT	81.95±2.73	12.2±0.41	···	11±1	11±1	102
J01090150−5100494	M8.5	OPT	57.8±3.5	17.3±1.05	···	17±2	17±2	147
J01095117−0343264	M9.0	OPT	104.23±2.29	9.59±0.21	10±1	12±1	11±1	102
J01231125−6921379	M7.5	OPT	···	···	···	20±2	21±3	···
J01243124−0027556	M7.0	OPT	···	···	···	20±2	21±3	···
J01282664−5545343	L2.0	OPT	···	···	···	19±2	19±2	···
J01311838+3801554	L4.0	OPT	···	···	···	20±2	20±3	···
J01410321+1804502	L1.0	OPT	···	···	23±3	24±3	24±3	···
J01443536−0716142	L5.0	OPT	···	···	13±2	13±1	13±2	···
J01483864−3024396	M7.5	OPT	···	···	···	20±2	20±3	···
J01490895+2956131	M9.5	OPT	44.4±0.7	22.52±0.36	18±2	24±3	21±3	87
J01550354+0950003	L4.0	SIMBAD	···	···	26±3	21±2	21±3	···
J02050344+1251422	L5.0	OPT	···	···	27±4	24±3	22±3	···
J02081833+2542533	L1.0	OPT	···	···	25±3	25±3	24±3	···

Table 5.6 Continued

Designation	Spectral Type		Parallax (*mas*)	Distance Type (pc)				Parallax Ref.
	Adopted	Flag		*Trigonometric*	*Color*	*NIR*	*WISE*	
J02115089+4728300	M8.0	NIR	···	···	23±2	24±3	25±3	···
J02132880+4444453	L1.5	OPT	···	···	···	19±2	20±2	···
J02150802−3040011	M8.0	OPT	···	···	···	14±2	14±2	···
J02182913−3133230	L3.0	OPT	···	···	···	24±3	23±3	···
J02192210−3925225	L4.0	NIR	···	···	···	29±4	···	···
J02271036−1624479	L1.5	OPT	···	···	···	19±2	19±2	···
J02284243+1639329	L0.0	OPT	···	···	···	20±2	20±2	···
J02284355−6325052	L1.0	OPT	···	···	···	21±2	22±3	···
J02354955−0711214	M7.0	OPT	···	···	25±3	23±3	24±3	···
J02355993−2331205	L1.5	OPT	47.15±0.27	21.21±0.12	···	19±2	···	186
J024029501+28325766	M7.5	OPT	···	···	21±2	24±3	24±3	···
J02484100−1651216	M8.0	OPT	61.6±5.4	16.23±1.42	17±2	21±2	21±3	185
J0251148−035245	L3.0	OPT	···	···	13±2	12±1	12±2	···
J02530084+1652532	M6.5	OPT	260.63±2.69	3.84±0.04	···	4±1	···	187
J0253202+271333	M8.0	OPT	···	···	···	21±2	21±3	···
J02540582−1934523	M9.0	OPT	···	···	···	23±3	22±3	···
J03061159−3647528	M8.0	OPT	76.46±1.42	13.08±0.24	···	14±2	14±2	136
J03122509+0021585	M7.0	OPT	···	···	···	21±3	22±3	···
J03140344+1603056	L0.0	OPT	···	···	···	15±2	15±2	···

Table 5.6 Continued

Designation	Spectral Type		Parallax (*mas*)	Distance Type (pc)				Parallax Ref.
	Adopted	Flag		*Trigonometric*	*Color*	*NIR*	*WISE*	
J03144011−0450316	M7.5	OPT	···	···	···	24±3	24±3	···
J03205965+1854233	M8.0	OPT	68.3±0.6	14.64±0.13	12±1	14±2	14±2	188
J03264453+1919309	M8.5	OPT	···	···	···	25±3	25±3	···
J03283463+1129515	M8.0	OPT	···	···	···	20±2	20±2	···
J03300506+2405281	M7.0	OPT	···	···	···	23±3	23±3	···
J03313025−3042383	M7.5	OPT	···	···	···	13±2	13±2	···
J03341218−4953322	M9.0	OPT	120.6±3.6	8.29±0.25	···	11±1	···	84
J03393521−3525440	M9.5	OPT	155.89±1.03	6.41±0.04	···	7±1	7±1	136
J03395284+2457273	M8.0	OPT	51.9±5.2	19.27±1.93	···	23±3	24±3	183
J03442102+3206158	M8.0	OPT	···	···	···	···	20±3	···
J03442694+3203494	M9.0	OPT	···	···	···	···	13±2	···
J034429979+32192276	L0.0	NIR	···	···	···	14±2	15±2	···
J03505737+1818069	M9.0	OPT	···	···	23±2	21±2	22±3	···
J03510004−0052452	M8.0	OPT	68.1±1.9	14.68±0.41	13±1	12±1	12±2	189
J03521086+0210479	M9.0	OPT	···	···	···	23±3	22±3	···
J03550477−1032415	M8.5	OPT	···	···	···	25±3	25±3	···
J03552337+1133437	L3.0	SIMBAD	···	···	16±3	13±2	8±1	···
J04013766+2849529	L3.0	SIMBAD	···	···	···	13±2	13±2	···
J04041807+4127398	L2.0	OPT	···	···	···	21±2	18±2	···

Table 5.6 Continued

Designation	Spectral Type		Parallax (*mas*)	Distance Type (pc)				Parallax Ref.
	Adopted	Flag		*Trigonometric*	*Color*	*NIR*	*WISE*	
J04082905−1450334	L2.0	OPT	···	···	···	24±3	23±3	···
J041539163+28185862	M9.0	NIR	···	···	12±1	7±1	6±1	···
J04173745−0800007	M7.5	OPT	···	···	···	19±2	19±2	···
J041807965+28260370	M8.0	NIR	···	···	13±1	13±1	13±2	···
J04210718−6306022	L5.0	OPT	···	···	···	22±3	19±2	···
J042154823+26423722	M8.0	NIR	···	···	29±3	18±2	19±2	···
J042353227−00065872	···	···	···	···	23±3	···	···	···
J042450211+26410066	M8.0	NIR	···	···	24±2	19±2	19±2	···
J04270723+0859027	M8.0	OPT	···	···	19±2	24±3	23±3	···
J042724678+26241993	M8.0	NIR	···	···	19±2	11±1	12±2	···
J04291842−3123568	M7.5	OPT	···	···	···	10±1	10±1	···
J04305157−0849007	M8.0	OPT	···	···	···	24±3	24±3	···
J04351455−1414468	M8.0	OPT	···	···	···	12±1	10±1	···
J04351612−1606574	M8.0	OPT	95.35±1.06	10.49±0.12	···	8±1	8±1	136
J04390101−2353083	L6.5	OPT	110.4±4.0	9.06±0.33	···	12±1	13±2	84
J04402325−0530082	M7.0	OPT	105.5±3.2	9.48±0.29	8±1	10±1	10±1	190
J044104244+25575612	M7.0	NIR	···	···	15±1	12±1	12±2	···
J04430581−3202090	L5.0	OPT	···	···	···	23±3	23±3	···
J04433761+0002051	M9.0	OPT	···	···	11±1	17±2	15±2	···

Table 5.6 Continued

Designation	Spectral Type		Parallax (*mas*)	Distance Type (pc)				Parallax Ref.
	Adopted	Flag		*Trigonometric*	*Color*	*NIR*	*WISE*	
J04455387−3048204	L2.0	OPT	78.5±4.9	12.74±0.8	···	16±2	16±2	84
J044806329+15512512	L2.0	NIR	···	···	···	17±2	14±2	···
J04510093−3402150	L0.5	OPT	47.46±1.51	21.07±0.67	···	23±3	22±3	136
J05002100+0330501	L4.0	OPT	73.85±1.98	13.54±0.36	···	13±1	13±2	136
J05004808+0442143	L1.0	NIR	···	···	···	24±3	23±3	···
J05012406−0010452	L4.0	SIMBAD	76.4±4.8	13.09±0.82	27±4	20±2	16±2	84
J050441399+25095440	M9.0	NIR	···	···	14±2	8±1	7±1	···
J05061292+0439272	M7.0	OPT	···	···	···	5±1	5±1	···
J050855063+33192721	L2.0	NIR	···	···	···	22±3	21±3	···
J05102012+2714032	M8.0	OPT	100.7±1.6	9.93±0.16	8±1	9±1	9±1	120
J05120636−29495400	L4.5	OPT	···	···	···	23±3	18±2	···
J05153094+5911185	M7.5	OPT	65.7±1.3	15.22±0.3	···	13±2	13±2	120
J05173766−3349027	M8.0	OPT	···	···	···	16±2	15±2	···
J05181131−3101529	M6.5	OPT	···	···	···	20±2	19±2	···
J05233822−1403022	L2.5	OPT	80.95±1.76	12.35±0.27	···	13±2	13±2	136
J05264316−1824315	M7.0	NIR	···	···	···	23±3	24±3	···
J05301261+6253254	L1.0	OPT	···	···	23±3	26±3	24±3	···
J05345844−1511439	M9.0	OPT	···	···	···	24±3	23±3	···
J05372332−0816055	M7.0	NIR	···	···	···	22±3	23±3	···

Table 5.6 Continued

Designation	Spectral Type		Parallax (*mas*)	Distance Type (pc)				Parallax Ref.
	Adopted	Flag		*Trigonometric*	*Color*	*NIR*	*WISE*	
J05392474+4038437	M8.0	OPT	···	···	···	11±1	11±1	···
J05394952+5253597	L5.0	NIR	···	···	···	18±2	18±2	···
J05395200−0059019	L5.0	OPT	76.12±2.17	13.14±0.37	13±2	13±2	14±2	84
J05431887+6422528	L1.0	OPT	···	···	···	20±2	19±2	···
J05441150−2433018	M8.0	OPT	···	···	···	21±2	21±3	···
J05480722+0033588	M7.0	OPT	···	···	13±2	25±3	15±2	···
J05500794+1610519	L2.0	NIR	···	···	···	25±3	23±3	···
J06022216+6336391	L1.0	OPT	···	···	25±3	27±3	24±3	···
J06023045+3910592	L1.0	OPT	···	···	···	11±1	10±1	···
J06091922−3549311	L3.0	NIR	45.16±0.34	22.14±0.17	···	15±2	···	186
J06145280+4536556	M9.0	OPT	···	···	···	22±3	22±3	···
J06154934−01004158	L2.0	OPT	···	···	22±3	20±2	22±3	···
J06244172+6626309	L1.0	SIMBAD	···	···	···	20±2	21±3	···
J06244595−4521548	L5.0	OPT	83.9±4.5	11.92±0.64	···	15±2	14±2	84
J06300140−1840143	M8.5	OPT	51.24±0.08	19.52±0.03	···	20±2	18±2	191
J06320617+8305014	L0.5	OPT	···	···	21±2	24±3	24±3	···
J06411840−4322329	L1.5	OPT	55.7±5.7	17.95±1.84	···	21±2	21±3	84
J06431685−1843375	M8.0	OPT	···	···	···	25±3	25±3	···
J06521977−2534505	L0.0	OPT	63.76±0.94	15.68±0.23	···	17±2	16±2	136

Table 5.6 Continued

Designation	Spectral Type		Parallax (*mas*)	Distance Type (pc)				Parallax Ref.
	Adopted	Flag		*Trigonometric*	*Color*	*NIR*	*WISE*	
J06523073+4710348	L4.5	OPT	···	···	···	10±1	9±1	···
J06572547−4019134	M7.5	OPT	···	···	···	25±3	24±3	···
J07003664+3157266	L3.5	OPT	82.0±2.0	12.2±0.3	···	10±1	9±1	84
J07025026−6102482	M7.0	SIMBAD	···	···	···	9±1	10±1	···
J07075327−4900503	M8.5	OPT	70.0±4.0	14.29±0.82	···	26±3	26±3	76
J07111138+4329590	M7.0	OPT	77.8±3.0	12.85±0.5	···	8±1	8±1	120
J07140394+3702459	M8.0	OPT	···	···	···	16±2	16±2	···
J071551828−11452847	L4.0	NIR	···	···	···	18±2	19±2	···
J07164790−0630369	L1.0	OPT	···	···	···	24±3	24±3	···
J07171626+5705430	L3.0	OPT	···	···	···	23±3	20±3	···
J07200325−0846499	M9.0	OPT	166.0±28.0	6.02±1.02	···	7±1	7±1	79
J07231462+5727081	L1.0	OPT	···	···	···	25±3	25±3	···
J07235262−3309435	L5.0	NIR	···	···	···	25±3	24±3	···
J07410681+1738459	M7.0	OPT	···	···	17±2	19±2	19±2	···
J07421169−1211516	L4.8	SPEX	···	···	···	8±1	15±2	···
J07464256+2000321	L0.5	OPT	86.2±4.6	11.6±0.62	9±1	10±1	10±1	84
J07511645−2530432	L2.5	OPT	59.15±0.84	16.91±0.24	···	14±2	16±2	136
J07522390+1612157	M7.0	OPT	53.7±3.3	18.62±1.14	12±1	11±1	12±1	190
J08040580+6153336	M9.0	OPT	···	···	···	19±2	19±2	···

Table 5.6 Continued

Designation	Spectral Type		Parallax (*mas*)	Distance Type (pc)				Parallax Ref.
	Adopted	Flag		*Trigonometric*	*Color*	*NIR*	*WISE*	
J08053189+4812330	L4.0	OPT	···	···	21±3	22±3	23±3	···
J08072607+3213101	M8.0	OPT	···	···	14±2	17±2	17±2	···
J08105865+1420390	M8.0	OPT	···	···	19±2	22±3	23±3	···
J08123170−2444423	L2.5	OPT	45.47±0.96	21.99±0.46	···	18±2	20±2	136
J08151407+1030117	M7.0	OPT	···	···	···	23±3	22±3	···
J08185804+2333522	M7.0	OPT	···	···	19±2	21±2	21±3	···
J08230313−4912012	L1.5	OPT	···	···	···	18±2	16±2	···
J08283419−1309198	L2.0	OPT	87.96±0.78	11.37±0.1	···	12±1	12±2	136
J08294949+2646348	M6.5	OPT	275.8±3.0	3.63±0.04	···	4±0	···	192
J08303256+0947153	M8.0	OPT	59.81±4.52	16.72±1.26	14±1	15±2	14±2	193
J08352366+1029318	M9.0	OPT	···	···	23±2	24±3	25±3	···
J08354256−0819237	L6.5	OPT	117.3±11.2	8.53±0.81	···	6±1	6±1	84
J08355829+05483080	L3.0	OPT	···	···	29±4	23±3	25±3	···
J08402975+1824091	M6.0	OPT	71.3±1.1	14.03±0.22	12±1	15±2	14±2	189
J08472872−1532372	L2.0	OPT	76.5±3.5	13.07±0.6	···	17±2	17±2	84
J08500174−1924184	M8.0	OPT	···	···	···	23±3	23±3	···
J08513558+7727182	M8.0	OPT	···	···	···	25±3	24±3	···
J08522464+2540591	M6.0	OPT	···	···	26±2	25±3	24±3	···
J08533619−0329321	M9.0	OPT	117.98±0.76	8.48±0.05	···	9±1	9±1	136

Table 5.6 Continued

Designation	Spectral Type		Parallax (*mas*)	Distance Type (pc)				Parallax Ref.
	Adopted	Flag		*Trigonometric*	*Color*	*NIR*	*WISE*	
J08581519+1945470A	M7.0	OPT	176.6±2.8	5.66±0.09	···	3±0	3±0	183
J08581519+1945470B	M7.0	NIR	190.0±3.0	5.26±0.08	···	···	3±0	184
J08593854+6341355	L0.0	OPT	···	···	23±3	26±3	24±3	···
J08594029+1145325	M8.0	OPT	···	···	15±2	22±3	21±3	···
J09002359+2150054	M6.0	OPT	156.87±2.67	6.37±0.11	6±1	7±1	7±1	187
J09020690+0033195	M7.0	OPT	50.1±3.8	19.96±1.51	19±2	20±2	21±3	183
J09054654+5623117	L5.0	OPT	···	···	31±4	23±3	23±3	···
J09083803+5032088	L5.0	OPT	···	···	11±2	16±2	15±2	···
J09095749−0658186	L0.0	OPT	42.5±4.2	23.53±2.33	···	28±3	27±3	84
J09111297+7401081	L0.0	OPT	···	···	···	19±2	18±2	···
J09113059+2248111	M7.0	OPT	···	···	···	17±2	18±2	···
J09161504+2139512	M9.0	OPT	···	···	17±2	24±3	23±3	···
J09211410−2104446	L1.0	OPT	···	···	···	15±2	15±2	···
J09230296−2300415	M8.2	SPEX	···	···	···	10±1	14±2	···
J09282562+4230545	M8.5	OPT	···	···	20±2	24±3	24±3	···
J09424604+5531025	M8.0	OPT	···	···	17±2	24±3	24±3	···
J09473829+3710178	M7.0	OPT	···	···	29±3	22±3	23±3	···
J09492223+0806450	M8.5	OPT	60.32±1.67	16.58±0.46	13±1	17±2	17±2	136
J09524622+0620410	M8.0	OPT	···	···	20±2	20±2	21±3	···

Table 5.6 Continued

Designation	Spectral Type		Parallax (*mas*)	Distance Type (pc)				Parallax Ref.
	Adopted	Flag		*Trigonometric*	*Color*	*NIR*	*WISE*	
J09532126−1014205	L0.0	OPT	···	···	···	23±3	21±3	···
J10031918−0105079	M7.0	OPT	···	···	17±2	22±3	22±3	···
J10042066+5022596	L2.0	SIMBAD	···	···	21±3	26±3	16±2	···
J10043929−33351889	L4.0	OPT	54.8±5.6	18.25±1.86	···	18±2	···	84
J10063197−1653266	M7.5	OPT	···	···	···	18±2	18±2	···
J10163470+2751497	M8.0	OPT	58.0±2.9	17.24±0.86	15±2	16±2	17±2	183
J10170754+1308398	L2.0	OPT	···	···	25±3	23±3	23±3	···
J101726800+07192609	M8.0	NIR	···	···	23±2	20±2	21±3	···
J10192447−2707171	L0.5	OPT	···	···	···	24±3	24±3	···
J10195684+7324087	M8.5	OPT	···	···	···	23±3	23±3	···
J10213232−2044069	M9.0	OPT	···	···	···	24±3	24±3	···
J10224821+5825453	L1.0	SIMBAD	···	···	21±2	20±2	20±2	···
J10240997+1815533	M8.0	OPT	···	···	21±2	18±2	19±2	···
J10292165+1626526	L2.5	OPT	···	···	26±3	21±3	19±2	···
J10451718−2607249	M8.0	OPT	···	···	···	23±3	23±3	···
J10452400−0149576	L1.0	OPT	···	···	17±2	17±2	17±2	···
J10471381+4026493A	M8.0	NIR	···	···	8±1	17±2	19±2	···
J10471381+4026493B	L0.0	NIR	···	···	14±2	23±3	15±2	···
J10473108−18155739	L2.5	OPT	···	···	···	22±3	25±3	···

Table 5.6 Continued

Designation	Spectral Type		Parallax (*mas*)	Distance Type (pc)				Parallax Ref.
	Adopted	Flag		*Trigonometric*	*Color*	*NIR*	*WISE*	
J10481258−1120082	M7.0	OPT	221.0±3.6	4.52±0.07	···	5±1	···	194
J10481463−3956062	M9.0	OPT	248.08±0.61	4.03±0.01	···	5±1	···	195
J10482788−5254180	L1.5	OPT	···	···	···	24±3	23±3	···
J10484281+0111580	L1.0	OPT	···	···	16±2	16±2	16±2	···
J10511900+5613086	L2.0	OPT	···	···	17±2	15±2	16±2	···
J10541102−8505023	M8.0	SIMBAD	···	···	···	22±3	22±3	···
J10544168+1214084	M7.5	OPT	···	···	22±2	22±3	23±3	···
J10554733+0808427	M9.0	OPT	···	···	14±2	18±2	18±2	···
J10584787−1548172	L3.0	OPT	66.5±4.4	15.04±0.99	···	19±2	18±2	84
J11040127+1959217	L4.0	OPT	···	···	20±3	18±2	19±2	···
J11061897+0428327	M7.0	OPT	48.1±3.1	20.79±1.34	19±2	22±3	23±3	185
J11073750−2759385	M7.0	NIR	···	···	···	22±3	24±3	···
J11083081+6830169	L1.0	OPT	···	···	···	16±2	14±2	···
J11122567+3548131	L4.5	OPT	46.04±0.9	21.72±0.42	18±2	17±2	15±2	84
J11214924−1313084	M8.0	OPT	65.83±2.02	15.19±0.47	···	16±2	14±2	136
J11232934+0154040	M7.0	OPT	···	···	20±2	23±3	23±3	···
J11240487+3808054	M8.5	OPT	···	···	···	21±2	19±2	···
J11263991−5003550	L5.0	OPT	59.38±1.64	16.84±0.47	···	14±2	···	136
J11345493+0022541	M9.0	OPT	···	···	18±2	21±2	21±3	···

Table 5.6 Continued

Designation	Spectral Type		Parallax (*mas*)	Distance Type (pc)				Parallax Ref.
	Adopted	Flag		*Trigonometric*	*Color*	*NIR*	*WISE*	
J113911077+0841121	M8.0	NIR	···	···	19±2	25±3	25±3	···
J11414406−2232156	M7.5	OPT	···	···	···	23±3	23±3	···
J11524266+2438079	M9.0	OPT	···	···	18±2	22±3	21±3	···
J11535267+0659561	M8.0	OPT	70.3±2.7	14.22±0.55	12±1	12±1	12±2	189
J11543399+0135545	M9.0	OPT	···	···	···	24±3	25±3	···
J11553952−3727350	L2.0	OPT	104.4±4.7	9.58±0.43	···	13±1	13±2	84
J11554286−2224586	M7.5	OPT	89.54±1.77	11.17±0.22	···	11±1	11±1	136
J11555389+0559577	L6.0	OPT	57.9±10.2	17.27±3.04	19±3	23±3	24±3	84
J11592743−5247188	M9.0	OPT	105.54±0.12	9.48±0.01	···	11±1	11±1	79
J120032924+2048513	···	···	···	···	24±2	···	···	···
J12035812+0015500	L3.0	OPT	···	···	17±2	18±2	17±2	···
J12130336−0432437	L5.0	OPT	···	···	···	17±2	18±2	···
J12210359+0857217	M7.0	NIR	···	···	24±2	21±3	22±3	···
J12212770+0257198	L0.5	OPT	···	···	18±2	19±2	19±2	···
J12245222−1238352	M9.0	OPT	58.6±3.8	17.06±1.11	···	18±2	17±2	185
J12281523−1547342	L5.0	OPT	49.4±1.9	20.24±0.78	···	15±2	15±2	84
J12321772−6856005	M8.0	OPT	···	···	···	19±2	19±2	···
J12392727+5515371	L5.0	OPT	···	···	19±3	16±2	15±2	···
J12405273+1129387	L1.0	OPT	···	···	···	10±1	13±2	···

Table 5.6 Continued

Designation	Spectral Type		Parallax (*mas*)	Distance Type (pc)				Parallax Ref.
	Adopted	Flag		*Trigonometric*	*Color*	*NIR*	*WISE*	
J12464678+4027150	L4.0	OPT	···	···	25±3	23±3	21±3	···
J12465176+3148104	M7.0	OPT	···	···	···	21±3	21±3	···
J12505265−2121136	M6.5	OPT	57.77±1.72	17.31±0.52	···	14±2	14±2	136
J12522264+0252058	M8.0	OPT	···	···	20±2	21±2	21±3	···
J12531092−5709248	L0.5	OPT	···	···	···	21±2	···	···
J12531240+4034038	M7.5	OPT	···	···	21±2	19±2	20±3	···
J12560215−1257217	M7.5	OPT	···	···	···	11±1	12±2	···
J12565688+0146163	L2.0	OPT	···	···	26±3	25±3	23±3	···
J12590470−4336243	M8.0	SIMBAD	128.0±nan	7.81±nan	···	8±1	8±1	79
J13004255+1912354	L1.0	OPT	···	···	12±1	15±2	···	···
J13054019−2541059A	L2.0	OPT	53.6±2.0	18.66±0.7	···	16±2	···	84
J13054019−2541059B	L3.5	OPT	···	···	···	19±2	12±1	···
J13054106+2046394	L4.0	OPT	···	···	25±4	24±3	21±3	···
J13082507+0725512	M9.0	OPT	···	···	19±2	24±3	24±3	···
J13092185−2330350	M8.0	OPT	69.33±1.33	14.42±0.28	···	14±2	15±2	136
J13113921+8032219	M8.0	OPT	···	···	···	23±3	24±3	···
J13142039+1320012	M7.0	OPT	61.0±2.8	16.39±0.75	1±0	7±1	7±1	120
J13153094−2649513	L5.5	OPT	···	···	···	19±2	19±2	···
J13171150+1849232	M9.0	OPT	···	···	···	17±2	18±2	···

Table 5.6 Continued

Designation	Spectral Type		Parallax (*mas*)	Distance Type (pc)				Parallax Ref.
	Adopted	Flag		*Trigonometric*	*Color*	*NIR*	*WISE*	
J13261625+5640448	M7.0	OPT	···	···	18±2	18±2	18±2	···
J13314894−0116500	L6.0	OPT	67.3±12.6	14.86±2.78	21±3	22±3	26±3	147
J13322442−0441126	M7.5	OPT	···	···	···	21±2	21±3	···
J13365044+4751321	M8.0	OPT	···	···	22±2	22±3	23±3	···
J13382615+4140342	L2.5	OPT	···	···	27±3	22±3	22±3	···
J13564148+4342587	M7.0	OPT	···	···	15±2	16±2	16±2	···
J13595510−4034582	L1.0	OPT	64.2±5.5	15.58±1.33	···	23±3	24±3	84
J14032232+3007547	M9.0	OPT	···	···	18±2	19±2	20±2	···
J14112131−2119503	M9.0	OPT	···	···	···	17±2	18±2	···
J14122449+1633115	L0.5	OPT	···	···	25±3	26±3	25±3	···
J14162408+1348263	L5.0	OPT	109.9±1.8	9.1±0.15	···	9±1	11±1	167
J14211873−1618201	M7.5	OPT	···	···	···	24±3	24±3	···
J14213145+1827407	L0.0	OPT	···	···	19±2	21±2	20±2	···
J14222424+2116076	M8.0	OPT	···	···	18±2	20±2	21±3	···
J14252798−3650229	L3.0	OPT	86.45±0.83	11.57±0.11	···	14±2	11±1	136
J1426316+155701	M9.0	OPT	···	···	19±2	21±2	21±3	···
J14280420+1356137	M7.5	OPT	82.8±4.1	12.08±0.6	13±1	11±1	12±1	120
J14283132+5923354	L4.0	OPT	···	···	25±3	22±3	22±3	···
J14284323+3310391	M9.0	OPT	90.8±1.3	11.01±0.16	11±1	14±2	13±2	189

Table 5.6 Continued

Designation	Spectral Type		Parallax (*mas*)	Distance Type (pc)				Parallax Ref.
	Adopted	Flag		*Trigonometric*	*Color*	*NIR*	*WISE*	
J14304358+2915405A	L2.0	OPT	···	···	25±3	24±3	···	···
J14304358+2915405B	L2.0	OPT	···	···	37±6	···	···	···
J14343616+2202463	L5.5	SDSS	···	···	29±3	16±2	25±3	···
J14380829+6408363	L0.0	OPT	···	···	17±2	18±2	18±2	···
J14392836+1929149	L1.0	OPT	69.6±0.5	14.37±0.1	14±2	15±2	···	84
J14402293+1339230	M8.0	OPT	45.0±1.11	22.22±0.55	···	19±2	20±3	136
J14422164+6603208	L0.0	OPT	91.18±0.3	10.97±0.04	···	10±1	···	186
J14442067−2019222	M9.0	OPT	61.2±5.1	16.34±1.36	···	20±2	···	84
J144506278+4409393	M8.0	NIR	···	···	23±2	20±2	21±3	···
J14460061+0024519	L6.0	OPT	46.7±14.6	21.41±6.69	30±5	23±3	24±3	84
J14480337+1554149	M7.0	OPT	···	···	26±3	24±3	24±3	···
J14482563+1031590	L4.0	OPT	···	···	18±2	18±2	15±2	···
J14501581+2354424	L4.0	OPT	55.03±0.34	18.17±0.11	···	14±3	···	196
J14540797−6604476	L3.5	OPT	84.88±1.71	11.78±0.24	···	11±1	11±1	136
J14562776+1755090	M7.0	OPT	···	···	17±2	19±2	18±2	···
J14563831−2809473	M7.0	OPT	145.3±3.25	6.88±0.15	···	7±1	8±1	102
J145638314−28094738	M7.0	OPT	145.3±3.25	6.88±0.15	···	7±1	8±1	102
J14573965+4517167	M9.0	OPT	···	···	19±2	23±3	23±3	···
J14582453+2839580	M8.5	OPT	···	···	19±2	24±3	24±3	···

Table 5.6 Continued

Designation	Spectral Type		Parallax (*mas*)	Distance Type (pc)				Parallax Ref.
	Adopted	Flag		*Trigonometric*	*Color*	*NIR*	*WISE*	
J15002635−0039281	M7.0	OPT	···	···	20±2	16±2	17±2	···
J15010818+2250020	M8.5	OPT	94.4±0.6	10.59±0.07	10±1	14±2	13±2	87
J15041621−2355564	M7.5	OPT	···	···	···	18±2	18±2	···
J15065441+1321060	L3.0	OPT	···	···	15±2	13±2	···	···
J15072779−2000431	M7.5	OPT	···	···	···	15±2	16±2	···
J15074769−1627386	L5.0	OPT	136.4±0.6	7.33±0.03	···	7±1	8±1	84
J15101685−0241078	M9.0	OPT	61.2±4.7	16.34±1.25	15±2	18±2	17±2	197
J15104786−2818174	M9.0	OPT	···	···	···	20±2	19±2	···
J15150083+4847416	L6.0	OPT	···	···	9±1	11±1	···	···
J15200224−4422419B	L4.5	SIMBAD	···	···	···	19±2	···	···
J15210103+5053230	M7.5	OPT	···	···	13±1	17±2	17±2	···
J15230657−2347526	L2.5	SIMBAD	···	···	···	22±3	21±3	···
J15242475+2925318	M7.5	OPT	···	···	···	12±1	12±2	···
J15261405+2043414	L7.0	OPT	48.5±8.7	20.62±3.7	24±3	19±2	21±3	84
J15291017+6312539	M8.0	NIR	···	···	···	14±2	14±2	···
J15345325+1219495	L6.0	OPT	···	···	26±4	20±2	21±3	···
J15345704−1418486	M7.0	OPT	···	···	···	14±2	14±2	···
J153824172−19531162	L6.0	SIMBAD	···	···	···	24±3	22±3	···
J15394189−0520428	L4.0	OPT	64.5±3.4	15.5±0.82	···	15±2	16±2	84

Table 5.6 Continued

Designation	Spectral Type		Parallax (*mas*)	Distance Type (pc)				Parallax Ref.
	Adopted	Flag		*Trigonometric*	*Color*	*NIR*	*WISE*	
J15394442+7437273	M9.0	OPT	···	···	···	21±2	20±3	···
J15404341−5101357	M7.0	OPT	228.0±24.0	4.39±0.46	···	5±1	···	79
J15445518+3301447	L6.0	OPT	···	···	27±4	22±3	24±3	···
J15460540+3749458	M7.5	OPT	···	···	21±2	21±3	22±3	···
J15464185−5534468	M7.5	OPT	149.0±40.0	6.71±1.8	···	8±1	6±1	79
J15485834−1636018	L2.0	OPT	···	···	···	21±2	22±3	···
J15510662+6457047	M8.0	OPT	···	···	···	24±3	23±3	···
J15525906+2948485	L1.0	SIMBAD	···	···	17±2	19±2	17±2	···
J15531993+1400337	M9.0	OPT	···	···	17±2	22±3	22±3	···
J15551573−0956055	L1.0	OPT	74.53±1.21	13.42±0.22	···	14±2	15±2	136
J16073123−0442091	M8.0	OPT	63.9±1.47	15.65±0.36	···	15±2	15±2	136
J16081603−3903042	M7.5	SIMBAD	···	···	···	21±2	20±2	···
J16095217−2136277	M7.0	OPT	···	···	···	25±3	24±3	···
J16134550+1708270	M9.5	OPT	···	···	23±3	25±3	24±3	···
J16141484−2427081	M7.0	OPT	···	···	···	24±3	24±3	···
J16154245+0546400	M9.0	OPT	···	···	16±2	21±2	20±2	···
J16154416+3559005	L4.0	OPT	···	···	25±3	19±2	19±2	···
J16271142−2348505	M8.8	SPEX	···	···	···	25±3	23±3	···
J16272794+8105075	M9.0	OPT	···	···	18±2	22±3	22±3	···

Table 5.6 Continued

Designation	Spectral Type		Parallax (*mas*)	Distance Type (pc)				Parallax Ref.
	Adopted	Flag		*Trigonometric*	*Color*	*NIR*	*WISE*	
J16325882−0631481	M7.0	OPT	53.31±1.48	18.76±0.52	17±2	26±3	25±3	136
J16331306−7553232	M9.5	OPT	···	···	···	23±3	23±3	···
J16334908−6808480	M8.0	NIR	···	···	···	11±1	8±1	···
J16351919+4223053	M9.0	OPT	···	···	17±2	21±2	21±3	···
J16452211−1319516	L1.5	OPT	109.9±6.1	9.1±0.51	···	12±1	12±1	84
J16553529−0823401	M7.0	OPT	154.5±0.7	6.47±0.03	7±1	7±1	7±1	189
J16573454+1054233	L2.0	OPT	···	···	26±3	23±3	23±3	···
J16580380+7027015	L1.0	OPT	53.9±0.7	18.55±0.24	···	18±2	18±2	84
J17054834−0516462	L0.5	OPT	44.5±12.0	22.47±6.06	···	20±2	20±2	84
J17065487−1314396	L5.0	SIMBAD	···	···	···	16±2	19±2	···
J17071830+6439331	M9.0	OPT	···	···	16±2	18±2	18±2	···
J17072343−0558249A	M9.0	SIMBAD	···	···	···	16±2	12±1	···
J17072343−0558249B	L3.0	SIMBAD	···	···	···	16±2	···	···
J17114559+4028578	L5.0	SIMBAD	73.8±5.1	13.55±0.94	25±3	22±3	···	183
J17125121−0507249	M9.5	SPEX	50.1±3.62	19.96±1.44	···	23±3	···	196
J17163523−0315431	L0.0	OPT	···	···	···	6±1	6±1	···
J17171408+6526221	L4.0	OPT	···	···	···	22±3	21±3	···
J17210390+3344160	L3.0	OPT	···	···	16±2	16±2	···	···
J17264070−2737593	L5.0	OPT	···	···	···	10±1	···	···

Table 5.6 Continued

Designation	Spectral Type		Parallax (*mas*)	Distance Type (pc)				Parallax Ref.
	Adopted	Flag		*Trigonometric*	*Color*	*NIR*	*WISE*	
J17312974+2721233	L0.0	OPT	113.8±7.0	8.79±0.54	10±1	13±1	13±2	183
J17331893+4633593	M9.5	OPT	···	···	···	22±3	21±3	···
J17334227−1654500	L0.5	OPT	···	···	···	23±3	18±2	···
J17335314+1655129	M7.0	OPT	···	···	···	5±1	5±1	···
J17343053−1151388	M8.5	OPT	···	···	···	24±3	23±3	···
J17351296+2634475	M7.5	OPT	···	···	9±1	12±1	12±2	···
J17395322+5532451	M7.5	NIR	···	···	20±2	19±2	19±2	···
J17410280−4642218	L7.0	SIMBAD	···	···	···	18±2	13±2	···
J17430860+8526594	L5.0	SIMBAD	···	···	···	18±2	22±3	···
J17453466−1640538	L1.5	OPT	···	···	···	20±2	22±3	···
J17461199+5034036	L5.0	OPT	···	···	23±3	21±2	22±3	···
J17502484−0016151	L4.5	OPT	108.5±2.6	9.22±0.22	15±2	10±1	11±1	84
J17534518−6559559	L4.0	OPT	58.0±4.9	17.24±1.46	···	15±2	15±2	147
J17562963−4518224	M9.0	OPT	···	···	···	17±2	16±2	···
J17565620−4805096	L0.0	OPT	···	···	···	23±3	23±3	···
J17571539+7042011	M7.5	OPT	52.4±1.1	19.08±0.4	···	14±2	14±2	120
J18000116−1559235	L5.5	OPT	···	···	···	9±1	11±1	···
J18071593+5015316	L1.5	OPT	···	···	···	14±2	15±2	···
J18212815+1414010	L4.5	OPT	106.55±0.19	9.39±0.02	···	10±1	9±1	198

Table 5.6 Continued

Designation	Spectral Type		Parallax (*mas*)	Distance Type (pc)				Parallax Ref.
	Adopted	Flag		*Trigonometric*	*Color*	*NIR*	*WISE*	
J18261131+3014201	M8.5	OPT	···	···	···	14±2	···	···
J18300760−1842361	M7.5	OPT	···	···	···	7±1	6±1	···
J18353790+3259545	M8.5	OPT	176.5±0.5	5.67±0.02	···	7±1	7±1	79
J18393308+2952164	M6.5	OPT	79.3±2.0	12.61±0.32	···	13±2	13±2	120
J18432213+4040209	M8.0	OPT	70.7±0.8	14.14±0.16	13±1	12±1	13±2	189
J18450541−6357475	M8.5	OPT	259.45±1.11	3.85±0.02	···	5±1	···	187
J18451889+3853248	M8.0	OPT	···	···	···	17±2	18±2	···
J18470342+5522433	M6.5	OPT	···	···	···	20±2	20±3	···
J19064801+4011089	L1.0	OPT	···	···	16±2	17±2	17±2	···
J19165762+0509021	M8.0	OPT	170.1±0.8	5.88±0.03	···	6±1	···	189
J19285196−4356256	L4.0	OPT	···	···	···	25±3	24±3	···
J19360187−5502322	L5.0	OPT	66.3±5.4	15.08±1.23	···	16±2	17±2	84
J19453551−2557215	M9.0	NIR	···	···	···	17±2	···	···
J20004841−7523070	M9.0	OPT	···	···	···	19±2	18±2	···
J20025073−0521524	L6.0	OPT	···	···	···	19±2	17±2	···
J20040620+1704125	L4.5	NIR	58.01±0.9	17.24±0.27	···	10±2	···	186
J201035392+06343676	M8.5	SIMBAD	···	···	···	19±2	19±2	···
J20140359−2016217	M7.5	OPT	···	···	···	22±3	22±3	···
J20282035+0052265	L3.0	OPT	···	···	26±3	20±2	20±3	···

Table 5.6 Continued

Designation	Spectral Type		Parallax (*mas*)	Distance Type (pc)				Parallax Ref.
	Adopted	Flag		*Trigonometric*	*Color*	*NIR*	*WISE*	
J20360316+1051295	L2.0	OPT	···	···	···	20±2	19±2	···
J20370715−1137569	M8.0	OPT	···	···	···	18±2	20±2	···
J20575409−0252302	L1.5	OPT	70.1±3.7	14.27±0.75	15±2	15±2	15±2	84
J21041491−1037369	L2.0	OPT	53.0±1.71	18.87±0.61	···	20±2	19±2	136
J21183174−4505522	M8.5	OPT	46.7±7.9	21.41±3.62	···	29±3	29±4	185
J213630294+05153290	M8.5	OPT	···	···	24±3	28±3	28±4	···
J21371044+1450475	L2.0	OPT	···	···	···	23±3	24±3	···
J21373742+0808463	L5.0	OPT	···	···	18±2	17±2	17±2	···
J21402931+1625183	M8.5	OPT	···	···	21±2	23±3	21±3	···
J21580457−1550098	L4.0	OPT	···	···	···	22±3	21±3	···
J22000201−3038327	L0.0	OPT	···	···	···	23±3	22±3	···
J22021125−1109461	M6.5	OPT	···	···	···	25±3	24±3	···
J22062280−2047058	M8.0	OPT	···	···	···	19±2	20±2	···
J22244381−0158521	L4.5	OPT	88.1±1.1	11.35±0.14	···	12±1	18±2	84
J22264440−7503425	M8.0	OPT	···	···	···	19±2	19±2	···
J22285440−1325178	M6.5	OPT	90.0±4.9	11.11±0.6	···	12±2	12±2	76
J22341394+2359559	M9.5	OPT	···	···	18±2	21±2	21±3	···
J22354905+1840298	M7.0	OPT	···	···	21±2	23±3	23±3	···
J22373255+3922398	M9.5	OPT	···	···	···	24±3	20±3	···

Table 5.6 Continued

Designation	Spectral Type		Parallax (*mas*)	Distance Type (pc)				Parallax Ref.
	Adopted	Flag		*Trigonometric*	*Color*	*NIR*	*WISE*	
J22380742+4353179	L1.5	OPT	···	···	···	22±3	23±3	···
J22425317+2542573	L3.0	OPT	···	···	30±4	24±3	22±3	···
J22490917+3205489	L5.0	OPT	···	···	25±4	23±3	23±3	···
J23062928−0502285	M8.0	OPT	82.58±2.58	12.11±0.38	10±1	12±1	12±2	193
J23065876−5008589	M9.0	OPT	46.59±1.57	21.46±0.72	···	26±3	25±3	136
J23072655+8753294	L3.0	OPT	···	···	···	25±3	23±3	···
J23081874+0629514	L0.5	PHOT	···	···	18±3	23±3	···	···
J23081888+0629551	M8.0	NIR	···	···	···	9±1	···	···
J23174712−4838501	L5.0	SIMBAD	···	···	···	19±2	17±2	···
J23224684−3133231	L0.0	OPT	58.6±5.6	17.06±1.63	···	24±3	24±3	84
J23272645−1741329	M7.0	SIMBAD	···	···	···	17±2	18±2	···
J23294790−1607551	M9.5	OPT	···	···	···	25±3	25±3	···
J23312174−2749500	M7.5	OPT	69.14±2.06	14.46±0.43	···	15±2	15±2	193
J23343945+1933041	M8.0	OPT	···	···	21±2	23±3	23±3	···
J23371491−0838084	M7.0	OPT	···	···	16±2	21±3	21±3	···
J23440624−0733282	L4.5	OPT	···	···	22±3	20±2	21±3	···
J23464599+1129094	M9.0	OPT	···	···	17±2	20±2	20±3	···
J23473680+2702068	M9.0	OPT	···	···	···	24±3	23±3	···
J23494899+1224386	M8.0	OPT	···	···	18±2	21±2	22±3	···

Table 5.6 Continued

Designation	Spectral Type		Parallax (*mas*)	Distance Type (pc)				Parallax Ref.
	Adopted	Flag		*Trigonometric*	*Color*	*NIR*	*WISE*	
J235122005+30105400	L5.5	OPT	···	···	28±4	25±3	24±3	···
J23515044−2537367	M8.0	OPT	···	···	···	19±2	19±2	···
J23520481−2208032	M9.5	NIR	···	···	···	20±2	23±3	···
J23535946−0833311	M8.5	OPT	···	···	19±2	24±3	24±3	···
J23540928−3316266	M9.0	OPT	44.38±2.09	22.53±1.06	···	23±3	23±3	136
J23561081−3426044	M9.0	OPT	52.37±1.71	19.09±0.62	···	22±3	22±3	136

References. — (76) Jenkins et al. (2009), (79) Burgasser et al. (2015b), (84) Faherty et al. (2012), (87) Dahn et al. (2002), (102) Costa et al. (2005), (120) Lépine et al. (2009), (137) Dieterich et al. (2014), (148) Marocco et al. (2013), (168) Dupuy & Liu (2012), (185) Dittmann et al. (2014), (186) Harrington & Dahn (1980), (187) Tinney (1996), (188) Lindegren et al. (2016), (189) Henry et al. (2006), (190) Reid & Cruz (2002), (191) Monet et al. (1992), (192) Shkolnik et al. (2012), (193) Sahlmann et al. (2015), (194) van Altena et al. (1995), (195) Costa et al. (2006), (196) Gliese & Jahreiß (1991), (197) Lurie et al. (2014), (198) van Leeuwen (2007), (199) Tinney et al. (1995), (200) Sahlmann et al. (2016).

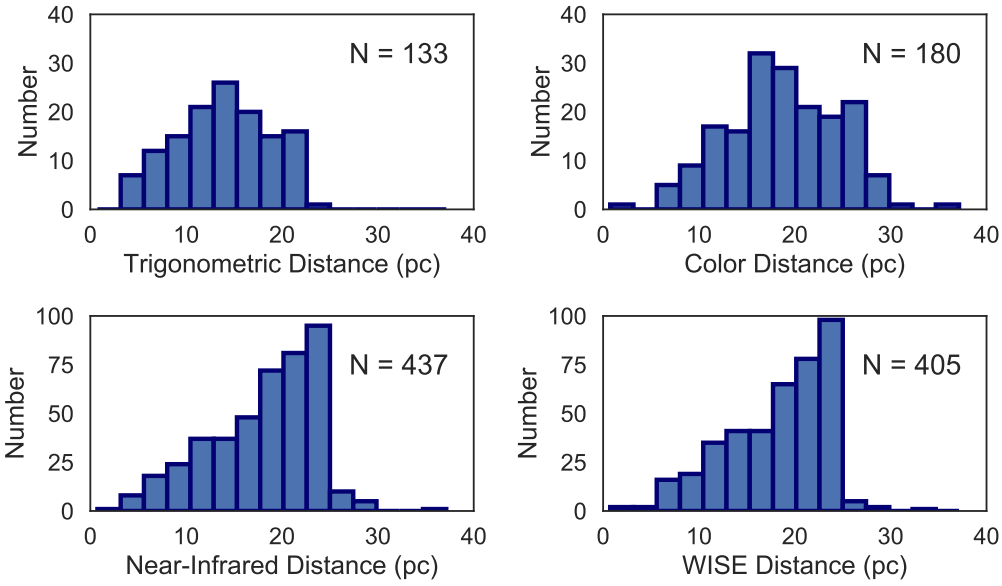

Figure 5.12 Distribution of distances by estimation method.

Our volume uncertainty was estimated by counting the number of sources that could be outside 25 pc within $1-\sigma$, and combining this error in quadrature with a Poisson counting error, $\sqrt{N}$. Taking into account only reliable distances, i.e. with errors $\simeq 20\%$, we find that 82 objects could fall outside our defined distance limit, using the adopted distance. Sources that could trickle into the sample despite being outside would fall in the category of young, overluminous objects or unresolved binary systems. This leads to an uncertainty in the number of objects of 85 sources, or 18.2%.

In order to estimate our volume completeness, we plotted cumulative histograms of each distance estimate and trigonometric distances, as shown in Figure 5.15. Assuming an isotropic distribution of sources for constant density and completeness up to 10 pc, 15 pc and 20 pc, we fit cube power law curves ($N \propto r^3$) to each distribution to find the expected number of sources at 25 pc. The completeness for each distance estimation is listed on Table 5.7.

Ideally, there would be trigonometric distances for the entire sample, or a single

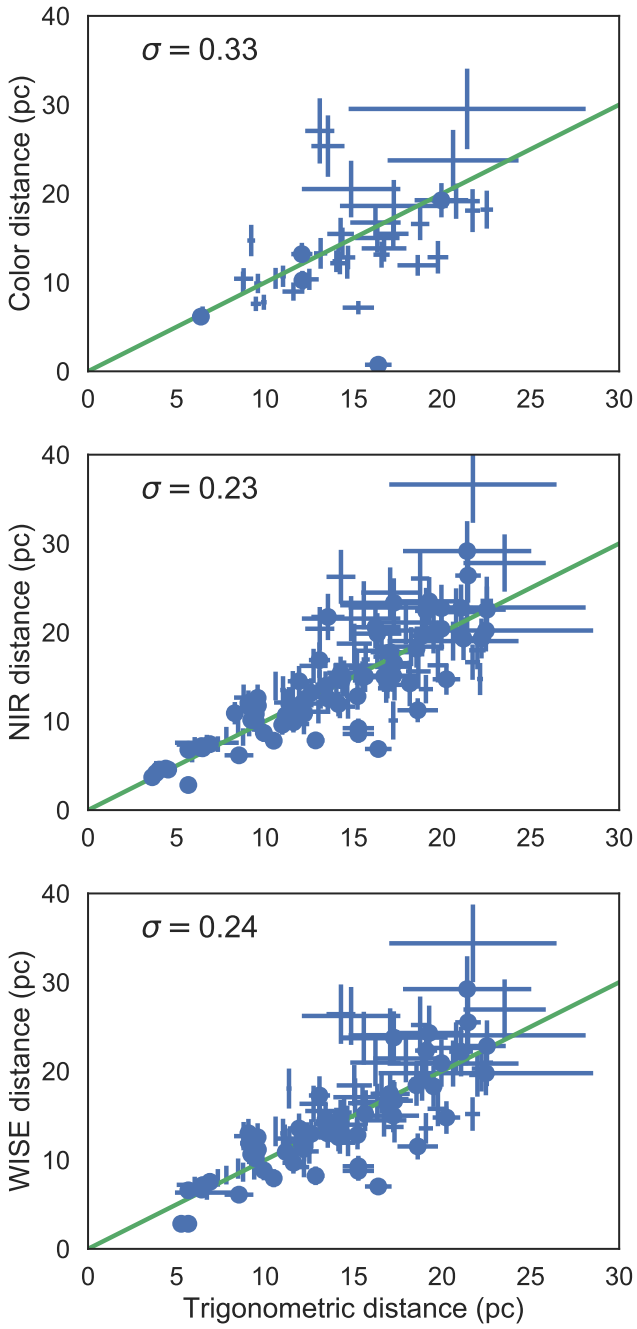

Figure 5.13 Spectrophotometric distance estimates compared to trigonometric distance measurements.

method of estimating spectrophotometric distances. Since these methods are fundamentally different, we calculate completeness for each one. We define an adopted distance

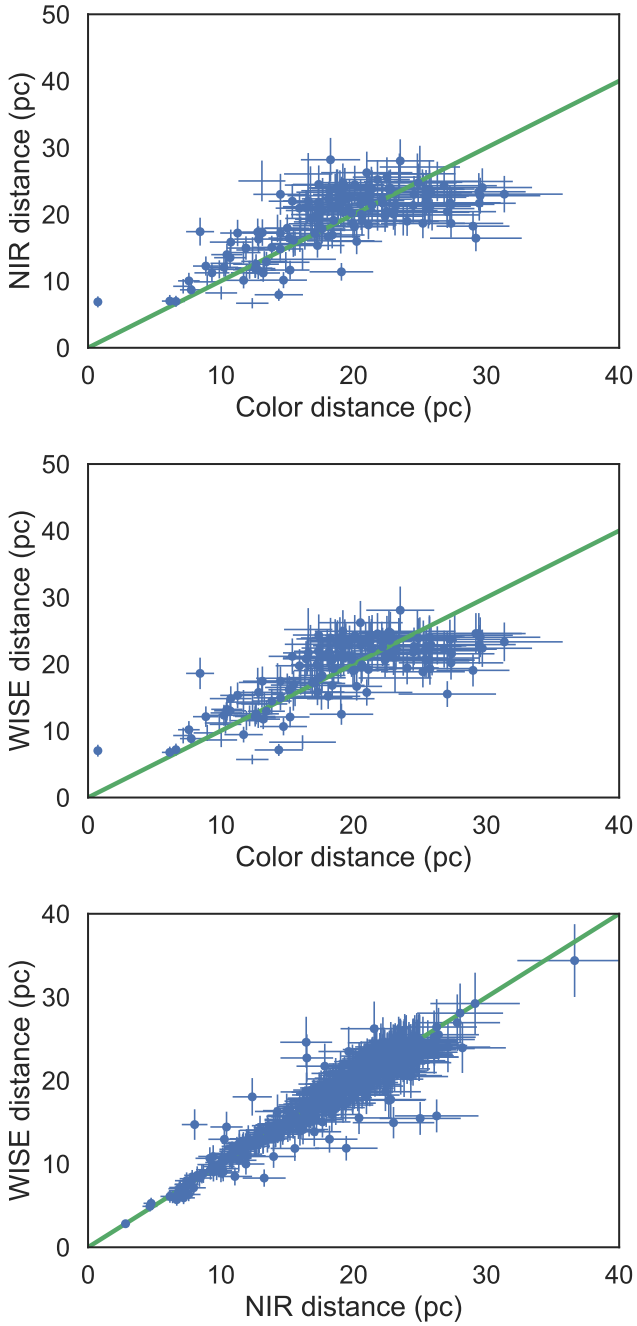

Figure 5.14 Comparison of spectrophotometric distances to each other. Near-infrared and WISE distances agree fairly well, while the color distance begins to diverge from the other two at around 20 pc.

Table 5.7 Estimated volume completeness.

	Distance Type (pc)				
Fit Range (pc)	Trigonometric	Color	NIR	WISE	Adopted
5 – 10	23%	84%	56%	68%	53%
5 – 15	33%	70%	66%	74%	64%
5 – 20	45%	70%	83%	87%	75%
Expected Number of Sources					
5 – 10	577	177	745	585	826
5 – 15	405	213	635	534	685
5 – 20	297	212	510	457	590

prioritized by trigonometric measurements, then the spectrophotometric estimate with the smallest uncertainty. Since only 28% of our sample has trigonometric distances, the large incompleteness is not surprising. We already know of roughly 350 sources included in this sample that lack parallax measurements and are most likely within 25 pc. We have estimated color distances for $\sim 50\%$ of the sample given the availability of SDSS optical magnitudes, and these account for a completeness of $69 - 78\%$.

WISE and near-infrared distance estimates are available for 92% and 98% of the sample. The assumptions of constant density and isotropic distribution lead to an estimated 79% completeness at best for both the WISE and near-infrared spectrophotometric distances, and $51 - 56\%$ for the worst case scenario. Combining distance measurements and estimations, we find a completeness of $44 - 70\%$ for the adopted distance. This is a 33% difference in completeness in the Solar Neighborhood, which could have an impact on the ratio of brown dwarfs to stars and our estimates of the initial mass function.

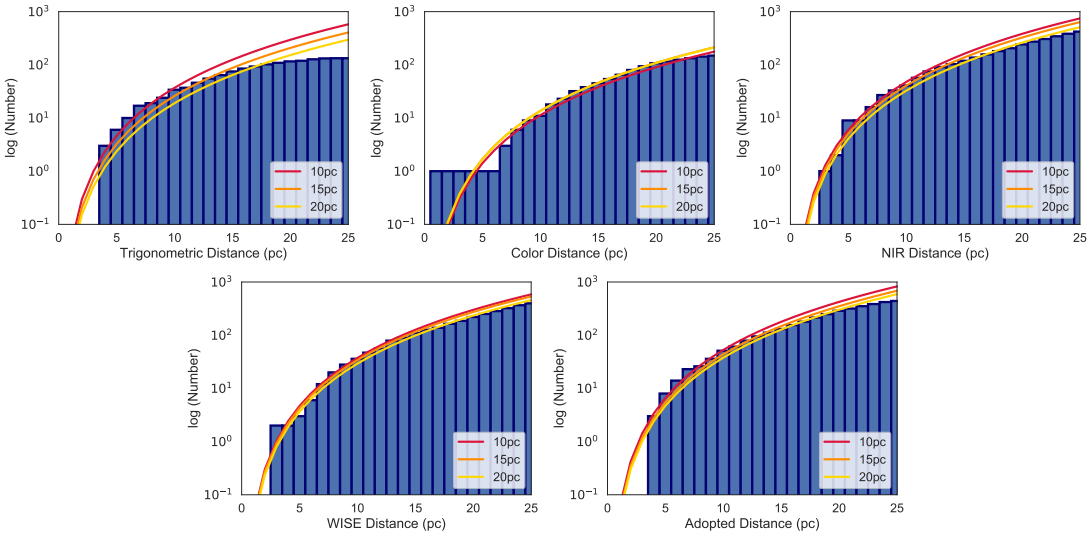

Figure 5.15 Cumulative histograms for each calculated distance with cube law fits assuming completeness in the $5-10$ pc (red), $5-15$ pc (orange), and $5-20$ pc (yellow) ranges.

5.4.6 Binaries

During sample clean-up, a number of binary systems were identified. Special care was taken to distinguish where the components had resolved photometry. We found cases were a sample member was associated with an earlier or later-type object such that only one of the two sources met our sample criteria, and also, where both components of an ultracool binary system were members (e.g. 2MASS J15200224−4422419, an L1+L4.5 binary; Burgasser et al. 2007b).

Additionally, we used the spectral binary technique for M7−L7 primaries described in Bardalez Gagliuffi et al. (2014) to identify spectral blends in the spectral sample. Through spectral indices, we found 3 strong candidates and 2 weak candidates, determined by the number of times the objects were found in the regions of interest from the 12 parameter spaces explored in the method[5]. These objects were compared to single and binary templates drawn from the full SpeX Prism Library using a χ^2 minimization routine. Spectral binary candidates are listed in Table 5.9.

[5]The boundaries of the parameter spaces were modified in Bardalez Gagliuffi et al. (2015) to include the newly discovered M9+T5 spectral binary WISE J072003.20−084651.2

Table 5.8 Ultracool Binaries with M7−L5 Primaries in the 25 pc Sample

Designation	Combined SpT	Primary SpT	Secondary SpT	Adopted Distance (pc)	Binary Reference
Ultracool Binaries					
J00275592+2219328AB	M7.5	M8	M9	15.27±0.89	122
J00413538−5621127AB	M6.5	···	···	19±2	66
J02192210−3925225AB	···	M6	L4	7±1	149
J06523073+4710348	L4.5	L3.5	L6.5 9±1	138	
J07003664+3157266	···	L3.5	L6	12.2±0.3	138
J07111138+4329590B	M5.5	M6.5	M7.5	12.85±0.5	199
J07200325−0846499	M9.0	M9.5	T5	6.02±1.02	129
J07464256+2000321	···	L0	L1.5	11.6±0.62	143
J08230313−4912012	L1.5	L1.5	L5.5	16±2	106
J08581519+1945470AB	M5.5	M7	M8	5.66±0.09	104
J10170754+1308398	L2.0	L2	L2 23±3	17	
J10471381+4026493AB	M9	M8.0	L0	14±2	14
J11122567+3548131	···	L4.5	L6:	21.72±0.42	158
J11214924−1313084	M8.0	M8	L7.5	15.19±0.47	129
J13054019−2541059AB	···	L2.0	L3.5	18.66±0.7	144
J13142039+1320012	M6	M6	M7.0	16.39±0.75	140
J13153094−2649513	L5.5	L3.5	T7 19±2	160	
J14162408+1348263	···	L5.0	T7.5	9.1±0.15	161
J14304358+2915405AB	L2.0	L2	L3.5	24±3	17
J15200224−4422419AB	L1	L1.5	L4.5	19±2	146
J17072343−0558249AB	···	M9.0	L3	12±1	19
J18450541−6357475	···	M8.5	T6	3.85±0.02	201
J18470342+5522433	M6.5	M7	M7.5	20±2	138
J21402931+1625183	···	M8.5	L2	21±2	167
Ultracool Companions to Main Sequence Primaries					
J00043484−4044058ABC	···	M4	L5+L5	13.01±0.67	143
···	L5	L5	L5	13.01±0.67	143
J02355993−2331205B	···	K3.5	L1.5	21.21±0.12	31
J06091922−3549311	···	M1	L3	22.14±0.17	153
J10043929−33351889	···	M4	L4	18.25±1.86	129
J14422164+6603208	···	M3	L0.0	10.97±0.04	163

Table 5.8 Continued

Designation	Combined SpT	Primary SpT	Secondary SpT	Adopted Distance (pc)	Binary Reference
J14501581+2354424ABC	···	F9IV	L4+L4	18.17±0.11	88
···	L4	L4	L4	18.17±0.11	88
J17114559+4028578	···	M4.5	L5.0	13.55±0.94	100
J17125121−0507249	···	M1	M9.5	19.96±1.44	200
J20040620+1704125	···	G0	L4.5	17.24±0.27	166
J23081888+0629551	···	M2	M8.0	9±1	115
J23540928−3316266	···	WD	M9.0	22.53±1.06	152

References. — (14) Close et al. (2003), (17) Wilson et al. (2003), (19) McElwain & Burgasser (2006), (31) Gizis et al. (2001), (66) Gagné et al. (2015c), (88) Goto et al. (2002), (100) Radigan et al. (2008), (104) Newton et al. (2014), (106) Folkes et al. (2012), (115) SpeX Prism Library, (122) Forveille et al. (2005), (129) Bardalez Gagliuffi et al. (2014), (139) Konopacky et al. (2010), (141) Dupuy et al. (2016), (144) Knapp et al. (2004), (145) Stumpf et al. (2008), (146) Radigan et al. (2013), (147) Burgasser et al. (2007b), (150) Artigau et al. (2015), (153) Burgasser et al. (in prep.), (154) Allers & Liu (2013), (159) Burgasser et al. (2010a), (161) Burgasser et al. (2011b), (162) Bowler et al. (2010), (164) Forveille et al. (2004), (167) Liu et al. (2002), (168) Dupuy & Liu (2012), (201) Montagnier et al. (2006), (202) Schneider et al. (2011), (203) Biller et al. (2006).

Table 5.9 Spectral binary candidates with M7−L7 primary components in the 25 pc Sample

Designation	Combined SpT	Primary SpT	Secondary SpT	Confidence	ΔJ	Binary Reference
Strong Candidates						
J08053189+4812330	T0.0	L4.3±0.4	T5.0±1.1	> 99%	1.521±0.340	165
J13153094−2649513	L5.0	L4.7±0.4	T5.4±3.0	95%	2.113±0.783	169
J14162408+1348263	L5.0	L4.0±0.2	T2.3±0.5	> 99%	1.207±0.118	170
Weak Candidates						
J02192210−3925225	M6.0	M6.3±0.2	T5.4±1.7	53%	4.835±0.646	157
J024029501+28325766	M7.0	M7.2±0.3	T5.7±1.5	61%	4.464±0.629	···
J04430581−3202090	L5.0	L4.4±0.1	T1.3±0.3	83%	1.112±0.074	134
J06431685−1843375	M9.0	M8.5±0.0	T6.1±1.3	86%	4.155±0.575	···
J09473829+3710178	M6.0	M6.2±0.4	T4.5±1.9	87%	4.725±0.668	···
J11061897+0428327	M7.0	M7.8±0.2	T7.0±0.6	52%	4.885±0.435	134
J11232934+0154040	M7.0	M7.9±0.4	T5.1±2.1	41%	4.121±0.621	···
J13261625+5640448	M7.0	M7.7±0.2	T5.5±1.9	58%	4.276±0.681	···
J14442067−2019222	M7.0	M7.8±0.2	T3.7±1.5	> 99%	3.536±0.297	134
J15150083+4847416	L5.0	L4.6±0.4	T1.8±0.6	94%	0.961±0.172	16
J15394189−0520428	L5.0	L2.9±0.9	T4.2±2.7	65%	2.433±0.613	85
J17334227−1654500	L1.0	L0.2±0.3	T4.2±1.7	80%	3.014±0.529	134
J17335314+1655129	M6.0	M6.2±0.3	T5.4±1.6	54%	4.930±0.639	···
J22021125−1109461	M7.0	M7.5±0.1	T5.4±1.7	83%	4.257±0.607	69
J22285440−1325178	M6.0	M7.1±0.5	T5.6±1.5	41%	4.484±0.607	134

Table 5.9 Continued

Designation	Combined SpT	Primary SpT	Secondary SpT	Confidence	ΔJ	Binary Reference
J23272645−1741329	M6.0	M7.3±0.4	T6.6±1.1	40%	4.850±0.543	···
J23312174−2749500	M8.0	M8.3±0.1	T6.1±1.3	74%	4.202±0.612	···

References. — (16) Liu & Leggett (2005); (69) Schmidt et al. (2010); (85) Scholz et al. (2004b); (134) Salim & Gould (2003); (157) Burgasser et al. (2007a); (165) Witte et al. (2011); (169) Burgasser & McElwain (2006); (170) Metodieva et al. (2015).

From the 20 index-selected candidates, only 5 had statistically better fits to binary templates rather than single templates, evaluated by a one-tailed F-test statistic. The three spectral binaries identified as strong candidates are in fact all confirmed or candidate spectral binaries. 2MASS J08053189+4812330 is an unusually blue spectral binary (Burgasser 2007b) confirmed by astrometric monitoring (Dupuy & Liu 2012) and radial velocity variability (Burgasser et al. 2016). 2MASS J13153094−2644313 is a candidate spectral binary of L3.5 and T7 components Bardalez Gagliuffi et al. (2014). SDSS J141624.08+134826.3 is a binary with both L7 and T7.5 unusually blue components (Burningham et al. 2010). However, this one is a resolved binary rather than a spectral binary, yet its blue colors have contaminated spectral binary selection criteria in the past (Bardalez Gagliuffi et al. 2014). The known M9.5+T5 spectral binary WISE J072003.20−084651.2 is a included in the sample, but was only selected in 3 regions, disqualifying it as a candidate spectral binary. We speculate that the spectral indices are sensitive to the signal-to-noise ratio of the spectrum.

The only two weak candidates with a confidence greater than 90% that the binary fit is statistically better than the single fit are 2MASSW J1515008+484742 and 2MASS J14432067−2019222. The only subtle signature of binarity in 2MASS J1515+4847 is the sloped peak in the *J* band, typically caused by the additional flux provided by the T dwarf secondary. The *H*-band dip is not particularly noticeable. For the case of 2MASS J1443−2019, we notice after further examination that this source is a subdwarf (Winters et al. 2015). Subdwarfs and unusually L dwarfs are known contaminants to spectral binary indices (Bardalez Gagliuffi et al. 2014).

There are four spectral binaries: 2MASS J0805+4812, 2MASS J1315−2647, 2MASSW J1515+4847 and WISE J0720−0846 in a sample of 370 ultracool dwarfs up to 25 pc for which we have SpeX spectra, leading to an observed spectral binary fraction of $0.95 \pm 0.14\%$. However, since we are working with small numbers, a Poisson uncertainty

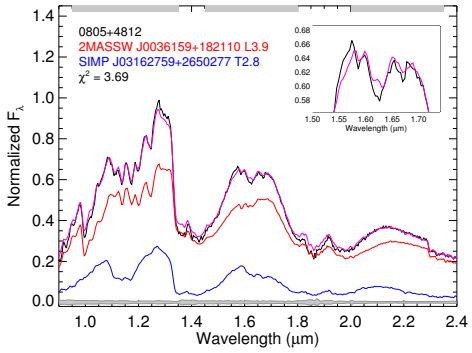

(a) 2MASS J0805+4812

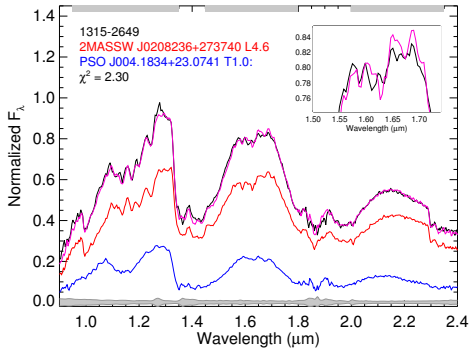

(b) 2MASS J1315−2647

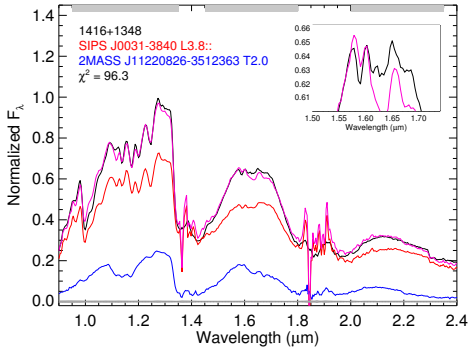

(c) SDSS J1416+1348

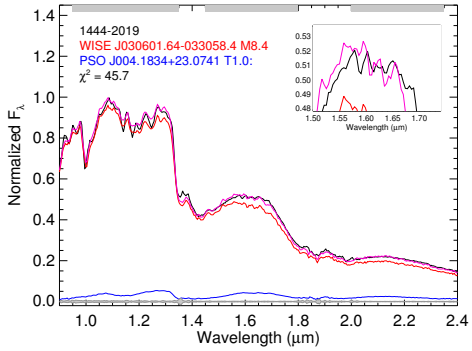

(d) 2MASS J1444−2019

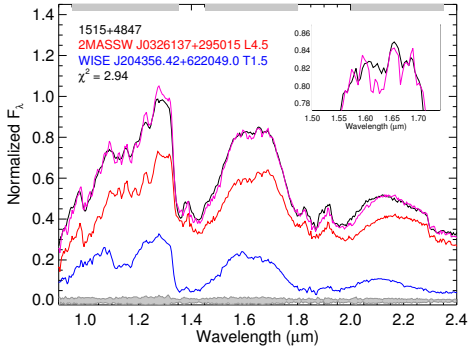

(e) J1515+4847

Figure 5.16 Spectral binary candidates with M7−L5 primaries in the 25 pc volume with a confidence $> 90\%$. 2MASS J0805−4812 and 2MASS J1315−2649 (top two) are strong candidates, SDSS J1416+1348 is a binary system with two unusually blue components (middle left), 2MASS J1443−2019 is a subdwarf, commonly mistaken as a spectral binary. 2MASS J1515+4847 is a new spectral binary candidate from this study.

is more realistic. This implies that the uncertainty on the binary fraction is $\sqrt{N}/370$, where N is the number of spectral binaries, in this case, 3.5 accounting for the one candidate. This estimation yields a spectral binary fraction of $0.95 \pm 0.5\%$. While this fraction is certainly low, it encompasses a very narrow range of component spectral types and a specific technique with its own biases, and can only be understood as a lower limit given our sample incompleteness. A large-scale binary population simulation described in Chapter 6 explores the significance of this spectral binary fraction with respect to the true binary fraction of ultracool dwarfs. A larger sample than 25 pc would be needed to reduce the large uncertainties on this fraction.

5.5 Discussion

The main difficulty in compiling a complete, volume-limited sample of ultracool dwarfs from the literature is the variety of selection criteria that goes into defining the surveys that discovered or characterized the sample members in the first place. In order to homogenize the piece-wise sample selection, we obtained low-resolution, near-infrared SpeX spectra of most of the sample.

We have selected objects from the literature where any of their spectral type classifications, be it optical, near-infrared or photometric estimate, was within M7−L5. As our analysis shows, most spectral type classification schemes are able to identify spectral type within a subtype. Therefore, it is likely that sources classified as M6 or L6, at the edges of our spectral type cut, have been included in the sample. We have also identified members of brown dwarf subpopulations, such as red and blue $J - K_s$ outliers, low gravity objects and one candidate binary to be followed up in the future.

The volume limit of this survey is a mix of trigonometric and spectrophotometric distances. We experienced contamination from bright, main sequence stars at distances

beyond 25 pc. These objects were eliminated from the sample by obtaining spectra and classifying it. Assuming constant density and an isotropic spatial distribution, we estimate our completeness at $49\% - 89\%$. This range implies an uncertainty in completeness of roughly a factor of two. Properly constraining the number of brown dwarfs in the Solar neighborhood has important consequences for determining the ratio of stars to brown dwarfs, the shape of the initial mass function and whether these objects share formation mechanisms or not.

Acknowledgments

The authors thank telescope operators Brian Cabreira, Dave Griep, and Tony Matulonis at IRTF for their support during observations. DBG and AJB acknowledge funding support from the National Aeronautics and Space Administration under Grant No. NNX15AI75G. This research has made heavy use of the VizieR catalogue access tool and SIMBAD database, operated at CDS, Strasbourg, France. The original description of the VizieR service was published in Ochsenbein et al. (2000), and the SIMBAD astronomical database was published in Wenger et al. (2000). This publication makes use of data from the SpeX Prism Spectral Libraries, maintained by Adam Burgasser at http://www.browndwarfs.org/spexprism. The authors wish to recognize and acknowledge the very significant cultural role and reverence that the summit of Mauna Kea has always had within the indigenous Hawaiian community. We are most fortunate to have the opportunity to conduct observations from this mountain.

This Chapter, in part, is currently being prepared for submission for publication of the material. Bardalez Gagliuffi, Daniella; Burgasser, Adam. The dissertation author was the primary investigator and author of this material.

Chapter 6

Brown Dwarf Population Simulations

6.1 Introduction

The essential mechanisms driving the formation of brown dwarfs is one of the fundamental open questions in stellar astrophysics. The distribution of stellar masses at birth is encapsulated in the initial mass function (IMF), which measures the number of objects dN formed within masses $M + dM$, and is typically represented as a power law, $dN \propto M^{-\alpha} dM$ (e.g. Salpeter 1955), a broken power law (Kroupa 2001) or a log-normal distribution (Chabrier 2005). Computing an accurate initial mass function across and below the hydrogen burning limit is crucial in order to better constrain the formation mechanisms. However, calculating mass functions for substellar objects is challenging because their inability to sustain core hydrogen fusion causes a mass-age-luminosity degeneracy, which obstructs their physical characterization.

Fortunately, ultracool binaries have the advantage of being coeval, cospatial and chemically homogeneous composition, and their population statistics can provide strong constraints on formation scenarios. Binary fractions have been calculated for numerous observed samples of ultracool dwarfs: $10-20\%$ for high resolution imag-

ing (e.g. Close et al. 2003; Gizis et al. 2003; Burgasser et al. 2003b), $2-30\%$ for radial velocity variability (e.g Basri & Reiners 2006; Joergens 2008; Blake et al. 2010), $22-60\%$ for overluminosity searches (e.g. Pinfield et al. 2003), 5% for astrometric monitoring (Sahlmann et al. 2014). Each one of these observational methods is sensitive to a different range of binary separations, and subject to a different set of biases.

An alternative, separation-independent binary identification technique is to select candidates from low-resolution, near-infrared spectra as blended-light systems known as spectral binaries (Burgasser et al. 2010a; Bardalez Gagliuffi et al. 2014). This technique has identified over 60 candidate binaries, about a dozen of which have been confirmed by follow-up, high-resolution observations (e.g. Burgasser et al. 2006c; Dupuy & Liu 2012; Burgasser et al. 2015b; Bardalez Gagliuffi et al. 2015). In the previous chapter, the spectral binary fraction was determined to be $0.80 \pm 0.12\%$ in a volume-limited spectroscopic sample up to 25 pc for M7$-$L5 ultracool dwarfs as primaries with T dwarf secondaries. However, in order to understand the implications and biases of this statistic and the origin of the statistical properties of brown dwarf binaries, we need to carry out a systematic study of the spectral binary technique.

Binary population simulations have been performed in the past to evaluate the observational biases in a controlled sample, especially to model distributions that are difficult to extract from observations, namely the IMF. Reid et al. (1999) first attempted to calculate the field substellar mass function using simulations of the solar neighborhood population and using observed L dwarf space densities and temperature distributions. Burgasser (2004) modeled the field substellar mass and luminosity functions of L and T dwarfs with Monte Carlo simulations, finding a minimum in mid-type L dwarfs numbers, and an increase in number density for T dwarfs. Burgasser (2007a) explicitly simulated L/T transition binaries and found that their observed excess is due to the rapid evolution of ultracool dwarfs across this transition, as evidenced by the flattening of the luminosity

scale. However, there are currently no binary population simulation that includes late-M dwarfs.

In this paper, we complement the results of Chapter 5 with an ultracool binary population simulation. Section 6.2 describes the design and methodology followed to generate a population of binaries with different assumptions of the IMF, age distribution, mass ratio distribution, and evolutionary models to obtain primary and secondary temperatures and spectral types. Section 6.3 presents the outcomes of the simulation in terms of the physical properties of the binary systems created. Section 6.4 explores the selection function of spectral binaries for our baseline model combination. Conclusions are presented in Section 6.5.

6.2 Methodology

The goal of this analysis is to quantify the selection function of the spectral binary technique, as the fraction of all binaries identified through this method, and accounting for variance in the underlying ultracool dwarf binary population. This was done by generating a population of binary brown dwarf properties, creating synthetic binary spectra based on those properties and subjecting them to the spectral binary selection technique (Bardalez Gagliuffi et al. 2014). In this manner, we can quantify the spectral binary selection, its biases and limitations and infer the true binary fraction of ultracool dwarfs. We want to learn the combinations of spectral types that this technique can recover, along with false negative and false positive rates. Different assumptions of the initial mass function, age distributions, and observed mass ratio distributions to generate masses for secondary components, are used to create a population of binary brown dwarfs. A suite of interpolated grid evolutionary models is used to retrieve effective temperatures, which are converted to spectral types and absolute magnitudes using empirical relations.

The spectral types are used to randomly draw spectral templates from the SpeX Prism Library and generate synthetic binary spectra.

This simulation relied on modular, multi-step Python and IDL codes with five general steps:

1. **Generate Binary Population**: generate physical properties for a population of brown dwarf binary systems. Properties include: primary and secondary masses, ages, mass ratios, effective temperatures, spectral types, and absolute magnitudes in 2MASS JHK_s.

2. **Synthetic Binaries**: create synthetic binaries by drawing single spectral templates from the SpeX Prism Library for a given spectral type.

3. **Spectral Index Selection**: calculate spectral indices from Bardalez Gagliuffi et al. (2014) for each synthetic binary, and select sources that match the spectral binary criteria.

4. **Selection function**: Assess selection function and calculate the true binary fraction.

   Below is an in-depth description of each piece of code.

6.2.1 Generate Binary Population

To generate a binary population means to create a suite of binary properties consistent with our assumptions. The IMF form dN/dM is a probability distribution function (PDF) that returns the number of stars created per mass bin. The integral of the PDF over the full range of masses is the cumulative distribution function (CDF). The CDF ranges from 0 to 1, such that random draws in that range will correspond to a frequency of masses. Primary masses are randomly drawn from an initial mass function distribution

using the `evolve.simulateMasses` function from SPLAT. The same process is followed to randomly draw ages from an age distribution with the `evolve.simulateAges` SPLAT function, and mass ratios from `evolve.simulateMassRatios`. By multiplying the mass ratios to the primary masses, we obtain the secondary masses.

Next, using the `evolve.modelParameters` function in SPLAT, effective temperatures can be estimated for each object, given its mass and age. There are several interpolated grid evolutionary models available for this step, including those from Saumon & Marley 2008; Baraffe et al. 2003, and Burrows et al. 1997a. The effective temperatures are converted to spectral types using the empirical relation of Filippazzo et al. (2015) interpolated in reverse, valid for types M6−T9. Absolute magnitudes in 2MASS JHK_s were then estimated from spectral types with the empirical relation of Dupuy & Liu (2012) with the SPLAT function `empirical.typeToMag`, also valid for M6−T9. Objects whose temperatures return spectral types later than T9 are given a Y spectral type, and thus ignored in subsequent steps due to this limitation in the applicability of empirical relations. However, we wanted to keep a record that these objects were generated in the first place, since they are possible binaries given our assumptions. All of these properties are saved in a Pandas DataFrame and subsequently onto a text file.

6.2.1.1 Input models

We used the Chabrier (2005) lognormal and the Kroupa (2001) broken power law IMFs to evaluate the differences in mass functions. For a more detailed description of the mass models, please refer to Section 1.4.3.1. We found an issue with the normalization of the Kroupa mass function that created a spike in the number of objects right at the hydrogen-burning minimum mass, where the exponents for the IMF change from $\alpha = 0.3$ for masses below $0.08\,M_\odot$ to $\alpha = 1.3$ for higher masses than$0.08\,M_\odot$. For age models, we used a uniform distribution and a Rujopakarn cosmic age distribution (Rujopakarn

et al. 2010), which assumes a peak in the star formation rate (SFR) of the universe at a redshift of $z \geq 1$ that declined to the present day SFR by an order of magnitude, as supported by observations (e.g. Lilly et al. 1996). For mass ratios, we use a uniform distribution and the Allen (2007) power law model which has a functional form of $f(q) \propto q^{1.8}$ and peaks at equal masses. Finally, to obtain temperatures from our mass and age assumptions, we used the evolutionary models of Baraffe et al. (2003), Burrows et al. (2001) and Saumon & Marley (2008).

6.2.1.2 Synthetic Binaries

Once the component spectral types have been defined, binary templates are created using single templates from the SpeX Prism Library using `splat.getSpectrum`. We use randomly-selected spectra as templates rather than spectral standards to account for the large diversity of sources for a given spectral type. Optical spectral type are used to draw near-infrared SpeX spectra for objects whose spectral type is earlier than L8.5, while near-infrared spectral types are used for T dwarfs. Spectral types later than T9 which had been excluded in the previous step do not retrieve a spectrum. In the case that the $> T9$ source is a primary, no binary spectrum is created, whereas if it is a secondary, the primary spectrum acts as the binary spectrum with the assumption that the late-type secondary is too faint to significantly modify the primary spectrum. Spectra from binaries, known and candidate spectral binaries, young sources, giants and subdwarfs are excluded from the retrieval.

Each individual spectrum is scaled to its absolute magnitude in J using the Dupuy & Liu (2012) relation, thus guaranteeing that all objects rest at a distance of 10 pc by definition. The flux component of the primary and secondary spectra are added to generate a synthetic binary spectrum. The binary spectra are classified by comparison to spectral standards using `splat.classifyByStandard` to find the combined spectral

type, an observable of a blended-light binary system.

6.2.2 Calculate Spectral Indices

The spectral indices defined in Bardalez Gagliuffi et al. (2014) and later modified in Bardalez Gagliuffi et al. (2015) are flux ratios obtained by integrating the flux density in small wavelength ranges for a given spectrum. The SPLAT function `splat.measureIndexSet` calculates the spectral indices used in the spectral binary technique. The spectral indices of the binary templates are saved to a Pandas DataFrame. If a NaN spectrum is found, as would be the case for both components $> T9$, this code returns NaN on for each spectral index.

6.2.3 Spectral Index Selection

A critical step of the spectral binary technique is to determine whether an object is an outlier in spectral index trends, indicative of a blended-light source. The objects which are consistent outliers in at least four index-index plots are selected as candidates. We use the matplotlib function `path.Path` to create a closed region in a plot given the vertices of a polygon, while also keeping track of the points falling inside with the `contains_points` attribute, thus identifying the spectral binary candidates and their count in regions of interest in the index-index plots.

While the full spectral binary technique uses template fitting to characterize the spectral types of the components and their relative magnitudes, this step was not performed due to computational limits.

6.3 Model Binary Populations

The simulations were run for $N = 100,000$ simulated systems in a parallel code in order to generate a sufficiently large sample of spectral binary candidates. Given the normalization issue with the Kroupa (2001) IMF, we only compare the last four models to each other, and use the model combination including the Chabrier (2005) IMF for the binary analysis in Section 6.4.

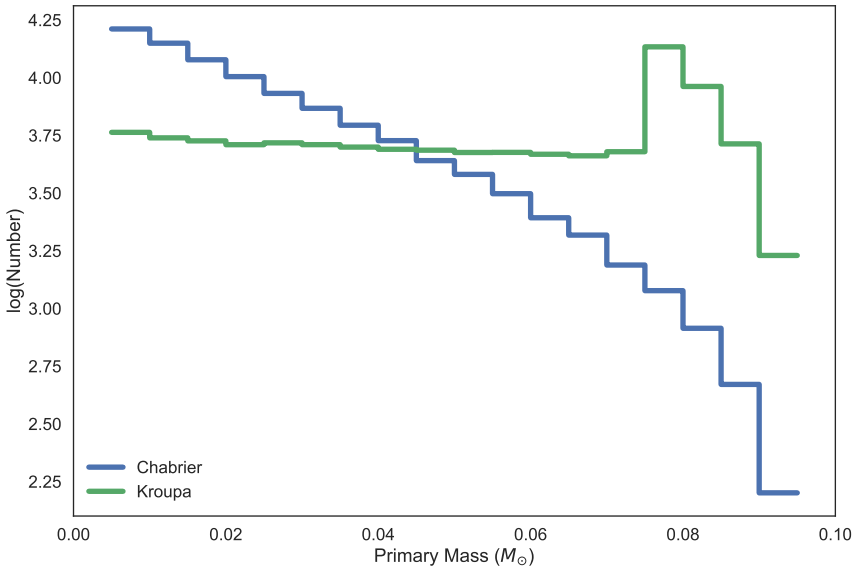

Figure 6.1 Mass distribution for the primary sources, according to the Chabrier and Kroupa IMFs. The Chabrier distribution has a log normal shape while the Kroupa IMF is a broken power law. Notice the normalization issue at $0.08\,M_\odot$, where the discontinuity in the Kroupa IMF occurs.

The primary mass, age and mass ratio distributions are our independent models. Figure 6.1 shows the differences between the Chabrier and Kroupa IMFs, with the Chabrier lognormal distribution increasing at lower masses, while the Kroupa mass function is discontinuous at $0.08\,M_\odot$, with an exponent of 0.3 for masses below that limit and 1.3 for masses above the limit. The shallow slope at lower masses for the Kroupa distribution is congruent with its exponent close to zero. These models show a normalization issue at the discontinuity, caused by a programming error.

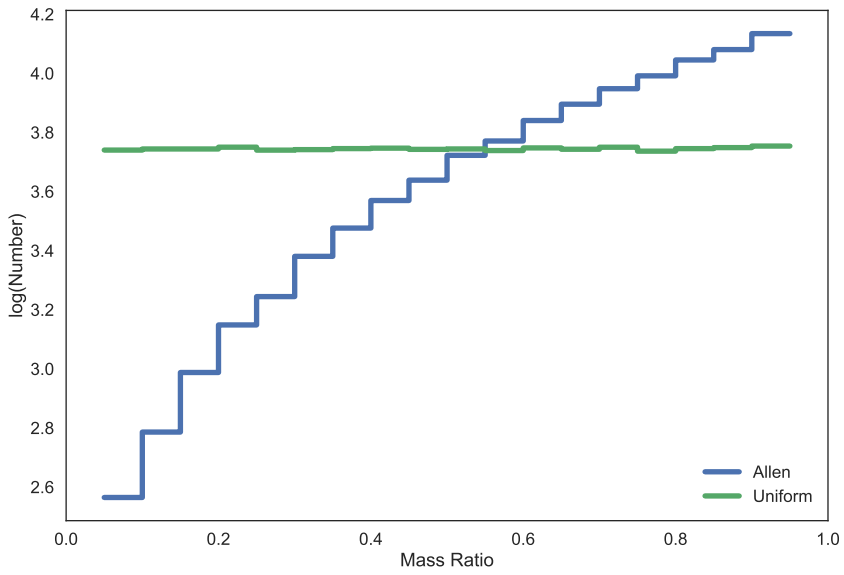

Figure 6.2 Uniform (green line) and Allen (blue line) mass ratio distributions. The uniform mass ratio distribution is equally likely for any mass ratio between 0 and 1, while the Allen distribution assumes a power law shape.

The mass ratio distributions used were a uniform distribution and the power law from Allen which increases towards equal masses, aligning with observations. Figure 6.2 shows precisely that behavior.

The secondary masses are the product of the mass function and the mass ratio distribution. For the Kroupa mass function and a uniform mass ratio distribution, we observe a shallow peak at $0.01\,M_{\odot}$, decreasing towards higher masses. The same mass function compared to an Allen mass ratio distribution yields secondary masses with a flatter distribution across the brown dwarf mass regime. For both of these cases there is a significant drop off after $0.08\,M_{\odot}$, signaling the discontinuity in the Kroupa power law. The Chabrier mass function with the Allen mass ratio distribution has a peak at $0.01\,M_{\odot}$ as well and continuously decreases towards higher masses. The secondary mass distribution for the Chabrier IMF is very similar in shape to the primary mass distribution because the Allen mass ratio peaks at 1, so most of the binaries generated in this model have components with equal masses. With only slight variations, in these three model

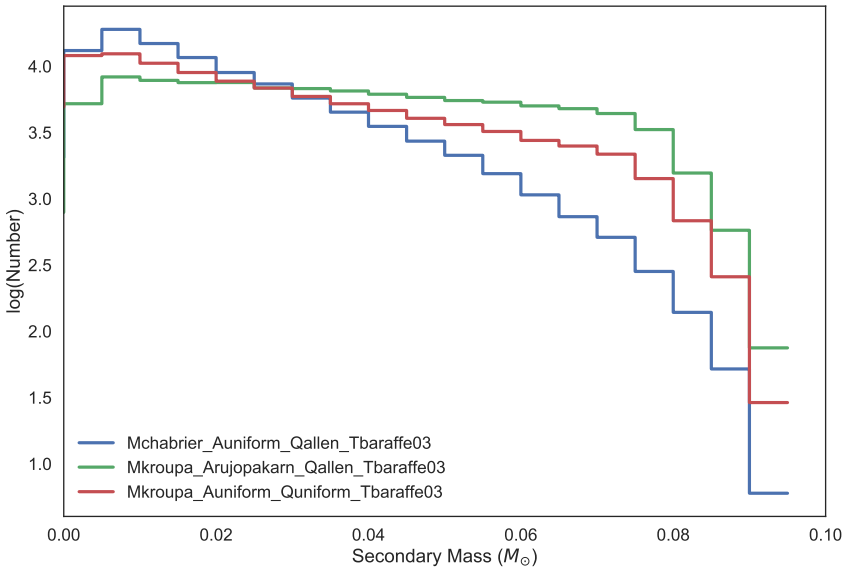

Figure 6.3 Mass distribution for the secondaries for a Kroupa IMF with both uniform and Allen mass ratio distributions (red and green lines, respectiverly), and for the Chabrier IMF and the Allen mass ratio distribution (blue line).

combinations, it is more common to find secondaries are at the lower end of the brown dwarf mass regime.

The age distributions used were a uniform distribution and a Rujopakarn cosmic age distribution. In the Rujopakarn age model, the star formation rate was higher in the past and has decreased to the current value. This is consistent with the age distribution peaking at old ages, as seen in Figure 6.4.

Combining masses and ages, we can obtain effective temperatures using evolutionary models. For the Kroupa mass function with uniform age and uniform mass ratio, the Baraffe 2003 models produce a primary effective temperature distribution with a peak at roughly 2300 K and a shallower peak at 500 K. The same mass function with a Rujopakarn age distribution and an Allen mass ratio peaking at unity shows a similar shape in the distribution, with a slightly deeper valley in the $1200 - 1800$ K range. The Chabrier mass function with a uniform age distribution and an Allen mass ratio produces a peak at low temperatures around 400 K, which steadily decreases towards

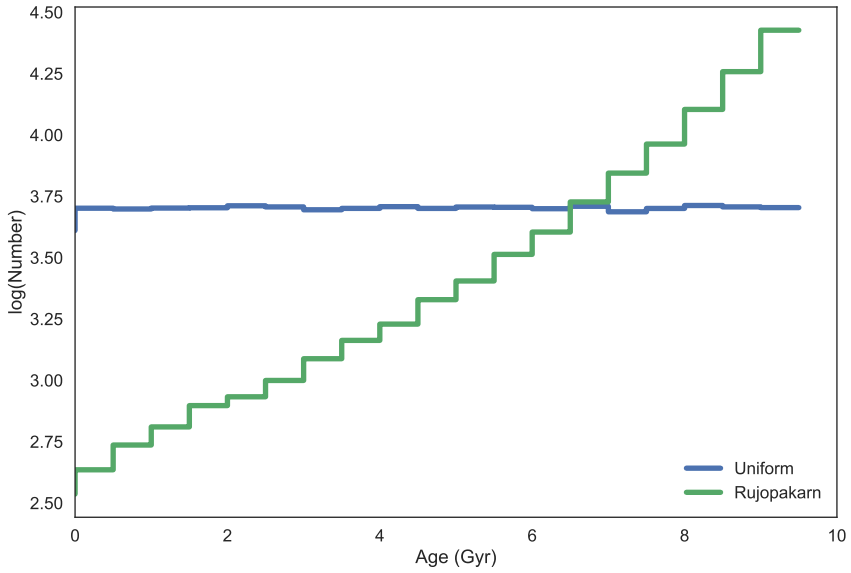

Figure 6.4 Age distributions for uniform (blue line) and Rujopakarn (green line) models. The uniform age distribution assumes a constant star formation rate throughout the history of the universe, while the Rujopakarn age model describes a higher star formation rate up to a redshift of $z = 1$ that flattens out to the present day.

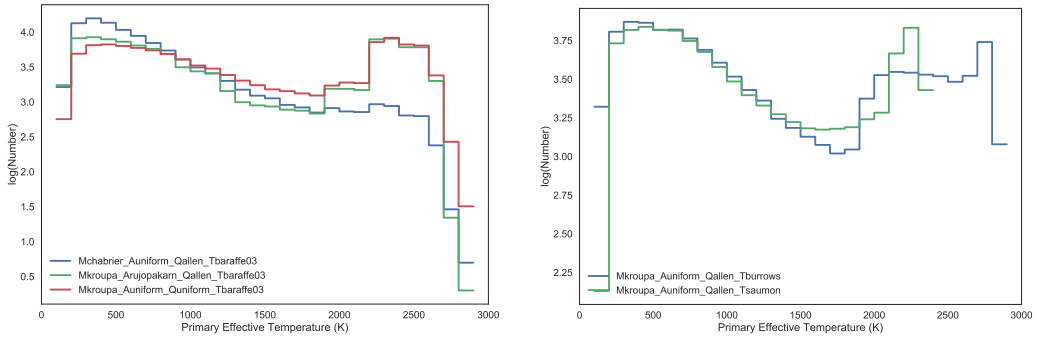

Figure 6.5 Effective temperature distributions for the primaries according to the Baraffe (left plot), Burrows (right plot, blue line) and Saumon (right plot, green line) models.

higher temperatures. This pile-up of objects at cool temperatures must contain both very low mass objects formed with low temperatures and massive, and older brown dwarfs that have cooled down to low temperatures over the course of their lifetime. The main difference between the Chabrier and Kroupa mass functions, given all other parameters constant, is in the number of high temperature objects created, with an order of magnitude

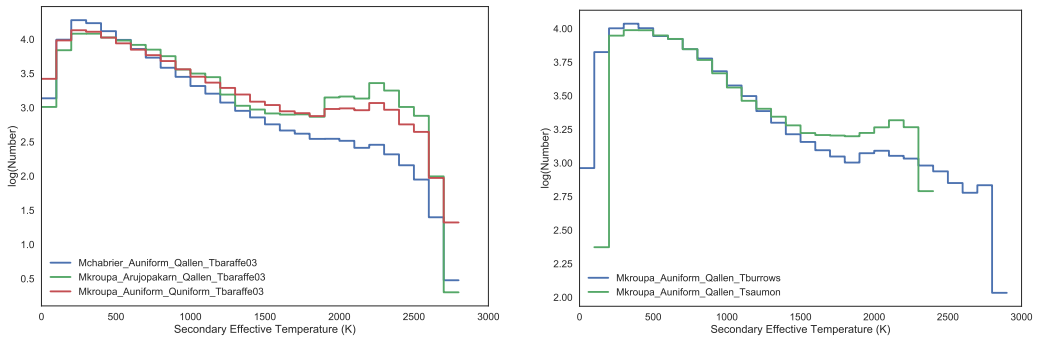

Figure 6.6 Effective temperature distributions for the secondaries according to the Baraffe (left plot), Burrows (right plot, blue line) and Saumon (right plot, green line) evolutionary models.

more $2000-3000$ K objects generated by the Kroupa IMF than the Chabrier IMF. The most interesting feature is the decline in all three model combinations around 1000 K to 2000 K, encompassing the later half of the L dwarf class. The drop off seen at ~ 2500 K corresponds to the $0.1\,M_{\odot}$ upper mass cut off, while the one seen at ~ 300 K is a feature of the $0.01\,M_{\odot}$ lower mass cut off.

Comparing the evolutionary models of Burrows and Saumon given a Kroupa IMF, a uniform mass function and an Allen mass ratio distribution, we see very similar behavior at low temperatures until about 1500 K. The valley between 1500-200 K, also seen for the other model combinations in a slightly wider range of temperatures, is deeper for the Burrows models than the Saumon models. The peak at higher temperatures occurs at 2300 K for the Saumon models and at 2700 K for the Burrows models. However, the steep increase and drop off of these high temperature peaks may be an artifact of the normalization problem at the Kroupa IMF discontinuity. Notice the different scales on the y-axis of the two subfigures of Figure 6.5 and the temperature cut off for the Saumon models at $T_{\rm eff} \sim 2200$ K.

Figure 6.6 shows the distributions for the effective temperatures of the secondaries. On the left figure, the secondary effective temperatures follow a similar pattern as

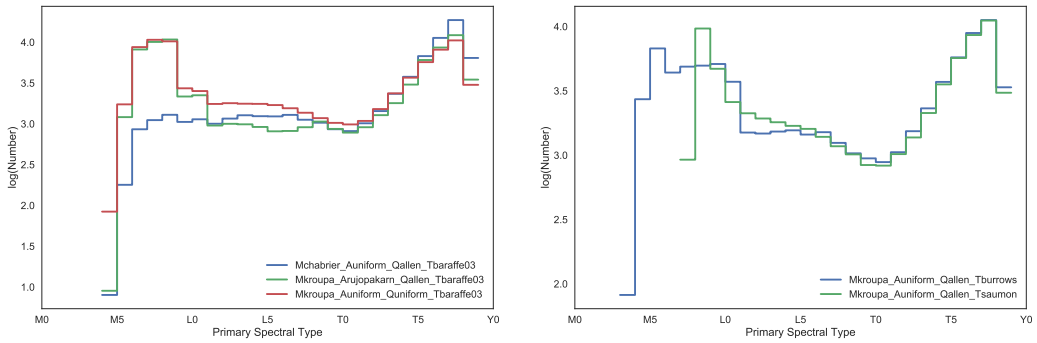

Figure 6.7 Spectral type distributions for the primaries according to the Baraffe (left plot), Burrows (right plot, blue line) and Saumon (right plot, green line) evolutionary models.

the primary effective temperatures, with the only difference in the height of the high temperature peak. By definition, the secondaries are the lower mass components of binary systems, and as such they are cooler than the primaries. The difference between the peaks around $2000 - 2500$ K are caused by the mass functions, the elevated peaks from Kroupa and the lower one from Chabrier. On the right figure, we evaluate the differences between the Burrows and Saumon evolutionary models, and observe that the overall shape is similar to the three model combinations of the left figure. The peak at high temperatures seems less pronounced for these two model combinations than for the Baraffe models.

Finally, we can transform the effective temperatures into spectral types using an empirical relation from Filippazzo et al. (2015). Figure 6.7 shows the spectral type distributions for the five model combinations analyzed. Spectral type is the observable proxy for effective temperature, and we see that the three distributions on the left are similar to each other, except in the late-M regime. This discrepancy between the Chabrier and Kroupa mass functions coincides with the primary effective temperature distributions at higher temperatures. On the right side of the same Figure, we also see a similar behavior to the primary effective temperatures shown earlier. The valley starting at mid-L

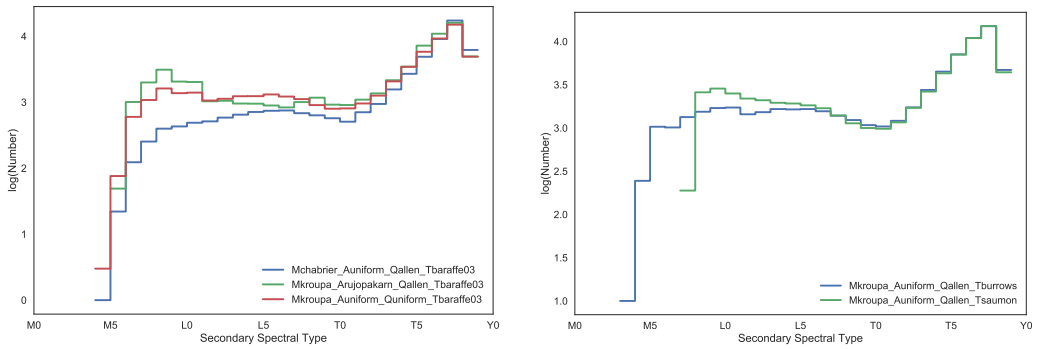

Figure 6.8 Spectral type distributions for the secondaries according to the Baraffe (left plot), Burrows (right plot, blue line) and Saumon (right plot, green line) evolutionary models.

and ending around mid-T dwarfs corresponds to the well-documented scarcity of L/T transition objects (e.g. Burgasser et al. 2002a), due to the short duration of the transition.

The distribution of secondary spectral types in Figure 6.8 also resembles the secondary effective temperature distribution. On the left we see a difference in the production of early-type objects between the Chabrier and Kroupa mass functions. Among the two model combinations with a Kroupa mass function, we see that the Rujopakarn age distribution produces more late-M dwarfs than the uniform age distribution, about 0.3 dex more than the Kroupa IMF and almost an order of magnitude more than the Chabrier IMF, both with a uniform age distribution. On the right side of this Figure, the only difference between the distributions is the evolutionary model used. The Burrows model goes to higher temperatures and spectral types, while the Saumon models are cut at roughly M7. The latter also predict a slightly higher number of late-M dwarfs than the Burrows model. In general, it seems that the population distributions are most sensitive to the choice of mass function.

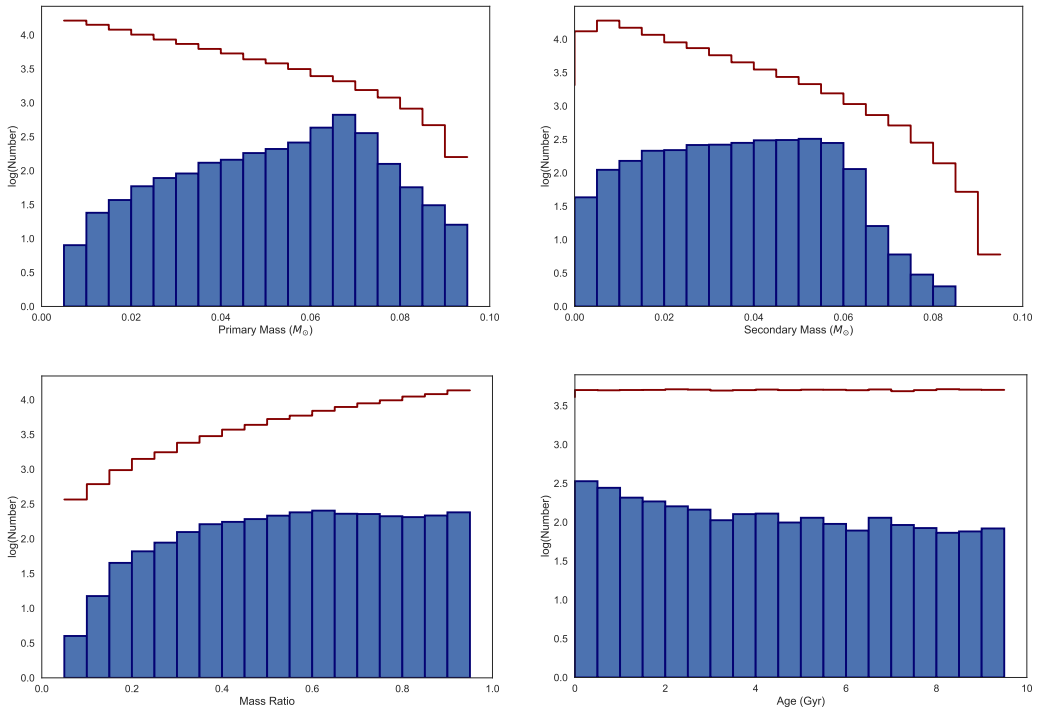

Figure 6.9 Primary masses, secondary masses, mass ratios and ages for our baseline model combination with a Chabrier IMF, a uniform age distribution, an Allen mass ratio distribution and the Baraffe evolutionary models. These distributions are shown as the dark red step function. Superimposed as a blue histogram are the objects selected as spectral binaries by the indices of Bardalez Gagliuffi et al. (2014).

6.4 Spectral Binary Selection Function and Biases

Each set of models produced a number of binary systems selected as spectral binaries using spectral indices. Figures 6.9 and 6.10 explore the parameter spaces covered by the spectral binaries in the sample. Spectral binary candidates were selected as the sources which fell on four or more of the twelve regions of interest in the index-index selection figures of Bardalez Gagliuffi et al. (2014). This includes both weak and strong spectral binary candidates.

Compared to the Chabrier mass function, spectral binaries have a clear peak around $0.07\,M_\odot$ for primary masses. The selected secondary masses span a broad range of brown dwarf masses uniformly from $0.03-0.06\,M_\odot$. However, this distribution

decreases slightly at the high end of this range, with a preference for lower masses. Secondaries with masses above $0.06 M_{\odot}$ are rare.

The range of mass ratios selected by the spectral binary technique is broad, as the technique is able to detect most values of mass ratio above 0.2. Below $q \sim 0.2$, it becomes increasingly rare to detect low mass ratio systems. While the selection function of spectral binaries flattens above $q = 0.2$, the distribution of binaries generated by an Allen mass ratio model increases towards unity. This implies that it is rare to identify systems with mass ratios below $q \sim 0.2$ and above $q \sim 0.6$ as spectral binaries, and conversely, the optimal identification range of the spectral binary technique are systems with $0.2 < q < 0.6$. Since the technique is based on detecting signatures of a faint companion in the spectra of the hotter primary, relying on the differences in the spectra of the components, it favors the identification of low mass ratio systems.

The fact that the ability to detect binary systems of this technique is in general unaffected by the mass ratio of the system suggests that the types of systems it detects are most likely straddling the hydrogen burning limit. In these case, both objects would have about the same mass, with one above and the other one below the HBMM, such that after the secondary has cooled to lower temperatures their spectral types are different from one another. This assumption would also suggest that the method is biased towards identifying older systems. However, the age distribution of the selected spectral binary candidates is flat across all ages with a slight increase towards young ages of roughly 0.5 dex.

Regarding the effective temperatures, the selected primaries have a broad peak around $1200 - 1600$ K which decreases towards higher temperatures. When analyzing primary spectral types, we see a symmetric distribution centered around L3, which roughly coincides with the effective temperatures. At spectral types earlier than L0, the primary dominates the combined-light flux so it becomes increasingly more difficult to

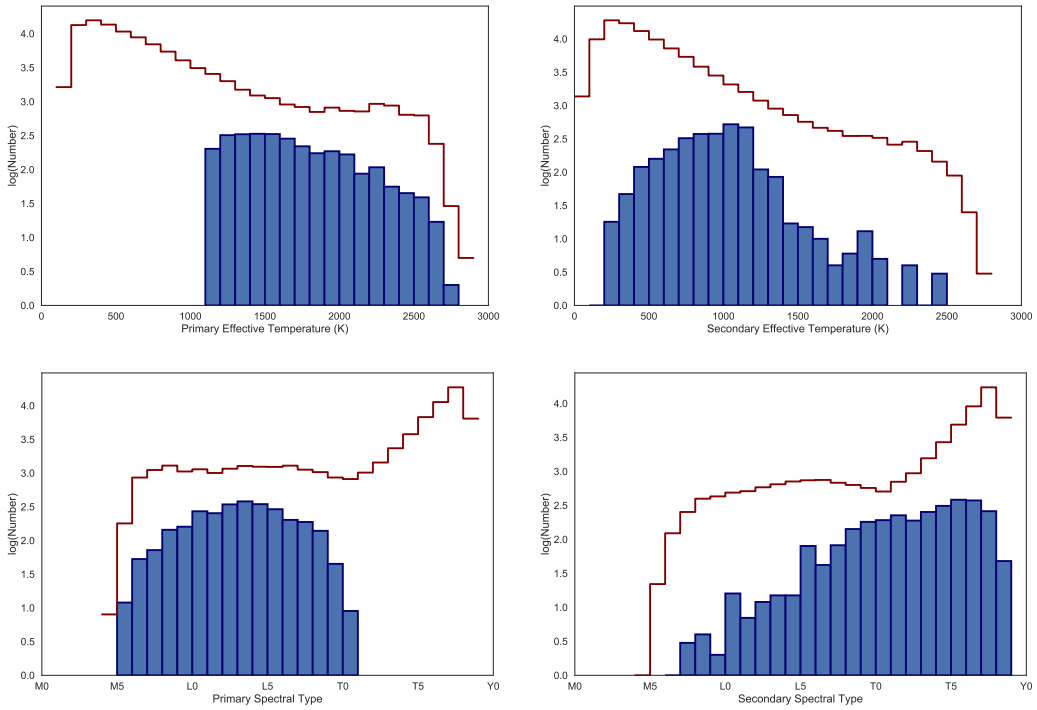

Figure 6.10 Primary and secondary temperatures and spectral types for the objects created by our baseline model combination with a Chabrier IMF, a uniform age distribution, an Allen mass ratio distribution and the Baraffe evolutionary models with the spectral binary selection function superimposed on the same scale. Same color-coding as in Figure 6.9.

detect faint T dwarf secondaries. The spectral binary technique for M/L+T dwarfs is defined for M7-L7 primaries, so at spectral types later than L5, it becomes less likely to identify binaries, possibly as methane absorption bands start to appear and deepen. The technique of Burgasser et al. (2010a) is better suited to identify spectral binaries with later-type primaries. For secondary temperatures, there is a clear peak around 1000 K that decreases in both directions, although the decrease is slower towards colder temperatures. Most objects detected as secondaries have temperatures above 200 K and below 1200 K, and spectral types later than L5. The technique is mostly sensitive to secondary spectral types in the L8-T2 range. It is likely that the candidate spectral binaries with secondaries earlier than T0 are false positives.

In Chapter 5 we found a spectral binary fraction of $0.95 \pm 0.5\%$ for the volume-limited sample of M7$-$L5 ultracool dwarfs. With these simulations we generated a population where we are guaranteed that 100% of objects are binary systems, we can calculate the correction factor of the spectral binary technique to estimate the true binary fraction. Table 7.2 presents the correction factors for each model combination. We will only analyze the Chabrier, Uniform, Allen, Baraffe model combination to avoid the Kroupa normalization problem. We counted the number of binary spectra created and spectral binaries selected compared to the full sample. We find a correction fraction of 0.029 or the inverse correction factor of 34.48 for the observed spectral binary fraction. This factor indicates a true binary fraction of $31 \pm 17\%$ given a Chabrier mass function. Additional analysis is needed to determine whether the disparity between the factors is due to the normalization issue with the Kroupa mass function. This true binary fraction indicates a possible range of fractions between $18-48\%$. The lower limit of this fraction overlaps with the upper limit of the binary fraction from some imaging surveys (e.g. $17^{+4}_{-3}\%$, Gizis et al. 2003) while being significantly larger than others ($7-10\%$, Bouy et al. 2003). The lower bound of this binary fraction overlaps with the results from

Table 6.1 Correction fraction for spectral binary technique.

Mass	Age	Mass Ratio	T_{eff}	Spectral Binaries	Correction Factor	True Binary Fraction
Chabrier	Uniform	Allen	Baraffe	2909	34.48	$31 \pm 17\%$
Kroupa	Rujopakarn	Allen	Baraffe	6944	14.49	$13 \pm 7\%$
Kroupa	Uniform	Uniform	Baraffe	8420	11.90	$11 \pm 6\%$
Kroupa	Uniform	Allen	Burrows	7708	12.99	$12 \pm 7\%$
Kroupa	Uniform	Allen	Saumon	6560	15.15	$14 \pm 8\%$

radial velocity surveys in the field (e.g $20-25\%$, Basri & Reiners 2006). For the case of astrometric monitoring surveys, both the observed sample and the resulting binary fraction are small and significantly lower than our derived binary fraction (5%, Sahlmann et al. 2015). However, these comparisons are driven by our large uncertainties. A larger observable volume is needed to identify more spectral binaries such that our uncertainties are not Poisson-limited.

6.5 Conclusions

We have simulated a population of binary systems given different assumptions of the IMF, age, mass ratio distributions, and evolutionary models. We selected five model combinations to analyze the primary and secondary masses, effective temperatures and spectral type distributions. We find that the distributions are mostly sensitive to the chosen mass function and slightly on the choice of evolutionary model. We calculate correction fractions for the selected spectral binaries selected and find a large discrepancy between the predictions from the Kroupa and Chabrier mass functions, presumably caused by the normalization problem on the Kroupa IMF code. Correcting for the observed spectral binary fraction found in Chapter 5 we find a true binary fraction of $31 \pm 17\%$ for a Chabrier IMF. The average value is larger than the observed binary fractions reported by high resolution imaging, radial velocity variability and astrometric monitoring surveys. However, our large uncertainties limit our ability to ascertain whether this fraction is

statistically significantly larger than previous results or not. A spectral survey in a larger observable volume is needed to reduce our uncertainties until the Poisson counting statistics are less dominant than our uncertainty from spectral binary candidacy. Future work will include a complete comparison of all combinations from the input models, and additional mass and age distributions. In particular, we want to include a variety of power law exponents for mass functions and exponential age distributions. These simulations and analysis will facilitate a more detailed analysis of the false positive and negative rates for the spectral binary technique.

Acknowledgements

This Chapter, in part, is currently being prepared for submission for publication of the material. Bardalez Gagliuffi, Daniella; Burgasser, Adam. The dissertation author was the primary investigator and author of this material.

Chapter 7

Young Spectral Binaries with Planetary-Mass Companions

7.1 WISE J1355−8258

Brown dwarfs span the mass range between the hydrogen and deuterium burning mass limits (13 $M_{\rm Jup} < M < 80\ M_{\rm Jup}$; Grossman & Graboske 1973). While the inability to sustain hydrogen fusion and consequent long-term cooling differentiates brown dwarfs from stars, differentiating low-mass brown dwarfs from giant planets is less straightforward. Signatures from different formation pathways that could distinguish between giant exoplanet and brown dwarf formation (e.g. gravitational collapse or core accretion) vanish within a couple hundred million years (Marley et al. 2007) while the direct detection of deuterium is inhibited by its low cosmic abundance (D/H $= (2.45 \pm 0.10) \times 10^{-5}$; Coc et al. 2015). Non-solar initial compositions could distinguish exoplanet spectra but such abundance differences have yet to be discerned (Konopacky et al. 2013).

Most of the directly-imaged giant exoplanets discovered to date have spectral types in the mid-L/early-T range, and are companions to young stars (e.g. Macintosh

et al. 2015). Isolated L and T dwarfs of the same age in young moving groups, are useful proxies for studying giant exoplanet atmospheres. In particular, the BASS-Ultracool Survey (BASS-UC; Gagné et al. 2015a, Gagné et al., in prep.) searches for the coolest late-L and T-type members of young moving groups using the Bayesian Analysis for Nearby Young AssociatioNs II (BANYAN II; Gagné et al. 2014; Malo et al. 2013) tool to assign membership probability based on sky position and kinematics. Targets for BASS-UC are selected from a photometric crossmatch of the 2MASS (Skrutskie et al. 2006) and AllWISE (Wright et al. 2010) catalogs with restrictions on proper motion ($\mu_{\rm total} > 30$ mas yr^{-1}) and customized color cuts. Sources are selected as young moving group candidates if their BANYAN II Bayesian probability exceeds 90% and their optimal position in UVW velocity space is within 5 km s^{-1} of the mean motion of the most probable moving group. This program identified the T5 SDSS J111010.01+011613.1 (Knapp et al. 2004) as a member of the AB Doradus moving group ($130-200$ Myr; Gagné et al. 2015a; Bell et al. 2015), implying an estimated mass ($\sim 10-12\ M_{\rm Jup}$) below the deuterium burning limit.

In this paper, we present the identification of WISE J135501.90−825838.9 (hereafter WISE J1355−8258) as a young spectral binary candidate with L-dwarf and T-dwarf components from the BASS-UC survey. Originally discovered by Kirkpatrick et al. (2016) and identified as a subdwarf, the near infrared spectrum of this source exhibits peculiarities which can be attributed to unresolved binarity. Additionally, its sky position and kinematics yield a high likelihood of membership in the AB Doradus moving group. In Section 7.2 we describe our spectroscopic observations of WISE J1355−8258. In Section 7.3 we examine evidence that this peculiar source is a spectral binary. In Section 7.4 we qualify its membership in the AB Doradus moving group. We discuss the implications of these results, including future young giant exoplanet searches with the spectral binary technique in Section 7.5.

7.2 FIRE Observations

WISE J1355−8258 was first identified as a "photometric" L7.1 in a high proper motion survey (Schneider et al. 2016) based on a crossmatch between AllWISE and the first pass of NEOWISE (Mainzer et al. 2014). It was independently selected as a low-mass, young AB Doradus candidate in the BASS-UC survey. Kirkpatrick et al. (2016) obtained a near-infrared spectrum of this object and classified it as an sdL5?, based on its blue near infrared spectral energy distribution (SED) as compared to the L5 standard 2MASS J08350622+1953050 (Kirkpatrick et al. 2010), attributed to stronger H_2 collision induced absorption. We obtained new spectroscopic observations of WISE J1355−8258 with the Folded-port InfraRed Echellete (FIRE; Simcoe et al. 2008) mounted on the 6.5 m Walter Baade Telescope, located at Las Campanas Observatory, La Serena, Chile. This object was observed in prism mode on 2016 January 22 with the $0\farcs6$ slit, which samples wavelengths $0.82-2.51\,\mu$m at a resolution ranging from R$\sim$500 at J band to R$\sim$300 at K_s band. The weather was clear with a seeing of $0\farcs3$. Eight exposures of 60 s each were taken at an airmass of 1.76, immediately followed by six 1 s exposures of the A0 star HD149818 at an airmass of 1.81. The A0 standard star was moved slightly off the slit to avoid saturation, leading to wavelength-dependent slit losses that limited our ability to calibrate the relative spectral response (see below). HeNeAr lamp exposures were obtained for wavelength calibration. Data were reduced with the Interactive Data Language (IDL) Firehose v2.0 package[1] (Bochanski et al. 2009; Gagné et al. 2015b) following standard procedures.

The de-centering of the A0 standard to avoid saturation causes unreliable overall slopes in the final reduced spectrum. To correct for this effect, synthetic 2MASS magnitudes for the final spectrum were measured and compared with the 2MASS photometry

[1] Available at https://github.com/jgagneastro/FireHose_v2/tree/v2.0 This package makes use of the telluric correction routines contained in SpeXtool (Vacca et al. 2003; Cushing et al. 2004), and the original FireHose pipeline.

of WISE J1355−8258. We applied a linear correction to the differences between the synthetic and measured J, H and K_s-band magnitudes, as a function of $\log \lambda_{\rm eff}$, where $\lambda_{\rm eff}$ is the effective wavelength of the filter (respectively 1.235 μm, 1.662 μm and 2.159 μm)[2]. This correction was applied to the spectrum so that its synthetic 2MASS magnitudes matched the observed ones, to within the photometric uncertainties ($\sim$0.1 mag).

Figure 7.1 shows the reduced spectrum of WISE 1355−8258. This spectrum displays strong H_2O absorption between $1.10-1.25\,\mu$m, $1.30-1.50\,\mu$m, and $1.80-2.00\,\mu$m. Methane absorption is visible at $\sim 1.6\,\mu$m, indicative of a T spectral classification. We determined formal near-infrared classifications of L9$\pm$0.9 using the indices of Burgasser et al. (2006b) and T0$\pm$0.5 by direct comparison to the spectral standards of Kirkpatrick et al. (2010) using the SpeX Prism Library Analysis Toolkit (SPLAT; Burgasser 2014). These are later than both the Schneider et al. (2016) photometric classification and the Kirkpatrick et al. (2016) near infrared spectral classification. A comparison between WISE J1355−8258 and a closely-matched T0 dwarf, WISE J015010.89+382724.1 (Kirkpatrick et al. 2011; Figure 7.1(a)) reveal a reasonable fit to the overall SED, but fails to match the absorption features in detail. In particular, methane typically emerges at 2.2 μm for L9 and at 1.6 μm at T0 (Burgasser et al. 2006a), whereas we see the opposite trend in WISE J1355−8258: clear methane at 1.6 μm but marginal at 2.2 μm. The spectrum of WISE J1355−8258 also has a slightly blue SED which motivated the subdwarf designation of Kirkpatrick et al. (2016). Both of these patterns have been previously seen in the blended-light spectra of L dwarf plus T dwarf spectral binaries (e.g. Cruz et al. 2004; Burgasser et al. 2010a), and we explore this possibility in Section 7.3.

[2]See http://svo2.cab.inta-csic.es/svo/theory/fps/index.php?mode=browse&gname=2MASS.

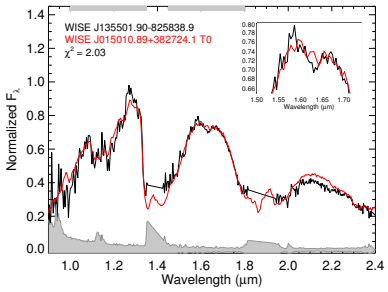

(a) Best single fit for field L and T dwarf templates

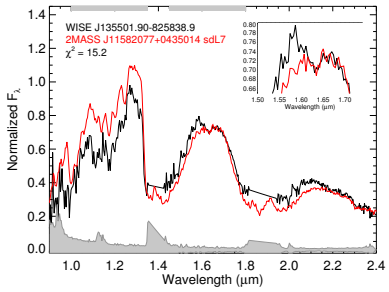

(b) Best single fit using only subdwarf templates

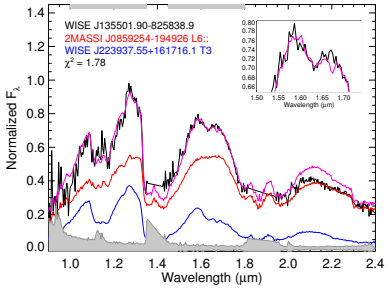

(c) Best binary fit solution for L6.5+T3 components with field L and T dwarf templates

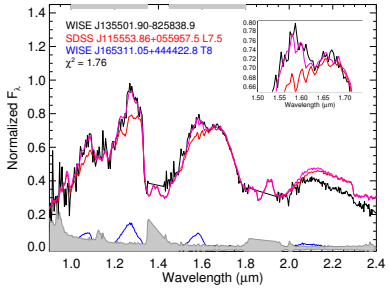

(d) Best binary fit solution for L7.5+T7.5 components with field L and T dwarf templates

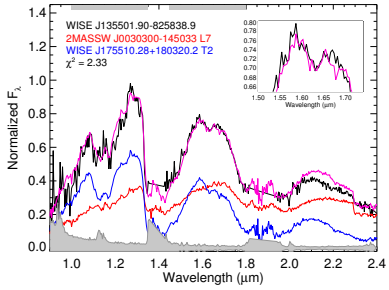

(e) Best fit binary using young templates for the primary and field templates for the secondary

Figure 7.1 Best single and binary fits for WISE J1355−8258 from various template subsamples. The spectrum of the source (black) is normalized to the peak flux in the 1.0?1.3 μm range. Single fit templates are shown in red. Binary fits (magenta) are built by adding primary (red) and secondary (blue) templates scaled by their absolute magnitudes according to Faherty et al. (2016). The methane dip feature at 1.62 μm is seen in the inset. Wavelength regions used for the fitting are noted as bars shaded in grey at the top of the plots. Noise spectrum is shaded in grey.

7.3 A Candidate L dwarf/T dwarf Binary

To assess the possibility of WISE J1355−8258 being an unresolved spectral binary, we followed the prescription of Burgasser et al. (2010a), comparing six sets of spectral indices to the loci of known L+T binaries. Blended-light measurements of WISE J1355−8258 satisfy three of the selection criteria, qualifying it as a strong spectral binary candidate.

We compared the FIRE prism spectrum, sampled to a resolution of R $\sim$ 100 with the same dispersion function as SpeX prism, to single and binary templates drawn from the SpeX Prism Library. Given our uncertainty about the relative flux calibration (Section 5.3) and the lack of binary-sensitive features in the K_s band, we restrict our analysis to the J and H bands of the spectrum, also excluding the telluric bands at $1.35-1.45\,\mu$m. We first compared the spectrum to all 1,169 single templates in the SpeX Prism Library, ignoring known and candidate spectral binaries. We found a best match to the spectrum of the T0 WISE J015010.89+382724.1 (Kirkpatrick et al. 2011) with a reduced chi squared[3] $\chi^2_r = 2.03$.

The spectrum of WISE J1355−8258 was then compared to 35,952 binary templates constructed from 321 L2−L7 primary and 112 T2−T7 secondary spectra, scaled according to the Faherty et al. (2016) field spectral type to absolute magnitude relation in J-band. The best match (Figure 7.1(c)) is a combination of the L6:: 2MASSI J0859254−194926 (Cruz et al. 2003) and the T3 WISE J223927.55+161716.1 (Kirkpatrick et al. 2011) which yielded a $\chi^2_r = 1.78$. An F-test comparison to the T0 best fit single yields a 63% confidence of improved fit, indicating marginal significance. However, there is clear improvement in the spectral shape of the binary template compared to

[3]We define reduced chi squared: $\chi^2_r \equiv \sum_\lambda \left[\frac{C[\lambda]-\alpha T[\lambda]}{\sigma_c[\lambda]}\right]^2 \cdot \frac{1}{dof}$ where $C[\lambda]$ is the candidate spectrum, $T[\lambda]$ is the template spectrum, α is a scaling factor minimizing χ^2, $\sigma_c[\lambda]$ is the noise spectrum for each candidate, and dof is the number of degrees of freedom, equal to the number of wavelength pixels divided by the slit width minus one.

the single template, particularly reproducing the slope in the J-band peak ($1.25-2.30\,\mu$m) and the dip in the H-band ($1.57-1.67\,\mu$m). The K_s-band flux is highly over-estimated as compared to the observed spectrum of WISE J1355−8258 but this could be attributed to flux calibration issues (see Section 5.3) or to a peculiar overall $J-K_s$ color. The ten binary fits with the smallest χ^2_r all had a primary with a spectral type in the L6−L7.5 range, while the secondaries accumulated around either T2−T3 or T7−T8 with similar χ^2_r; we therefore consider both possibilities.

In order to optimize the solutions for late-T secondaries, we also constrained the spectral type ranges to L5−L9 for the primary and T5−T9 for the secondary, with 147 and 95 templates, respectively. From a total of 13,818 binary templates, the best binary fit was a combination of the L7.5 SDSS J115553.86+055957.5 (Knapp et al. 2004) and the T8 WISE J165311.05+444422.8 (Kirkpatrick et al. 2011) with a $\chi^2_r = 1.76$, a very slight improvement compared to the solution with a T3 secondary (Figure 7.1(d)). While the spectral features and shape are well reproduced by this combination, the flux of the secondary is only slightly above the noise level. Averaging over our fits, weighted by the F-statistic, we determine mean spectral types of L6.5±T3 or L7.5±T7.5.

Taking into account that WISE J1355−8258 is a suspected member of AB Doradus (see Section 7.4), we also compared its spectrum to single and binary templates constructed of 83 L dwarfs previously reported as young in the literature and 112 field-age T2−T7 dwarfs.[4] The primary templates were scaled following the young J-band spectral type to absolute magnitude relation of Faherty et al. (2016). The best fit binary out of 11,200 templates ($\chi^2_r = 2.33$) is composed of the L7 2MASSW J0030300-145033 (Kirkpatrick et al. 2000), a possible member of the 40 Myr Argus young association (Torres et al. 2008), and the T2 WISE J175510.28+180320.2 (Mace et al. 2013), shown in

[4]Only three verified young T dwarfs are known, the aforementioned SDSS J111010.01+011613.1, GU Psc b (Naud et al. 2014) and 51 Eri b (Macintosh et al. 2015). We would unnecessarily restrict our binary template sample using just these spectra as a secondary templates.

Figure 7.1(e). The lack of known young late L and T dwarf spectra limits our ability to reproduce the near-infrared spectrum of WISE 1355−8258 using young template binaries.

We also examined the hypothesis of Kirkpatrick et al. (2016), that the peculiarities in the spectrum of WISE J1355−8258 are due to subsolar metallicity. We compared the prism spectrum to 8 L subdwarf spectra; Figure 7.1(b) shows the best match, the sdL7 2MASS J11582077+0435014 (Kirkpatrick et al. 2010) with a reduced chi squared of $\chi^2_r = 15.2$. The template is a poor match to the spectrum of WISE J1355−8258, failing to reproduce the absorption feature at $1.55 - 1.6\,\mu$m and having a blue SED as compared to WISE J1355−8258. Despite our small subdwarf comparison subsample, low metallicity is not a compelling explanation for the peculiar spectrum of WISE J1355−8258. If the secondary is a T3 dwarf, our binary template fitting predicts magnitude differences of $\Delta J = 0.9\pm0.5$ and $\Delta H = 1.6\pm0.7$. For the case of a T7.5 secondary, the magnitude differences are predicted to be $\Delta J = 2.2 \pm 0.4$ and $\Delta H = 3.4 \pm 0.4$. Using these relative magnitudes and the system magnitudes from 2MASS, we estimated individual magnitudes for the two components of the system for each secondary spectral type case, and used the Faherty et al. (2016) absolute magnitude relation for field objects for the L6 primary to compute a mean spectrophotometric distance of 27 ± 4 pc for the L6.5+T3 case, and 24 ± 4 pc for the L7.5+T7.5 case. While signatures of unresolved multiplicity are robust in our analysis, the lack of unambiguous indicators of youth in the spectrum of WISE J1355−8258, means that AB Doradus membership is tentative and requires validation.

7.4 Signatures of youth

In the BASS-UC survey, potentially young sources are assigned a moving group membership probability, which determines their priority for follow-up. The location of WISE J1355−8258 in a J versus $J-K$ color-magnitude diagram ($J = 16.14$, $J-K = 1.42$) is consistent with a field L9 dwarf at the AB Doradus kinematic distance. This, in addition to its red $W1-W2$ color ($W1-W2 = 0.57$), made it a high priority target for radial velocity measurements.

The radial velocity of WISE J1355−8258 was measured by comparing the FIRE echelle spectrum of Kirkpatrick et al. (2016) with zero-velocity CIFIST 2011 BT-Settl models (Allard et al. 2012; Baraffe et al. 2015) using the IDL implementation of the amoeba Nelder-Mead downhill simplex method (Nelder & Mead 1965) to minimize the χ^2 between the model and data. The free parameters were radial velocity, width of the instrumental line spread function (assumed Gaussian), and a linear polynomial to account for slope systematics in the observed spectrum. The fitting procedure was applied in the $1.5100-1.5535\,\mu$m region of the H-band, where the signal-to-noise ratio and absorption feature density are high in L dwarfs. The wavelength range was divided in fifteen evenly-distributed $0.02\,\mu$m-wide regions to perform model fits, leading to RV$= 20.0 \pm 3.6\,\mathrm{km\,s^{-1}}$. Including the systematic RV uncertainty of $\pm 3\,\mathrm{km\,s^{-1}}$ (Gagné et al. 2015a) yielded a final measurement of $20.0 \pm 4.7\,\mathrm{km\,s^{-1}}$. Combining sky position, proper motion from 2MASS to AllWISE (Schneider et al. 2016) and RV, BANYAN II gives a Bayesian probability of 94.8% for AB Doradus membership, with a 5.2% chance of being a field interloper. BANYAN II estimates a kinematic distance of 17 ± 2 pc, marginally consistent (2σ) with the spectrophotometric distance estimates.

We place the system on spectral type versus absolute magnitude diagrams using this kinematic distance (Figure 7.2). The unresolved system (purple star) follows the

Table 7.1 Equivalent widths of K I doublets for WISE 1355−8258 compared to field and young single and synthetic binaries. Obtained from FIRE echelle spectra (R∼6000; Simcoe et al. 2008)

	Source	1.169μm	1.177μm	1.243μm	1.254μm
	WISE J135501.90−825838.9	10.2±0.6	9.7±0.7	5.7±0.4	5.6±0.4
Case 1: L6.5+T3					
Field L5	2MASS J15074769−1627386	9.2±1.9	12.3±2.3	7.8±1.4	9.3±1.8
Field T3	2MASS J10210969−0304197	6.1±1.9	5.8±2.6	5.0±0.9	7.5±1.3
Field L5 + Field T3	Synthetic binary	8.7±1.8	11.0±2.2	6.9±1.2	8.9±1.7
Case 2: L7.5+T7.5					
Field L8	2MASS J16322911+1904407	5.1±1.2	7.1±1.6	3.1±0.7	3.9±1.2
Field T6.5	2MASS J10475385+2124234	−8.5 ± 23.4	−6.4 ± 6.0	1.1±0.2	3.2±0.3
Field L8 + Field T6.5	Synthetic Binary	5.6±1.4	7.3±1.6	2.4±0.6	3.6±0.8
Young L7	PSO J318.5-22	2.4±1.2	2.5±1.3	1.5±0.6	1.8±0.6
Field T6.5	2MASS J10475385+2124234	−8.4±24.1	−6.4±6.0	1.1±0.2	3.2± 0.3
Young L7 + Field T6.5	Synthetic binary	3.1±1.1	4.0±1.1	1.5±0.4	2.6± 0.4

field and young sequences (in blue and gold, respectively), noting the dearth of examples around the L/T transition. We infer individual absolute magnitudes for *J* and *H* bands from the spectral binary template fitting. For the case of L6+T3 components at the kinematic distance, the secondary is significantly fainter for its spectral type, while the primary lies within the scatter of the sequence. For the L7.5+T8 case, the components are well placed in the sequence individually. An intriguing aspect of the absolute magnitude calculations is that the combined-light source remains fainter in the mid-infrared bands $W1$ and $W2$, despite flux redistribution in young objects (Faherty et al. 2016). Again, the scarcity of young T dwarf examples in this spectral type range prevents us from a conclusive interpretation of either the peculiar colors due to youth or the possibility that WISE J1355−8258 is a field interloper to AB Doradus.

While the Allers & Liu (2013) near infrared gravity classification scheme[5] cannot be applied to this object because its combined spectral type exceeds their defined range, the temperature and gravity-sensitive K I doublets at 1.17 μm and 1.25 μm can provide an independent measure of youth. Lower surface gravity brown dwarfs exhibit narrower alkali lines and weaker equivalent widths compared to field-age objects due to their lower

[5] Young brown dwarfs (ages $\gtrsim$ 100 Myr; Burrows et al. 2001) generally have lower surface gravity than equivalent-temperature field dwarfs due to their lower mass and inflated radii.

atmospheric pressure (McGovern et al. 2004; McLean et al. 2007; Martin et al. 2017).

Table 7.1 compares K I equivalent widths for WISE J1355−8258 FIRE echelle data and similarly classified field single sources and combined-light synthetic binaries. For the case of L6.5+T3 components, WISE J1355−8258 has K I equivalent widths statistically equal to the field L5 2MASS J15074769−1627386 for the 1.17 μm doublet, but weaker for the 1.25 μm doublet. For the case of L7.5+T7.5 components, WISE J1355−8258 has all K I equivalent widths stronger than the field L8 2MASS J16322911+1904407.

We also compare the K I equivalent widths of WISE J1355−8258 against a synthetic binary of field L5 and T3 components. We find that WISE J1355−8258 is statistically as strong for the 1.169 μm line as the synthetic field binary, while the other three lines are weaker, on average suggesting a younger age. For the case of a synthetic binary with a young L5 and field T3 components, WISE J1355−8258 has stronger equivalent widths for the 1.17 μm doublet and statistically equal strengths as the synthetic binary for the 1.25 μm doublet.

Comparing to a synthetic binary of field L8 and T6.5 sources, we find that WISE J1355−8258 has stronger equivalent widths for both doublets. We observe the same trend when compared against a synthetic binary composed of young L7 and field T6.5 dwarfs, whose primary component is PSO J318.5−22, a member of the 12 Myr β-Pictoris association (Liu et al. 2013) and significantly younger than the age considered for WISE J1355−8258. The stronger K I equivalent widths of WISE J1355−8258 for both field and partially young synthetic binaries seems to disfavor the case for L7.5+T8 spectral binary components, introducing an inconsistency with the analysis of absolute magnitudes that favors this case. However, given the lack of appropriately-aged templates, we cannot make a conclusive determination on whether K I lines are indicative of either youth or AB Doradus membership.

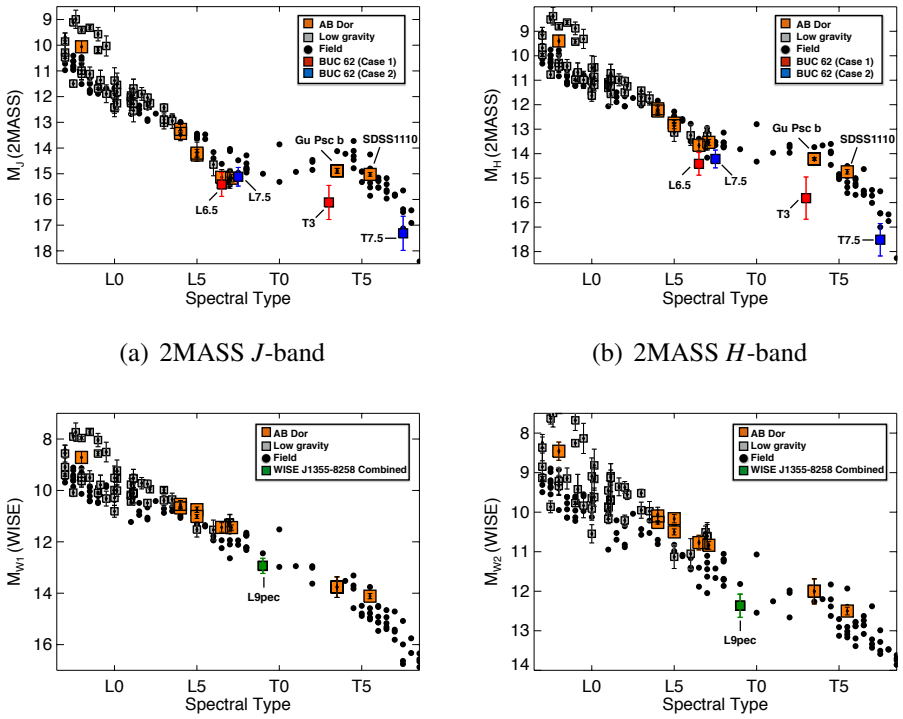

(a) 2MASS J-band

(b) 2MASS H-band

(c) WISE $W1$-band

(d) WISE $W2$-band

Figure 7.2 Spectral Type versus absolute magnitude diagrams of WISE J1355−8258, at the AB Doradus kinematic distance. Field objects are displayed as blue circles and young objects as gold triangles. The binary solutions are shown as red and green stars for the L6+T3 and L7.5+T8 cases, respectively. The combined-light system, classified as L9, is also shown as purple stars. For both binary cases, the components and unresolved systems are 2σ under-luminous compared to field objects.

7.5 Discussion

Our compilation of measurements and analyses lead us to conclude that WISE J1355−8258 is a candidate young binary system, composed of brown dwarfs with L6.5+T3 or L7.5+T7.5 spectral type combinations. While we cannot conclusively distinguish between these two possibilities or establish youth with the available data, they are compelling and resolved photometry, spectroscopy or a parallax measurement would settle current ambiguities. Given the potential close binary nature of WISE J1355−8258, RV measurements may be required to determine whether binary motion influences the kinematic analysis in this study.

Assuming AB Doradus membership, the inferred temperatures (Table 7.2) and the evolutionary models of Saumon & Marley (2008), we estimate component masses of 19±4 $M_{\rm Jup}$ and 14±4 $M_{\rm Jup}$ for the L6.5+T3 case and 16±3 $M_{\rm Jup}$ and 10±1 $M_{\rm Jup}$ for the L7.5+T7.5 case. Corresponding mass ratios are $q = 0.73\pm0.17$ and $q = 0.66\pm0.14$, respectively. WISE J1355−8258 appears to be a binary composed of a low-mass brown dwarf and an object straddling the deuterium burning limit, i.e. potentially planetary-mass. Comparable systems are 2MASS J12073346−3932539b, a binary system in the $\sim$ 10 Myr TW Hydra association (Barrado Y Navascués 2006) composed of a 33 $M_{\rm Jup}$ brown dwarf and a 5 $M_{\rm Jup}$ giant planet (Chauvin et al. 2004), separated by 45 AU and discovered through direct imaging or WISEPC J121756.91+162640.2, a field T+Y binary with estimated masses of 11.5±1.1 $M_{\rm Jup}$ and 7.4±0.5 $M_{\rm Jup}$ (assuming 1 Gyr and evolutionary models from Burrows et al. 2003), separated by 8.0±1.3 AU (Liu et al. 2012).

Table 7.2 Properties of the WISE J1355−8258 system

Property	System	Case 1		Case 2		Reference
		A	B	A	B	
NIR Spectral Type	L9pec	L6.5±1.2	T3±1.6	L7.5±1.5	T7.5±0.7	1
χ^2_r	···	1.78		1.76		1
2MASS J	16.14±0.13	16.6±0.2	17.3±0.4	16.3±0.1	18.5±0.4	1,2
2MASS H	15.31±0.13	15.6±0.2	17.0±0.6	15.4±0.1	18.7±0.4	1,2
2MASS K_s	14.72±0.14	···	···	···	···	2
WISE $W1$	14.12±0.03	···	···	···	···	2
WISE $W2$	13.55±0.03	···	···	···	···	2
WISE $W3$	12.54±0.28	···	···	···	···	2
WISE $W4$	$\leq$ 9.670					2
Δ 2MASS J	···	0.7±0.5		2.2±0.4		1
Δ 2MASS H	···	1.3±0.7		3.4±0.4		1
RV (km s^{-1})	20.0±4.7	···	···	···	···	1
$\mu_\alpha \cos\delta$ (mas yr^{-1})	-241±13.7	···	···	···	···	2
μ_δ (mas yr^{-1})	-142±11.9	···	···	···	···	2
$d_{\rm kin}$ (pc)	17±2	···	···	···	···	1
U (km s^{-1})[a]	···	-8.6±3.7		···		1
V (km s^{-1})[a]	···	-26.3±3.9		···		1
W (km s^{-1})[a]	···	-12.7±2.1		···		1
If member of AB Doradus						
Age (Myr)	130 − 200	···	···	···	···	3
$T_{\rm eff}$ (K)	···	1230±230	1020±200	1140±230	760±200	1
Mass ($M_{\rm Jup}$)	···	19±4	14±1	16±3	10±1	1
Mass ratio	···	0.77±0.16		0.62±0.10		1
If field object						
Age (Gyr)	2 − 5	···	···	···	···	···
$T_{\rm eff}$ (K)	···	1460±150	1130±140	1380±150	780±130	1
Mass ($M_{\rm Jup}$)	···	70±3	58±6	68±4	38±6	1
Mass ratio	···	0.823±0.08		0.57±0.07		1
d_J (pc)	···	24±7	25±7	22±7	23±8	1
d_H (pc)	···	34±10	35±14	26±7	26±9	1

Table 7.2 Continued

Property	System	Case 1		Case 2		Reference
		A	B	A	B	
$d_{\rm avg}$ (pc)	···	27±4		24±4		1
U (km s^{-1})[b]	···	-19.5±5.2		-16.5±5.2		1
V (km s^{-1})[b]	···	-32.5±4.5		-30.0±4.4		1
W (km s^{-1})[b]	···	-15.9±2.7		-14.9±2.6		1

[a]UVW velocities based on kinematic distance.

[b]UVW velocities based on spectrophotometric distance.

References. — (1) This paper; (2) Schneider et al. 2016; (3) Bell et al. 2015.

Regardless of whether WISE J1355−8258 is a young binary or not, our analysis demonstrates the spectral binary method as a novel technique in the discovery of planetary-mass companions to low-mass objects. If confirmed as a young binary system, it will be one of a very few age-calibrated, very low-mass binary brown dwarfs with potentially measurable dynamical masses. Equivalent systems could be found in other young moving groups and star formation regions through this technique. Assuming an effective limiting magnitude of $J = 19$ (appropriate for FIRE in prism mode; Sullivan & Simcoe 2012), data to identify these systems could be obtained for distances up to 650 pc for young M7 dwarfs, and up to 165 pc for young L5 dwarfs. Several $1 - 200$ Myr moving groups and clusters can be found within the latter sphere[6] Identifying such systems in multiple clusters and moving groups over a range of ages would allow the exploration of planetary-mass companions as a function of time, and future confirmation and characterization with the James Webb Space Telescope.

Acknowledgements

The authors thank telescope operators for their assistance during our observations. This publication makes use of data and analysis routines from the SpeX Prism Library Analysis Toolkit (SPLAT) maintained at http://www.browndwarfs.org/splat. This publication is based on data obtained with the Magellan Telescope and the Infrared Telescope Facility, operated by the University of Hawaii under Cooperative Agreement No. NNX-08AE38A with the National Aeronautics and Space Administration, Science Mission Directorate, Planetary Astronomy Program. A.J.B. acknowledges funding support from the National Science Foundation under award No. AST-1517177. The material presented

[6] e.g. Taurus (1 Myr at 140 pc; Luhman et al. 2017), Chameleon (2 Myr at 160 pc; Luhman 2007; Bayo et al. 2017), TW Hydra ($7 - 13$ Myr at $40 - 62$ pc; Bell et al. 2015), Tucana Horologium ($20 - 40$ Myr at $40 - 50$ pc; Torres et al. 2008), AB Doradus ($130 - 200$ Myr at $20 - 50$ pc; Bell et al. 2015; Zuckerman et al. 2004).

here is based upon work supported by the National Aeronautics and Space Administration under Grant No. NNX15AI75G. The authors wish to recognize and acknowledge the very significant cultural role and reverence that the summit of Mauna Kea has always had within the indigenous Hawaiian community. We are most fortunate to have the opportunity to conduct observations from this mountain.

Facilities: Magellan FIRE.

This Chapter, in full, has been submitted for publication of the material as it may appear in The Astrophysical Journal Letters, 2017, Bardalez Gagliuffi, Daniella; Gagné, Jonathan; Faherty, Jacqueline; Burgasser, Adam. The dissertation author was the primary investigator and author of this paper.

Chapter 8

Conclusions

Brown dwarfs are objects intermediate between stars and giant planets, sharing physical characteristics with both. While brown dwarfs most likely form as stars, their atmospheres closely resemble those of giant exoplanets. Their inability to fuse hydrogen determines their physical properties and evolution, which observationally, it translates to a degeneracy between mass, age and luminosity that challenges their characterization. The fundamental question of brown dwarf formation, and which are the essential processes that determine their low mass at birth or that halt their accretion of surrounding material during formation remains unanswered, and should be part of any complete star formation theory.

Multiplicity is a key statistic for understanding their formation. Several binary detection techniques are used to identify a diversity of ultracool binary systems, each one with its own set of biases. The observed binary population statistics retrieved through these different methods can constrain formation scenarios. However, the separation distribution of VLM binaries remains poorly constrained at small separations (< 1 AU), leading to uncertainty in the overall binary fraction. We approach this problem by searching for late-M/early-L plus T dwarf spectral binaries whose combined light spectra

exhibit distinct peculiarities, allowing for separation-independent identification. We define a set of spectral indices designed to identify these systems, and use a spectral template fitting method to confirm and characterize spectral binary candidates from a library of 815 spectra from the SpeX Prism Spectral Libraries. We present 11 new binary candidates, confirm 3 previously reported candidates, and rule out 2 previously identified candidates, all with primary and secondary spectral types in the range M7−L7 and T1−T8, respectively. We find that subdwarfs and blue L dwarfs are the primary contaminants in our sample and propose a method for segregating these sources. If confirmed by follow-up observations, these systems may add to the growing list of tight separation binaries, whose orbital properties may yield further insight into brown dwarf formation scenarios.

We followed up some of these spectral binary candidates with high resolution Laser Guide Star Adaptive Optics at Keck/NIRC2. We imaged 43 late-M, L and T dwarf systems, including 17 spectral binary candidates. We resolved three systems: 2MASS J1341−3052, SDSS J1511+0607 and SDSS J2052−1609; the first two were resolved for the first time. All three have projected separations < 8 AU and estimated periods of $14-80$ years. We also reported a preliminary orbit determination for SDSS J2052−1609 based on six epochs of resolved astrometry between 2005 and 2010. Among the 14 unresolved spectral binaries, 5 systems were confirmed binaries but remained unresolved, implying a minimum binary fraction of $47^{+12}_{-11}\%$ for this sample. Our inability to resolve most of the spectral binaries, including the confirmed binaries, supports the hypothesis that a large fraction of very low mass systems have relatively small separations and are missed with direct imaging.

While this follow up was crucial to confirm three spectral binaries, the sample was small and inhomogeneous in terms of distance and spectral type completeness. In order to obtain better statistics, we compiled a volume-limited, near-infrared spectroscopic sample

of M7−L5 ultracool dwarfs up to 25 pc. The sample contains 443 sources, of which 91% have been observed with low-resolution, near-infrared SpeX spectra. We characterized the sample, providing near-infrared spectral types and gravity classifications. We identify subpopulations including spectral binaries, young sources, and red and blue $J-K_s$ color outliers. We calculate the spectral binary fraction of this volume-limited sample to be $0.95 \pm 0.50\%$. We find that the completeness cannot be constrained to less than a factor of two thirds, between $47\% - 72\%$, therefore indicating a significant uncertainty in the total number of ultracool dwarfs.

In order to estimate the true binary fraction of ultracool dwarfs, we performed binary population simulations with different assumptions of the initial mass function, age, mass ratio distributions and evolutionary models. We analyze five model combinations and the binary properties they produce, particularly the primary and secondary masses, temperatures and spectral types. We find that the population distributions are most sensitive to the chosen mass function. We identified spectral binaries in the simulated population and estimate their selection function given each set of model combinations, along with a correction factor to be applied to the observed spectral binary fraction. The true ultracool binary fraction is $11 - 14\%$ or $31 \pm 17\%$, for either a Kroupa or a Chabrier mass function, although the lower values may be altered by a normalization issue.

Finally, we present the identification of WISE J135501.90−825838.9 as a candidate spectral binary system with a planetary-mass secondary in the $130 - 200$ Myr AB Doradus moving group. Peculiarities in the near-infrared spectrum of this source suggest it to be a blended-light binary with either L6.5±1.2 and T3±1.6 or L7.5±1.5 and T7.5±0.7 components. Its proper motion and radial velocity as a combined-light source yield a high membership probability for AB Doradus. However, there is a 2σ difference between the kinematic and spectrophotometric distance estimates that challenges the young characterization. If confirmed as a member of AB Doradus, we estimate masses of

$19\pm4\,M_{\rm Jup}$ and $14\pm1\,M_{\rm Jup}$ or $16\pm3\,M_{\rm Jup}$ and $10\pm1\,M_{\rm Jup}$, for each spectral type combination respectively, with the secondary component mass straddling the deuterium burning mass limit. Our identification of WISE J135501.90−825838.9 as a candidate young spectral binary introduces the spectral binary technique as a new method for detecting and characterizing planetary-mass companions to young brown dwarfs.

Bibliography

Ackerman, A. S., & Marley, M. S. 2001, ApJ, 556, 872, 872

Adelman-McCarthy, J. K., Agüeros, M. A., Allam, S. S., et al. 2007, ApJS, 172, 634, 634

Ahmic, M., Jayawardhana, R., Brandeker, A., et al. 2007, ApJ, 671, 2074, 2074

Allard, F., & Hauschildt, P. H. 1995, ApJ, 445, 433, 433

Allard, F., Hauschildt, P. H., Alexander, D. R., & Starrfield, S. 1997, ARA&A, 35, 137, 137

Allard, F., Homeier, D., Freytag, B., & Sharp, C. M. 2012, in EAS Publications Series, Vol. 57, EAS Publications Series, ed. C. Reylé, C. Charbonnel, & M. Schultheis, 3–43

Allen, P. R. 2007, ApJ, 668, 492, 492

Allen, P. R., Koerner, D. W., McElwain, M. W., Cruz, K. L., & Reid, I. N. 2007, AJ, 133, 971, 971

Allen, P. R., Koerner, D. W., Reid, I. N., & Trilling, D. E. 2005, ApJ, 625, 385, 385

Allers, K. N., & Liu, M. C. 2013, ApJ, 772, 79, 79

Allers, K. N., Liu, M. C., Dupuy, T. J., & Cushing, M. C. 2010, ApJ, 715, 561, 561

Allers, K. N., Jaffe, D. T., Luhman, K. L., et al. 2007, ApJ, 657, 511, 511

Allers, K. N., Liu, M. C., Shkolnik, E., et al. 2009, ApJ, 697, 824, 824

Alonso-Floriano, F. J., Morales, J. C., Caballero, J. A., et al. 2015, A&A, 577, A128, A128

Alves de Oliveira, C., Moraux, E., Bouvier, J., & Bouy, H. 2012, A&A, 539, A151, A151

Andre, P., & Montmerle, T. 1994, ApJ, 420, 837, 837

Andre, P., Ward-Thompson, D., & Barsony, M. 2000, Protostars and Planets IV, 59, 59

Andrei, A. H., Smart, R. L., Penna, J. L., et al. 2011, AJ, 141, 54, 54

Apai, D., Luhman, K., & Liu, M. C. 2008, in Astronomical Society of the Pacific Conference Series, Vol. 384, 14th Cambridge Workshop on Cool Stars, Stellar Systems, and the Sun, ed. G. van Belle, 383

Artigau, É., Gagné, J., Faherty, J., et al. 2015, ApJ, 806, 254, 254

Artigau, É., Lafrenière, D., Doyon, R., et al. 2011, ApJ, 739, 48, 48

Attwood, R. E., Goodwin, S. P., Stamatellos, D., & Whitworth, A. P. 2009, A&A, 495, 201, 201

Baines, D., Oudmaijer, R. D., Porter, J. M., & Pozzo, M. 2006, MNRAS, 367, 737, 737

Baraffe, I., Chabrier, G., Allard, F., & Hauschildt, P. H. 1997, A&A, 327, 1054, 1054

Baraffe, I., Chabrier, G., Barman, T. S., Allard, F., & Hauschildt, P. H. 2003, A&A, 402, 701, 701

Baraffe, I., Homeier, D., Allard, F., & Chabrier, G. 2015, A&A, 577, A42, A42

Bardalez Gagliuffi, D. C., Gelino, C. R., & Burgasser, A. J. 2015, AJ, 150, 163, 163

Bardalez Gagliuffi, D. C., Burgasser, A. J., Gelino, C. R., et al. 2014, ApJ, 794, 143, 143

Barman, T. S., Macintosh, B., Konopacky, Q. M., & Marois, C. 2011, ApJ, 735, L39, L39

Barrado Y Navascués, D. 2006, A&A, 459, 511, 511

Barrado y Navascués, D., Bouvier, J., Stauffer, J. R., Lodieu, N., & McCaughrean, M. J. 2002, A&A, 395, 813, 813

Basri, G., Marcy, G. W., & Graham, J. R. 1995, in Bulletin of the American Astronomical Society, Vol. 27, American Astronomical Society Meeting Abstracts #186, 1214

Basri, G., Marcy, G. W., & Graham, J. R. 1996, ApJ, 458, 600, 600

Basri, G., & Martín, E. L. 1999, AJ, 118, 2460, 2460

Basri, G., Mohanty, S., Allard, F., et al. 2000, ApJ, 538, 363, 363

Basri, G., & Reiners, A. 2006, AJ, 132, 663, 663

Bate, M. R. 2009, MNRAS, 392, 590, 590

—. 2012, MNRAS, 419, 3115, 3115

Bate, M. R., Bonnell, I. A., & Bromm, V. 2002a, MNRAS, 332, L65, L65

—. 2002b, MNRAS, 336, 705, 705

—. 2003, MNRAS, 339, 577, 577

Bayo, A., Barrado, D., Allard, F., et al. 2017, MNRAS, 465, 760, 760

Beamín, J. C., Minniti, D., Gromadzki, M., et al. 2013, A&A, 557, L8, L8

Becklin, E. E., & Zuckerman, B. 1988, Nature, 336, 656, 656

Béjar, V. J. S., Martín, E. L., Zapatero Osorio, M. R., et al. 2001, ApJ, 556, 830, 830

Bell, C. P. M., Mamajek, E. E., & Naylor, T. 2015, MNRAS, 454, 593, 593

Bennett, D. P., Bond, I. A., Udalski, A., et al. 2008, ApJ, 684, 663, 663

Bergfors, C., Brandner, W., Janson, M., et al. 2010, A&A, 520, A54, A54

Bergin, E. A., & Tafalla, M. 2007, ARA&A, 45, 339, 339

Berriman, B., Kirkpatrick, D., Hanisch, R., Szalay, A., & Williams, R. 2003, in IAU Joint Discussion, Vol. 8, IAU Joint Discussion

Bessell, M. S. 1991, AJ, 101, 662, 662

Best, W. M. J., Magnier, E. A., Liu, M. C., et al. 2017, ArXiv e-prints, arXiv:1701.00490

Biller, B. A., Kasper, M., Close, L. M., Brandner, W., & Kellner, S. 2006, ApJ, 641, L141, L141

Billères, M., Delfosse, X., Beuzit, J.-L., et al. 2005, A&A, 440, L55, L55

Blake, C. H., Charbonneau, D., & White, R. J. 2010, ApJ, 723, 684, 684

Blake, C. H., Charbonneau, D., White, R. J., et al. 2008, ApJ, 678, L125, L125

Blitz, L. 1993, in Protostars and Planets III, ed. E. H. Levy & J. I. Lunine, 125–161

Bochanski, J. J., Hawley, S. L., Covey, K. R., et al. 2010, AJ, 139, 2679, 2679

Bochanski, J. J., Hawley, S. L., & West, A. A. 2011, AJ, 141, 98, 98

Bochanski, J. J., Hennawi, J. F., Simcoe, R. A., et al. 2009, PASP, 121, 1409, 1409

Boeshaar, P. C., & Tyson, J. A. 1985, AJ, 90, 817, 817

Bonnell, I. A., Clark, P., & Bate, M. R. 2008, MNRAS, 389, 1556, 1556

Boss, A. P. 1997, Science, 276, 1836, 1836

—. 2001, ApJ, 551, L167, L167

Bouy, H., Brandner, W., Martín, E. L., et al. 2003, AJ, 126, 1526, 1526

Bouy, H., Martín, E. L., Brandner, W., & Bouvier, J. 2005, AJ, 129, 511, 511

Bowler, B. P., Liu, M. C., & Dupuy, T. J. 2010, ApJ, 710, 45, 45

Boyd, D. F. A., & Whitworth, A. P. 2005, A&A, 430, 1059, 1059

Briceño, C., Luhman, K. L., Hartmann, L., Stauffer, J. R., & Kirkpatrick, J. D. 2002, ApJ, 580, 317, 317

Burbidge, E. M., Burbidge, G. R., Fowler, W. A., & Hoyle, F. 1957, Reviews of Modern Physics, 29, 547, 547

Burgasser, A. J. 2001, PhD thesis,

—. 2002, PhD thesis,

—. 2004, ApJS, 155, 191, 191

—. 2007a, ApJ, 659, 655, 655

—. 2007b, AJ, 134, 1330, 1330

Burgasser, A. J. 2008, in Astronomical Society of the Pacific Conference Series, Vol. 384, 14th Cambridge Workshop on Cool Stars, Stellar Systems, and the Sun, ed. G. van Belle, 126

—. 2009, ArXiv e-prints, arXiv:0903.1390

Burgasser, A. J. 2014, in Astronomical Society of India Conference Series, Vol. 11, Astronomical Society of India Conference Series, 7–16

Burgasser, A. J., Bardalez-Gagliuffi, D. C., & Gizis, J. E. 2011a, AJ, 141, 70, 70

Burgasser, A. J., & Blake, C. H. 2009, AJ, 137, 4621, 4621

Burgasser, A. J., Blake, C. H., Gelino, C. R., Sahlmann, J., & Bardalez Gagliuffi, D. 2016, ApJ, 827, 25, 25

Burgasser, A. J., Burrows, A., & Kirkpatrick, J. D. 2006a, ApJ, 639, 1095, 1095

Burgasser, A. J., Cruz, K. L., Cushing, M., et al. 2010a, ApJ, 710, 1142, 1142

Burgasser, A. J., Cruz, K. L., & Kirkpatrick, J. D. 2007a, ApJ, 657, 494, 494

Burgasser, A. J., Geballe, T. R., Leggett, S. K., Kirkpatrick, J. D., & Golimowski, D. A. 2006b, ApJ, 637, 1067, 1067

Burgasser, A. J., Kirkpatrick, J. D., Cruz, K. L., et al. 2006c, ApJS, 166, 585, 585

Burgasser, A. J., Kirkpatrick, J. D., Liebert, J., & Burrows, A. 2003a, ApJ, 594, 510, 510

Burgasser, A. J., Kirkpatrick, J. D., & Lowrance, P. J. 2005, AJ, 129, 2849, 2849

Burgasser, A. J., Kirkpatrick, J. D., Reid, I. N., et al. 2003b, ApJ, 586, 512, 512

Burgasser, A. J., Liu, M. C., Ireland, M. J., Cruz, K. L., & Dupuy, T. J. 2008a, ApJ, 681, 579, 579

Burgasser, A. J., Looper, D., & Rayner, J. T. 2010b, AJ, 139, 2448, 2448

Burgasser, A. J., Looper, D. L., Kirkpatrick, J. D., Cruz, K. L., & Swift, B. J. 2008b, ApJ, 674, 451, 451

Burgasser, A. J., Looper, D. L., Kirkpatrick, J. D., & Liu, M. C. 2007b, ApJ, 658, 557, 557

Burgasser, A. J., Luk, C., Dhital, S., et al. 2012, ApJ, 757, 110, 110

Burgasser, A. J., Marley, M. S., Ackerman, A. S., et al. 2002a, ApJ, 571, L151, L151

Burgasser, A. J., & McElwain, M. W. 2006, AJ, 131, 1007, 1007

Burgasser, A. J., McElwain, M. W., Kirkpatrick, J. D., et al. 2004, AJ, 127, 2856, 2856

Burgasser, A. J., Melis, C., Todd, J., et al. 2015a, ArXiv e-prints, arXiv:1508.06332

Burgasser, A. J., Melis, C., Zauderer, B. A., & Berger, E. 2013, ApJ, 762, L3, L3

Burgasser, A. J., Reid, I. N., Siegler, N., et al. 2007c, Protostars and Planets V, 427, 427

Burgasser, A. J., Sitarski, B. N., Gelino, C. R., Logsdon, S. E., & Perrin, M. D. 2011b, ApJ, 739, 49, 49

Burgasser, A. J., Kirkpatrick, J. D., Brown, M. E., et al. 2002b, ApJ, 564, 421, 421

Burgasser, A. J., Kirkpatrick, J. D., Burrows, A., et al. 2003c, ApJ, 592, 1186, 1186

Burgasser, A. J., Gillon, M., Melis, C., et al. 2015b, AJ, 149, 104, 104

Burningham, B., Smith, L., Cardoso, C. V., et al. 2014, MNRAS, 440, 359, 359

Burningham, B., Leggett, S. K., Lucas, P. W., et al. 2010, MNRAS, 404, 1952, 1952

Burrows, A., Hubbard, W. B., Lunine, J. I., & Liebert, J. 2001, Reviews of Modern Physics, 73, 719, 719

Burrows, A., Hubbard, W. B., Lunine, J. I., et al. 1997a, in Astronomical Society of the Pacific Conference Series, Vol. 119, Planets Beyond the Solar System and the Next Generation of Space Missions, ed. D. Soderblom, 9

Burrows, A., & Liebert, J. 1993, Reviews of Modern Physics, 65, 301, 301

Burrows, A., Saumon, D., Guillot, T., Hubbard, W. B., & Lunine, J. I. 1995, Nature, 375, 299, 299

Burrows, A., & Sharp, C. M. 1999, ApJ, 512, 843, 843

Burrows, A., Sudarsky, D., & Lunine, J. I. 2003, ApJ, 596, 587, 587

Burrows, A., Marley, M., Hubbard, W. B., et al. 1997b, ApJ, 491, 856, 856

Caballero, J. A. 2007, ApJ, 667, 520, 520

Carson, J. C., Marengo, M., Patten, B. M., et al. 2011, ApJ, 743, 141, 141

Casewell, S. L., Jameson, R. F., & Burleigh, M. R. 2008, MNRAS, 390, 1517, 1517

Castro, P. J., Gizis, J. E., Harris, H. C., et al. 2013, ApJ, 776, 126, 126

Chabrier, G. 2002, ApJ, 567, 304, 304

Chabrier, G. 2005, in Astrophysics and Space Science Library, Vol. 327, The Initial Mass Function 50 Years Later, ed. E. Corbelli, F. Palla, & H. Zinnecker, 41

Chabrier, G., & Baraffe, I. 2000, ARA&A, 38, 337, 337

Chabrier, G., Baraffe, I., Allard, F., & Hauschildt, P. H. 2005, ArXiv Astrophysics e-prints, arXiv:astro-ph/0509798

Chabrier, G., Gallardo, J., & Baraffe, I. 2007, A&A, 472, L17, L17

Chappelle, R. J., Pinfield, D. J., Steele, I. A., Dobbie, P. D., & Magazzù, A. 2005, MNRAS, 361, 1323, 1323

Chauvin, G., Lagrange, A.-M., Dumas, C., et al. 2004, A&A, 425, L29, L29

Chiu, K., Fan, X., Leggett, S. K., et al. 2006, AJ, 131, 2722, 2722

Choi, J.-Y., Han, C., Udalski, A., et al. 2013, ApJ, 768, 129, 129

Close, L. M., Richer, H. B., & Crabtree, D. R. 1990, AJ, 100, 1968, 1968

Close, L. M., Siegler, N., Freed, M., & Biller, B. 2003, ApJ, 587, 407, 407

Coc, A., Petitjean, P., Uzan, J.-P., et al. 2015, Phys Rev D, 92, 123526, 123526

Comerón, F., Fernández, M., Baraffe, I., Neuhäuser, R., & Kaas, A. A. 2003, A&A, 406, 1001, 1001

Costa, E., Méndez, R. A., Jao, W.-C., et al. 2005, AJ, 130, 337, 337

—. 2006, AJ, 132, 1234, 1234

Cowley, A. P., & Hartwick, F. D. A. 1982, ApJ, 253, 237, 237

Crifo, F., Phan-Bao, N., Delfosse, X., et al. 2005, A&A, 441, 653, 653

Cruz, K., Faherty, J., Rice, E., Riedel, A., & Núñez, A. 2013, in Protostars and Planets VI, Heidelberg, July 15-20, 2013. Poster #2G022, 22

Cruz, K. L., Burgasser, A. J., Reid, I. N., & Liebert, J. 2004, ApJ, 604, L61, L61

Cruz, K. L., Kirkpatrick, J. D., & Burgasser, A. J. 2009, AJ, 137, 3345, 3345

Cruz, K. L., Reid, I. N., Liebert, J., Kirkpatrick, J. D., & Lowrance, P. J. 2003, AJ, 126, 2421, 2421

Cruz, K. L., Reid, I. N., Kirkpatrick, J. D., et al. 2007, AJ, 133, 439, 439

Cushing, M. C., Rayner, J. T., Davis, S. P., & Vacca, W. D. 2003, ApJ, 582, 1066, 1066

Cushing, M. C., Vacca, W. D., & Rayner, J. T. 2004, PASP, 116, 362, 362

Cushing, M. C., Roellig, T. L., Marley, M. S., et al. 2006, ApJ, 648, 614, 614

Cushing, M. C., Marley, M. S., Saumon, D., et al. 2008, ApJ, 678, 1372, 1372

Cushing, M. C., Kirkpatrick, J. D., Gelino, C. R., et al. 2011, ApJ, 743, 50, 50

Cutri, R. M., Skrutskie, M. F., van Dyk, S., et al. 2003, VizieR Online Data Catalog, 2246, 0, 0

Dahn, C. C., Harris, H. C., Vrba, F. J., et al. 2002, AJ, 124, 1170, 1170

Dahn, C. C., Harris, H. C., Levine, S. E., et al. 2008, ApJ, 686, 548, 548

Daly, R. A., & McLaughlin, G. C. 1992, ApJ, 390, 423, 423

D'Antona, F., & Mazzitelli, I. 1996, ApJ, 456, 329, 329

Davenport, J. R. A., Ivezić, Ž., Becker, A. C., et al. 2014, MNRAS, 440, 3430, 3430

Davison, C. L., White, R. J., Henry, T. J., et al. 2015, AJ, 149, 106, 106

Day-Jones, A. C., Marocco, F., Pinfield, D. J., et al. 2013, MNRAS, 648, 648

De Rosa, R. J., Patience, J., Vigan, A., et al. 2012, MNRAS, 422, 2765, 2765

De Rosa, R. J., Patience, J., Wilson, P. A., et al. 2014, MNRAS, 437, 1216, 1216

Deacon, N. R., Hambly, N. C., & Cooke, J. A. 2005, A&A, 435, 363, 363

Deacon, N. R., Hambly, N. C., King, R. R., & McCaughrean, M. J. 2009, MNRAS, 394, 857, 857

Deacon, N. R., Liu, M. C., Magnier, E. A., et al. 2014, ApJ, 792, 119, 119

Delfosse, X., Tinney, C. G., Forveille, T., et al. 1999, , 135, 41, 41

—. 1997, A&A, 327, L25, L25

Delfosse, X., Beuzit, J.-L., Marchal, L., et al. 2004, in Astronomical Society of the Pacific Conference Series, Vol. 318, Spectroscopically and Spatially Resolving the Components of the Close Binary Stars, ed. R. W. Hilditch, H. Hensberge, & K. Pavlovski, 166–174

Delgado-Donate, E. J., Clarke, C. J., Bate, M. R., & Hodgkin, S. T. 2004, MNRAS, 351, 617, 617

Deshpande, R., Martín, E. L., Montgomery, M. M., et al. 2012, AJ, 144, 99, 99

Dhital, S., Burgasser, A. J., Looper, D. L., & Stassun, K. G. 2011, AJ, 141, 7, 7

Dieterich, S. B., Henry, T. J., Jao, W.-C., et al. 2014, AJ, 147, 94, 94

Dittmann, J. A., Irwin, J. M., Charbonneau, D., & Berta-Thompson, Z. K. 2014, ApJ, 784, 156, 156

Duchêne, G., Bouvier, J., Moraux, E., et al. 2013, A&A, 555, A137, A137

Dupuy, T. J. 2010, PhD thesis,

Dupuy, T. J., Forbrich, J., Rizzuto, A., et al. 2016, ApJ, 827, 23, 23

Dupuy, T. J., & Liu, M. C. 2011, ApJ, 733, 122, 122

—. 2012, ApJS, 201, 19, 19

—. 2017, ArXiv e-prints, arXiv:1703.05775

Dupuy, T. J., Liu, M. C., & Bowler, B. P. 2009a, ApJ, 706, 328, 328

Dupuy, T. J., Liu, M. C., Bowler, B. P., et al. 2010, ApJ, 721, 1725, 1725

Dupuy, T. J., Liu, M. C., & Ireland, M. J. 2009b, ArXiv e-prints, arXiv:0912.0738

—. 2014, ApJ, 790, 133, 133

Duquennoy, A., & Mayor, M. 1991, A&A, 248, 485, 485

Durisen, R. H., & Sterzik, M. F. 1994, A&A, 286, 84, 84

Einstein, A. 1936, Science, 84, 506, 506

Elmegreen, B. G. 1999, ApJ, 522, 915, 915

Epchtein, N., de Batz, B., Capoani, L., et al. 1997, The Messenger, 87, 27, 27

EROS Collaboration, Goldman, B., Delfosse, X., et al. 1999, A&A, 351, L5, L5

Esplin, T. L., Luhman, K. L., & Mamajek, E. E. 2014, ApJ, 784, 126, 126

Faherty, J., Cruz, K., Rice, E., & Riedel, A. 2013a, in Protostars and Planets VI, Heidelberg, July 15-20, 2013. Poster #2G024, 24

Faherty, J. K., Burgasser, A. J., Cruz, K. L., et al. 2009, AJ, 137, 1, 1

Faherty, J. K., Cruz, K. L., Rice, E. L., & Riedel, A. 2013b, , 84, 955, 955

Faherty, J. K., Tinney, C. G., Skemer, A., & Monson, A. J. 2014, ApJ, 793, L16, L16

Faherty, J. K., Burgasser, A. J., Walter, F. M., et al. 2012, ApJ, 752, 56, 56

Faherty, J. K., Riedel, A. R., Cruz, K. L., et al. 2016, ApJS, 225, 10, 10

Fan, X., Knapp, G. R., Strauss, M. A., et al. 2000, AJ, 119, 928, 928

Fegley, Jr., B., & Lodders, K. 1994, Icarus, 110, 117, 117

—. 1996, ApJ, 472, L37, L37

Filippazzo, J. C., Rice, E. L., Faherty, J., et al. 2015, ApJ, 810, 158, 158

Fischer, D. A., & Marcy, G. W. 1992, ApJ, 396, 178, 178

Folkes, S. L., Pinfield, D. J., Jones, H. R. A., et al. 2012, MNRAS, 427, 3280, 3280

Fontaine, G., Brassard, P., & Bergeron, P. 2001, PASP, 113, 409, 409

Forveille, T., Ségransan, D., Delorme, P., et al. 2004, A&A, 427, L1, L1

Forveille, T., Beuzit, J.-L., Delorme, P., et al. 2005, A&A, 435, L5, L5

Foy, R., & Labeyrie, A. 1985, A&A, 152, L29, L29

Furlan, E., Luhman, K. L., Espaillat, C., et al. 2011, ApJS, 195, 3, 3

Gagné, J., Burgasser, A. J., Faherty, J. K., et al. 2015a, The Astrophysical Journal Letters, 808, L20, L20

Gagné, J., Lafrenière, D., Doyon, R., Malo, L., & Artigau, É. 2014, ApJ, 783, 121, 121

Gagné, J., Lambrides, E., Faherty, J. K., & Simcoe, R. 2015b, Firehose v2.0, Zenodo,

Gagné, J., Faherty, J. K., Cruz, K. L., et al. 2015c, The Astrophysical Journal Supplement Series, 219, 33, 33

Gagné, J., Faherty, J. K., Burgasser, A. J., et al. 2017, ArXiv e-prints, arXiv:1705.01625

Gaidos, E., Mann, A. W., Lépine, S., et al. 2014, MNRAS, 443, 2561, 2561

Gammie, C. F. 2001, ApJ, 553, 174, 174

García, B., & Mermilliod, J. C. 2001, A&A, 368, 122, 122

Gaudi, B. S. 2012, ARA&A, 50, 411, 411

Gauza, B., Béjar, V. J. S., Pérez-Garrido, A., et al. 2015, ApJ, 804, 96, 96

Geballe, T. R., Knapp, G. R., Leggett, S. K., et al. 2002, ApJ, 564, 466, 466

Geißler, K., Metchev, S., Kirkpatrick, J. D., Berriman, G. B., & Looper, D. 2011, ApJ, 732, 56, 56

Gelino, C. R., & Burgasser, A. J. 2010, AJ, 140, 110, 110

Gelino, C. R., Kirkpatrick, J. D., Cushing, M. C., et al. 2011, AJ, 142, 57, 57

Gillon, M., Jehin, E., Delrez, L., et al. 2013, in Protostars and Planets VI Posters

Gizis, J. E. 1997, AJ, 113, 806, 806

—. 2002, ApJ, 575, 484, 484

Gizis, J. E., Kirkpatrick, J. D., & Wilson, J. C. 2001, AJ, 121, 2185, 2185

Gizis, J. E., Monet, D. G., Reid, I. N., Kirkpatrick, J. D., & Burgasser, A. J. 2000a, MNRAS, 311, 385, 385

Gizis, J. E., Monet, D. G., Reid, I. N., et al. 2000b, AJ, 120, 1085, 1085

Gizis, J. E., Reid, I. N., & Hawley, S. L. 2002, AJ, 123, 3356, 3356

Gizis, J. E., Reid, I. N., Knapp, G. R., et al. 2003, AJ, 125, 3302, 3302

Gizis, J. E., Troup, N. W., & Burgasser, A. J. 2011, ApJ, 736, L34, L34

Gliese, W., & Jahreiß, H. 1991, Preliminary Version of the Third Catalogue of Nearby Stars,

Golimowski, D. A., Leggett, S. K., Marley, M. S., et al. 2004a, AJ, 127, 3516, 3516

Golimowski, D. A., Henry, T. J., Krist, J. E., et al. 2004b, AJ, 128, 1733, 1733

Gomes, J. I., Pinfield, D. J., Marocco, F., et al. 2013, MNRAS, 431, 2745, 2745

Goodwin, S. P., Whitworth, A. P., & Ward-Thompson, D. 2004, A&A, 414, 633, 633

Goto, M., Kobayashi, N., Terada, H., et al. 2002, ApJ, 567, L59, L59

Gould, A. 2000, ApJ, 542, 785, 785

Gray, R. O., & Corbally, J., C. 2009,

Gray, R. O., Corbally, C. J., Garrison, R. F., et al. 2006, AJ, 132, 161, 161

Griffith, C. A., & Yelle, R. V. 1999, ApJ, 519, L85, L85

Grossman, A. S., & Graboske, H. C. 1973, ApJ, 180, 195, 195

Guenther, E. W., & Wuchterl, G. 2003, A&A, 401, 677, 677

Guillot, T. 1999, Science, 286

Gullbring, E., Hartmann, L., Briceño, C., & Calvet, N. 1998, ApJ, 492, 323, 323

Haisch, Jr., K. E., Lada, E. A., & Lada, C. J. 2001, ApJ, 553, L153, L153

Hall, P. B. 2002, ApJ, 580, L77, L77

Hambly, N. C., Steele, I. A., Hawkins, M. R. S., & Jameson, R. F. 1995, MNRAS, 273, 505, 505

Han, C., Jung, Y. K., Udalski, A., et al. 2013, ApJ, 778, 38, 38

Hanel, R., Conrath, B., Herath, L., Kunde, V., & Pirraglia, J. 1981, J. Geophys. Res., 86, 8705, 8705

Hansen, C. J., Kawaler, S. D., & Trimble, V. 2004,

Haro, G., & Chavira, E. 1966, Vistas in Astronomy, 8, 89, 89

Harrington, R. S., & Dahn, C. C. 1980, AJ, 85, 454, 454

Harvey, P. M., Henning, T., Liu, Y., et al. 2012, ApJ, 755, 67, 67

Hastings, W. K. 1970, Biometrika, 57, 97, 97

Hawley, S. L., Covey, K. R., Knapp, G. R., et al. 2002, AJ, 123, 3409, 3409

Hayashi, C., & Nakano, T. 1963, Progress of Theoretical Physics, 30, 460, 460

Heller, R., Schwope, A. D., & Østensen, R. H. 2011, in Astronomical Society of the Pacific Conference Series, Vol. 447, Evolution of Compact Binaries, ed. L. Schmidtobreick, M. R. Schreiber, & C. Tappert, 177

Henry, T. J., Jao, W.-C., Subasavage, J. P., et al. 2006, AJ, 132, 2360, 2360

Henry, T. J., Subasavage, J. P., Brown, M. A., et al. 2004, AJ, 128, 2460, 2460

Herbig, G. H. 1956, PASP, 68, 531, 531

Hester, J. J., Scowen, P. A., Sankrit, R., et al. 1996, AJ, 111, 2349, 2349

Hillenbrand, L. A., Strom, S. E., Calvet, N., et al. 1998, AJ, 116, 1816, 1816

Hwang, K.-H., Udalski, A., Han, C., et al. 2010, ApJ, 723, 797, 797

Innes, R. T. A. 1907, The Observatory, 30, 310, 310

Irwin, M., McMahon, R. G., & Reid, N. 1991, MNRAS, 252, 61P, 61P

Janson, M., Hormuth, F., Bergfors, C., et al. 2012, ApJ, 754, 44, 44

Jayawardhana, R., Ardila, D. R., Stelzer, B., & Haisch, Jr., K. E. 2003, AJ, 126, 1515, 1515

Jeans, J. H. 1902, Philosophical Transactions of the Royal Society of London Series A, 199, 1, 1

Jenkins, J. S., Ramsey, L. W., Jones, H. R. A., et al. 2009, ApJ, 704, 975, 975

Joergens, V. 2006, A&A, 448, 655, 655

—. 2008, A&A, 492, 545, 545

Joergens, V., & Guenther, E. 2001, A&A, 379, L9, L9

Joergens, V., Janson, M., & Müller, A. 2012, A&A, 537, A13, A13

Joergens, V., Müller, A., & Reffert, S. 2010, A&A, 521, A24, A24

Jung, Y. K., Udalski, A., Sumi, T., et al. 2015, ApJ, 798, 123, 123

Kang, M., Choi, M., Stutz, A. M., & Tatematsu, K. 2015, ApJ, 814, 31, 31

Kendall, T. R., Delfosse, X., Martín, E. L., & Forveille, T. 2004, A&A, 416, L17, L17

Kendall, T. R., Jones, H. R. A., Pinfield, D. J., et al. 2007, MNRAS, 374, 445, 445

Kendall, T. R., Mauron, N., Azzopardi, M., & Gigoyan, K. 2003, A&A, 403, 929, 929

Khandrika, H., Burgasser, A. J., Melis, C., et al. 2013, AJ, 145, 71, 71

Kirkpatrick, J. D. 2005, ARA&A, 43, 195, 195

Kirkpatrick, J. D., Allard, F., Bida, T., et al. 1999a, ApJ, 519, 834, 834

Kirkpatrick, J. D., Dahn, C. C., Monet, D. G., et al. 2001, AJ, 121, 3235, 3235

Kirkpatrick, J. D., Henry, T. J., & Irwin, M. J. 1997, AJ, 113, 1421, 1421

Kirkpatrick, J. D., Henry, T. J., & Liebert, J. 1993, ApJ, 406, 701, 701

Kirkpatrick, J. D., Henry, T. J., & McCarthy, Jr., D. W. 1991, ApJS, 77, 417, 417

Kirkpatrick, J. D., Henry, T. J., & Simons, D. A. 1995, AJ, 109, 797, 797

Kirkpatrick, J. D., Reid, I. N., Liebert, J., et al. 1999b, ApJ, 519, 802, 802

—. 2000, AJ, 120, 447, 447

Kirkpatrick, J. D., Cruz, K. L., Barman, T. S., et al. 2008, ApJ, 689, 1295, 1295

Kirkpatrick, J. D., Looper, D. L., Burgasser, A. J., et al. 2010, ApJS, 190, 100, 100

Kirkpatrick, J. D., Cushing, M. C., Gelino, C. R., et al. 2011, ApJS, 197, 19, 19

Kirkpatrick, J. D., Schneider, A., Fajardo-Acosta, S., et al. 2014, ApJ, 783, 122, 122

Kirkpatrick, J. D., Kellogg, K., Schneider, A. C., et al. 2016, ApJS, 224, 36, 36

Knapp, G. R., Leggett, S. K., Fan, X., et al. 2004, AJ, 127, 3553, 3553

Koen, C. 2013, MNRAS, 428, 2824, 2824

Koen, C., Kilkenny, D., van Wyk, F., & Marang, F. 2010, MNRAS, 403, 1949, 1949

Koerner, D. W., Kirkpatrick, J. D., McElwain, M. W., & Bonaventura, N. R. 1999, ApJ, 526, L25, L25

Konopacky, Q. M., Barman, T. S., Macintosh, B. A., & Marois, C. 2013, Science, 339, 1398, 1398

Konopacky, Q. M., Ghez, A. M., Barman, T. S., et al. 2010, ApJ, 711, 1087, 1087

Kouwenhoven, M. B. N., Brown, A. G. A., Goodwin, S. P., Portegies Zwart, S. F., & Kaper, L. 2009, A&A, 493, 979, 979

Kouwenhoven, M. B. N., Brown, A. G. A., Portegies Zwart, S. F., & Kaper, L. 2007, A&A, 474, 77, 77

Kouwenhoven, M. B. N., Brown, A. G. A., Zinnecker, H., Kaper, L., & Portegies Zwart, S. F. 2005, A&A, 430, 137, 137

Kraus, A. L., & Hillenbrand, L. A. 2012, ApJ, 757, 141, 141

Kraus, A. L., Ireland, M. J., Martinache, F., & Hillenbrand, L. A. 2011, ApJ, 731, 8, 8

Kraus, A. L., Ireland, M. J., Martinache, F., & Lloyd, J. P. 2008, ApJ, 679, 762, 762

Kraus, A. L., White, R. J., & Hillenbrand, L. A. 2006, ApJ, 649, 306, 306

Kroupa, P. 1998, MNRAS, 300, 200, 200

Kroupa, P. 2001, in Astronomical Society of the Pacific Conference Series, Vol. 228, Dynamics of Star Clusters and the Milky Way, ed. S. Deiters, B. Fuchs, A. Just, R. Spurzem, & R. Wielen, 187

Kroupa, P., & Bouvier, J. 2003a, MNRAS, 346, 369, 369

—. 2003b, MNRAS, 346, 343, 343

Kumar, S. S. 1962, Models for Stars of Very Low Mass,

—. 1963, ApJ, 137, 1121, 1121

Lada, C. J., & Wilking, B. A. 1984, ApJ, 287, 610, 610

Lafrenière, D., Jayawardhana, R., Brandeker, A., Ahmic, M., & van Kerkwijk, M. H. 2008, ApJ, 683, 844, 844

Larson, R. B. 1972, MNRAS, 157, 121, 121

—. 1973, MNRAS, 161, 133, 133

—. 1985, MNRAS, 214, 379, 379

Larson, R. B. 1999, in Star Formation 1999, ed. T. Nakamoto, 336–340

Lawrence, A., Warren, S. J., Almaini, O., et al. 2007, MNRAS, 379, 1599, 1599

Lazorenko, P. F., Mayor, M., Dominik, M., et al. 2009, A&A, 505, 903, 903

Leggett, S. K., Allard, F., Geballe, T. R., Hauschildt, P. H., & Schweitzer, A. 2001, ApJ, 548, 908, 908

Leggett, S. K., Fan, X., Geballe, T. R., Golimowski, D. A., & Knapp, G. R. 2003, in IAU Symposium, Vol. 211, Brown Dwarfs, ed. E. Martín, 317

Leggett, S. K., Hauschildt, P. H., Allard, F., Geballe, T. R., & Baron, E. 2002, MNRAS, 332, 78, 78

Lépine, S., Rich, R. M., Neill, J. D., Caulet, A., & Shara, M. M. 2002a, ApJ, 581, L47, L47

Lépine, S., Rich, R. M., & Shara, M. M. 2003, AJ, 125, 1598, 1598

Lépine, S., & Shara, M. M. 2005, AJ, 129, 1483, 1483

Lépine, S., Shara, M. M., & Rich, R. M. 2002b, AJ, 124, 1190, 1190

Lépine, S., Thorstensen, J. R., Shara, M. M., & Rich, R. M. 2009, AJ, 137, 4109, 4109

Liebert, J. 1976, PASP, 88, 232, 232

Liebert, J., & Ferguson, D. H. 1982, MNRAS, 199, 29P, 29P

Liebert, J., & Gizis, J. E. 2006, PASP, 118, 659, 659

Liebert, J., Kirkpatrick, J. D., Cruz, K. L., et al. 2003, AJ, 125, 343, 343

Liebert, J., Kirkpatrick, J. D., Reid, I. N., & Fisher, M. D. 1999, ApJ, 519, 345, 345

Lilly, S. J., Le Fevre, O., Hammer, F., & Crampton, D. 1996, ApJ, 460, L1, L1

Lindegren, L., Lammers, U., Bastian, U., et al. 2016, A&A, 595, A4, A4

Linsky, J. L. 1969, ApJ, 156, 989, 989

Lissauer, J. J. 1993, ARA&A, 31, 129, 129

Liu, M. C., Dupuy, T. J., & Allers, K. N. 2016, ApJ, 833, 96, 96

Liu, M. C., Dupuy, T. J., Bowler, B. P., Leggett, S. K., & Best, W. M. J. 2012, ApJ, 758, 57, 57

Liu, M. C., Dupuy, T. J., & Leggett, S. K. 2010, ApJ, 722, 311, 311

Liu, M. C., Fischer, D. A., Graham, J. R., et al. 2002, ApJ, 571, 519, 519

Liu, M. C., & Leggett, S. K. 2005, ApJ, 634, 616, 616

Liu, M. C., Delorme, P., Dupuy, T. J., et al. 2011, ApJ, 740, 108, 108

Liu, M. C., Magnier, E. A., Deacon, N. R., et al. 2013, ApJ, 777, L20, L20

Lodders, K. 2002, ApJ, 577, 974, 974

Lodders, K., & Fegley, Jr., B. 2006, Chemistry of Low Mass Substellar Objects, ed. J. W. Mason, 1

Lodieu, N., Hambly, N. C., Jameson, R. F., et al. 2007, MNRAS, 374, 372, 372

Lodieu, N., Scholz, R.-D., & McCaughrean, M. J. 2002, A&A, 389, L20, L20

Lodieu, N., Scholz, R.-D., McCaughrean, M. J., et al. 2005, A&A, 440, 1061, 1061

Lodieu, N., Zapatero Osorio, M. R., Rebolo, R., Martín, E. L., & Hambly, N. C. 2009, A&A, 505, 1115, 1115

Looper, D. L., Gelino, C. R., Burgasser, A. J., & Kirkpatrick, J. D. 2008a, ApJ, 685, 1183, 1183

Looper, D. L., Kirkpatrick, J. D., & Burgasser, A. J. 2007, AJ, 134, 1162, 1162

Looper, D. L., Kirkpatrick, J. D., Cutri, R. M., et al. 2008b, ApJ, 686, 528, 528

Lovis, C., & Fischer, D. 2010, Radial Velocity Techniques for Exoplanets, ed. S. Seager, 27–53

Luhman, K. L. 2004a, ApJ, 617, 1216, 1216

—. 2004b, ApJ, 614, 398, 398

Luhman, K. L. 2005, in Astrophysics and Space Science Library, Vol. 327, The Initial Mass Function 50 Years Later, ed. E. Corbelli, F. Palla, & H. Zinnecker, 115

—. 2007, ApJS, 173, 104, 104

—. 2013, ApJ, 767, L1, L1

—. 2014, ApJ, 786, L18, L18

Luhman, K. L., Esplin, T. L., & Loutrel, N. P. 2016, ApJ, 827, 52, 52

Luhman, K. L., Joergens, V., Lada, C., et al. 2007, Protostars and Planets V, 443, 443

Luhman, K. L., Mamajek, E. E., Allen, P. R., Muench, A. A., & Finkbeiner, D. P. 2009, ApJ, 691, 1265, 1265

Luhman, K. L., Mamajek, E. E., Shukla, S. J., & Loutrel, N. P. 2017, AJ, 153, 46, 46

Luhman, K. L., & Sheppard, S. S. 2014, ApJ, 787, 126, 126

Luhman, K. L., Stauffer, J. R., Muench, A. A., et al. 2003, ApJ, 593, 1093, 1093

Luhman, K. L., Loutrel, N. P., McCurdy, N. S., et al. 2012, ApJ, 760, 152, 152

Lunine, J. I., Hubbard, W. B., Burrows, A., Wang, Y.-P., & Garlow, K. 1989, ApJ, 338, 314, 314

Lurie, J. C., Henry, T. J., Jao, W.-C., et al. 2014, AJ, 148, 91, 91

Luyten, W. J. 1979, in New Luyten Catalogue of stars with proper motions larger than two tenths of an arcsecond, Vol. 2, p. 0 (1979), Vol. 2, 0

Mace, G. N., Kirkpatrick, J. D., Cushing, M. C., et al. 2013, ApJS, 205, 6, 6

Macintosh, B., Graham, J. R., Barman, T., et al. 2015, Science, 350, 64, 64

Mainzer, A., Bauer, J., Cutri, R. M., et al. 2014, ApJ, 792, 30, 30

Malo, L., Doyon, R., Lafrenière, D., et al. 2013, ApJ, 762, 88, 88

Manjavacas, E., Goldman, B., Reffert, S., & Henning, T. 2013, A&A, 560, A52, A52

Marcy, G. W., & Butler, R. P. 2000, PASP, 112, 137, 137

Marley, M. S., Fortney, J. J., Hubickyj, O., Bodenheimer, P., & Lissauer, J. J. 2007, ApJ, 655, 541, 541

Marley, M. S., Saumon, D., Guillot, T., et al. 1996, Science, 272, 1919, 1919

Marocco, F., Andrei, A. H., Smart, R. L., et al. 2013, AJ, 146, 161, 161

Marocco, F., Jones, H. R. A., Day-Jones, A. C., et al. 2015, MNRAS, 449, 3651, 3651

Martin, E. C., Mace, G. N., McLean, I. S., et al. 2017, ArXiv e-prints, arXiv:1703.03811

Martin, E. L., Basri, G., Delfosse, X., & Forveille, T. 1997, A&A, 327, L29, L29

Martin, E. L., Brandner, W., & Basri, G. 1999, Science, 283, 1718, 1718

Martín, E. L., Delfosse, X., Basri, G., et al. 1999, AJ, 118, 2466, 2466

Martín, E. L., Basri, G., Brandner, W., et al. 1998, ApJ, 509, L113, L113

Martín, E. L., Phan-Bao, N., Bessell, M., et al. 2010, A&A, 517, A53, A53

Mason, B. D., Gies, D. R., Hartkopf, W. I., et al. 1998a, AJ, 115, 821, 821

Mason, B. D., Henry, T. J., Hartkopf, W. I., ten Brummelaar, T., & Soderblom, D. R. 1998b, AJ, 116, 2975, 2975

Maxted, P. F. L., & Jeffries, R. D. 2005, MNRAS, 362, L45, L45

Maxted, P. F. L., Jeffries, R. D., Oliveira, J. M., Naylor, T., & Jackson, R. J. 2008, MNRAS, 385, 2210, 2210

Mayor, M., Queloz, D., Marcy, G., et al. 1995, , 6251

McCarthy, Jr., D. W., Probst, R. G., & Low, F. J. 1985, ApJ, 290, L9, L9

McCaughrean, M. J., Scholz, R.-D., & Lodieu, N. 2002, A&A, 390, L27, L27

McElwain, M. W., & Burgasser, A. J. 2006, AJ, 132, 2074, 2074

McGovern, M. R., Kirkpatrick, J. D., McLean, I. S., et al. 2004, ApJ, 600, 1020, 1020

McLean, I. S., McGovern, M. R., Burgasser, A. J., et al. 2003, ApJ, 596, 561, 561

McLean, I. S., Prato, L., McGovern, M. R., et al. 2007, ApJ, 658, 1217, 1217

Metchev, S. A., Kirkpatrick, J. D., Berriman, G. B., & Looper, D. 2008, ApJ, 676, 1281, 1281

Metodieva, Y., Antonova, A., Golev, V., et al. 2015, MNRAS, 446, 3878, 3878

Metropolis, N., Rosenbluth, A. W., Rosenbluth, M. N., Teller, A. H., & Teller, E. 1953, J. Chem. Phys., 21, 1087, 1087

Miller, G. E., & Scalo, J. M. 1979, ApJS, 41, 513, 513

Mizuno, H. 1980, Progress of Theoretical Physics, 64, 544, 544

Mohanty, S., Jayawardhana, R., & Barrado y Navascués, D. 2003, ApJ, 593, L109, L109

Monet, D. G., Dahn, C. C., Vrba, F. J., et al. 1992, AJ, 103, 638, 638

Monet, D. G., Levine, S. E., Canzian, B., et al. 2003, AJ, 125, 984, 984

Montagnier, G., Ségransan, D., Beuzit, J.-L., et al. 2006, A&A, 460, L19, L19

Moraux, E., Bouvier, J., Stauffer, J. R., & Cuillandre, J.-C. 2003, A&A, 400, 891, 891

Motte, F., Andre, P., & Neri, R. 1998, A&A, 336, 150, 150

Murray, N. 2011, ApJ, 729, 133, 133

Nakajima, T., Oppenheimer, B. R., Kulkarni, S. R., et al. 1995, Nature, 378, 463, 463

Nakajima, T., Tsuji, T., & Yanagisawa, K. 2004, ApJ, 607, 499, 499

Naud, M.-E., Artigau, É., Malo, L., et al. 2014, ApJ, 787, 5, 5

Nelder, J. A., & Mead, R. 1965, The Computer Journal, 7, 308, 308

Neuhäuser, R., Brandner, W., Alves, J., Joergens, V., & Comerón, F. 2002, A&A, 384, 999, 999

Neuhäuser, R., Guenther, E. W., Petr, M. G., et al. 2000, A&A, 360, L39, L39

Newton, E. R., Charbonneau, D., Irwin, J., et al. 2014, AJ, 147, 20, 20

Noll, K. S., Geballe, T. R., Leggett, S. K., & Marley, M. S. 2000, ApJ, 541, L75, L75

Noll, K. S., Geballe, T. R., & Marley, M. S. 1997, ApJ, 489, L87, L87

Ochsenbein, F., Bauer, P., & Marcout, J. 2000, , 143, 23, 23

Oppenheimer, B. R., Kulkarni, S. R., Matthews, K., & van Kerkwijk, M. H. 1998, ApJ, 502, 932, 932

Oppenheimer, B. R., Baranec, C., Beichman, C., et al. 2013, ApJ, 768, 24, 24

Padoan, P., Kritsuk, A., Michael, Norman, L., & Nordlund, Å. 2005, , 76, 187, 187

Padoan, P., & Nordlund, Å. 2002, ApJ, 576, 870, 870

—. 2004, ApJ, 617, 559, 559

Parker, R. J., & Meyer, M. R. 2014, MNRAS, 442, 3722, 3722

Pérez Garrido, A., Lodieu, N., Béjar, V. J. S., et al. 2014, A&A, 567, A6, A6

Phan-Bao, N. 2011, Astronomische Nachrichten, 332, 668, 668

Phan-Bao, N., & Bessell, M. S. 2006, A&A, 446, 515, 515

Phan-Bao, N., Crifo, F., Delfosse, X., et al. 2003, A&A, 401, 959, 959

Phan-Bao, N., Bessell, M. S., Martín, E. L., et al. 2006, MNRAS, 366, L40, L40

—. 2008, MNRAS, 383, 831, 831

Pinfield, D. J., Dobbie, P. D., Jameson, R. F., et al. 2003, MNRAS, 342, 1241, 1241

Pokorny, R. S., Jones, H. R. A., & Hambly, N. C. 2003, A&A, 397, 575, 575

Pokorny, R. S., Jones, H. R. A., Hambly, N. C., & Pinfield, D. J. 2004, A&A, 421, 763, 763

Pollack, J. B., Hubickyj, O., Bodenheimer, P., et al. 1996, Icarus, 124, 62, 62

Pravdo, S. H., Shaklan, S. B., Wiktorowicz, S. J., et al. 2006, ApJ, 649, 389, 389

Preibisch, T., Balega, Y., Hofmann, K.-H., Weigelt, G., & Zinnecker, H. 1999, , 4, 531, 531

Prinn, R. G., & Barshay, S. S. 1977, Science, 198, 1031, 1031

Radigan, J., Jayawardhana, R., Lafrenière, D., et al. 2012, ApJ, 750, 105, 105

—. 2013, ApJ, 778, 36, 36

Radigan, J., Lafrenière, D., Jayawardhana, R., & Doyon, R. 2008, ApJ, 689, 471, 471

Raghavan, D., McAlister, H. A., Henry, T. J., et al. 2010, ApJS, 190, 1, 1

Rajpurohit, A. S., Reylé, C., Allard, F., et al. 2013, A&A, 556, A15, A15

Ratzka, T., Köhler, R., & Leinert, C. 2005, A&A, 437, 611, 611

Rayner, J. T., Toomey, D. W., Onaka, P. M., et al. 2003, PASP, 115, 362, 362

Rebolo, R., Martin, E. L., Basri, G., Marcy, G. W., & Zapatero-Osorio, M. R. 1996, ApJ, 469, L53, L53

Rebolo, R., Zapatero Osorio, M. R., Madruga, S., et al. 1998, Science, 282, 1309, 1309

Rebolo, R., Zapatero Osorio, M. R., & Martín, E. L. 1995, Nature, 377, 129, 129

Reggiani, M. M., & Meyer, M. R. 2011, ApJ, 738, 60, 60

Reid, I. N., Burgasser, A. J., Cruz, K. L., Kirkpatrick, J. D., & Gizis, J. E. 2001a, AJ, 121, 1710, 1710

Reid, I. N., & Cruz, K. L. 2002, AJ, 123, 2806, 2806

Reid, I. N., Cruz, K. L., & Allen, P. R. 2007, AJ, 133, 2825, 2825

Reid, I. N., Cruz, K. L., Burgasser, A. J., & Liu, M. C. 2008a, AJ, 135, 580, 580

Reid, I. N., Cruz, K. L., Kirkpatrick, J. D., et al. 2008b, AJ, 136, 1290, 1290

Reid, I. N., & Gizis, J. E. 1997a, AJ, 113, 2246, 2246

—. 1997b, AJ, 114, 1992, 1992

—. 2005, PASP, 117, 676, 676

Reid, I. N., Gizis, J. E., & Hawley, S. L. 2002a, AJ, 124, 2721, 2721

Reid, I. N., Gizis, J. E., Kirkpatrick, J. D., & Koerner, D. W. 2001b, AJ, 121, 489, 489

Reid, I. N., & Hawley, S. L. 2005,

Reid, I. N., Kirkpatrick, J. D., Gizis, J. E., et al. 2000, AJ, 119, 369, 369

Reid, I. N., Kirkpatrick, J. D., Liebert, J., et al. 2002b, AJ, 124, 519, 519

Reid, I. N., Lewitus, E., Allen, P. R., Cruz, K. L., & Burgasser, A. J. 2006, AJ, 132, 891, 891

Reid, I. N., Kirkpatrick, J. D., Liebert, J., et al. 1999, ApJ, 521, 613, 613

Reid, I. N., Cruz, K. L., Allen, P., et al. 2003, AJ, 126, 3007, 3007

—. 2004, AJ, 128, 463, 463

Reipurth, B., & Clarke, C. 2001, AJ, 122, 432, 432

Reipurth, B., Clarke, C. J., Boss, A. P., et al. 2014, Protostars and Planets VI, 267, 267

Reipurth, B., Guimarães, M. M., Connelley, M. S., & Bally, J. 2007, AJ, 134, 2272, 2272

Reipurth, B., & Zinnecker, H. 1993, A&A, 278, 81, 81

Reylé, C., Scholz, R.-D., Schultheis, M., Robin, A. C., & Irwin, M. 2006, MNRAS, 373, 705, 705

Riaz, B. 2013, , 84, 1113, 1113

Riaz, B., Briceno, C., Whelan, E., & Heathcote, S. 2017, ArXiv e-prints, arXiv:1705.01170

Ricci, L., Testi, L., Natta, A., et al. 2014, ApJ, 791, 20, 20

Rice, W. K. M., Lodato, G., & Armitage, P. J. 2005, MNRAS, 364, L56, L56

Ruiz, M. T., & Takamiya, M. Y. 1995, AJ, 109, 2817, 2817

Rujopakarn, W., Eisenstein, D. J., Rieke, G. H., et al. 2010, ApJ, 718, 1171, 1171

Sahlmann, J., Lazorenko, P. F., Bouy, H., et al. 2016, MNRAS, 455, 357, 357

Sahlmann, J., Lazorenko, P. F., Ségransan, D., et al. 2014, A&A, 565, A20, A20

—. 2015, A&A, 577, A15, A15

—. 2013, A&A, 556, A133, A133

Salim, S., & Gould, A. 2003, ApJ, 582, 1011, 1011

Salim, S., Lépine, S., Rich, R. M., & Shara, M. M. 2003, ApJ, 586, L149, L149

Salpeter, E. E. 1955, ApJ, 121, 161, 161

Sargent, A. I., & Welch, W. J. 1993, ARA&A, 31, 297, 297

Saumon, D., & Marley, M. S. 2008, ApJ, 689, 1327, 1327

Saumon, D., Marley, M. S., Cushing, M. C., et al. 2006, ApJ, 647, 552, 552

Saumon, D., Marley, M. S., & Lodders, K. 2003, ArXiv Astrophysics e-prints, astro-ph/0310805

Scally, A., Clarke, C., & McCaughrean, M. J. 1999, MNRAS, 306, 253, 253

Schmidt, S. J., Cruz, K. L., Bongiorno, B. J., Liebert, J., & Reid, I. N. 2007, AJ, 133, 2258, 2258

Schmidt, S. J., Hawley, S. L., West, A. A., et al. 2015, AJ, 149, 158, 158

Schmidt, S. J., West, A. A., Bochanski, J. J., Hawley, S. L., & Kielty, C. 2014, PASP, 126, 642, 642

Schmidt, S. J., West, A. A., Hawley, S. L., & Pineda, J. S. 2010, AJ, 139, 1808, 1808

Schneider, A., Melis, C., Song, I., & Zuckerman, B. 2011, ApJ, 743, 109, 109

Schneider, A. C., Cushing, M. C., Kirkpatrick, J. D., et al. 2014, AJ, 147, 34, 34

Schneider, A. C., Greco, J., Cushing, M. C., et al. 2016, ApJ, 817, 112, 112

Schneider, A. C., Windsor, J., Cushing, M. C., Kirkpatrick, J. D., & Shkolnik, E. L. 2017, AJ, 153, 196, 196

Schneider, D. P., Knapp, G. R., Hawley, S. L., et al. 2002, AJ, 123, 458, 458

Scholz, R.-D. 2010, A&A, 510, L8, L8

—. 2013, ArXiv e-prints, arXiv:1311.2716

—. 2014, A&A, 561, A113, A113

Scholz, R.-D., Lodieu, N., Ibata, R., et al. 2004a, MNRAS, 347, 685, 685

Scholz, R.-D., Lodieu, N., & McCaughrean, M. J. 2004b, A&A, 428, L25, L25

Scholz, R.-D., & Meusinger, H. 2002, MNRAS, 336, L49, L49

Scholz, R.-D., Meusinger, H., & Jahreiß, H. 2001, A&A, 374, L12, L12

Scholz, R.-D., Storm, J., Knapp, G. R., & Zinnecker, H. 2009, A&A, 494, 949, 949

Seifahrt, A., Röll, T., Neuhäuser, R., et al. 2008, A&A, 484, 429, 429

Sheppard, S. S., & Cushing, M. 2009a, in Bulletin of the American Astronomical Society, Vol. 41, American Astronomical Society Meeting Abstracts #213, 291

Sheppard, S. S., & Cushing, M. C. 2009b, AJ, 137, 304, 304

Shkolnik, E., Liu, M. C., & Reid, I. N. 2009, ApJ, 699, 649, 649

Shkolnik, E. L., Anglada-Escudé, G., Liu, M. C., et al. 2012, ApJ, 758, 56, 56

Shu, F. H., Adams, F. C., & Lizano, S. 1987, ARA&A, 25, 23, 23

Silvestri, N. M., Lemagie, M. P., Hawley, S. L., et al. 2007, AJ, 134, 741, 741

Simcoe, R. A., Burgasser, A. J., Bernstein, R. A., et al. 2008, in , Vol. 7014, Ground-based and Airborne Instrumentation for Astronomy II, 70140U

Simons, D. A., & Tokunaga, A. 2002, PASP, 114, 169, 169

Skrutskie, M. F., Forrest, W. J., & Shure, M. A. 1987, ApJ, 312, L55, L55

Skrutskie, M. F., Cutri, R. M., Stiening, R., et al. 2006, AJ, 131, 1163, 1163

Skrzypek, N., Warren, S. J., & Faherty, J. K. 2016, A&A, 589, A49, A49

Skrzypek, N., Warren, S. J., Faherty, J. K., et al. 2015, A&A, 574, A78, A78

Slesnick, C. L., Hillenbrand, L. A., & Carpenter, J. M. 2008, ApJ, 688, 377, 377

Stamatellos, D., & Whitworth, A. 2010, in Astronomical Society of the Pacific Conference Series, Vol. 424, 9th International Conference of the Hellenic Astronomical Society, ed. K. Tsinganos, D. Hatzidimitriou, & T. Matsakos, 159

Stamatellos, D., & Whitworth, A. P. 2008, A&A, 480, 879, 879

—. 2009a, MNRAS, 392, 413, 413

—. 2009b, MNRAS, 392, 413, 413

Stassun, K. G., Mathieu, R. D., & Valenti, J. A. 2006, Nature, 440, 311, 311

Stephens, D. C., Leggett, S. K., Cushing, M. C., et al. 2009, ApJ, 702, 154, 154

Stephenson, C. B. 1986, AJ, 92, 139, 139

Sterzik, M. F., Durisen, R. H., & Zinnecker, H. 2003, A&A, 411, 91, 91

Stumpf, M. B., Brandner, W., Bouy, H., Henning, T., & Hippler, S. 2010, A&A, 516, A37, A37

Stumpf, M. B., Brandner, W., Henning, T., et al. 2008, ArXiv e-prints, arXiv:0811.0556

Stumpf, M. B., Geißler, K., Bouy, H., et al. 2011, A&A, 525, A123, A123

Sullivan, P. W., & Simcoe, R. A. 2012, PASP, 124, 1336, 1336

Taylor, M. B. 2005, in Astronomical Society of the Pacific Conference Series, Vol. 347, Astronomical Data Analysis Software and Systems XIV, ed. P. Shopbell, M. Britton, & R. Ebert, 29

Teegarden, B. J., Pravdo, S. H., Hicks, M., et al. 2003, ApJ, 589, L51, L51

Testi, L. 2009, A&A, 503, 639, 639

Testi, L., Natta, A., Scholz, A., et al. 2016, A&A, 593, A111, A111

Testi, L., & Sargent, A. I. 1998, ApJ, 508, L91, L91

Thies, I., & Kroupa, P. 2007, ApJ, 671, 767, 767

Thompson, M. A., Kirkpatrick, J. D., Mace, G. N., et al. 2013, PASP, 125, 809, 809

Thorstensen, J. R., & Kirkpatrick, J. D. 2003, PASP, 115, 1207, 1207

Tinney, C. G. 1996, MNRAS, 281, 644, 644

Tinney, C. G., Burgasser, A. J., & Kirkpatrick, J. D. 2003, AJ, 126, 975, 975

Tinney, C. G., Delfosse, X., Forveille, T., & Allard, F. 1998, A&A, 338, 1066, 1066

Tinney, C. G., Mould, J. R., & Reid, I. N. 1993, AJ, 105, 1045, 1045

Tinney, C. G., Reid, I. N., Gizis, J., & Mould, J. R. 1995, AJ, 110, 3014, 3014

Tokunaga, A. T., Simons, D. A., & Vacca, W. D. 2002, PASP, 114, 180, 180

Toomre, A. 1964, ApJ, 139, 1217, 1217

Torres, C. A. O., Quast, G. R., Melo, C. H. F., & Sterzik, M. F. 2008, Young Nearby Loose Associations, ed. B. Reipurth, 757

Tremblin, P., Amundsen, D. S., Chabrier, G., et al. 2016, ApJ, 817, L19, L19

Tsuji, T. 1995, in Astronomical Society of the Pacific Conference Series, Vol. 81, Laboratory and Astronomical High Resolution Spectra, ed. A. J. Sauval, R. Blomme, & N. Grevesse, 566

Tsuji, T., Ohnaka, K., & Aoki, W. 1996a, A&A, 305, L1, L1

Tsuji, T., Ohnaka, K., Aoki, W., & Nakajima, T. 1996b, A&A, 308, L29, L29

Vacca, W. D., Cushing, M. C., & Rayner, J. T. 2003, PASP, 115, 389, 389

van Altena, W. F., Lee, J. T., & Hoffleit, E. D. 1995,

van Biesbroeck, G. 1961, AJ, 66, 528, 528

van Dam, M. A., Bouchez, A. H., Le Mignant, D., et al. 2006, PASP, 118, 310, 310

van den Bos, W. H. 1927, , 3, 261, 261

van Leeuwen, F. 2007, A&A, 474, 653, 653

Verschueren, W., David, M., & Brown, A. G. A. 1996, in Astronomical Society of the Pacific Conference Series, Vol. 90, The Origins, Evolution, and Destinies of Binary Stars in Clusters, ed. E. F. Milone & J.-C. Mermilliod, 131

Vrba, F. J., Henden, A. A., Luginbuhl, C. B., et al. 2004, AJ, 127, 2948, 2948

Ward-Thompson, D. 2002, Science, 295, 76, 76

Wenger, M., Ochsenbein, F., Egret, D., et al. 2000, , 143, 9, 9

West, A. A., Hawley, S. L., Bochanski, J. J., et al. 2008, AJ, 135, 785, 785

West, A. A., Morgan, D. P., Bochanski, J. J., et al. 2011, AJ, 141, 97, 97

Whitworth, A., Bate, M. R., Nordlund, Å., Reipurth, B., & Zinnecker, H. 2007, Protostars and Planets V, 459, 459

Whitworth, A. P., & Zinnecker, H. 2004, A&A, 427, 299, 299

Williams, J. P., Blitz, L., & McKee, C. F. 2000, Protostars and Planets IV, 97, 97

Wilson, J. C., Kirkpatrick, J. D., Gizis, J. E., et al. 2001, AJ, 122, 1989, 1989

Wilson, J. C., Miller, N. A., Gizis, J. E., et al. 2003, in IAU Symposium, Vol. 211, Brown Dwarfs, ed. E. Martín, 197

Winters, J. G., Henry, T. J., Lurie, J. C., et al. 2015, AJ, 149, 5, 5

Witte, S., Helling, C., Barman, T., Heidrich, N., & Hauschildt, P. H. 2011, A&A, 529, A44, A44

Wizinowich, P. L., Le Mignant, D., Bouchez, A. H., et al. 2006, PASP, 118, 297, 297

Wright, E. L., Eisenhardt, P. R. M., Mainzer, A. K., et al. 2010, AJ, 140, 1868, 1868

York, D. G., Adelman, J., Anderson, Jr., J. E., et al. 2000, AJ, 120, 1579, 1579

Zacharias, N., Finch, C. T., Girard, T. M., et al. 2012, VizieR Online Data Catalog, 1322

Zapatero Osorio, M. R., Béjar, V. J. S., Martín, E. L., et al. 2000, Science, 290, 103, 103

Zhang, Z. H., Homeier, D., Pinfield, D. J., et al. 2017, MNRAS, 468, 261, 261

Zhang, Z. H., Pokorny, R. S., Jones, H. R. A., et al. 2009, A&A, 497, 619, 619

Zhang, Z. H., Pinfield, D. J., Day-Jones, A. C., et al. 2010, MNRAS, 404, 1817, 1817

Zinnecker, H. 1984, , 99, 41, 41

Zucker, S., & Mazeh, T. 2000, ApJ, 531, L67, L67

Zuckerman, B., Song, I., & Bessell, M. S. 2004, ApJ, 613, L65, L65